R-07-49

Hydrogeological conceptual model development and numerical modelling using CONNECTFLOW, Forsmark modelling stage 2.2

Sven Follin, SF GeoLogic AB

Per-Olof Johansson, Artesia Grundvattenkonsult AB

Lee Hartley, Peter Jackson, David Roberts
Serco TAS

Niko Marsic, Kemakta Konsult AB

December 2007

Svensk Kärnbränslehantering AB
Swedish Nuclear Fuel
and Waste Management Co
Box 250, SE-101 24 Stockholm
Tel +46 8 459 84 00

ISSN 1402-3091
SKB Rapport R-07-49
ID 1187021
Updated 2024-11

Hydrogeological conceptual model development and numerical modelling using CONNECTFLOW, Forsmark modelling stage 2.2

Sven Follin, SF GeoLogic AB

Per-Olof Johansson, Artesia Grundvattenkonsult AB

Lee Hartley, Peter Jackson, David Roberts
Serco TAS

Niko Marsic, Kemakta Konsult AB

December 2007

Keywords: Forsmark, Hydrogeology, Hydrochemistry, Modelling, Calibration.

This report concerns a study which was conducted for SKB. The conclusions and viewpoints presented in the report are those of the authors and do not necessarily coincide with those of the client.

Update notice

The original report, dated December 2007, was found to contain both factual and editorial errors which have been corrected in this updated version. The corrected factual errors are presented below.

Updated 2024-11

The original report, updated 2013-08, was found to contain editorial errors which have been corrected in this updated version.

Updated 2013-08

Location	Original text	Corrected text
Page 68, Table 3-7, column 3	Wrong data in table	Table updated with correct data
Page 68, Table 3-7, column 6, row 6	(–7.0, 1.2)	(–6.7, 1.2)
Page 227, Table F-1, column 3	Wrong data in table	Table updated with correct data
Page 227, Table F-1, column 4, row 2	(0.038, 2.75)	(0.038, 2.70)
Page 227, Table F-1, column 6, row 6	(–7.0, 1.2)	(–6.7, 1.2)
Page 228, Table F-2, column 3	Wrong data in table	Table updated with correct data
Page 228, Table F-3, column 3	Wrong data in table	Table updated with correct data

The updated tables show what was actually used in the groundwater flow modelling for SDM-Site Forsmark.

Abstract

Three versions of a site descriptive model (SDM) have been completed for the Forsmark area. Version 0 established the state of knowledge prior to the start of the site investigation programme. Version 1.1 was essentially a training exercise and was completed during 2004. Version 1.2 was a preliminary site description and concluded the initial site investigation work (ISI) in June 2005. Three modelling stages are planned for the complete site investigation work (CSI). These are labelled stage 2.1, 2.2 and 2.3, respectively. An important component of each of these stages is to address and continuously try to resolve discipline-specific uncertainties of importance for repository engineering and safety assessment. Stage 2.1 included an updated geological model for Forsmark and aimed to provide a feedback from the modelling working group to the site investigation team to enable completion of the site investigation work. The present work refers to stage 2.2 and describes the conceptual understanding and the numerical modelling of the bedrock hydrogeology in the Forsmark area based on data freeze 2.2. The final data freeze in Forsmark, data freeze 2.3, will be reported in stage 2.3.

Data freeze 2.2 is the major data freeze of the site investigations in the Forsmark area and constitutes the basis for the hydrogeological description to be presented in the site descriptive model for Forsmark. It contains single-hole hydraulic test data from 21 core-drilled and 32 percussion-drilled boreholes in the bedrock, and from 58 monitoring wells (stand-pipes) drilled in the regolith (mainly Quaternary deposits). Furthermore, it contains cross-hole (interference) test data from observation wells as far as c. 2 km away from the pumped wells, which is a significant improvement compared to database available for modelling in version 1.2. In comparison, data freeze 2.3 will be considerably smaller than data freeze 2.2 but it will contain several important single-hole and cross-hole tests as a means to test the hypotheses developed in stage 2.2. The numerical modelling planned for stage 2.3 will address the sensitivity of the stage 2.2 groundwater flow and solute transport model to parameter heterogeneity.

Another significant improvement of the hydrogeological database in stage 2.2, relative to version 1.2, concerns the hydrogeological and hydrochemical monitoring data, i.e. groundwater levels, surface water levels, surface water runoff measurements and hydrochemistry of these waters. These measurements allow for a more elaborated analysis and discussion of potential recharge and discharge areas, hence a better assessment of the top boundary conditions to be used in the numerical modelling. The monitoring data provide a possibility for an improved integration between bedrock hydrogeology, surface hydrology/near-surface hydrogeology and hydrochemistry.

The addition of pore water hydrochemistry data from fresh, in-situ rock samples is an example of a vital improvement of the premises for the palaeohydrological modelling. For instance the pore water hydrochemistry allows for a more elaborated analysis and discussion of the initial hydrochemical conditions at the suggested start of the palaeohydrological modelling (8000 BC), as well as the role of rock matrix diffusion. Thus, pore water hydrochemistry data provide a better integration between bedrock hydrogeology, bedrock hydrochemistry and bedrock transport property modelling.

The numerical simulations carried out demonstrate that the conceptual model developed from the interpretation of Forsmark data in stage 2.2 can be used to predict a wide range of different types of data such as 1) large-scale cross-hole tests, 2) natural point-water heads in the bedrock and in the Quaternary deposits, and 3) hydrochemical profiles along the many cored boreholes drilled in close proximity to the so-called target volume. It is noted that a primary idea in stage 2.2 is that the same groundwater flow and solute transport model is used for each type of simulation to make it transparent that a single implementation of the conceptual model could be calibrated against all three types of field observations, although it may have been possible to improve the modelling of a particular data type by refining the model around a relevant observation borehole, for example.

In the process of calibrating the numerical model to cross-hole tests, natural point-water head measurements and hydrochemistry samples, a number of lessons were learnt in terms of the key features, processes and parameters required to mimic the observed behaviour of the hydrogeological system. Sensitivities to various features and parameters had to be considered to find one or more ways to honour the field data. This prompted relatively few changes to the initial implementation of the conceptual model within the reasonable ranges of uncertainty on parameters. Among the lessons learnt we note in particular:

- **HCD model:** The description of the hydraulic properties and the depth dependency of deformation zones developed in the conceptual model appear to give simulation results consistent with the hydraulic and hydrochemistry measurements, although it is important to condition individual zones where data is available to the single-hole test data.
- **HRD model:** Using the Hydro-DFN fracture set orientation model derived from data freeze 2.2 rather than the model derived based on data freeze 1.2, improved the calibration of the flow and solute transport model, primarily by defining fractures in the sub-horizontal set to be more sub-parallel, which reduced the vertical connectivity and hence increased the hydraulic anisotropy. Further mechanisms for hydraulic anisotropy such as a lower transmissivity in the sub-vertical sets may also make the simulations correspond better to the observations, although this hypothesis was not tested here.
- **HSD model:** The hydraulic properties of the simplistic HSD model used to represent the complex geometry and stratification of the regolith model suggested for stage 2.2 required considerable calibrations of the hydraulic properties to find consistency with the hydraulic interference test and point-water head measurements. The introduction of anisotropy (lower vertical hydraulic conductivity) in the Quaternary deposits being the key step.
- **Solute transport model:** Changes to the initial ECPM bedrock transport parameters were necessary for the solute transport modelling of salt including (*i*) increasing the kinematic porosity about one order of magnitude from the initial empirical relationship used to relate fracture transport aperture to transmissivity, and (*ii*) increasing the flow wetted fracture surface area per unit volume of rock compared to the frequency of water bearing fractures measured by the PFL-f technique.
- **Initial conditions:** The Alternative Case hydrochemical initial condition suggested in the work reported here assumes a persistence of an interglacial groundwater composition over the Holocene. This hypothesis gave better predictions for both fracture and pore water samples than the Base Case hydrochemical initial condition used in version 1.2. The Alternative Case requires further consideration since it has implications for the description of the long term stability of hydrochemical conditions over glacial cycles.
- **Boundary conditions:** The simulations imply poor hydraulic contacts between the surface and upper bedrock within the target area, which raise questions about the locations of possible discharge areas. The role of topography is likely to be less important due to geological structures, and hence hydraulic gradients in major deformation zones need to be considered as well as their contact to the sea.

In conclusion, the implementation of the hydrogeological conceptual model in a numerical model has been used to demonstrate its consistency with a wide range of field observations, and hence build confidence in its applicability to the Forsmark area. The calibration process has helped narrow uncertainties on some parameters and helped our understanding of the character of the hydrogeological system in the Forsmark area. It is emphasised that the results obtained from stage 2.2 represent a single realisation. Uncertainties relating to spatial variability in the geometrical and/or hydraulic properties will be quantified in stage 2.3, e.g. sensitivity studies to spatial heterogeneity with deformation zones, and multiple Hydro-DFN realisations.

A vital characteristic of the Forsmark area is the hydrogeological conditions in the uppermost part of the bedrock. Besides outcropping deformation zones and a high frequency of single fractures in the near-surface rock masses between the zones, the percussion drilling and hydraulic testing have also identified a system of large, transmissive sub-horizontal fractures, which are interpreted to be sheet joints formed through stress release. Sheet joints commonly have their highest intensities near the bedrock surface and decrease rapidly with depth. Being related to the present surface, the sheet joints are recently-formed, especially compared with the ductile and brittle deformation zones and the discrete fracture networks in between the deformation zones.

Together, the three types of geological features (outcropping deformation zones, a high frequency of rock mass fractures and large, sub-horizontal sheet joints) form a dense network of structures. Hydraulic diffusivity data from interference tests indicate that this network is highly connected laterally, if heterogeneously, and locally very transmissive. The network is presumably confined to within 150 m of the surface and largely parallels the undulations of the topography (horizontal anisotropy). It is noteworthy that the groundwater levels in the regolith are found to be higher than the groundwater levels in the uppermost part of the bedrock below the regolith.

Hydraulic data suggest that the transmissive network of structures in the uppermost part of the bedrock may have a finite lateral extent. In the work reported here it is given the form of a triangle bounded to the northeast by the Singö deformation zone, (WNW0001), to the southeast by the NE0062A deformation zone, and to the west by the expression of the sheath fold structure in rock domains 32 and 44. This hypothesis will be tested hydraulically in stage 2.3 by means of an interference test conducted at percussion-drilled borehole HFM33 located on the SFR peninsula.

The significant hydraulic diffusivity and horizontal anisotropy of the uppermost part of the bedrock reduce the hydraulic gradients across the deeper bedrock flow system in the target area below c. 150 m depth. In a way, the near-surface flow system acts like a "hydraulic cage phenomenon", though unlike a true hydraulic cage, the shallow network of transmissive structures only covers one side of the deeper bedrock flow system. It does not eliminate the hydraulic gradients entirely. Hence, a more appropriate hydrogeological analogue of the hydraulic short circuit phenomenon observed in the uppermost part of the bedrock is a shallow, anisotropic, bedrock "aquifer" on top of thicker segment of bedrock with "aquitard" type properties. Despite the risk of misconception, we used the term "hydraulic cage phenomenon" in the work reported here to emphasise the significant hydraulic diffusivity and anisotropy associated with the near-surface network of geological structures.

Since the sheet joints are not mapped to a very large detail in the site investigations, they are difficult to implement with a high degree of certainty due to uncertainties in their spatial extent and hydraulic heterogeneity. However, the chosen numerical approach to model the sheet joints in terms of three deterministic, hydraulically heterogeneous so-called "cage features", along with the interpreted deformation zones, communicates hydraulic disturbances across large distances in the numerical model that by and large are consistent with the field observations observed in the upper parts of the bedrock.

Finally, it is vital to note that the sheet joints do not exclude flow at repository depth. The simulations carried out with different model domains (version 1.2) suggest that the recharge area of the deeper flow system largely coincides with the topographic heights located in between the candidate area and the Forsmark deformation zone. The crest of these heights forms a regional water divide that clearly affects the runoff pattern of northern Uppland.

Sammanfattning

Tre versioner av den platsbeskrivande modellen för Forsmark har färdigställts. Version 0 beskrev kunskapsläget innan platsundersökningarna påbörjades. Version 1.1, som var en övningsversion, färdigställdes år 2004 och version 1.2 färdigställdes i juni år 2005. Version 1.2 utgör den preliminära platsbeskrivningen för Forsmark och beskriver kunskapsläget efter det inledande platsundersökningsskedet. För det avslutande platsundersökningsskedet planeras tre s k modelleringssteg, vilka betecknas 2.1, 2.2 och 2.3. En viktig uppgift för arbetet inom var och ett av dessa steg är att tydligt redovisa kunskapsläget samt osäkerheter av betydelse för projektering och säkerhetsanalys

Steg 2.1 syftade till att ge feedback till genomförandet av de återstående platsundersökningarna och innehåller dessutom en uppdaterad geologisk modell över Forsmark. Steg 2.2 och 2.3 karaktäriseras av ett stort antal ämnesspecifika underlagsrapporter. Den föreliggande rapporten ingår i steg 2.2 och beskriver det hydrogeologiska kunskapsläget i Forsmark och den numeriska modellering som utförts baserat på datafrys 2.2. Kunskapsläget efter den slutliga datafrysen i Forsmark, datafrys 2.3, kommer att avrapporteras i en särskild rapport i steg 2.3.

Datafrys 2.2 är den största datafrysen från platsundersökningarna i Forsmark och utgör grunden för den hydrogeologiska beskrivningen i Forsmark platsmodell. Den innehåller data från hydrauliska enhålstester borrade i 21 kärnborrhål och 32 hammarborrhål i berggrunden, samt data från 58 observationsbrunnar borrade i det kvartära jordtäcket. Vidare innehåller datafrys 2.2 data från mellanhålstester (interferenstester) med observationsbrunnar upp till ett avstånd av ca 2 km från pumpbrunnarna. Data från mellanhålstesterna är ett väsentligt tillskott till beskrivningen av de hydrogeologiska förhållandena i Forsmarksområdet. Datafrys 2.3 kommer att innehålla kompletterande data från flera viktiga enhålstester och mellanhålstester, som planeras bli genomförda i syfte att testa de hypoteser som redovisas i steg 2.2. Den numeriska modelleringen som planeras för steg 2.3 kommer att beskriva känsligheten hos den grundvattenflödes- och transportmodell som redovisas i steg 2.2.

En annan betydande förbättring av den hydrogeologiska databasen, relativt version 1.2, är moniteringen av de hydrogeologiska förhållandena, dvs grundvattennivåer, ytvattennivåer, mätning av ytvattenavrinning och hydrokemi. Mätningarna medger en mer genomtänkt analys och diskussion av potentiella in- och utströmningsområden och följaktligen en bättre ansättning av topprandvillkor vid numerisk modellering. Moniteringsdata möjliggör även en bättre integrering mellan hydrogeologin i berggrunden och jordlagren, ythydrologin samt hydrokemin hos dessa.

Porvattenkemidata från nyupptagna borrkärnor är ett exempel på en vital förbättring av förutsättningarna för den palaeohydrogeologiska modelleringen. Porvattnets hydrokemi möjliggör en mer genomtänkt analys och diskussion av de initiala hydrokemiska förhållandena i berggrunden vid den föreslagna starttidpunkten för den palaeohydrogeologiska modelleringen (8000 BC). Kunskap om porvattnets hydrokemi möjliggör även en fördjupad analys av betydelsen av matrisdiffusion, vilket ger förutsättningar för en bättre integration mellan modelleringen av hydrogeologin i berggrunden, berggrundens hydrokemi samt transportegenskaper.

De genomförda numeriska simuleringarna visar att den konceptuella modellen som baserar sig på tolkningen av data från datafrys 2.2 kan användas för att prediktera olika datatyper som 1) storskaliga mellanhålstester, 2) naturliga grundvattennivåer i berggrunden och i det kvartära jordtäcket och 3) hydrokemiska profiler längs med ett stort antal kärnborrhål borrade i närheten av det potentiella förvarsområdet. Det konstateras att en grundläggande utgångspunkt i steg 2.2 är att samma grundvattenflödes- och transportmodell används för varje simulering. Det bör påpekas att en huvudtanke i steg 2.2 har varit att använda en och samma grundvattenflödes- och transportmodell för de olika simuleringarna, dvs skapa transparens och konsistens i modelleringen.

Kalibreringen av den numeriska modellen mot hydrauliska mellanhålstester, grundvattennivåmätningar och hydrokemisk provtagning gav insikt och kunskap om vilka egenskaper, processer och parametrar som har störst betydelse för att efterlikna det hydrogeologiska systemets observerade beteende. Känsligheten för olika parameterändringar studerades i syfte att finna ett eller flera sätt att kalibrera modellen mot fältdata. Detta föranledde relativt få ändringar av den initiala implementeringen av den konceptuella modellen, dvs de slutliga ändringarna låg inom rimliga gränser för vad som kan betraktas som parameterosäkerheter på grund av heterogeniteten hos fältdata. Bland gjorda erfarenheter konstateras ska särskilt nämnas:

- **HCD-modell:** Den generella konceptuella beskrivningen av deformationszonernas hydrauliska egenskaper, samt djupberoendet hos dessa, ger simuleringsresultat som är förenliga med de uppmätta hydrauliska och hydrokemiska data, men det är viktigt att betinga modelleringen av zonernas egenskaper där data finns tillgängligt från enhålstester.

- **HRD-modell:** Spricknätverksmodellen för datafrys 2.2 ger en bättre beskrivning av bergets hydrauliska egenskaper än den modell som baseras på datafrys 1.2. Den huvudsakliga skillnaden mellan de två modellerna ligger i en högre grad av parallellitet hos de subhorisontella sprickorna i steg 2.2. Detta reducerar den vertikala konnektiviteten och ger en större hydraulisk anisotropi. En antagen lägre transmissivitet hos de subvertikala sprickorna kan eventuellt ge en ännu högre överensstämmelse med mätta data men denna hypotes har inte prövats i det arbete som redovisas här.

- **HSD-modell:** Modelleringen av de hydrauliska egenskaperna hos det kvartära jordtäcket krävde en betydande kalibrering för att uppnå överensstämmelse mellan uppmätta och simulerade responser vid interferenstesterna. En nyckelfaktor var införandet av hydraulisk anisotropi i jordlagren, vilket gav en lägre vertikal hydraulisk konduktivitet, dvs lägre läckage från jordlager och ytvattendrag till berget.

- **Transportmodell:** De initialt ansatta transportegenskaperna ECPM-formuleringen i CONNECTFLOW ändrades på två punkter: (*i*) en ökning av flödesporositeten med ca en tiopotens från det initiala värdet, som grundas på det empiriska samband som vanligtvis används för att relatera sprickvidd till transmissivitet, och (*ii*) en ökning av den flödesvätta ytan per enhetsvolym berg relativt frekvensen av vattenförande sprickor som uppmätts med PFL-f metoden. Värdet på den flödesvätta ytan per enhetsvolym berg varierar i detta arbete mellan 0,15–0,6 m^2/m^3 beroende på sprickdomän och djup.

- **Initialvillkor:** Det alternativ till hydrokemiskt initialvillkor som föreslås i detta arbete innebär att grundvattnet i sprickor och porer i berggrunden på ett par hundra meters djup bär spår av tidigare interglacialer/-stadialer. Hypotesen gav bättre prediktioner för både spricks- och porvatten än för det hydrokemiska initialvillkor som användes i version 1.2. Hypotesen är av intresse för beskrivningen av långtidsstabiliteten av de hydrokemiska förhållandena över glacialcyklerna.

- **Randvillkor:** Fältdata indikerar dålig hydraulisk kontakt mellan grundvattnet i jordlagren och grundvattnet i berg, vilket ger upphov till frågor angående läget för möjliga utströmningsområden. Troligen spelar topografin mindre roll än de geologiska strukturerna, vilket medför att hydrauliska gradienter i större deformationszoner måste beaktas liksom zonernas kontakt med havet.

Sammanfattningsvis konstateras att den framtagna numersika modellen kan efterlikna en rad olika fältobservationer, vilket stärker den konceptuella modellens trovärdighet. Utförda kalibreringar har reducerat en del osäkerheter vad gäller valet av parametervärden där data saknas. Det betonas att vi i detta arbete endast arbetat med en enskild realisering och att osäkerheter som beror på rumsliga variationer i de geometriska och hydrauliska egenskaperna kommer att studeras närmare i steg 2.3.

En mycket viktig hydrogeologisk egenskap i Forsmark är att den ytnära berggrunden förutom utgående deformationszoner och en hög intensitet av enskilda sprickor i bergmassan mellan deformationszonerna även innehåller uthålliga, subhorisontella bankningsplan. Hydrauliska data från enhålstester och mellanhålstester visar att bankningsplanen är heterogena men att de lokalt kan vara mycket transmissiva med varaktigt höga flöden. De hydrotestade borrhålen indikerar att bankningsplanen är oregelbundet fördelade inom de översta ca 150 m av berggrunden. Den hydrauliska diffusiviteten hos den övre delen av berggrunden bedöms vara mycket stor med en påtaglig horisontell anisotropi. Vi har av denna anledning i denna rapport liknat grundvattenströmningen i den övre delen av berggrunden vid en ”hydraulisk bur”, dvs ett kortslutet hydrologiskt system. Det är viktigt att notera att eftersom kortslutningen bara gäller strömningen i ytberget är liknelsen vid en ”hydraulisk bur” i viss mån missvisande. En mer adekvat hydrogeologisk liknelse är möjligen ”en ytlig bergakvifer med anisotropa egenskaper ovanpå en tjockare bergmassa med akvitardliknande egenskaper”.

En av hypoteserna som presenteras i denna rapport är antagandet att bankningsplanen som påträffats inom det s k ”målområdet” är så pass uthålliga att de konnekterar detsamma med Singözonen. Denna hypotes kommer att prövas i steg 2.3 med hjälp av en mellanhålstest. Planen är att provpumpa hammarborrhål HFM33 ute vid SFR anläggningens ovanjordsdel.

Den numeriska modelleringen som redovisas här visar att förekomsten av ytnära flacka sprickor/bankningsplan och utgående djupa deformationszoner ger en hydraulisk påverkan över stora avstånd i den numeriska modellen. Detta är samstämmigt med de fältobservationer som gjorts i de övre delarna av berggrunden. Dock är de horisontella sprickorna/bankningsplanen svåra att modellerna i detalj på grund av osäkerheter i rumslig utbredning och hydraulisk heterogenitet.

Avslutningsvis noteras att såväl data som simuleringar visar att grundvattenflöde förekommer på förvarsnivå. Simuleringar med olika stora modelldomäner (version 1.2) indikerar att grundvattenbildningen för det djupare flödet genom målområdet sker huvudsakligen sker i höjdområdet mellan kandidatområdet och Forsmarkszonen. Höjdområdet utgör en regional vattendelare som tydligt påverkar avrinningen i de norra delarna av Uppland.

Contents

1 Introduction

1.1 Context

Three versions of a site descriptive model (SDM) have been completed for the Forsmark area. Version 0 /SKB 2002/ established the state of knowledge prior to the start of the site investigation programme. Version 1.1 was essentially a training exercise and was completed during 2004 /SKB 2004/. Version 1.2 was a preliminary site description and concluded the initial site investigation work (ISI) in June 2005 /SKB 2005a/. Three modelling stages are planned for the complete site investigation work (CSI). These are labelled stage 2.1, 2.2 and 2.3, respectively. An important component of each of these stages is to address and continuously try to resolve uncertainties of importance for repository engineering and safety assessment. Stage 2.1 /SKB 2006a/ included an updated geological model for Forsmark and aimed to provide a feedback from the modelling working group to the site investigation team to enable completion of the site investigation work. The present work refers to stage 2.2 and describes the conceptual understanding and the numerical modelling of the bedrock hydrogeology in the Forsmark area based on data freeze 2.2. The final data freeze in Forsmark, data freeze 2.3, will be reported in stage 2.3.

1.2 Overview of hydrogeological reports

The development of the bedrock hydrogeological model is closely related to the development of the bedrock geological model and the hydraulic investigations conducted in boreholes. Table 1-1 shows the cumulative number of boreholes providing hydraulic information about the bedrock in the Forsmark area in relation to the three versions (0, 1.1 and 1.2) and the three stages (2.1, 2.2 and 2.3) carried out during the period 2002–2007. It is noted that stage 2.2 is the major stage from a data acquisition and conceptual modelling point of view.

Table 1-1 also shows the reference numbers of all reports that contain hydrogeological information about the bedrock in the Forsmark area. For instance, the results from the initial site investigation (ISI) phase are summarised in the preliminary site descriptive model (SDM) report R-05-18 /SKB 2005a/. For the complete site investigation (CSI) phase the reporting is split between the 2.2 and 2.3 stages. The upcoming stage 2.3 report (referred to as R-08-23 /Follin et al. 2008/ in Table 1-1) plays the role of model verification. The basis for the stage 2.3 report are the findings reported in R-07-48 /Follin et al. 2007b/ and in the present report, i.e. R-07-49. R-07-48 presents the interpretation of single-hole hydraulic data, the assignment of hydraulic properties of the deformation zones, and the derivation of hydrogeological discrete fracture network models (Hydro-DFN) for the bedrock between the deformation zones. In the present report we implemented the hydraulic properties and models reported in R-07-48 into the CONNECTFLOW code and performed groundwater flow and solute transport simulations.

It is noted that the report referred to as R-07-20 /Follin et al. 2007a/ is not a model update report, but a preparatory modelling study presenting a procedure for the integration of different kinds of data in the groundwater flow and solute transport modelling as a means of approaching the issue of confirmatory testing during the complete site investigation (CSI) phase, i.e. stages 2.2 and 2.3. The methodology outlined in /Follin et al. 2007a/ is applied in the work reported here.

Table 1-1. The cumulative number of boreholes providing hydraulic information about the bedrock in the Forsmark candidate area at the end of each of the three versions and three stages carried out during the period 2002–2007. KFM = core-drilled boreholes, HFM = percussion-drilled boreholes. The reports with reference numbers typed in italics describe the hydraulic data gathered and the hydrogeological modelling undertaken. The reports with underlined reference numbers summarise the development of the hydrogeological model in general terms along with the developments achieved within the other disciplines.

Existing data	Initial site investigation (ISI)		Strategy	Complete site investigation (CSI)	
Version 0	**Version 1.1**	**Version 1.2**	**Stage 2.1**	**Stage 2.2**	**Stage 2.3**
0 KFM (0%)	1 KFM (4%)	5 KFM (21%)	9 KFM (38%)	20 KFM (83%)	24 KFM (100%)
0 HFM (0%)	8 HFM (21%)	19 HFM (50%)	22 HFM (58%)	32 HFM (84%)	38 HFM (100%)
R-02-32	R-04-15	R-05-18	R-06-38	*R-07-48*	*R-08-23*
		R-05-32	*R-07-20*	*R-07-49*	
		R-05-60			

1.3 Background

As part of the preliminary SDM for the initial site investigation phase at Forsmark, Simpevarp and Laxemar, a methodology was developed for constructing hydrogeological models of the crystalline bedrock. The methodology combined a deterministic representation of the major deformation zones (DZ) with a stochastic representation of the less fractured bedrock outside these zones using a discrete fracture network (DFN) concept.

The deformation zone and discrete fracture network models were parameterised hydraulically with data from single-hole difference flow logging pumping tests and single-hole double-packer injection tests, see /Follin et al. 2005/ and /Hartley et al. 2005/. The hydrogeological descriptions of the major deformation zones and the less fractured bedrock outside these zones were referred to as Hydraulic Conductor Domains (HCD) and Hydraulic Rock Domains (HRD), respectively, cf. /Rhén et al. 2003/.

The division into HCD and HRD formed the basis for constructing regional-scale equivalent continuous porous medium (ECPM) flow models, which were used to simulate the palaeo-hydrogeological-hydrochemical evolution over the last 10,000 years (Holocene), as a coupled process between groundwater flow and the hydrodynamic transport of several so called reference waters including the process of rock-matrix diffusion. Results obtained from these simulations included a prediction of hydrochemical constituents (e.g. major ions and environmental isotopes) for the present-day situation along boreholes which could be compared with corresponding groundwater samples acquired from the sites. By comparing the model predictions with measurements, the models developed could be partially calibrated to improve model parameterisation, improve our understanding of the hydrogeological system, and help build confidence in the conceptual models developed for the sites.

The methodology achieved reasonable success given the restricted amounts and types of data available at the time. Notwithstanding, several issues of concern surfaced following the reviews of the preliminary site descriptions of the three sites conducted internally by SKB's modelling teams, by SKB's external review group (SIERG) and by SKI's and SSI's international review groups (INSITE and OVERSITE). Moreover, the safety implications of the preliminary site descriptions were assessed in the Preliminary Safety Evaluations (PSE) and in SR-Can. The issues raised both internally and externally, as well as the feedback obtained from the safety assessment work, are essentially in agreement and are briefly summarised in /Follin et al. 2007a/.

For the complete site investigation phase, new types of hydrogeological data are available and in greater amounts, and hence the issues of concern require satisfactory resolution as the site investigation work moves towards completion. In particular, the use of the integrated geological, hydrogeological, hydrochemical and solute transport models has identified the need for more robust 'partially validated' models, consistent between disciplines, which are to be produced by the final stage of the site descriptive modelling.

Possible solutions to parts of the problems have been discussed and an integrated view and strategy forward has been formulated, see Figure 1-1. The "updated strategy" is not an entire shift in methodology, however, but a refocusing on and clarification of the key aspects of the hydrogeological SDM, i.e.:

- assess the current understanding of the hydrogeology at the analysed area, and
- provide the hydrogeological input descriptions needed by the end users, Repository Design, Safety Assessment and Environmental Impact Assessment. The input descriptions should especially focus on properties in the potential repository volumes of the explored sites and assess the distribution of flow paths at potential repository depth.

/Follin et al. 2007a/ suggested a procedure for integrating different kinds of data in the groundwater flow and solute transport modelling, see Figure 1-2, as a means of approaching the issue of confirmatory testing (Step 4 in Figure 1-1). For its demonstration /Follin et al. 2007a/ used the HCD and HRD models derived in version 1.2 and the hydrogeological and hydrochemical data from data freeze 2.1. Hence, the modelling study by /Follin et al. 2007a/ was not aimed at a model update, but a preparatory modelling study intended to provide some insight into new aspects of the suggested procedure and the use of field data (e.g. interference tests and groundwater levels), and therefore provide background support for the work reported here.

The general approach applied in the numerical modelling was to first parameterise the deformation zones and fracture domains hydraulically using fracture and inflow data from individual boreholes (Task A in Figure 1-2). Second, the confirmatory step relies on using essentially the same groundwater flow and solute transport model in terms of grid discretisation and parameter settings for matching three types of independent field data (Tasks B–D). Using the three types of data, a unified conceptual description of the groundwater system has been atttempted.

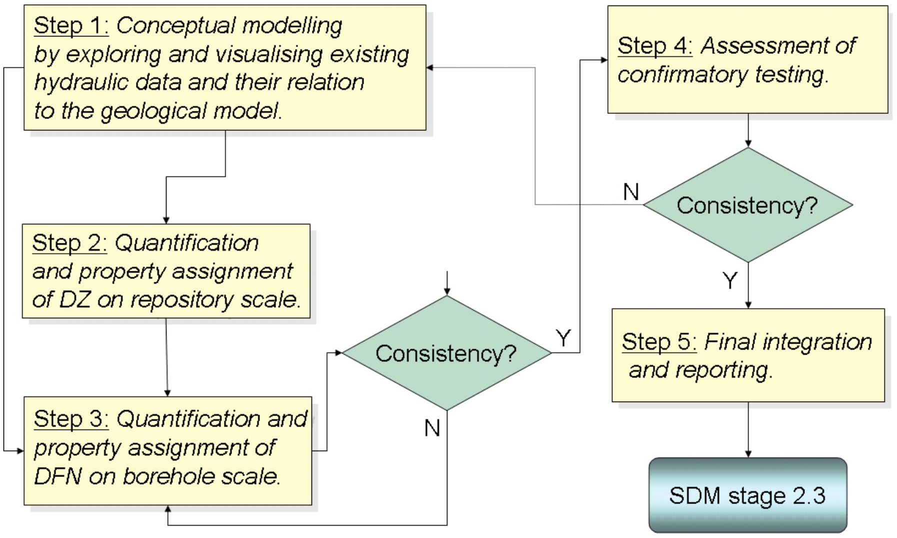

Figure 1-1. Flow chart of the five steps suggested for the hydrogeological modelling of the complete site investigation (CSI) phase. Reproduced from /Follin et al. 2007b/.

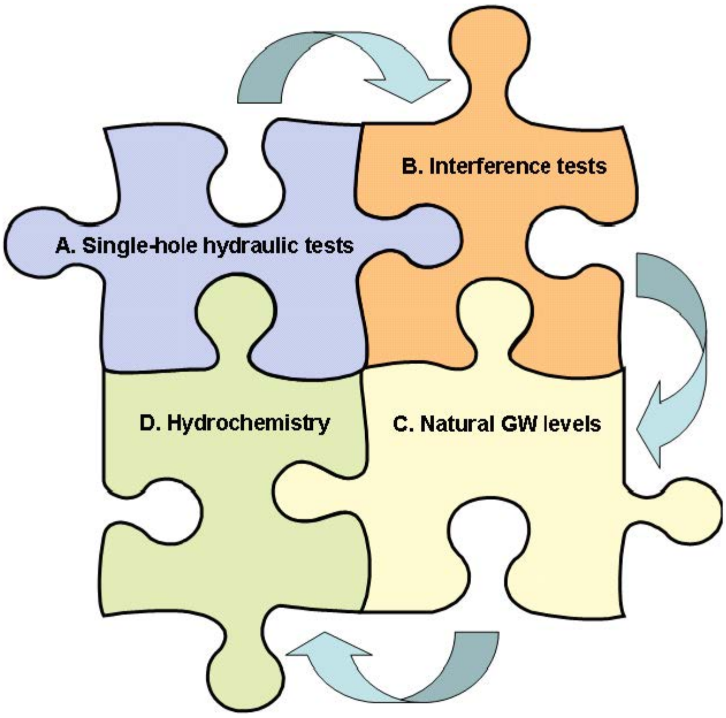

Figure 1-2. *Four kinds of data are used in the numerical modelling a means of approaching the issue of confirmatory testing, cf. Step 4 in Figure 1-1: A) Hydraulic properties of deformation zones and discrete fracture networks as deduced from single-hole hydraulic tests; B) Interference tests; C) Natural groundwater levels[1]; D) Hydrochemistry. The data sets used as calibration targets (B–D) are presented in Section 4. Reproduced from /Follin et al. 2007b/.*

1.4 Scope and objectives

The primary objectives of the work reported here are:

- to assess and illustrate the hydrogeological conceptual understanding of the Forsmark area, in particular the target volume and its boundaries, and
- to build a numerical groundwater flow and solute transport model and test its representation against different types of data as a means of approaching Step 4 in Figure 1-1.

Numerical modelling is necessary in order to gain credibility for the SDM in general and the site hydrogeological description in particular. This is important since the numerical model is to serve as a basis for describing the present hydrogeological conditions as well as for forthcoming predictions of future hydrogeological conditions and transport pathways. Equally important is the need to illustrate the role of field data in reducing uncertainty.

A major effort of the work reported here concerns the practical implementation of the hydrogeological conceptual model in CONNECTFLOW. We simulate the confirmatory testing tasks B–D in Figure 1-2 by means of a single realisation. Uncertainties caused by spatial variability in the geometrical and/or hydraulic properties will be quantified in stage 2.3 in terms of multiple realisations.

---

[1] The salinity of groundwater in the Forsmark area varies in space. The groundwater levels in Forsmark are point-water heads. In order to interpret the measurements in terms of recharge and discharge it is necessary to convert the data to environmental-water heads. The transformation from point-water head to environmental-water head is explained in Appendix K.

1.5 Structure of this report

The work is divided into three main parts:

Part 1 presents a summary of the hydrogeological conceptual model development in the Forsmark area and how the conceptual model is implemented in the CONNECTFLOW code /Hartley and Holton 2004, Hartley et al. 2004ab, Hoch and Jackson 2004/. Part 1 is completely covered by Sections 2–3.

Part 2 describes the numerical modelling of groundwater flow and solute transport modelling carried out with the CONNECTFLOW code. The data used for model calibration represent data freeze 2.2 is described in Section 4. Part 2 is wholly covered by Sections 5–7.

Part 3, finally, consists of twelve appendices. Appendix A describes how the transport of solutes in the Forsmark area, which gives rise to variations in salinity and hence variable-density flow, is coupled to groundwater flow in CONNECTFLOW. Appendix B describes the location of boreholes and the type of investigations carried out. Remaining Appendices, C–L, describe particular hydrogeological issues discussed in the report in greater detail.

The contents of the different sections is summarised below as:

- Section 2 presents SKB's systems approach to hydrogeological modelling in the SDM.
- Section 3 presents a summary of the hydrogeological conceptual model of the Forsmark area and how this conceptual model is implemented in CONNECTFLOW in stage 2.2. (For the sake of a simplified reading the implementation of the conceptual model in the CONNECTFLOW code is described alongside with the description of the conceptual model. In this way the additional assumptions and simplifications made in the numerical model can be readily noted.)
- Section 4 presents the data sets used for model calibration.
- Section 5 treats the parameterisation of HCD and HRD and groundwater flow calibration.
- Section 6 treats solute transport calibration.
- Section 7 demonstrates the behaviour of the calibrated numerical model in terms of solute transport and particle tracking simulations. The discussion of the simulations focuses on the pattern of recharge and discharge within the so-called target area in Forsmark.
- Section 8 presents the conclusions drawn with regard to the primary objectives of the work.

2 Hydrogeological modelling in the SDM

2.1 Hydraulic domains

The three-dimensional, large-scale numerical flow models considered by the Swedish Nuclear Fuel and Waste Management Company (SKB) for the geological disposal of spent nuclear fuel in low-temperature, fractured crystalline rock simulate the shore level displacement in the Fennoscandian Shield during the Holocene i.e., between 8000 BC and 2000 AD. The models include descriptions of the geometry of discrete geological features (fractures and deformation zones), transient hydrological and chemical boundary conditions, strong spatial heterogeneity in the hydraulic properties, density driven flow, advective transport and rock matrix diffusion of different water types (solutes). It has been suggested that an understanding of the evolution throughout geological time is a powerful tool to predict the future development of groundwater flow and its chemical composition, see e.g. /NEA-OECD 1993, Bath and Lalieux 1999/. Testing and developing tools for coupled hydrogeological-hydrochemical modelling over time was also the focus of an international project referred to as *Task 5*, which was based on multidisciplinary data from the Äspö Hard Rock Laboratory in Sweden /Laaksoharju and Wallin 1997, Wikberg 1998, Rhén and Smellie 2003/.

Figure 2-1 illustrates schematically the division of the groundwater system into hydraulic domains as used in the hydrogeological SDM for Forsmark and Laxemar. The groundwater system consists of three hydraulic domains, HSD, HCD and HRD, where:

- HSD represents the regolith,
- HCD represents deformation zones, and
- HRD represents the fractured rock masses between the deformations zones.

The division into hydraulic domains constitute the basis for the conceptual modelling, the planning of the site investigations and the numerical simulations carried out in support of the SDM. How the modelling is structured is described in Section 3.2.

It is noted that the groundwater flow and solute transport modelling is split between the surface systems modelling group and the bedrock hydrogeology modelling group due to both practical and historical reasons (large amounts of data, different objectives, etc). For instance, the surface systems modelling group describes, among other things, the hydrologic cycle on a diurnal basis, i.e. the different components in the water mass balance equation including precipitation, evapotranspiration, surface runoff, unsaturated flow in the regolith and groundwater flow in the regolith and the upper 150 m of the bedrock. The bedrock hydrogeology modelling group,

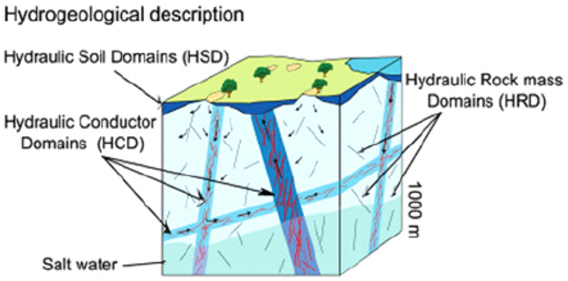

Figure 2-1. *Cartoon showing the division of the crystalline bedrock and the regolith above it (Quaternary deposits mainly) into three hydraulic domains. Reproduced from /Rhén et al. 2003/.*

on the other hand, describes the deeper parts of hydrologic cycle with an emphasis on (i) structural-hydraulic pathways-properties in the deformation zones and the bedrock in between, and (ii) the transport of variable-density solutes in the fracture system and the bedrock matrix over long time periods (thousands of years). The discrete analysis of open fractures vis-à-vis flowing fractures at repository depth is an example of key assignment for the bedrock hydrogeology modelling group. Figure 2-2 shows a cartoon of how the modelling of the hydrologic cycle is split between the two modelling groups. The surface-based modelling is carried out with the MIKE SHE code /DHI 2004/ and the bedrock-based modelling is carried out with the CONNECTFLOW code /Hartley and Holton 2004, Hartley et al. 2004ab, Hoch and Jackson 2004/.

The integration of the different works carried out by the two modelling groups is essential to the hydrological-hydrogeological description in general and to the description of the recharge-discharge conditions in particular. Embryos to the updated strategy for integrated numerical modelling outlined in /Follin et al. 2007a/ are found in /Follin et al. 2005, Hartley et al. 2005, Werner et al. 2006, Bosson and Berglund 2006, Werner et al. 2007/. The recharge-discharge conditions in the Forsmark area are discussed and analysed analytically in several reports, see in particular /Tröjbom et al. 2007/ and /Johansson 2008/. The present report and the works by /Bosson et al. 2008/ and /Follin et al. 2008/ deal with recharge and discharge in terms of numerical models.

2.2 Evaluation of single-hole hydraulic tests

A cornerstone of the bedrock hydrogeological description concerns the hydraulic characterisation of the more intensely fractured deformation zones and the less fractured bedrock in between. The approach taken by SKB combines a deterministic representation of the major deformation zones (DZ) with a stochastic representation of the less fractured bedrock in between using a discrete fracture network (DFN) concept /Munier 2004, Follin et al. 2007b/. The deformation zones and fracture domains are parameterised hydraulically with data from single-hole Posiva Flow Log (PFL) pumping tests and single-hole Pipe String System (PSS) injection tests.

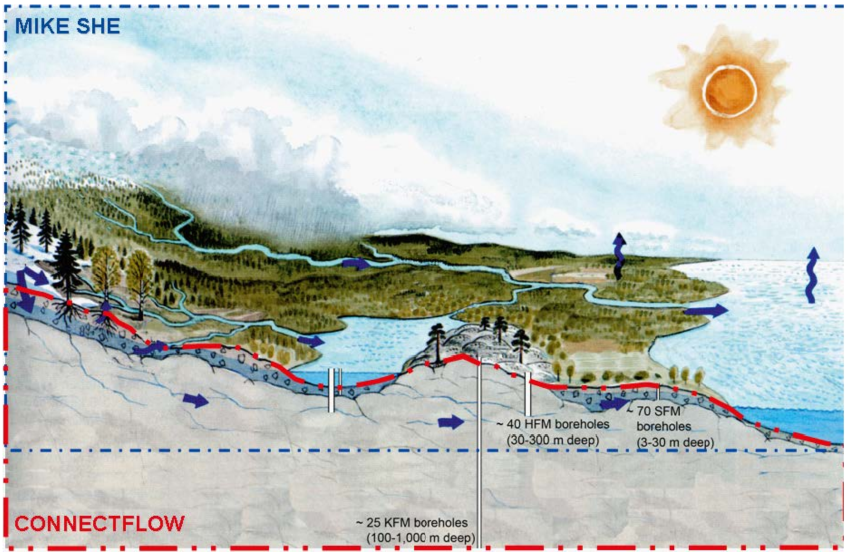

Figure 2-2. *Cartoon showing how the modelling of the hydrologic cycle is divided into a surface-based system and a bedrock-based system. The former is modelled with the MIKE SHE code and the latter with the CONNECTFLOW code.*

The hydraulic characterisation of the less fractured bedrock between the deformation zones at repository depth is a vital part of the bedrock hydrogeological description. The modelling is based on data from investigations in cored boreholes drilled from the surface, and the current understanding of the groundwater system at depth is bound to be constrained by this fact. With regard to the advantages and disadvantages of the two different methods used for hydraulic borehole investigations in Forsmark, PFL and PSS, the hydraulic characterisation of less fractured bedrock between the deformation zones may be envisaged as illustrated in Figure 2-3. The constituent parameters measured where the fractures intersects the borehole are the flow rate Q and the pressure difference Δp. Since these are coupled, the studied parameter is the specific capacity $Q/\Delta p$.

The advantages and disadvantages of the two test methods, PFL and PSS, are described in /Follin et al. 2007b/. From a site descriptive modelling point of view, it is noted that the modelling approach taken by SKB focuses on the conductive fracture frequency (CFF) gathered by the so-called PFL-f method, which identifies individual flowing features with a resolution of 0.1 m. This decision means, among other things, that fracture network situations such as A–C are not analysed in stage 2.2[2]. Ignoring situations like A–C does not mean that they are unimportant, however. On the contrary, the role of compartmentalised fracture systems is well recognised by the hydrogeological modelling group and a procedure for its handling in the open repository modelling carried out in the forthcoming safety assessment project SR-Site has been suggested. However, situations such as D–F are regarded as more important for the groundwater flow modelling addressed in the SDM, see /Follin et al. 2007c/.

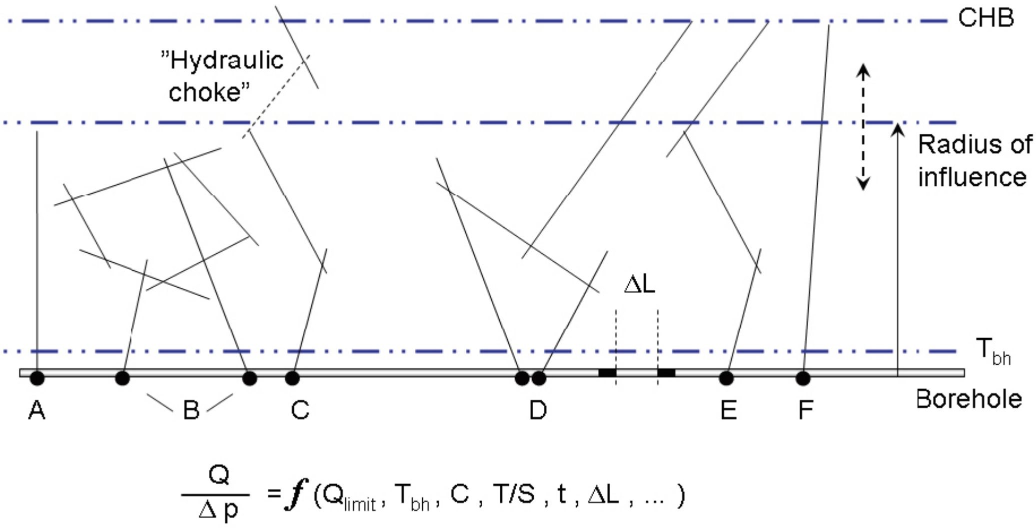

Figure 2-3. Cartoon showing a borehole with six different symbolic fracture network situations, cases A–F. The specific discharge $Q/\Delta p$ measured at the boreholes is dependent on several factors, e.g. the measurement limit Q_{limit} of the test method, the transmissivity of the fracture intersecting the borehole T_{bh}, the fracture connectivity C, the hydraulic diffusivity T/S of the fracture network, the test time t, the length of the test section ΔL, etc. The hydraulic characterisation of the fracture system varies depending on the method used as well as on the in-situ conditions, e.g. the occurrence of "hydraulic chokes". Cases A–C represent isolated fracture networks and cases D–F represent fracture networks connected to the overall hydrogeological system. The latter is here indicated by a "constant head boundary" (CHB) suggesting a steady-state flow at long test times. The cartoon is rotated 90° to improve the readability. Modified after /Follin et al. 2007b/.

---

[2] The reason why the PFL method cannot address situations like A–C in Figure 2-3, in contrast to the PSS method, is explained in /Follin et al. 2007b/. There it is also explained why the PSS method has problems in distinguishing situations A–C from situations D–F.

2.3 The tectonic continuum approach

Figure 2-4 illustrates the structural-hydraulic approach used to separate single fractures from deformation zones in the hydrogeological work for Forsmark. A tectonic continuum is envisaged where the data at depth intersecting the boreholes are combined with lineaments or deformation zones. The approach used in /Follin et al. 2007b/ is fairly similar to the tectonic continuum modelling discussed in /Fox et al. 2007/. In the SDM, features up to L = 1,000 m ($r \approx$ 564 m) are regarded as uncertain and treated stochastically using the DFN concept.

The parameterisation of the deformation zones is based on all transmissivity data between the upper and lower bounds of a deformation zone interval, as determined in the single-hole geological interpretation are considered. That is, the transmissivity data from consecutive tests are summed up to form a single transmissivity value for that interval, see Figure 2-4. This implies that the hydraulic thickness is initially assumed to be equal to the geological. The hydraulic heterogeneity of a deformation zone is assessed by means of single-hole transmissivity determinations measured at different locations.

2.4 Equivalent continuous porous medium (ECPM)

The numerical modelling of groundwater flow and solute (salt) transport in the SDM is carried out with the equivalent continuous porous medium (ECPM) approach, see Figure 2-5. Since each ECPM model is based on a particular underlying stochastic realisation, the ECPM models are also stochastic. Uncertainties relating to spatial variability in the geometrical and/or hydraulic properties will be quantified in stage 2.3 by means of multiple realisations.

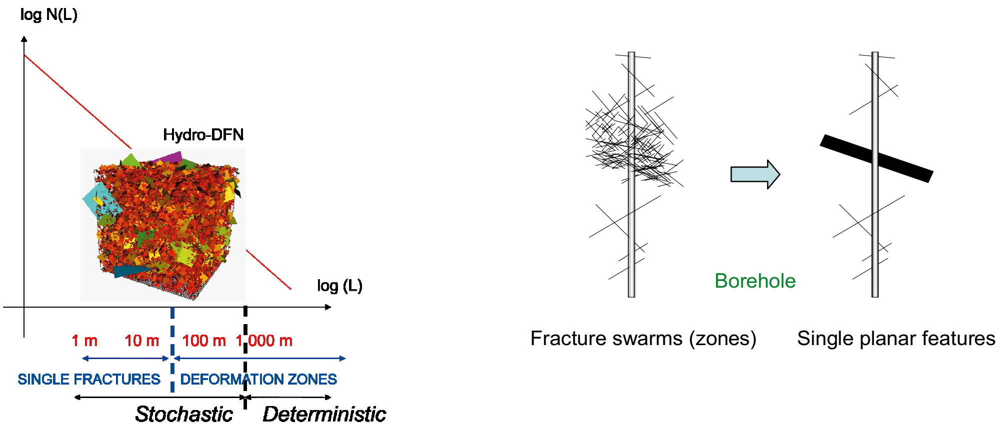

Figure 2-4. *Cartoons showing the structural-hydraulic approach used for the treatment of single fractures and deformation zones (certain, as well as possible) in the hydrogeological SDM. Left: A tectonic continuum is envisaged in the hydrogeological modelling where the number of features of different sizes follows a power-law relationship. All features up to L = 1,000 m (r ≈ 564 m) are regarded as uncertain and treated stochastically using the DFN concept. Right: The fracture data gathered between the upper and lower bounds of a deformation zone interval are lumped together to form a single planar feature. In the same fashion, all hydraulic data in the interval are also lumped together, to form a single transmissivity value.Reproduced from /Follin et al. 2007b/.*

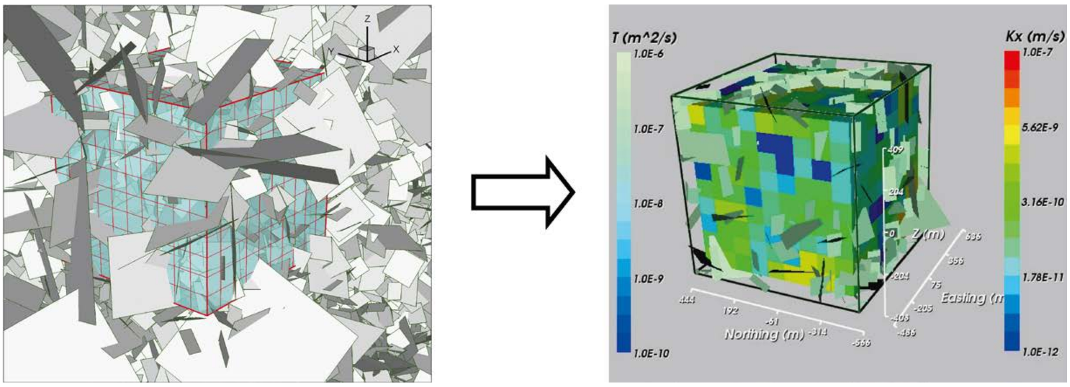

Figure 2-5. *Illustrations showing the ECPM approach in CONNECTFLOW. The geometrical and hydraulic properties of planar discrete features (left) are transformed into a 3D equivalent continuous porous medium (right).*

2.5 Additional assumptions and simplifications in the numerical modelling using CONNECTFLOW

Key assumptions and simplifications made in the numerical groundwater flow and solute transport modelling reported here are summarised below as:

- The deformation zone models provided by the geological modelling group represent hydraulically active features. However, based on hydraulic interpretation of /Follin et al. 2007b/ some zones, or parts of zones, have very low transmissivities of around 10^{-10} m^2/s at depth.
- The transmissivity of each deformation zone varies linearly with depth, but is here assumed to be uniform horizontally. The linear variation is transformed into step-wise 100 m thick intervals of constant values.
- The kinematic porosity of HCD correlates with transmissivity.
- Fracture geometric and flow statistics are defined for each fracture domain, but may vary with depth.
- Flow and transport within the network of fractures can be represented by an ECPM on an appropriate grid. Grid elements are of length 20 m around the candidate area and 100 m on the regional scale.
- Properties in the HRD outside the fracture domains modelled in the work reported here are treated as homogeneous bulk continuum porous medium (CPM) properties due to a lack of fracture data outside the candidate area. Some hydraulic data are available from Finnsjön /Andersson et al. 1991/ that are used as an indication of the general properties.
- The hydraulic properties of the Quaternary deposits are homogeneous within each layer, and the hydraulic properties of layers of different soil types can be represented by equivalent hydraulic conductivities in the horizontal and vertical directions, respectively.
- The top surface flow boundary condition can be specified as an average flux over an appropriate time scale. For the long term palaeohydrological simulations, the flux is based on the average annual precipitation minus evapotranspiration (specific discharge). For the short term interference test simulations, the flux is based on the detailed precipitation minus evapotranspiration during the duration of the test. In both cases, the flux is reduced or allowed to be negative (i.e. discharge) where the calculated head is at or above the surface.
- Initial and boundary hydrochemical conditions for the palaeohydrological simulations (Task D in Figure 1-2) are best conceptualised in terms of reference water types with the water at any point being a mixture of each of the reference waters defined in terms of mass fractions.

- The chemical composition of the reference waters is derived by a principal component analysis using the Multivariate Mixing and Mass-balance (M3) analysis /Laaksoharju et al. 1999/. This is used to make straightforward conversion between mass fractions, concentrations of individual ions, and/or stable isotopes, and fluid density.
- The reference water mass fractions are transported as conservative entities by advection and dispersion with groundwater flow within the fracture system. Diffusion into the inter-fracture matrix pore water is included, i.e. rock matrix diffusion (RMD), but there is no advection within the pore water.
- The palaeohydrological simulations are calibrated primarily against borehole measurements of Cl, Br/Cl, and $\delta^{18}O$, which are considered to be conservative tracers. Mg and HCO_3 are considered as secondary indicators. Measured groundwater samples vary in their integrity as representative indicators of natural conditions according to the level of contamination by drilling mud and charge balance. Those samples with a low contamination and charge balance are given more credence as quantitative calibration targets, but since such samples are quite sparse, the available supplementary measurements of less credence are used as a more qualitative guide of the hydrochemical conditions.
- Pore water measurements of Cl and $\delta^{18}O$ are also considered as calibration targets. In the simulations, the model of RMD calculates a spatial profile of solute concentrations within each idealised matrix volume, which could vary considerably from the surface of the fracture to the centre of the matrix volume. However, for simplicity the average concentration with the matrix volume is compared with the measured pore water concentration irrespective of how far the core sample may have been from a water-bearing fracture.
- The palaeohydrological simulations were started at 8000 BC and the evolution of the hydrochemistry was calculated according to the changes in sea level and salinity. The initial conditions model assumed in version 1.2 /Follin et al. 2005, Hartley et al. 2005/ was here replaced by an alternative initial conditions model. The latter model is here referred to as the Alternative Case model and the initial condition assumed in version 1.2 as the Base Case model.

3 Conceptual model development and implementation in CONNECTFLOW

3.1 Introduction

A key characteristic of the hydrogeological description of the bedrock in the Forsmark area is the notion of interdisciplinary correlations between, on one side, structural and geophysical data observed on outcrops and in boreholes, and, on the other, hydrogeological and hydrochemical data gathered in boreholes, lakes and brooks. This correlation is assumed to be reinforced by the observed anisotropy in the current stress field in the bedrock, although it may be difficult to delineate in explicit terms due to scale differences between different types of data. In short, the reasons for strong interdisciplinary correlations in the Forsmark area can in a broad context be explained by two important processes:

- the more than 1.85 billion years old tectonic evolution of the Forsmark area, which has formed characteristic patterns of deformation zones of different orientations and character,
- the shore level displacement of the Fennoscandian Shield during the Holocene and the associated changes of the sea water salinity in the Baltic basin.

A significant improvement of the hydrogeological description of the Forsmark area during stage 2.2 concerns the incorporation of hydrogeological and hydrochemical monitoring data, i.e. groundwater levels, surface water levels, surface water runoff measurements and hydrochemistry. These measurements allow for a more elaborated analysis and discussion of potential recharge and discharge areas, hence a better assignment of the top boundary conditions and integration between bedrock hydrogeology and surface hydrology/near-surface hydrogeology. The hydrogeological monitoring data represent both natural (undisturbed) conditions and conditions sampled under stress, e.g. hydraulic interference tests.

The incorporation of pore water hydrochemistry from fresh rock samples is another vital improvement of the palaeohydrological modelling during stage 2.2. The pore water hydrochemistry allows for a more elaborated analysis and discussion of the initial hydrochemical conditions at the start of the palaeohydrological modelling 8000 BC, hence a better integration between bedrock hydrogeology and bedrock hydrochemistry.

We present below excerpts from the disciplinary specific descriptions presented in /Stephens et al. 2007, Follin et al. 2007b/ and /Laaksoharju et al. 2008/. The excerpts focus on those aspects that are important for the objectives of this report; i.e.:

- to assess and illustrate the conceptual hydrogeological understanding of the Forsmark area, in particular the target volume and its boundaries, and
- to build a numerical groundwater flow and solute transport model and test its functionality against different types of data as a means of approaching Step 4 in Figure 1-1.

3.2 Model structure and organisation

The numerical model consists of six elements:

- Hydraulic Conductor Domain model – representing interpreted deformation zones.
- Hydraulic Rock mass Domain model – representing the bedrock between the zones.
- Hydraulic Soil Domain model – representing the regolith (Quaternary deposits).

- Solute transport model for the modelling of matrix diffusion.
- Initial conditions for groundwater flow and hydrochemistry.
- Boundary conditions for groundwater flow and hydrochemistry.

The six elements are based on altogether 13 different submodels, see Table 3-1. The shaded fields below the submodels show the key field/laboratory data used to conceptualise and parameterise the model elements. The bottommost row (text in *italics*) lists the key modelling groups in terms of integration. Some of the submodels are multidisciplinary (shared by two or more modelling groups) and some of the submodels are essential to more than one model element. The hydrogeological modelling group is in charge of how the six elements are parameterised and used in the groundwater flow and solute (salt) transport modelling. In particular, it is responsible for the development of the Hydraulic Conductor Domain and the Hydraulic Rock mass Domain models. We provide here a detailed description of the 13 submodels and how they merged in the numerical model. This means that a fully integrated modelling approach was attempted in stage 2.2.

Table 3-1. The top row shows the six elements of the hydrogeological model in the SDM-Site project for Forsmark. The six model elements consist of altogether 13 different submodels. The shaded fields below the submodels show the key field/laboratory data used to conceptualise and parameterise the six model elements. The bottommost row (text in *italics*) lists the key modelling groups in terms of conceptual/quantitative integration.

HCD, Hydraulic conductor domain model	**HRD, Hydraulic rock mass domain model**	**HSD, Hydraulic soil domain model**	**Solute transport model**	**Initial conditions**	**Boundary conditions**
2. Deformation zone model	1. Rock domain model	8. Regolith model	7. Hydro-DFN model	10. Palaeo-hydrological model	3. Digital elevation model
5. Bedrock hydrogeological model	4. Fracture domain model	3. Digital elevation model	13. Bedrock transport properties model		11. Shore level displacement model
	5. Bedrock hydrogeological model	9. Quaternary deposits hydrogeological model			12. Baltic Sea salinity model
	6. Geo-DFN model				
	7. Hydro-DFN model				
Single-hole hydraulic tests (PSS and PFL)	Single-hole hydraulic tests (PFL)	Slug-tests BAT tests	Single-hole hydraulic tests (PFL)	Hydrochemical database	Hydrochemical database
Borehole core description	Borehole fracture data		Dilution tests SWIW tests Tracer tests Laboratory tests		Hydrological monitoring data
Geology	*Geology*	*Geology* *Surface systems*	*Bedrock transport properties*	*Surface systems* *Hydrogeochemistry*	*Surface systems* *Hydrogeochemistry*

3.3 The Forsmark area

The Forsmark area is located in northern Uppland within the municipality of Östhammar, about 120 km north of Stockholm. The candidate area is located along the shoreline of Öregrundsgrepen and it extends from the Forsmark nuclear power plant and the access road to the SFR in the northwest to Kallrigafjärden in the southeast (Figure 3-1). The bedrock was formed between 1,890 and 1,850 million years ago and it has been affected by both ductile and brittle deformation. The ductile deformation has resulted in large-scale ductile high-strain zones and the brittle deformation has given rise to large-scale fracture zones. Tectonic lenses, in which the bedrock is much less affected by ductile deformation, are enclosed between the ductile high-strain zones. The candidate area is located in the north-westernmost part of one of these tectonic lenses that extends from north-west of the nuclear power plant south-eastwards to Öregrund (Figure 3-1).

3.4 Model volumes

3.4.1 Regional and local model volumes

The site descriptive modelling is performed using two different scales of model volume, a regional model volume and a local model volume. Generally, the local model is required to cover the volume within which the repository is expected to be placed, including accesses and the immediate environs. In addition to the description on the local scale, a description is also devised for a much larger volume, the regional model, in order to place the local model in a larger context and to allow for a sensitivity analysis of, mainly, hydrogeological boundary conditions.

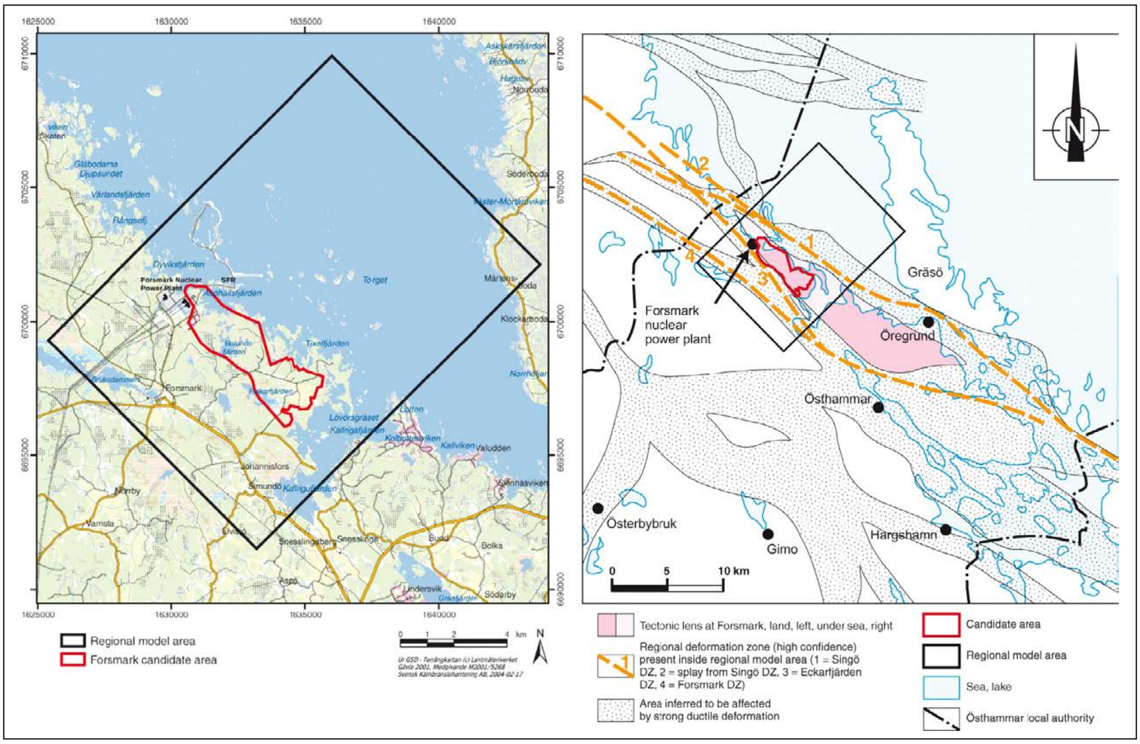

Figure 3-1. *Left: The Forsmark candidate area (red) and the regional model area (black). Right: The extension of the tectonic lens within which the candidate area at Forsmark is situated. Reproduced from /SKB 2006a/.*

In selecting the model volumes some rules of thumb, taken from the SKB strategy document for integrated evaluation /Andersson 2003/ have been applied. These rules also apply for stage 2.2. It needs also to be understood that the distinct model sizes primarily concern the development of the geological model in the SKB Rock Visualisation System, RVS. This is also the reason why the model areas and volumes have a rectangular shape. The motivation for the model areas shown in Figure 3-2 are found in /SKB 2006a/. It is noted that the north-western part of the candidate area has been selected as the target area for the Complete Site Investigation phase /SKB 2005b/. This is the main reason why the local model area since stage 2.1 is smaller than the local model area up to version 1.2.

The coordinates defining the regional model volume are (in metres):

RT90 (RAK) system; (Easting, Northing): (1625400, 6699300), (1636007, 6709907), (1643785, 6702129), (1633178, 6691522)

RHB 70; elevation: +100, –2,100

The coordinates defining the local model volume are (in metres):

RT90 (RAK) system; (Easting, Northing): (1629171, 6700562), (1631434, 6702824), (1634099, 6700159), (1631841, 6697892)

RHB 70; elevation: +100, –1,100

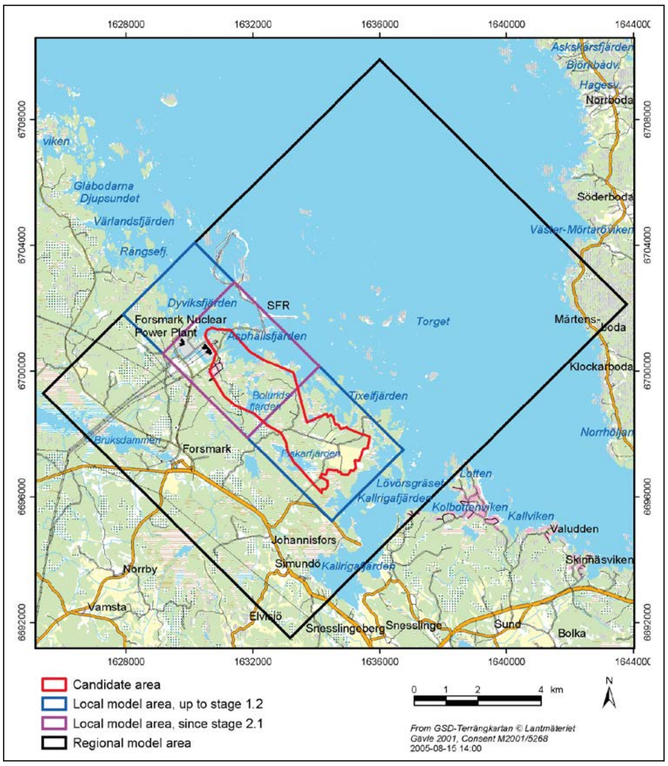

***Figure 3-2.** Regional (black) and local (purple) model area in stage 2.2. The regional model area is the same as in versions 0, 1.1 and 1.2 and 2.1. The local model area is smaller than in version 1.2 (blue line) and covers the north-western part of the candidate area selected as target area for a potential repository /SKB 2005b/. Reproduced from /SKB 2006a/.*

3.4.2 Repository target volume

The repository target volume refers to the bedrock volume within the local model used for detailed planning, design and modelling purposes. It is noted that the main objective of the site investigations carried out since version 1.2 has been to characterise the geological, rock mechanics, thermal, hydrogeological, hydrochemical and transport properties of the repository target volume. Figure 3-3 shows a map of the regional model area, the candidate area, the local model area and the target model area. The final layout is being developed on the basis of the site SDM, and the layout shown here is an older version referred to as layout D1 /SKB 2006a/. The elevation of repository for spent fuel is about –500 m RHB 70.

3.4.3 Hydrogeological model volume and investigations

Digital elevation model (DEM) and model area

Topographic data for stage 2.2 were supplied as a digital elevation model with a spatial resolution a 20 m scale in the horizontal. The digital elevation model is used both to define the model area and to set boundary conditions on the top surface.

In CONNECTFLOW it is possible to construct unstructured meshes with irregular boundaries, and hence it is possible to choose boundaries that follow significant surface water divides. The regional and local surface water divides in the Forsmark area were identified already in version 1.1 /SKB 2004/. Figure 3-4 shows the hydrogeological model area and the location of the upstream boundary with regard to the surface water divides used in this study. The sensitivity of the groundwater flow within the target volume with regard to the location of the upstream boundary was studied in version 1.2. The groundwater flow (GWF) model area and the location of the upstream boundary shown in Figure 3-4 are considered appropriate both for the SDM and the forthcoming SR-Site safety assessment /Follin et al. 2005/.

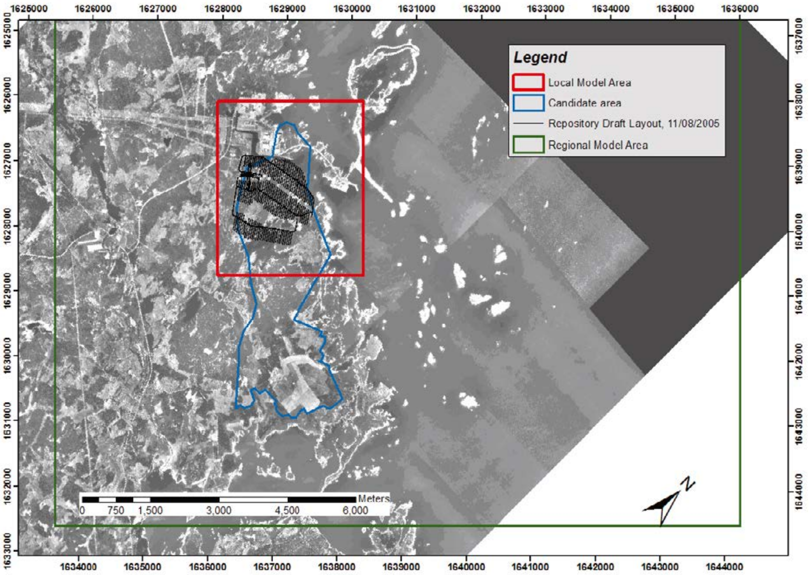

Figure 3-3. Map showing the regional model area (green), the candidate area (blue), the local model area (red) and a repository target area (black). However, the repository layout shown here is an older version, referred to as layout D1 /SKB 2006a/. An updated layout, D2, is being developed on the basis of the site SDM.

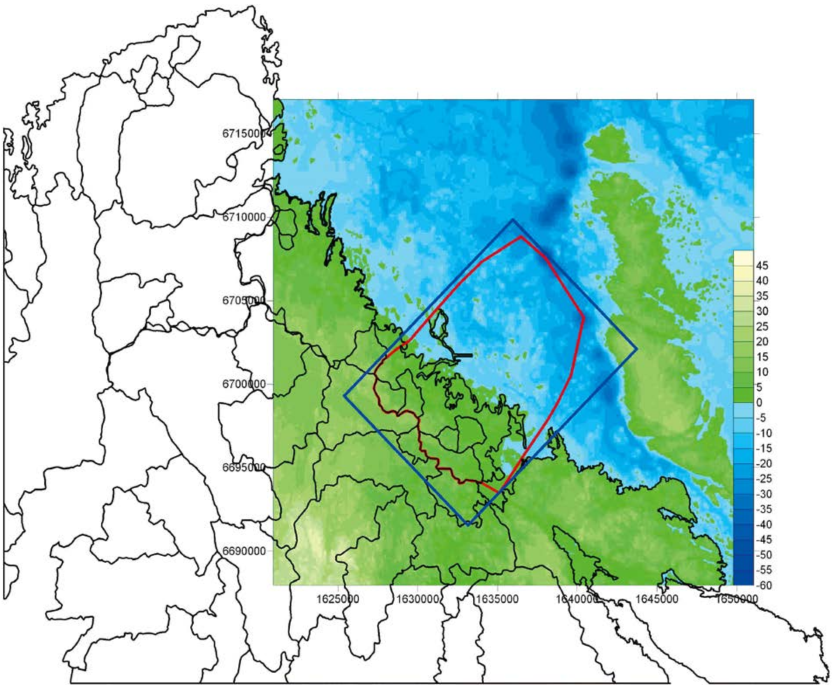

Figure 3-4. *Surface hydrology catchments used to define the hydrogeological model area (red lines). The regional model domain used for the structural model definition by the blue lines. (Geographic data ©Lantmäteriverket Gävle 2007. Consent I 2007/1092).*

Model thickness

The base of the hydrogeological model volume in version 1.2 was set to –2,100 m RHB 70. In stage 2.2, the elevation of the base of the hydrogeological model volume was changed to –1,200 m RHB 70. The major motive for this change is the significant depth dependency in the transmissivity of the deformation zones and the fracture domains below –400 m RHB 70, see /Follin et al. 2007b/. Flowing features below this depth are extremely rare and have a maximum transmissivity of less than 10^{-7} m^2/s. For FFM01, the mean hydraulic conductivity for all boreholes sections outside of deformation zones below –400 m RHB 70 drops to less than 10^{-10} m/s. Taking this into account together with the high salinities seen below about –700 m RHB 70, which is likely to form a lower boundary to flow, then it is unlikely that there are deep circulating flows of any significance.

Selection of grid resolution

CONNECTFLOW allows refined sub-domains to be embedded within a coarser grid with appropriate conditions at the interface to ensure conservation of fluxes and continuity of variables. The grid resolution in version 1.2 was 50 m for the candidate area and 100 m for the regional-scale. Limiting the area and the thickness of the hydrogeological model domain as described above made it tractable to use more refined grids within the candidate area. Since data on the topography and fracture domains was supplied on a 20 m scale, then this was chosen as an appropriate finite-element size around the candidate area to avoid the need to interpolate the data within this area. A less refined grid of either 60 m or 100 m was used for the wider regional scale. 60 m was used for the interference test and point-water head simulations, but 100 m was used for the more computationally intensive palaeohydrological simulations, requiring around 500 time-steps of coupled flow and transport calculations.

The refined sub-domain was chosen to be about 3 km by 3 km horizontally and 700 m deep. This extent was chosen so as to cover all of the core-drilled boreholes within the target volume (note that borehole KFM03A is outside the target volume), and the local scale deformation zones. Many local deformation zones have been identified in the mapping of the target volume, and hence a fine-scale grid is needed to represent the contrasts between the deformation zones and the background rock, and also many deformation zones are characterised as being only a few metres thick. Figure 3-5 shows the borehole locations and deformation zones that were considered in choosing an appropriate grid refinement.

A horizontal slice through the embedded grid around the target area is shown in Figure 3-6. As can be seen, the 20 m grid covers all core drilled boreholes apart from borehole KFM03A, which is outside the target area. Here, a 60 m grid is used for the coarser regional-scale. How the deformation zone transmissivities are mapped onto this grid is explained below Section 3.10.

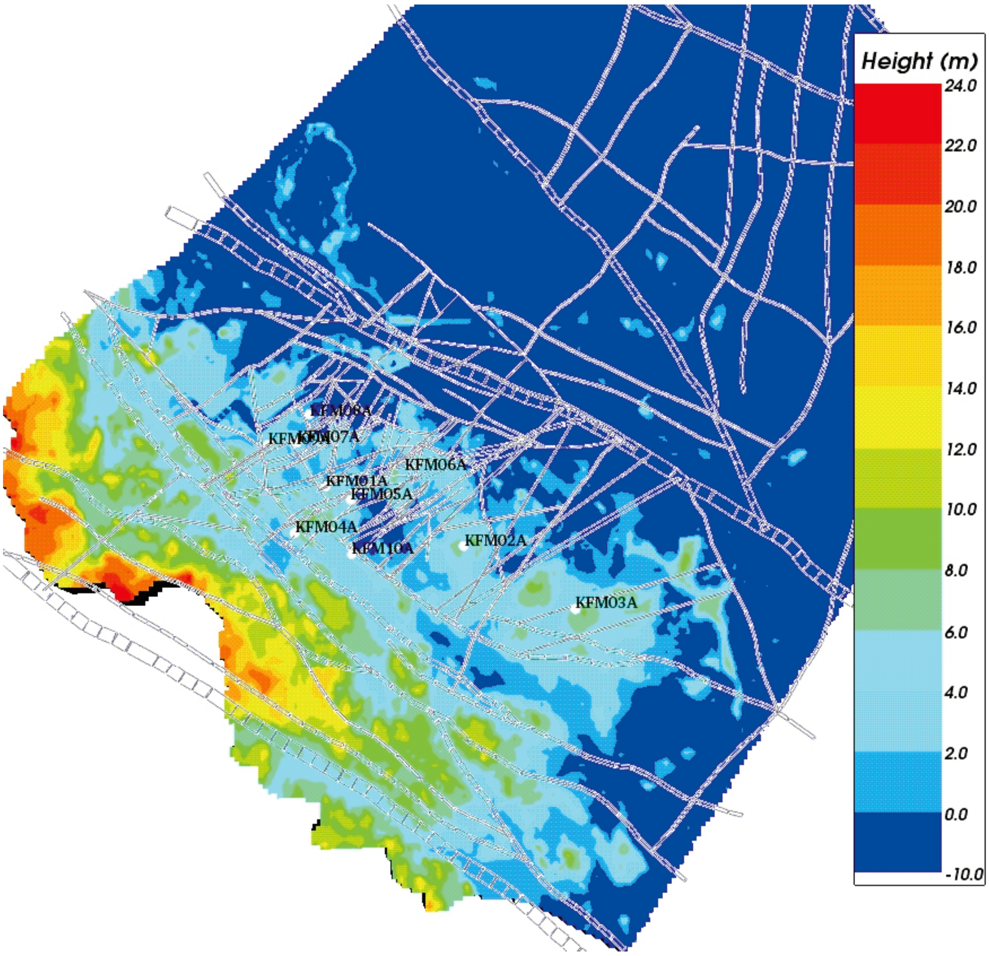

Figure 3-5. *A visualisation of the topography of the regional-scale hydrogeological model together with the core-drilled boreholes with calibration data and the features that were considered in selecting the grid resolution. The geometry of the deformation zones represents a horizontal slice through the deformation zone model at 0 m RHB 70.*

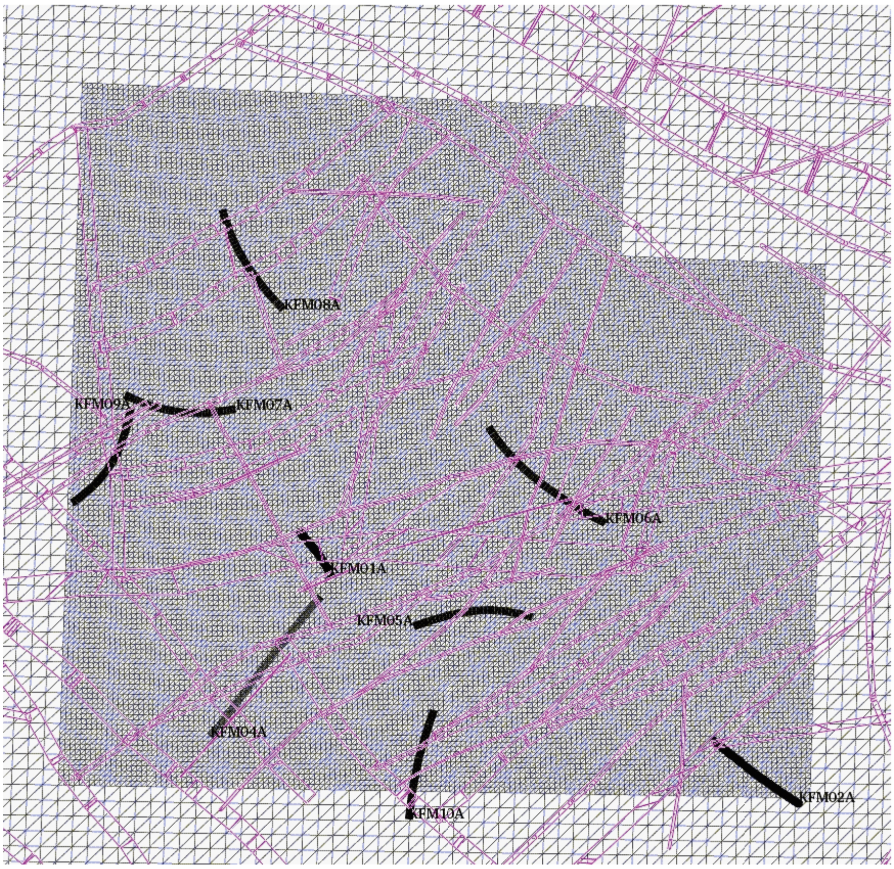

Figure 3-6. *Embedded refined finite-element grid around the target area with size 20 m square. Here, a 60 m grid was used on the regional-scale outside the target area. The elements have a square horizontal cross-section, but are visualised here as artificially split into 2 triangles. The positions of some of the boreholes drilled are shown in black. A horizontal slice through the deformation zone model at 0 m RHB 70 is superimposed and the intercepted zones are coloured purple.*

Investigations

The location of drill sites, boreholes and type of hydrogeological investigations carried out in the bedrock and in the Quaternary deposits within the model volume are described in Appendix B. The reading of this report is eased if Appendix B is read early on.

3.5 Rock domain model

The bedrock at Forsmark is divided into rock domains. A rock domain refers to a rock volume in which rock units that show similar composition, grain size, degree of bedrock homogeneity, and degree and style of ductile deformation have been combined and distinguished from each other. Rock volumes that show early-stage alteration (albitisation) are also distinguished as separate rock domains. The different rock domains at Forsmark are referred to as RFM in SKB’s 3D geometric modelling work and rock visualisation system (RVS). The dominant rock domains within the local model area are referred to as RFM029 and RFM045, see Figure 3-7. The extent in 3D of these two rock domains defines by and large the repository target volume for Forsmark in stage 2.2. The modelling of the rock domains shown in Figure 3-7 and their petrophysical properties, e.g. the porosity of fresh bedrock samples without visible fractures, are described in detail in /Stephens et al. 2007/.

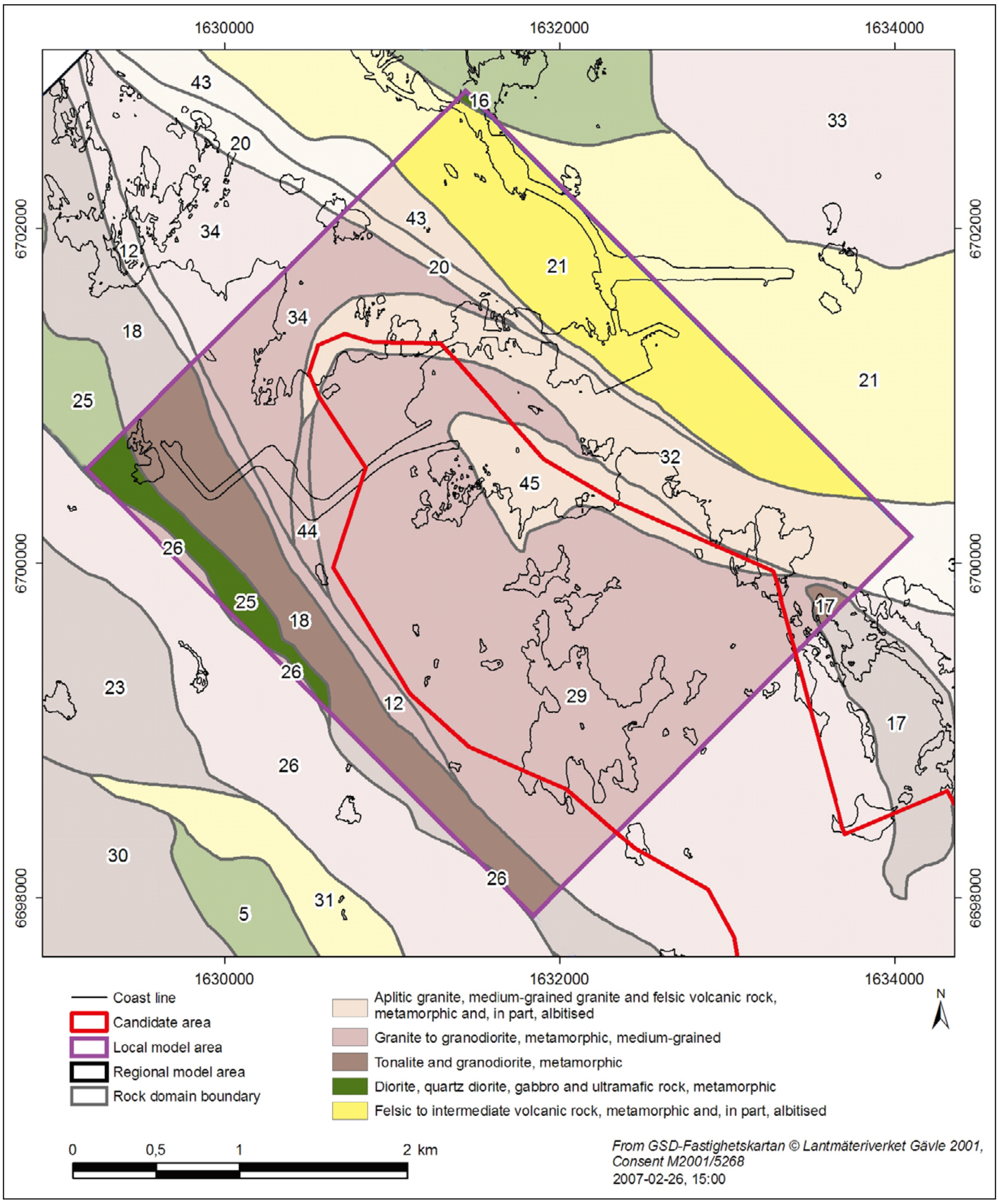

From GSD-Fastighetskartan © Lantmäteriverket Gävle 2001, Consent M2001/5268
2007-02-26, 15:00

Figure 3-7. *Horizontal slice at the surface for rock domains inside and immediately around the local model area in Forsmark. Reproduced from /Stephens et al. 2007/.*

3.6 Deformation zone model

The term deformation zone is used at all stages in the geological work, bedrock surface mapping, single-hole interpretation and 3D geometric modelling and visualisation. A deformation zone is a general term referring to an essentially 2D structure along which there is a concentration of brittle, ductile or combined brittle and ductile deformation. The term fracture zone is used to denote a brittle deformation zone without any specification whether there has or has not been a shear sense of movement along the zone. A fracture zone that shows a shear sense of movement is referred to as a fault zone. Table 3-2 presents the terminology for brittle structures based on trace length and thickness as presented in /Andersson et al. 2000/.

Table 3-2. Terminology and general description (length and width are approximate) of brittle structures /Andersson et al. 2000/.

Terminology	Length	Width	Geometrical description
Regional deformation zone	> 10 km	> 100 m	Deterministic
Local major deformation zone	1–10 km	5–100 m	Deterministic (with scale-dependent description of uncertainty)
Local minor deformation zone	10 m–1 km	0.1–5 m	Statistical (if possible, deterministic)
Fracture	< 10 m	< 0.1 m	Statistical

The borderlines between the different structures are approximate. The so called 3D DZ block model for Forsmark stage 2.2 described in /Stephens et al. 2007/ contains 103 deterministically modelled deformation zones. These are referred to as ZFM. All but 11 of the 103 deformation zones have trace lengths longer than one kilometre, which implies that the 3D DZ block model, in principle, consists of regional or local major deformation zones, cf. Table 3-2. The 11 deformation zones with trace lengths shorter than one kilometre are either a part (splay) of a nearby deformation zone longer than one kilometre, or gently dipping.

In addition to the 103 deterministically modelled deformation zones, /Stephens et al. 2007/ describe 28 minor deformation zones deterministically, i.e. deformation zones with trace lengths shorter than one kilometre. These are also referred to as ZFM, but *not* part of the 3D DZ block model. Finally, /Stephens et al. 2007/ discuss 43 so called "possible deformation zones". These are probably shorter than one kilometre, hence judged to be minor deformation zones, and modelled stochastically.

Conceptually, the 28 minor deformation zones are no different than the possible deformation zones not modelled deterministically. Despite the conceptual inconsistency created, it was decided by the hydrogeological modelling group to incorporate the 28 deterministically modelled minor deformation zones in the deformation zone model. The motive for this decision is purely pragmatic; that is, it is better to use the geometrical data available and model them as hydraulically heterogeneous than having them modelled as large, random features with homogeneous hydraulic properties. Hence, the final deformation zone model for the hydrogeological SDM contains 131 deterministically modelled deformation zones. It was decided by the hydrogeological modelling group to leave the stochastic discrete fracture network (DFN) model unaffected by this decision.

Figure 3-8 shows a 3D visualisation of the 131 deformation zones modelled deterministically in the hydrogeological SDM for Forsmark stage 2.2. The steeply-dipping deformation zones (107) are shaded in different colours and labelled with regard to their principle direction of strike. The gently-dipping zones (24) are shaded in pale grey and denoted by a G. The inset shows the direction of the main principal stress, cf. /Stephens et al. 2007/. All of the 28 minor deformation zones modelled deterministically by /Stephens et al. 2007/, but not included in the 3D DZ block model, occur inside the local model domain, see Figure 3-9. The local model domain encompasses the target volume defined in stage 2.1 /SKB 2006a/, hence investigated to a greater extent than the regional model domain. The bottom of the local model ends at elevation –1,100 m, which means that it matches fairly well the maximum penetration depths of the deepest cored boreholes.

Table 3-3 shows a summary of the information presented above. We note in particular:

- 39 (28+11) deformation zones have trace lengths shorter than one kilometre and 45 deformation zones have trace lengths longer than three kilometres.

- 31 of the 103 deformation zones contained by the 3D deformation zone model occur inside the local model domain solely, 43 major deformation zones occur outside the local model domain solely and 29 major deformation zones occur both inside and outside. All of the 28 minor deformation zones modelled deterministically in the hydrogeological SDM are steeply dipping and occur inside the local model domain.
- There are 43 possible deformation zones identified in the geological single-hole interpretation but not modelled deterministically for Forsmark in stage 2.2; 34 of these intersect cored boreholes and nine the percussion-drilled holes.

The 43 possible deformation zones not modelled deterministically were reported as borehole intervals with "deformation zone type properties". Their orientations may be tentatively estimated from the fracture poles. However, there are no other strands of evidence to support a more deterministic interpretation, such as, e.g., magnetic lineaments or seismic reflectors. The lack of constraining deterministic information implies that they should be treated stochastically, i.e. as discrete fracture network (DFN) features.

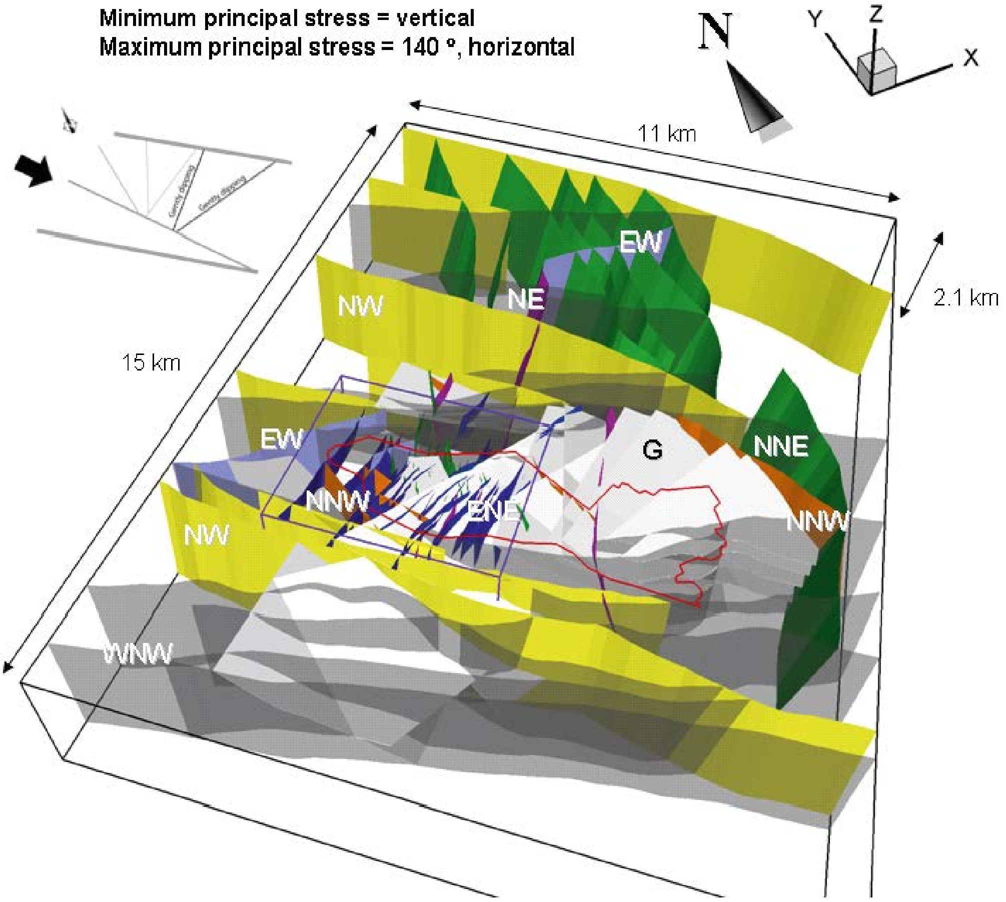

Figure 3-8. *3D visualisation of the regional model domain and the 131 deformation zones modelled deterministically for Forsmark stage 2.2 /Stephens et al. 2007/. The steeply-dipping deformation zones (107) are shaded in different colours and labelled with regard to their principle direction of strike. The gently-dipping zones (24) are shaded in pale grey and denoted by a G. The border of the candidate area is shown in red and regional and local model domains in black and purple, respectively. The inset in the upper left corner of the figure shows the direction of the main principal stress. Reproduced from /Follin et al. 2007b/.*

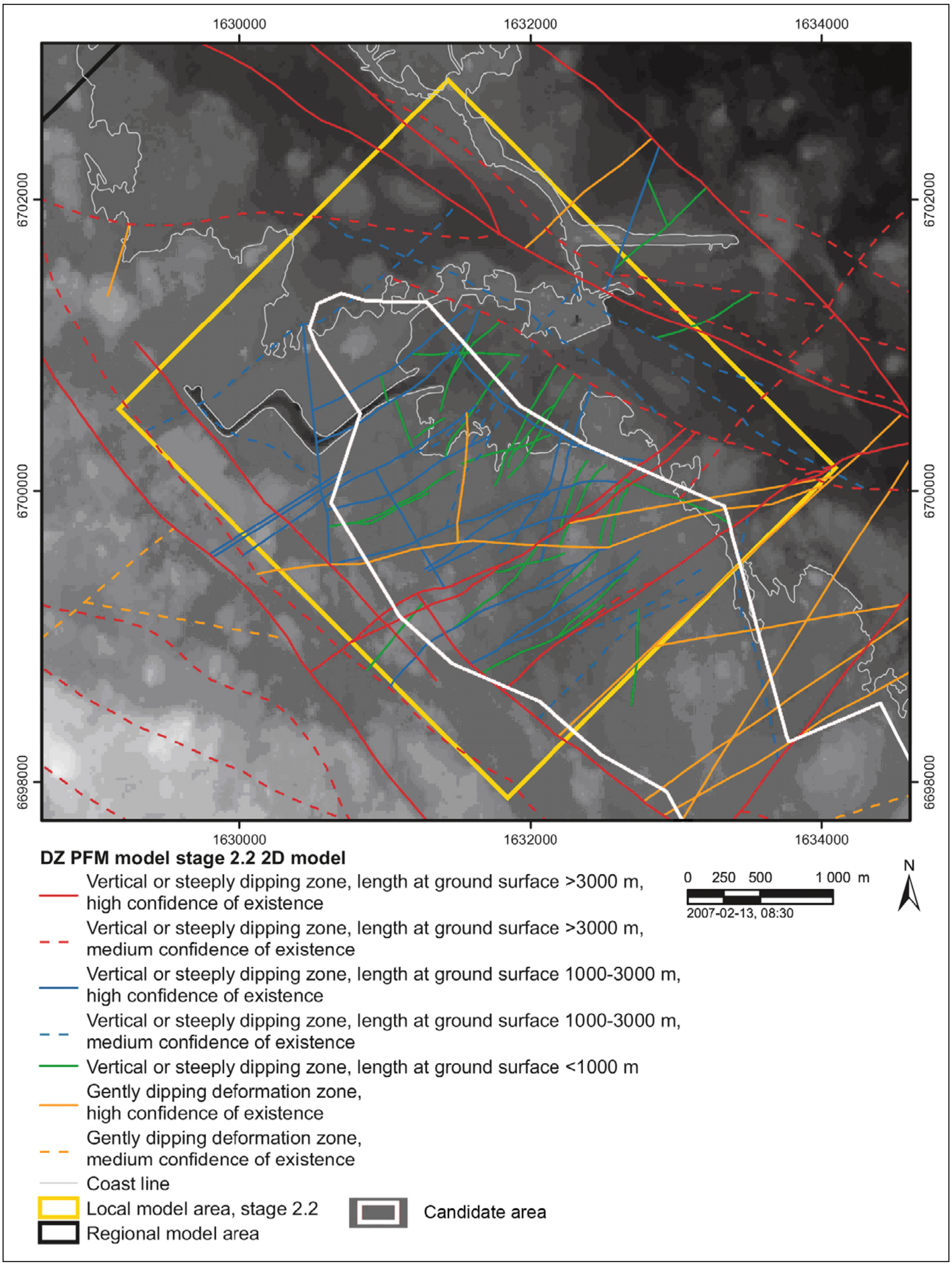

Figure 3-9. *Surface intersection of deterministically modelled deformation zones in the local model area, stage 2.2. The background corresponds to the digital elevation model for the site. Coordinates are provide using the RT90 (RAK) system. The 28 minor deformation zones modelled deterministically and included in the hydrogeological SDM have a green colour. Modified after /Olofsson et al. 2007/.*

Table 3-3. Summary of trace length data (L) for the deterministically modelled deformation zones tabulated with regard to orientation. Note that ten of the 24 gently-dipping deformation zones do not outcrop. The two numbers separated by a slash in the second and fifth columns show the number of major and minor deformations zones, respectively. All minor deformation zones are steeply-dipping and shorter than 1 km. The colours shown in the table correspond to the colours used in Figure 3-8.

Orientation category	No. of DZ major/minor	No. of DZ L ≥ 3 km	No. of DZ 3 km > L ≥ 1 km	No. of DZ L < 1 km major/minor	No. Of DZ Possible
G	24 / –	6	6	2 / –	17
WNW	23 / 1	15	7	1 / 1	3
NW	9 / –	9	0	0 / –	0
NNW	4 / 3	1	2	1 / 3	7
NNE	13 / 10	8	4	1 / 10	6
NE	4 / 6	2	1	1 / 6	0
ENE	24 / 7	2	17	5 / 7	9
EW	2 / 1	2	0	0 / 1	0
Total	103 / 28	45	37	11 / 28	42[1]

[1] One of the 43 possible deformation zones interpreted has no orientation data.

3.6.1 Structural differences above and below deformation zones A2 and F1

Figure 3-10 shows three cross-sections; one WNW-ESE cross-section along the central part of the candidate volume, and two parallel WSW-ENE cross sections in the eastern and central parts of the local model volume, respectively. The WNW-ESE cross-section demonstrates the significant structural difference in the deformation zone pattern on both sides of the gently-dipping and sub-horizontal deformation zones A2 and F1, respectively. The bedrock above these zones is here referred to as the hanging wall and the bedrock below as the footwall. The hanging wall bedrock contains a number of gently-dipping deformation zones, many of which extend down to one kilometre depth, or more. In contrast, there are very few gently dipping zones in the footwall bedrock.

The difference in the deformation pattern between the hanging wall and the footwall is steered by, among other things, the older anisotropy at the site, with-gently dipping ductile structures and rock contacts in the south-eastern part of the candidate volume and more steeply-dipping structures and contacts in the north-western part, in different parts of a major, sheath fold structure /Stephens et al. 2007/. It should be noted that the bedrock to the north-west of the steeply dipping deformation zone referred to as NE65, both above and below zones A2 and F1, is intersected by a number of steeply-dipping brittle deformation zones (fracture zones), many of which strike NNE and ENE. For purposes of simplicity, however, only the two zones that are included in the regional model are shown in Figure 3-10, i.e. NE60A and NE62A. The significance of zones with trace lengths shorter than 3 km can be appreciated from Figure 3-9.

Cross-section (c) in Figure 3-10 is shown in Figure 3-11. It is located 1,255 m north-west of cross-section (b) in Figure 3-10 and parallel. The cross-section in Figure 3-11 is closer the north-west boundary of the tectonic lens and visualises how the thickness and width of rock domain RFM029R narrow as the sheath fold structure gets steeper and the major Eckarfjärden and Singö deformation zones come closer to each other. The only major gently-dipping deformation zone detected with reflection seismics in this part of the candidate volume is A1 (cf. cross-section (a) in Figure 3-10).

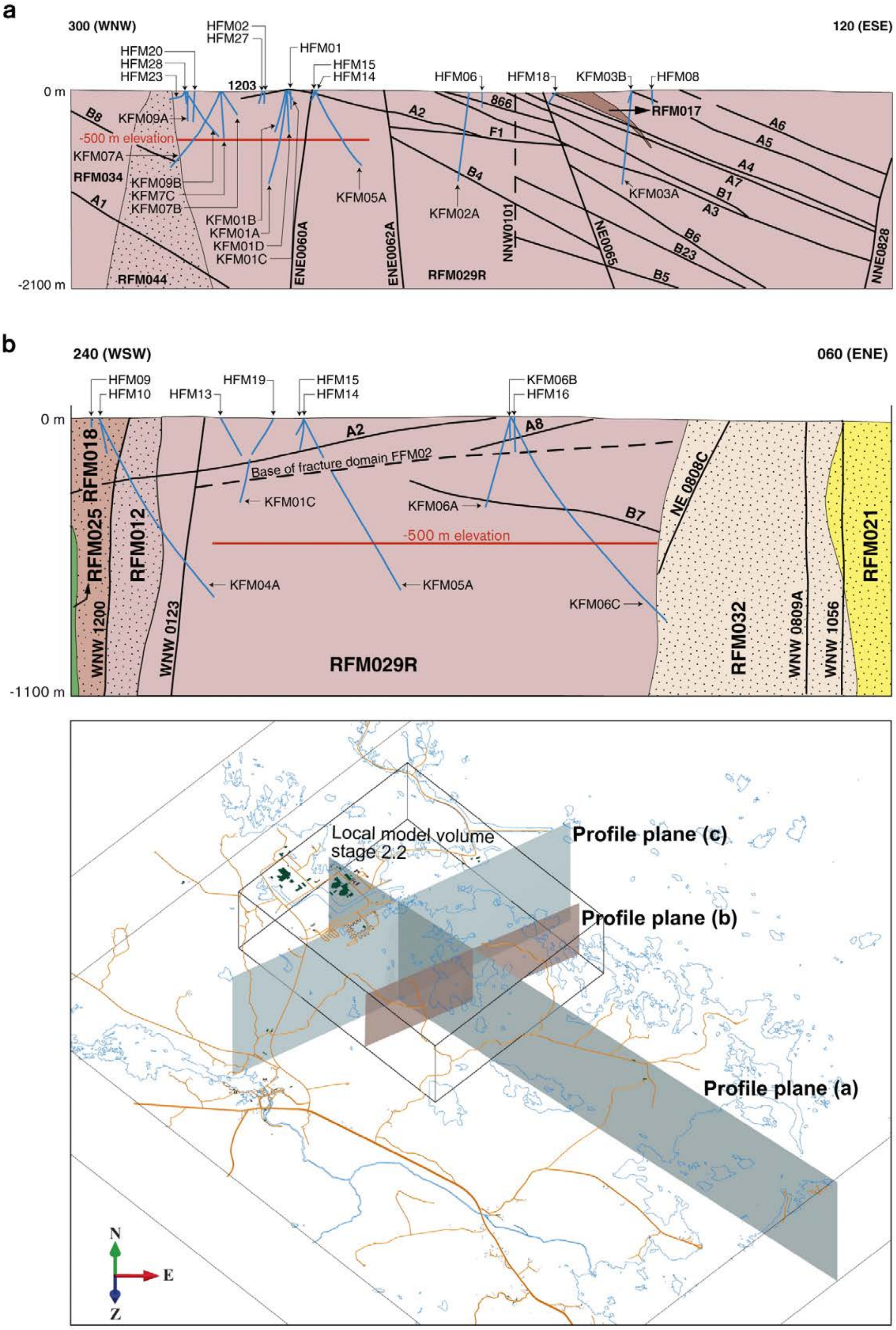

Figure 3-10. *(a) A c. 7 km long WNW-ESE cross-section along the central part of the candidate volume and (b) A c. 3 km long WSW-ENE cross-section along the south-eastern part of the local model volume. The important gently-dipping deformation zones identified with reflection seismics are highlighted in these cross-sections. The bedrock above and below deformation zones A2 and F1 are referred to here as the hanging wall and the footwall, respectively. RFM029R is a regional rock domain. On a local scale RFM029R is split into the local rock domains RFM029 and RFM045, see Figure 3-7 Modified after /Stephens et al. 2007/.*

3.7 Fracture domain model

A fracture domain refers to a rock volume between deformation zones in which rock units show similar fracture frequency characteristics. Fracture domains are defined on the basis of the single-hole interpretation work and the results of the initial statistical treatment of fractures. The minor modifications of the single-hole interpretation performed during the stage and the higher-resolution, extended single-hole interpretation work are also accounted for in the recognition of fracture domains. The different fracture domains at Forsmark are referred to as FFM.

An embryo to the fracture domain concept was suggested from a hydrogeological point of view for Forsmark already in version 1.2 by /Follin et al. 2005/. The fracture domain definition presented above was first introduced in stage 2.1 /SKB 2006a/ and elaborated for stage 2.2 /Olofsson et al. 2007/. The fracture domain concept constitutes a basis for the geological DFN modelling carried out by /Fox et al. 2007/ as well as for the hydrogeological DFN modelling carried out by /Follin et al. 2007b/.

The fractured bedrock outside the deterministically modelled deformation zones intersecting the rock domains RFM012, RFM018, RFM029, RFM032, RFM044 and RFM045, see Figure 3-7, is divided into six fracture domains, FFM01–06. Four of the six fracture domains outcrop, FFM02–05, see Figure 3-12. The key fracture domains for the target volume, FFM01 and FFM06 occur below fracture domain FFM02, see Figure 3-13.

Fracture domain FFM01: This domain is situated within rock domain RFM029 inside the target volume. It lies beneath the gently dipping or sub-horizontal zones A2, A3 and F1, and north-west of the steeply dipping zone NE0065, at a depth that varies from greater than c. –40 m RHB 70 (large distance from A2) to greater than c. –300 m RHB 70 (close to A2). Relative to the overlying fracture domain FFM02, the bedrock in this domain shows a lower frequency of especially open and partly open fractures. Gently dipping or sub-horizontal deformation zones are not common inside this domain. In particular, they have not been recognised in the critical depth interval 400–500 m in the north-western part of this domain. It has been suggested that high in-situ rock stresses have been able to accumulate inside this volume at one or more times during geological history, in connection with, for example, sedimentary loading processes /SKB 2006a/. It should be noted that some fracture assigned to FFM01 lie between zones A2 and F1, which in fact are considered to be possible deformation zones. In consequence, the model may over-predict the amount of the stochastic fractures within FFM01.

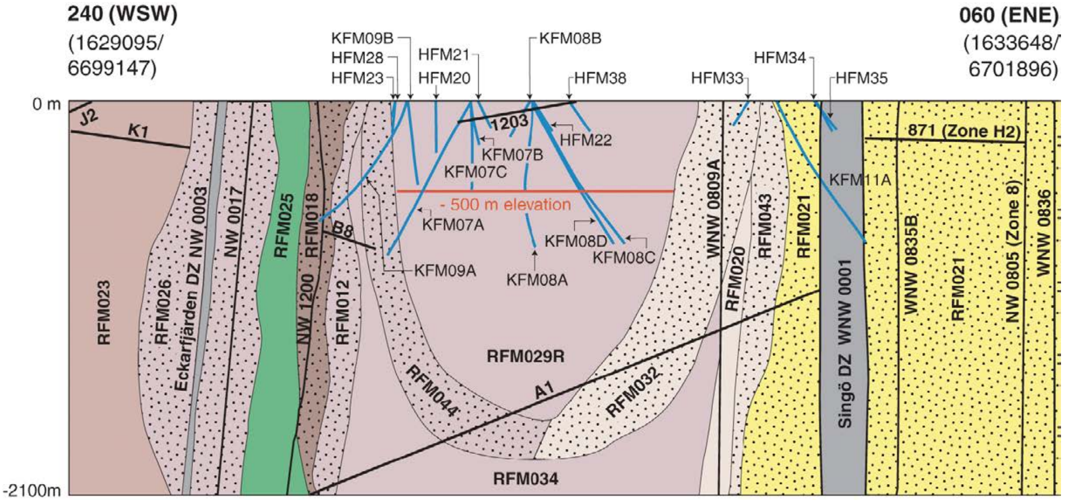

Figure 3-11. *A c. 5 km long WSW-ENE cross-section along the north-western part of the local model volume. Reproduced from /Stephens et al. 2007/.*

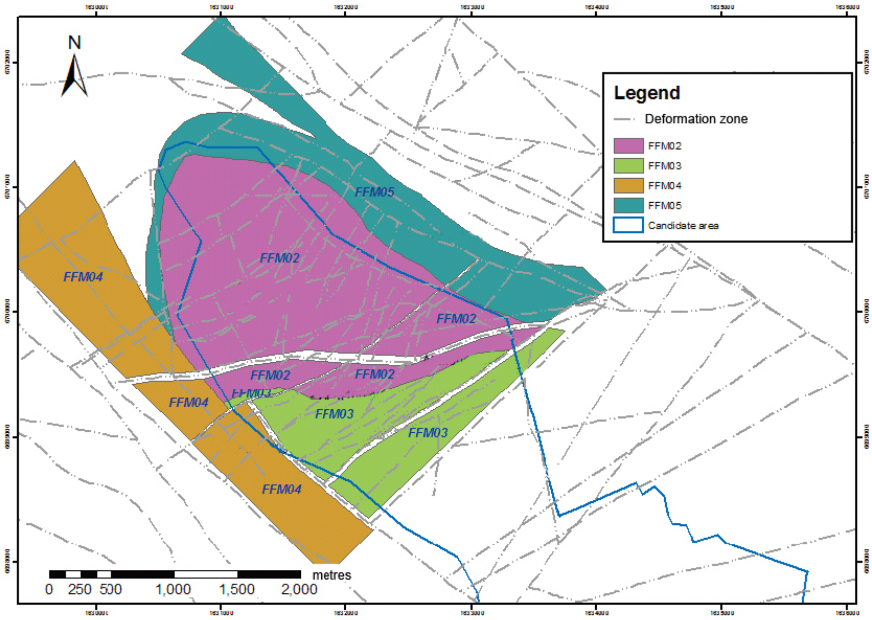

Figure 3-12. *Simplified horizontal slice at the surface showing outcropping fracture domains within the local model area for Forsmark stage 2.2. Modified after /Fox et al. 2007/.*

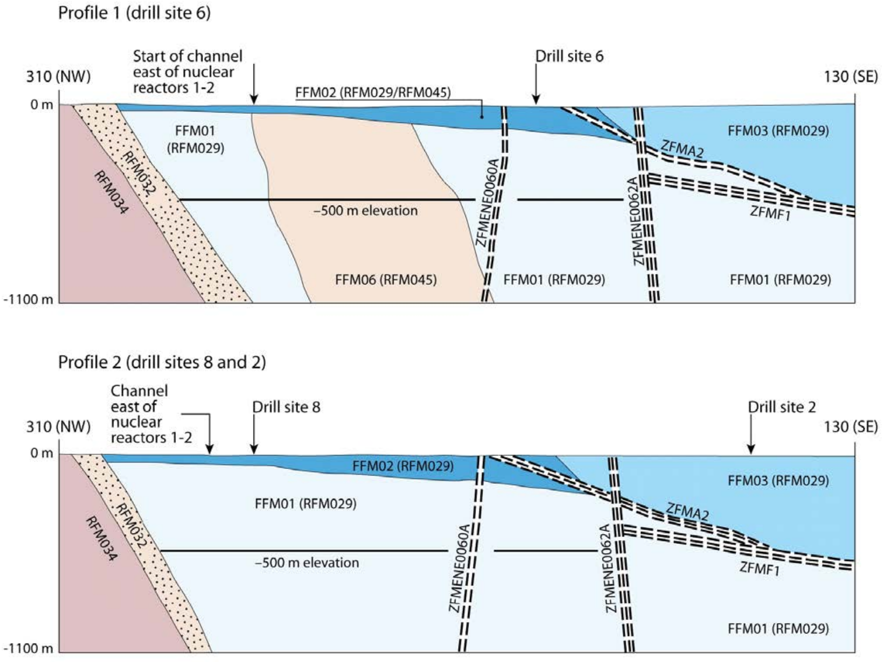

Figure 3-13. *Simplified profiles in a NW-SE direction (310°–130°) that pass through drill sites 2 and 8 (lower profile) and drill site 6 (upper profile). The labelled fracture domains (FFM01, FFM02, FFM03 and FFM06) occur inside rock domains RFM029 and RFM045. Only the high confidence deformation zones A2 (gently dipping), F1 (sub-horizontal), ENE0060A (steeply dipping, longer than 3,000 m) and ENE0062A (steeply dipping, longer than 3,000 m) are included in the profiles. Note the increased depth of fracture domain FFM02 as zone A2 is approached in the footwall to the zone, and the occurrence of this domain close to the surface directly above A2. Reproduced from /Olofsson et al. 2007/.*

Fracture domain FFM02: This domain is situated close to the surface inside the target volume, directly above fracture domain FFM01 (Figure 3-13). The domain is characterised by a complex network of gently dipping and sub-horizontal, open and partly-open fractures, which, beneath drill site 7, are known to merge into minor zones. The gently dipping and sub-horizontal fractures are oriented at a high angle to the present day minimum principal stress in the bedrock. This relationship favours their reactivation as extensional joints in the present stress regime, the development of conspicuous apertures along several fractures, and the release of high stress. The occurrence of this domain at greater depths close to A2 at drill site 1, and even above this zone at drill sites 5 and 6, is related to an inferred higher frequency of such older fractures in the vicinity of this zone, to higher rock stresses around zone A2 or to a combination of these two possibilities.

Fracture domain FFM03: This domain is situated within rock domains RFM017 and RFM029, outside the target volume. It lies structurally above zones A2, A3 and F1, north-west of the steeply dipping zone NE0065, and south-east of zone NE0065 (Figure 3-13). The domain is characterised by a high frequency of gently dipping deformation zones, which contain both open and sealed fractures. It is suggested that this structural feature inhibited the build-up of rock stresses in connection with, for example, sedimentary loading processes /SKB 2006a, Section 3.2.2, p. 121–126/. The development of a significant stress-release fracture domain, close to the surface, with the characteristics of domain FFM02 is also not favoured.

Fracture domain FFM04: This domain is situated within rock domains RFM012 and RFM018 along the south-western margin of and outside the target volume. Strong bedrock anisotropy with high ductile strain and ductile structures that dip steeply to the south-west are prominent in this domain.

Fracture domain FFM05: This domain is situated within rock domains RFM044 and RFM032 along the north-western and north-eastern margins of and outside the target volume. Strong bedrock anisotropy with high ductile strain and folded ductile structures, as well as the occurrence of fine-grained, felsic meta-igneous rocks characterise this domain.

Fracture domain FFM06: This domain is situated within rock domain RFM045, inside the target volume. It resembles fracture domain FFM01 in the sense that it lies beneath both zone A2 and fracture domain FFM02. It is distinguished from domain FFM01 on the basis of the common occurrence of fine-grained, altered (albitised) granitic rock, with slightly higher contents of quartz compared to unaltered granitic rock.

In summary, fracture domains FFM01–03 occur in rock domain RFM029, with FFM01–02 in the footwall bedrock and FFM03 in the hanging wall bedrock. Fracture domains FFM04 and FFM05 coincide with rock domains RFM012+RFM018 and RFM032+RFM044, respectively. Fracture domain FFM06 coincides with rock domain RFM045. In conclusion, the target volume consists of three fracture domains, FFM01, FFM02 and FFM06. Since the target volume lies within rock domains RFM029 and RFM045, north-west of the steeply dipping zone NE0065 and structurally beneath the gently dipping and sub-horizontal zones A2, A3 and F1, it is apparent that statistical modelling of fractures and possible minor deformation zones needs to be implemented in fracture domains FFM01, FFM02 and FFM06.

Figure 3-14 and Figure 3-15 show two 3D visualisations of the fracture domain model as modelled in RVS. The two views show the geometrical relationships between domains FFM01, FFM02, FFM03 and FFM06. Fracture domain FFM01 dominates in the lowermost part of the view. The volume coloured dark grey shows the position of FFM06. The uppermost part of the bedrock, in the north-western part of the model, is fracture domain FFM02. This domain dips gently towards the south. Fracture domain FFM03 is situated directly above the gently dipping and sub-horizontal zones A2 and F1 at depth, and above domain FFM02 close to the surface.

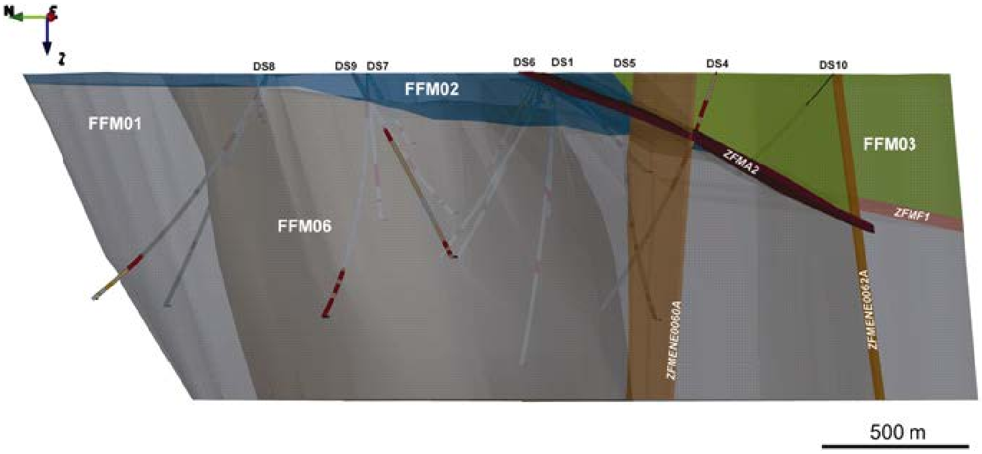

Figure 3-14. Three-dimensional view of the fraction domain model, viewed towards the east-north-east. Fracture domains FFM01, FFM02, FFM03 and FFM06 are coloured grey, dark grey, blue and green, respectively. The gently dipping and sub-horizontal zones A2 and F1 as well as the steeply dipping deformation zones ENE0060A and ENE0062A are also shown. Reproduced from /Olofsson et al. 2007/.

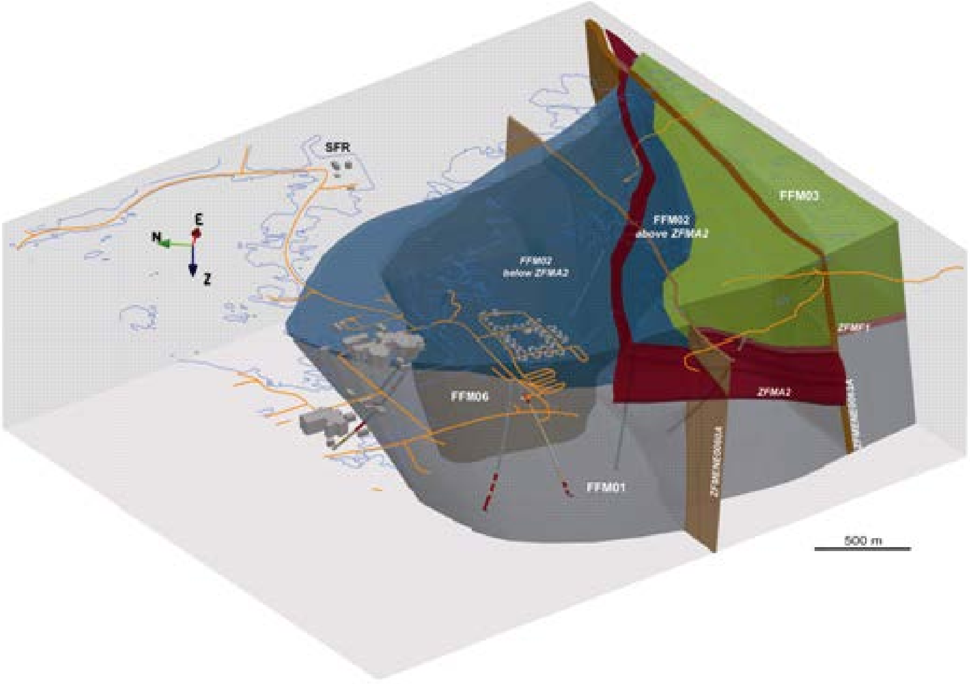

Figure 3-15. Three-dimensional view to the east-north-east showing the relationship between deformation zone A2 (red) and fracture domain FFM02 (blue). Reproduced from /Olofsson et al. 2007/.

3.8 Discrete fracture network (DFN) model

In essence, the geological DFN approach adopted by SKB is based on four types of fracture data: fracture orientations, fracture trace lengths, fracture frequencies and fracture locations. From this information fracture sets are defined. Each set is assigned a specific size distribution and intensity. If the fracture locations are clustered, a fractal spatial model may be invoked. If the fracture locations are uniformly distributed in space and uncorrelated, a so-called Poissonian spatial model may be invoked. In addition to the four types of fracture data specified above, a hydrogeological DFN (Hydro-DFN) model also requires information about fracture transmissivity (or hydraulic aperture) and fracture connectivity. That is, a network of flowing fractures consists of open (transmissive) fractures that are geometrically connected.

The geological DFN (Geo-DFN) modelling conducted in stage 2.2 /Fox et al. 2007/ entails different sorts of data (geometrical and geophysical) and data on different spatial scales (lineament data, outcrop data and borehole data). The data are analysed with regard to a number of different orientation, size, intensity and spatial models. The modelling addresses the geological DFN properties of fracture domains FFM01–03 and FFM06. It is made without consideration to fracture aperture; that is, the identification of fracture sets and their specific properties (sizes and intensities) are deduced for all fractures (no distinction between sealed and open fractures are made). Moreover, the geological DFN modelling undertaken does not consider fracture connectivity.

In comparison, the Hydro-DFN modelling conducted in stage 2.2 is based on data gathered on a single spatial scale, i.e. fracture data and hydraulic data from boreholes. In order to circumvent the lack of geometrical information that follows from this constraint, several geometrical assumptions are invoked. We note in particular that a tectonic continuum is envisaged where the number of features of different sizes follows a power-law relationship (Figure 2-4). The exact locations of features with a fracture surface area less than 10^6 m^2 are regarded as uncertain and are therefore treated stochastically using the DFN concept. The Hydro-DFN approach adopted by SKB focuses on flowing fractures, i.e. fractures that are both open *and* connected. The methodology was developed in version 1.2 /Follin et al. 2005/ and elaborated for stage 2.2 /Follin et al. 2007b/. The Geo-DFN and Hydro-DFN modelling tasks are run in parallel in stage 2.2. Appendix C provides a simplified comparison between the Geo-DFN and the Hydro-DFN results deduced for fracture domain FFM01, one of the two key fracture domains for a repository in the Forsmark area, the other being FFM06.

Table 3-4 shows a summary of the open fracture statistics and the flowing fracture statistics for the three fracture domains FFM01–03, respectively, as reported for stage 2.2 by /Follin et al. 2007b/. The decreasing frequency of flowing fractures with depth is based on the conductive fracture frequency (CFF) measured with the PFL-f method. The data observed suggest that the network of open and connected fractures is considerably compartmentalised and close to or below the percolation threshold. This result implies a restricted groundwater circulation at repository depth.

Figure 3-16 shows an example realisation of the regional Hydro-DFN. The realisation is shown as a NW-SE cross-section and two horizontal trace planes at –30 and –500 m RHB 70, respectively. The images in the left column show the traces of "All Open" fractures. The images in the right column show the traces of the "Connected Open" fractures. The effect of the low connectivity below –400 m RHB 70 is obvious. For the bedrock outside the mapped fracture domains, i.e. outside the tectonic lens, there is no fracture information available, and so a simplified property assignment must be used to specify homogeneous continuum porous medium (CPM) properties.

Table 3-4. Summary of fracture statistics for three of the fracture domains in the tectonic lens (FFM01–FFM03). Terzaghi corrected values of the intensity of open and flowing fractures are shown for different elevation intervals. There are significant differences between the three fracture domains and a substantial decrease with depth of both open and flowing fractures /Follin et al. 2007b/.

Fracture domain	**FFM01**			**FFM02**	**FFM03**	
Elevation, m RHB 70	–100 to –200	–200 to –400	–400 to –1,200	–100 to –200	–100 to –400	–400 to –1,200
Intensity of observed open fractures, m^{-1}	1.13	1.02	0.54	3.17	1.10	0.77
Intensity of observed flowing fractures, m^{-1}	0.15	0.04	< 0.01	0.33	0.09	0.05

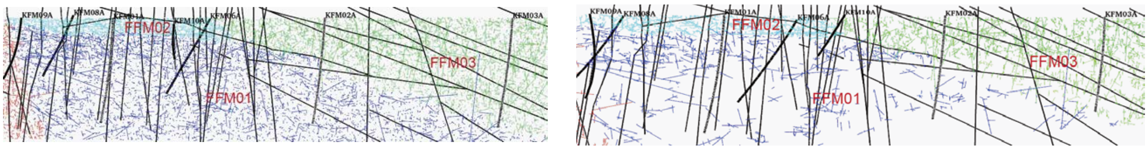

NW–SE cross-section: All Open

NW–SE cross-section: Connected Open only

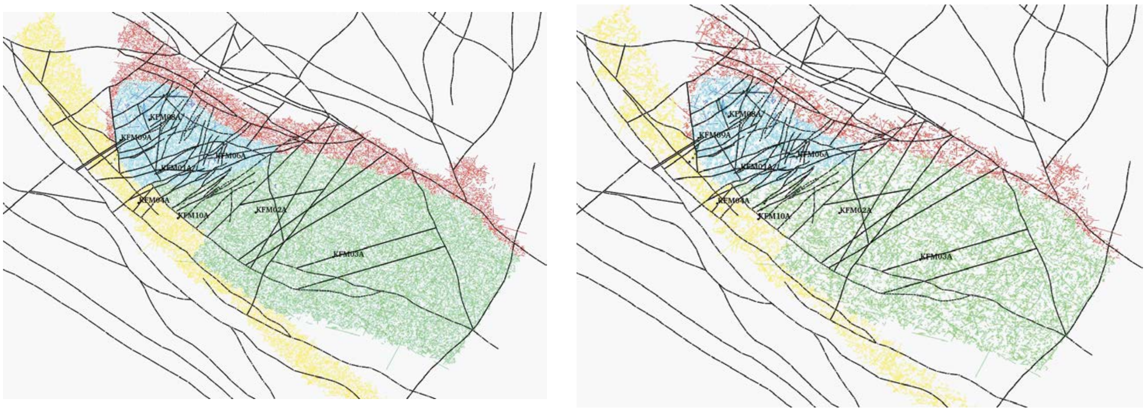

Horizontal slice at –30 m RHB 70: All Open

Horizontal slice at –30 m RHB 70: Connected Open only

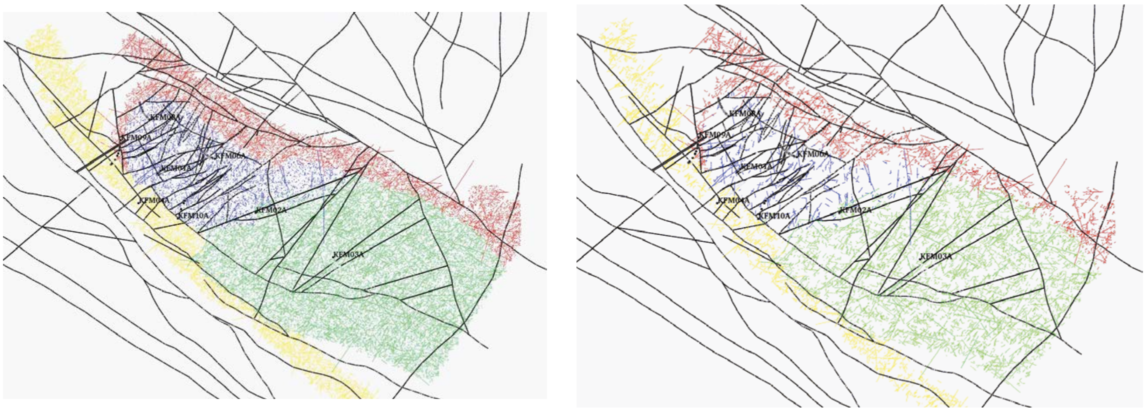

Horizontal slice at –500 m RHB 70: All Open

Horizontal slice at –500 m RHB 70: Connected Open only

Figure 3-16. *An example realisation of the regional Hydro-DFN shown as a NW-SE cross-section and two horizontal trace planes at –30 and –500 m RHB 70, respectively. The thickness of the cross-section is c. 1.2 km and the length is c. 5 km. The images in the left column show the traces of "All Open" fractures. The images in the right column show the traces of the "Connected Open" fractures. The fracture traces are coloured by fracture domain: FFM01 and FFM06 are dark blue, FFM02 is light blue, FMM03 is green, FFM04 is yellow, and FFM05 is red. Slices through the deformation zones at the same elevations are superimposed in black. Here, the stochastic fractures are generated with radii between 5.64–564 m.*

Figure 3-17 shows a view of the fracture domains in the target volume below FFM02, i.e. FFM01 and FFM06, and the core-drilled boreholes available for Hydro-DFN modelling in stage 2.2. None of the available boreholes provide hydraulic information about FFM06. Therefore, a new borehole, KFM08D, will be drilled into FFM06 as shown in Figure 3-18. A prediction of the hydraulic properties along KFM08D is shown in Appendix D.

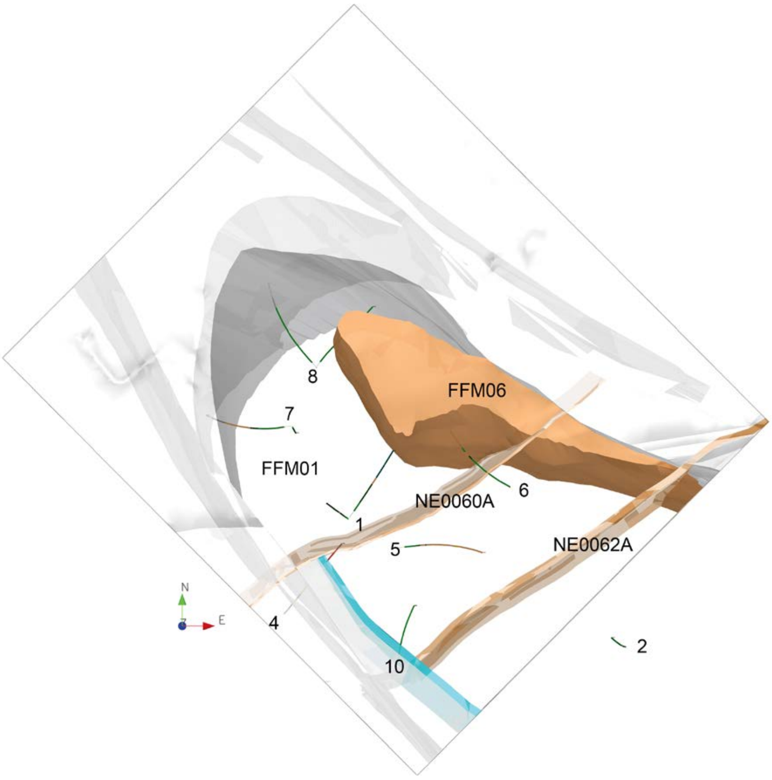

Figure 3-17. *The core-drilled boreholes available for Hydro-DFN modelling of the target volume in stage 2.2 did not investigate fracture domain FFM06.*

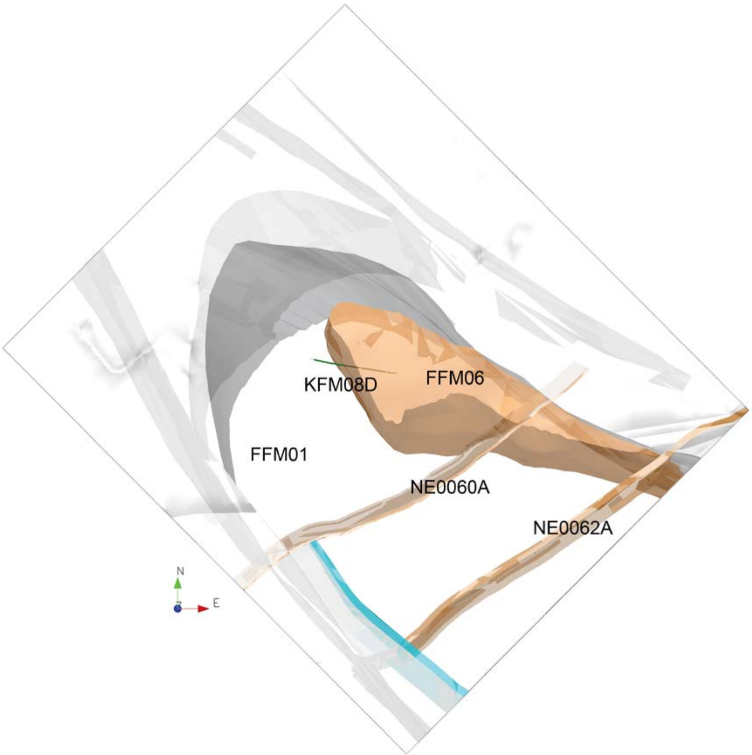

Figure 3-18. *A view of the KFM08D borehole that will be drilled into FFM06. Appendix D contains a summary of the structural-hydraulic prediction made for this borehole. The data from KFM08D will be available for a comparison with the prediction in stage 2.3.*

3.9 Bedrock hydrogeological model

/Follin et al. 2007b/ provide an overview of the hydraulic data gathered from the single-hole hydraulic test information contained in data freeze 2.2. The majority of the fractures observed in the cored boreholes are sealed, both inside and outside the intervals with deformation zone type properties. Moreover, the vast majority of the flowing open fractures detected with the PFL tool are gently dipping, see Appendix E. The bedrock hydrogeological model addresses the hydraulic properties of the target volume and its boundaries. The structural segments treated in stage 2.2 are:

1. The deterministically modelled deformation zones within the candidate area.
2. The superficial bedrock above repository depth (FFM02).
3. The bedrock bordering the target volume (FFM04–05).
4. The bedrock at repository depth (FFM01 and FFM06).

3.9.1 The deterministically modelled deformation zones

The role of the deterministically modelled deformation zones for regional GWF was a key aspect of version 1.2, which studied, among other things, the need for far-field realism by means of three regional deformation zone models. It was concluded by means of modelling that detailed geometrical and hydraulic information about the deformation zones within the tectonic lens are much more important for the bedrock hydrogeological description within the target volume than the positions and hydraulic properties of deformation zones outside the tectonic lens /Follin et al. 2005/.

The assignment of hydraulic properties to the different deformation zones in version 1.2 was based on simple depth trend regression analyses of single-hole transmissivity data acquired at a limited number of borehole intercepts /Follin et al. 2005/. Although the observed differences in transmissivity between steeply-dipping and gently-dipping was found to be considerable at repository depth (c. two orders of magnitude), it was concluded that a simplified description of the deformation zone heterogeneity within the tectonic lens undoubtedly affected the matching against hydrochemical data, which were gathered in borehole intervals with "deformation zone type properties".

In version 1.2, 44 deformation zone intercepts representing 28 different deformation zones were investigated hydraulically. In stage 2.2 these numbers have increased to 116 and 57, respectively, which implies a more or less doubled information density. Figure 3-19 shows a plot of transmissivity versus depth for the 57 deformation zones investigated hydraulically in stage 2.2. The colour legend used is the same as the legends used in Figure 3-8 and Table 3-3. Figure 3-19 shows that, at each elevation, the gently-dipping deformation zones occurring in the hanging wall bedrock are the most transmissive. The bordering steeply-dipping deformation zones that strike WNW and NW form structures with a second order of importance as far as transmissivity is concerned. The steeply-dipping deformation zones that strike ENE and NNE occur in the footwall bedrock mainly. These are significantly more heterogeneous from a hydraulic point of view. In summary, these observations suggest a pronounced hydraulic anisotropy, where the largest transmissivities observed are associated with deformation zones parallel with the orientation of the maximum principal stress, WNW, (see also /Juhlin and Stephens 2006/).

Figure 3-19 suggests that all deformation zones in the uppermost one kilometre of bedrock are affected by a substantial depth trend (vertical heterogeneity) in transmissivity. The depth trend in transmissivity spans four to six orders of magnitude, from 10^{-4}–10^{-3} m^2/s near the bedrock surface to 10^{-9}–10^{-8} m^2/s at –1,000 m RHB 70. However, of equal importance, Figure 3-19 also reveals that the lateral heterogeneity in transmissivity at each elevation is considerable.

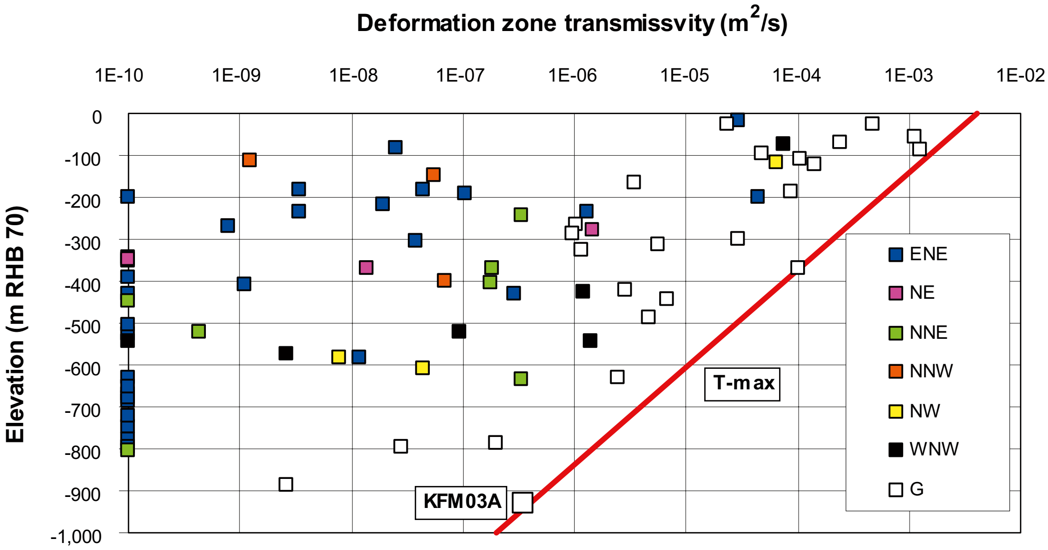

Figure 3-19. Transmissivity versus depth for the deterministically modelled deformation zones observed in cored boreholes. The transmissivities are coloured with regard to the orientations of the deformation zones. For the purpose of this plot, deformation zones with little or no flow are assigned arbitrary low transmissivity value of $1 \cdot 10^{-10}$ m²/s in order to make them visible on the log scale. The red line is inserted to indicate a possible depth variation of the maximum transmissivity ***observed*** *at each elevation. Reproduced from /Follin et al. 2007b/.*

A closer analysis of the data shown in Figure 3-19 reveals that the transmissivities vary laterally (at the same depth) by several orders of magnitude between zones with similar orientation, as well as between different parts of a specific zone. The conclusion drawn from these findings is that the previously described structural-mechanical anisotropy is not only accompanied by a significant hydraulic anisotropy, but also a substantial lateral hydraulic heterogeneity. This observation may cause a more channelised flow-field than otherwise.

3.9.2 The superficial bedrock above repository depth

The current hydrogeological understanding of the uppermost part of the bedrock is based on the impeller flow logging carried out in 32 percussion-drilled boreholes, HFM01–32, see Figure B-7 in Appendix B, and two large-scale interference tests conducted in boreholes HFM01 and in HFM14. The two interference tests were carried out for three weeks each during the summers of 2005 and 2006, respectively. The borehole lengths of HFM01–32 vary between 26 and 301 m and the borehole inclinations vary between 49° and 88°. The median penetration depth is c. 140 m /Follin et al. 2007b/.

Figure 3-20 shows the inferred flow logging transmissivities in intervals of 50 m for the uppermost 200 m of bedrock. The pattern is quite heterogeneous, i.e. high and low values can occur at any depth and location. However, the high transmissivities are in many cases exceptionally high, in particular in the north-western part of the candidate area. The uppermost bedrock in this area more or less corresponds to fracture domain FFM02, cf. Figure 3-12.

In /SKB 2006a/, it was suggested that there can be a network of high-transmissive structures that shorts the recharge from above as well as the discharge from below, see Figure 3-21. The network is probably heterogeneous but it is imagined to follow the undulations of the bedrock surface implying that many of them do not outcrop, but stay below the bedrock surface as this dips under the Baltic Sea, see Figure 3-21.

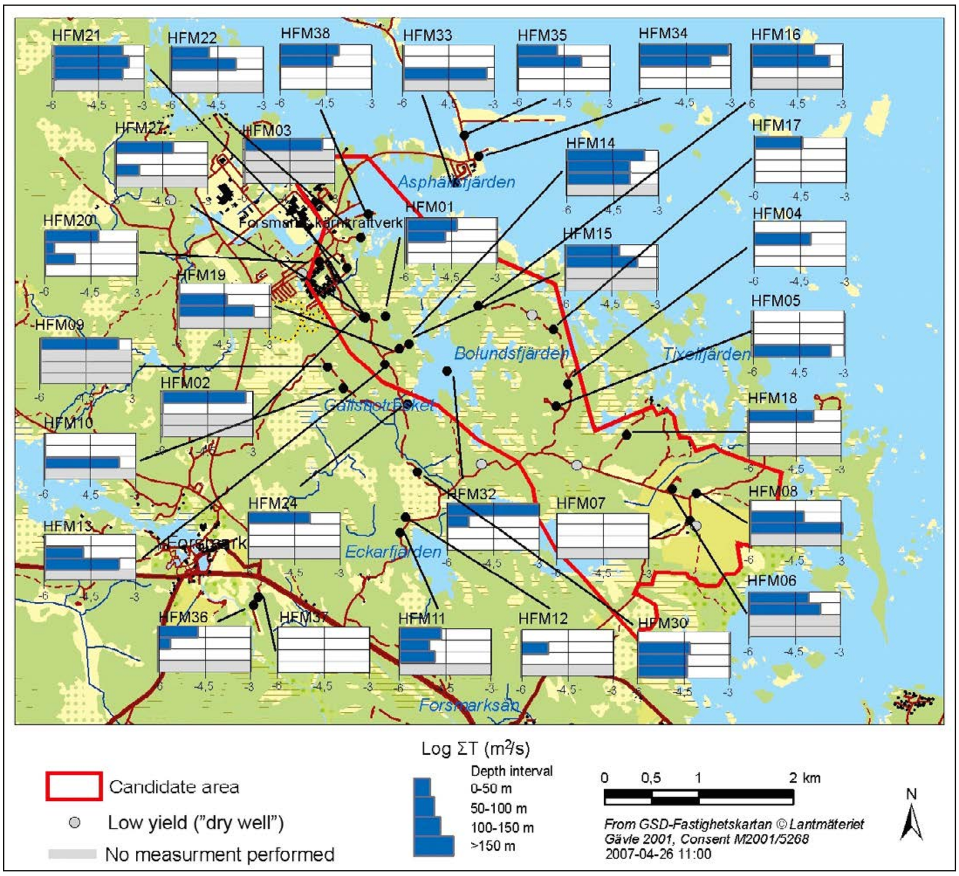

Figure 3-20. *HTHB transmissivities lumped into intervals of 50 m for the uppermost 200 m of bedrock. The logarithmic transmissivity scale ranges from* 10^{-6} *to* 10^{-3} m^2/s*. Reproduced from /Follin et al. 2007b/.*

Understanding the horizontal extent and the hydraulic properties of the horizontal fractures/sheet joints is an important component of the description of the hydrogeological system in the Forsmark area. There are several observations that the "hydraulic cage phenomenon" is more pronounced in the superficial rock mass in the footwall bedrock of the gently-dipping zone A2 than in the hanging wall bedrock of this zone. Among the structural evidence we note in particular the picture of the horizontal fractures/sheet joints encountered along the entire excavation of the more than one kilometre long and 13 m deep canal between the Baltic Sea and the nuclear power reactors in Forsmark, see Figure 3-22. The observations reported by /Carlsson and Christiansson 2007/ suggest the horizontal fractures/sheet joints seen in Figure 3-22 connect the candidate area to the Singö deformation zone. This hypothesis will be tested in stage 2.3 by means of an interference test at percussion-borehole HFM33 located on the SFR peninsula, see Figure B-7 in Appendix B. The interference test will also study the hydraulic properties transverse the Singö deformation zone by means of measurements in the boreholes located on the other side of this zone including the boreholes at the SFR. The hydraulic properties of the Singö deformation zone will also be investigated in stage 2.3 by means of a core-drilled borehole KFM11A, see Figure B-6 in Appendix B.

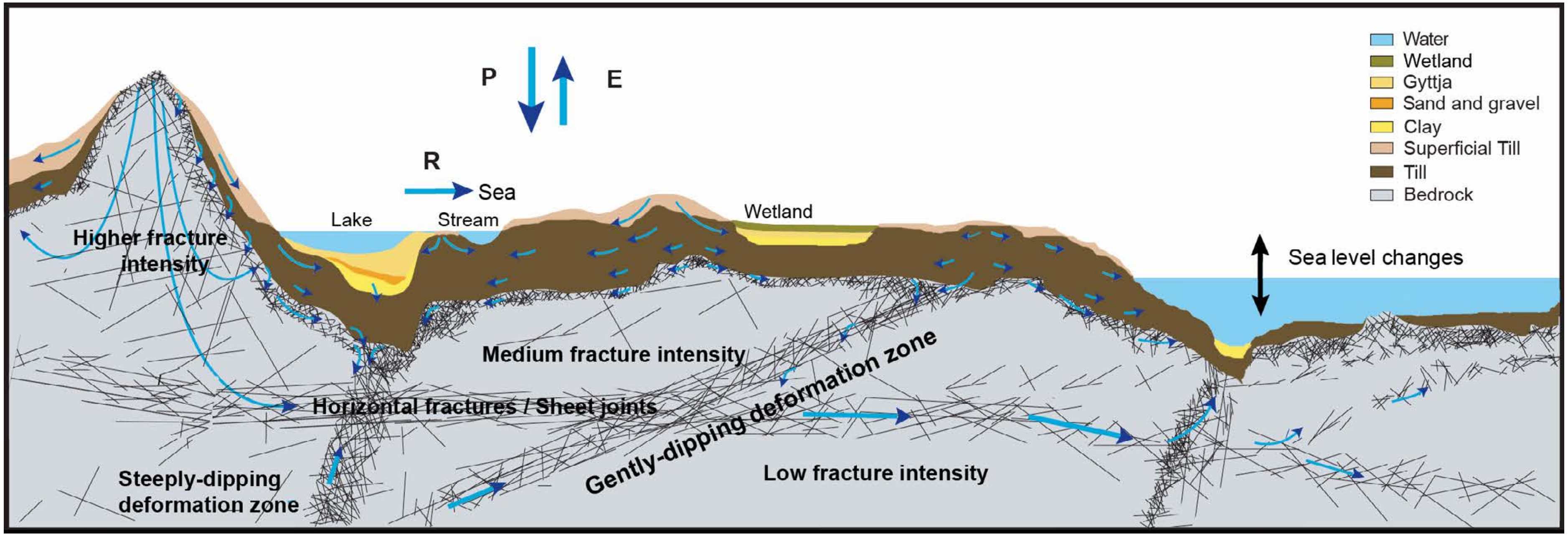

Figure 3-21. *Cross-section cartoon visualising the notion of a near-surface network of high-transmissive structures that acts like a short circuit for the recharge from above as well as the discharge from below. P=precipitation, E=evapotranspiration, R=runoff. The network is thought to consist of extensive, horizontal fractures/sheet joints, which intersect outcropping deformation zones and the frequency of discrete fractures in fracture domain FFM02. The network is probably hydraulically heterogeneous but in many places it is highly transmissive, cf. Figure 3-20. The sheet joints are imagined to follow the undulations of the bedrock surface implying that many of them do not outcrop, but stay below the bedrock surface as this dips under the Baltic Sea. Strands of evidence that support this notion are found in the works presented by /Carlsson and Christiansson 2007/. Modified after /Follin et al. 2007b/.*

Figure 3-22. *Picture from the construction of the 13 m deep and more than one kilometre long canal between the Baltic Sea and the nuclear power reactors. Horizontal fractures/sheet joints are encountered along the entire excavation. There are several "horizons" of extensive sheet joints on top of each other. The picture is taken from the southern side of the canal where the bridge crosses the canal between drill sites 7 and 8, see Figure B-1 in Appendix B.*

There are three strands of hydrogeological evidence that support the hypothesis that the near-surface network of structures is highly conductive:

1. Exceptional high well yields for the percussion boreholes drilled inside the target area, see Figure 3-23. The median yield of the first 22 percussion-drilled boreholes within the candidate area is c. 12,000 L/h, which is c. twenty (20) times higher that the mean yield in the nearby domestic water wells, which is no different than the median yield of all bedrock water wells in Sweden (c. 200,000 wells) /Berggren 1998/. An example of a high yielding percussion-drilled borehole within the candidate area is shown in Figure 3-24.
2. The near uniform groundwater levels in the uppermost 100 m of bedrock inside the tectonic lens. In particular, the groundwater levels in the target area suggest a well connected network of superficial fractures of high transmissivity, see Figure 3-25.
3. The extensive and rapid transmission of fluid pressure changes during two large-scale interference tests conducted within the target area /Gokall-Norman et al. 2005, Gokall-Norman and Ludvigson 2006/, see Figure 3-26 through Figure 3-30. Figure 3-30 suggests that the Baltic Sea is a positive hydraulic boundary while pumping in HFM14.

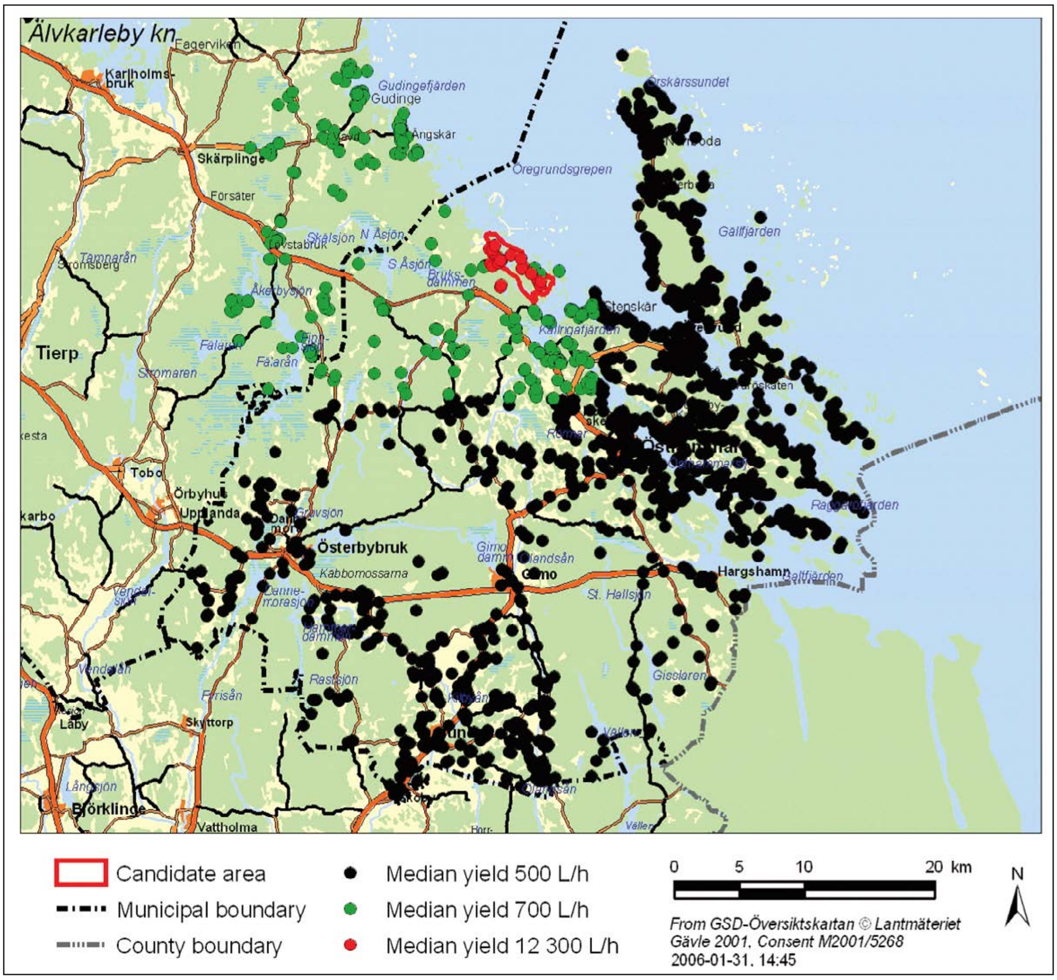

From GSD-Översiktskartan © Lantmäteriet Gävle 2001. Consent M2001/5268 2006-01-31, 14:45

Figure 3-23. *The median yield of the HFM01–HFM22 boreholes (red dots) is c. 20 times higher than the median yield of the nearby domestic wells (green and black dots). Reproduced from /Gentzschein et al. 2006/.*

Figure 3-24. *The yield in the superficial bedrock is exceptional in some boreholes. At HFM02 the yield is about 60,000 L/h. At HFM16, which is about 1 km away from HFM02, the yield is about 72,000 L/h. Reproduced from /Gentzschein et al. 2006/.*

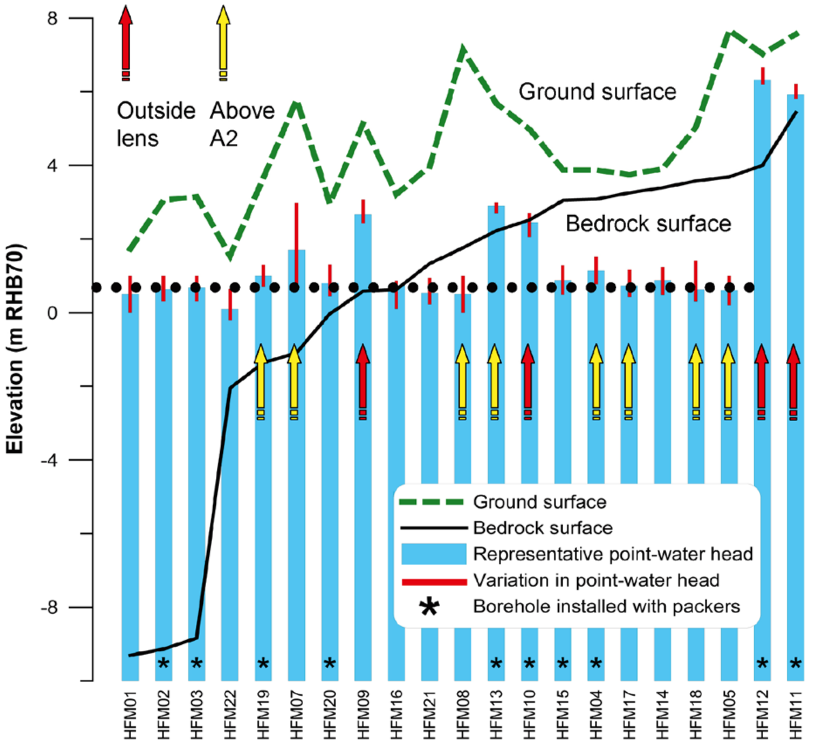

Figure 3-25. Mean groundwater levels (point-water heads) in the superficial bedrock in the north-western part of the tectonic lens. The percussion boreholes are ordered with regard to the bedrock elevation. The groundwater levels are insensitive to the ground elevation as well as to the bedrock elevation. Modified after /Gentzschein et al. 2006/.

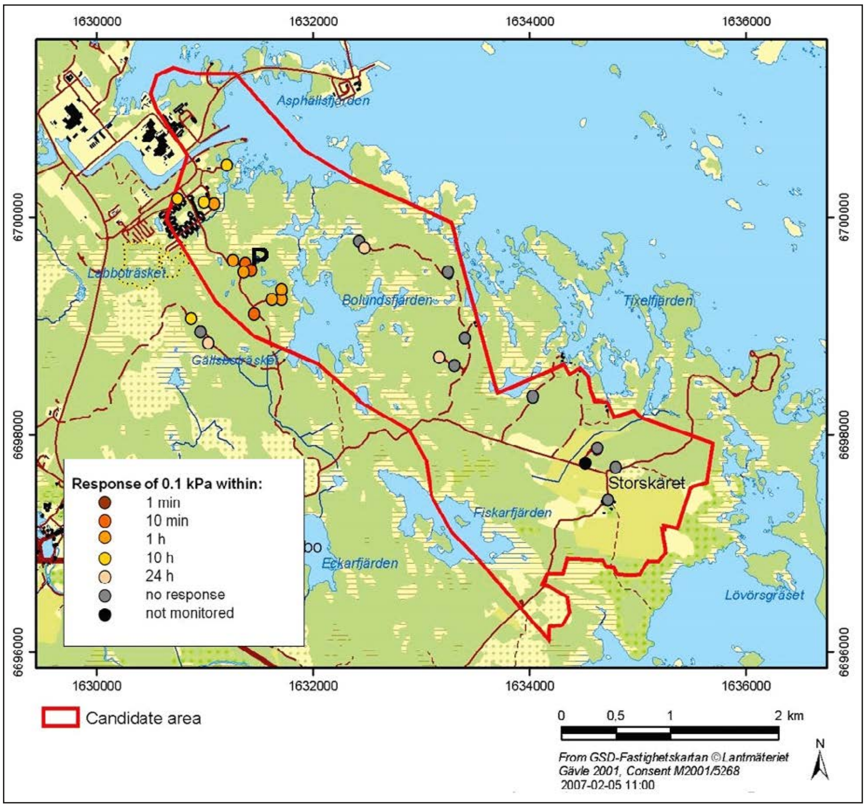

Figure 3-26. Map showing response times in the bedrock to the 2005 interference conducted in HFM01 (P). The test responses were monitored at 37 "observation points", see /Gokall-Norman et al. 2005/.

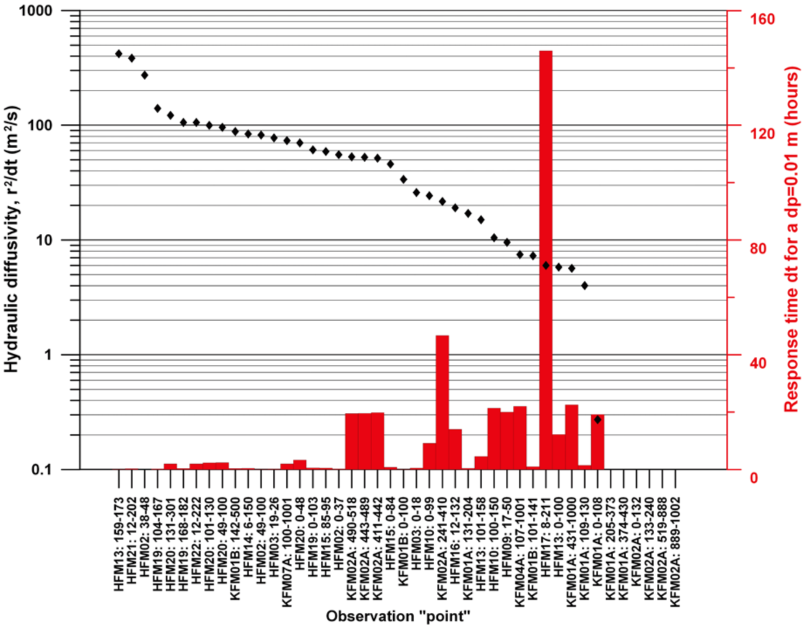

***Figure 3-27.** Hydraulic diffusivities, r^2/dt, (evaluated according to /Streltsova 1988/) and "breakthrough times" for the 37 "observation points" monitored during the 2005 interference test in HFM01, cf. Figure 3-26. The interpreted diffusivity values range between 4–500 m^2/s, which implies a fairly transmissive network of flow paths of little or no storativity.*

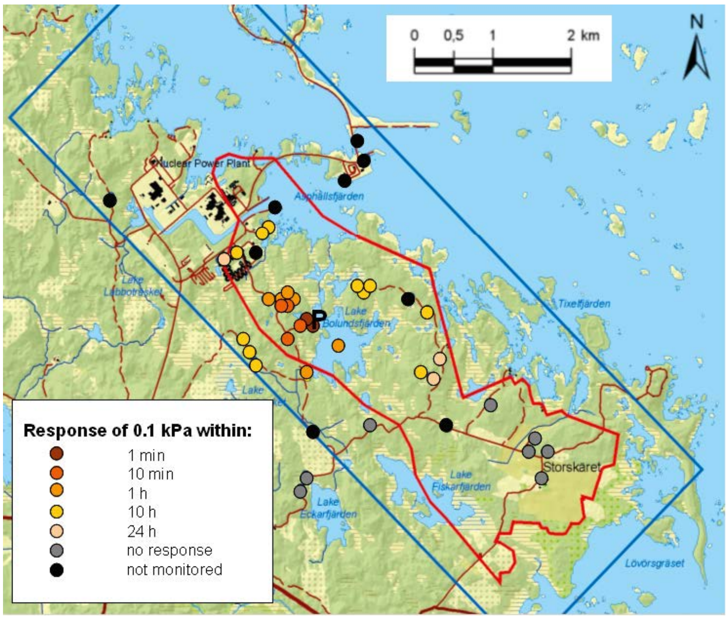

***Figure 3-28.** Map showing response times in the bedrock to the 2006 interference test conducted in HFM14 (P). The test responses were monitored at 71 "observation points", see /Gokall-Norman and Ludvigson 2006/.*

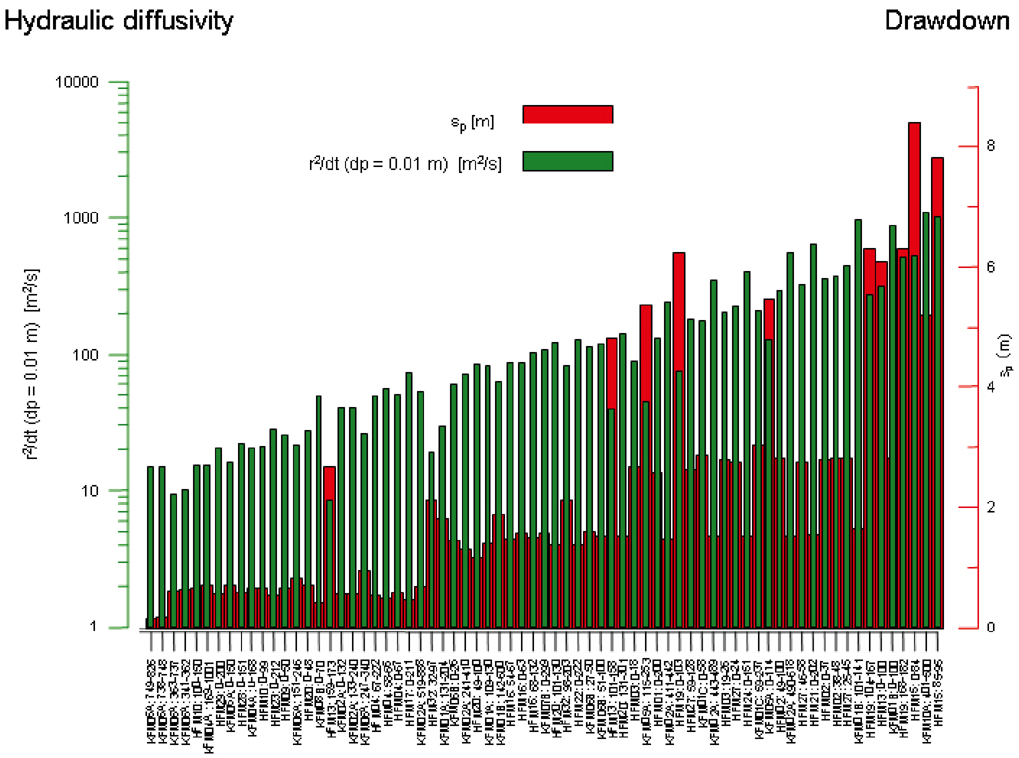

Figure 3-29. *Hydraulic diffusivities, r^2/dt, (evaluated according to /Streltsova 1988/) and maximum drawdowns for the 71 "observation points" that reacted to the 2006 interference test in HFM014, cf. Figure 3-28. The interpreted values of r^2/dt range between 10–1,000 m^2/s, which implies a transmissive network of flow paths of little or no storativity.*

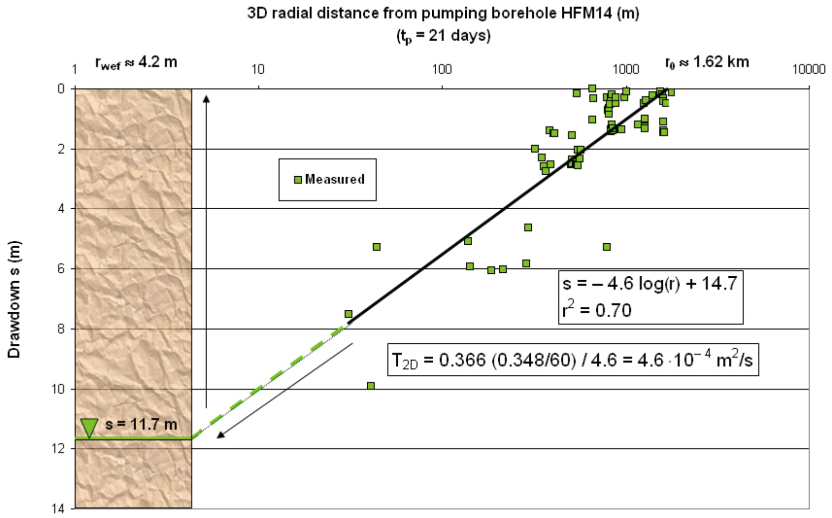

Figure 3-30. *Plot of measured drawdowns vs. log(3D radial distance) at the end of the 21-day log interference test in HFM14. The drawdown in HFM14 was 11.7 m and the flow rate was c. 348 L/min implying a specific capacity of approximately $5 \cdot 10^{-4}$ m^2/s. The black line shows a least-square fit to the measurements. The value of the correlation coefficient (r^2 = 0.70) indicates a heterogeneous system. A steady-state, radial flow approximation using the slope of the least-squares fit for an estimate of Δs renders a large-scale effective transmissivity of $5 \cdot 10^{-4}$ m^2/s. An extrapolation of the regression model suggests an effective radius of HFM14 of about four metres, which corresponds to a negative skin of about –4.1.*

In summary, the significant hydraulic diffusivity and horizontal anisotropy of the uppermost part of the bedrock reduce the hydraulic gradients across the deeper bedrock flow system in the target area below c. 150 m depth. In a way, the near-surface flow system acts like a “hydraulic cage phenomenon” /Follin et al. 2007a/, though unlike a true hydraulic cage, the shallow network of transmissive structures only covers one side of the deeper bedrock flow system. It does not eliminate the hydraulic gradients entirely. Hence, a more appropriate hydrogeological analogue of the hydraulic short circuit phenomenon observed in the uppermost part of the bedrock is a shallow, anisotropic, bedrock “aquifer” on top of thicker segment of bedrock with “aquitard” type properties. Despite the risk of misunderstanding, we use the term “cage feature” in the work reported here to emphasise the significant hydraulic diffusivity and horizontal anisotropy associated with the near-surface network of geological structures.

Structural and hydrogeological data suggest that the “hydraulic cage phenomenon” is centred geographically in the north-western part of the candidate area, i.e. to the northwest of the area where the gently-dipping deformation zone A2 is outcropping. We note in particular that the phenomenon continues under Lake Bolundsfjärden to the southeast. This suggests fairly impervious sediments at the bottom of the lake. Another important result from the interference testing is the hydraulic response in the gently dipping deformation zone A2 in borehole KFM02A at drill site 2. The depth to A2 in this “vertical” borehole is c. 400 m. The hydraulic responses observed in A2 in borehole KFM02A due to a precipitation event during the 2005 interference test at HFM01 are discussed in Appendix G. In Appendix H we discuss the hydraulic responses observed at depth in the target area in the inclined borehole KFM06A at drill site 6 during the 2006 interference test in HFM14.

The horizontal extent of the transmissive network of structures was hypothesised based on the occurrence of high transmissivities to correspond approximately to the domain for FFM02 but stretching north all the way to the Singö deformation zone (WNW001) as shown in Figure 3-31.

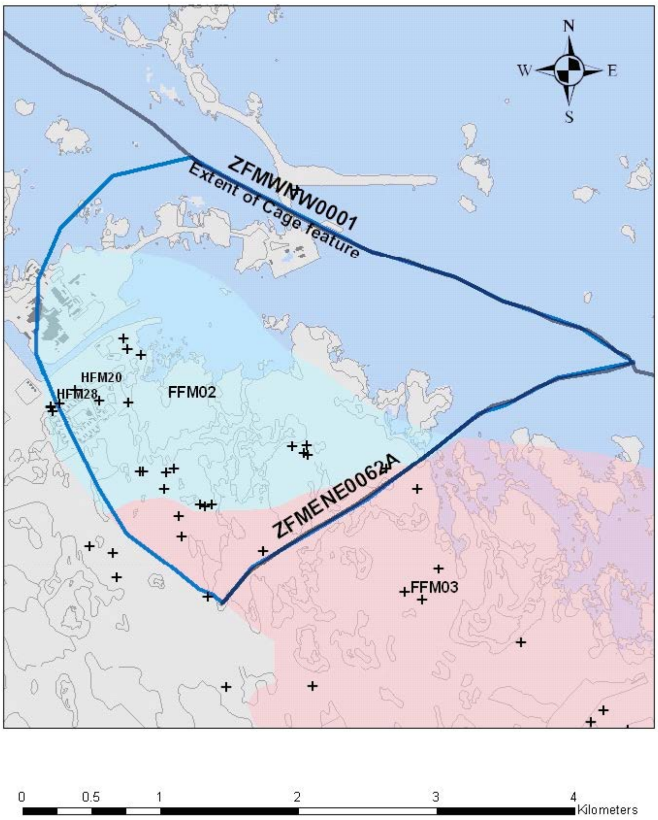

***Figure 3-31.** The hypothesised horizontal extent of the discrete features implemented in this study to model the “hydraulic cage phenomenon”. The crosses mark the positions of percussion and cored-drilled boreholes for which transmissivity measurements were available.*

The chosen bounds of the discrete features implemented in this study to model the "hydraulic cage phenomenon" are deformation zone WNW001 in the north, and deformation zone ENE0062A in the southeast. The rest of the features follow the boundary of the FFM02 domain with a modification so that the boundary passes between boreholes HFM20 and HFM28. The crosses in Figure 3-31 mark the positions of percussion-drilled and core-drilled boreholes for which transmissivity measurements are available.

In the south-eastern part of the candidate area the groundwater flow appears to be governed by a sequence of gently dipping deformation zones (A2–A8 and -B1) rather. These zones were first predicted by the reflection seismics and later confirmed by the drilling and the hydraulic testing of KFM02A and KFM03A, cf. /Follin et al. 2005/. Two hydraulic interference tests have been conducted in the hanging wall to test the interference between KFMA2 and KFM03 (A3) /Gokall-Norman et al. 2004/ and the interference between HFM18 and KFM03A (A4) /Gokall-Norman et al. 2006/ as indicated in Table B-5 in Appendix B. The interference tests reveal hydraulic connectivity across large distances in the hanging wall of A2, but that more efforts are needed to fully understand the structural-hydraulic connections between the zones.

3.9.3 The bedrock bordering the target volume

Strong bedrock anisotropy with high ductile strain and ductile structures that dip steeply to the south-west are prominent in the bedrock bordering the tectonic lens to the southwest of the target volume. The area corresponds to fracture domain FFM04 in Figure 3-12. Along the north-western and north-eastern margins of the tectonic lens strong bedrock anisotropy with high ductile strain and folded ductile structures are prominent. This area corresponds to fracture domain FFM05 in Figure 3-12.

FFM04 and FFM05 are investigated by several boreholes and for an illustration we comment here the findings in three nearby boreholes, KFM04A, KFM09A and KFM07A. The three borehole locations and their inclinations are readily appreciated in Figure 3-32.

KFM04A is located in the intensely fractured bedrock bordering the tectonic lens and is inclined 60° towards the lens. It enters the sparsely fractured bedrock inside the lens as it reaches repository depth (–400 m RHB 70).

KFM09A is located on the border of the lens and also inclined 60° but outwards; that is, it investigates the intensely fractured bedrock bordering the tectonic lens mainly.

KFM07A is located close to KFM09A but inside the tectonic lens. It investigates at first the intensely fractured superficial bedrock within the tectonic lens (FFM02) and then the sparsely fractured bedrock (FFM01) as it reaches repository depth. KFM07A approaches the intensely fractured bedrock bordering the lens at the very end (FFM05).

It is noted that KFM07A intercepts a fairly transmissive deformation zone at depth, see Figure 3-32 and /Follin et al. 2007b/. The groundwater composition at this elevation is fairly saline. To some extent the situation is the same in KFM09A and at about the same elevation. In fact, the highest salinities in the Forsmark area recorded so far come from these two boreholes. It is unclear whether the observations are typical for the intensely fractured bedrock bordering the target volume or if the high salinities are due to upconing of more saline water at depth during the drilling and flushing of the two boreholes. The chemical observations are treated further in Section 3.17.

3.9.4 The bedrock at repository depth

Figure 3-33 shows fracture transmissivity data versus depth in boreholes KFM01A and KFM03A. The transmissivity data are coloured with regard to the identified fracture domains and deformation zones. These two boreholes are both located along the longitudinal axis of the tectonic lens but represent quite different structural conditions, cf. Figure 3-10 and Figure 3-16. Borehole KFM01A is located in the footwall (FFM01) and borehole KFM03A in hanging wall (FFM03) bedrock of deformation zone A2.

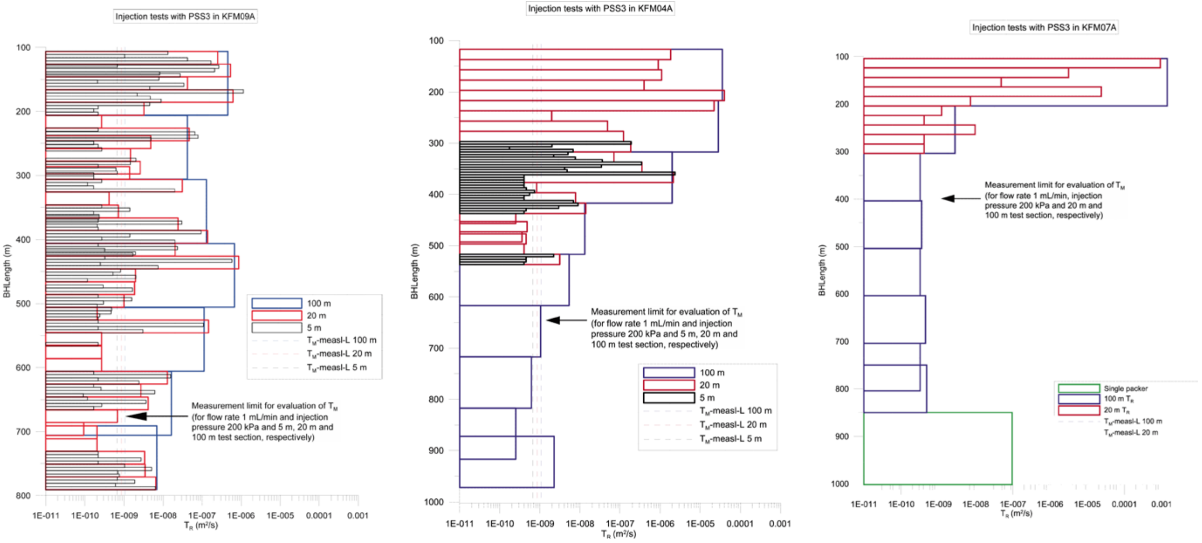

Figure 3-32. *Hydraulic comparison of PSS transmissivity data gathered in the bedrock bordering the target volume the bedrock inside the target volume. Left: KFM09A; Middle: KFM04A; Right: KFM07A. Note that the PSS measurements are made with three different spacings (sections) between the inflatable packers; 100 m (blue), 20 m (red) and 5 m (black). A telescopic measurement strategy was used; that is, if a 100 m section is impervious (meaning that T_{100m} ≤ the measurement limit) no further testing is made with 20 m sections in that interval. In KFM09A this procedure is repeated for the 20 m vis-à-vis 5 m sections. In conclusion, all 100 m intervals in KFM04A and KFM07A that are without 20 m interval data are regarded as impervious. In contrast, all 100 m section and almost all 20 m sections in KFM09A are pervious. This example demonstrates the hydraulic difference between the intensely fractured bedrock bordering the target volume and the bedrock within the latter.*

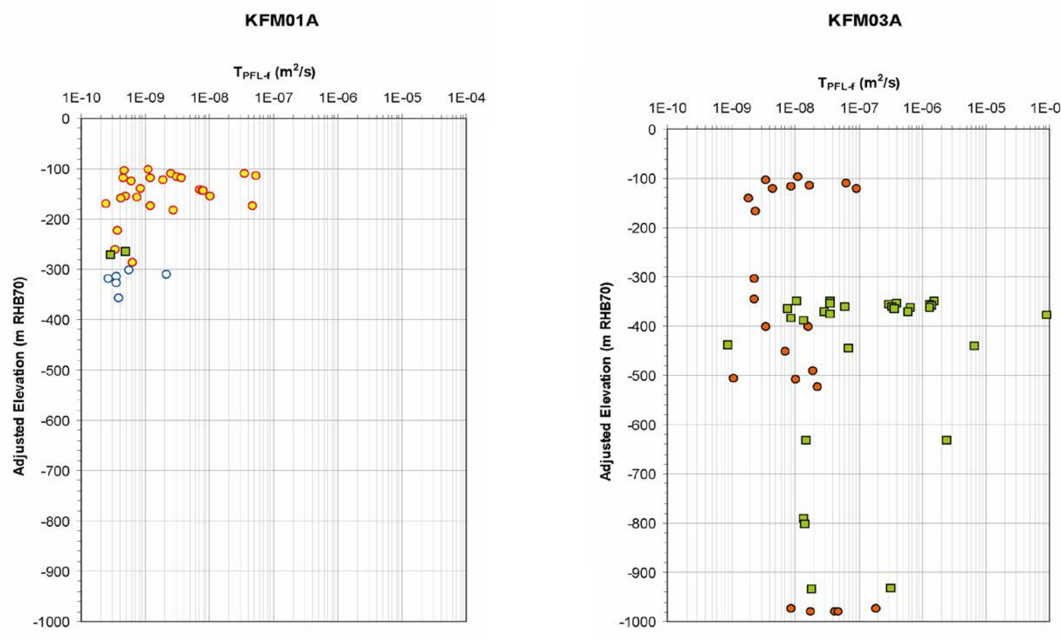

Figure 3-33. *Fracture transmissivity data from boreholes KFM01A and KFM03A, see cf. Figure 3-14. Yellow/red dots denote flowing fractures associated with FFM02, white/blue dots denote flowing fractures associated with FFM01, orange/black dots denote flowing fractures associated with FFM03, and green/black squares denote flowing fractures associated with deformation zones, see /Follin et al. 2007b/. Reproduced from /Follin et al. 2007b/.*

Below –400 m RHB 70 in FFM01 the rock stresses are inferred to be twice as high compared to the stresses in FFM03 at this elevation /Martin 2007/. Furthermore, there are far fewer flowing fractures in fracture domain FFM01 compared to the conditions in fracture domains FFM03 (and FFM02). It should be noted that FFM03 is intersected by a series of high-transmissive, gently-dipping deformation zones, whereas the open fractures within the steeply-dipping deformation zones intersected by KFM01A below –400 m RHB 70 are found to be as impervious as the intact rock. Furthermore, the steeply-dipping deformation zones are oriented at a high angle (NE to ENE) to the maximum principal stress (NW).

The moderate decrease in fracture transmissivity with depth in the bedrock between the deformation zones, see Table 3-5, suggests that it is the significant decrease with depth in the observed intensity of flowing fractures that governs the groundwater flow at depth and not the transmissivity. For instance, below –400 m RHB 70 in FFM01 there is less than one flowing fracture per hundred metres. The fracture intensities shown in Table 3-4 are so-called Terzaghi corrected /Terzaghi 1965/.

The left image in Figure 3-34 shows an example of the rock quality observed at repository depth (400–700 m depth). The large number of unbroken core pipes supports the few hydraulic observations made with the PFL-f method. The right image in Figure 3-34 shows the envisaged conceptual model of the network of flowing features in FFM01 and FFM06. The present-day groundwater flow in the target volume at repository depth in FFM01 and FFM06 is imagined to be formed by ordinary sized NS-NE steeply-dipping fractures and, relatively speaking, larger gently-dipping fractures. The plots shown in Appendix C suggest, very roughly, that there is, on the average, “one potentially flowing 4 m radius, NS steeply-dipping fracture every 100 m”, “one potentially flowing 2 m radius, NE steeply-dipping fracture every 100 m” and “one potentially flowing 40 m radius, gently-dipping fracture every 100 m”. Alternatively, the spacing between potentially flowing fractures of 100 m radius is, on average, 0.8 km, 2 km and 0.2 km for the NS set, NE set and the HZ set, respectively. It is envisaged that an open repository (here shown as deposition drift with canister holes) will contribute to the fracture connectivity since the natural system is so poorly connected.

3.10 Hydraulic conductor domain (HCD) model

The assignment of hydraulic properties to the deterministically modelled deformation zones suggested by /Follin et al. 2007b/ is used here as initial input to GWF modelling undertaken. Clearly, the observations of strong vertical trends, anisotropy, intra-zone and inter-zone spatial heterogeneity create a complex situation to model. Therefore, we started with a simplified model and then gradually increased the complexity and scope of the model once the effects of the primary features of the deformation zones had been quantified.

Table 3-5. Values of the minimum and maximum PFL-f fracture transmissivities (PFL-f T) for the three fracture domains FFM01, FFM02 and FFM03. Based on information reported by /Follin et al. 2007b/.

Fracture domain	FFM01			FFM02	FFM03	
Elevation, m RHB 70	–100 to –200	–200 to –400	–400 to –1,200	–100 to –200	–100 to –400	–400 to –1,200
PFL-f T_{min}, m^2/s	$2.5 \cdot 10^{-10}$	$2.7 \cdot 10^{-10}$	$6.2 \cdot 10^{-10}$	$2.5 \cdot 10^{-10}$	$1.9 \cdot 10^{-9}$	$1.1 \cdot 10^{-9}$
PFL-f T_{max}, m^2/s	$4.7 \cdot 10^{-5}$	$1.8 \cdot 10^{-7}$	$8.9 \cdot 10^{-8}$	$7.3 \cdot 10^{-6}$	$6.8 \cdot 10^{-7}$	$1.9 \cdot 10^{-7}$

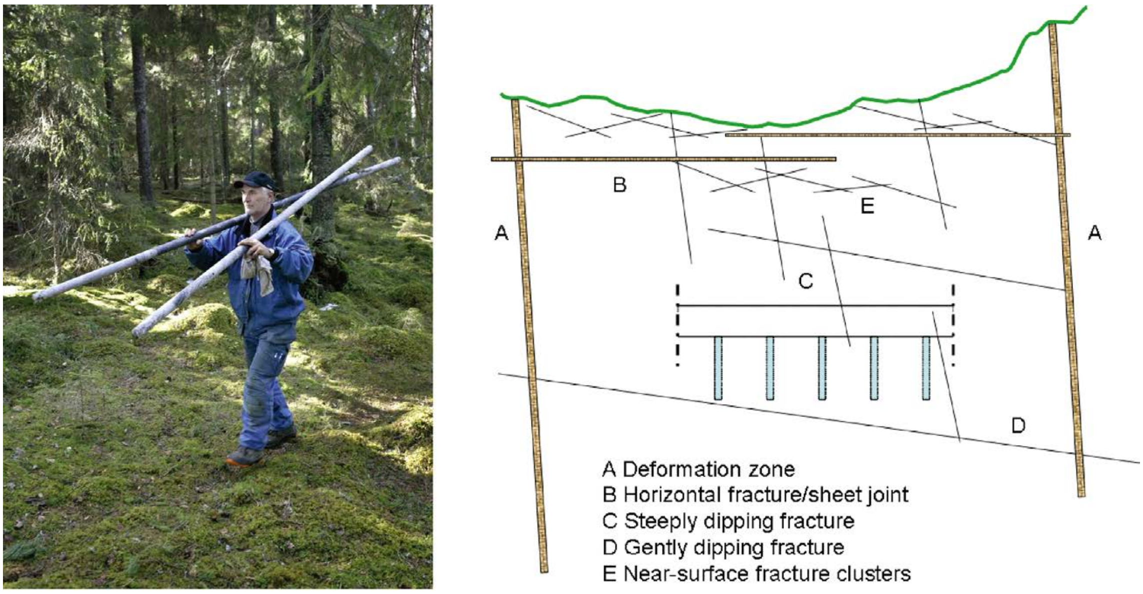

a **b**

Figure 3-34. *Left: The bedrock at repository depth (< –450 m RHB 70) in the north-western part of the tectonic lens is sparsely fractured by open fractures. About 200 unbroken three-metre long rock cores have been gathered during the coring drillings (total core length c. 15 km). Right: The present-day groundwater flow in the target volume at repository depth in FFM01 and FFM06 is imagined to be close to the percolation threshold. The pattern of flow paths is probably channelised in a network consisting of short NS-NE steeply-dipping fractures and long gently-dipping fractures.*

3.10.1 Initial deterministic model

Since there are hydraulic measurements in many of the zones an appropriate initial model is a deterministic one, that honours the values measured in the zone, but is also consistent with the depth trend seen generally within the data. The following algorithm was applied to assign the transmissivity of the HCD /cf. Follin et al. 2007b/:

1. An exponential model for the vertical heterogeneity in transmissivity is used for all deformation zones regardless of orientation:

   $$T(z) = T(0)\ 10^{z/k} \qquad (3\text{-}1a)$$

   where $T(0)$ is the transmissivity at zero elevation and k is the depth at which the transmissivities have declined an order of magnitude.

   We use here a linear model of the common logarithm of Equation (3-1a):

   $$\log(T(z)) = (z - m) / k \qquad (3\text{-}1b)$$

   where k is derived from the slope of the red line denoted by "T-max" in Figure 3-19:

   $$T_{max}(0\text{ m}) = 4 \cdot 10^{-3}\text{ m}^2\text{/s}\ ;\ T_{max}\ (-1{,}000\text{ m}) = 2 \cdot 10^{-7}\text{ m}^2\text{/s} \rightarrow k = 232.50\text{ m} \qquad (3\text{-}2)$$

2. The value of m for the red line is readily computed from $T_{max}(0\text{ m}) = 4 \cdot 10^{-3}\text{ m}^2\text{/s}$:

   $$m_{max} = -\ 232.50 \log(4 \cdot 10^{-3}) = 557.53 \qquad (3\text{-}3)$$

3. For any deformation zone in which a hydraulic test was performed at elevation z_{obs}, the k-value is fixed as given in Equation (3-2) using the measurement value $\log(T(z_{obs}))$ to give a corresponding m-value as calculated from Equation (3-1):

   $$m_{obs} = z_{obs} - k \log(T_{obs}) \qquad (3\text{-}4)$$

If there are several measurements in the same zone, then the arithmetic mean *m*-value is used within that zone.

The resultant model is used to assign properties to the hydrogeological model. Where the simulated hydraulic conductivities in borehole intervals associated with deformation zone intercepts is significantly different to that interpreted from the Pipe string system (PSS) data, then the K-value and width of the interval are adjusted manually. For the deformation zones not tested hydraulically, the zone orientation category is used to condition the values assigned. For instance, for all NNE deformation zones not tested hydraulically, the arithmetic mean *m*-value of the tested NNE deformation zones is used.

Since many measured HCD transmissivities are small or below the detection limit, the above local conditioning process results in conductivities at depth below both the detection limit and values assigned to the HRD. Since conceptually, HCD are expected to give hydraulic conductivities equal or greater than the surrounding rock, then a minimum hydraulic transmissivity is assigned. The minimum hydraulic conductivity for the HRD outside the fracture domains is set to 10^{-9} m/s, and so a minimum transmissivity of $b \cdot 10^{-9}$ is used for regional and 'regional and local' HCD, where *b* is the hydraulic thickness[3]. For the local and minor zones, a minimum transmissivity of 10^{-10} m^2/s is used. The corresponding minimum hydraulic conductivity for the HRD within the fracture domains is 10^{-11} m/s.

The resulting property model is shown in Figure 3-35. Here, the zones are coloured by the hydraulic conductivity within the zones and drawn as volumes to show their assigned hydraulic width. The depth dependency is clearly apparent. A final step would be to add lateral heterogeneity within each zone, but this is not performed until stage 2.3. Because the heterogeneity away from the measurement boreholes is undetermined, this necessarily requires a stochastic modelling approach using at least several realisations.

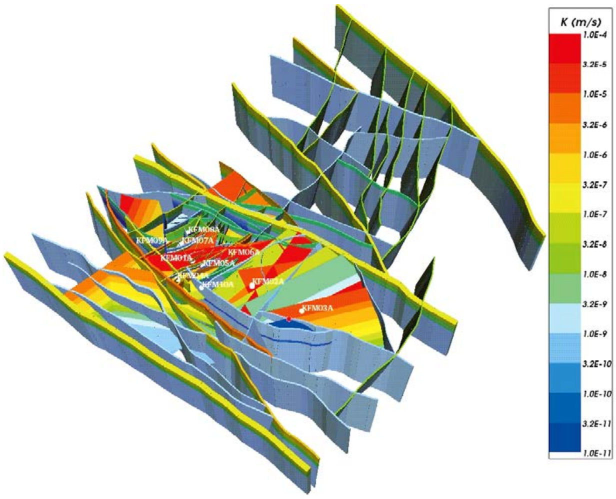

Figure 3-35. *Implementation of hydraulic property model on regional and local scale deterministic deformation Zones (HCD). Each section of fracture is coloured by its hydraulic conductivity and drawn with their defined hydraulic thicknesses. The properties of the deformation zones were represented as step-wise depth variations divided into 100 m thick intervals with homogeneous properties.*

---

[3] The hydraulic thickness of the zones was set to be equal to the interpreted geological thickness, although it has been concluded that the hydraulic response associated with a zone often only corresponded to one or two narrow intervals logged by the PFL-f method /Follin et al. 2007b/.

3.10.2 Spatial heterogeneity and uncertainty

Data suggests that lateral heterogeneity within a zone could lead to 2–4 orders of magnitude variability in transmissivity. This is not as large as the vertical heterogeneity. However, lateral heterogeneity could lead to more vertical flow channelling, whereas the current deterministic model with only vertical heterogeneity will tend to force flow into horizontal channels, and hence stochastic HCD models could perturb the flow pattern in the deformation zones to a moderate extent. The notion of HCD heterogeneity was addressed already in version 1.2 and found to be important for the groundwater flow field /Follin et al. 2005/. Stochastic HCD modelling, however, will be reserved until stage 2.3, while here the focus will be on quantifying how well the deterministic HCD model can be used to simulate field data, and broader issues such as modelling the fracture domains, the Quaternary deposits and the palaeohydrological evolution.

In the ECPM approach, properties of the HCD are represented by an implicit method by adjusting the properties of the finite-elements crossed by the volume of the deformation zone to represent the effective hydraulic conductivity of the combined background rock and the zone. The hydraulic conductivity is implemented as a full symmetric tensor, so that anisotropy along the plane of the zone can be represented. If a zone is thicker than the element size, then the properties in elements surrounding the central plane of the zone will be modified, whereas if the zone is thinner than element size, the transmissivity of the zone will be smeared over the elements that the zone crosses. An example of the resolution of the HCD on the finite-element mesh is shown in Figure 3-36. There is a strong contrast in hydraulic conductivity between the major HCD and the rock in between, which as shown in Figure 3-36 seems to be appropriately represented by the 20 m grid used for the candidate area.

As well as an update to the deformation zone model in terms of its geological description, many new concepts have been introduced into the description of their hydrogeological properties. A number of general trends have been identified such as depth dependency and directional dependency within a zone. These trends have been implemented in the numerical model, but where data is available from single-hole interpretations of transmissivity or drawdowns in the interference test, there is scope for conditioning the properties of particular deformation zones to improve the agreement with measurements. Stochastic spatial heterogeneity is not considered

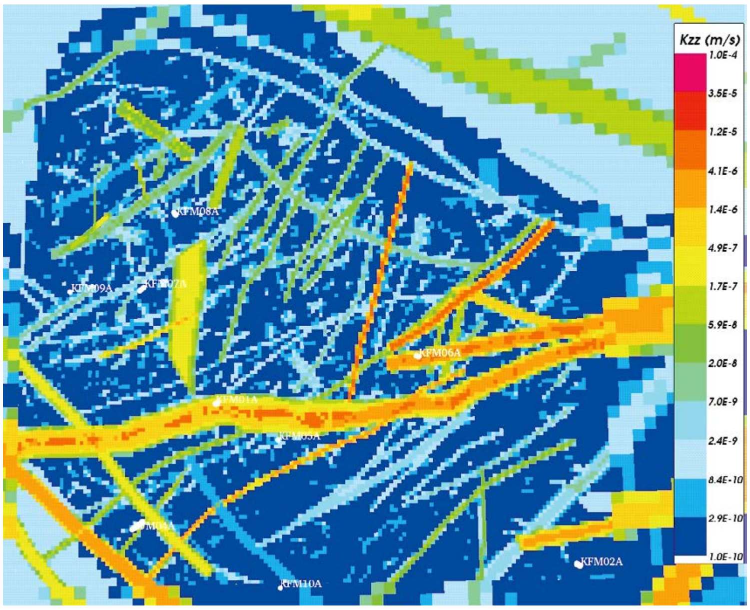

Figure 3-36. An example of the representation of the HCD using an implicit method of hydraulic property assignment. Hydraulic conductivity is shown here on a slice at –50 m RHB 70 in an area of approximately 3 km by 3 km centred on the north-western part of the candidate area.

at this stage. Instead, the properties of the deformation zones are represented as step-wise depth variations divided into 100 m thick intervals with homogeneous properties. The hydraulic conductivity within these depth intervals is calibrated where data is available. In broad terms, the objectives were to test (*i*) whether the specification of the hydraulic properties in the conceptual model gave simulation results consistent with the transmission of the HFM14 interference test disturbance and the palaeohydrological evolution, and (*ii*) the sensitivity of the calibration to the properties of particular key zones such as the gently-dipping A2 zone.

3.10.3 Horizontal sheet joints

In addition to the deformation zones, deterministic structures were added to the HCD model to represent the horizontal sheet joints. The sheets joints are here referred to as "cage features" since they can act to flatten hydraulic gradients within the bedrock, and reduce vertical infiltration of meteoric water (cf. Section 3.9.2). In the previous study /Follin et al. 2007a/, the impact of a single, thin and homogeneous "cage feature" of about $5 \cdot 10^{-4}$ m^2/s was studied. Here, more effort was made to honour the available hydraulic data for the upper bedrock. Still, the computational grid geometry was idealised into three parallel layers within the intervals 0 to –50, –50 to –100 and –100 to –150 m RHB 70 to represent the horizontal sheet joints. In the model implementation, three 1 m thick layers are included at approximately the mid-elevations of these three intervals running parallel to the topographic surface to avoid outcropping on the top surface, cf. Figure 3-21. The three layers were given the form of triangles bounded to the northeast by the Singö deformation zone, (WNW0001), to the southeast by the NE0062A deformation zone, and to the west by the expression of the sheath fold structure in rock domains 32 and 44 as shown in Figure 3-31. The next decision is how to apply hydraulic properties to the three layers. Hydraulic data for the near-surface is available from a combination of PFL-f, PSS and HTHB data, all of which have been interpreted to identify intervals with anomalously high flows. The data were used as follows:

- The total transmissivity in each borehole in the three intervals 0 to –50, –50 to –100 and –100 to –150 m RHB 70 is summed.
- Some data are in the same region as mapped gently-dipping deformation zones; they are still assumed to contribute to the "hydraulic cage phenomenon". That is, we do not exclude a simultaneous occurrence of outcropping deformation zones and horizontal fractures/sheet joints.
- Some boreholes do not have any flow in a particular depth interval, or at least the flow is below the detection threshold of the pumping test technique used. They are assigned a default transmissivity of 10^{-7} m^2 s^{-1} (relatively low for this depth).
- If a core-drilled borehole did not record any PFL-f or PSS data it is excluded from the analysis. The reason for the different treatment is that the core-drilled boreholes are in general cased down to approximately –100 m RHB 70, thus excluding any chance for data acquisition.

The resulting distribution of transmissivity data for the three layers is summarised in Appendix I. The values suggest a high degree of heterogeneity in all three layers. Using these values, the distribution of transmissivity is interpolated for each of the three layers. There are various approaches one might take to producing the interpolated values such as Kriging, nearest neighbour or using an inverse distance weighting. Variograms calculated from the data do not suggest a coherent correlation structure and hence a Kriging approach is not supported. For simplicity, a nearest neighbour approach is used for the final model as this best preserved the varying scale of heterogeneity observed in the measurements and honoured the data at the measurement points. Illustrations of how this affected the property assignment on the finite-element grid is shown in Figure 3-37 and Figure 3-38. The geostatistical analyses undertaken are reported in Appendix I. In the following, the three layers are referred to as "cage features".

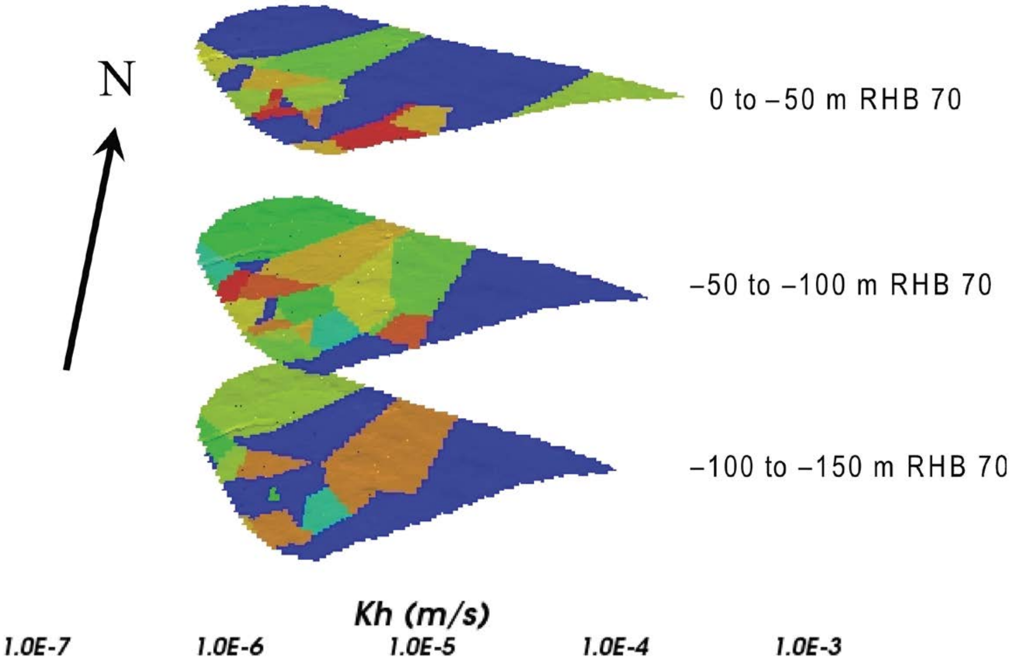

Figure 3-37. *Visualisation of the three layers forming the "cage features". The vertical scale has been exaggerated. The colour scale refers to the horizontal conductivity (m/s).*

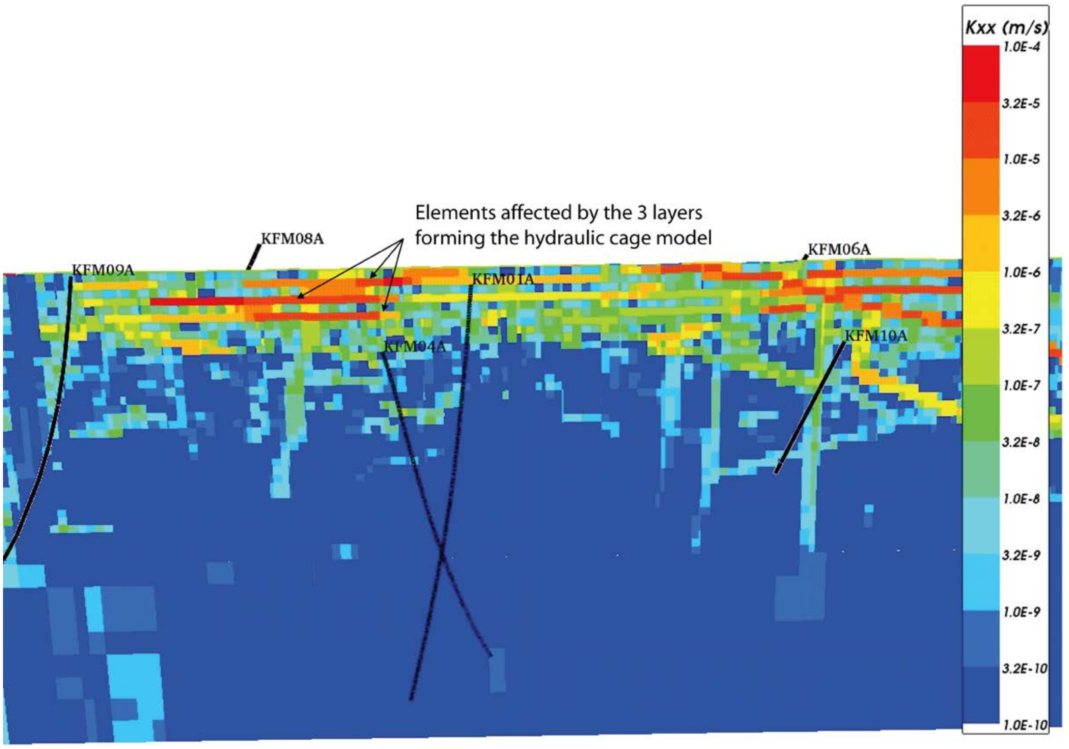

Figure 3-38. *An illustration of the horizontal hydraulic conductivity in CONNECTFLOW on a N115E vertical slice through the target volume. Note the effect of the three layers forming the hydraulic "cage features".*

3.11 Hydraulic rock domain (HRD) model

The HRD correspond to the six defined fracture domains, FFM01–FFM06, together with the remaining rock in which there is no borehole information. Each finite-element with the ECPM is assigned to either of the FFM or the remaining rock based on a 3D geological model, as illustrated in Figure 3-39.

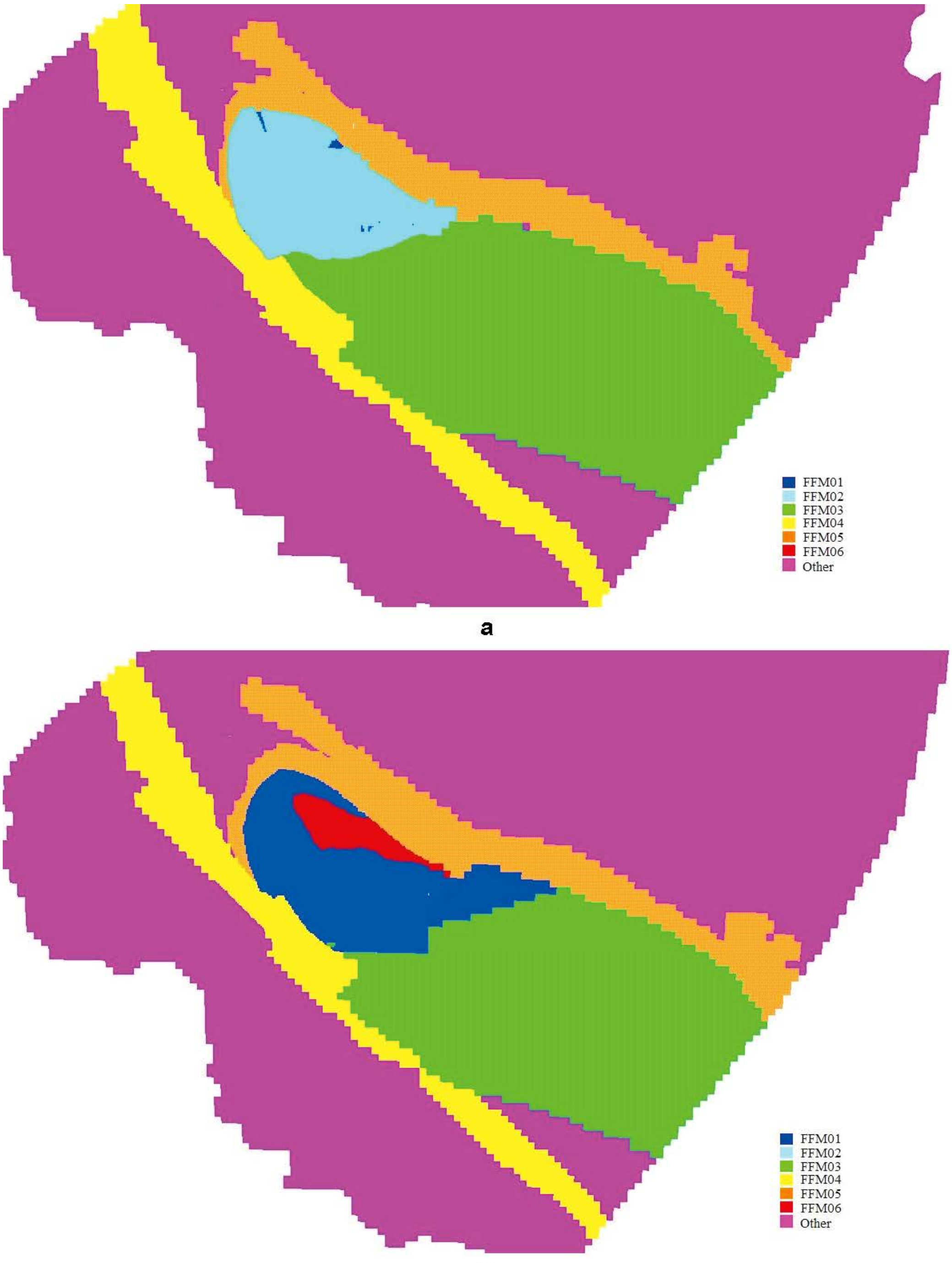

Figure 3-39. *The implementation of fracture domains, FFM01–FFM06 in the ECPM model. Horizontal slices through the fracture domains are shown at –30 m RHB 70 (a) and at –500 m RHB 70 (b). Only the southern half of the regional model is shown. Definitions of the fracture domain volumes were supplied on a 20 m regular grid within the local model area and on a 100 m grid elsewhere.*

3.11.1 Hydro-DFN

Based on borehole core-, image-logging and PFL-f hydraulic testing, a Hydro-DFN model has been interpreted for fracture domains FFM01, FFM02 and FFM03 /Follin et al. 2007b/. The Hydro-DFN is defined in terms of a statistical parameterisation of fracture intensity, orientation probability distribution functions (PDF), fracture length PDF, and alternative transmissivity relationships. Additional refinements of the fracture domain volumes were recommended in /Follin et al. 2007b/ according to depth trends apparent in the frequency and magnitudes of flowing features measured in the PFL-f tests. The lengths of borehole logged for constructing these models was 5,156 m for FFM01, 366 m for FFM02, and 1,334 m for FFM03. Only 100–200 m of borehole length was logged for FFM04–FFM06, which was considered too little to build a quantitative stochastic Hydro-DFN model for these fracture domains. FFM06 is within the candidate area, but has very little data as of data freeze 2.2. Based on the description of the fracture domains it is assumed that FFM06 can be modelled by analogy to the Hydro-DFN in FFM01. FFM04 and FFM05 lie in the periphery of the candidate area. Based on the limited statistical data available, FFM05 seems to be similar to FFM03, while FFM04 is of slightly higher hydraulic conductivity. Therefore, FFM05 is assumed to have the same Hydro-DFN properties as FFM03, and FFM04 also has the same properties apart from having a transmissivity twice that of FFM03.

Using the Hydro-DFN model for the six fracture domains, realisations of the regional-scale DFN model are generated for the purpose of deriving equivalent hydraulic and transport properties for an ECPM. The Hydro-DFN model assumes statistical homogeneity within each fracture domain and is based on a Poisson point process, but the particular locations, lengths, orientations and transmissivities of fractures vary between realisations. Since each ECPM model is derived based on an underlying DFN realisation, then the ECPM approach is also stochastic. However, as with the HCD, we only consider single realisations in this work. Sensitivities to stochastic variability will be quantified in stage 2.3.

For the HRD rock outside the mapped fracture domains, there is no fracture information available, and so a simplified property assignment is used to specify homogeneous continuum porous medium (CPM) properties. Approximate values for this rock are taken from hydraulic single-hole tests in deep boreholes at Finnsjön /Andersson et al. 1991/ using their results given for the geometric mean for 3 m PSS tests in the bedrock between deformation zones, see Table 3-6. Again, a depth dependency is suggested by the data, which is simplified here to a step-wise model consistent with the depth zonations used in FFM01 /cf. Follin et al. 2007b/.

The statistical parameterisations of the Hydro-DFN for FFM01–06 are tabulated in Appendix F. As an example, data for FFM01 and FFM06 are repeated in Table 3-7. The Hydro-DFN parameterisation comprises data for the intensity, orientation, length and transmissivity parameters. These parameters are used to generate a realisation of a Hydro-DFN model on the regional scale. A DFN is generated using the same grid as used in the ECPM model. The algorithm then: loops over each grid element; checks which fracture domain it is in; generates fractures centred within that element according to the fracture statistics for the corresponding fracture domain. Fractures may extend in to neighbouring elements depending on the fracture size value sampled. For practical reasons, only fractures with radii between 5.64–564 m are generated on the regional-scale since this gives about five million fractures. However, since large fractures tend to be responsible for the large scale connections for sparse networks, then it is expected this

Table 3-6. Homogeneous hydrogeological properties used outside the FFM based on Table 4-8 in /Andersson et al. 1991/.

Elevation (m RHB 70)	HRD properties outside FFM K (m/s)	Kinematic porosity
> –200	$1 \cdot 10^{-7}$	$1 \cdot 10^{-5}$
–200 to –400	$1 \cdot 10^{-8}$	$1 \cdot 10^{-5}$
< –400	$3 \cdot 10^{-9}$	$1 \cdot 10^{-5}$

Table 3-7. Description of Hydro-DFN parameters for FFM01 and FFM06 with depth dependency above –200 m, –200 m to –400 m and below –400 m RHB 70 /Follin et al. 2007b/.

Fracture domain (m RHB 70)	Fracture set name	Orientation set pole: (trend, plunge), conc.	Size model, power-law (r_0, k_r) (m, –)	Intensity ($P_{32,open}$) valid size interval: (r_0, 564 m) (m^2/m^3)	Transmissivity model Eq. (11-3) Eq. (11-2) Eq. (11-4) in /Follin et al. 2007b/
FFM01 > –200 m	NS	(292, 1) 17.8	(0.038, 2.50)	0.073	Semi-correlated: $(a,b,\sigma) = (6.3\cdot10^{-9}, 1.3, 1.0)$; Correlated: $(a,b) = (6.7\cdot10^{-9}, 1.4)$; Uncorrelated: $(\mu, \sigma) = (-6.7, 1.2)$
	NE	(326, 2) 14.3	(0.038, 2.70)	0.319	
	NW	(60, 6) 12.9	(0.038, 3.10)	0.107	
	EW	(15, 2) 14.0	(0.038, 3.10)	0.088	
	HZ	(5, 86) 15.2	(0.038, 2.38)	0.543	
FFM01 –200 m to –400 m	NS	As above	(0.038, 2.50)	0.142	Semi-correlated: $(a,b,\sigma) = (1.3\cdot10^{-9}, 0.5, 1.0)$; Correlated: $(a,b) = (1.6\cdot10^{-9}, 0.8)$; Uncorrelated: $(\mu, \sigma) = (-7.5, 0.8)$
	NE	As above	(0.038, 2.70)	0.345	
	NW	As above	(0.038, 3.10)	0.133	
	EW	As above	(0.038, 3.10)	0.081	
	HZ	As above	(0.038, 2.38)	0.316	
FFM01 < –400 m	NS	As above	(0.038, 2.50)	0.094	Semi-correlated: $(a,b,\sigma) = (5.3\cdot10^{-11}, 0.5, 1.0)$; Correlated: $(a,b) = (1.8\cdot10^{-10}, 1.0)$; Uncorrelated: $(\mu, \sigma) = (-8.8, 1.0)$
	NE	As above	(0.038, 2.70)	0.163	
	NW	As above	(0.038, 3.10)	0.098	
	EW	As above	(0.038, 3.10)	0.039	
	HZ	As above	(0.038, 2.38)	0.141	

truncation is adequate for considering regional-scale groundwater flow. However, it is noted that smaller scale fractures need to be considered in safety assessment calculations.

An example realisation of the regional Hydro-DFN model is shown in Figure 3-16. An open fracture is defined as connected if it is connected via a network of fractures to the top surface boundary. The removal of isolated fracture clusters reduces the fracture count from about 5 million to about 1.5 million, and the total fracture surface area from $2.2\cdot10^9$ m^2 to $1.4\cdot10^9$ m^2.

The methodology used to generate the ECPM model is:

- generate all fractures according to the Hydro-DFN parameters,
- perform a connectivity analysis on the regional scale to identify network clusters connected to the top surface of the model,
- remove also isolated or dead-end clusters, and
- derive ECPM properties for each grid element for the remaining fractures.

The isolated fractures are removed based on a regional-scale connectivity analysis, so that ECPM properties are derived only for the network of fractures that contributes to regional-scale flow. If hydraulic conductivity were calculated for an element where connectivity were calculated on the scale of the element, then a higher hydraulic conductivity would probably result, and may be quite scale dependent.

The resulting hydrogeological property assignment for the ECPM model is illustrated by Figure 3-40 through Figure 3-42, which show the distribution of East-West horizontal hydraulic conductivity on three different horizontal slices chosen to cut through three different elevations of FFM01. The figures show the results of the combined HRD and HCD features. These slices show the clear reduction in hydraulic conductivity in both the HCD and the HRD in between. They also show that the finer grid discretisation within the 20 m scale embedded grid leads to a more heterogeneous spatial distribution since it is able to resolve many individual features, while the coarser grid tends to give more homogenised fracture network properties on the scale of either 60 m or 100 m elements.

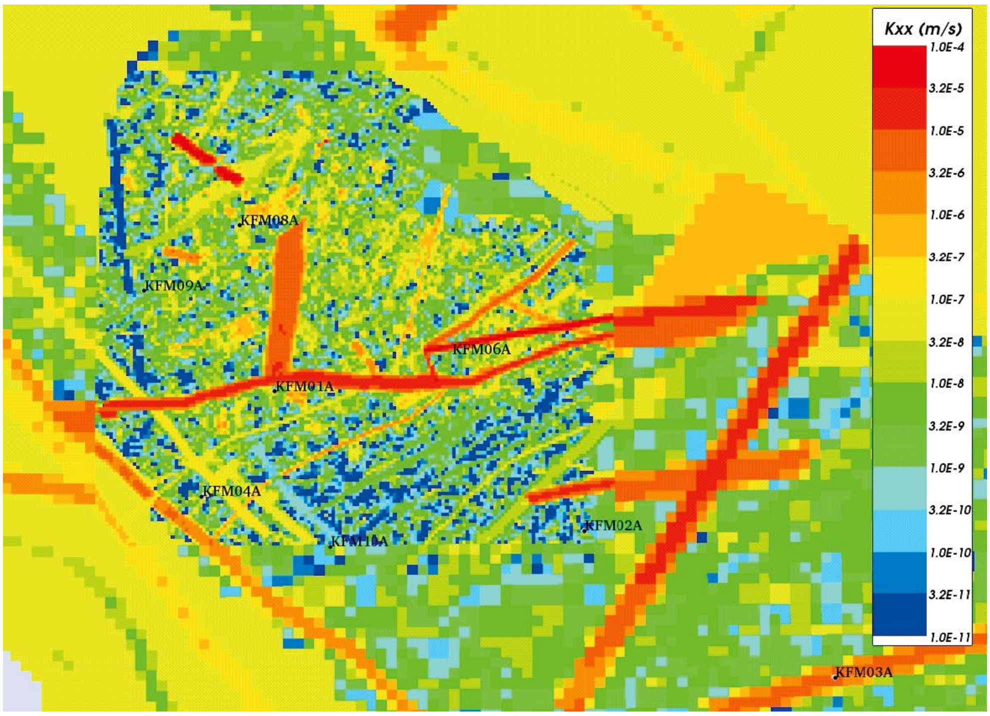

Figure 3-40. *An example of the distribution of hydraulic conductivity for a realisation of the ECPM model. A horizontal slice is shown at –20 m RHB 70. The hydraulic conductivity tensor is potentially anisotropic, but only the E-W diagonal component is shown here. Properties are more heterogeneous within the finer scale embedded grid.*

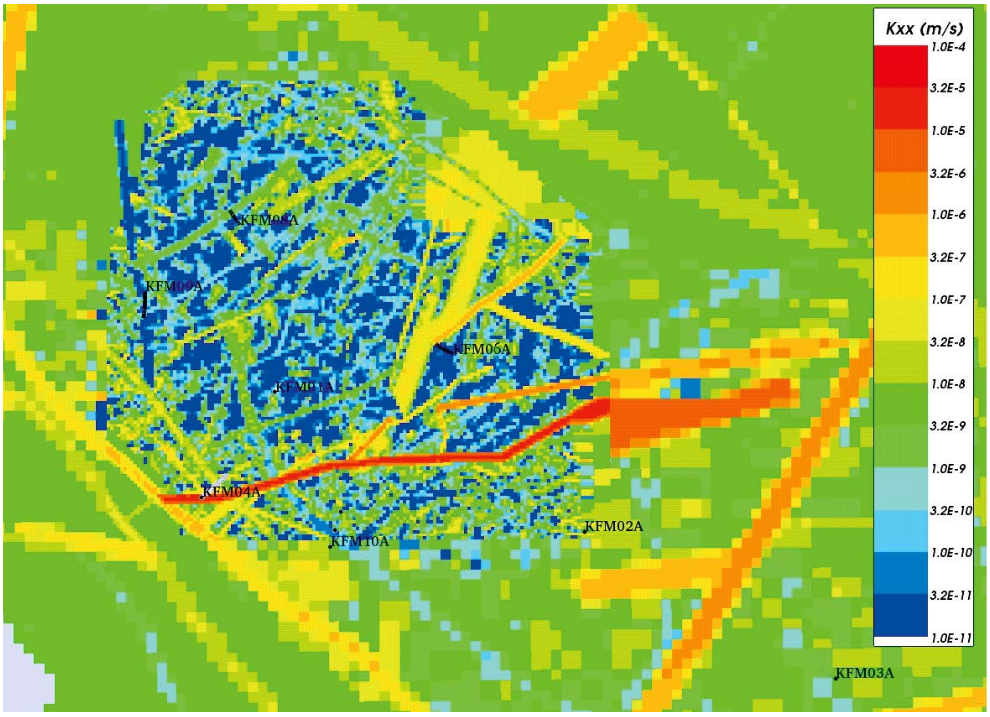

Figure 3-41. *An example of the distribution of hydraulic conductivity for a realisation of the ECPM model. A horizontal slice is shown at –250 m RHB 70. The hydraulic conductivity tensor is potentially anisotropic, but only the E-W diagonal component is shown here. Properties are more heterogeneous within the finer scale embedded grid.*

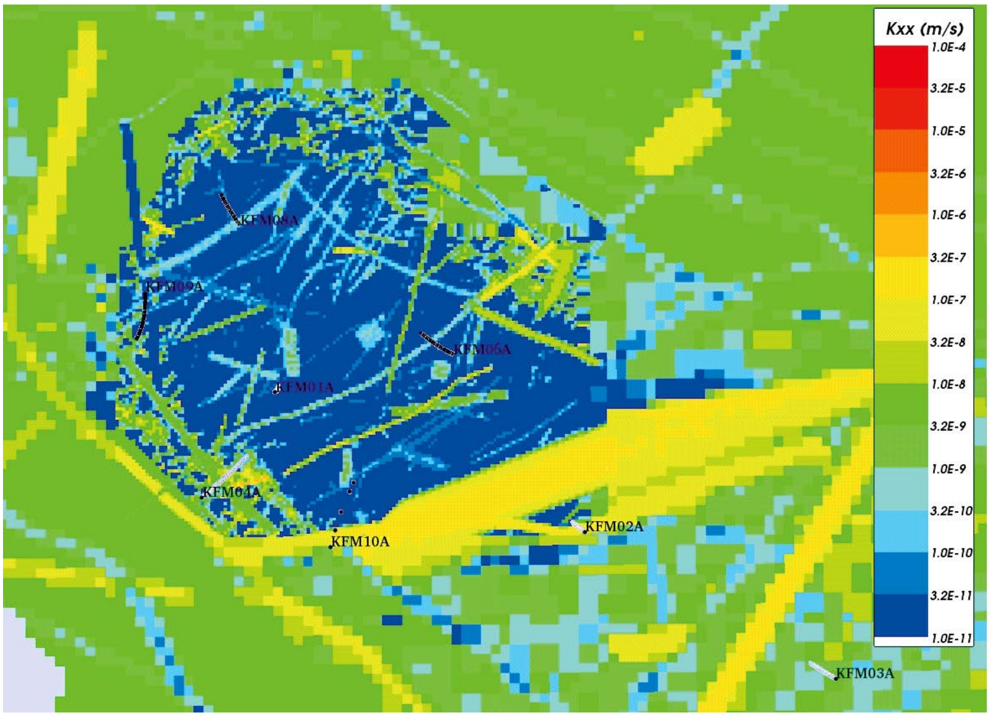

Figure 3-42. *An example of the distribution of hydraulic conductivity for a realisation of the ECPM model. A horizontal slice is shown at –450 m RHB 70. The hydraulic conductivity tensor is potentially anisotropic, but only the E-W diagonal component is shown here. Properties are more heterogeneous within the finer scale embedded grid.*

3.11.2 Uncertainties

Two of the main uncertainties inherited from the Hydro-DFN model are the hydraulic anisotropy and the fracturing in the top 100 m of bedrock. Although the Hydro-DFN model in principle explicitly represents the orientation of fracturing according to the definition of fracture sets and the Univariate Fisher distribution of angles, the Hydro-DFN derived in stage 2.2 applies the definition of fracture sets and Fisher angle PDF concluded in version 1.2, and hence does not fully condition the fracture orientations to all available data. Suggestions for alternative Fisher orientation distributions were made by /Follin et al. 2007b/ for updating the fracture set definitions and parameters for Fisher angle PDF as given in Table 3-8. Significant differences compared to the distributions shown in Table 3-7 are the higher Fisher concentration in the sub-horizontal (HZ) set and the convergence of the NS and NE sets, which will lead to stronger horizontal versus vertical anisotropy of flow, and toward NNE within the horizontal directions.

In addition, the PFL-f tests used to calibrate the DFN hydraulic parameters are performed in steeply dipping boreholes (60–90°), so they are largely measuring radial horizontal flow. Hence, our understanding of vertical flows through the fracture network is more uncertain. However, vertical flows will affect the interference test since responses are measured at various depths in some deep boreholes, and other indications are given to the vertical movement of solutes by the hydrochemical data.

Simple ways to quantify the sensitivities to anisotropy are to alter the vertical component of hydraulic conductivity tensor obtained in the ECPM model or to change the Fisher angle PDF in the underlying Hydro-DFN model using Table 3-8 to create a network with a more concentrated sub-horizontal set.

Table 3-8. A suggestion for alternative hard sector set definitions and recommended Univariate Fisher distribution parameters based on open fractures in borehole data belonging to data freeze 2.2. Reproduced from /Follin et al. 2007b/.

Set	Orientation Fisher distribution (trend, plunge), concentration	Trend	Plunge	Dip	Strike
1 NS	(292, 1) 17.8	90–130, 270–310	0–40	50–90	0–40, 180–220
2 NE	(326, 2) 14.3	130–170, 310–350	0–40	50–90	40–80, 220–260
3 NW	(60, 6) 12.9	30–90, 210–270	0–40	50–90	120–180, 300–360
4 EW	(15, 2) 14.0	350–30, 170–210	0–40	50–90	80–120, 260–300
5 HZ	(5, 86) 15.2	0–360	40–90	0–50	0–360

3.12 ECPM Solute transport model

In the CONNECTFLOW model of solute transport, the total connected pore-space available to solutes is divided between a mobile porosity, known as the “kinematic porosity”, in which both groundwater flow and solute transport takes place, and an immobile porosity, referred to as “diffusion accessible porosity”, in which only solute transport through diffusive exchange with the kinematic porosity is considered. In the context of Forsmark, the kinematic porosity may be interpreted as the open fracture channels that are connected and responsible for the circulation of groundwater, and the diffusion accessible porosity is the rest of the total connected porosity including inter-granular porosity and micro-fractures. The diffusion accessible porosity may also include contributions from fractures in which there is negligible flow (which would typically be a subset of the smaller fractures) and from regions of nearly immobile water in the larger fractures (resulting from constrictions in fracture aperture or the presence of gouge material). In practice, it may be difficult to estimate either type of porosity accurately by direct measurement, and hence one purpose of the solute transport modelling of natural tracers is to confirm the interpretation of transport properties.

In the mobile porosity, groundwater flow is modelled and solute transport takes place by advection, dispersion and diffusion through the kinematic porosity together with diffusion of solute between the groundwater in the kinematic porosity and immobile groundwater in the diffusion accessible porosity. Processes such as radioactive decay and sorption can also be taken into account. The process of rock matrix diffusion between groundwater in the kinematic porosity and the diffusion accessible porosity (RMD) can lead to a significant retardation of solute migration relative to migration in the kinematic porosity alone. ECPM models in CONNECTFLOW use a simple model of RMD which represents the process in terms of a 1D model of diffusion between groundwater flowing in infinite, parallel, equidistant, constant-aperture, planar fractures and immobile groundwater in the intervening rock. The parameters used in the RMD model are:

- the effective (or intrinsic) diffusion coefficient (for diffusion in the diffusion accessible porosity),
- the diffusion accessible porosity,
- the maximum distance available for diffusion into the diffusion accessible porosity,
- the area of fracture surface per unit volume (the flow-wetted surface per unit volume) over which there may be diffusion between the groundwater flowing in the fractures and the diffusion accessible porosity, and
- the kinematic porosity.

Estimates of the effective diffusion coefficient and the diffusion accessible porosity are available from in-diffusion experiments. Although it is recognised that these are based on small-scale experiments, and there may be important scaling issues when considering transport on the intra-fracture scale. Parameters relating to the fracture spacing can be derived from information about the hydraulic fracture network (Hydro-DFN). This may be derived based on the frequency of water conducting fractures mapped using the PFL-f method. Because this frequency can be biased by the relative orientation of fractures to the borehole trajectory, it is more appropriate to estimate the 'true' fracture intensity, $P_{10,corr}$, rather than the 'apparent' intensity, P_{10}, measured directly in the borehole. The maximum distance available for diffusion into the diffusion accessible porosity can be based on the spacing of the fractures (if it is considered that all of the rock between the fractures is potentially accessible) or based on the dimensions of alteration halos around fractures (if it is considered that only the rock within a limited distance of fractures is accessible). Similarly, the flow-wetted fracture surface area per unit volume can be estimated from the unbiased fracture intensity, $P_{10,corr}$.

Measurement of the kinematic porosity is difficult, particularly in fractured rocks. In practice, it may be necessary to infer the kinematic porosity on the basis of DFN models of the flowing fractures. Even if tracer tests are performed, the amount of porosity seen by the test may depend on the time and spatial scales considered. Also, in fractured rock, porosity may show anisotropy according to the orientation of fractures and their connections, and hence the assumption that porosity is a scalar entity is an approximation. The relative importance of the kinematic porosity and diffusion accessible porosity depends on the timescales considered. In terms of palaeohydrology, the transient changes in surface water chemistry and marine transgressions occur over long time scales, allowing time for solutes to access at least some of the diffusion accessible porosity by RMD. Hence, the influence of both types of porosity on solute transport needs to be quantified.

For the sake of the work reported here, the kinematic porosity, n_e, is derived based on the underlying Hydro-DFN calculated element-by-element as the total connected volume divided by the element volume. The fracture volume for an individual fracture is calculated as the fracture area within an element multiplied by the transport aperture, and this is parameterised based on Äspö Task Force 6c results /Dershowitz et al. 2003/, which assumes a direct correlation between the transport aperture e_t and the transmissivity T, such that:

$$e_t = a\ T^b \tag{3-5}$$

The values suggested from Äspö Task Force 6c are $a = 0.46$ and $b = 0.5$. Although this approach provides a direct link between the assignment of kinematic porosity in the ECPM model and the underlying Hydro-DFN model, it relies on several approximations, including that the full fracture surface area contributes to advection and that the contribution to porosity of fractures below the truncation of fracture sizes in the regional DFN model is not significant[4]. Nevertheless, the derived kinematic porosity can be used as an initial guess to the calibration, and any adjustments made as part of the calibration can be used to inform a more appropriate description of the fracture transport properties. Figure 3-43 and Figure 3-44 show examples of the kinematic porosity distribution at different depths.

The flow wetted fracture surface area per unit volume of rock used to parameterise RMD of solutes in the palaeohydrological modelling task was initially set uniformly as 0.17 m^2m^{-3}, which is derived from the intensity of flowing features identified in the PFL-f tests reported for use in version 1.2 and assumed to be appropriate in /Follin et al. 2007a/. That is,

$$a_r \approx 2\ P_{10,PFL,corr} \tag{3-6}$$

---

[4] The size truncation applied in Section 3.11.1, i.e. $r_{\min} = 5.64$ m, rendered a connected fracture porosity for FFM02 of $2 \cdot 10^{-5}$. For $r_{\min} = r_0$, where $r_0 = 0.038$ (see Table 3-7), a value of $6 \cdot 10^{-5}$ was obtained, i.e. a factor 3 higher.

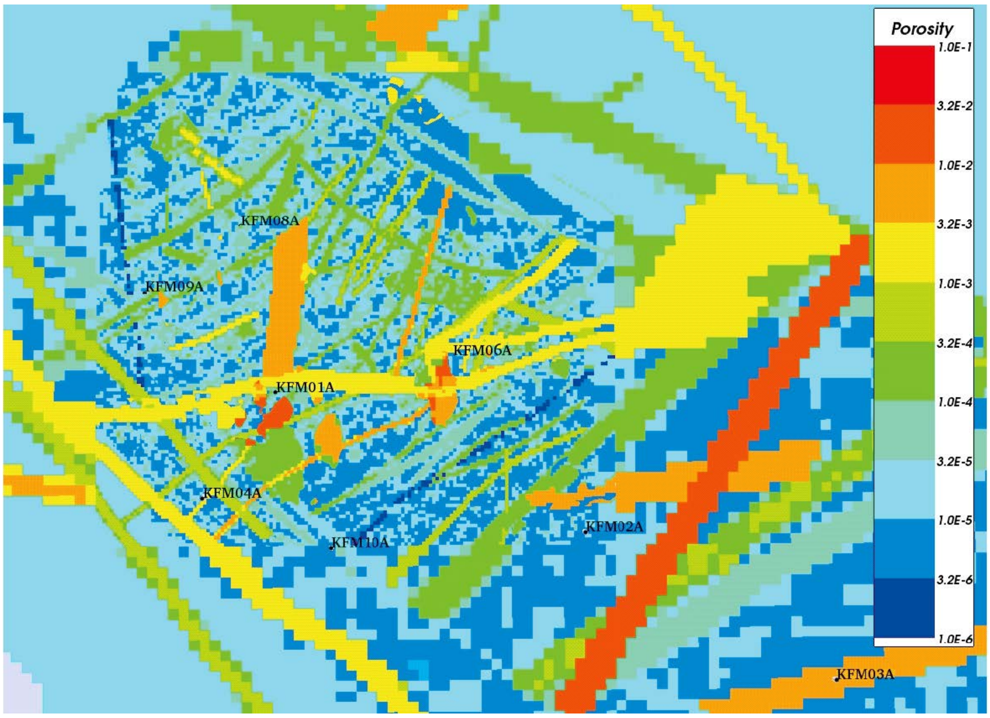

Figure 3-43. *An example of the distribution of kinematic porosity for a realisation of the ECPM model. A horizontal slice is shown at –20 m RHB 70. Properties are more heterogeneous within the finer scale embedded grid.*

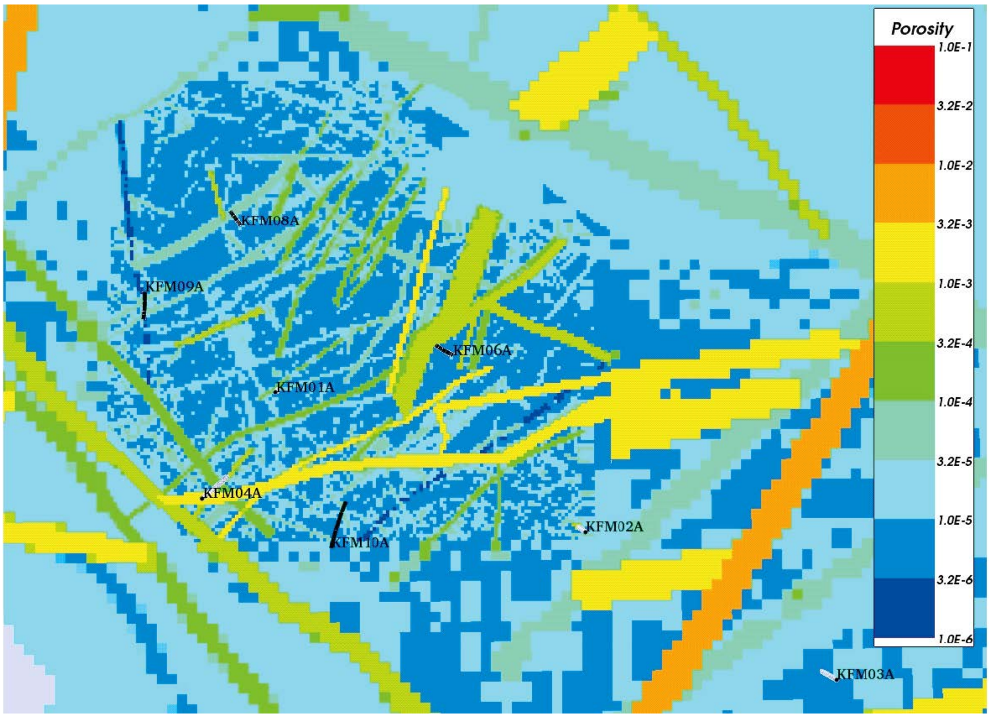

Figure 3-44. *An example of the distribution of kinematic porosity for a realisation of the ECPM model. A horizontal slice is shown at –250 m RHB 70. Properties are more heterogeneous within the finer scale embedded grid.*

Since the conceptual model has been updated to reflect spatial variations in the intensity of flowing features, see /Follin et al. 2007b/, then a_r is modified to reflect these spatial variations. The results for the different fracture domains are given in Table 3-9. Other transport properties used are based on either the SR-Can simulations of palaeohydrology for version 1.2 /Hartley et al. 2006/ or the preparatory modelling study using data from stage 2.1 /Follin et al. 2007a/ and are listed in Table 3-10.

Below –400 m RHB 70 in FFM01, a_r would actually be < 0.01 m^2m^{-3} according to Table 3-4. However, for such low values the 1D approximation of the solute profile in the matrix requires a prohibitively large number of terms in the numerical solution, and hence for pragmatic reasons a minimum value of 0.15 m^2m^{-3} is used. Below about 0.3 m^2m^{-3}, there is a time lag of a few thousands of years between the solute concentration in the matrix and fracture systems, and for 0.15 m^2m^{-3}, the lag is about 10,000 years. Hence, using a minimum value of 0.15 m^2m^{-3} reproduces the expected behaviour of large matrix blocks with non-equilibrium in solute concentrations between the matrix and fracture systems over the simulation time of 10,000 years.

It is noted that in safety assessment calculations, such as SR-Can /Hartley et al. 2006/ and the upcoming SR-Site, flow wetted fracture surface area per unit volume of rock is calculated explicitly along migration pathways obtained from DFN flow simulations implemented in CONNECTFLOW.

3.13 Regolith model

The term regolith refers to the loose deposits overlying the bedrock. In the Forsmark area, all known regolith was deposited during the Quaternary period, thus referred to as Quaternary deposits (QD) in the work reported here. In addition, most of the QD in the Forsmark area were probably deposited during or after the latest deglaciation.

Table 3-9. Alternative spatial variation of flow wetted fracture surface area per unit volume of rock based on Terzaghi corrected PFL-f intensities, i.e. $a_r \approx 2\, P_{10,PFL,corr}$.

HRD	Flow wetted fracture surface area per unit volume a_r (m^2m^{-3})
FFM01, FFM06	0.30 above –200 m RHB 70 0.15 < –200 m RHB 70
FFM02	0.60
FFM03, FFM04, FFM05	0.15
Outside FFM01–06	0.60 > –200 m RHB 70 0.30 < –200 m RHB 70

Table 3-10. Matrix porosity, dispersion lengths, RMD length and intrinsic porosity.

Property	Value	Comment
Matrix porosity n_m (–)	$3.7\cdot10^{-3}$	Based on /Hartley et al. 2006/
Dispersion lengths a_L (m) and a_T (m)	Longitudinal a_L = 40 m on the regional-scale, 20 m on the local-scale, transverse a_T = 5 m	Minimal values for grid size
RMD length, L_D	$1/a_r$	Assume can potentially diffuse into full matrix volume
Intrinsic diffusivity, D_i (m^2s^{-1})	$1\cdot10^{-13}$	Based on /Hartley et al. 2006/

The geographical and stratigraphical distributions of the QD observed in the boreholes drilled, excavations and geophysical investigations have been used to construct a model showing the distribution of QD depths /Hedenström et al. 2008/. The QD model consists of nine layers (L1–L3, Z1–Z6). Not all layers exist everywhere, and the thickness of individual layers varies significantly. The overall thickness of the QD varies from less than a decimetre to a maximum of 42 m. Figure 3-45 shows a conceptual model of the spatial location of the layers. The definition of the nine layers is given in Table 3-11. The stratigraphical units shown have been characterised with respect to physical and chemical properties. Most of the data used for that characterisation have been obtained from the site investigation but some data were taken from the literature. The QD model was developed for the area shown in Figure 3-46, which covers most of the site descriptive regional model area. However, it is truncated in the south slightly more than in the regional-scale hydrogeological model. The interpreted thickness of the QD over both land and sea are also shown in Figure 3-46. Compiling data obtained from several investigations has produced this model. The accuracy of the map varies therefore and the most detailed information was obtained from the central part of the model area and in the near shore coastal area. The profile in Figure 3-46 shows show the stratification of the Quaternary deposits layers beneath Lake Bolundsfjärden.

Table 3-11. Definition of Quaternary deposits layers /Hedenström et al. 2008/.

Layer	Description and comments
L1	Layer consisting of different kinds of gyttja/mud/clay or peat. Is interpolated from input data, thickness will therefore vary.
L2	Layer consisting of sand and gravel. Is interpolated from input data, thickness will therefore vary.
L3	Layer consisting of different clay (glacial and postglacial). Is interpolated from input data, thickness will therefore vary.
Z1	Surface affected layer present all over the model, except where peat is found and under lakes with lenses. Thickness is 0.10 m on bedrock outcrops, 0.60 m elsewhere. If total regolith thickness is less than 0.60 m, Z1 will have the same thickness as the total, i.e. in those areas only Z1 will exist.
Z2	Surface layer consisting of peat. Zero thickness in the sea. Always followed by Z3.
Z3	Middle layer of sediments. Only found where surface layers are other than till, clay or peat.
Z4a	Middle layer consisting of postglacial clay. Always followed by Z4b.
Z4b	Middle layer of glacial clay.
Z5	Corresponds to a layer of till. No min or max range. The bottom of layer Z5 corresponds to the bedrock surface.
Z6	Upper part of the bedrock. Fractured rock. Constant thickness of 0.5 m. Calculated as an offset from Z5.

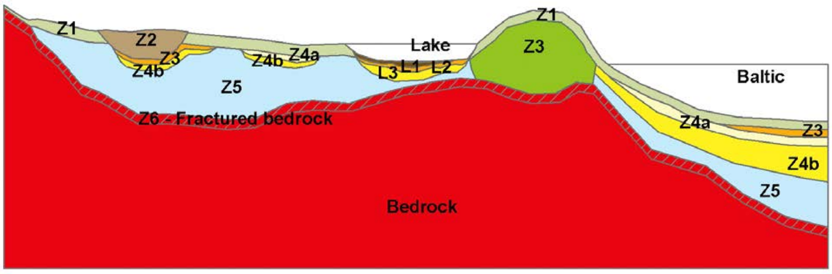

Figure 3-45. *Conceptual model for layering of Quaternary deposits in Forsmark /Hedenström et al. 2008/. The different layers are explained in Table 3-11.*

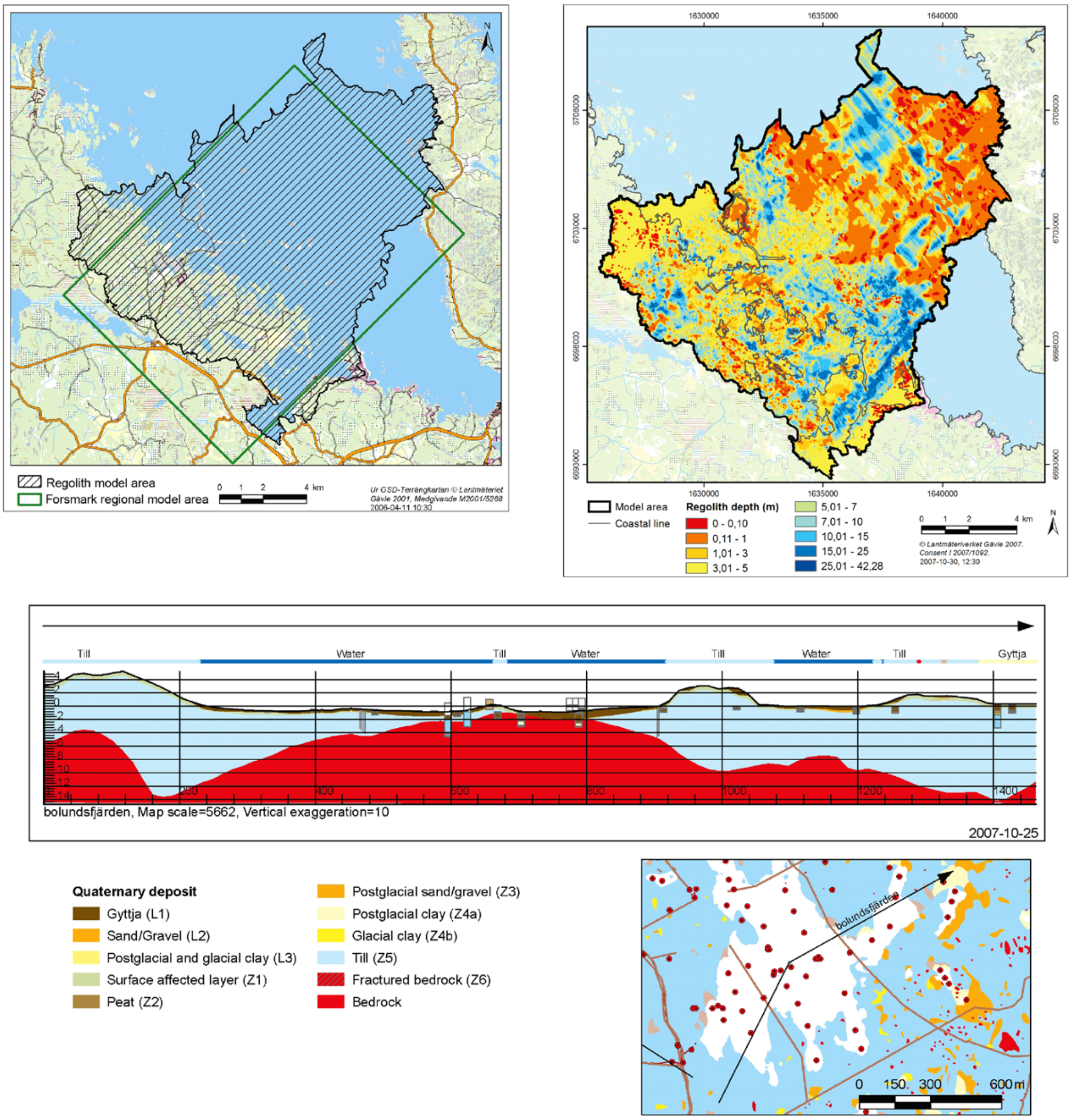

Figure 3-46. Top left: Extent of the Regolith model developed for Forsmark stage 2.2. Top right: Interpreted total thickness of the Quaternary deposits. Bottom: Example cross-section showing the interpreted stratification and thicknesses of the Quaternary deposits layers beneath Lake Bolundsfjärden. Reproduced from Appendix 2 in /Hedenström et al. 2008/.

3.14 Quaternary deposits hydrogeological model

The groundwater levels in the superficial bedrock within the target area are generally low and the hydraulic gradient between adjacent boreholes is fairly flat, see Figure 3-25. The average groundwater levels range between 0.0 and 1.14 m RHB70 in all percussion-drilled boreholes with the exception of two sections with very little water, see Figure 3-47 and Figure 3-48.

The groundwater levels in the Quaternary deposits are quite different. In contrast to the groundwater levels in bedrock, the groundwater levels in the Quaternary deposits are strongly correlated to the topography, see Figure 3-49 and Figure 3-50.

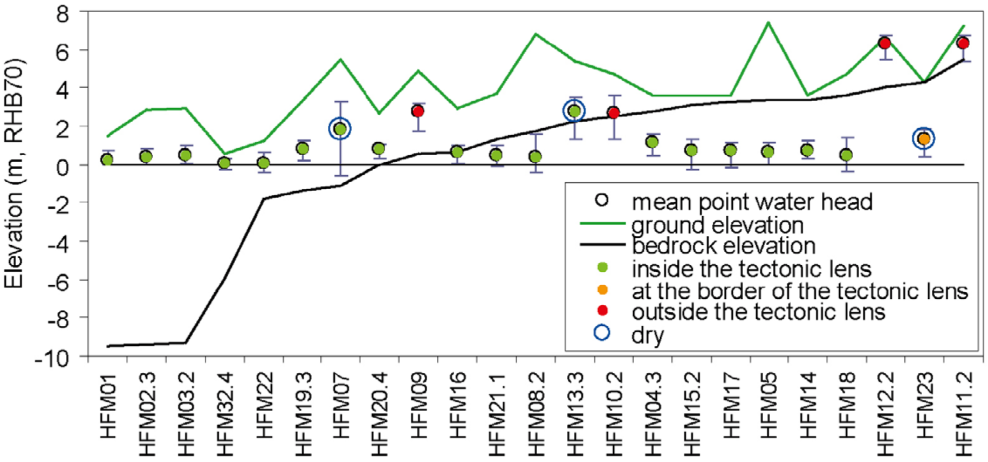

Figure 3-47. *Mean groundwater levels in the percussion-drilled boreholes (cf. Figure 3-25). With exception for two "dry" sections in HFM07 (open hole) and HFM13:3, the groundwater levels within the tectonic lens vary very little, from 0.0 to 1.14 m RHB70 (only wells with more than 150 days of level data are included). Modified after /Werner et al. 2007/.*

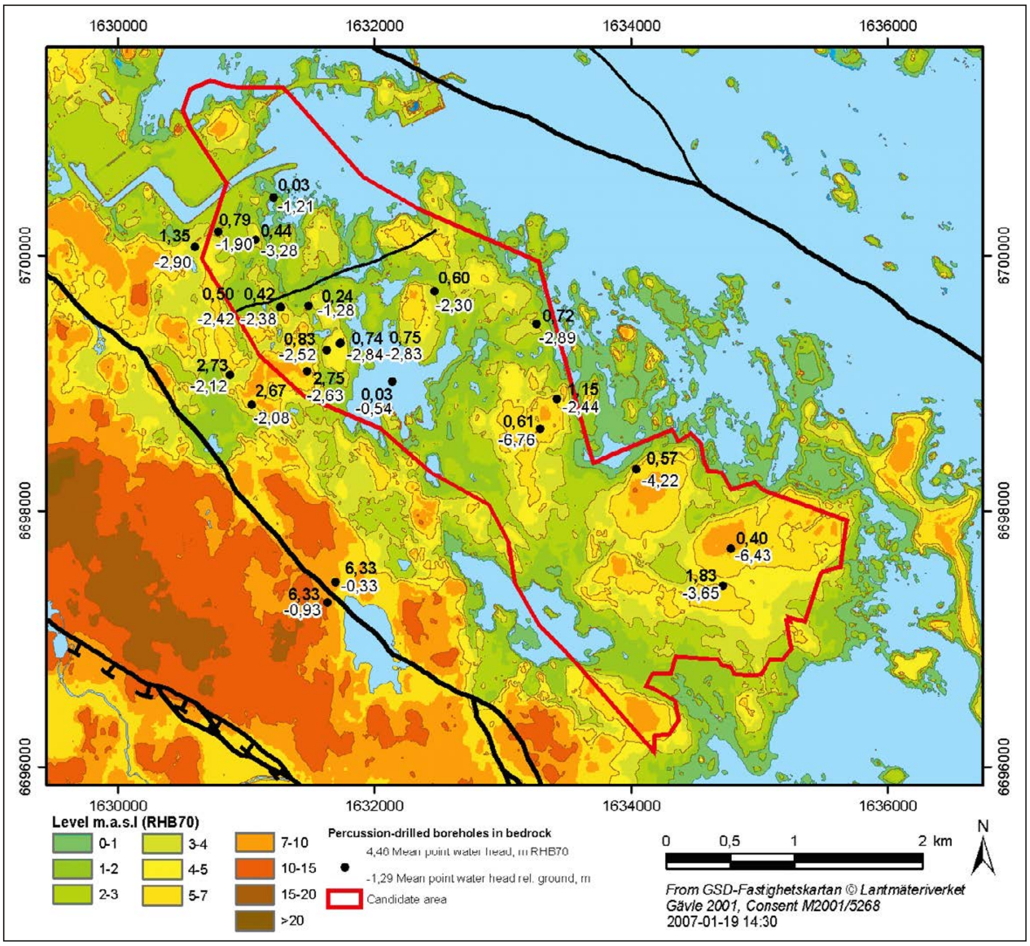

Figure 3-48. *Mean groundwater levels in the percussion-drilled boreholes in the uppermost part of the bedrock expressed as elevation in RHB70 (black) and depth relative to ground surface (grey). Reproduced from /Werner et al. 2007/.*

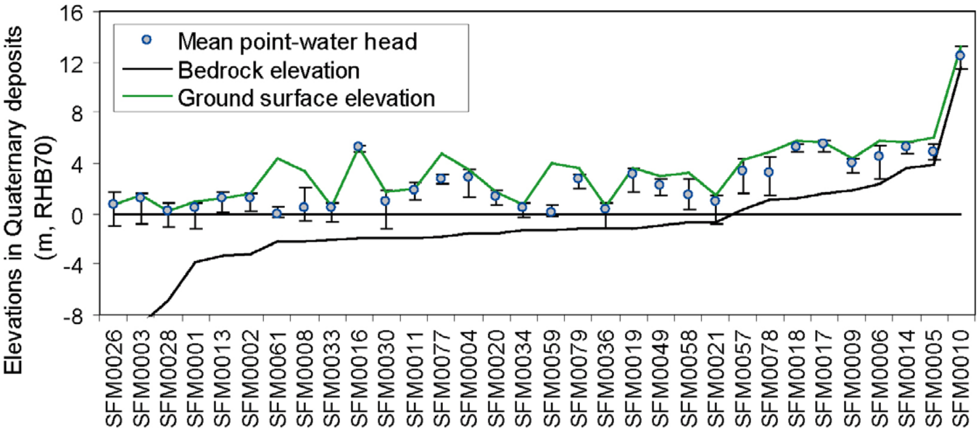

***Figure 3-49.** Mean groundwater levels in Quaternary deposits (only wells with more than 150 days of level data are included). The close correlation of groundwater levels and ground levels is clear. The only exceptions are SFM0059 and SFM0061, which are located in a glaciofluvial deposit, Börstilåsen. Modified after /Werner et al. 2007/.*

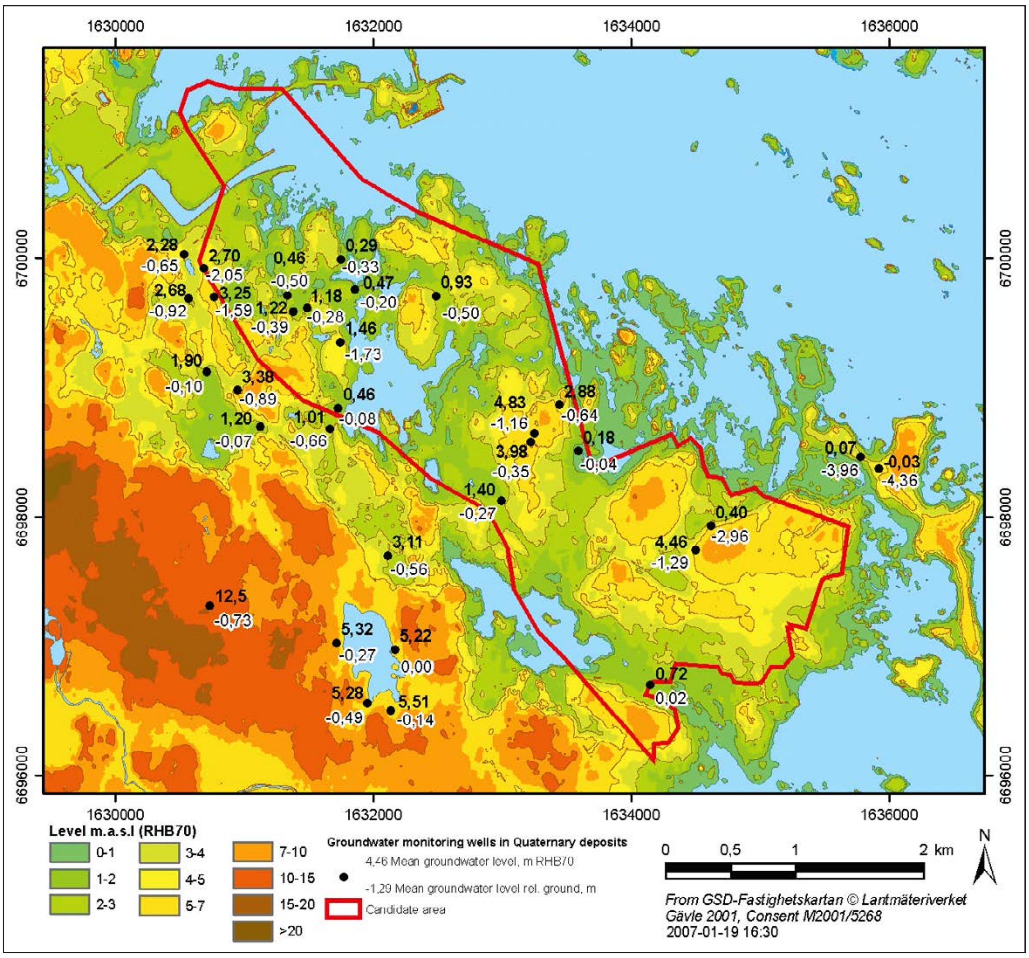

***Figure 3-50.** Mean groundwater levels in the monitoring wells in the Quaternary deposits expressed as elevation in RHB70 (black) and depth relative to ground surface (grey) /Werner et al. 2007/.*

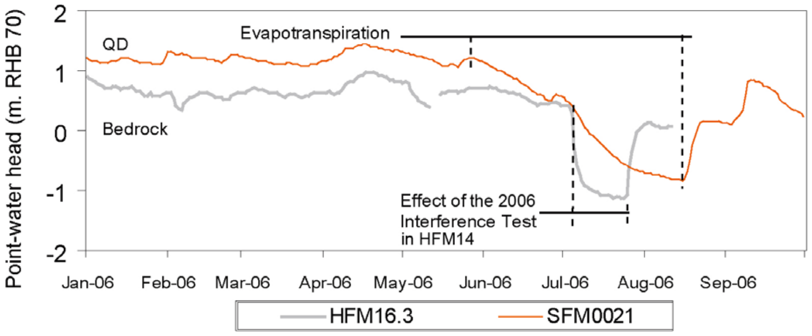

Figure 3-51. *Groundwater levels in bedrock (HFM16:3) and in the Quaternary deposits (SFM0021) in close proximity to drill site 6. The head in the Quaternary deposit is generally greater than in the bedrock except during dry summer periods when the evapotranspiration is large. Modified after /Werner et al. 2007/.*

At locations where the wells for groundwater level measurements in the Quaternary deposits are close to the wells in the bedrock, the heads in the bedrock are often considerably lower than in the Quaternary deposits. This feature is most pronounced within the target area. There are no examples within the target area of a situation where the groundwater level in the Quaternary deposits is constantly below the groundwater level in the bedrock for nearby wells. However, such conditions can occur during dry summer periods when the evapotranspiration is large. Figure 3-51 shows an example from drill site 6.

The general situation with lower groundwater levels in superficial bedrock than in the Quaternary deposits shown in Figure 3-47 and Figure 3-49 has been observed even below the middle of Lake Bolundsfjärden, which is located in the major topographical depression in the centre of the target area in Forsmark, see Figure 3-55. Since the water level in the lake is generally higher than in the Quaternary deposits beneath the lake, the two observations combined suggest that the lake may be a potential source for groundwater recharge rather than a discharge area. Appendix J shows examples of time series of point-water head data in the bedrock, in the Quaternary deposits, in the lake and in the sea and discusses the vertical gradients observed. The time series covers the period between 2006-02-01 and 2007-03-31, which encompasses a dry summer period and a three-week long interference test in HFM14. In order to account for variable-density flow the point-water head data were transformed to environmental water head data. The transformation is explained in Appendix K.

3.15 Hydraulic soil domain (HSD) model

Table 3-12 shows the preliminary suggestion for hydraulic properties of the different QD layers provided by the surface systems modelling group at the onset of the groundwater flow modelling reported here. Layers L1, Z1 and Z5 are geologically heterogeneous with spatially varying occurrence of the deposits. For stage 2.2 the variations within a layer were not considered, rather the hydraulic conductivity of individual layers was assumed to be homogeneous and varied accordingly in order to understand how the values affected the calibration. Table 3-12 shows this leads to variations in hydraulic conductivity of up to two orders of magnitude. Considering the upper bedrock properties, sediments with hydraulic conductivities of around 10^{-8} to 10^{-7} m/s can act as semi-impermeable cover to reduce the hydraulic contact between the soil and the bedrock. Of the layering shown in Figure 3-45 layers Z1 and Z5 make up most of the volume of the overburden in the area, hence where these are of either the clayey Z1 or fine-grained till of Z5, then the QD may restrict recharge/discharge to the bedrock. Equally, where there is clay (L3) or gyttja (L1) sediments the hydraulic contact between the lakes and bedrock may be poor. Hence, sensitivities to the HSD properties need to be considered in the calibration.

Table 3-12. Summary of the preliminary effective hydraulic properties of Quaternary deposits provided by the surface systems modelling group as an initial trial data set for the GWF modelling reported here. L1–L3: lake sediments, Z1–Z6: terrestrial deposits.

Layer	K (m/s)	Total porosity	Specific yield
L1	Gyttja: $3\cdot10^{-7}$ Peat, upper 0.6 m: $1\cdot10^{-6}$ Peat, depth > 0.6 m: $3\cdot10^{-7}$	Gyttja: 0.5 Peat, upper 0.6 m: 0.6 Peat, depth > 0.6 m: 0.40	0.03 0.20 0.05
L2	Sand and gravel: $1.5\cdot10^{-4}$	0.35	0.20
L3	Glacial clay and post-glacial clay: Upper 0.6 m: $1\cdot10^{-6}$ Depth > 0.6 m: $1.5\cdot10^{-8}$	0.55 0.45	0.05 0.03
Z1	Weathered deposits: Till: $3\cdot10^{-5}$ Clay: $1\cdot10^{-6}$ Sand: $1.5\cdot10^{-4}$	0.35 0.55 0.35	0.15 0.05 0.20
Z2	Peat: $3\cdot10^{-7}$	0.40	0.05
Z3	Sand/gravel, glaciofluvial deposits: $1.5\cdot10^{-4}$	0.35	0.20
Z4a	Post-glacial clay, clayey gyttja: $1.5\cdot10^{-8}$	0.45	0.03
Z4b	Glacial clay: $1.5\cdot10^{-8}$	0.45	0.03
Z5	Coarse till: $1.5\cdot10^{-6}$ Fine-grained till: $1\cdot10^{-7}$	0.25 0.25	0.05 0.03
Z6	Bedrock surface: $1.5\cdot10^{-5}$ (from slug tests)	No data	No data

It should be noted that the data shown in Table 3-12 represent a very preliminary estimate based on site specific data, when available, and generic data. An updated and calibrated parameterisation of the QD properties is expected once the hydrological-hydrogeological modelling with the MIKE SHE code is completed /Bosson et al. 2008/.

The horizontal grid refinement of the regolith model shown in Figure 3-46 is 20 m by 20 m. The thickness of the Quaternary deposits within the model area varies from less than a decimetre to over 25 m, not all layers exist everywhere, and the thickness of individual layers varies significantly. Hence, it would be difficult to produce a 3D hydrogeological model in CONNECTFLOW that explicitly honoured the geometrical complexity of the soil layering. Instead, an effective treatment of the hydrogeology of the QD model is adopted. This implies a considerable simplification of the detailed description of the near-surface system in comparison with the hydrological-hydrogeological modelling conducted with the MIKE SHE code, cf. Section 2.2 and Figure 2-2.

In version 1.2, the hydrogeological modelling of the HSD in the Forsmark area used a simple homogeneous model with 3–4 thin layers of elements of constant thickness (about 1 m) /Hartley et al. 2005, 2006/. The hydraulic conductivity of these layers was $7.5 \cdot 10^{-6}$ m/s. This was generally higher than the bedrock, so it had little effect on hydrogeology in the bedrock apart perhaps where it controlled the hydrogeological contact between the deformation zones and surface hydrology. For stage 2.2, we substitute the complex multi-layer QD model by four element layers each of a constant 1 m thickness. The same hydraulic conductivity tensor is specified for each vertical stack of four grid elements, but varies horizontally from element-to-element, and is anisotropic between horizontal and vertical components. The horizontal component is calculated as the arithmetic average of transmissivities of the QD layers for the corresponding QD data cell divided by the 4 m thickness, while the vertical component is based on the harmonic average.

For the 20 m computational grid used in the centre of the model area there is a one-to-one horizontal correspondence with the grid refinement of the QD data, making the averaging straightforward. For the area surrounding the centre, where a coarser computational grid of 60 m or 100 m is used, then additional averaging has to be performed. The approach first calculates the horizontal and vertical hydraulic conductivity for each 20 m block within the element corresponding to a vertical stack of QD layers using arithmetic and harmonic averages, respectively, then for the vertical component, the arithmetic average of blocks is calculated.

For the horizontal components there are potentially several blocks of 20 m QD cells within the horizontal extent of the hydrogeological grid element (60–100 m). Here, the approach is illustrated by Figure 3-52 for the hydraulic conductivity in the E-W direction as an example. Using the effective hydraulic conductivity of the 20 m blocks, the harmonic average of each row of blocks is first calculated, and then the arithmetic average of these values is taken. Therefore, for the coarse grid elements, the hydraulic conductivity can differ in all three directions according to the spatial distribution of the QD layering.

An example of a resulting hydraulic conductivity distribution is illustrated in Figure 3-53. Note: In the areas outside the QD model area shown in Figure 3-53, an isotropic and homogeneous value of $7.5 \cdot 10^{-6}$ m/s is used by default.

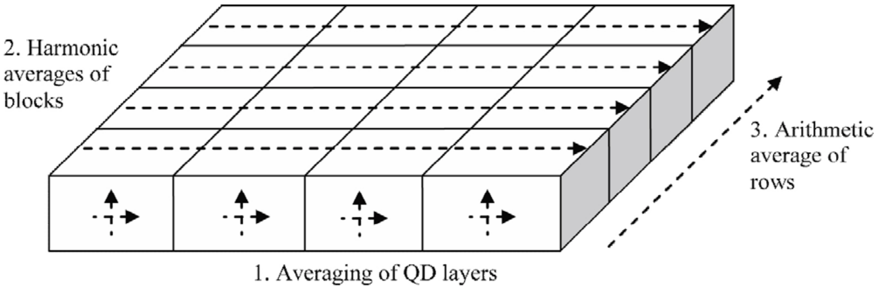

Figure 3-52. *Steps in averaging of QD layers to calculate the effective E-W component (left to right here) of hydraulic conductivity of the HSD where the computational grid elements are larger than the grid refinement of the QD data (here 4 to 1 for illustration).*

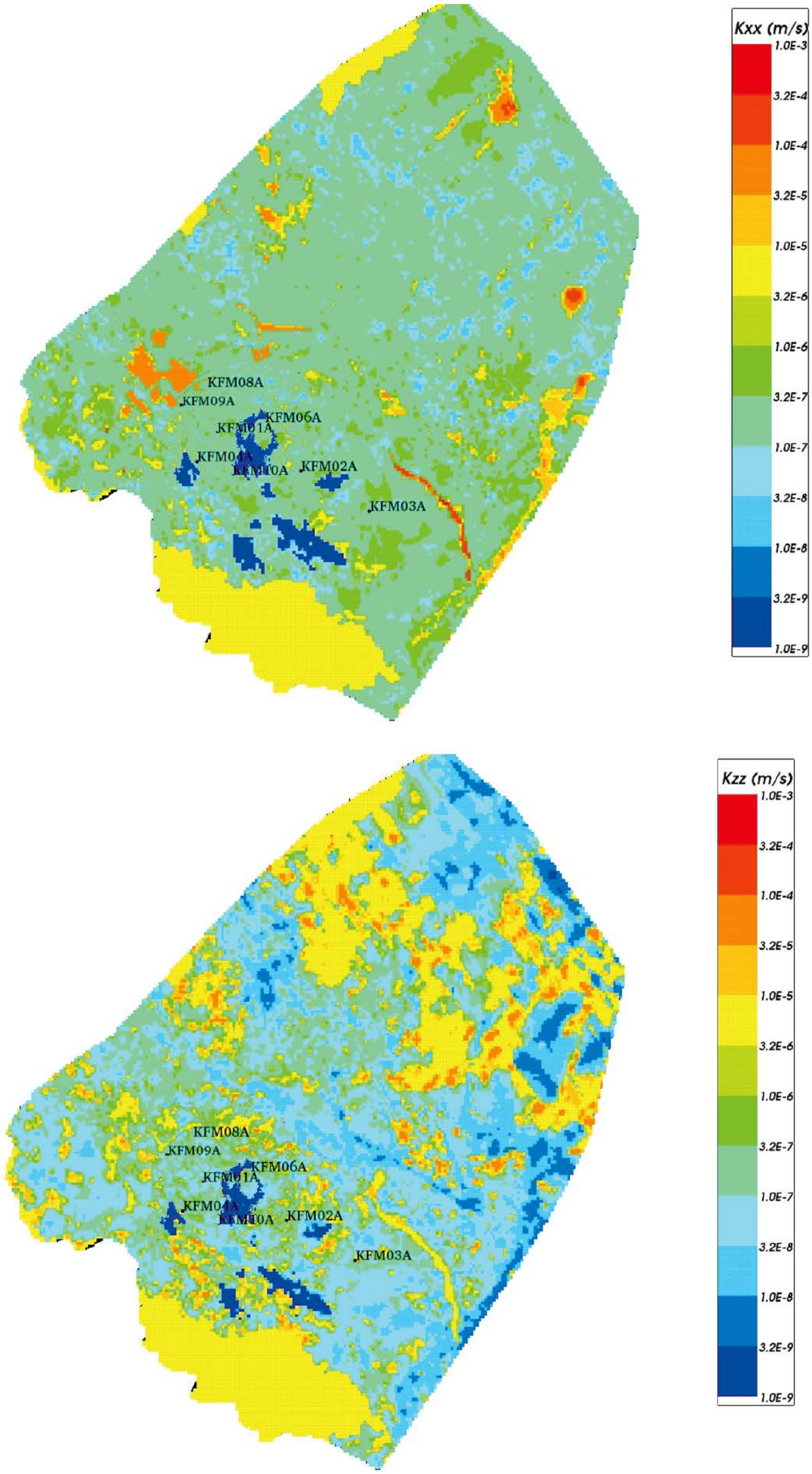

Figure 3-53. *Resulting effective hydraulic conductivity for HSD top layer based on QD layer thicknesses and hydraulic properties. Top: E-W horizontal component; Bottom: vertical component.*

3.16 Palaeohydrological model

Figure 3-54 illustrates some important phases in the climate (interglacials, stadials and interstadials) after the Eem interglacial. The illustrations suggest that the Forsmark area has been subjected to meteoric, glacial and marine/lacustrine water influences for relatively long periods of time prior to the start of the main phase of the most recent glaciation, the Weichselian.

A major crustal phenomenon that has affected, and continues to affect northern Europe, following the melting of the Weichselian glaciation, is the interplay between isostatic recovery on the one hand and eustatic sea-level variations on the other. During the main phase of the Weichselian glaciation, the global sea-level was in the order of 120 m lower than at present, due to the large amounts of water stored in ice /Fairbanks 1989/. In northern Sweden, the heavy continental ice depressed the Earth's crust by as much as 800 m below its present altitude. A marked improvement in climate took place about 18,000 years ago, shortly after the last glacial maximum and the ice started to retreat, a process that was completed after some 10,000 years. There was a major standstill and, in some areas, a re-advance of the ice front during a cold period c. 13,000–11,500 years ago. The end of this period marked the onset of the present interglacial, the Holocene (the last 10,000 years). The ice retreated more or less continuously during the early part of the Holocene.

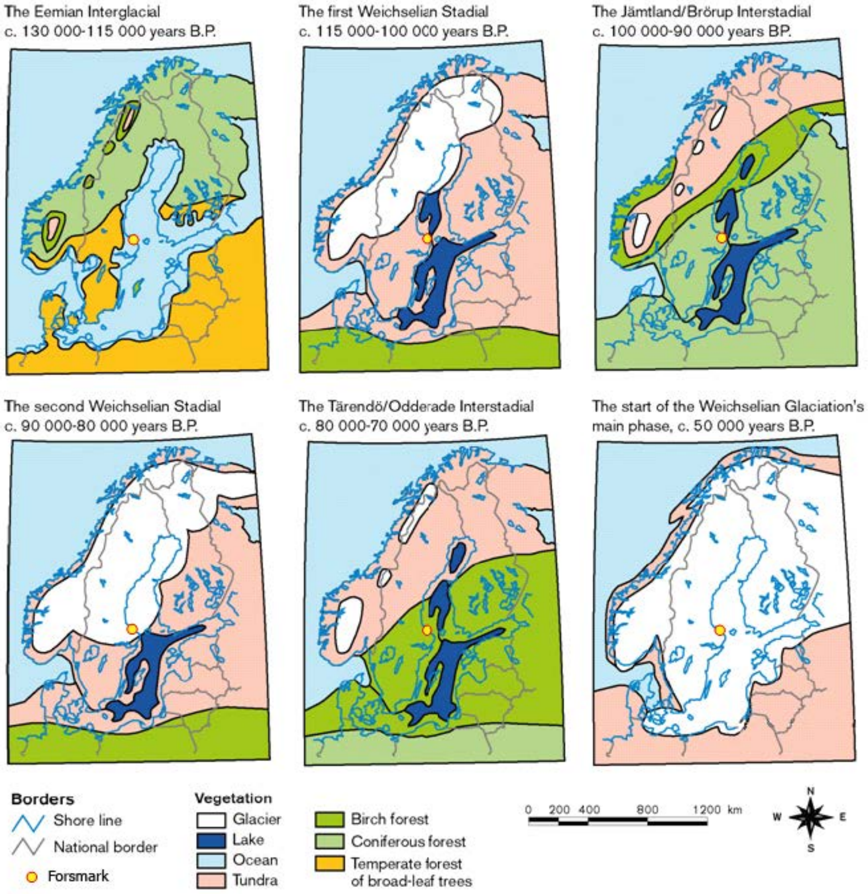

Figure 3-54. Map of Fennoscandia with some important phases in the Quaternary climate since the Eem interglacial. The location of the Forsmark area is denoted by a yellow dot. Modified after /Fredén 2002/.

As soon as the vertical stress started to decrease, due to thinner ice coverage, the crust started to rise (isostatic land uplift). The net effect of the interplay between isostatic recovery on the one hand and eustatic sea-level variations on the other is called shore level displacement, a process modelled by, among others, /Påsse 1996, 1997, 2001, Morén and Påsse 2001/.

The shore level displacement started before the final deglaciation and is still an active process in most of Sweden. For instance, the displacement rate in the Forsmark area around 10,000 years ago was very rapid at about 5 cm per annum, but has now reduced to about 7 mm per annum. About 10,000 years from today the accumulated displacement is predicted to be c. 40 m. Thus, the present-day hydrological conditions in the Forsmark area are not at steady-state and the site will not be a coastal site in the future provided that the current shore-level displacement process continues.

Figure 3-55 shows the shore level specified for stage 2.2. Comparing with the curve used previously for version 1.2, the displacement rate for stage 2.2 is slightly reduced. Still, given the low altitudes of the Forsmark area, which range between 0–20 m, then it is only the last 3,000 years that any part of the regional area has been above sea level, and only in about the last 1,000 years has any part of the candidate area been above sea level.

The changes in the salinity of the aquatic systems in the Baltic basin during the Holocene are closely coupled to the shore-level displacement. The changes are divided into four main stages /Björck 1995, Fredén 2002/ and are summarised in Table 3-13 and Figure 3-56. The most saline period during the Holocene occurred c. 6500–5000 BP, when the surface water salinity in the so-called Littorina Sea was 10–15‰ compared with approximately 5‰ today in the Baltic Sea /Westman et al. 1999/, see Figure 3-57.

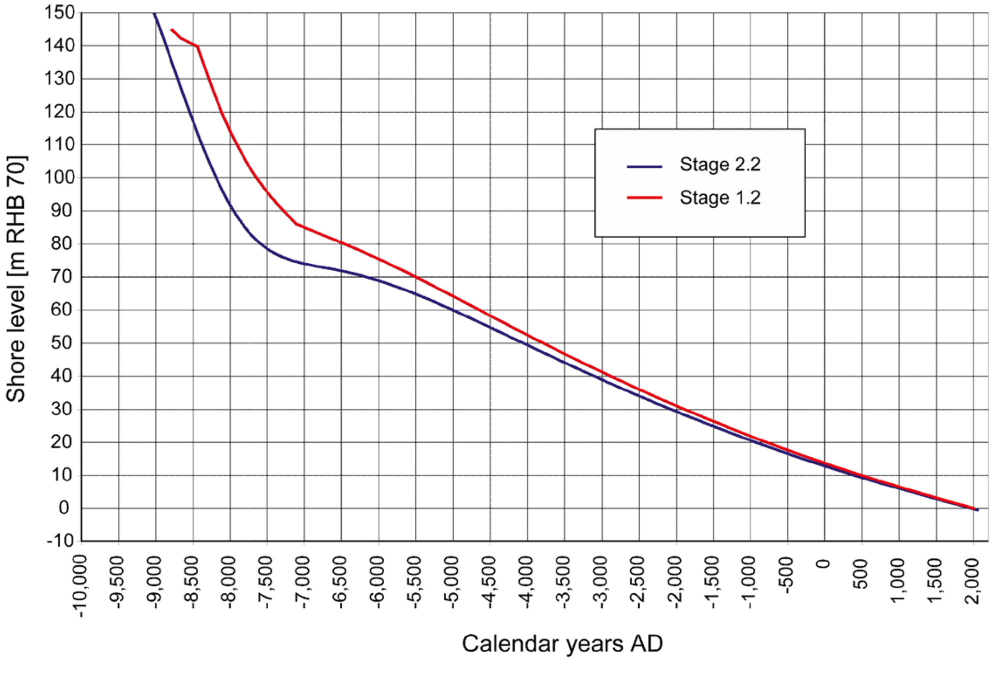

Figure 3-55. *Shore level displacement specified for Forsmark stage 2.2 and compared to the evolution used in version 1.2. Based on /Påsse 1997, 2001/.*

Table 3-13. Summary of the stages in the development of the Baltic Sea, presented as years before present (BP; 0 BP = 2000 AD). Note that the Littorina Sea stage is based on the palaeogeography in the threshold areas and includes e.g. the so-called Mastogloia Sea stage and the present Baltic Sea conditions. Note also that the altitudes and ages are approximate values. Based on data reported by /Björck 1995, Fredén 2002, Westman et al. 1999/.

Baltic stage	Calendar year BP	Salinity	Environment in Forsmark
Baltic Ice Lake (not applicable in Forsmark)	15,000–11,500	Glacio-lacustrine	Covered by inland ice.
Yoldia Sea (perhaps not applicable in Forsmark)	11,500–10,800	Lacustrine/Brackish /Lacustrine	At the rim of the retreating inland ice.
Ancylus Lake	10,800–9500	Lacustrine	Regressive shore level from c. 140–75 m RHB 70.
Littorina Sea (→ Baltic Sea)	9500–present	Brackish	Regressive shore level from c. 75–0 m RHB 70. Most saline period 6500–5000 BP. Present-day Baltic Sea conditions have prevailed during the last c. 2,000 years.

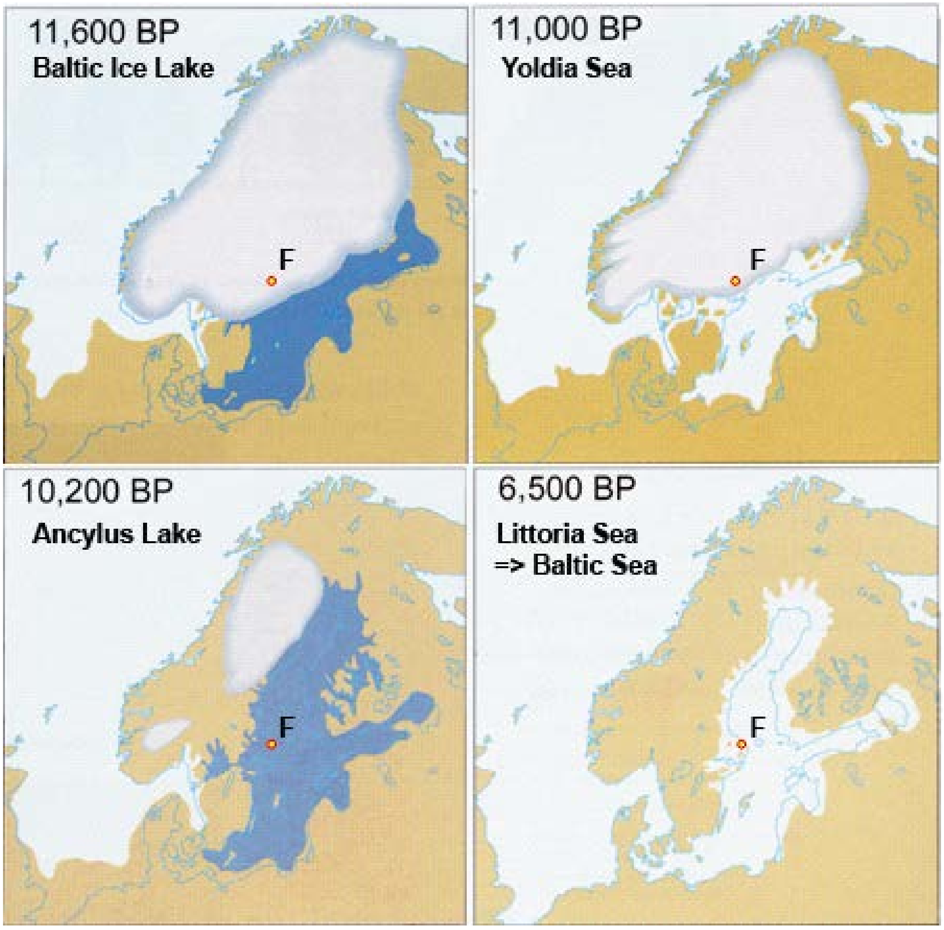

Figure 3-56. *Map of Fennoscandia with some important stages during the Holocene. Four main stages characterise the development of the aquatic systems in the Baltic basin since the latest deglaciation: the Baltic Ice Lake (15,000–11,500 BP), the Yoldia Sea (11,500–10,800 BP), the Ancylus Lake (10,800–9500 BP) and the Littorina Sea (9500 BP–present). Fresh water is symbolised with dark blue and marine/brackish water with light blue. The Forsmark area (notated F) was probably at the rim of the retreating ice sheet during the Yoldia Sea stage. Modified after /Fredén 2002/.*

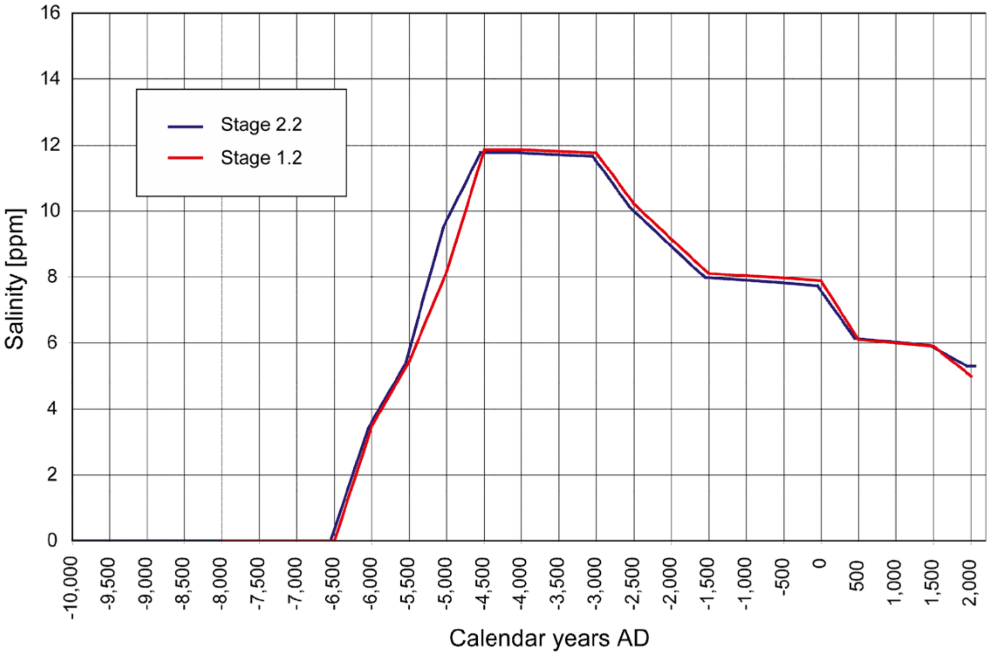

Figure 3-57. *Changes in the salinity of the aquatic systems in the Baltic basin specified for Forsmark stage 2.2 and version 1.2. Based on /Westman et al. 1999/.*

3.17 Hydrochemical model

3.17.1 Background

In the hydrochemical modelling it is suggested that the mixing of several so-called *reference* (or *end-member*) *water types* contribute to the groundwater composition in the Forsmark area /SKB 2005c/. Conceptually, the reference water types together reflect important aspects of the changes in the climate and the evolution of the hydrological conditions. The focus on mixing rather than on chemical reactions as a dominant process for the present-day hydrochemical conditions in low-temperature, fractured crystalline bedrock is not new. /Laaksoharju et al. 1999/ presented a multivariate mixing and mass balance (M3) method for decoding the hydrochemical information gathered in 3D by means of deep boreholes.

The assumption that mixing rather than reaction is the dominant hydrochemical process in the Forsmark area remains in stage 2.2, but the hydrochemical modelling is more diversified. Reactions involving ion exchange and microbiologically mediated processes clearly affect the composition of the listed non-conservative constituents and may mislead the interpretation of the physical system studied, if mixing alone is assumed for model calibration. Nevertheless, magnesium, for instance, which is a reactive caution, has been an excellent qualitative indicator in distinguishing between marine versus non-marine saline water conditions /SKB 2005a, 2006b/. The strong correlation between geological-hydrogeological-hydrochemical data evident from the multidisciplinary modelling undertaken in previous stages /SKB 2005a, 2006a/ is key to the hydrogeological conceptual modelling in general and to the long-term groundwater flow and solute transport modelling in particular, i.e.palaeohydrology. We present below a summary of the hydrochemical conceptual model development of the Forsmark area. The description is based on the nomenclature and modelling reported by the hydrogeochemical modelling group /Laaksoharju et al. 2008/.

3.17.2 Conceptual model

The chronological order of the reference water types associated with the changes in the climate shown in Figure 3-56 may be written as:

Deep Saline Water (oldest) > *Holocene Glacial Melt Water* > *Littorina Sea Water* (→ *Baltic Sea Water*) > *Present-day Meteoric Water* (most recent).

The intrusion of brackish *Littorina Sea Water* during the Holocene is an important hydrological event in the Forsmark area. The intrusion can be regarded as a natural tracer experiment, with a potentially much greater imprint in the hanging wall relative to the footwall, due to the significant differences in the structural-mechanical-hydraulic properties of these two bedrock segments. However, in order for the intrusion to take place, the resident groundwater at the time must have been less dense than the *Littorina Sea Water*, which is an indirect support for the hypothesis of a preceding period of flushing by *Holocene Glacial Melt Water*. A direct support for the flushing by *Holocene Glacial Melt Water* is the observed occurrence of glaciofluvial sediments in some of the fractures and deformation zones penetrated by boreholes and excavations.

The penetration depth of the *Littorina Sea Water* intrusion is constrained by the gravitational force on the displaced mass, i.e. it cannot be deeper than the interface with *Deep Saline Water* at depth, which has a much higher salinity. However, the data gathered from the hydrochemical investigations suggest that this interface is not sharp and that its mobility is also governed by the hydraulic properties of the deformation zones. Finally, the flushing of the Forsmark area by *Present-day Meteoric Water* is a recent process that began c. 900 AD when the highest terrains became islands in the Baltic Sea archipelago, see Figure 3-58. Data show that the flushing is governed by the structural-mechanic-hydraulic properties in the uppermost c. 100 m of the bedrock, where the occurrence and transmissivity of newly formed, sub-horizontal sheet joints, as well as the transmissivity of ancient, gently dipping fractures reactivated as joints, are steered by the release of stress in the bedrock, following the retreat of the land ice.

Table 3-14 shows the major ion components and stable isotope compositions for the four reference water types. The composition of the *Present-day Meteoric Water* is quite different than the composition of the present-day precipitation of meteoric water. That is, the composition of the *Present-day Meteoric Water* refers to the composition in the bedrock after infiltration and percolation through the Quaternary deposits. Hence, the original composition of the present-day precipitation of meteoric water is altered by a number of near-surface chemical processes. Probably, this reasoning is also valid for the *Littorina Sea Water*.

Table 3-14. Compilation of reference water composition for Forsmark in stage 2.2 based on end-member data reported by /Laaksoharju et al. 2008/.

Reference water	Na mg/L	K mg/L	Ca mg/L	Mg mg/L	HCO_3 mg/L	Cl mg/L	SO_4 mg/L	Br mg/L	δ^2H ‰SMOW	$\delta^{18}O$ ‰SMOW
Deep Saline Water (DS)	8,200	45.5	19,300	2.12	14.1	47,200	10	323	–44.9	–8.9
Holocene Glacial Melt Water (HGM)	0.17	0.4	0.18	0.1	0.12	0.5	0.5	0	–158	–21
Littorina Sea Water (L)	3,674	134	151	448	92.5	6,500	890	22.2	–37.8	–4.7
Present-day Meteoric Water (PM)	274	5.6	41.1	7.5	466	181	85.1	0.6	–80.6	–11.1

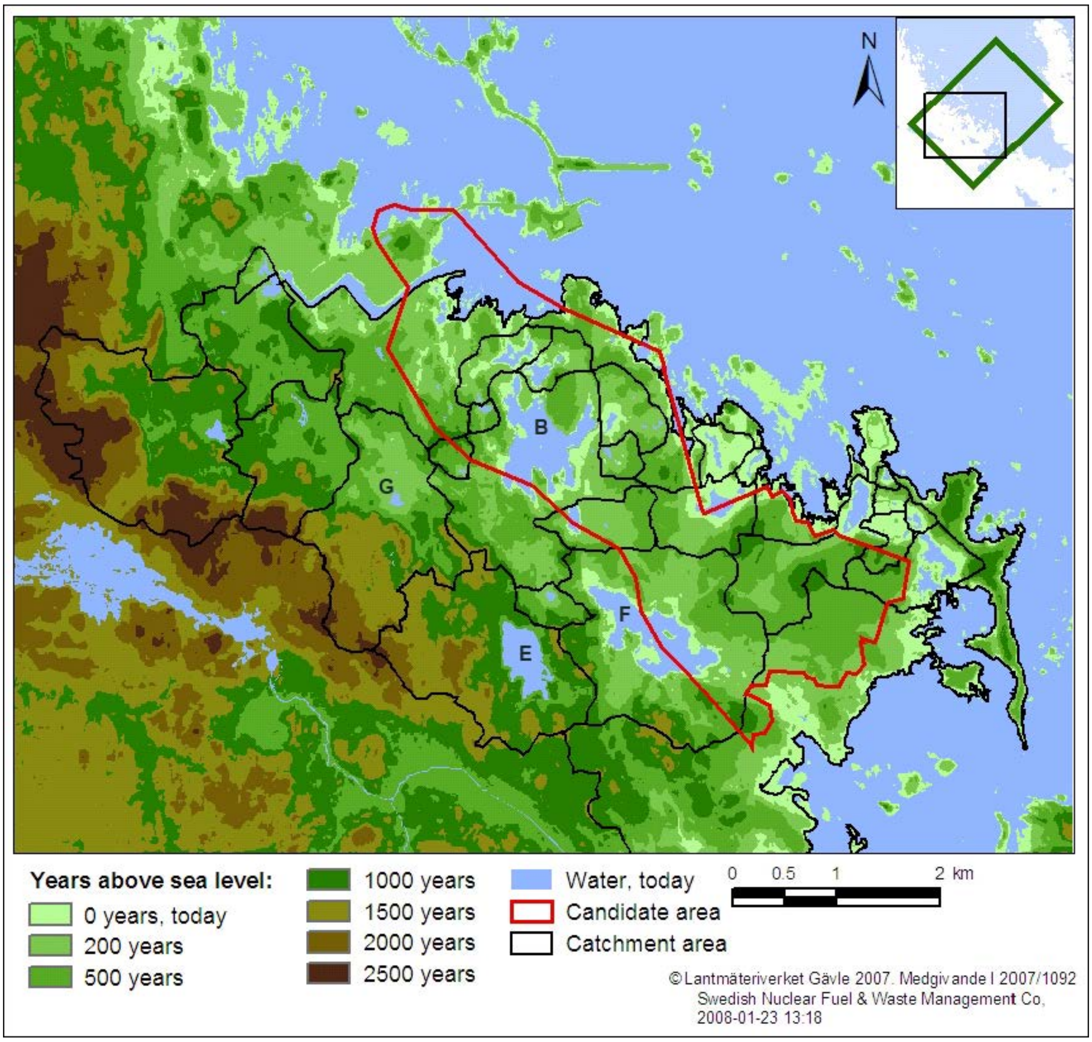

Figure 3-58. *Iso-chronic map showing the time elapsed since the land in the proximity of the Forsmark area emerged from the Baltic Sea. Modified after /SKB 2005a/. The letters inserted denote lakes in the major catchments: G = L. Gällsboträsket; B = L. Bolundsfjärden; E = L. Eckarfjärden; F = L. Fiskarfjärden. The altitudes of L. Eckarfjärden and L. Gällsboträsket are c. 5 m and c. 2 m RHB 70, respectively. The other two lakes have much lower altitudes and are occasionally subjected to sea water transgressions. The borders of the catchments coinciding with the highest altitudes in the map constitute a regional water divide, which separates the Forsmark area from the rest of northern Uppland from a hydrological point of view /Brunberg and Blomqvist 1998/.*

Using chloride, magnesium and $\delta^{18}O$, the four water types above can be classified for discussion purposes as follows:

Deep Saline Water

Strong saline source → high chloride content (> 20,000 mg/L)

Non-marine origin → low magnesium content (< 20 mg/L)

Enriched $\delta^{18}O$

Holocene Glacial Melt Water

Non-saline source → low chloride content (< 8 mg/L)

Non-marine origin → low magnesium content (< 8 mg/L)

Significantly depleted δ^{18}O

Littorina Sea Water

Brackish saline source → moderate chloride content (max. ~ 5,500 mg/L)

(The chloride content of the present-day *Baltic Sea Water* is ~ 3,000 mg/L)

Marine origin → high magnesium content (max. 250–350 mg/L)

Enriched δ^{18}O (> –10‰ SMOW)

Present-day Meteoric Water

Non-saline source → low chloride content (< 200 mg/L)

Non-marine origin → low magnesium content (< 50 mg/L)

Intermediate δ^{18}O (–12 to –11‰ SMOW)

The *Present-day Meteoric Water* and *Littorina Sea Water* type groundwaters are based on hydrochemical measurements /SKB 2005c/, the *Deep Saline Water* type groundwater on measured data from the Laxemar site in south-east Sweden /SKB 2006c/ and the *Holocene Glacial Melt Water* type groundwater from the open literature /e.g. Brown 2002/. It should be pointed out also that the original water types have undergone mixing and alterations (water/rock reactions) since their introduction into the bedrock, and that the *Holocene Glacial Melt Water* type groundwater only exists as a residual component in the deeper, brackish *Littorina Sea Water* and the non-marine, more saline, *Deep Saline Water* type groundwaters. The general evolutionary sequence is illustrated in Figure 3-59, which plots Ca/Mg against Br/Cl. This plot provides the opportunity to differentiate between groundwaters of modern marine origin (e.g. present *Baltic Sea Water*), of old marine origin (e.g. *Littorina Sea Water*) and of non-marine origin (*Deep Saline Water* and *Present-day Meteoric Water*). Further, the data are presented with respect to the different structural-hydraulic units (i.e. the different fracture domains) presented and discussed above.

Figure 3-59 clearly shows the difference between, on one hand, modern, brackish, shallow, marine type groundwaters characterised by a *Baltic Sea Water* signature, and, on the other hand, saline, non-marine, groundwaters acquired at depth in the cored boreholes. Most of the groundwater data gathered in the Forsmark area actually plots between these two characteristic groups. The dashed arrow shows the direction towards the deeper, saline, non-marine type groundwaters. Much of the data along this direction represent groundwaters with an increasing content of *Deep Saline Water*. At the other extreme in the plot, some of the data are identified as *Present-day Meteoric Water* (> –150 m RHB 70) which are in close contact with older, brackish, marine groundwaters characterised by a strong *Littorina Sea Water* signature (–150 to –600 m RHB 70). At greater depths (–500 to –900 m RHB 70) there is a transition towards brackish, non-marine, groundwaters; some mixing at this transition has resulted in some brackish groundwaters having a weak *Littorina Sea Water* signature. At still greater depths (< –1,000 m RHB 70), the brackish groundwaters become increasingly more saline with the highest value of 14,800 mg/L of chloride originating from a deformation zone just outside the tectonic lens.

The δ^{18}O data gathered show that a cold climate water component persists within the brackish, non-marine and deeper saline groundwaters, and probably also within the brackish, marine (*Littorina Sea Water*) type groundwaters; any *Holocene Glacial Melt Water* signature, however, in the Littorina-type groundwaters is masked by the enriched δ^{18}O signature of these groundwaters.

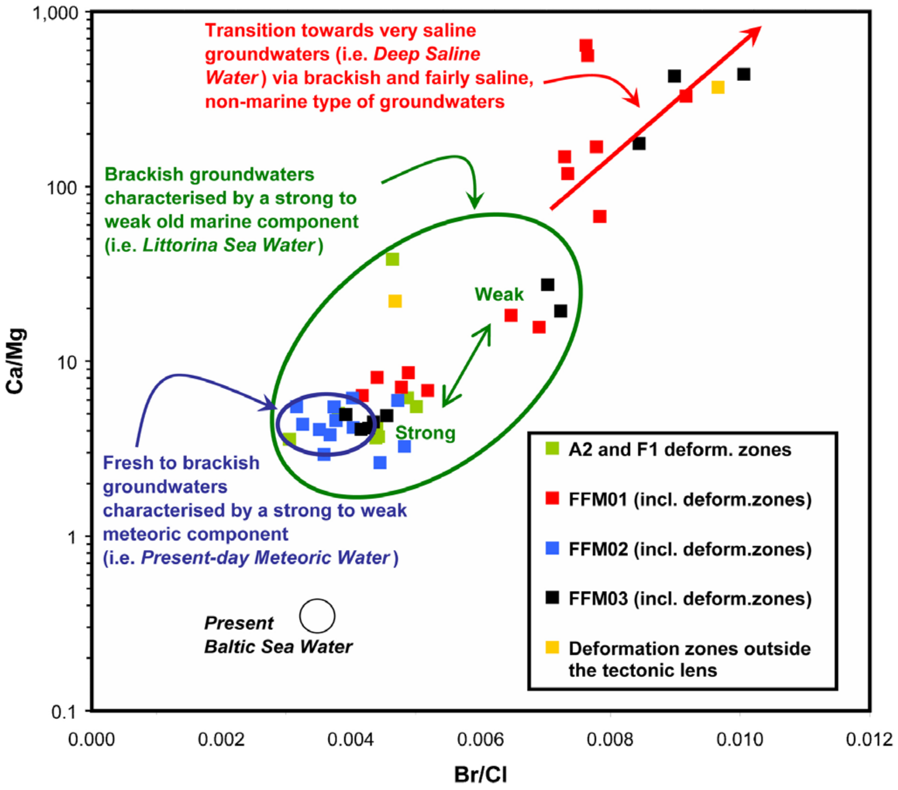

Figure 3-59. *Plot of Ca/Mg versus Br/Cl differentiating between the saline sources in the main groundwater types constituting the Forsmark site. Hydrochemical evolution of the groundwater system with depth is along the direction of the dashed arrow. Modified after Appendix 1, Figure 4-30 in /SKB 2005c/.*

Figure 3-60 attempts to illustrate the importance of the data locations for the interpretation of the magnesium and chloride data with regard to the structural-mechanical-hydraulic model. The left scatter plot shows magnesium concentration versus elevation and the right scatter plot shows chloride concentrations versus elevation. The data gathered in deformation zones are shown as filled triangles whereas the data acquired in fracture domains are shown as filled circles. The three fracture domains are notated by different colours; red for FFM01, blue for FFM02 and black for FFM03. Moreover, hydrochemical data representing the A2 and F1 deformation zones are shown in a green colour.

Figure 3-60 suggests that both magnesium and chloride show variability with regard to elevation, structural geology and hydraulic properties. For instance, magnesium-rich samples extend to considerably greater depths along gently dipping deformation zones in the hanging wall bedrock, relative to that observed in the footwall bedrock in fracture domain FFM01. Furthermore, chloride concentrations in the water along gently dipping deformation zones in the hanging wall bedrock and in the underlying zones A2 and F1 are greater than the concentrations in the footwall bedrock (FFM01) down to c. –400 m RHB 70. However, below this elevation, the salinity in the footwall bedrock seems to be greater than the *Littorina Sea Water* salinity in the hanging wall. Hence, both plots indicate that the groundwater at depth in fracture domain FFM01 is of a non-marine origin at depth. This view is supported by the high chloride and low magnesium concentrations observed in the adjacent deformation zones bordering the tectonic lens where the footwall bedrock is situated, cf. the yellow triangles shown in Figure 3-60. The dashed lines in the two plots are inserted to improve the visualisation of the characteristics of the hydrochemical situation in the hanging wall bedrock.

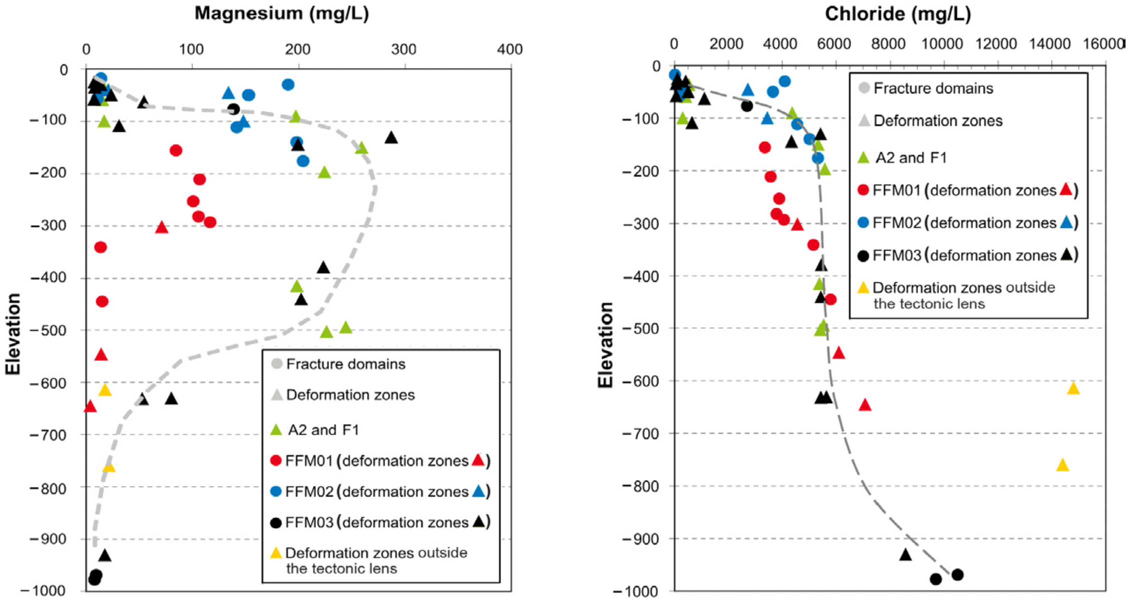

Figure 3-60. *Scatter plots showing magnesium concentration versus elevation (left) and chloride concentration versus elevation (right). Triangles denote deformation zones and circles the intervening fracture domains. The dashed lines indicate the conditions prevailing along the gently dipping deformation zones in the hanging wall bedrock and the gently dipping zones A2 and F1. Modified after /Olofsson et al. 2007/.*

Moreover, Figure 3-60 indicates that the conditions in FFM01 vary with depth in a complex manner. The samples gathered in the interval –150 to –400 m RHB 70 are less saline in FFM01 than they are in the interval –50 to –200 m RHB 70 in the intensely fractured domain FFM02 that lies above FFM01, cf. Figure 3-16. The same situation applies to magnesium. Presumably, this condition is an indication of a shallower impact of the *Littorina Sea Water* intrusion in the footwall bedrock below c. –150 m RHB 70 than in the hanging wall bedrock. It is recalled that the flowing fracture network system is significantly compartmentalised and poorly connected in FFM01, whereas the conditions are the opposite in the overlying fracture domain FFM02, cf. Figure 3-16 and Table 3-4. The shallow flushing of the *Littorina Sea Water* imprint in FFM02 by the *Present-day Meteoric Water* in Figure 3-60 is due to the pronounced structural-mechanical-hydraulic horizontal anisotropy observed near the bedrock surface.

The data shown in Figure 3-59 and Figure 3-60 represent *fracture water* chemistry. A vital contribution to the site investigation database in stage 2.2 is the sampling and hydrochemical analysis of bedrock *pore water* data. The work performed in the Forsmark area is described in /Waber and Smellie 2008/. We show in Figure 3-61 an example of the data gathered in borehole KFM01D, which penetrates the sparsely fractured FFM01 at drill site 1. The chloride data in Figure 3-61 suggest that:

- The chloride concentrations in the pore water and in the fracture water appear to be almost in equilibrium (steady-state) down to c. –200 m RHB 70, i.e. more or less down to the boundary between fracture domains FFM01 and FFM02. The magnesium concentration in the fracture water is high, cf. Figure 3-60, which indicates that salinity in the fracture water at this depth is of marine origin, e.g. *Littorina Sea Water*. In addition, the steady-state salinity conditions indicate that the mean spacing between the flowing fractures is small (tens of a metre to metre). This notion is supported by the frequency of PFL-f transmissivity data shown as blue dots in Figure 3-61.

- Between –200 and –500 m RHB 70, the conditions appear to be more transient with ongoing diffusion of chloride from the more saline fracture water to the less saline pore water. The observed pore water compositions suggest an ancient hydrochemical condition of more dilute water in both fractures and pores down to c. –500 m RHB 70, before the appearance of more brackish water in the fractures. It is noted that the magnesium content in the fracture water is low though, cf. Figure 3-60, which indicates that the origin of the brackish saline fracture water is non-marine, e.g. *Deep Saline Water* remnants. This interpretation is not necessarily unique, however. There is certainly a risk of upconing the *Deep Saline Water* while (pumping) in fractures. If the observations are correct, the difference in chloride concentrations between the fracture water and the pore water implies that the mean spacing between the flowing fractures is large (tens of metres). This view is supported by the PFL-f transmissivity data shown as red dots in Figure 3-61.
- Below c. –500 m RHB 70 in fracture domain FFM01, the chloride concentrations in the pore water samples increase considerably, reaching magnitudes close to or greater than the maximum values associated with the surrounding brackish, non-marine type groundwater in the fractures (c. 6,000 mg/L), which indicates (*i*) a pre-glacial circulation of more dilute water in the fractures and the pores down to c. –500 m RHB 70, and (*ii*) that the pore water at greater depth may be in equilibrium with the non-marine, *Deep Saline Water* type groundwater in the fractures.

In summary, the observations above suggest:

- A circulation of dilute water in the fractures and the pore water between –200 and –500 m RHB 70.
- At greater depth, the pore water may be in equilibrium with non-marine *Deep Saline Water*.

The resolution of the $\delta^{18}O$ stable isotope data in Figure 3-61 is considerably lower than for the chloride data, as indicated by the uncertainty bars shown. The reasons for these wide uncertainties are discussed in /Waber and Smellie 2008/. If we assume that the mean values are of some relevance for the conceptual modelling, the data shown in Figure 3-61 indicate that:

- The $\delta^{18}O$ values in the pore water and in the fracture water are in not in equilibrium but in a transient state in the interval –250 to –400 m RHB 70. The differences observed support the hypothesis that the mean spacing between the flowing fractures is increasing below c. –200 m RHB 70.
- The $\delta^{18}O$ content in the pore water is fairly enriched, which may indicate a warmer origin than normally associated with *Holocene Glacial Melt Water*. The interpretation of these high values is still subject to scrutiny, however.

The differences in fracture water and pore water hydrochemistry at repository depth indicate that the hydrochemistry in the sparsely fractured rock mass in fracture domain FFM01 is affected by hydrological surface conditions prior to the start of the main phase of the Weichselian glaciation, c. 50,000 years ago. Figure 3-54 illustrates some important phases in the climate (interglacials, stadials and interstadials) after the Eem interglacial. Indeed, Fennoscandia has been affected by very different climate conditions during the last 130,000–115,000 years BP. The evolution portrayed in Figure 3-54 indicates that the Forsmark area may have been subjected to various water influences for relatively long periods of time prior to the start of the main phase of the Weichselian glaciation.

The hydrochemical conceptual model development suggested in the work reported here is illustrated in Figure 3-62, which shows a 2D NW-SE cross-section of the present-day hydrochemical conditions in the Forsmark area. The cartoon highlights:

- the differences observed in the *Littorina Sea Water* intrusion in the hanging wall and footwall deformation zones, and
- the possibility for pre-Weichselian water influences at depth in the less fractured footwall and hanging wall bedrock segments.

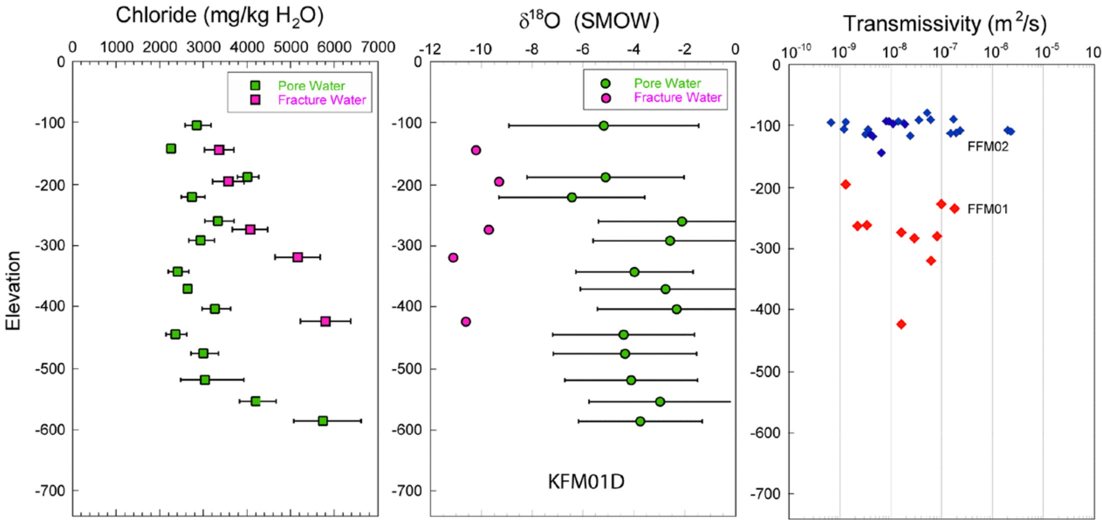

Figure 3-61. *Measured concentrations of chloride and $\delta^{18}O$ in fracture water and pore water samples gathered in cored borehole KFM01D /Waber and Smellie 2007/. The plot to the right shows PFL-f fracture transmissivity data from the same borehole /Follin et al. 2007b/.*

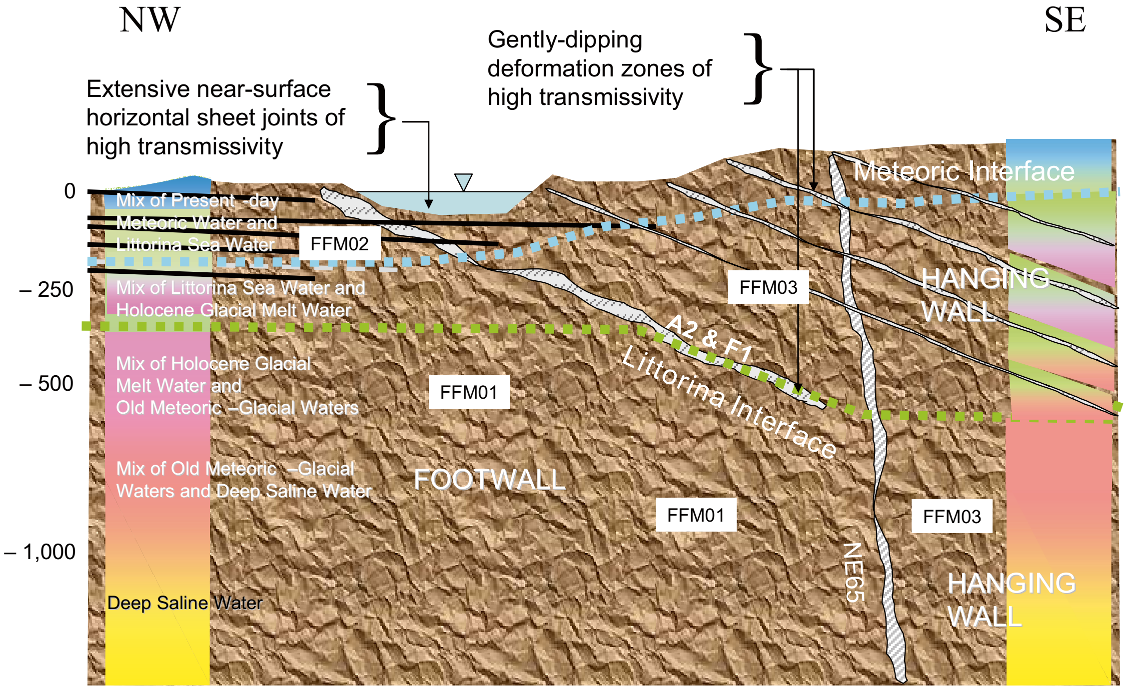

Figure 3-62. *NW-SE cross-section cartoon showing a conceptual model of the present-day hydrochemical conditions in the Forsmark area. The cartoon highlights (i) the differences observed in the Littorina Sea Water intrusion in the hanging wall and footwall deformation zones and (ii) the possibility for pre-Weichselian water influences at depth in the less fractured footwall and hanging wall bedrock segments. Blue = Present-day Meteoric Water, Green = Littorina Sea Water, Pink = Holocene Glacial Melt Water, Red = Old Meteoric-Glacial Waters and Yellow = Deep Saline Water.*

In conclusion, Figure 3-62 suggests five sources for the hydrochemistry observed with the following relative chronology in terms of hydrochemical influence: *Deep Saline Water* (oldest) > *Old Meteoric-Glacial Waters* (hypothesis) > *Holocene Glacial Melt Water* > *Littorina Sea Water* > *Present-day Meteoric Water* (most recent). At the present time, the hydrochemical composition of the hypothesised *Old Meteoric-Glacial Waters* can only be speculated. Indeed, since it is conceived as a melange of ancient water influences, it may not be possible to define it as a particular water type. However, the concept of residual, pre-Weichselian, water influences in the pore water hydrochemistry is an interesting view. Its role for the understanding of the palaeohydrological evolution in the Fennoscandian Shield is scrutinised as more pore water samples are gathered in the footwall bedrock, in the hanging wall bedrock and in the bedrock bordering the tectonic lens in the Forsmark area.

3.17.3 Boundary conditions in CONNECTFLOW

The boundary conditions for palaeohydrological modelling with CONNECTFLOW must represent the changes of the water composition at the upper surface, which mainly varies as a consequence of changes in shore level displacement (Figure 3-55) and the variations in the salinity of the Baltic Sea (Figure 3-57). The combination of these two plots suggests that prior to 6500 BC, the area would have been beneath a more or less freshwater lake (cf. the Ancylus Lake in Figure 3-56). Therefore, whatever is assumed for the initial condition, the surface water will have an equal or lower density than the groundwater beneath, and so there is no driving force for water to infiltrate the bedrock.

Hydraulic boundary conditions

For groundwater flow, there are two main possible boundary conditions that could be applied: specified head or a specified flux type boundary condition.

- For the area under the sea, it is most natural to use a specified head type boundary condition, where the head is equal to the depth of the sea multiplied by the relative salinity of the Baltic Sea.
- For the area onshore the specified flux type boundary condition is the most natural. It is complicated to implement because in reality the flux to the saturated zone will vary spatially, both in magnitude and direction since in some areas groundwater is recharging and in others it is discharging. This distribution of flux varies according to the amount of potential groundwater recharge and the hydraulic properties. /Follin et al. 2007a/ tested a flux boundary condition on the top surface, and found that the observed point-water head measurements in the uppermost part of the bedrock could be roughly reproduced with a groundwater recharge equal to about 100–150 mm/year and a homogeneous transmissivity of the single "cage feature" implemented around $5 \cdot 10^{-4}$ to $1 \cdot 10^{-3}$ m²/s.

The standard approach in CONNECTFLOW for specifying an infiltration type condition is to define the recharge flux, *R*, into or out of the model as a function of the current head, *h*, in the model, the topographic surface height, *z*, and the maximum potential groundwater recharge, R_p. The maximum potential groundwater recharge is equal to the precipitation minus evapotranspiration ($P - E$) and surface run-off. Surface run-off is subtracted because we are only interested in the potential recharge to the sub-surface. Appropriate functions for the flux, *R*, must have certain characteristics. For recharge areas, the head, *h*, or water table, is below ground surface and so the recharge must be equal to the full recharge, R_p. In discharge areas, the water table is just above ground surface and so head is just above ground surface, which can be achieved by taking a suitably large flux out of the model, i.e. a negative value of *R,* whenever the head goes above ground surface. The standard function used in CONNECTFLOW is:

$$R = \begin{cases} R_p & h \le z - \varepsilon \\ -R_p\,(h-z)/\varepsilon & h > z - \varepsilon \end{cases} \tag{3-7}$$

where ε is a small distance (2cm was used). This function implies that if the water table is more than ε below the topographic surface then recharge equals the full potential groundwater recharge. Above that, the recharge reduces until the water table is at the surface. If the water table is above the topographic surface, then recharge becomes negative, i.e. discharge, and an appropriate flux of groundwater is taken from the model to reduce the head until the water table is restored to the topographic height. Hence, this boundary condition is a non-linear equation (the flux depends on the free-variable head) that ensures a specified flux if the water table is low and a specified head where the water table is at or above ground surface. The non-linearity requires that multiple iterations of the groundwater flow equations be performed at each time-step to reach convergence, which implies longer run times for this boundary condition. The topographic surface is not constant in time due to post-glacial rebound and marine transgressions, and hence $z = z(t)$. Newton-Raphson iteration was used to achieve convergence of the non-linear equations at each time-step. This technique works best for systems with smooth gradients. The standard function given above for flux has a discontinuous derivative at $h = z - \varepsilon$ and this can lead to a slow rate of convergence; typically 3–5 Newton-Raphson iterations were required at each time-step. Hence, an alternative smooth function for recharge was used:

$$R = R_p \left(\exp\left(\frac{h - z}{0.5} \right) - 1 \right) \tag{3-8}$$

This has similar characteristics to the standard function, but has smooth derivatives around $h = z$. This often gives convergence in two Newton-Raphson iterations, and hence gives quicker and more robust solutions. There are other candidates for this function, such as a modification to the standard function but using a hyperbola to give a smooth transition around $h = z$.

It should be noted that in this model any groundwater that discharges through the top surface exits the model and does not enter a separate surface model that allows recharge downstream. Alternative approaches, are to couple the groundwater model to a surface hydrology model, or to add a surface layer with very high hydraulic conductivity to model the surface flow explicitly. In the second of these approaches, a flux is specified over the onshore region not covered by lakes, a head is specified in the sea and lakes, and the unsaturated flow equations should be solved in the near-surface layers. In this case, the flux should be set to precipitation minus evapotranspiration, and these in principle can vary spatially.

When simulating the palaeohydrological evolution over the last 10,000 years, transient variations in surface boundary conditions have to be considered both due to changes in the shore-level and in the salinity of the Littorina/Baltic Sea. The approach used is to apply the same definition of the boundary conditions as detailed above, but to calculate heads and elevations relative a sea-level datum that evolves in time. CONNECTFLOW uses residual pressure, P^R, as the independent flow variable which is related to total pressure, P^T, by

$$P^R = P^T + \rho_0 \, g \, (z - z_0) \tag{3-9}$$

where ρ_0 is the density of freshwater, g is acceleration due to gravity, and $(z - z_0)$ is the elevation of a point in the model relative to a datum. Hydraulic head scales with residual pressure as

$$h = P^R / \rho_0 \, g \tag{3-10}$$

For transients, then the datum, i.e. sea-level, varies in time, $z_0 = z_0(t)$.

Hydrochemical boundary conditions

In order to implement the evolving hydrochemical condition described in Section 3.17.2, a time varying specified value hydrochemical boundary condition is used on the top surface where there is an advective flow into the model (recharge area), or an outflow condition where there is flow out (discharge). Because the flows are transient, the areas of recharge and discharge evolve in time, and hence it is important to have an automatic way of determining where to have a specified concentration of infiltrating surface water and where to have an outflow of solute with discharging groundwater. The difficulty in achieving this is that it requires mixing a Neumann (specified flux) type boundary condition on outflow with a Dirichlet (specified concentration) type boundary condition on inflow; and since the recharge/discharge areas change in time, the type of boundary condition has to be changed in time. Our solution is to specify a flux of solute through the top surface that changes depending on the direction of flow across the surface. Where an inflow of groundwater at a specified input concentration is required (i.e. a Dirichlet condition), flux is equated to a penalty weight function based on the difference between solute concentration in the model and the required input concentration. Therefore, the magnitude of the flux of solute out of the model, F_c, is then given by the equation:

$$F_C = \begin{cases} (\boldsymbol{q}\cdot\boldsymbol{n})\,C & \boldsymbol{q}\cdot\boldsymbol{n} \geq 0 \\ (C - C_0)/\delta & \boldsymbol{q}\cdot\boldsymbol{n} < 0 \end{cases} \tag{3-11}$$

where $(\boldsymbol{q} \cdot \boldsymbol{n})$ is the magnitude of the advective flux of water out of the model, i.e. the groundwater flux, $\boldsymbol{q}$, in the direction parallel to the outward normal to the surface, $\boldsymbol{n}$, C is the solute concentration or mixing fraction, and δ is a small value (an inverse flow-rate, 10^{-4} s/m is used). For $(\boldsymbol{q} \cdot \boldsymbol{n}) \geq 0$, the flux corresponds to an outflow condition. For $(\boldsymbol{q} \cdot \boldsymbol{n}) < 0$, a specified value condition, $C = C_0$, is implemented as a penalty function such that solute is removed if $C > C_0$, and injected if $C < C_0$. This effectively ensures that $C \approx C_0$.

The hydrochemical boundary condition on the vertical sides of the model domain is assumed to be zero flux of solutes. On the base of the model at –1,200 m RHB 70, the mixture of reference waters is held fixed (i.e. equal to the initial condition) since it is expected that groundwater is mostly ancient high salinity stable water subject to very little advective flow below this elevation.

3.17.4 Initial conditions in CONNECTFLOW

The initial condition guess at 8000 BC considered in stages 1.2 and 2.1, as well as in the SR-Can project, was based on data from data freeze 1.2. It is shown to the left in Figure 3-63 and is here referred to as the "Base Case model". The "Alternative Case" initial condition guess at 8000 BC used in the work reported here is shown to the right in Figure 3-63. It is based on data from data freeze 2.2 and the hydrochemical conceptual model presented in Section 3.17.2. In short, the major difference between the Base Case and the Alternative Case initial condition models is:

- The Base Case model assumes that the less saline groundwater above the *Deep Saline Water* at 8000 BC was a mixture of *Deep Saline Water* and *Holocene Glacial Melt Water*. Hence, the Base Case model assumed that fresh, glacial melt water was injected deep into the bedrock under high pressures during the Weichselian period.
- The Alternative Case model assumes that the less saline groundwater above the *Deep Saline Water* at 8000 BC was a mixture of *Deep Saline Water*, *Old Meteoric-Glacial Waters and Holocene Glacial Melt Water*. Thus, the Alternative Case model assumes that the flushing with *Holocene Glacial Melt Water* did not completely replace the pre-existing waters above the *Deep Saline Water*, e.g. waters of pre-Weichselian origin.

To implement the Alternative Case model in CONNECTFLOW, we treated that *Old Meteoric-Glacial Waters* as a fifth reference water with the same hydrochemical composition as the *Present-day Meteoric Water*, except that the levels of bicarbonate were reduced to those of the ancient *Deep Saline Water* in accordance with low bicarbonate levels measured at depths below about –200 m RHB 70. The difference this makes to the initial profile of $\delta^{18}O$ is demonstrated in Figure 3-64 along with a comparison to the measured levels of $\delta^{18}O$ in groundwater samples. Only samples taken below –400 m RHB 70 are shown since these may reflect groundwater chemistry from the past more relevant to initial conditions than samples nearer the surface. As can be seen, the alternative model predicts initial $\delta^{18}O$ levels closer to those seen in present-day samples at depth. The $\delta^{18}O$ ratio will increase with time from these initial profiles as *Littorina Sea Water* and *Present-day Meteoric Water* infiltrates into the upper bedrock.

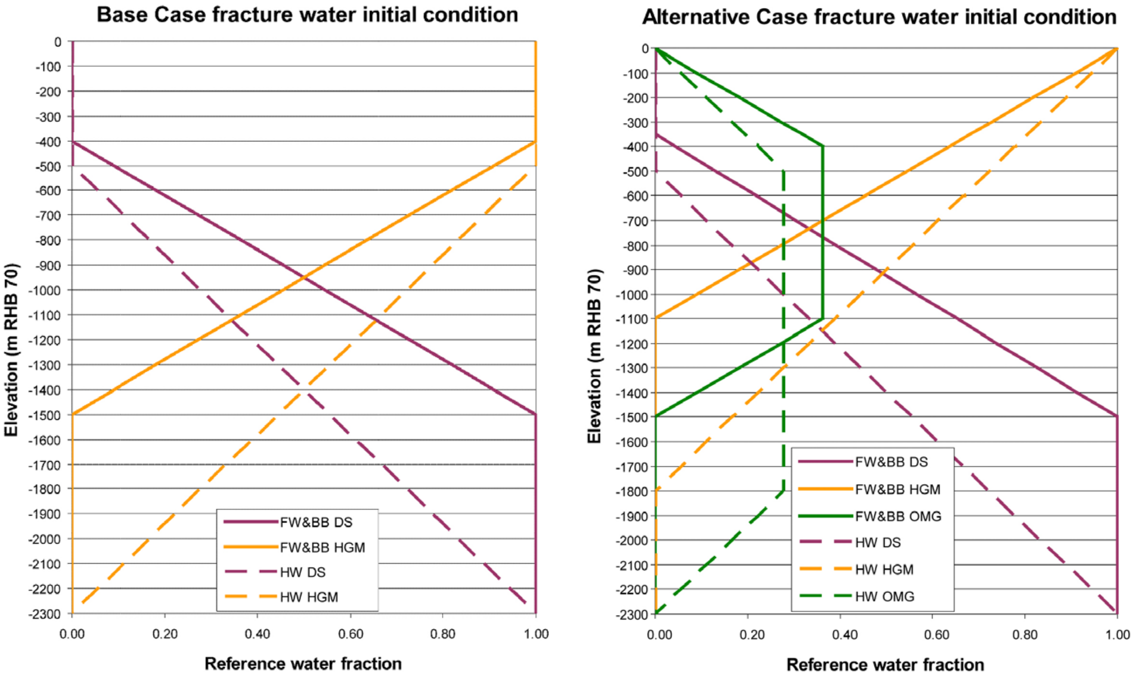

Figure 3-63. *Left: The Base Case model assumes that the fracture water chemistry at 8000 BC was a mixture of Deep Saline Water and Holocene Glacial Melt Water (HGM). Right: The Alternative Case model assumes that the fracture water chemistry at 8000 BC was as a mixture of Deep Saline Water (DS), Holocene Glacial Melt Water (HGM) and Old Meteoric-Glacial Waters. In both models, different profiles were assumed for the footwall (FW) and border borehole (BB) regions of deformation zone A2 compared to the hanging wall (HW) bedrock of zone A2.*

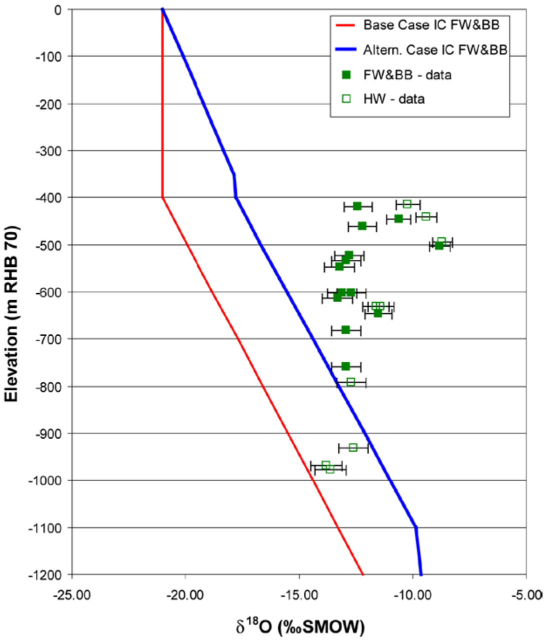

Figure 3-64. *Comparison of initial $\delta^{18}O$ for the Base Case (red) and the Alternative Case (blue) models. The measured levels of $\delta^{18}O$ from the fracture water samples from below –400 m RHB 70 are shown in green, where the filled squares represent the data gathered in the footwall and bordering bedrock of deformation zone A2 and the open squares represent the data gathered in the hanging wall (HW) of zone A2.*

The basis for choosing the initial fractions of *Deep Saline Water* shown in Figure 3-63 is demonstrated in Figure 3-65 by comparing the initial fractions of *Deep Saline Water* used in the Alternative Case model with those interpreted with the M3 method /Laaksoharju et al. 2008/. This shows why the different slopes and intercept were chosen for the hanging wall and footwall of the gently dipping deformation zone A2. It is also clear that levels of *Deep Saline Water* seem to rise rapidly in some boreholes at around –300 m to –400 m RHB 70 while in others it is a more gradual increase. Another way of considering the choice for the initial condition of *Deep Saline Water* would be to use the ratio of Br/Cl without relying on any M3 results, although for the reference water compositions given it only informs where *Deep Saline Water* starts to be encountered. Such plots confirm the choice for the onset of *Deep Saline Water* in the initial condition.

For freshwater, the division between *Holocene Glacial Melt Water* and *Old Meteoric-Glacial Waters* partly justified by considering $\delta^{18}O$ in Figure 3-64, but also by considering what fraction of meteoric water was interpreted by M3. One needs some caution here as the M3 analysis for stage 2.2 did not consider *Old Meteoric-Glacial Water* as one of the principal components. It only considered *Present-day Meteoric Waters* as a principal meteoric component. The difference in chemical composition between infiltrating *Present-day Meteoric Water* and *Old Meteoric-Glacial Waters* is going to be hard to discriminate by methods such as M3. However, here we assume that the fractions of *Present-day Meteoric Water* identified by the M3 method at depths below –400 m RHB 70, where groundwater flux is generally low, are indicative of the levels of *Old Meteoric-Glacial Waters* that may persist over long times at such depths used for deriving the Alternative Case initial condition. Figure 3-66 shows a comparison of the mass fraction of *Old Meteoric-Glacial Waters* used in the initial condition and the fractions of *Present-day Meteoric Water* interpreted by the M3 method using groundwater samples from elevations below –400 m RHB 70. This shows levels of around 30–40% are appropriate at these depths.

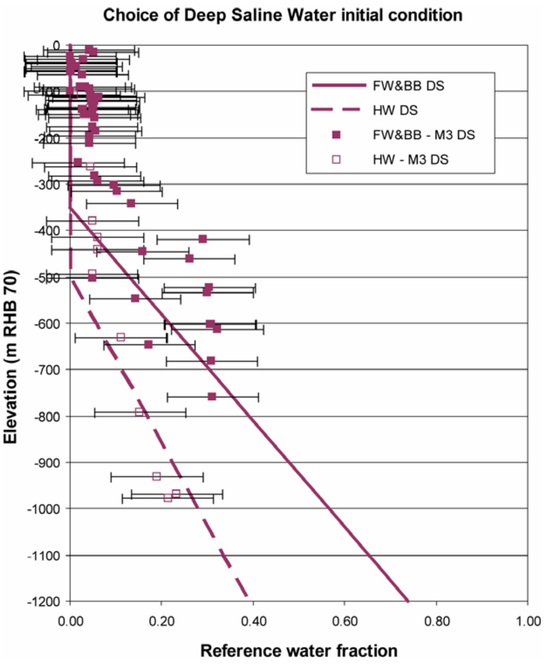

***Figure 3-65.** Comparison of mass fraction of Deep Saline Water (DS) in the fractures between the Alternative Case model and the M3 method. The M3 method has an interpretation error of at least ± 10%. Different profiles were assumed for the footwall (FW) and border borehole (BB) regions of deformation zone A2 compared to the hanging wall (HW) bedrock of zone A2.*

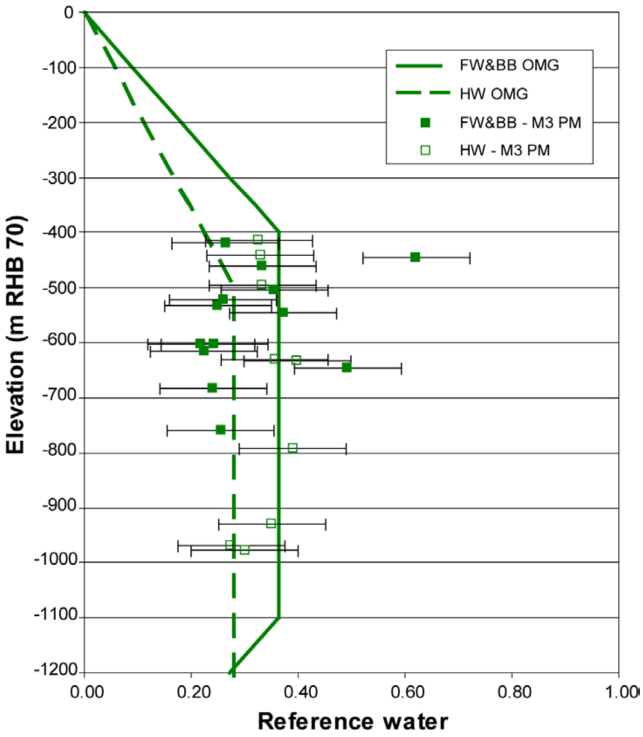

***Figure 3-66.** Comparison of mass fraction of Old Meteoric-Glacial Waters (OMG) used in the Alternative Case initial condition with the fraction interpreted for Present-day Meteoric Water (PM) using the M3 method on groundwater samples below an elevation of –400 m RHB 70. The M3 method has an interpretation error of at least 10% as indicated by the error bars shown. A different profile is used for the footwall (FW) of deformation zone A2 and border borehole (BB) regions (solid lines and data points) and the hanging wall (HW) of zone A2 (dashed lines and open data points).*

The above discussions only consider an appropriate initial condition for groundwater in the connected fracture system since it is based on samples of groundwater that have flowed into a borehole section. Since we also model diffusion of reference waters into the rock matrix pore water between fractures, then an initial condition is also required for reference water fractions in the rock matrix pore water.

In the Base Case model it was assumed that the initial reference water fractions at 8000 BC are the same in the matrix as in the fracture system (i.e. a mixture of *Deep Saline Water* and *Holocene Glacial Melt Water*), see the plot to the left in Figure 3-67. For such a situation to arise in the sparsely fracture rock at Forsmark, the *Holocene Glacial Melt Water* must have infiltrated deep into the bedrock over tens of thousands of years and reached a diffusive equilibrium with the matrix pore water.

Analysis of pore water taken from cores in the intact bedrock indicates high δ^{18}O ratios, however, thus suggesting *Old Meteoric-Glacial Water*. In the Alternative Case model it was assumed that the initial reference water fractions are different in the matrix than in the fracture system. δ^{18}O is not necessarily conservative over hundred of thousands of years, but it should be sufficiently conservative to indicate the evolution of groundwater since the last ice age, say 50,000–100,000 years. Only Cl and δ^{18}O and δD have been measured for the matrix pore water samples, making it harder to guess the origin of the mixture of reference waters. The Cl levels are similar to those of the modern Baltic Sea, and generally lower than in the fracture system at similar depths. However, the water in the fractures cannot be of a marine origin because the magnesium content in the fractures is low. It seems that this would require that the water in the matrix to be a mix *Old Meteoric-Glacial Water* and *Deep Saline Water*, see the plot to the right in Figure 3-67, whereas the water in the fractures is a mix of *Holocene Glacial Melt Water*, *Old Meteoric-Glacial Water* and *Deep Saline Water* (Figure 3-63) As mentioned, this interpretation is not necessarily unique, though. There is certainly a risk for an upconing of *Deep Saline Water* while pumping in transmissive fractures.

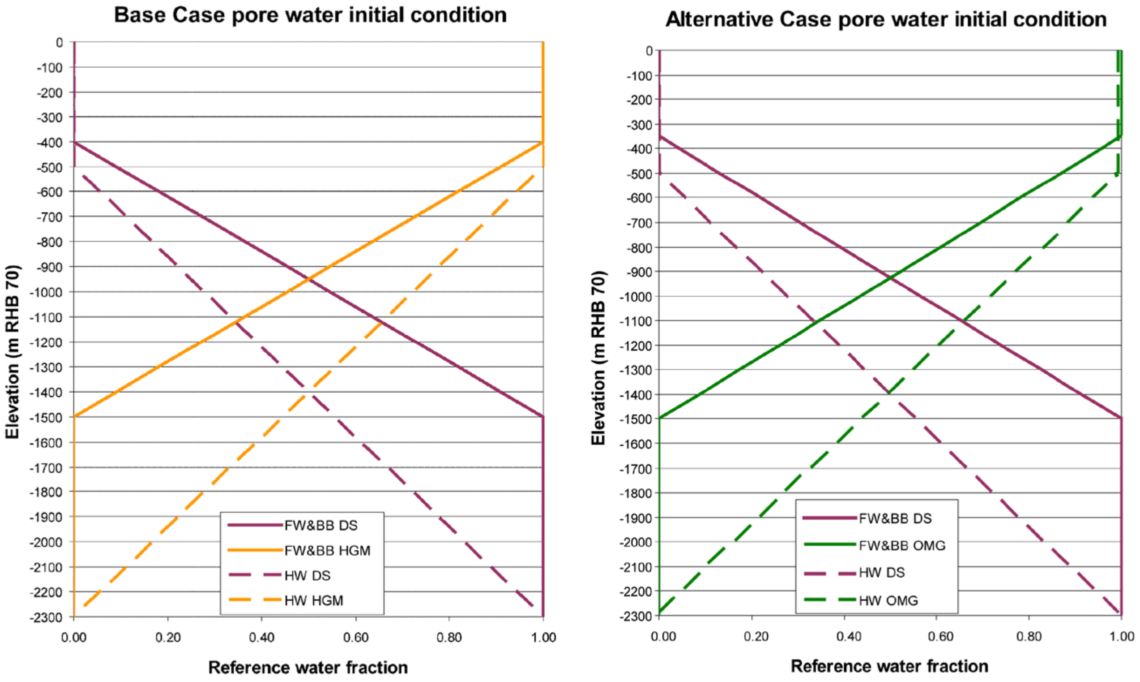

__Figure 3-67.__ Left: The Base Case model assumes that the groundwater in the pores at 8000 BC was a mixture of Deep Saline Water and Holocene Glacial Melt Water (HGM). Right: The Alternative Case model assumes that the groundwater in the pores at 8000 BC was as a mixture of Deep Saline Water (DS) and Old Meteoric-Glacial Waters. In both models, different profiles were assumed for the footwall (FW) and border borehole (BB) regions of deformation zone A2 compared to the hanging wall (HW) bedrock of A2.

3.17.5 Recharge and discharge

Several attempts have been made to assess and classify the distribution of recharge and discharge of near-surface groundwater in the Forsmark area. /Werner et al. 2007/ provide a comparison between different recharge/discharge methods based on data from the Quaternary deposits belonging to data freeze 2.1. /Werner et al. 2007/ compare “continuous classification recharge/discharge methods”, i.e. topographical modelling, map overlays and hydrological-hydrogeological flow modelling, and “discrete classification recharge/discharge methods”, i.e. field-based and hydrochemistry based classifications of groundwater monitoring well locations. The best agreement between models was found for the topography-based model and hydrological-hydrogeological flow modelling. For the monitoring wells located in areas classified in the field as recharge areas, there is a good agreement with the hydrochemistry-based (Piper plot). The agreement is less good for the monitoring wells located in areas classified in the field as discharge areas. In addition, using tritium concentration as an age-dating indicator shows low variability among recharge wells, but a large spread among discharge wells. The usefulness of a hydrochemistry-based recharge/discharge classification of the Quaternary deposits in the Forsmark area is thought to be limited due to, among other things, the calcite-rich soils and local/shallow groundwater flow systems.

The hydrochemical data from data freeze 2.2 are collated and analysed in, among others, /Tröjbom et al. 2007/, who focused on the understanding of important processes and factors that affect the hydrochemistry in the surface systems. One major issue discussed in /Tröjbom et al. 2007/ is if any evidence of deep groundwater discharge to the surface system can be found. Consistent with the hydrological-hydrochemical conceptual model, observations in surface water and shallow groundwater indicate that there is probably no ongoing deep discharge into the freshwater surface system within the area covered by horizontal sheet joints, see Figure 3-31. In restricted areas outside these structures there are, however, indications of relict marine remnants, which also include deep saline signatures, in the groundwater at relatively shallow depths in the Quaternary deposits. One such area, suggested by /Tröjbom et al. 2007/, is Lake Gällsboträsket, cf. Figure 3-58. /Johansson 2008/ made a hydrochemical budget for Lake Gällsboträsket with regard to the mass flux of chloride discharging from the lake and concluded that with the current rate of outflow of chloride (c. 8 tonnes/year), the total quantity of chloride in the Quaternary deposits of the Gällsboträsket depression (c. 500 tonnes) should be depleted in c. 60 years. The lake threshold of Lake Gällsboträsket rose above the sea level c. 225 years ago. The current rate of outflow of chloride raises the question of an additional source of chloride besides the relict marine remnants alone. We note here that the location of Lake Gällsboträsket coincides with the Eckarfjärden deformation zone.

3.17.6 Hydrochemical conditions outside the candidate area

The hydrochemical conditions in the bedrock bordering the tectonic lens are briefly investigated. Figure 3-60 shows that high chloride concentrations were obtained between –600 to –750 m RHB 70 while sampling in two deformation zones bordering the north-western part of the candidate area, see Figure 3-67. The two zones are referred to as NNW0100 and NW1200 and are found to be transmissive /Follin et al. 2007b/. It is unclear whether the high chloride concentrations are natural due to upconing during the drilling operations.

It is known from the study site investigations in the Finnsjön area /Andersson et al. 1991, Ahlbom and Svensson 1991/ that near-surface, gently-dipping deformation zones can short circuit the groundwater circulation at depth. /Thunehed and Pitkänen 2007/ have investigated the Forsmark area with transient electromagnetic soundings. Seven transmitter loops were used, see Figure 3-69. Figure 3-70 shows an interpretation of the data gathered along the profile connecting transmitter loops 1–4. The dislocation at the Forsmark deformation zone is mainly based on interpretation of the sounding data from transmitter loop 5 NW of the profile, see Figure 3-69. Data freeze 2.3 will contain results from the investigations of the Singö and Forsmark deformations at drill sites 11 (KFM11A) and 12 (KFM12A), cf. Figure B-2 in Appendix B.

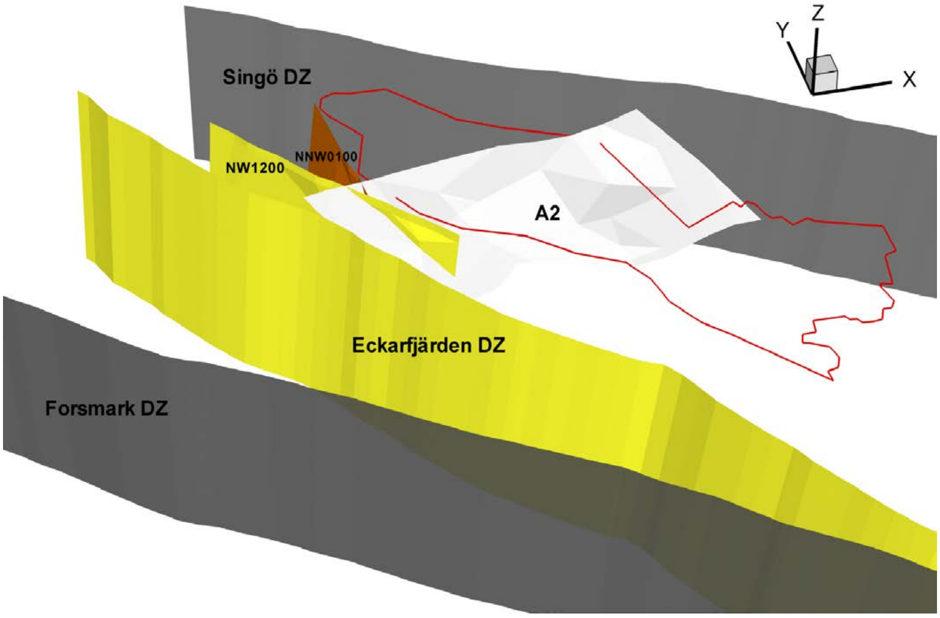

Figure 3-68. *The deformation zones referred to as NNW0100 and NW1200 border the south-eastern side of the target area. Hydrochemical data from these zones reveal high chloride concentrations at –600 to –750 m RHB 70 in boreholes KFM07A and KFM09A intersecting the two zones, respectively, cf. Figure 3-60.*

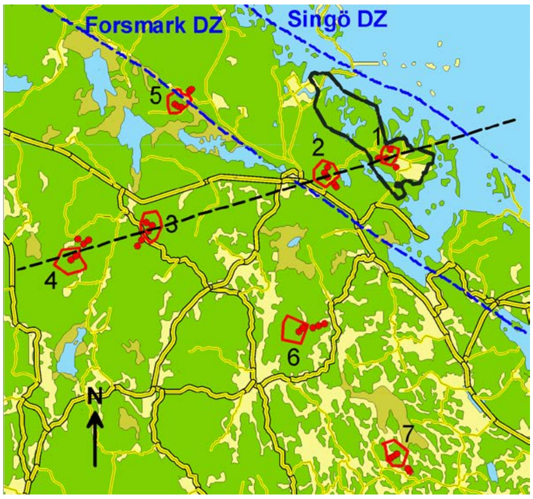

***Figure 3-69.** Map showing the position of the vertical section in Figure 3-70 as a dashed black line. The Singö and Forsmark deformation zones are shown with dashed blue lines together with the candidate area. Modified after /Thunehed and Pitkänen 2007/.*

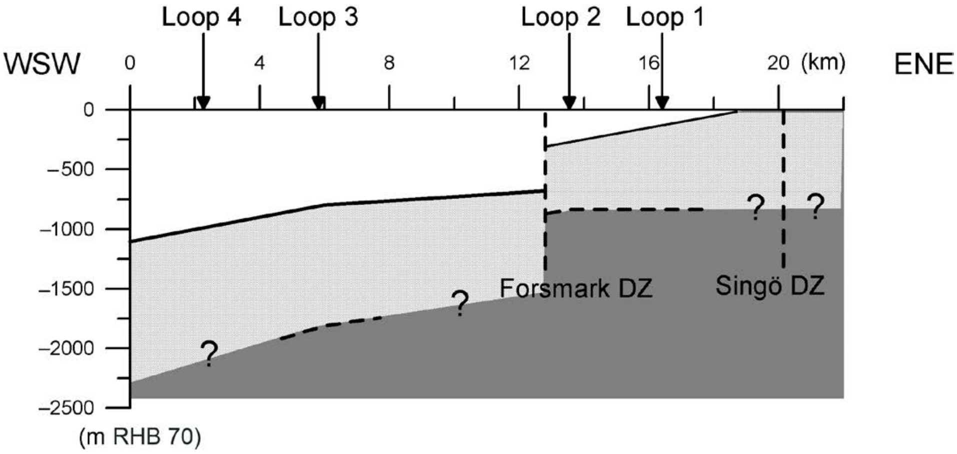

***Figure 3-70.** Vertical section showing a generalised interpretation of the sounding data. The layers represent, from top to bottom, rock saturated by fresh, brackish and saline water respectively. The dislocation at the Forsmark deformation zone is mainly based on interpretation of the sounding data from transmitter loop 5 NW of the profile, see Figure 3-69. Modified after /Thunehed and Pitkänen 2007/.*

3.18 Summary

The key features and assumptions of the hydrogeological conceptual model in stage 2.2 are summarised as:

HCD

- A pronounced structural anisotropy, established at an early stage in the geological history in the ductile regime, steered the overall occurrence and character of younger brittle structures in the Forsmark area. The candidate area is located in the north-westernmost part of one of these tectonic lenses that extends from north-west of the nuclear power plant south-eastwards to Öregrund.
- The gently-dipping deformation zones A2 and F1 divide the bedrock inside the tectonic lens into two structural segments, which are here referred to as the footwall and hanging wall bedrock of A2, respectively.

- The hanging wall bedrock is intersected by several gently-dipping deformation zones, many of which extend down to one kilometre depth, or more. It is primarily composed of a single fracture domain, FFM03. By contrast, the footwall bedrock has very few gently-dipping deformation zones but a number of steeply-dipping deformation zones with a north-eastern strike. The footwall bedrock is primarily composed of fracture domains FFM01, FFM02 and FFM06.
- The hydraulic measurements in boreholes reveal that the hydraulic properties of the deformation zones are very heterogeneous. Besides a striking depth trend there is also a considerable horizontal heterogeneity. At each elevation the gently-dipping deformation zones are found to be the most transmissive. Apparently, the number of gently-dipping deformation zones is lower in the footwall segment of deformation zone A2 than in the hanging wall segment of zone A2.
- It is assumed that the observed spatial variability of the transmissivity data associated with the deterministically modelled deformation zones inside the candidate area is representative for deformation zones in general, both inside and outside the candidate area. This hypothesis will be tested in stage 2.3 when boreholes KFM08D, KFM11A and KFM12A will be drilled.

HRD

- The repository target volume is located in the north-western part of the lens and consists of fracture domains FFM01, FFM02 and FFM06. Fracture domains FFM04 and FFM05 border the lens (and the target volume) to the southwest, to the northwest and to the northeast. Fracture domain FFM03, which occurs within the lens, borders the target volume to the southeast.
- Fracture domain FFM02 is situated closest to the surface and is substantially more fractured than fracture domain FFM01. Available data from fracture domains FFM04 and FFM05 indicate that the bordering bedrock is also considerably more fractured than fracture domain FFM01. Below –400 m RHB 70 in fracture domain FFM01, the connected network of open fractures is considerably compartmentalised and the frequency close to the percolation threshold, which implies a restricted groundwater circulation at repository depth.
- It is assumed that fracture domain FFM06, which is poorly investigated at this stage, is structurally and hydraulically similar to fracture domain FFM01. This hypothesis will be tested in stage 2.3 when the KFM08D borehole is drilled into FFM06.
- Sub-horizontal and gently-dipping single fractures are more predominant in FFM02. Release of vertical stress across sub-horizontal and gently dipping fractures near the surface leads to these features being often more transmissive than the steeply-dipping single fractures, and hence a high degree of horizontal versus vertical anisotropy in flow is expected.

HSD

- The Quaternary deposits consist mainly of till with a mean thickness of a few metres. Till is the oldest Quaternary deposit in the area and is subsequently resting directly upon the bedrock surface. Below the lakes, the stratigraphy of the Quaternary deposits is more complex; the till is here often overlain by more impermeable gyttja-clay sediments.

Solute transport model

- The evolution of the salinity of the aquatic systems in the Baltic basin during the Holocene is closely coupled to the shore level displacement. The most saline period during the Holocene occurred c. 4500–3000 BC, when the area was entirely covered by Littorina Sea implying a surface water salinity of 10–15‰ compared with approximately 5‰ today in the Baltic Sea.

- The hydrochemical conditions in the bedrock bordering the tectonic lens are briefly investigated. High chloride concentrations were obtained between –600 to –750 m RHB 70 while sampling in two deformation zones bordering the north-western part of the candidate area. It is unclear whether the high chloride concentrations are natural due to upconing during the drilling operations. Regional geophysical measurements support a hypothesis of a varying depth to the deep saline water, where the depth to the interface is deeper to the southwest of the Forsmark deformation zone than it is in the candidate area.

Initial conditions

- From a palaeohydrological point it is envisaged that the Forsmark area has been subjected to meteoric, glacial and marine/lacustrine water influences for relatively long periods of time prior to the start of the main phase of the most recent glaciation, the Weichselian. Remnants of these waters creates may still exist in the groundwater system making it harder to certain about the initial hydrochemical conditions at 8000 BC, which is the selected starting point of the palaeohydrological simulations.
- The Alternative Case hydrochemical model suggested here assumes that the water in the matrix at 8000 BC was a mix of two reference waters: *Old Meteoric-Glacial Water* and *Deep Saline Water*, whereas the water in the fractures was a mix of *Holocene Glacial Melt Water*, *Old Meteoric-Glacial Water* and *Deep Saline Water*. As mentioned, this interpretation is not necessarily unique, though. There is certainly a risk of upconing of *Deep Saline Water* during sampling in transmissive fractures caused by pumping.

Boundary conditions

- The shore-level displacement started before the final deglaciation and is still an active process in the Forsmark area with about 7 mm per annum. About 10,000 years from today the accumulated displacement is predicted to be c. 40 m. Thus, the present-day hydrological conditions in the Forsmark area are not at steady-state and the site will not be a coastal site in the future provided that the current shore level displacement process continues at its expected rate.
- It is only during the last 3,000 years that any part of the regional model area has been above sea-level, and only in about the last 1,000 years has any part of the candidate area been above sea-level.
- Several attempts have been made to assess and classify the distribution of recharge and discharge of near-surface groundwater in the Forsmark area. According to observations in surface water and shallow groundwater, and to the hydrological-hydrochemical conceptual model, there is probably no ongoing deep discharge into the freshwater surface system within the area covered by horizontal sheet joints. In restricted areas outside these structures there are, however, indications of relict marine remnants, which also include deep saline signatures, in the groundwater at relatively shallow depths in the Quaternary deposits. One such area is Lake Gällsboträsket, which lays in a topographic depression that coincides with the Eckarfjärden deformation zone.

Besides older, single fractures (HRD) and outcropping deformation zones (HCD), the percussion drilling and hydraulic testing programme has identified a system of shallow, sub-horizontal fractures/sheet joints. Together, these structures form a “shallow bedrock aquifer”. This fracture network is presumably confined to within 150 m of the surface and largely parallels the undulations of the topography. Evidence from groundwater levels suggest that the network is poorly connected vertically to the regolith above the bedrock (mainly Quaternary deposits). However, hydraulic diffusivity data from interference tests indicate that the network is well connected laterally, if heterogeneously, and very transmissive.

Current hydraulic data suggest that the transmissive shallow bedrock aquifer overlying the target repository volume may have a finite lateral extent having the form of a triangle bounded to the northeast by the Singö deformation zone, (WNW0001), to the southeast by the NE0062A deformation zone, and to the west by the expression of the sheath fold structure in rock domains 32 and 44. This hypothesis will be tested hydraulically in stage 2.3 by means of an interference test conducted at percussion-drilled borehole HFM33 located on the SFR peninsula. see Figure B-7 in Appendix B.

In terms of regional flow, the high transmissivity and diffusivity of the shallow fracture aquifer serves to reduce hydraulic gradients across the deeper bedrock flow system. As such, this reduction of gradient in a way acts like a “hydraulic cage”, though unlike a hydraulic cage it does not eliminate gradients entirely. Indeed, both data and simulations indicate that there is flow across the connected heterogeneous deformation zones in the target area at repository depth toward the shallow fracture aquifer, which becomes the main conduit for transport form the site.

Despite the risk of misunderstanding, we use the term “hydraulic cage phenomenon” in the work reported here to emphasise the significant hydraulic diffusivity of the near-surface network, which shorts the groundwater flow pattern in the uppermost part of the bedrock. Since the horizontal fractures/sheet joints are not mapped to a very large detail in the site investigations, they are difficult to implement due to uncertainties in their spatial extent and hydraulic heterogeneity. The chosen numerical approach to model the near-surface horizontal fractures/sheet joints in terms of three so-called “cage features”, along with interpreted deformation zones, communicates hydraulic disturbances across large distances in the numerical model, which by and large are consistent with the field observations observed in the upper parts of the bedrock.

4 Calibration targets

4.1 Modelling concepts and methodology

The work reported here focuses on studying the gross performance and sensitivity of an ECPM flow model representation (cf. Figure 2-5) to different major model assumptions and code settings. As mentioned in Section 1.3, we study single realisations representing different scenarios at this stage. Hence, the objective function in stage 2.2 is not to propose a best fit model, but to try to discriminate among alternative major assumptions (what controls the system?) and look for major sensitivities and/or potential sources for interpretation errors in the hydrogeological conceptual model development presented in Section 3.

Forward model calibration consists of changing values of model input parameters in an attempt to match field conditions within some acceptable criteria. The general approach used here is to use essentially the same groundwater flow and solute transport model in terms of grid discretisation and parameter settings for simulating (matching) the three types of field data associated with Tasks B–D in Figure 1-2. By comparing the model predictions with different types of field data/measurements, the overall model development could be partially calibrated to improve the parameterisation, improve our understanding of the hydrogeological system, and help build confidence in the hydrogeological conceptual model of the Forsmark area.

However, to become a meaningful activity in a highly heterogeneous and anisotropic medium such as the crystalline bedrock in the Forsmark area, ECPM model calibration with regard to groundwater flow and solute transport requires that the structural-hydraulic conditions be fairly properly characterised and implemented from the on-set. Lack of a proper structural-hydraulic numerical implementation may result in a calibrated groundwater flow and solute transport model that is not representative for use in other applications/scenarios /Konikow and Bredehoeft 1992/. Therefore, an initial model calibration step was applied in this study (Task A) prior to the modelling of the three calibration targets focusing on groundwater flow and solute transport (Tasks B–D). The initial step is here referred to as “Local conditioning on single-hole hydraulic tests”.

4.2 Task A – Local conditioning on single-hole hydraulic tests

ECPM model parameterisation is a two step process. First, transmissivities inferred from the hydraulics tests are used to parameterise the deformation zone (HCD) and the fracture domain (HRD) models, see /Follin et al. 2007b/. Secondly, the geometrical and hydraulic properties of these two discrete models are transformed into ECPM hydraulic conductivities using a specified grid resolution, see Figure 2-5.

/Follin et al. 2007b/ suggested that in addition to a depth dependency model, local conditioning of the ECPM model should be attempted, which implies that measured data should be honoured in the final ECPM model as far as possible. Thus, the ‘objective function’ of Task A in the work reported here was to condition the hydraulic conductivity values of the ECPM model on the measured transmissivity data gathered on the same support scale as the ECPM grid. The data used are the 20 m constant-head, double-packer injection tests gathered with PSS method, see Figure 4-1 for an example.

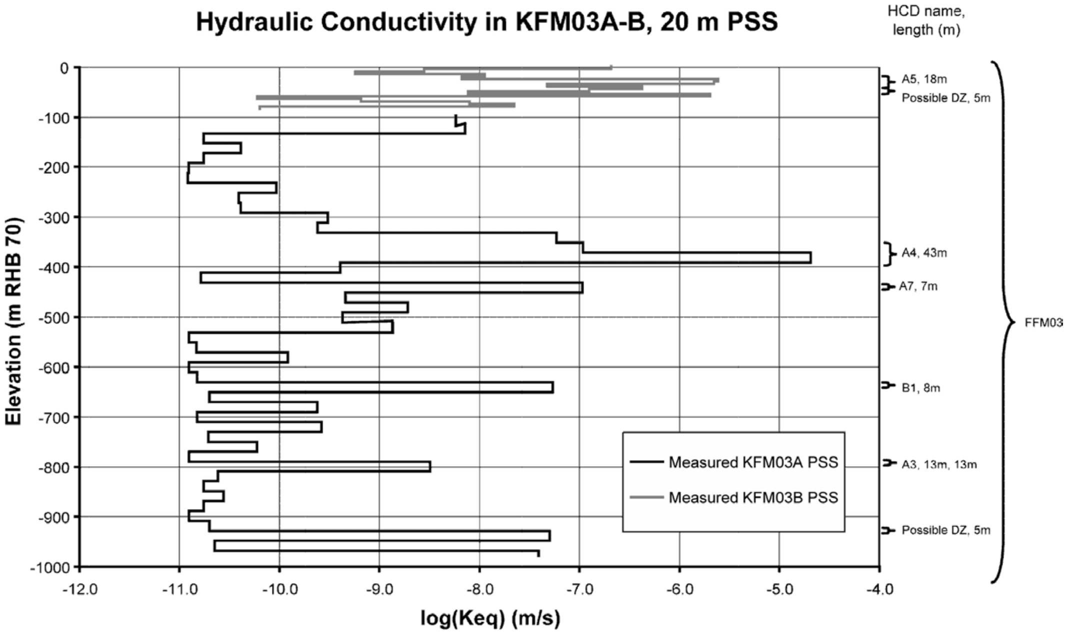

Figure 4-1. *Hydraulic conductivity data from 20 m section PSS measurements in KFM03A and KFM03B. Based on data reported by /Källgården et al. 2004/ and /Hjerne et al. 2004/.*

4.2.1 Uncertainties in data

Measurement uncertainties

There are several issues of ongoing concern regarding the performance and interpretation of hydraulic investigations in fractured rocks, e.g. test disturbances, measurement thresholds (limits), flow regimes, fracture connectivity (chokes), skin effects, well-bore storage effects, etc. The reliability of the hydraulic investigations conducted in the Forsmark area using PSS injection tests and PFL-f difference flow logging tests is discussed in /Follin et al. 2007b/.

Handling uncertainties

Some other examples of handling uncertainties are: (*i*) interpretation of hydraulic thickness versus geological, (*ii*) upscaling of a scalar entity (test transmissivity) to a model tensor (hydraulic conductivity), (*iii*) treatment of inferred depth dependencies and our suggested method for local hydraulic conditioning, and (i*v*) interpretation of horizontal fractures/sheet joints in the near-surface bedrock.

4.2.2 Expected contribution

It is envisaged that comparing ECPM profiles of hydraulic conductivity predicted in boreholes against measured PSS data provides a simple test that the numerical implementation of conceptual is broadly consistent with the hydraulic properties at the measurement points. We expect the model to have the right conductivities where the boreholes intercept deformation zones to verify the model for the HCDs is appropriate. In the background rock, HRD, we expect the model to predict a generally low hydraulic conductivity at depth with *occasional* stochastic transmissive features with a similar frequency and magnitude of hydraulic conductivity to that observed. If the model can reproduce such behaviour, then the right distribution of flow-rates can be expected. The main focus of this calibration step is the HCD, since these dominate the flow regime at Forsmark.

4.3 Task B – Matching the 2006 interference test in HFM14

4.3.1 Data selected for calibration

The 2006 interference test in HFM14 was performed by pumping in HFM14 and at the same time monitoring pressure responses in different observation sections in surrounding boreholes. In total, 105 observation sections in 36 observation boreholes were included in the interference test. 12 of the 36 boreholes are core-drilled and have 55 sections included in the interference test. 24 boreholes are percussion-drilled with a total of 50 monitoring sections. For each observation section, the estimated drawdown was supplied as a time-series over the 21 days of pumping. Additional data was supplied for a second later interference test performed in HFM14 at approximately the same flow-rate with monitoring only in KFM10A, but for only 3 days of pumping, although this was enough to achieve a response at the borehole intercepts with zone A2.

Figure 4-2 shows the observed drawdowns at the end of the 2006 interference test in HFM14, cf. Figure 3-28 thorough Figure 3-30. The observation points are ordered with regard to the radial distance between the point and the sink (HFM14). Here, the ‘objective function’ is not to reproduce every single response, but to understand what controls the near-field and far-field responses, i.e. what mechanisms/properties that make the model responses mimic the measured responses.

4.3.2 Uncertainties in data

Measurement uncertainties

Two examples of measurement uncertainties are: (*i*) uncertainties associated with the gathering of representative point-water head data in a heterogeneous groundwater system with a spatially a varying fluid density, and (*ii*) uncertainties associated with disturbances due to seasonal trends, precipitation events, etc. These matters were partly discussed in /Gokall-Norman and Ludvigson 2006/. The data treated in the work reported here is corrected for seasonal trends but not for precipitation, thus accounted for in the simulations. The role of precipitation for the interpretation of bedrock interference test responses is exemplified in Appendix G, which display and analyse data observed during the 2005 HFM01 interference test /Gokall-Norman et al. 2005/.

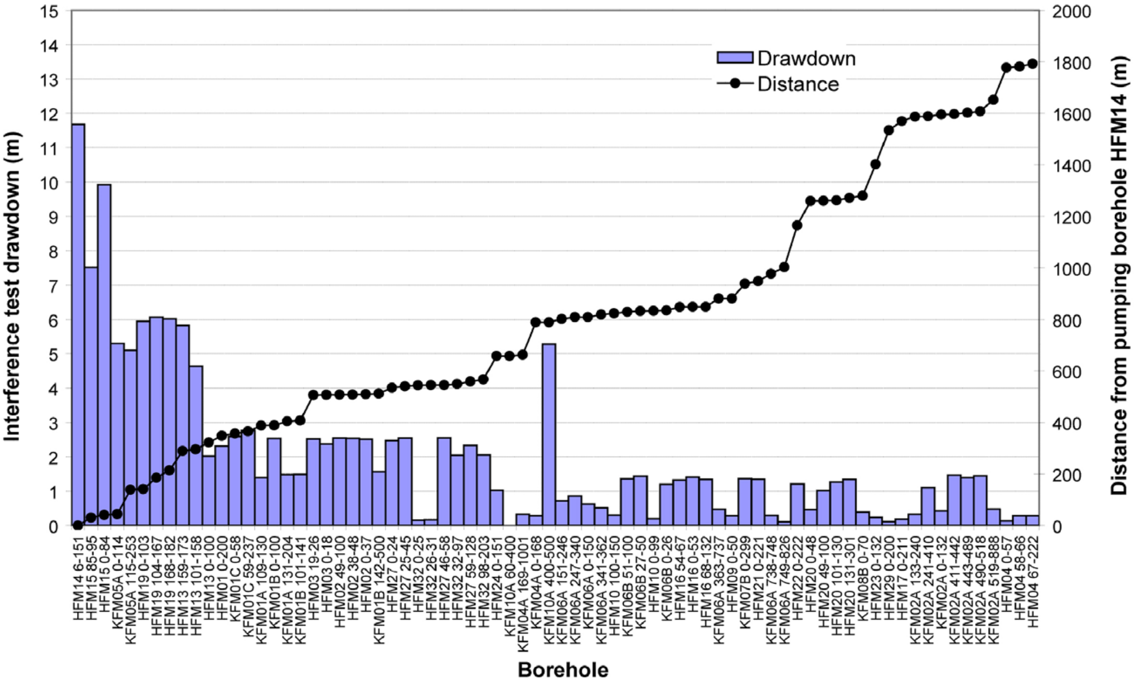

Figure 4-2. *Plot of observed drawdowns at the end of the 2006 interference test in HFM14. Monitoring intervals are sorted by distance from the abstraction well.*

Handling uncertainties

Two examples of handling uncertainties are: (*i*) How should the abstraction rate in be distributed amongst the continuum finite-elements modelling HFM14 in order to mimic the real sink, which is located in fractured rock?, and (*ii*) How shall the comparison be made between measured heads observed in a packed off multi-packer monitoring system and the pressures representing variable-density flow in a continuum grid?

4.3.3 Expected contribution

Calibrating against the 2006 interference test is expected to test model predictions of hydraulic communications on the scale of a kilometre or so. The high transmissivity HCD are expected to dominate the hydraulic responses, and so Task B should provide a good test of the structural model and hydraulic property assignment, such as the transmissivity of zone A2 and its connections to sub-vertical zones and the "cage features". Several boreholes have been monitored at different depths, and where there are differences in the responses at different depths, the data will provide a way of understanding distinctions in the hydraulic properties of the HCD, the bedrock, and the quaternary deposits. In contrast to the PSS and PFL-f hydraulic test data that essentially only informs horizontal flows, the interference test also provides information on the vertical transmission of hydraulic disturbances. HFM14 is very close to Lake Bolundsfjärden which provides a possible source of recharge to the abstraction. Calibrating the model on hydraulic responses in monitoring holes surrounding the lake will provide a means of understanding the vertical hydraulic contact between the lake, underlying soil and bedrock. In summary, Task B is likely to prove a useful calibration for all 3 hydraulic domains: HCD, HRD and HSD.

4.4 Task C – Matching natural point-water heads

4.4.1 Data selected for calibration

Figure 4-3 and Figure 4-4 show natural (undisturbed) point-water heads in the Quaternary deposits and the near-surface bedrock available for modelling in stage 2.2. The observation points are ordered with regard to the elevation of the bedrock. Here, the 'objective function' is to reproduce the spatial distribution of natural mean point-water heads in the Quaternary deposits as well as in the near-surface bedrock. The agreement can be evaluated by comparing graphs such as these with model predictions and/or by calculating functions such as the root-mean-square of difference in heads.

4.4.2 Uncertainties in data

Measurement uncertainties

Two examples of measurement uncertainties are: (*i*) uncertainties associated with the gathering of representative point-water head data in a heterogeneous groundwater system with a spatially varying fluid density, and (*ii*) uncertainties associated with the computation of representative mean point-water head data in a heterogeneous groundwater system subjected to disturbances due to seasonal variations, precipitation events, nearby pumping, etc.

These matters were partly discussed in /Johansson et al. 2005, SKB 2006a, Juston et al. 2007/ and /Johansson and Öhman 2008/. The mean data treated in the work reported here represent the best data available considering the listed uncertainties.

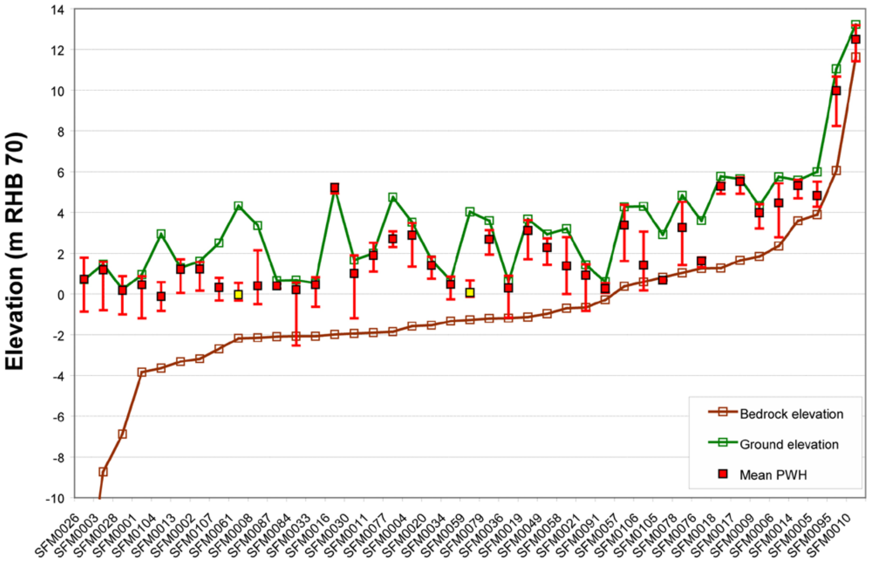

Figure 4-3. *Mean natural (undisturbed) point-water heads in the Quaternary deposits available for modelling in stage 2.2. The time series behind these plots are discussed in /Johansson et al. 2005, Juston et al. 2007, Werner et al. 2007/ and /Johansson and Öhman 2008/. The bars show the observed spread between the maximum and minimum values. The observations points referred to as SFM0061 and SFM0059 are located in an esker, which explains why the unsaturated zone is thicker at these two points than elsewhere.*

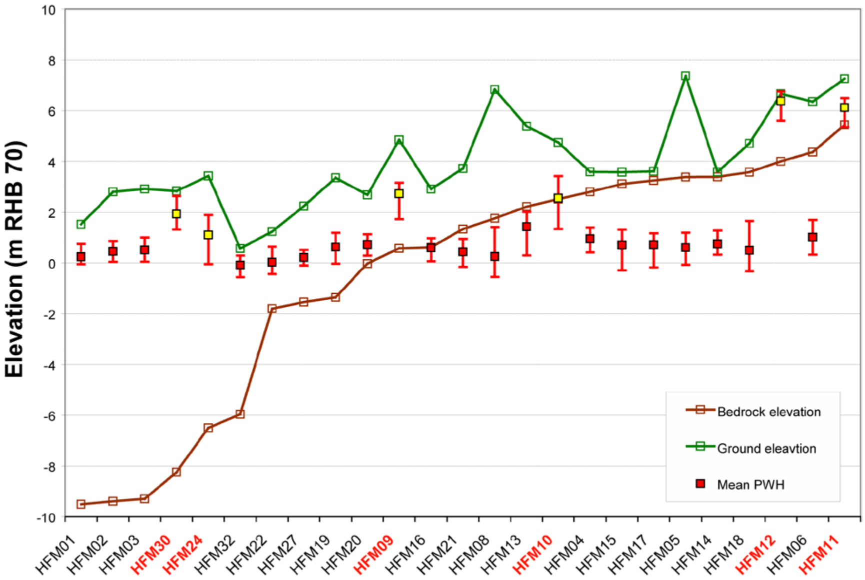

Figure 4-4. *Mean natural (undisturbed) mean point-water heads in the uppermost part of the bedrock available for modelling in stage 2.2. The time series behind these plots are discussed in /Johansson et al. 2005, Juston et al. 2007, Werner et al. 2007/ and /Johansson and Öhman 2008/. The bars show the observed spread between the maximum and minimum head values. The observations points referred to as HFM30, HFM24, HFM09, HFM10, HFM12 and HFM11 are located outside the area where the "hydraulic cage phenomenon" has been observed, which may explain why the heads at these point are closer to the surface elevation.*

Handling uncertainties

An example of a pertinent handling uncertainty is: How shall the comparison be made between heads observed in a packed off multi-packer monitoring system and the pressures representing variable-density flow in a continuum grid?

4.4.3 Expected contribution

The natural point-water head measurements are located in the quaternary deposits and upper bedrock, and hence calibrating on this type of data is expected to inform the interaction between the groundwater in the superficial bedrock and the groundwater in the Quaternary deposits, in particular the discussion about the net recharge to the bedrock and the distribution of the recharge-discharge pattern. Therefore, Task C is likely to be focussed on the hydraulic properties of the HSD and upper HRD, as well as providing confirmatory testing of the hydraulic boundary conditions.

4.5 Task D – Matching hydrochemistry profiles in boreholes

4.5.1 Salinity data

The constituents encompassed by the hydrochemical programme in stage 2.2 are listed in Appendix B. In Table 4-1, a summary of the constituents and boreholes considered in the model calibration reported here is presented. Figure B-1 and Figure B-2 in Appendix B show the location of the boreholes of interest.

If one would limit the selection of data used to only those that fulfil criteria such as a low level of drilling water residue and full coverage of major ions and isotopes, it would leave a large number of unused samples. Some of these samples are found at elevations where more representative data are missing. It was therefore decided to use some of these samples as *supplementary data* in this study in order to provide more data for the comparison. Samples with drilling water residue less than 15% were selected, but only if there were no other data available for that particular elevation. Samples having such high contents of drilling water must of course be used with a great deal of caution and may serve only as *indicative* data.

The delivery of hydrochemistry data makes use of a colour code in order to show the degree of representativity. In Table 4-2, these codes are defined for samples taken from the core-drilled boreholes. In total, c. 1,700 data samples were delivered for modelling in stage 2.2. Eleven samples (5 HFM and 6 KFM) were judged as representative (orange colour code) and 41 samples (19 HFM and 22 KFM) were judged as less representative (green colour code). Another 29 samples were selected as supplementary data (grey colour code) using the criteria defined above. See Figure 4-5 for a plot summary of all available salinity data for the KFM boreholes.

For the ease of presentation, and to allow results from different boreholes to be combined in a single plot with colours used to distinguish the values for the different boreholes, a modified scheme is used in the plots here:

- The 11 data samples considered representative and the 41 data samples considered less representative (orange and green colour coding in Table 4-2, respectively) were grouped together and are indicated by large filled squares in the plots shown in Section 5.
- The 29 supplementary data (grey colour coding in Table 4-2) are indicated by small filled circles in the plots shown in Section 5. It is emphasised that the supplementary data are included only because of the lack of representative and less representative data. That is, the supplementary data are uncertain and should be used with great caution in the calibration.
- The pore water data are indicated by blue-white circles (for those boreholes where such data were available).

Table 4-1. Coverage of hydrochemistry data in the boreholes used as calibration targets in stage 2.2. Table 4-2 contains a detailed specification of the quality classification system used for the data samples.

Name	Salinity	Major ions	Iso-topes	Water types	Pore water	No. of samples [representative / less representative / supplementary / total number]	Highest elevation of data (m RHB 70)	Lowest elevation of data (m RHB 70)
KFM01A	Yes	Yes	Yes	Yes	–	2 / 1 / 0 / 3	–47	–176
KFM01B	Yes	Yes	Yes	Yes	–	0 / 0 / 1 / 1	–37	–37
KFM01D	Yes	Yes	Yes	Yes	Yes	0 / 6 / 0 / 6	–156	–445
KFM02A	Yes	Yes	Yes	Yes	–	1 / 4 / 7 / 12	–52	–962
KFM03A	Yes	Yes	Yes	Yes	–	2 / 4 / 4 / 10	–137	–978
KFM04A	Yes	Yes	Yes	Yes	–	0 / 1 / 2 / 3	–11	–197
KFM05A	Yes	Yes	Yes	Yes	–	0 / 1 / 0 / 1	–90	–90
KFM06A	Yes	Yes	Yes	Yes	Yes	1 / 2 / 3 / 6	–15	–645
KFM07A	Yes	Yes	Yes	Yes	–	0 / 1 / 5 / 6	–316	–760
KFM08A	Yes	Yes	Yes	Yes	–	0 / 1 / 1 / 2	–564	–648
KFM08C	–	–	–	–	Yes	0 / 0 / 0 / 0	–	–
KFM09A	Yes	Yes	Yes	Yes	–	0 / 1 / 5 / 6	–56	–614
KFM09B	Yes	Yes	Yes	Yes	Yes	0 / 0 / 1 / 1	–65	–65

Table 4-2. Colour coding with respect to representativity of the used hydrochemistry data.

Colour coding	Specification
Orange	Considered representative or suitable. A charge balance of ± 5%. Less than or close to 1% drilling water.
Green	Less representative or of a limited suitability. A charge balance of ± 5%. Less than or close to 5% drilling water. Should be used with caution.
Grey	*Supplementary data* for elevations where no representative data are present. Less representative or of a limited suitability. A charge balance of ± 5%. Less than or close to 15% drilling water. Should be used with a great deal of caution and may serve only as *indicative* data.
White	Not used in calibration.

In the present study, the main focus is on the results for salinity (expressed as TDS), Cl, Br/Cl-ratio, Mg, HCO_3 and $\delta^{18}O$, primarily in the hanging wall bedrock of zone A2 (KFM03A) as well as in the footwall bedrock of zone A2 (KFM01D, KFM06A and KFM08A predominantly). Salinity is a very important natural tracer because variations in salinity lead to one of the driving forces for groundwater flow.

The main comparison of the results of the flow model with observations is a visual comparison of the trends of salinity along the boreholes with interpreted field data. The comparison is made in this way, rather than in terms of a quantitative measure defined at the data points.

The salinity for a given water composition in the model is calculated as the sum of the products of each reference water fraction and the salinity of that reference water (i.e. Br, Ca, Cl, HCO_3, K, Mg, Na and SO_4). The modelled salinities were compared with those observed through a visual comparison of the profiles along the boreholes, comparing the trends and major features in the boreholes.

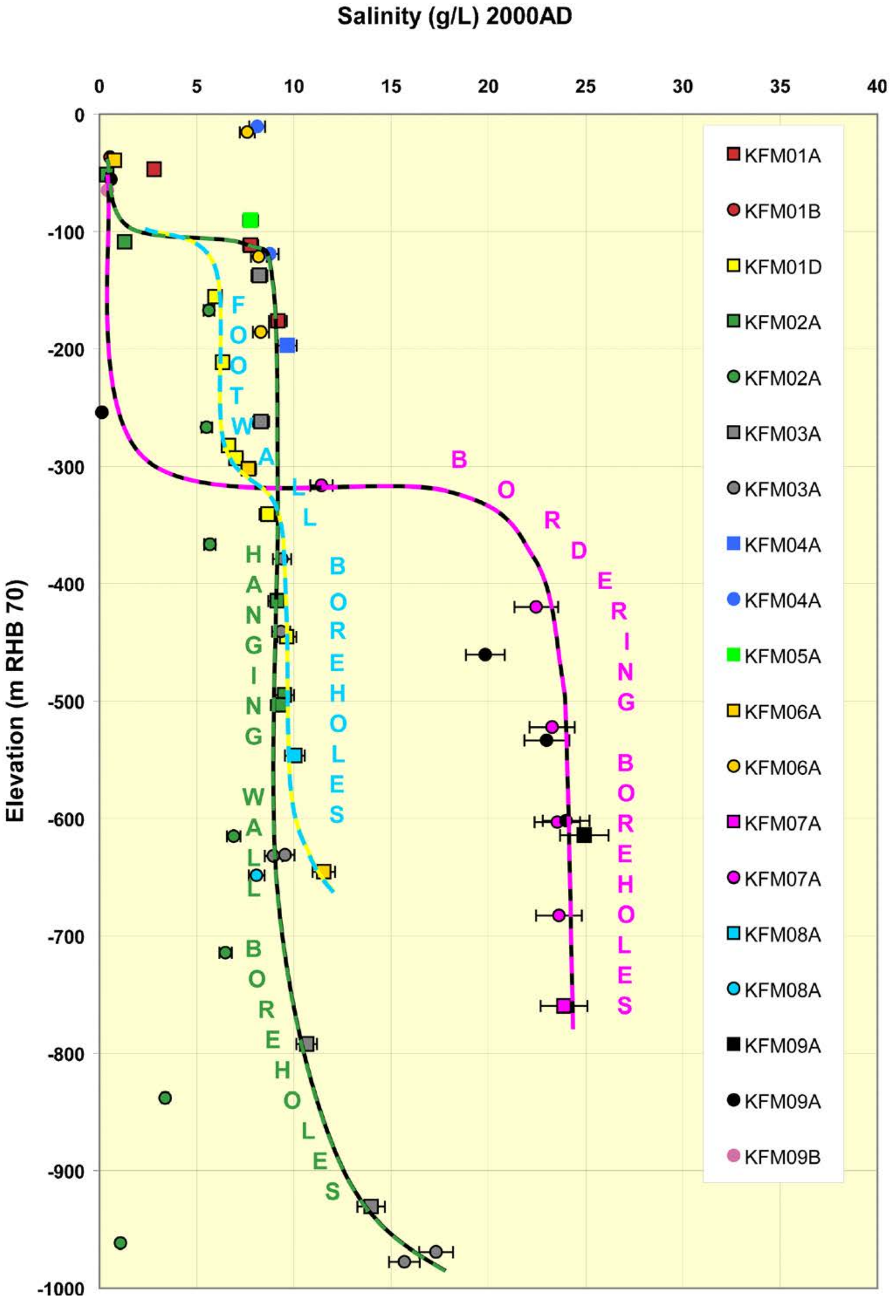

Figure 4-5. *Plot of all available salinity data from the core-drilled boreholes. For the sake of comparison, the reference water salinities (g/L) are: Deep Saline Water = 100; Old Meteoric-Glacial Water = 1.5; Holocene Glacial Melt Water = 0; Littorina Sea Water = 12; Present-day Meteoric Water = 1.5. The hypothetical trend lines shown are based on data from KFM01D+KFM08A, KFM02A+KFM03A and KFM07A+KFM09A. The footwall boreholes sample the groundwater in the FFM02 and FFM01 fracture domains. The hanging wall boreholes sample the groundwater in the FFM03 fracture domain, whereas the bordering boreholes sample the groundwater in the FFM04 and FFM05 fracture domains. Data samples considered representative (or somewhat less representative) are indicated by large filled squares, the supplementary data are indicated by small filled circles, and the pore water data are indicated by blue-white circles (for those boreholes where such data are available). It is noted that the supplementary data (small filled circles) are uncertain and should be used with great caution. For instance, the supplementary data at depth in KFM02A are not regarded as representative.*

There are different approaches for estimating the total dissolved solids (TDS) in the groundwater. Since chloride is the main anion in the groundwater at Forsmark, a strong correlation between chloride concentrations and groundwater salinity expressed as TDS, is expected. This correlation may be used to estimate approximate values for chloride concentrations if TDS is known, and vice-versa. An empirical relation has been found when analysing groundwater chemistry samples from Forsmark, Laxemar, Simpevarp and Äspö/Ävrö /Auqué et al. 2006/:

$$TDS(Cl^-) = 1.65\, Cl^- \qquad (4\text{-}1)$$

The TDS can also be calculated from the electric conductivity (EC) using the following empirical relation:

$$TDS(EC) = 6.30\, EC \qquad (4\text{-}2)$$

In the model, the TDS is calculated as the sum of all ions that have been considered (i.e. Br, Ca, Cl, HCO_3, K, Mg, Na and SO_4). In Figure 4-6, a comparison of the different approaches for estimating the TDS is presented. The three approaches discussed above (as well as only the chloride fraction) are all compared to the TDS obtained from calculations with the computer software Phreeq C. It is clear that pure chloride concentration and TDS based on chloride consequently are lower than the TDS values calculated with Phreeq C. The TDS calculated from electric conductivity however is generally higher than with Phreeq C. This is also the case for TDS calculated as the sum of all ions, even if the situation is the opposite for lower concentrations. This discrepancy also depends upon the scale used for presentation. In this case, a logarithmic scale is used, which emphasises the differences in the lower end of the range of values. In the model calibration only the TDS values calculated with Phreeq C were used. As seen in Figure 4-6 this estimate is in the middle of the range of values computed using the different methods presented above.

In the model calibration only data from the core-drilled boreholes were used since the samples from the percussion-drilled boreholes are obtained from water pumped from the boreholes, and hence are subject to more disturbances by the sample acquisition. Because of the complex geology at Forsmark, the boreholes were split into three main groups for presentation purposes, see Table 4-3.

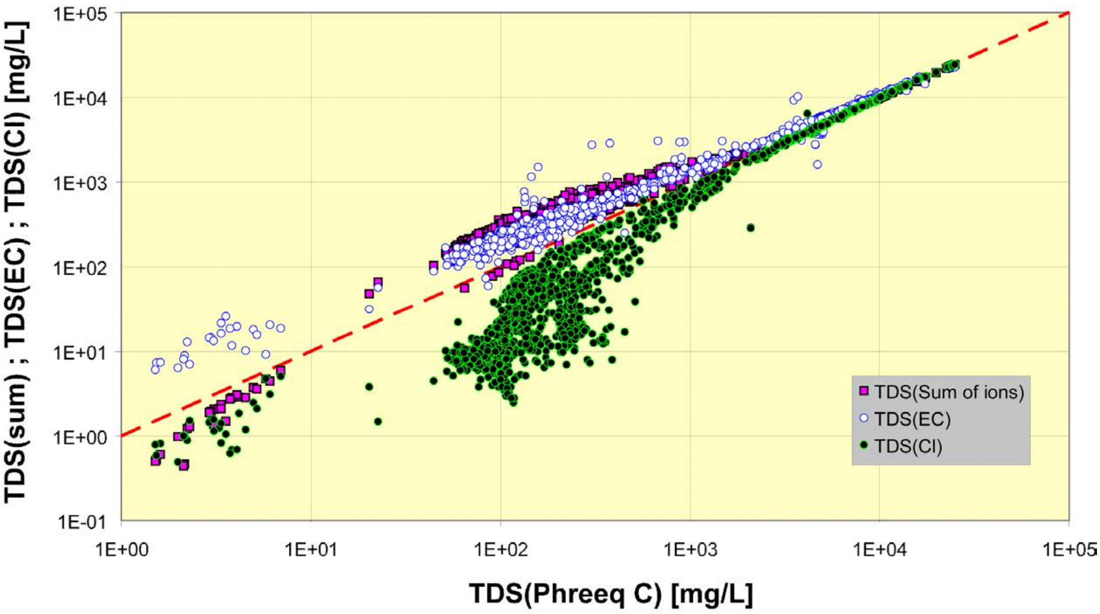

Figure 4-6. *Comparison of different approaches for estimating the total dissolved solids, TDS, in the groundwater.*

Table 4-3. Suggested division of the boreholes used in the model calibration.

Hanging wall boreholes	Fracture domain	Interval
KFM02A	FFM03	< –515 m RHB 70
KFM03A	FFM03	Entire length
KFM03B	FFM03	Entire length
KFM10A	FFM03	Entire length

Footwall boreholes	Fracture domain	Interval
KFM01A–D	FFM02 & FFM01	Entire length
KFM02A	FFM01	> –515 m RHB 70
KFM04A	FFM01	> –400 m RHB 70
KFM05A	FFM02 & FFM01	Entire length
KFM06A–C	FFM02 & FFM01	Entire length
KFM07A	FFM02 & FFM01	< 700 m RHB 70
KFM07B	FFM02 & FFM01	Entire length
KFM08A–C	FFM02 & FFM01	Entire length
KFM09A	FFM02 & FFM01	> –179 m RHB 70
KFM09B	FFM02 & FFM01	Entire length

Bordering boreholes	Fracture domain	Interval
KFM04A	FFM04	< –400 m RHB 70
KFM07A	FFM05	> –700 m RHB 70
KFM09A	FFM04 & FFM05	< –232 m RHB 70

4.5.2 Major ions and isotope data

Fracture water

The transport of reference waters is here simulated as chemically non-reactive fluids in the groundwater flow model. The reference water compositions in the fracture system are given in Table 3-14. The concentrations of the major ions and the isotope ratios (and the salinity) can be readily determined from the fractions of the reference waters. In this study, these concentrations are compared with those observed, which represent in a sense raw data. This was considered preferable to comparing the calculated mixing fractions of the reference waters with the M3 mixing fractions inferred from the data (using a principal component analysis), because there are substantial errors (at least 10%) associated with the M3 mixing fractions.

It is perhaps worth noting that CONNECTFLOW could have directly simulated the transport of the major ions and isotopes. However, it was more convenient to specify the boundary and initial conditions in terms of the reference waters. Also, although some chemical constituents, such as Cl and $\delta^{18}O$, are transported conservatively (i.e. no chemical reaction takes place during transport), others are likely to be non-conservative, such as HCO_3 and SO_4, which can be affected by chemical and microbial processes. As mentioned previously, Mg is not a conservative tracer either, but it is a useful indicator to differentiate between *Deep Saline Water* at depth and shallower *Littorina Sea Water* near the top surface of the model domain. However, because of the ion exchange mechanisms involving Mg great caution should be taken when using these non-conservative tracers for model calibration purposes. Actually, even a qualitative evaluation might be misleading. The Br/Cl ratio can be used as an alternative to indicate the transition zone from *Littorina Sea Water* to *Deep Saline Water*. The environmental isotopes δD and $\delta^{18}O$ help to differentiate between *Holocene Glacial melt Water* and meteoric reference waters such as *Old Meteoric-Glacial Waters* and *Present-day Meteoric Water*.

Pore water

The hydrochemistry delivery for stage 2.1 contained pore water data (Cl) extracted from fresh core samples collected in KFM06A. The hydrochemistry delivery for stage 2.2 contains additional pore water data (Cl, δD (or δ^2H) and $\delta^{18}O$) extracted from fresh core samples collected in KFM01D, KFM08C and KFM09B. All boreholes are situated in the footwall. The pore water from fresh core samples is here referred to as matrix pore water.

For KFM01D, a depth profile of 14 matrix pore water samples, down to an elevation of –603 m RHB 70, have been reported for the Cl concentration and 13 samples for the components $\delta^{18}O$ and δD, see Table 4-4 and Figure 4-7 to Figure 4-9. The pore water isotope composition is strongly enriched in the heavy isotopes compared to the fracture groundwater. The pore water isotope compositions from these depths appear to be more of Littorina-type composition. The lack of equilibrium between pore water and fracture groundwater suggests that the pore water contains a component that is significantly older than the fracture groundwater (because the groundwater is predominantly flowing in the fractures). The behaviour of the chloride concentration in KFM01D is consistent with that of $\delta^{18}O$ and δD.

For KFM06A, a depth profile of 20 matrix pore water samples, down to an elevation of –865 m RHB 7, have been reported for the Cl concentration, see Table 4-4 and Figure 4-10. No data were reported for the isotope components $\delta^{18}O$ and δD in KFM06A. The situation in KFM06A is similar to that in KFM01D. In addition, pore water data for KFM06A are available at greater depths compared to KFM01D. The data at depths below –700 m RHB 7 indicate the presence of *Deep Saline Water* in the rock matrix.

For KFM08C, a depth profile of ten matrix pore water samples, down to an elevation of –771 m RHB 70, have been reported for the Cl concentration and eight samples for the components $\delta^{18}O$ and δD, see Table 4-4 and Figure 4-11 to Figure 4-13. The isotopes show that the upper 400 m of the rock matrix in KFM08C has been flushed. At depths greater than –400 m RHB 70, the salinity in the matrix increases. Around –400 to –500 m RHB 70 there seems to be some *Littorina Sea Water* left in the matrix. Beneath this level, the water is more of a *Deep Saline Water* type.

For KFM09B, a depth profile of eight matrix pore water samples, at an elevation of approximately –440 m RHB 70, have been reported for the Cl concentration and three samples for the components $\delta^{18}O$ and δD, see Table 4-4 and Figure 4-11 to Figure 4-13. The isotope content of KFM09B is similar to KFM08C at the corresponding elevation. The chloride content in KFM09B indicates Deep Saline at higher elevations compared to the other boreholes where matrix pore water data are reported.

In general, there are few samples available for comparison between the fracture water and the matrix pore water. However, it can be noted that in KFM01D there is a poor connection between the fracture water and the matrix pore water. This also seems to be the situation in KFM08C.

Table 4-4. Coverage of the matrix pore water data. The pore water measurement error of the studied components for each sample was specified in the delivery, see Figure 3-61 for an example.

Borehole	Number of samples for each component			Depth interval
ID	Cl	δD	$\Delta^{18}O$	(m RHB 70)
KFM01D	14	13	13	–112 to –603
KFM06A	20	–	–	–126 to –865
KFM08C	10	8	8	–131 to –771
KFM09B	8	3	3	–436 to –445

Apart from the salinity, the focus here is also on the results for Cl, Br/Cl-ratio, Mg, HCO_3 and $\delta^{18}O$, primarily in the hanging wall bedrock of A2 (KFM03A) as well as in the footwall bedrock of A2 (KFM01D, KFM06A and KFM08A predominantly). Because of the conservative nature of Cl and $\delta^{18}O$, they can be used quantitatively in the model calibration. The use of Mg, HCO_3 and potentially other ions, must be used in a more qualitative way. The main comparison of the results of the flow model with observation is a visual comparison of the trends of these major ions along the boreholes with interpreted field data. The comparison is made in this way, rather than in terms of a quantitative measure defined at the data points. Again only data from the core-drill boreholes were used.

4.5.3 Uncertainties in data

Measurement uncertainties

A lot of data samples were rejected by the hydrochemical modelling group in the hydrochemistry delivery for stage 2.2. These data samples may not be of the same quality as the orange or green data, but could still be of a qualitative interest for the model calibration. In effect, only 28 data samples for the core-drilled boreholes were classified as useful (representative and less representative). The inclusion of supplementary data needs to be treated with great caution.

The analytical error on each major ion concentration is about ± 5% except for Cl for which the error is ± 10 to 15% and Br for which the error is ± 15%. The errors in the Br/Cl-ratio are therefore shown as ± 25%.

Other examples of measurement uncertainties are:

- The observed salinity (TDS) is calculated from the sum of the major ion concentrations. The analytical error on each major ion concentration is about ± 5%. This is also the error that was used for the TDS in the presentation of the results.
- Upconing of Deep Saline Water.
- Drawdown of superficial waters.
- Drilling fluid contamination.
- Position of pore water sample with regard to the location of flowing fractures.

Handling uncertainties

Two examples of handling uncertainties are:

(i) The upper and lower elevations of the packer section used for the measurements were missing in the hydrochemistry delivery for stage 2.2. This information can be very useful since it is used in the model calibration for indicating the vertical error of the taken sample. The sample is actually reflecting the entire interval that is pumped rather than just a point in the middle of the interval.

(ii) The treatment of all components forming the base for the TDS as conservative tracers. This is far from true, especially in the case of HCO_3 and Mg.

4.5.4 Expected contribution

The modelling of the palaeohydrological evolution and its effects on the groundwater system during the Holocene (last 10,000 years) is an essential part of the SDM. In this context, the calibration on hydrochemistry is fundamental to the understanding of the hydrogeological processes in the fractured rock, assessing the impact of variable-density flow, and assessing the solute transport interaction between the fracture system and matrix. During the Littorina Sea phase, salinity infiltrates the bedrock and sinks vertically. The model parameters governing this process are primarily the vertical hydraulic conductivity of the HRD and the transport properties (kinematic porosity and RMD parameters). Hence, salinity data is likely to provide confirmatory testing of the solute transport model and boundary conditions, as well as a calibration of the HRD hydraulic and transport properties. The calibration on major ions and isotopes in fracture water provides a further test of these model elements, while the pore water, as a remnant of past hydrogeological and hydrochemical conditions, provides an insight into appropriate initial conditions. It also confirms the spacing between flowing fractures, i.e. the conductive fracture frequency (CFF), as an important parameter for the modelling of matrix diffusion. (See Section 3.12 for how rock matrix diffusion of solutes is modelled and parameterised).

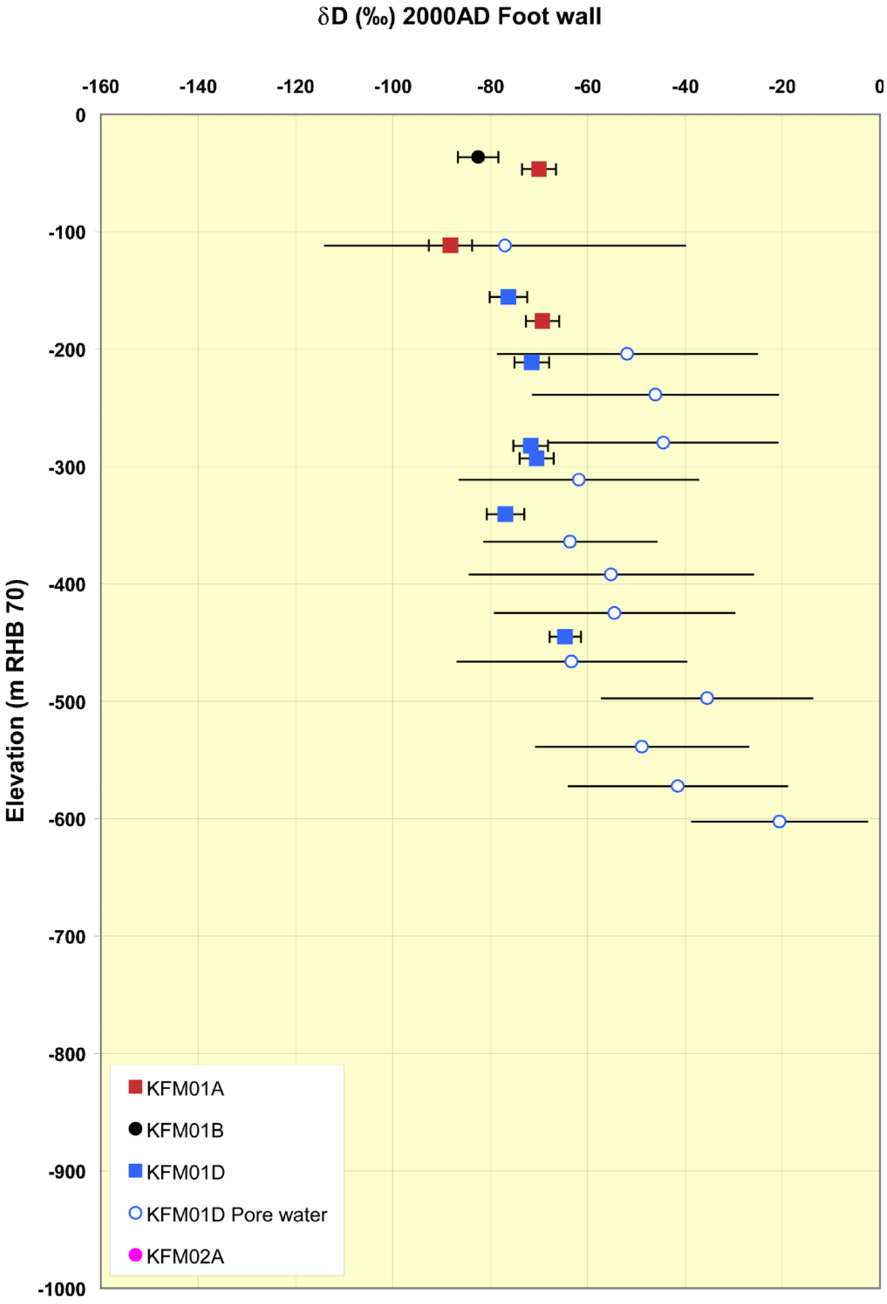

***Figure 4-7.** Pore water data showing the δD content in the samples for KFM01D. For the sake of comparison, the reference water δD values (‰SMOW) are: Deep Saline Water = –44.9; Old Meteoric-Glacial Water = –80.6; Holocene Glacial Melt Water = –158; Littorina Sea Water = –37.8; Present-day Meteoric Water = –80.6. Data samples considered representative (or somewhat less representative) are indicated by large filled squares, the supplementary data are indicated by small filled circles, and the pore water data are indicated by blue-white circles (for those boreholes where such data are available).*

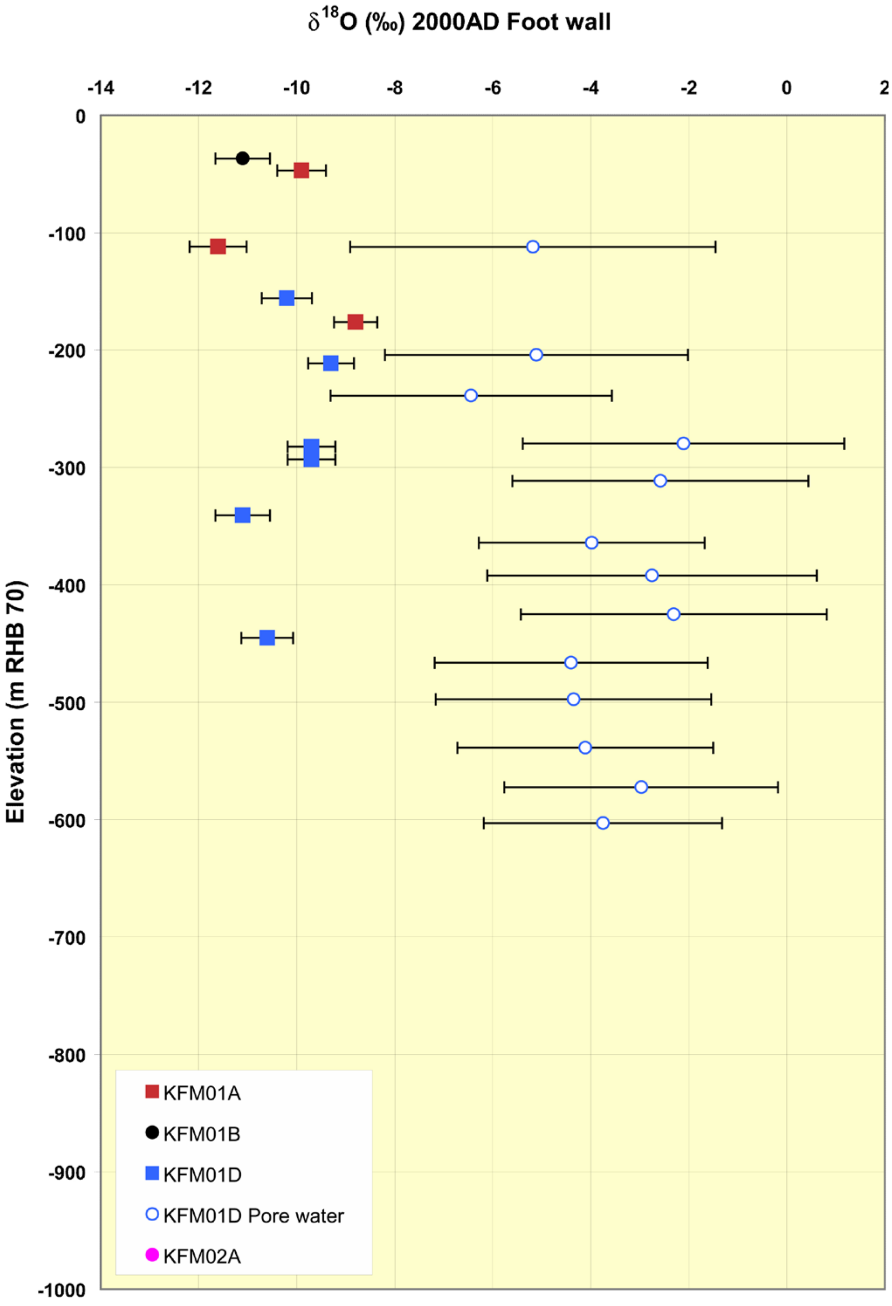

Figure 4-8. *Pore water data showing the δ^{18}O content in the samples for KFM01D. For the sake of comparison, the reference water δ^{18}O values (‰SMOW) are: Deep Saline Water = –8.9; Old Meteoric-Glacial Water = –11.1; Holocene Glacial Melt Water = –21; Littorina Sea Water = –4.7; Present-day Meteoric Water = –11.1. Data samples considered representative (or somewhat less representative) are indicated by large filled squares, the supplementary data are indicated by small filled circles, and the pore water data are indicated by blue-white circles (for those boreholes where such data are available).*

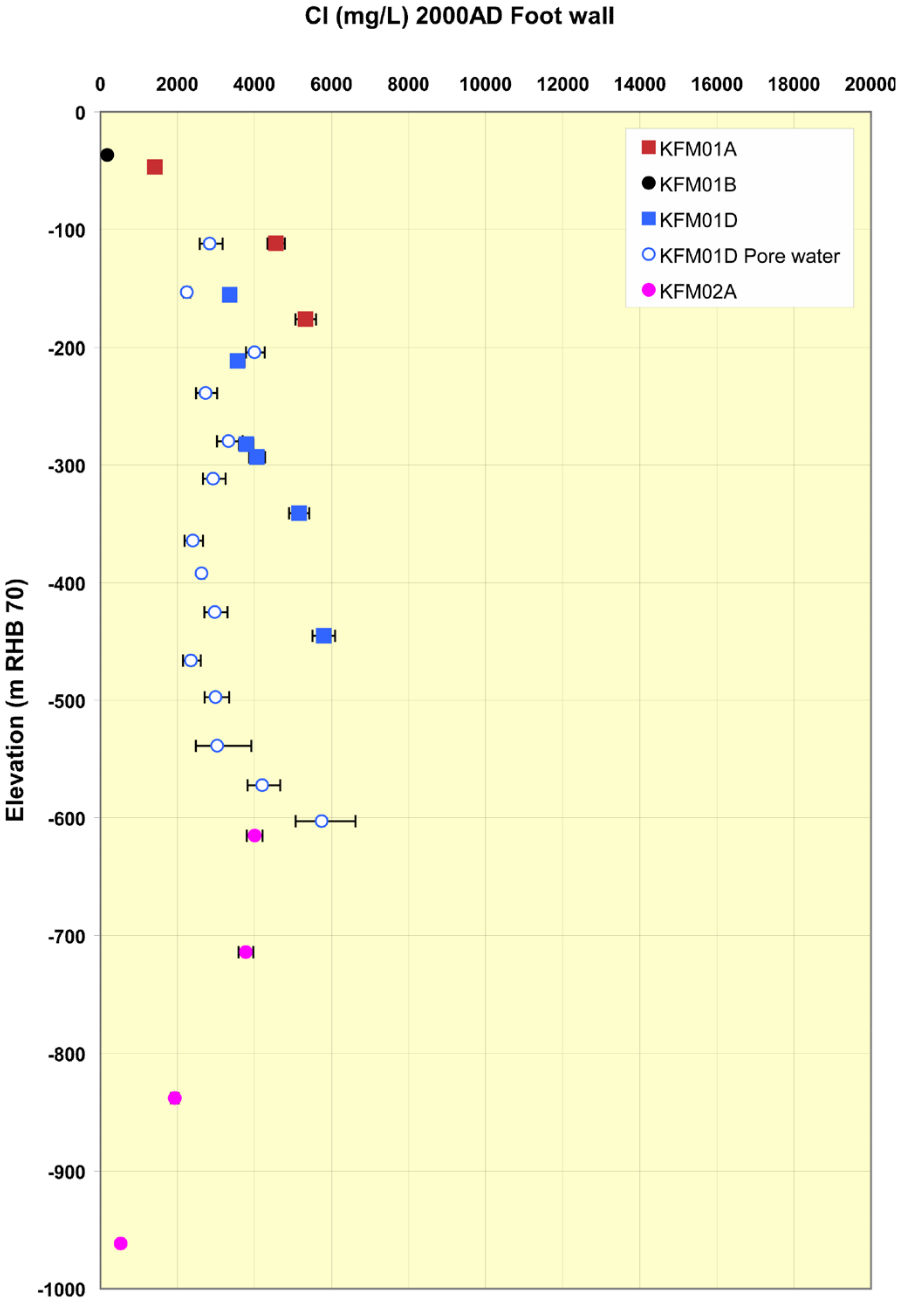

***Figure 4-9.** Pore water data showing the Cl content in the samples for KFM01D. For the sake of comparison, the reference water chloride concentrations (mg/L) are: Deep Saline Water = 47,200; Old Meteoric-Glacial Water = 181; Holocene Glacial Melt Water = 0.5; Littorina Sea Water = 6,500; Present-day Meteoric Water = 181. Data samples considered representative (or somewhat less representative) are indicated by large filled squares, the supplementary data are indicated by small filled circles, and the pore water data are indicated by blue-white circles (for those boreholes where such data are available). The supplementary data at depth in KFM02A are not regarded as representative.*

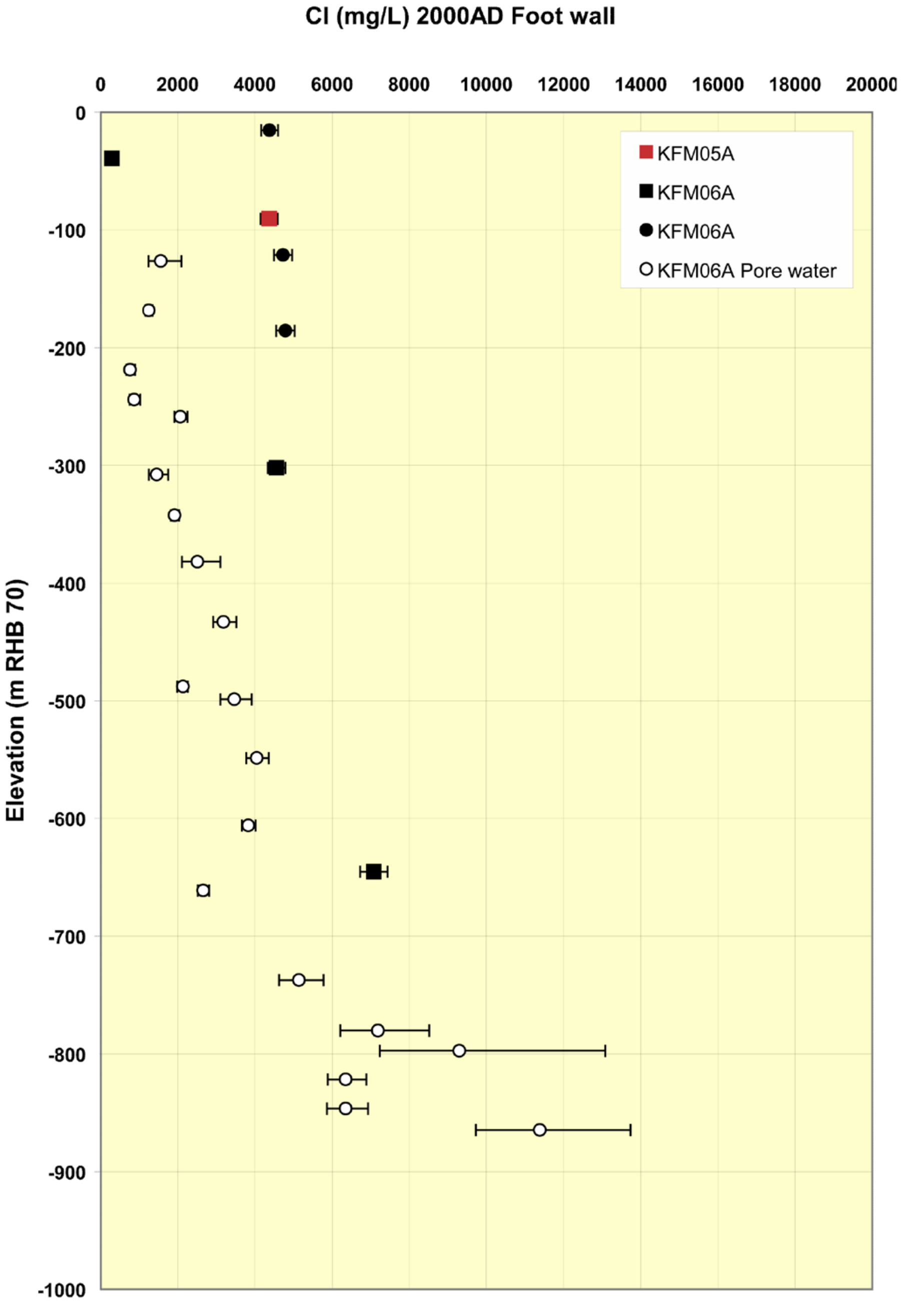

Figure 4-10. Pore water data showing the Cl content in the samples for KFM06A. For the sake of comparison, the reference water chloride concentrations (mg/L) are: Deep Saline Water = 47,200; Old Meteoric-Glacial Water = 181; Holocene Glacial Melt Water = 0.5; Littorina Sea Water = 6,500; Present-day Meteoric Water = 181. Data samples considered representative (or somewhat less representative) are indicated by large filled squares, the supplementary data are indicated by small filled circles, and the pore water data are indicated by black-white circles (for those boreholes where such data are available).

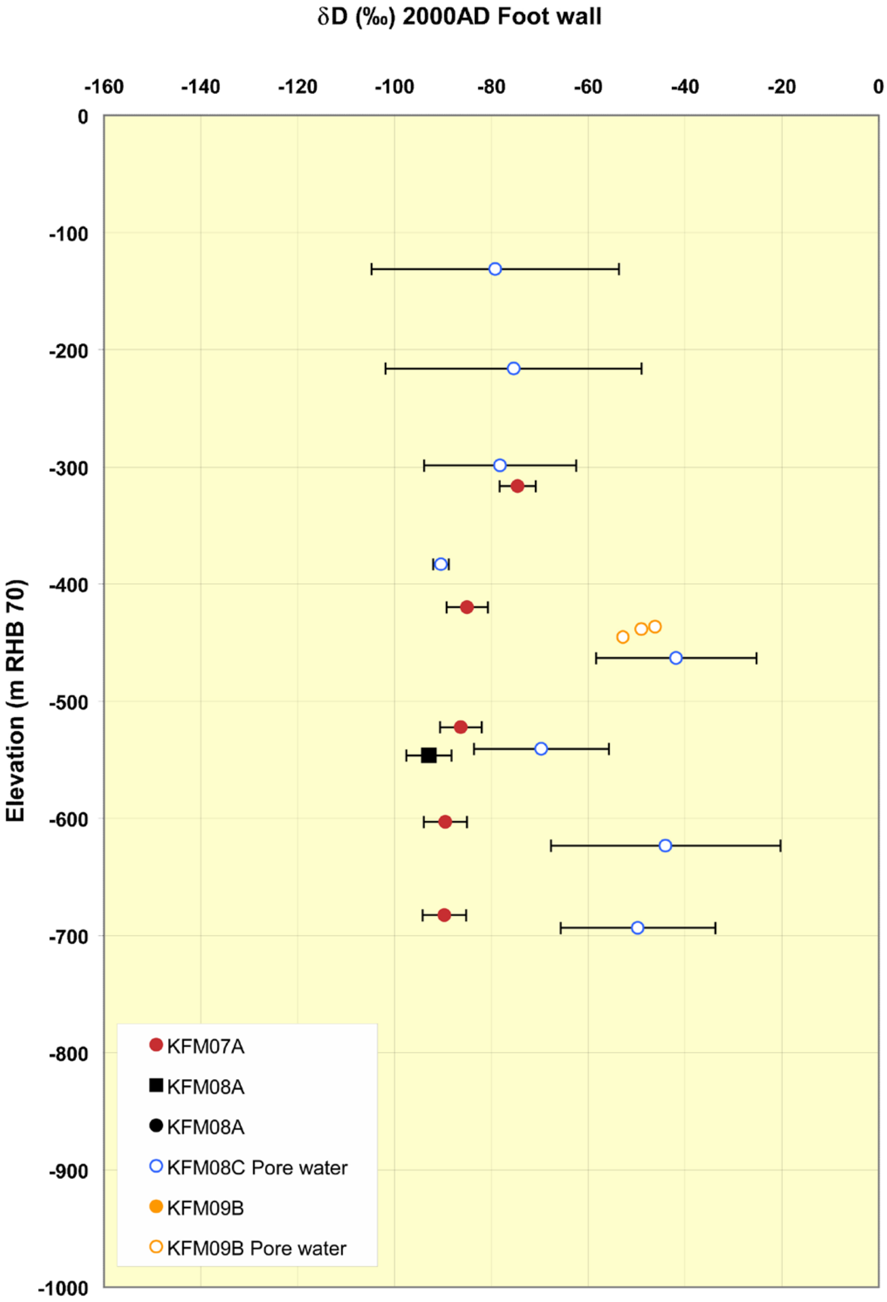

Figure 4-11. *Pore water data showing the δD content in the samples for KFM08C and KFM09B. For the sake of comparison, the reference water δD values (‰SMOW) are: Deep Saline Water = –44.9; Old Meteoric-Glacial Water = –80.6; Holocene Glacial Melt Water = –158; Littorina Sea Water = –37.8; Present-day Meteoric Water = –80.6. Data samples considered representative (or somewhat less representative) are indicated by large filled squares, the supplementary data are indicated by small filled circles, and the pore water data are indicated by blue-white circles (for those boreholes where such data are available).*

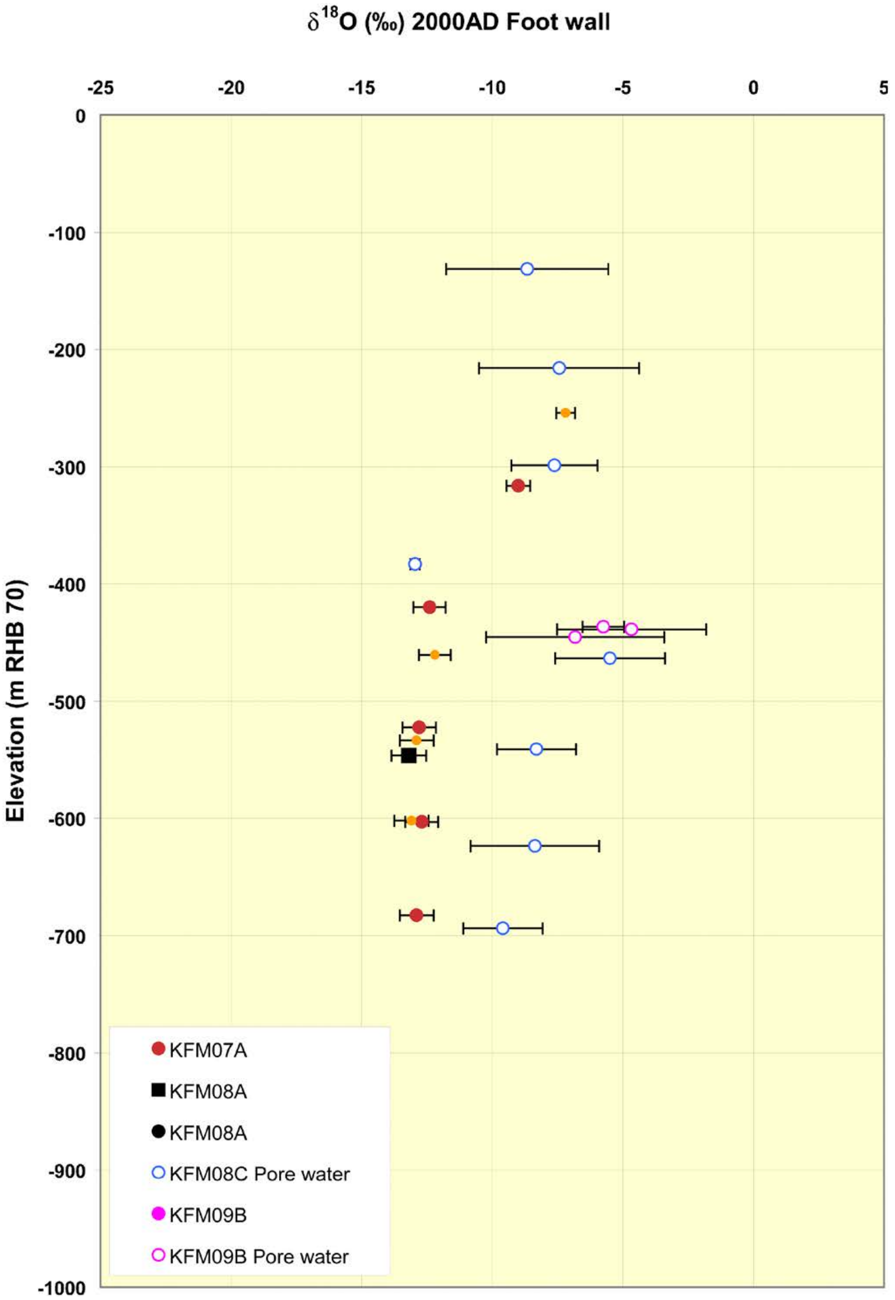

Figure 4-12. *Pore water data showing the $\delta^{18}O$ content in the samples for KFM08C and KFM09B. For the sake of comparison, the reference water $\delta^{18}O$ values (‰SMOW) are: Deep Saline Water = –8.9; Old Meteoric-Glacial Water = –11.1; Holocene Glacial Melt Water = –21; Littorina Sea Water = –4.7; Present-day Meteoric Water = –11.1. Data samples considered representative (or somewhat less representative) are indicated by large filled squares, the supplementary data are indicated by small filled circles, and the pore water data are indicated by blue-white circles (for those boreholes where such data are available).*

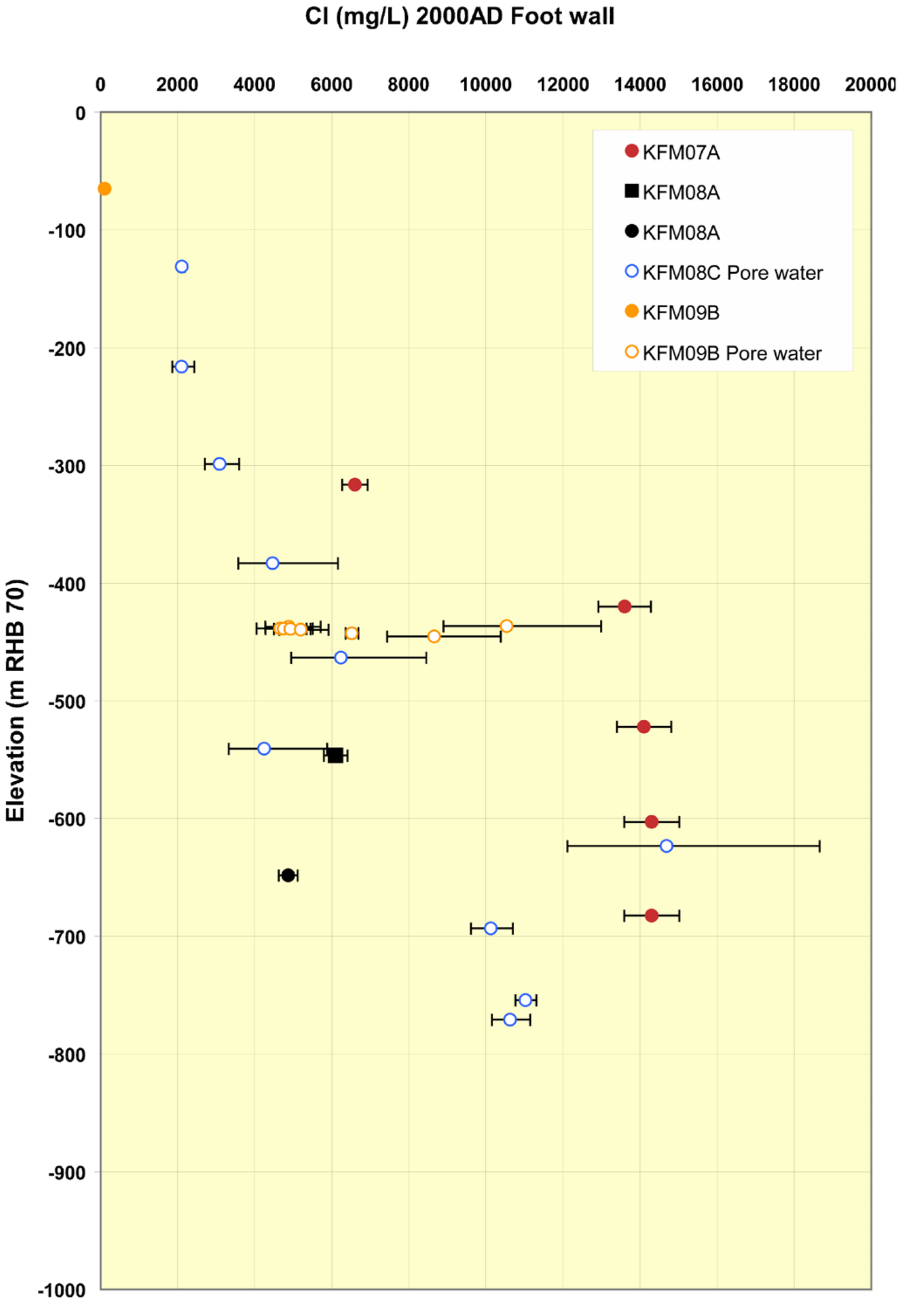

Figure 4-13. *Pore water data showing the Cl content in the samples for KFM08C and KFM09B. For the sake of comparison, the reference water chloride concentrations (mg/L) are: Deep Saline Water = 47,200; Old Meteoric-Glacial Water = 181; Holocene Glacial Melt Water = 0.5; Littorina Sea Water = 6,500; Present-day Meteoric Water = 181. Data samples considered representative (or somewhat less representative) are indicated by large filled squares, the supplementary data are indicated by small filled circles, and the pore water data are indicated by blue-white circles (for those boreholes where such data are available).*

5 Calibration on hydraulic tests and monitoring data

In this section the numerical implementation of the conceptual model is tested against single-hole and cross-hole hydraulic tests together with measurements of point-water heads in the near-surface bedrock and Quaternary deposits, and depending on its performance it is modified to give better agreement with the data. The main model parameters considered are the hydraulic properties of the HCD, HSD and HRD.

5.1 Task A – Local conditioning on single-hole hydraulic tests

5.1.1 Methodology

The properties of the ECPM model grid are first defined in terms of the HRD model described in Section 3.11. That is, the structural-hydraulic properties of a HRD model realisation are upscaled to give equivalent properties for a 20 m grid scale ECPM model. The deformation zones are then superimposed implicitly by altering the properties of the finite-elements that they intersected according to the 'first guess' HCD model described in Section 3.10. The consistency of the resulting spatial distribution of hydraulic conductivity on a 20 m grid is then tested against measured PSS transmissivity data from 20 m long borehole sections in a large number of core-drilled boreholes (20). This gives both a check of the parameter settings of the HRD and HCD models, but also the methods used to upscale the DFN and represent the deformation zones on a 20 m ECPM model grid.

The following boreholes are simulated and used for comparisons with measured PSS transmissivity data from 20 m long borehole sections: KM01A/C, KFM01D/C, KFM02A, KFM03A/B, KFMF04A, KFM05A, KFM06A/B, KFM06C/B, KFM07A, KFM08A/B, KFM08C/B and KFM09A/9B. Where large discrepancies in the hydraulic conductivity of more than an order of magnitude are apparent, the cause of the difference is investigated to see if the borehole interval is affected by a HCD. In which case, alternative methods of defining the properties of the HCD or localised conditioning of their properties are tried. Otherwise, it is considered whether the discrepancy is simply due to spatial heterogeneity arising from the upscaling of the stochastic Hydro-DFN. Mainly the calibration focussed on the HCD since these account for the majority of high flow regions. Due to the requirements of CONNECTFLOW input, depth dependency in the HCD is represented by step changes in hydraulic conductivity, with depth intervals of 100 m being used to approximate the depth trend.

5.1.2 Calibration steps

As a brief summary of the sequence of modifications made to the property specification for the HCD, the following steps are made:

1. The depth dependency for HCD is based on a fixed slope, *k*, and the value of *m* in Equation (3-1) is based on the maximum transmissivity measured in a zone (blue graph in Figure 5-1).
2. The value of *m* in Equation (3-1) is based on the mean *m* value calculated within a zone where there are multiple measurements of *T* (red graph in Figure 5-1).
3. Local conditioning of particular HCD is made by adjusting the *k* value within one or more 100 m depth intervals where it is difficult to use a single linear depth variation in log(*T*) (green graph in Figure 5-1).

4. Initially, the hydraulic thicknesses are set to the geometric mean of values given for the geological thicknesses. Individual changes to the thicknesses of zones are made where the model gives a different number of 20 m elements affected by a HCD than observed in the 20 m PSS data.
5. Finally, a minimum hydraulic conductivity is set for each deformation zone, otherwise the HCD could become much tighter at depth than the surrounding rock because a minimum hydraulic conductivity of 10^{-11} m/s is used within FFM01–06 and 10^{-9} m/s outside the FFM. To avoid this situation, transmissivity divided by thickness is set to a minimum of 10^{-9} m/s for zones described geologically as "regional", and 10^{-11} m/s is used in zones described as either "local" or "local and regional".

The measured values indicate the clear lateral heterogeneity in the zones. Therefore, the procedure above in effect steps through a number of alternative implementations of a simplified deterministic model of the HCD with only vertical heterogeneity modelled. The appropriateness of these alternatives as an approximation to the HCD properties is then assessed by comparison with the hydraulic data. Two examples of how this procedure affects the depth trends in transmissivity considered in zones with multiple measurements are shown in Figure 5-1 for deformation zones A2 and ENE0060. For each zone three alternative trend profiles are shown corresponding to Steps 1 (blue), 2 (red) and 3 (green) above. It is noted that Step 2 is a far better approach than Step 1 and that Step 3, which is derived by means of some local conditioning of the vertical heterogeneity, is a manual improvement of Step 2. As of stage 2.2, we have not yet developed a tool to automate the local conditioning, but this is planned for stage 2.3. The calibrated model resulting from Step 3 is referred to as the *stage 2.2 base model simulation* in the work reported here.

5.1.3 Resulting calibration

Some examples comparing the very first models and the *stage 2.2 base model simulation* are shown in Figure 5-2 to Figure 5-4 for the profiles of hydraulic conductivity in KFM02A, KFM03A and KFM04A. These examples illustrate the improvement in matching the hydraulic conductivity of zones affected by deformation zones whose intercept with the boreholes is indicated on the right axis of the graphs. They also indicate that the hydraulic conductivity has the right order of magnitude between the deterministic deformation zones with variations consistent with magnitudes of hydraulic conductivity measured for sections where a "possible deformation zone" was identified in the geological description (as shown on the right axis). A few discrepancies in hydraulic conductivity remain as can be seen in the figures, since the local conditioning as described in step 3 above is made manually and focuses on those borehole intervals where the discrepancies are greater than an order of magnitude. It should be noted that all the models considered are constructed within the general framework of the HCD interpretation made in /Follin et al. 2007b/. The changes made represent alternative decisions that are made in the detailed implementation of this conceptual framework in a numerical model. In a sense, these alternatives reflect the uncertainty in the interpretation of the data, which can to some extent be addressed by model calibration exercises.

KFM03A is the only borehole located outside the 20 m embedded grid area where the grid refinement is reduced to either 60 m or 100 m. As can be seen in Figure 5-3, the hydraulic conductivity becomes more homogeneous due to upscaling the DFN to a larger grid size.

The final prescription of hydraulic thickness and transmissivity with depth of the HCD incorporated in the *stage 2.2 base model simulation* used for groundwater flow and solute transport modelling is given in Appendix L.

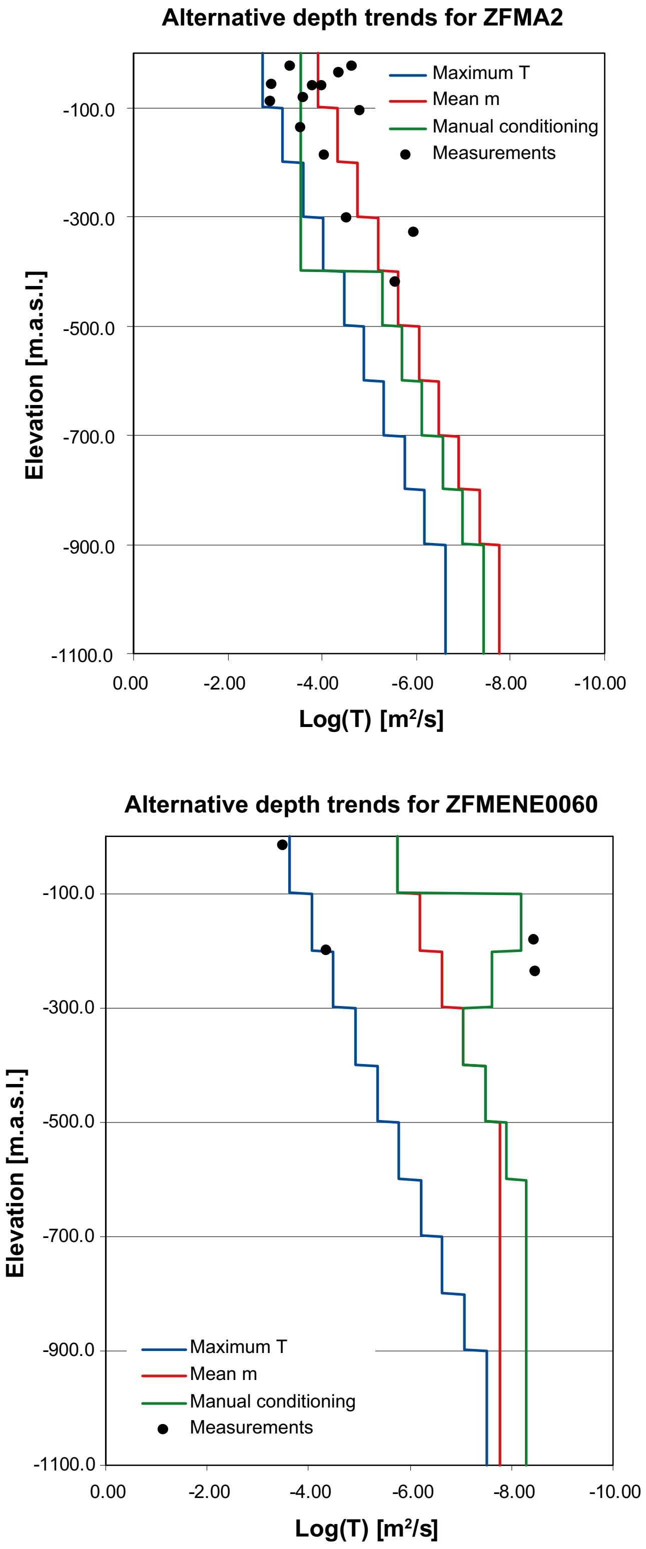

Figure 5-1. *Two examples, A2 and ENE0060, of the modifications made to the depth trends in transmissivity for zones with multiple measurements. The black dots indicate measured transmissivities. The blue profiles are based on values of m in Equation (3-1) derived using the maximum transmissivity measured in the zone; the red profiles are based on the mean value of m value calculated by Equation (3-1) from the data; and the green profiles are based on some local conditioning of the vertical heterogeneity. The locally conditioned case is here referred to as the stage 2.2 base model simulation.*

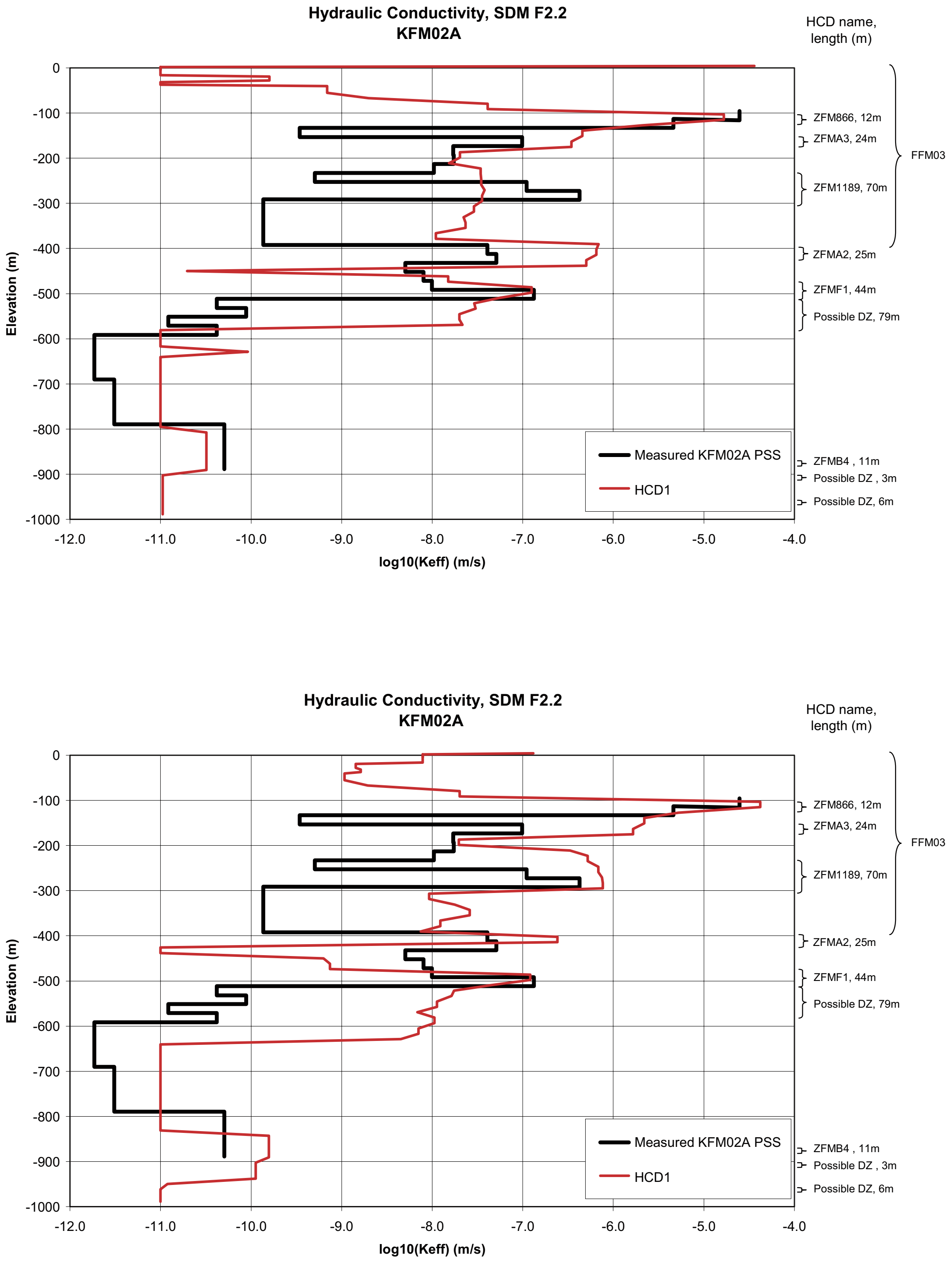

Figure 5-2. *Example profiles of ECPM hydraulic conductivity in borehole KFM02A before conditioning (top) and after conditioning (bottom) against 20 m section PSS transmissivity measurements. The black lines show the geometric mean horizontal hydraulic conductivity in the model, while the red lines show the measurements. The intercept by deformation zones is indicated on the right axis.*

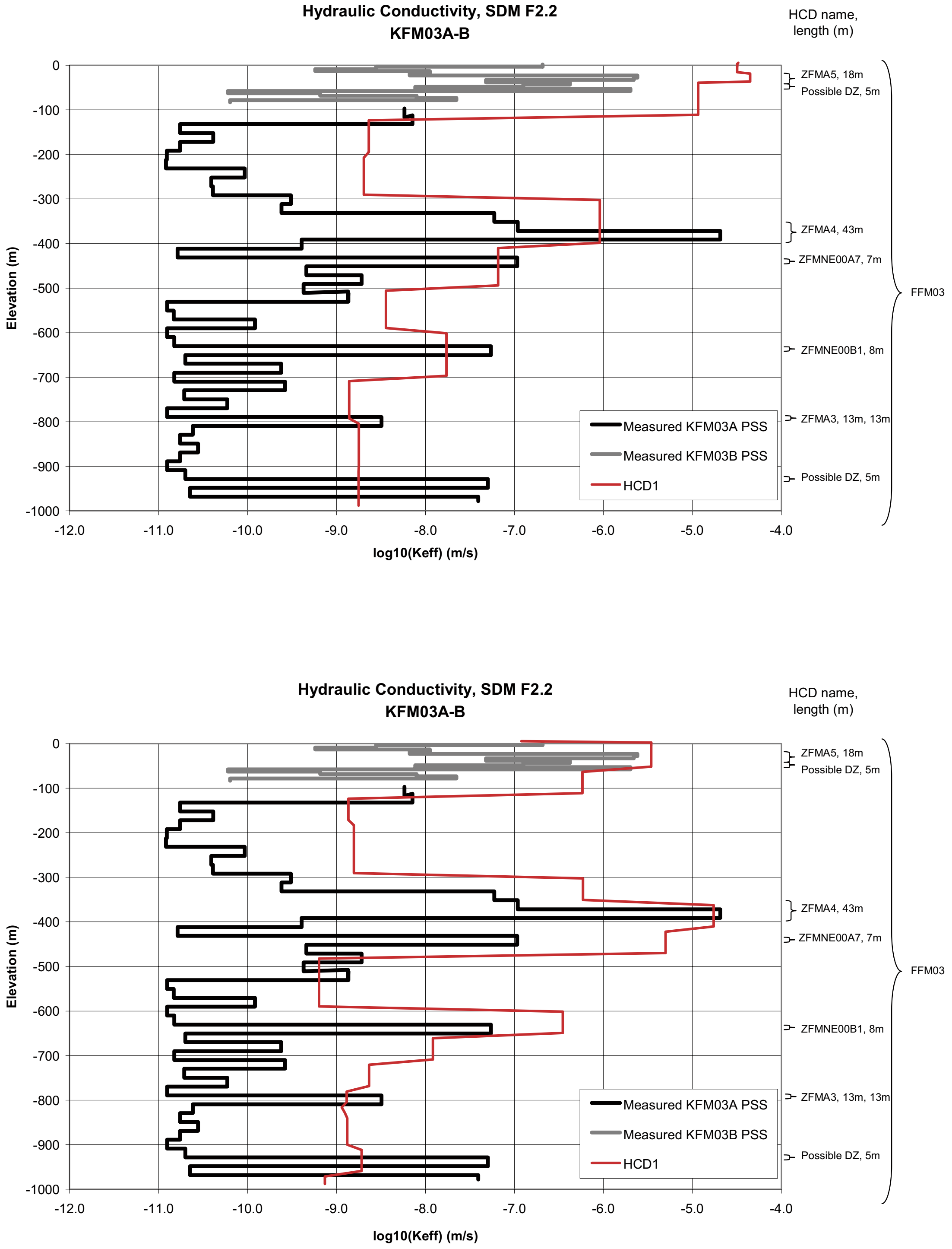

Figure 5-3. *Example profiles of ECPM hydraulic conductivity in borehole KFM03A before conditioning (top) and after conditioning (bottom) against 20 m section PSS transmissivity measurements. The black lines show the geometric mean horizontal hydraulic conductivity in the model, while the red lines show the measurements. The intercept by deformation zones is indicated on the right axis.*

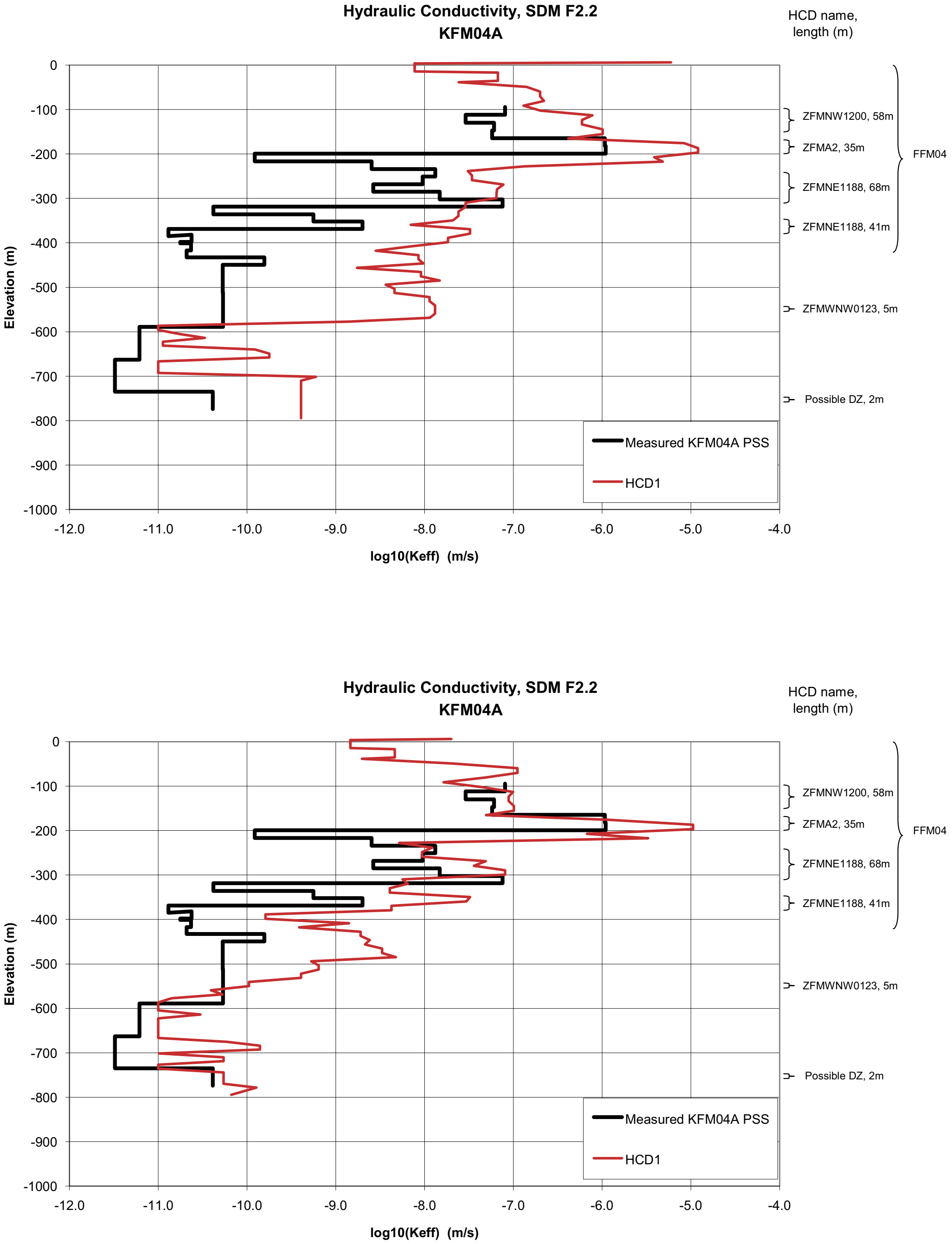

Figure 5-4. *Example profiles of ECPM hydraulic conductivity in borehole KFM02A before conditioning (top) and after conditioning (bottom) against 20 m section PSS transmissivity measurements. The black lines show the geometric mean horizontal hydraulic conductivity in the model, while the red lines show the measurements. The intercept by deformation zones is indicated on the right axis.*

5.2 Task B – Matching the 2006 interference test in HFM14

The simulations of the HFM14 hydraulic interference test and the point-water heads followed on from the calibration against PSS single-hole hydraulic tests described in Section 5.1. They were performed independently to consider the parameters that appeared most important for the individual tests. This led to conclusions that had to be reconciled to give a final model that was consistent with both types of data. We discuss the calibration on the hydraulic interference test first since this was sensitive to more aspects of the model than the point-water heads.

5.2.1 Methodology

The monitoring scheme was designed to indicate the hydraulic connections of features in the near-surface and downwards along some key deformations zones intersected by intervals in KFM01A, KFM02A, KFM04A, KFM05A, KFM06A and KFM10A. The performance of the simulations is assessed by comparing the profiles of measured and modelled drawdown after 21 days of pumping in each monitoring interval ordered according to their 3D distances from the abstraction boreholes, and by plotting the vertical distribution of drawdown at appropriately selected times in boreholes where there are multiple monitoring intervals. These are presented as plots. A full set of examples is given for the *stage 2.2 base model simulation* in Section 5.2.3. HFM14 intersects the high transmissivity gently dipping zone A2, so that the distribution of drawdowns against distance for monitoring points within about 500 m of HFM14 is dominated by the transmissivity of this zone. Further away, greater than about 600 m, the drawdown depends on other structures such as sub-vertical zones or the "cage features" and the role of the boundary conditions that control recharge through the HSD. Hence, the drawdown versus distance plot is important for guiding the properties and connections of the major hydraulic features and the hydraulic connection to the surface. Plots of drawdown profiles along the lengths of boreholes help to define the contrasts in hydraulic properties between HCD, the surrounding HRD, and HSD at the surface. A second interference test was performed in HFM14 at about the same abstraction rate with monitoring only in packer intervals within KFM10A. The measurements from this follow-up test were added to the measurement data for the calibration.

The simulations of the hydraulic interference test are performed by first modelling the steady-state flow-field without pumping, and then switching on the abstraction at HFM14 to model the transient drawdown over the pumping period of 21 days. The boundary conditions are no flow on the vertical boundaries and a non-linear infiltration condition as defined in Section 3.17.3 with an effective infiltration of only 20 mm/year to reflect the relatively dry conditions prevalent during the interference test. The abstraction rate in HFM14 is 348 L/min distributed over the uncased length of the borehole according to the transmissivity of the grid elements it intercepts, i.e. a greater flux was removed from elements with a higher hydraulic conductivity (the geometric mean of the axial components of hydraulic conductivity is used). Using a fully implicit scheme, the time-step used in the transient simulations was successively increased by starting with 0.015 days (36 minutes) for 10 time-steps, then 0.15 days (3.6 hours) for 9 time-steps, then 1.5 days until 21 days. The drawdown distributions were compared with the measured data after 1.5, 3.0, 7.5, 13.5 and 21.0 days after pumping started. For the drawdown comparisons made at these times, the results were not strongly sensitive to further reductions in the time-step size. The 20 m local-scale grid embedded within a 60 m regional-scale grid was used for the spatial discretisation.

5.2.2 Calibration steps

The initial parameter assignment of deformation zones was based on Section 3.10 with the modifications to the HCD properties described in Section 5.1. Parameter settings were then changed in a stepwise manner to try to improve different aspects of the match to the measured drawdowns and to identify those parameters to which the simulations of the interference tests were most sensitive. Many different simulation cases were performed to gain insight into what hydrogeological features and parameters governed the hydraulic interference test.

Rather than exhaustively document each simulation, we here describe the sequence of steps taken in developing what is considered to be an acceptable overall match, and then present the results for this *stage 2.2 base model simulation* in Section 5.2.3. Then in Section 5.2.4 we present a series of sensitivity cases that are centred on the *stage 2.2 base model simulation*, but variations were made to quantify by how much and where the match deteriorates, or sometimes improves, as the parameters considered during the calibration process are varied within plausible ranges of uncertainty. This is not intended as a comprehensive sensitivity analysis, merely as an illustration of the sensitivity to parameters considered during the calibration. More comprehensive analyses of sensitivity to uncertainties such as lateral heterogeneity in HCD and multiple DFN realisations will be made as part of stage 2.3.

The model calibration is non-unique in that different combinations of parameter settings may achieve equally good and plausible matches to the interference test data. However, one also needs to consider the performance of the simulation cases against other sorts of data, such as the point-water heads and the palaeohydrological development described in Sections 5.3 and 6, respectively. Therefore, some extra sensitivity cases were made to try and integrate the findings of the different calibration exercises to seek model settings that could describe the different types of measurement.

As a brief summary the key steps made in order to achieve an acceptable match to the hydraulic interference tests were:

- A low specific storage coefficient around 10^{-8} m^{-1} for the bedrock and 10^{-3} m^{-1} for the soil was required to obtain the rapid responses seen in monitoring intervals even those a kilometre or more from the HFM14. Typical hydraulic diffusivities inferred from the test are in the range 10 to 1,000 m^2/s /Gokall-Norman and Ludvigson 2006/. A tentative empirical relationship, obtained from the modelling of the hydraulic responses in the superficial bedrock in the Forsmark area, between specific storativity and hydraulic conductivity might be $S_s \sim 10^{-5} K^{1/2}$. It is noted that the empirical relationship reported from the investigations in the Äspö area is 10–100 times greater or $S_s \sim 7 \cdot 10^{-4} K^{1/2}$ /Rhén et al. 1997/. The validity of these relationships is of course a bit uncertain, but they indicate that there is a clear difference in the bedrock hydrogeological conditions between the two areas.
- The transmissivity of A2 had to be increased to give $T = 2.8 \cdot 10^{-4}$ m^2/s in the upper 100 m to give the correct drawdown of about 12 m in HFM14 and boreholes close to the abstraction.
- The hydraulic thickness of deformation zones A2, ENE0060, ENE0401 and A8 was reduce to be thinner than the 20 m finite-element size, nominally 5 m was used. This change was made to ensure a more discrete response propagated rapidly along a smaller hydraulic volume associated with a few key deformation zones.
- The hydraulic conductivity of the hydraulic soil domains had to be reduced to decrease the recharge from the top surface that otherwise diluted the response in monitoring intervals further than about 1 km for the abstraction point. In particular, the responses that propagate under Lake Bolundsfjärden from HFM14 to boreholes KFM06A, KFM06B and HFM16 on the opposite shore of the lake required the lake sediments to be made tighter, and also benefited from a general reduction in the hydraulic conductivity of Quaternary deposits.
- A reduction in the vertical hydraulic conductivity of the hydraulic rock domains to reproduce the very discrete propagation of the drawdown along deformation zones especially to deep intervals and to reduce the recharge to depth from ground surface via the background rock. This was considered both in terms of the context of fracture orientations by considering the alternative Hydro-DFN fracture orientation distributions proposed in /Follin et al. 2007b/ that have a higher Fisher orientation concentration in the dominant sub-horizontal set, or by simply implementing a general order of magnitude reduction in vertical hydraulic conductivity in the top 400 m of bedrock.

The effects that these changes and others have on the simulation results are illustrated by sensitivity cases described in Section 5.2.4, and their significance is interpreted in Section 5.4. First though, we present results for the *stage 2.2 base model simulation* to demonstrate how we judge the performance of the calibration in reproducing the measurements and the level of match that was possible.

5.2.3 Resulting calibration

As an overall representation of the match against the measurements in all monitored intervals, the drawdown after 21 days is plotted as a bar diagram for each interval ordered according to ascending 3D distance between the monitoring interval and the abstraction as shown in Figure 5-5. The comparison for near monitoring intervals on the left side of the graph is controlled by the hydraulic properties close to the abstraction borehole HFM14. Mainly this relates to the transmissivity of the extensive sub-horizontal A2 deformation zone and the "cage features" These are the key controls for most intervals up to about 500–600 m from HFM14. Beyond this, the responses are controlled by a more complex balance of parameters representing the hydraulics of the deformation zones, the "cage features", the Quaternary deposits and, most likely, the Baltic Sea. The pumping in HFM14 equates to an effective sink of about 183,000 m^3/year. For the infiltration rate of 20 mm/year used in the simulations, this is equal to the total per annum recharge from an area of about 1,700 m radius. However, this radius of influence is reached already within 3 weeks of testing, see Figure 3-30. This suggests a low leakage from the Quaternary deposits and/or the HRD above the "cage features". Moreover, 1,700 m is beyond the shortest distance to the Baltic Sea, see Figure 3-28, which implies that the Baltic Sea may at some point become a positive hydraulic boundary depending on the laterally extent of the "cage features".

Of particular importance to the behaviour of the interference test are:

- The responses in KFM06A, KFM06B and HFM16 to the north of Lake Bolundsfjärden, and HFM32 in the centre of the lake, that provide a guide for the properties of ENE deformation zones ENE0401, ENE0060 and A8, and the properties of the HSD beneath and surrounding the lake.
- The responses in HFM20, which is about 1.5 km away, but shows a large response associated with the "cage features".
- The responses in KFM02A at c. –400 m RHB 70 about 1.5 km away from HFM14, which provides a guide to the far-field hydrogeological conditions in A2.
- The responses in KFM10A which are also large at depth around the intercept with A2 about 800 m away from HFM14.

Reproducing the nature of these responses gave the greatest challenge in trying to obtain a satisfactory model. The match shown in Figure 5-5 is considered to be adequate at this stage given the model does not yet consider heterogeneity in deformation zones which is likely to have a strong control on the transmission of the hydraulic disturbance caused by pumping in HFM14. Some of the sensitivities considered in Section 5.2.4 give possible routes for improving the match further, such as an increased transmissivity in ENE0060 which increases the drawdown in KFM06A, KFM06B and HFM16.

The other type of comparison made in the matching process was to consider the spatial and temporal distribution of the drawdown in some key boreholes. Multiple drawdown measurements in the same borehole are available for a few deep core drilled boreholes and several percussion drilled boreholes, some of which show marked depth variations in the magnitude and time of response, suggesting heterogeneity and contrasts between HCD, HRD and HSD. Six key boreholes were highlighted for more detailed study: HFM13, HFM19, HFM20, HFM32, KFM02A and KFM06A, all having at least 3 measurement intervals. The positions of these boreholes relative to HFM14 and the key deformation zones that influence the hydraulic interference test are shown in Figure 5-6.

Figure 5-7 to Figure 5-12 show the results for these 6 key boreholes for the *stage 2.2 base model simulation*. The positions of mapped deformation zones intersecting the zones are marked. The drawdown is plotted as a vertical line to show the elevation range of the monitoring packer

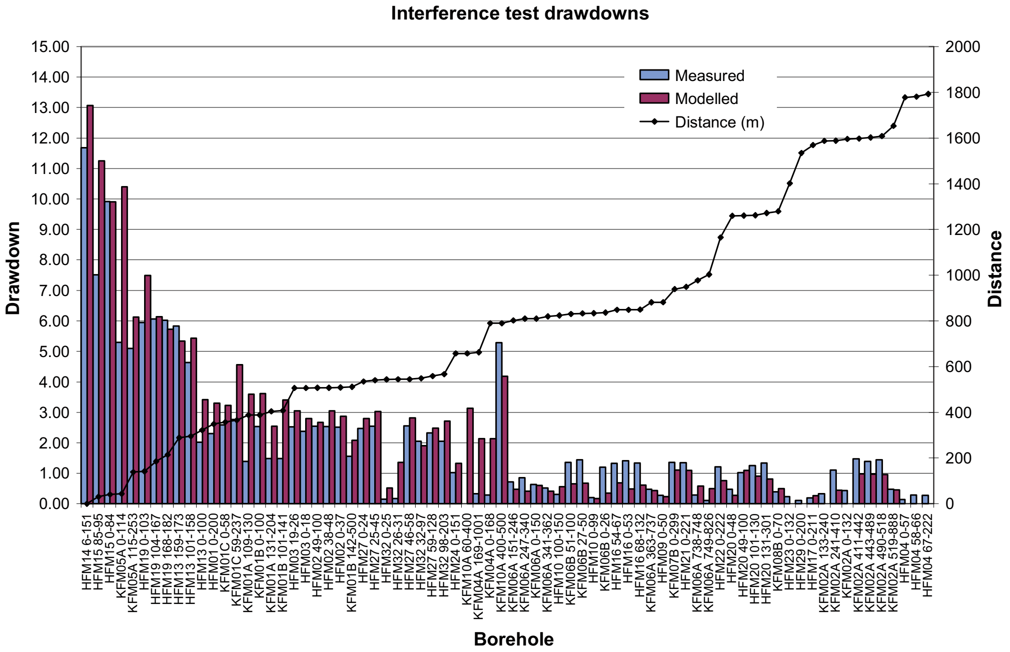

Figure 5-5. *Comparison of measured (blue) and modelled (red) drawdown at the end of pumping (21 days) for all monitored borehole intervals for the stage 2.2 base model simulation. The borehole intervals are ordered according to the three-dimensional distance (the right axis) of the monitoring intervals to the abstraction borehole HFM14.*

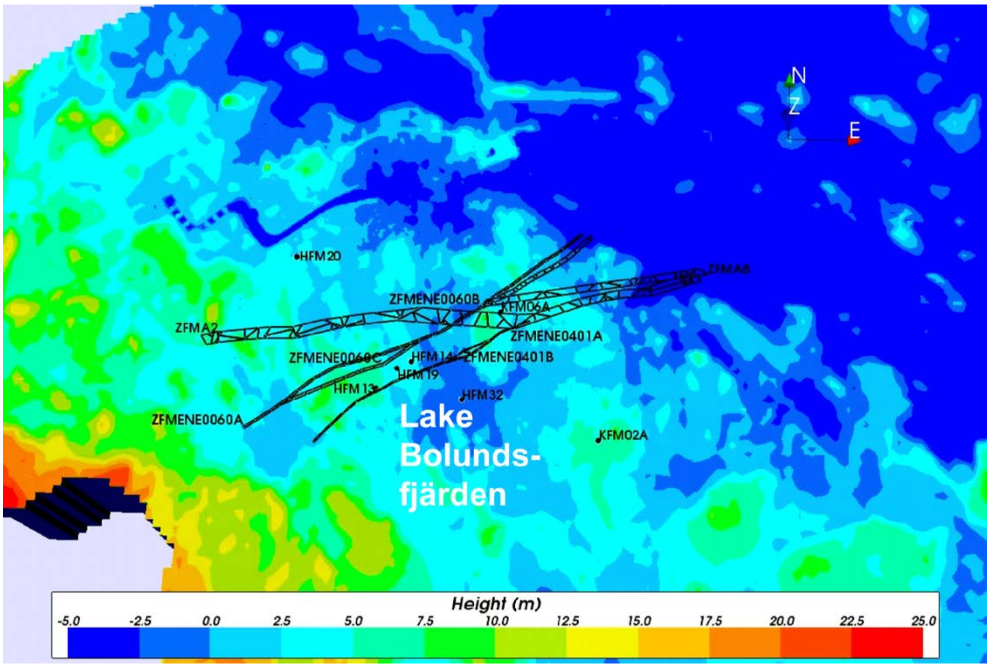

Figure 5-6. *Positions of abstraction borehole, HFM14, key monitoring boreholes used in the calibration and key deformation zones studied in theFM14 interference test. The deformation zones are shown as their modelled position at the surface.*

interval, and is shown at 3 appropriate times after the start of pumping. The ECPM simulation model yields a continuous spatial distribution of drawdown, which is drawn as the variation in drawdown along the borehole. Some of the monitoring intervals are several hundreds of metres long, and so it is not possible to discern what governs the drawdown within the interval. However, the variation in drawdown within the model is shown continuously rather than averaged to help understand where the model predicts there will be variations in the drawdown.

In HFM13, HFM20, HFM32 and KFM02A the upper most packer interval indicates a smaller and slower response than in deeper intervals, which may suggest either a lower hydraulic diffusivity in the Quaternary deposits or a poor hydraulic contact between the soils and the bedrock. The other 2 boreholes do respond in the upper packer interval, but these intervals span at least 80 m of elevation, and so it is difficult to know what hydrogeological features the response is associated with.

HFM13 is relatively close to HFM14, and the simulation predicts an overall response of the right magnitude, and a lower response in the top interval compared to the deep bedrock.

HFM19 is also close to HFM14, but the measurements show a more homogeneous response, but that may just be due to the length of the intervals. The simulations, when averaged over the interval lengths would appear to give good agreement, and suggest a slower response in the Quaternary deposits that cannot be verified by available data.

HFM20 is about 1.3 km from HFM14 toward the power plant, and is an interesting borehole because it shows a relatively high response given its distance from the sink which is thought to be a result of the "cage features". This is partly reproduced by the simulations at the right depths, but could perhaps be improved by a higher transmissivity and a different interpretation of the "cage features".

HFM32 is about 500 m from HFM14 on an island in the middle of Lake Bolundsfjärden. The model simulates well the depth variation in drawdown in this borehole. The low drawdown in the top interval compared to the intervals beneath suggests either a poor contact with the Quaternary deposits or low vertical hydraulic conductivity in the upper bedrock.

KFM02A is a deep borehole 1.6 km from HFM14 in which a high drawdown response was measured soon after the start of pumping in intervals associated with A2. The same intervals respond in the simulations, although not to quite as high a magnitude as seen in the measurements. The simulated response extends deeper than in the data. This is thought to be due to an extensive stochastic sub-horizontal fracture generated at about –600 m RHB 70 in the only realisation of the HRD considered. Clearly, more stochastic realisations of the HRD have to be considered. The broader response predicted in the simulation may also be a result of the 20 m embedded grid only just about extending as far as KFM02A. A more discrete response may have been simulated if the fine-scale grid was extended a bit further east, and perhaps if yet finer grids were used.

KFM06A is about 900 m from HFM14 to the north on the far shore of Lake Bolundsfjärden. Therefore, the drawdown has to propagate through the bedrock beneath a large potential source of recharge which could counteract the drawdown from HFM14. It is intersected by several mapped deformation zones and monitoring intervals. Hence, this is a very interesting and important borehole for the hydraulic interference test calibration. It shows a high response, about 1 m in the 3 upper intervals including those associated with ENE0060A and ENE0060B. KFM06B recorded an even higher drawdown, possibly associated with A8 as well as ENE0060, although this only had 2 monitoring intervals. These responses suggest a poor hydraulic contact between the lake and the bedrock, and a high transmissivity pathway connecting A2 at the source, HFM14, and one or more of the ENE deformation zones ENE0060 and ENE0401, and possibly also the sub-horizontal feature A8 that occurs possibly forming a splay off A2 in this area to the north-east of the site. The simulation predicts drawdowns of the right magnitude and largely position, although this central case probably under-predicts the transmissivity of ENE0060 and over-predicts that of NNE0725 at depth. Referring to Figure 5-1, ENE0060 displays four orders of magnitude in lateral heterogeneity making it difficult to parameterise. Hence, sensitivities to the properties of some of these zones were considered in the present study.

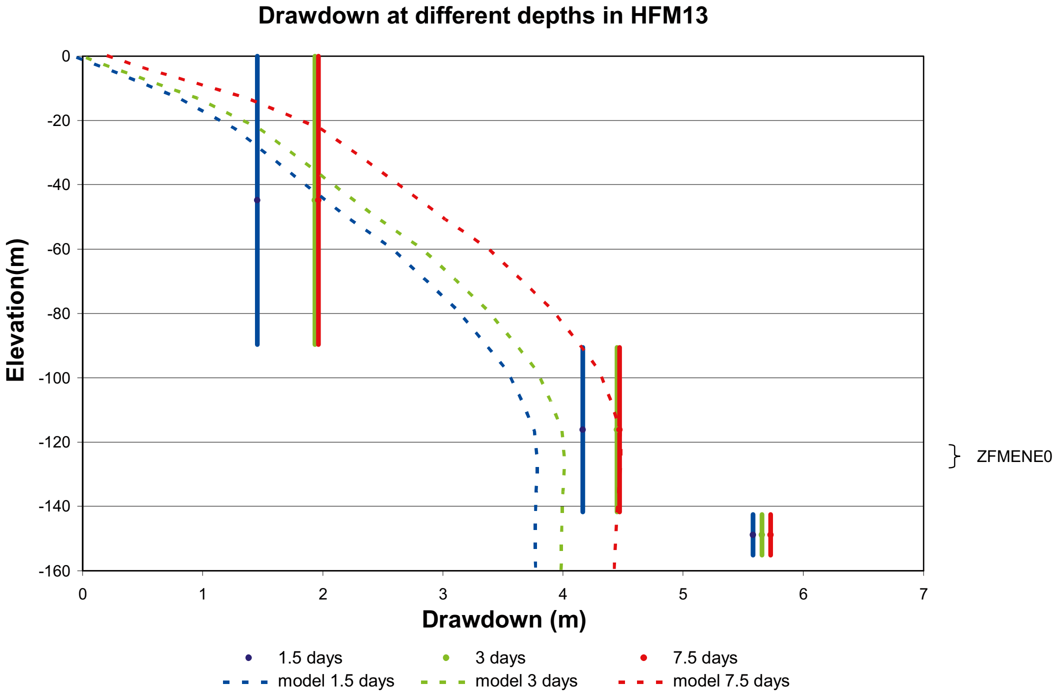

Figure 5-7. Comparison of measured (solid) and stage 2.2 base model simulation (dashed) drawdown at 3 times for the HFM13 monitoring hole. For the data, a vertical line shows the extent of the monitoring section with the drawdown representing an average within the interval, while the simulated spatial variation in drawdown in the borehole is shown for the model.

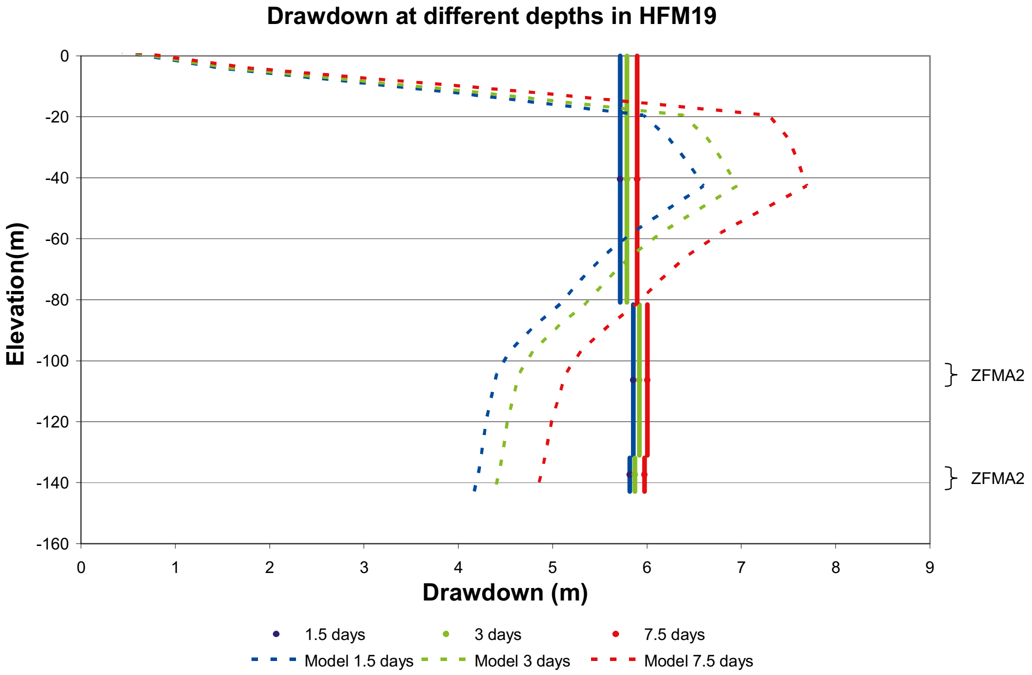

Figure 5-8. Comparison of measured (solid) and stage 2.2 base model simulation (dashed) drawdown at 3 times for the HFM19 monitoring hole. For the data, a vertical line shows the extent of the monitoring section with the drawdown representing an average within the interval, while the simulated spatial variation in drawdown in the borehole is shown for the model.

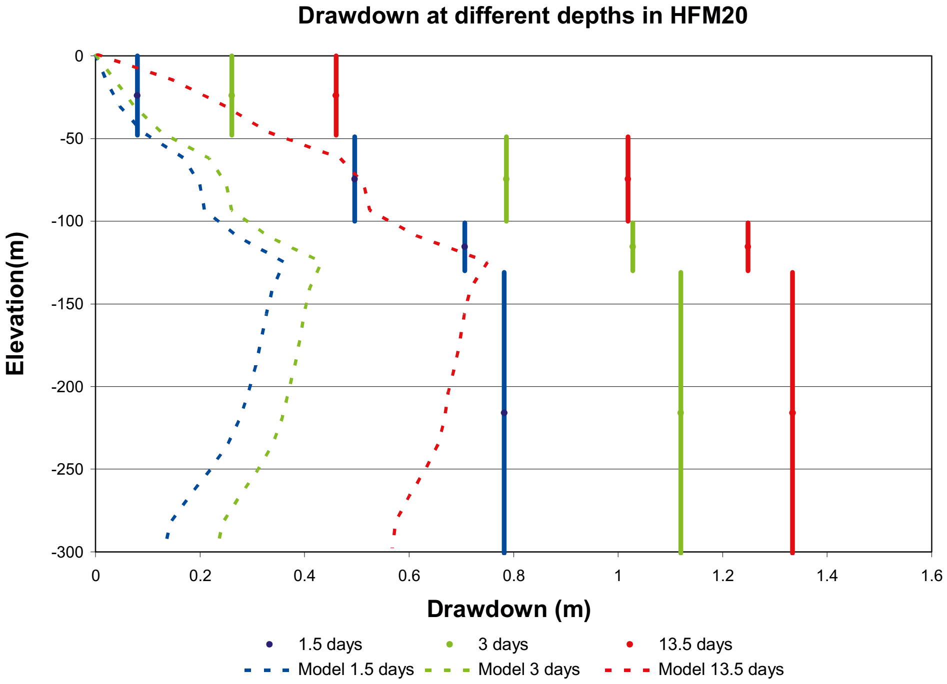

Figure 5-9. Comparison of measured (solid) and stage 2.2 base model simulation (dashed) drawdown at 3 times for the HFM20 monitoring hole. For the data, a vertical line shows the extent of the monitoring section with the drawdown representing an average within the interval, while the simulated spatial variation in drawdown in the borehole is shown for the model.

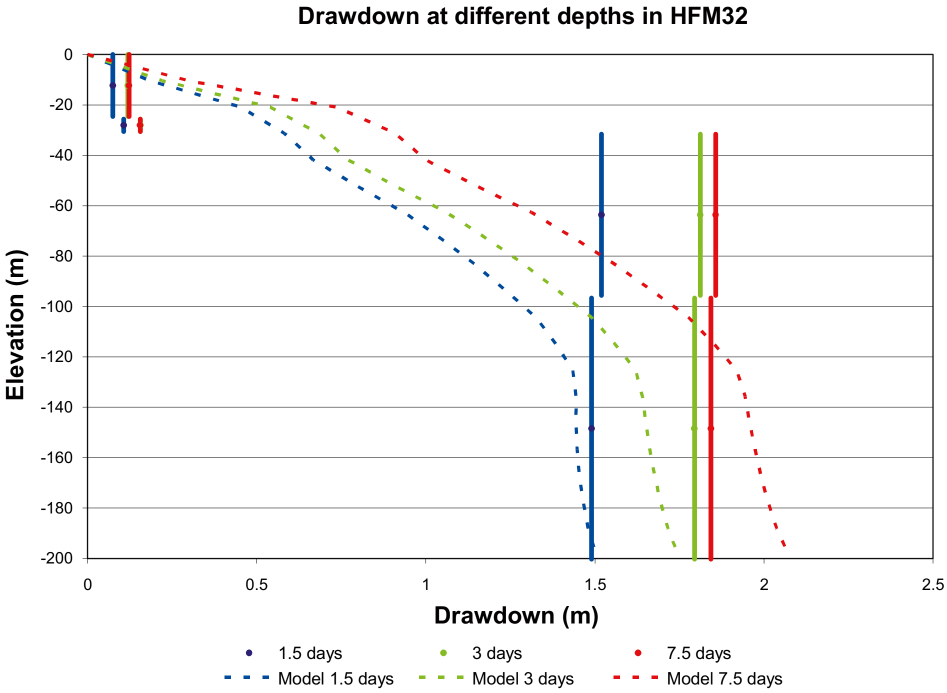

Figure 5-10. Comparison of measured (solid) and stage 2.2 base model simulation (dashed) drawdown at 3 times for the HFM32 monitoring hole. For the data, a vertical line shows the extent of the monitoring section with the drawdown representing an average within the interval, while the simulated spatial variation in drawdown in the borehole is shown for the model.

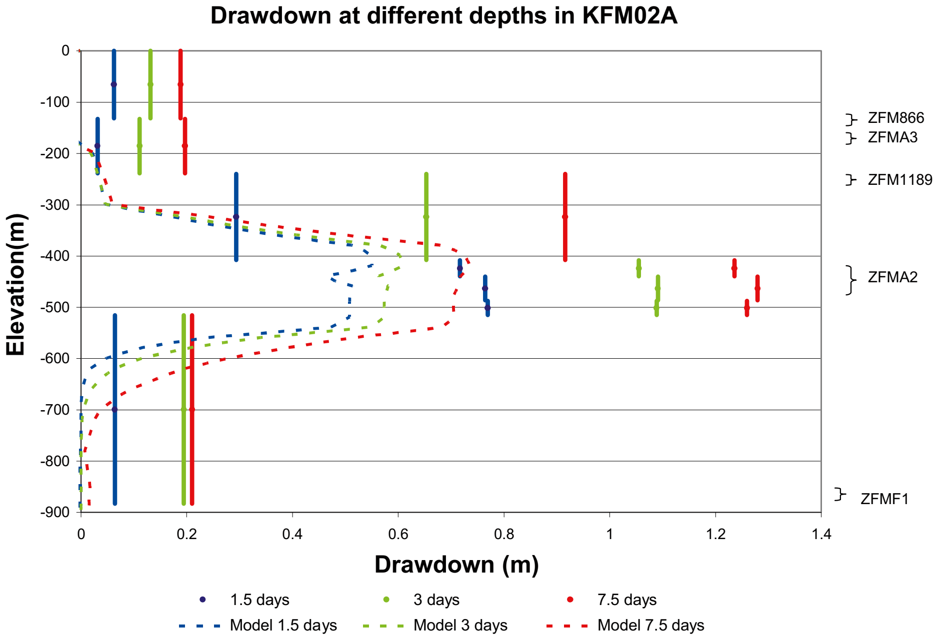

Figure 5-11. *Comparison of measured (solid) and stage 2.2 base model simulation (dashed) drawdown at 3 times for the KFM02A monitoring hole. For the data, a vertical line shows the extent of the monitoring section with the drawdown representing an average within the interval, while the simulated spatial variation in drawdown in the borehole is shown for the model.*

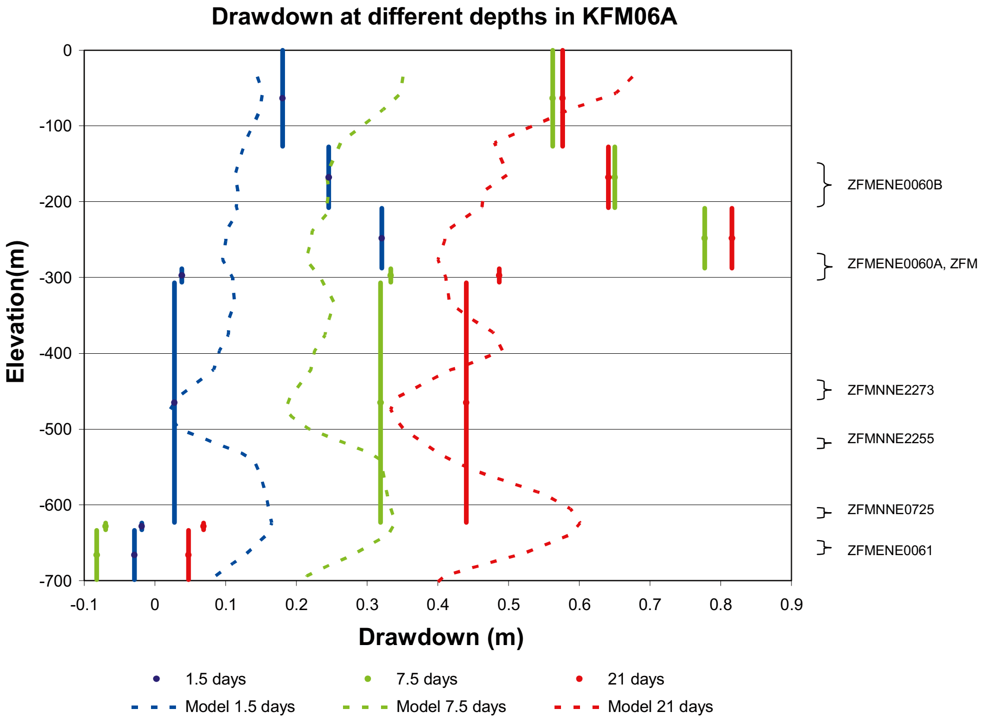

Figure 5-12. *Comparison of measured (solid) and stage 2.2 base model simulation (dashed) drawdown at 3 times for the KFM06A monitoring hole. For the data, a vertical line shows the extent of the monitoring section with the drawdown representing an average within the interval, while the simulated spatial variation in drawdown in the borehole is shown for the model.*

5.2.4 Illustration of sensitivities considered during calibration

In this section, the results of sensitivity cases about the *stage 2.2 base model simulation* are reported to illustrate why certain steps were made in the calibration process on the hydraulic interference test, and to quantify sensitivities to a few of the uncertainties. The sensitivity cases are here collated according to the model elements: HCD, HSD and HRD.

Sensitivities to hydraulic conductor domains (HCD)

The first sensitivity case is included to show the effects of using the HCD property assignment based on calibration to the single-hole hydraulic measurements prior to considering the HFM14 cross-hole test. That is, all other properties are preserved from the central calibrated case, but no adjustments are made to the transmissivity of zones or their hydraulic thickness to match the interference test. This sensitivity case essentially corresponds to the HCD property assignment that is specified in /Follin et al. 2007b/. The overall final drawdown is shown in Figure 5-13. Clearly, the drawdown for near boreholes is too high, and that in far boreholes too low. Individual responses for KFM02A and KFM06A are shown in Figure 5-14 and Figure 5-15. This motivates an increase in the transmissivity of A2 in the top 400 m to $2.8 \cdot 10^{-4}$ m^2/s and a reduction in the hydraulic thickness of zones A2, A8, ENE0401 and ENE0060 to 5 m thick to give a more discrete response. Although these changes are a slight deviation from the properties proposed in /Follin et al. 2007b/, neither change is inconsistent with the underlying data. The hydraulic thicknesses are uncertain, with the geological thicknesses only indicating an upper limit. The transmissivity depth profile used in zone A2 for the *stage 2.2 base model simulation* is illustrated by the green line shown in the top plot of Figure 5-1. The red and blue lines represent 2 alternative ways of interpreting /Follin et al. 2007b/ by either using the mean calculated *m*-value or the *m*-value based on the maximum transmissivity measured in the zone. Generally, using the mean *m*-value was found to be the better interpretation, but the one used for zone A2 in the stage 2.2 base case is essentially a hybrid of the 2 possible implementations of /Follin et al. 2007b/. In terms of the hydrogeology of A2, it suggests that there are connected high transmissivity channels with A2 that persist throughout the top 400 m although the average transmissivity may reduce with depth.

Sensitivity cases were also performed to scope the effects of the two extensive ENE striking zones ENE0401 and ENE0060 that pass close to the abstraction. In both cases the transmissivity was increased by reducing the parameter *m* such that the depth trend in transmissivity passed through the maximum measured value in that zone. For ENE0401A and B, this meant using $m = 680$ to honour $T = 2.91 \cdot 10^{-4}$ m^2/s at $z = -141$ m RHB 70, which amounts to increasing T by a factor of about 20. The overall drawdown for this sensitivity case is shown in Figure 5-16. The impact is not great apart from a general lowering of drawdowns as the zone now provides an additional source of water, diluting the response in A2. On balance, it is probably a slightly poorer match, but still indicates the sensitivity to this major ENE zone in the area. For ENE0060A it meant using $T = 1.48 \cdot 10^{-3}$ m^2/s for the interval –100 to –200 m RHB 70 as used for ENE0060B in the calibration to single-hole tests in KFM06A, rather than using the $T = 3.48 \cdot 10^{-9}$ m^2/s measured at $z = -181$ m RHB 70 in KFM01C. The overall drawdown for this case is shown in Figure 5-17, and the response in KFM06A is shown in Figure 5-18. The magnitude and depth variation of responses in KFM06A is improved, although now too high, and the overall level of response is slightly decreased at short to medium distances as more water is supplied to HFM14 from ENE0060 resulting in less drawdown in A2. A compromise could be to use $T \sim 5 \cdot 10^{-4}$ m^2/s in ENE0060A, and reduce the transmissivity in NNE0725 which has a relatively high transmissivity based on the measurement in KFM06A of $T = 3.4 \cdot 10^{-7}$ m^2/s at $z = -634$ m RHB 70 in the single-hole tests.

The sub-horizontal zone A8 that runs near parallel to A2 in the north of the site was also considered by making *m* = 700 to honour $T = 5.26 \cdot 10^{-4}$ m^2/s at $z = -38$ m RHB 70, a factor 1.6 increase. This gave very little change to the drawdown responses. However, A8 intercepts KFM06B which shows a higher response than KFM06A, which may be due to a hydraulic connection via ENE0060A and A8. Hence, it is recommended that a case be considered with higher transmissivity in zones ENE0060A and A8, possibly coupled with zone A8 having a structural connection to zone A2 to form a splay.

A final sensitivity case considered to the HCD structures was to illustrate the role of the "cage features" by simply removing the "cage features" altogether. The results of this simulation are shown by the overall drawdown profile shown in Figure 5-19. This results in an almost doubling of the simulated drawdown in HFM14 since a high transmissivity structure intercepts this borehole. Very little drawdown is predicted in HFM20 without the "cage features" as it is the main hydraulic connection between HFM14 and HFM20. These results indicate the key importance of a handful of features – A2, ENE0060 and the "cage features" – in determining the response to the interference test.

Sensitivities to hydraulic soil domains (HSD)

The next most important factor in simulating the interference test is the properties of the Quaternary deposits, HSD. A set of sensitive cases were constructed to illustrate the role of the HSD properties to the interference test. These properties are also important to simulating the point-water head measurements, so this discussion has to be considered in parallel to those for the point-water head calibration.

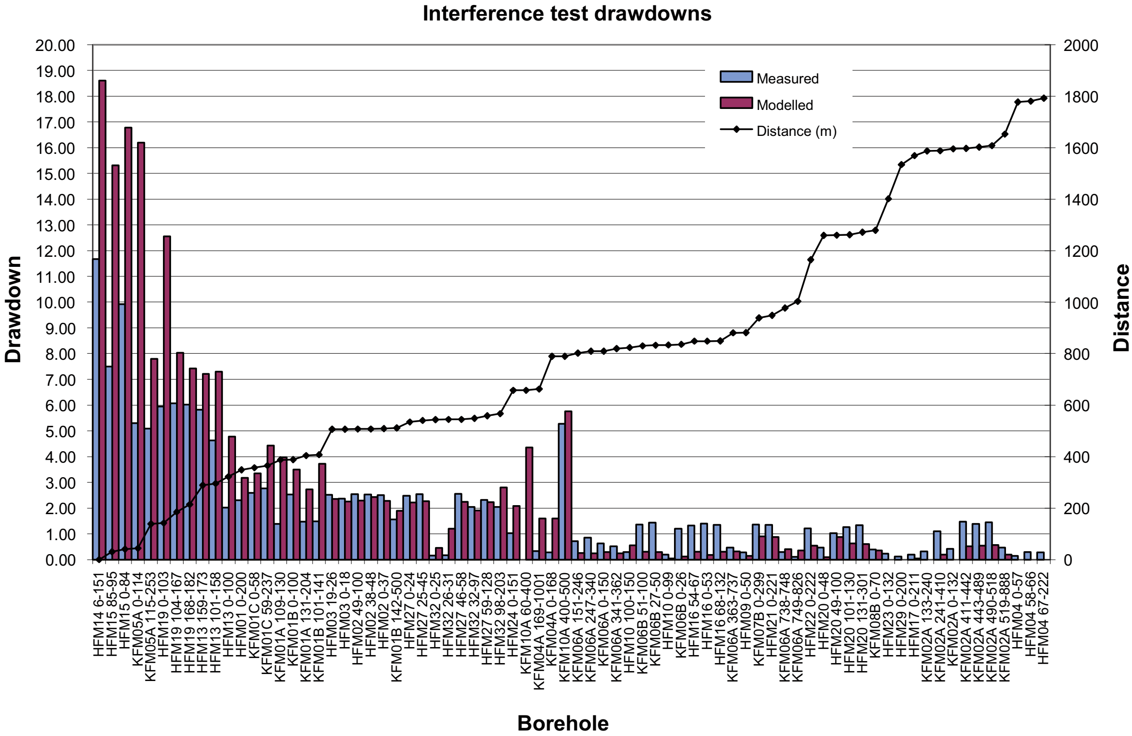

Figure 5-13. Comparison of measured (blue) and modelled (red) drawdown at the end of pumping (21 days) for all monitored borehole intervals for the sensitivity case without any calibration of A2 on the interference test. The borehole intervals are ordered according to the 3D distance (the right axis) of the monitoring intervals to the abstraction at HFM14.

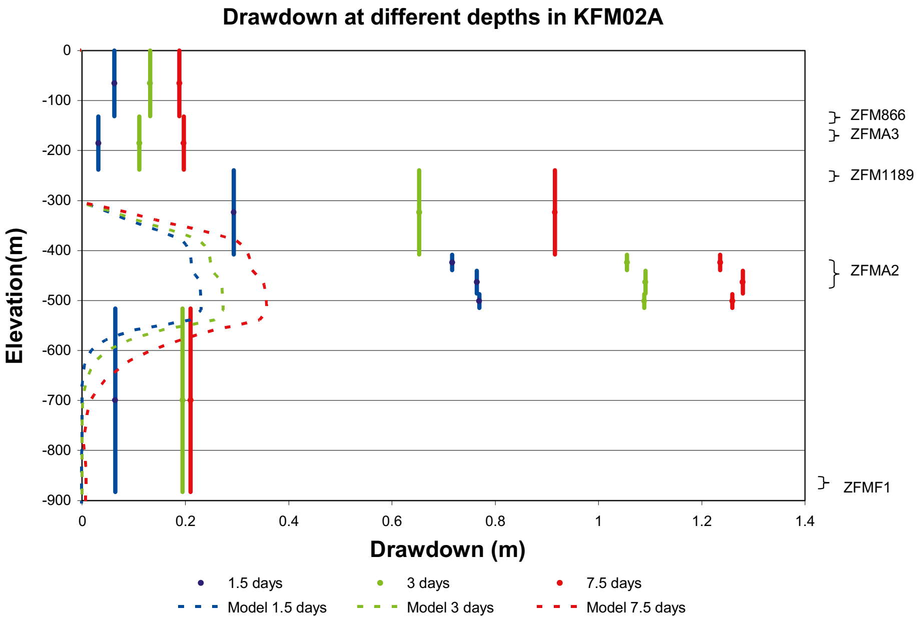

Figure 5-14. *Comparison of measured (solid) and modelled (dashed) drawdown at 3 times for the KFM02A monitoring hole. For the data, a vertical line shows the extent of the monitoring section with the drawdown representing an average within the interval. The model is shown as a spatial variation in drawdown in the borehole for the sensitivity case without any calibration of zone A2.*

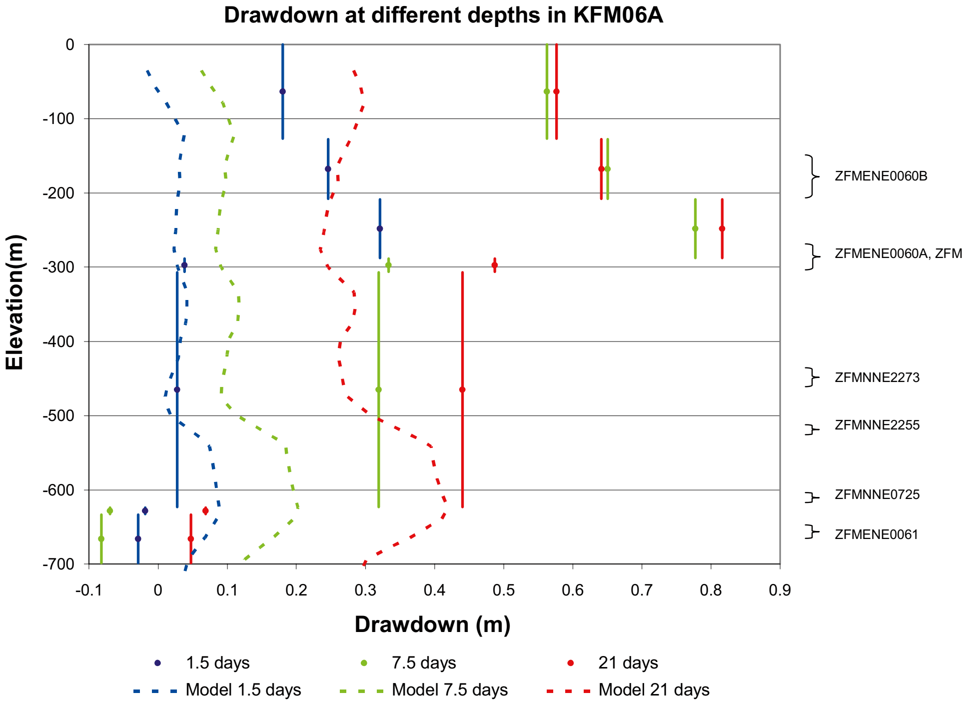

Figure 5-15. *Comparison of measured (solid) and modelled (dashed) drawdown at 3 times for the KFM06A monitoring hole. For the data, a vertical line shows the extent of the monitoring section with the drawdown representing an average within the interval. The model is shown as a spatial variation in drawdown in the borehole for the sensitivity case without any calibration of zone A2.*

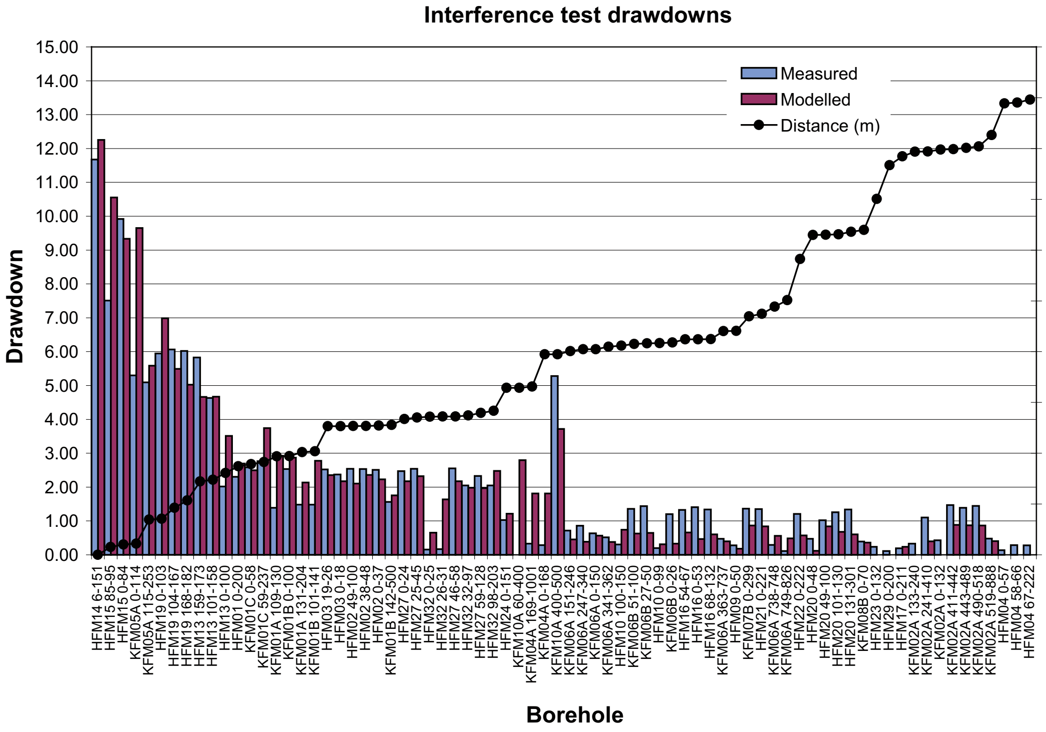

Figure 5-16. *Comparison of measured (blue) and modelled (red) drawdown at the end of pumping (21 days) for all monitored borehole intervals for the sensitivity case with increased transmissivity in zone ENE0401A. The borehole intervals are order according to the 3D distance of the monitoring intervals to the abstraction at HFM14.*

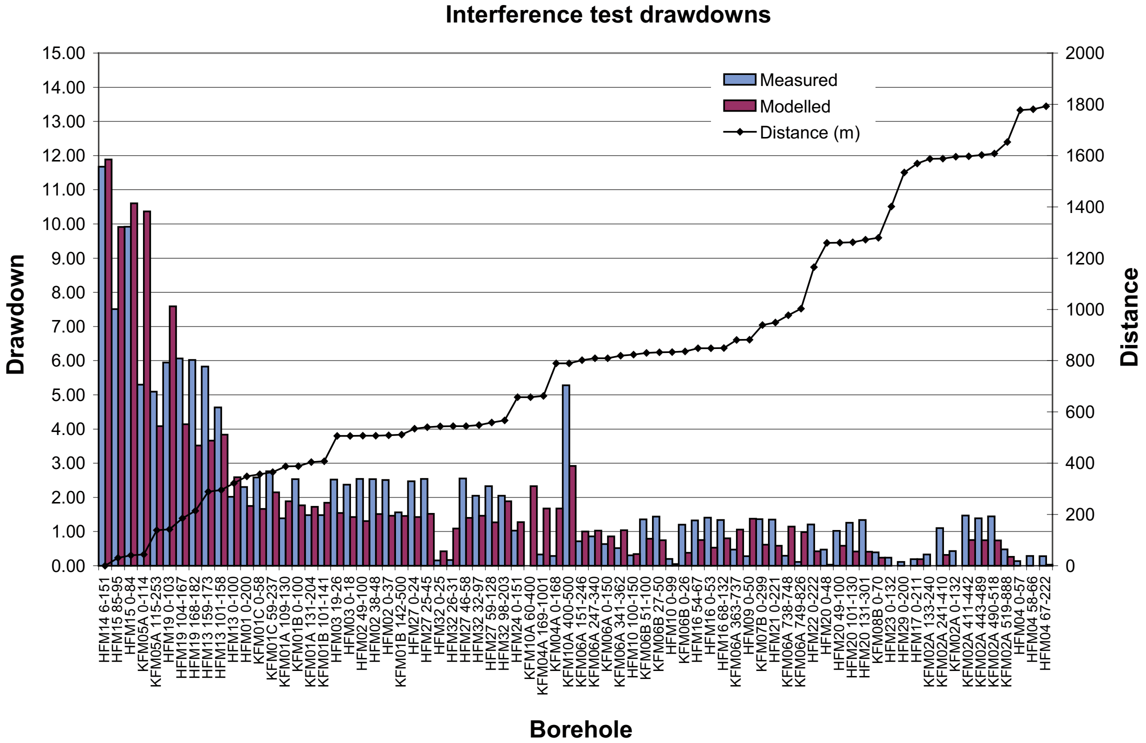

Figure 5-17. *Comparison of measured (blue) and modelled (red) drawdown at the end of pumping (21 days) for all monitored borehole intervals for the sensitivity case with increased transmissivity in zone ENE0060A. The borehole intervals are order according to the 3D distance of the monitoring intervals to the abstraction at HFM14.*

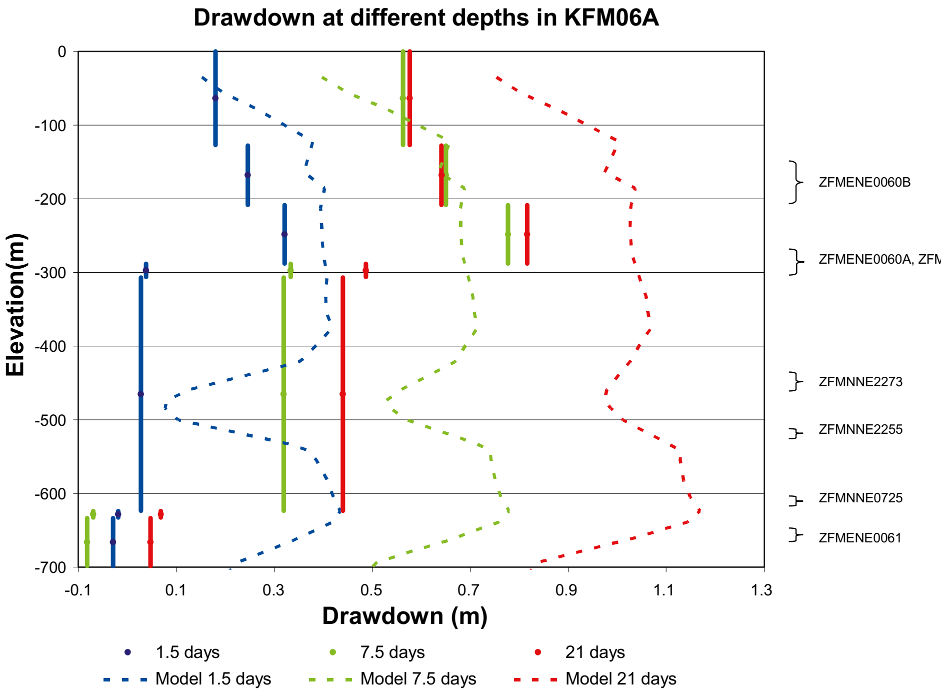

Figure 5-18. *Comparison of measured (solid) and modelled (dashed) drawdown at 3 times for the KFM06A monitoring hole. For the data, a vertical line shows the extent of the monitoring section with the drawdown representing an average within the interval. The model is shown as a spatial variation in drawdown in the borehole for the sensitivity case increased transmissivity in zone ENE0060A.*

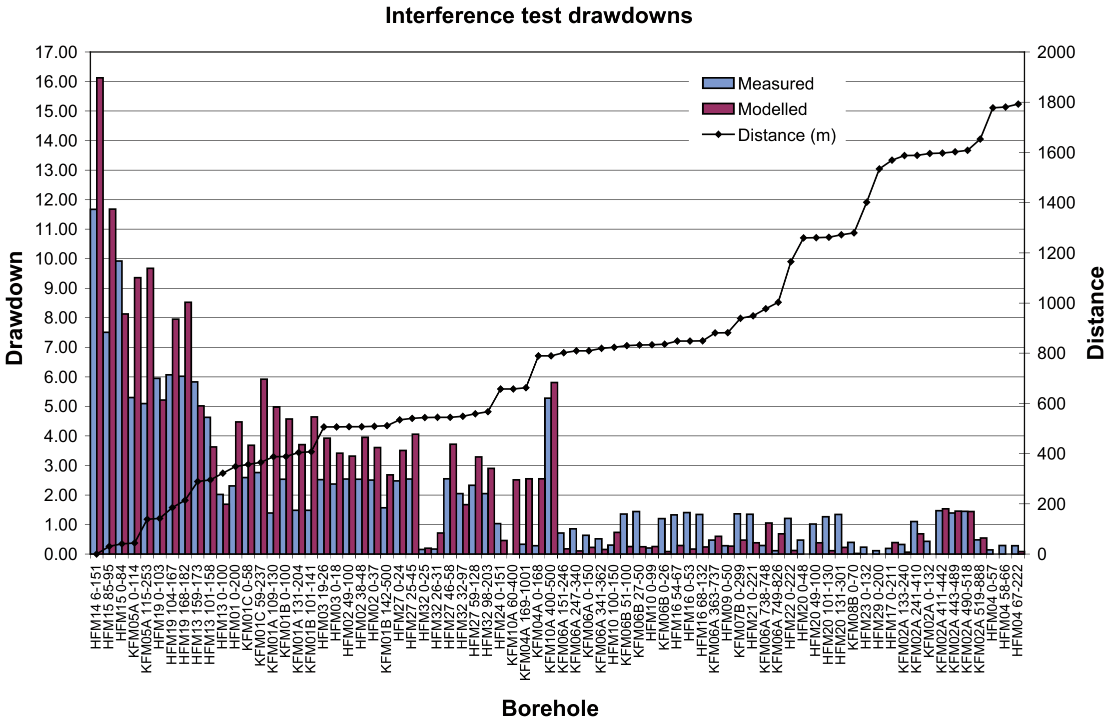

Figure 5-19. *Comparison of measured (blue) and modelled (red) drawdown at the end of pumping (21 days) for all monitored borehole intervals for the sensitivity case without the "cage features". The borehole intervals are ordered according to the 3D distance of the monitoring intervals to the abstraction at HFM14.*

One step in the calibration was to make all soils corresponding to the lake sediments L1–L3 tighter. To show why this was done, a sensitivity cases was made with the change reversed to the properties used in the *stage 2.2 base model simulation*, i.e. we used the properties as specified in Table 3-12. (In the *stage 2.2 base model simulation* the L1–L3 layers are tighter by a factor 1/300, 1/150,000, 1/15, respectively.) For such a case, the general pattern of drawdown is not changed for most boreholes apart from KFM06A, KFM06B and HFM16 on the opposite side of Lake Bolundsfjärden, where the simulated drawdown is much reduced below that measured (see Figure 5-20 and Figure 5-21). Hence, it confirms the decision to have a much lower effective vertical hydraulic conductivity the lake sediments to reduce the hydraulic connection with the bedrock.

In the *stage 2.2 base model simulation* the properties chosen from Table 3-12 for Z1 were based on clay and Z5 was on fine-grained till, i.e. the lowest possible values for soil types within those layers. Using the highest possible values gave lower drawdowns at all monitoring points more than 500 m away as it gave a good contact between the bedrock and surface, and hence away from HFM14, the bedrock was replenished by recharge or the Baltic Sea as shown in Figure 5-22 and Figure 5-23. Unfortunately, for the point-water head calibration, the choice of properties for Z1 and Z5 corresponding to these high values gave the better match to that type of data. Two possible interpretations were considered to try and reconcile this contradiction. The first was to consider that the low lying areas to the north and east where the problem monitoring boreholes are located may be characterised by finer grain sediments than the rest of the site area. There is evidence from site to support higher clay content to the east. The other was to consider the effective properties of the HSD to be anisotropic, such that the coarse grain sediment properties are used for the effective horizontal hydraulic conductivity and the fine grained sediment properties are used for the effective vertical hydraulic conductivity. Both these scenarios seem to be able to largely reconcile the calibration on the interference test and point-water heads.

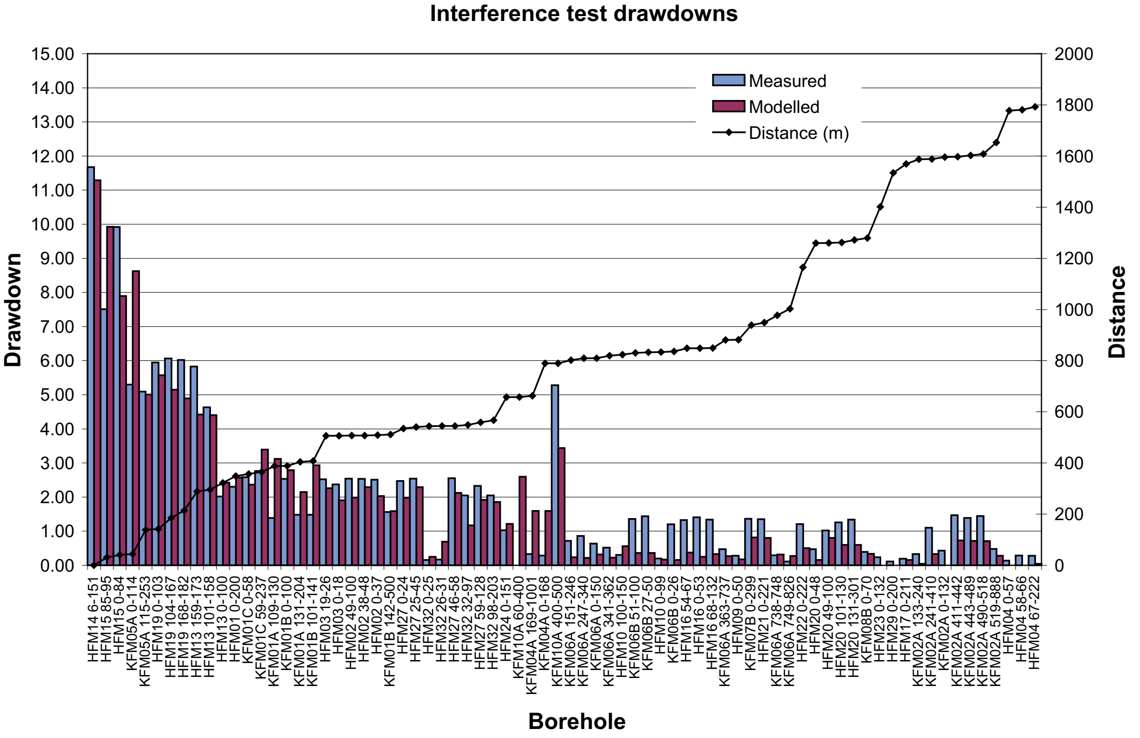

Figure 5-20. *Comparison of measured (blue) and modelled (red) drawdown at the end of pumping (21 days) for all monitored borehole intervals for the sensitivity case with more permeable lake sediments. The borehole intervals are ordered according to the 3D distance of the monitoring intervals to the abstraction at HFM14.*

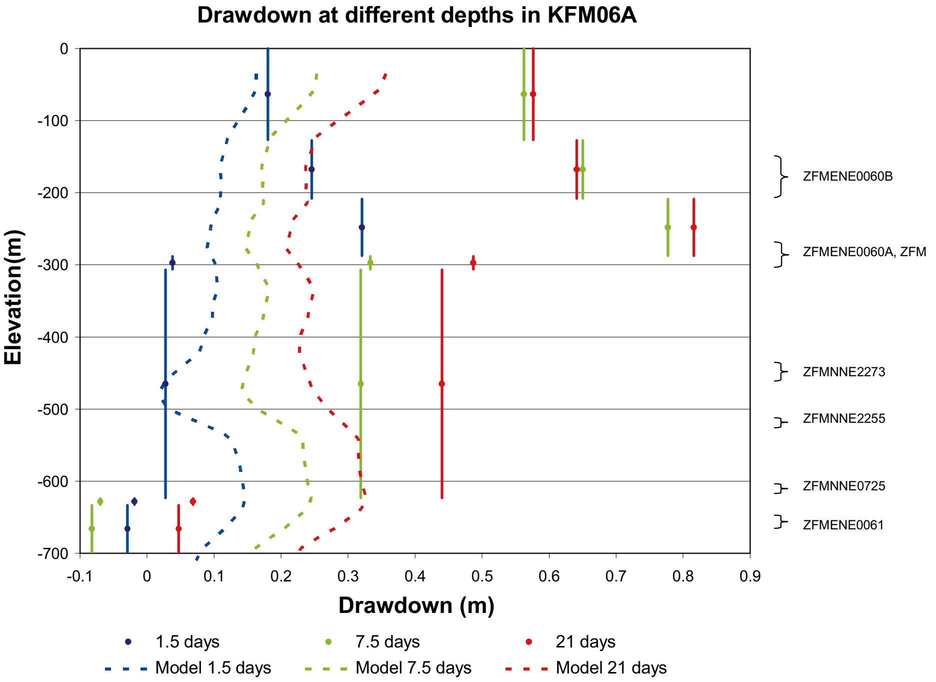

Figure 5-21. *Comparison of measured (solid) and modelled (dashed) drawdown at 3 times for the KFM06A monitoring hole. For the data, a vertical line shows the extent of the monitoring section with the drawdown representing an average within the interval. The model is shown as a spatial variation in drawdown in the borehole for the sensitivity case with more permeable lake sediments.*

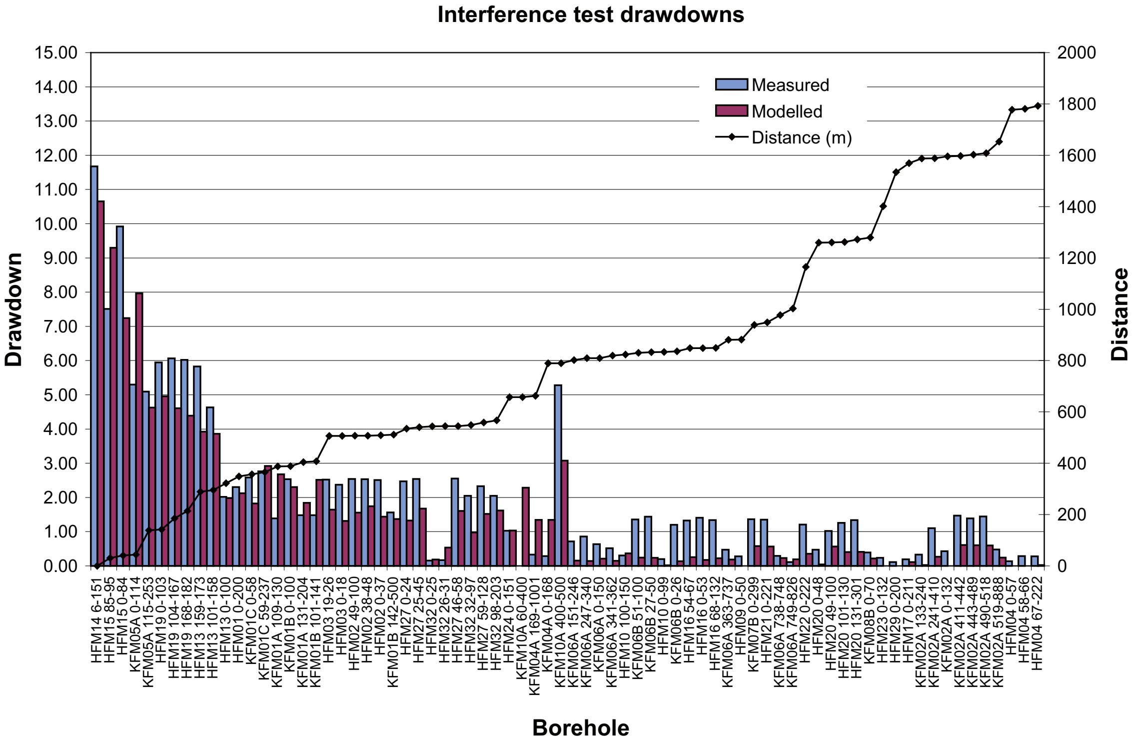

Figure 5-22. *Comparison of measured (blue) and modelled (red) drawdown at the end of pumping (21 days) for all monitored borehole intervals for the sensitivity case with more permeable layers Z1 and Z5. The borehole intervals are ordered according to the 3D distance of the monitoring intervals to the abstraction at HFM14.*

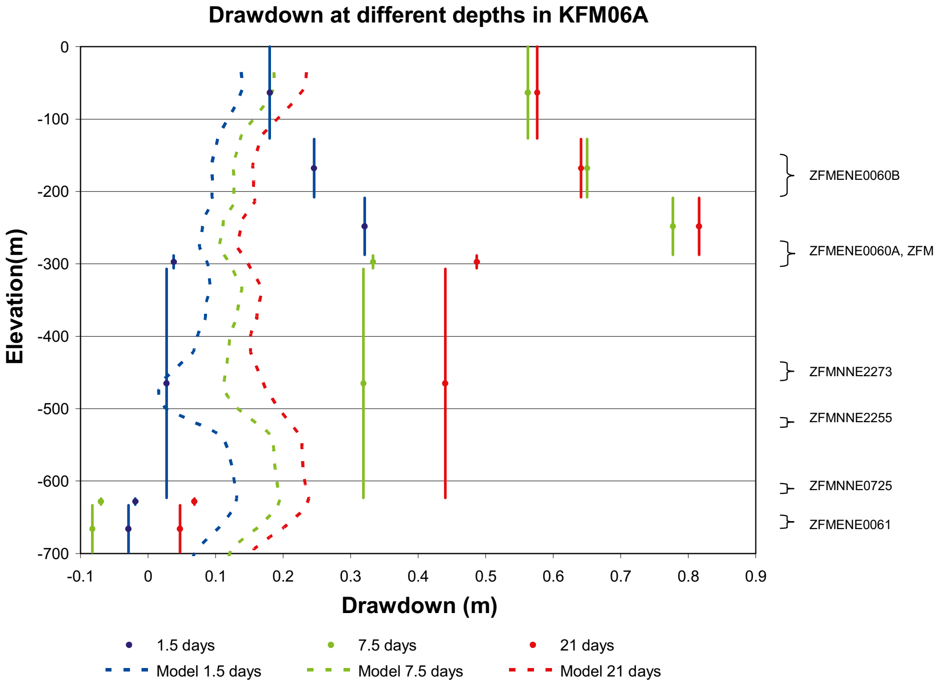

Figure 5-23. *Comparison of measured (solid) and modelled (dashed) drawdown at 3 times for the KFM06A monitoring hole. For the data, a vertical line shows the extent of the monitoring section with the drawdown representing an average within the interval. The model is shown as a spatial variation in drawdown in the borehole for the sensitivity case with more permeable layers Z1 and Z5.*

The sensitivity case with fine-grained properties in low lying areas assumed, for simplicity, such properties for Z1 and Z5 below a topographic surface height of 2 m, which covers the area around the shore of the Baltic and lakes. Figure 5-24 shows that this gives results similar to the central calibrated case for the interference test, and improved agreement to the point-water heads, as will be seen in Section 5.3.

Sensitivities to hydraulic rock domains (HRD)

In the previous section we focussed on the importance of how the properties of the Quaternary deposits affect recharge to the bedrock and vertical infiltration of groundwater vertically through the system to counteract the water extracted from HFM14. Equally important to this process is the vertical hydraulic conductivity of the bedrock. At present, there remain large uncertainties in the vertical hydraulic connectivity of the bedrock based on direct measurements from the field. Partly, this is because the description of fracture sets and orientations and their description in terms of DFN models for the different fracture domains using the available data from data freeze 2.2 were not yet fully mature. There are also limited core-logs, image-logs, and hydraulic measurements of fracturing in the upper 100 m of rock, and finally because the hydraulic tests principally measure radial flow toward vertical or steeply inclined boreholes, making it difficult to interpret the vertical hydraulic connectivity and hydraulic properties. Hence, the interference tests and the palaeohydrological measurements probably give us the best indication of the vertical drainage and transport through the bedrock. Clearly, such measurements do not yield a description of fracture geometrical and hydraulic parameters directly, more they provide a consistency check for properties assumed from what information we do have, and a means for evaluating possible ranges for uncertain parameters. Hence, here we consider several sensitivity cases that quantify the effects of varying the fracture orientation, and hydraulic conductivity and anisotropy of the upper bedrock.

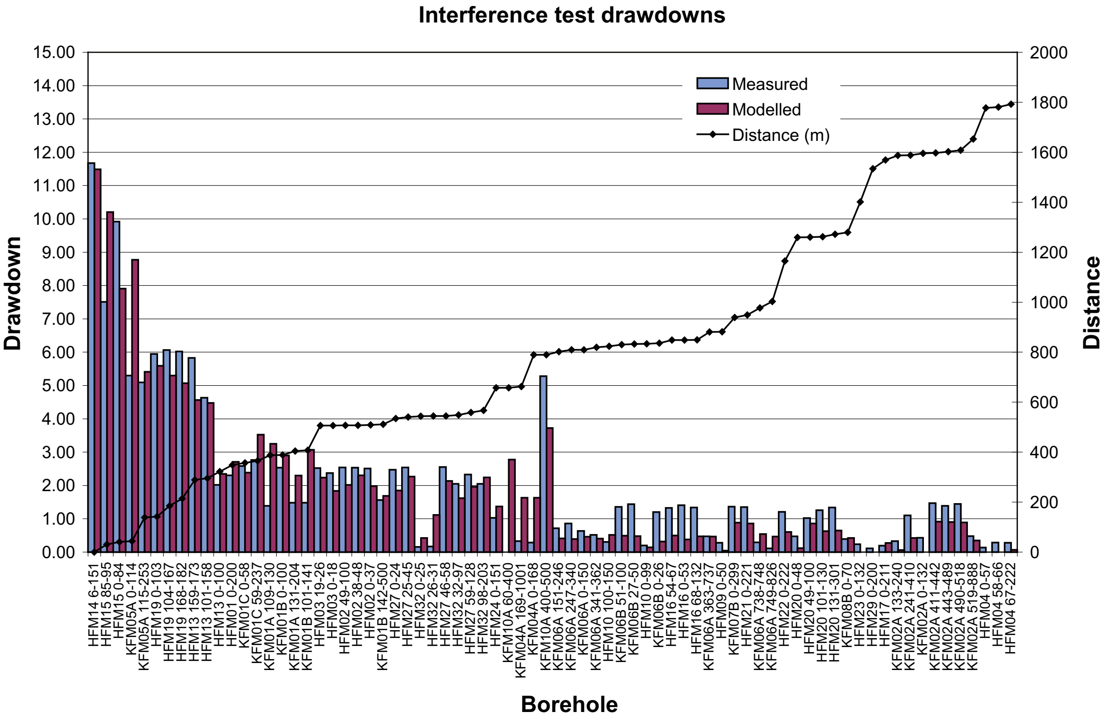

***Figure 5-24.** Comparison of measured (blue) and modelled (red) drawdown at the end of pumping (21 days) for all monitored borehole intervals for the sensitivity case with more permeable layers Z1 and Z5 where topography > 2 m. The borehole intervals are ordered according to the 3D distance of the monitoring intervals to the abstraction at HFM14.*

The *stage 2.2 base model simulation* used the alternative Hydro-DFN fracture orientations distributions shown in Table 3-8 recommended by /Follin et al. 2007b/ in preference to the Hydro-DFN fracture orientations derived in version 1.2, cf. Table 3-7. This change in orientation was applied to all fracture domains: FFM01–06. The key difference between the two models from a hydrogeological point of view is the higher Fisher concentration in the dominant sub-horizontal set ($\kappa = 15.2$ instead of 8.2) specified in the alternative Hydro-DFN model, which will lead to a greater horizontal versus vertical anisotropy due to the reduced vertical connectivity. The implications of using a more isotropic fracture network are here illustrated by a sensitivity case that reverts to the Hydro-DFN fracture orientation distributions used in version 1.2 to assign the ECPM properties. The vertical hydraulic conductivity of the HRD was still reduced by one order of magnitude in the upper 400 m of bedrock as in the *stage 2.2 base model simulation*, i.e. only the probability distributions functions were changed for the underlying Hydro-DFN model fracture orientations. The overall drawdown responses at the end of pumping for this case are shown in Figure 5-25. Generally, the drawdown is reduced due to a greater amount of recharge through the bedrock. This is an interesting result since it suggests that by merely changing the orientation distributions of the fracture sets, then the hydraulic behaviour can be altered a significant amount. More often, such small changes in fracture orientations have a relatively weak control on hydraulics, but at Forsmark the dominance of the sub-horizontal set means that flow is anisotropic and sensitive to such changes in the orientation parameters.

This sensitivity to the fracture orientations suggests that more effort should be put on analysing the fracture sets and orientation parameters for individual fracture domains, especially the near-surface FFM02 and FFM06 once data is available from KFM08D in stage 2.3.

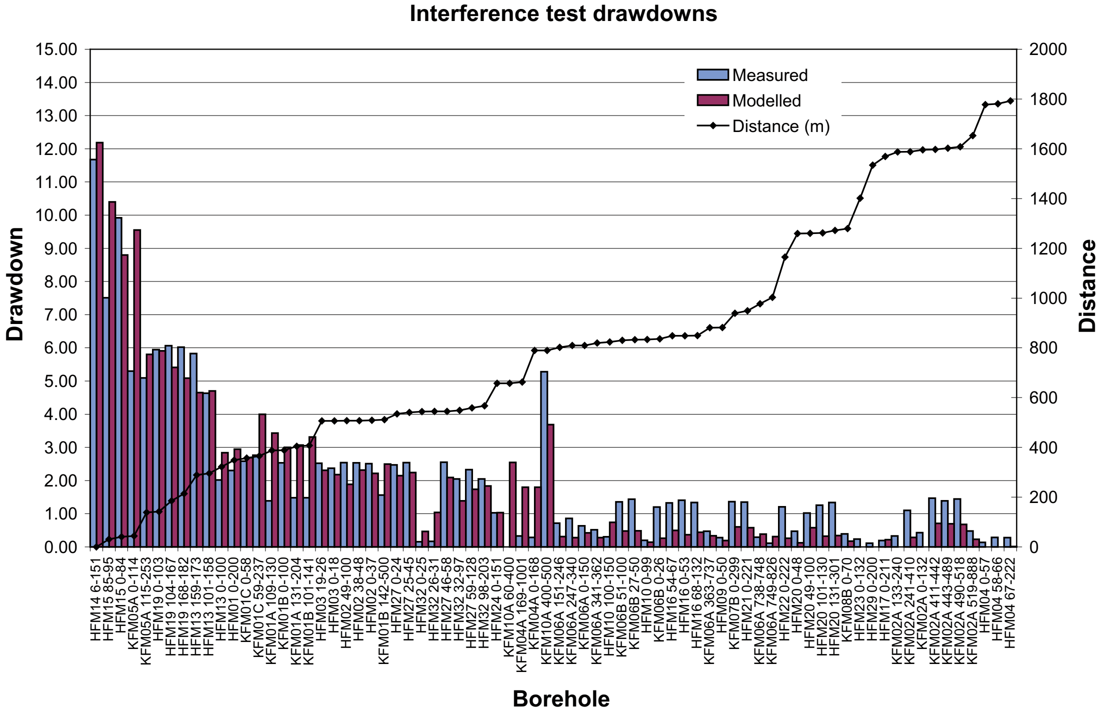

***Figure 5-25.** Comparison of measured (blue) and modelled (red) drawdown at the end of pumping (21 days) for all monitored borehole intervals for the sensitivity case with version 1.2 fracture orientation distributions. The borehole intervals are ordered according to the 3D distance of the monitoring intervals to the abstraction at HFM14.*

In the *stage 2.2 base model simulation*, the vertical hydraulic conductivity of the HRD was reduced by one order of magnitude in the upper 400 m of bedrock. Such a scenario would arise if the sub-horizontal fracturing in FFM02 were near parallel (i.e. large Fisher concentration) or the transmissivity of sub-vertical sets are lower than those in the sub-horizontal set due to the effect of the large horizontal rock stresses at Forsmark. Both of these possibilities are likely to occur. The overall drawdown distribution for a sensitivity case without the reduction in vertical hydraulic conductivity is shown in Figure 5-26. This has a similar, but slightly smaller effect to that for the alternative fracture orientations.

Given this sensitivity to the hydraulic properties of the upper bedrock, two additional cases were considered to scope the impact of the HRD properties. These were to use the ECPM properties derived from the alternative Hydro-DFN fracture orientations (higher Fisher concentration in sub-horizontal set) suggested by /Follin et al. 2007b/, but apply a one order of magnitude reduction in horizontal and vertical hydraulic conductivity in the upper 400 m of relatively more permeable bedrock, results shown in Figure 5-27, and a two orders of magnitude reduction, shown in Figure 5-28. Both cases give similar results that are also very close to the results obtained for the *stage 2.2 base model simulation*. Based on these results we conclude that it is the vertical hydraulic conductivity in the HRD that affects the interference test by controlling the infiltration of surface recharge, and that this control is secondary to the properties of the HCD as reductions in hydraulic conductivity larger than about one order of magnitude have no further change in the hydraulic interference test.

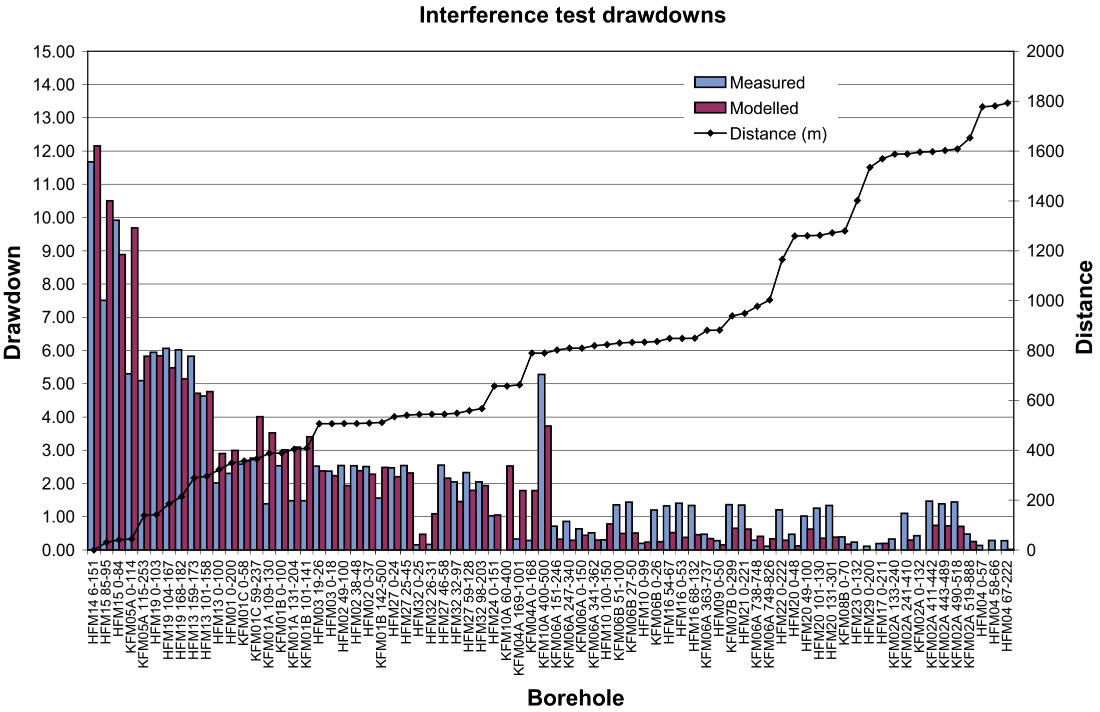

Figure 5-26. *Comparison of measured (blue) and modelled (red) drawdown at the end of pumping (21 days) for all monitored borehole intervals for the sensitivity case without a reduction in hydraulic conductivity of HRD. The borehole intervals are ordered according to the 3D distance of the monitoring intervals to the abstraction at HFM14.*

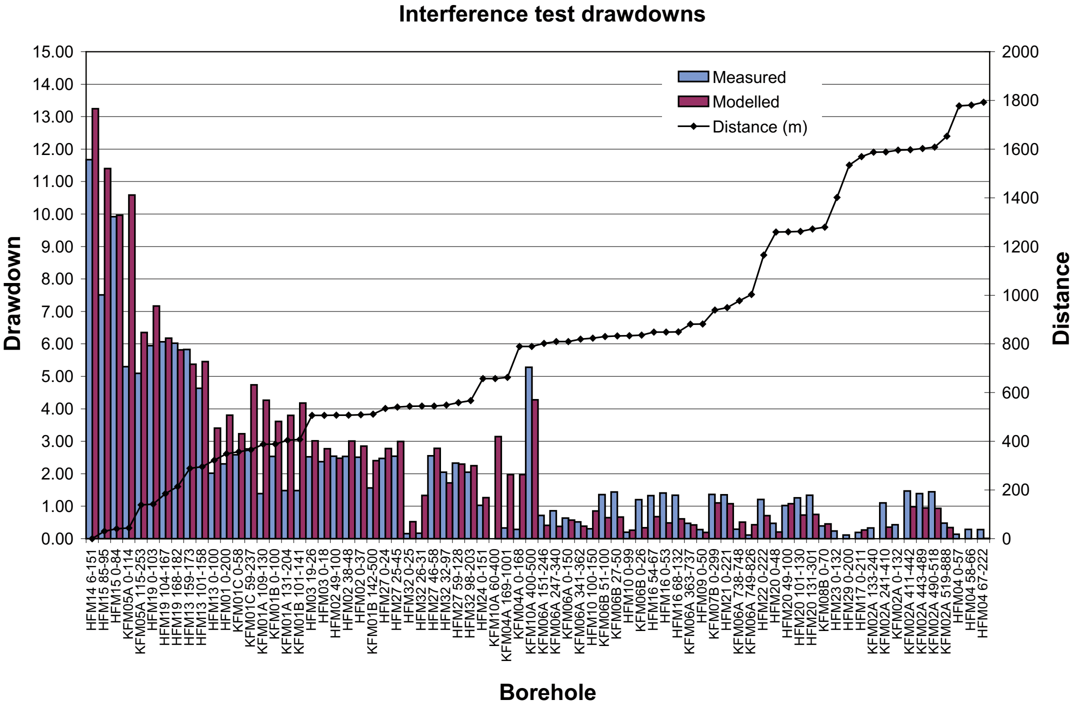

Figure 5-27. *Comparison of measured (blue) and modelled (red) drawdown at the end of pumping (21 days) for all monitored borehole intervals for the sensitivity case with a order of magnitude lower hydraulic conductivity of HRD. The borehole intervals are order according to the 3D distance of the monitoring intervals to the abstraction at HFM14.*

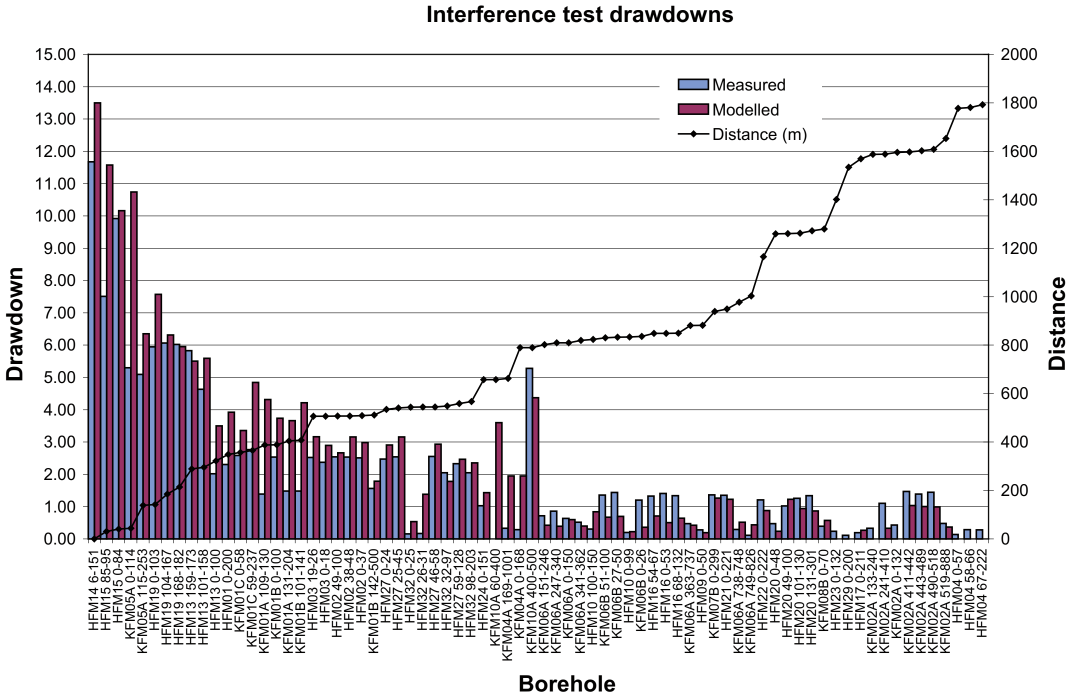

Figure 5-28. *Comparison of measured (blue) and modelled (red) drawdown at the end of pumping (21 days) for all monitored borehole intervals for the sensitivity case with two orders of magnitude lower hydraulic conductivity of HRD. The borehole intervals are ordered according to the 3D distance of the monitoring intervals to the abstraction at HFM14.*

5.3 Task C – Matching natural point-water heads

The simulations of the point-water heads were originally performed independently of those for the hydraulic interference test, and were generally found to be less challenging to reproduce the measurements. Therefore, the simulations of point-water heads were repeated using the *stage 2.2 base model simulation* and sensitivity cases used in the interference test described above once these had been decided. As already mentioned, the point-water head measurements did create a seeming contradiction that the sensitivity cases that compared best for the point-water head measurements gave a poorer match to the interference test. This prompted extra sensitivity cases to be considered primarily focussed in the properties of the HSD.

5.3.1 Methodology

Measurements of natural point-water heads were available in both the percussion-drilled boreholes in the bedrock (HFM) and the boreholes in the Quaternary deposits (SFM). Measurements were made at several different times to yield a mean point-water head and indicate seasonal variations recorded simply as a minimum and maximum head. It should be noted that these are all measurements from the soil or upper bedrock, top 100–200 m, and hence we are not calibrating against depth variations in the natural head deep into the rock, or considering the effects of variable-density flow.

The simulation model used exactly the same grid and parameters as those used for the interference test. The top surface boundary condition was based on the estimated average annual precipitation minus evapotranspiration and overland flow (often notated as *P–E*) of 150 mm/year. Calculations were performed under steady-state conditions to indicate a temporal average head distribution in the rock and Quaternary deposits.

To compare simulation results with measurements, the calculated mean head was calculated within each HFM borehole along its length and compared to the mean measured head.

Dry HFM holes were omitted, since the head measurements from these holes were likely to be unrepresentative. For the data, the seasonal variation was shown on the comparison plots to indicate the uncertainties in the measurements, while for the simulations, the head at the very top of the HFM boreholes was plotted as well as the mean over the borehole length to indicate the predicted direction of vertical flow, i.e. recharge or discharge. For the HFM boreholes, an arithmetic average along the borehole was used for both the simulations and the data. An alternative may have been to weight by hydraulic conductivity. For the SFM data, the simulated mean heads were compared with the mean measurement, again with the seasonal variation shown to quantify data uncertainties. In addition, the mean and root mean square of the differences between the simulated heads and the mean measured heads were calculated to give a numeric objective function or quantification of "goodness of fit". Both measures were found to correlate well as the models tended to predict heads consistently slightly higher than the measurements, and so only the mean difference is given here. A good match was judged to have been achieved where the general distribution of heads within the candidate area was reproduced and when the mean discrepancy was less than the mean seasonal variation in the measurements.

5.3.2 Calibration steps

Initial simulations used the parameterisation described in Section 3 and sensitivities focussed on the uncertainties in the HSD properties. Most simulations yielded average head discrepancies of around 0.6–1.7 m for the HFM and SFM data. The best matches were found to be obtained when the more permeable options given in Table 3-12 were used.

Following on from the hydraulic interference test, the *stage 2.2 base model simulation* was considered which gave average head discrepancies from the data of just under 2 m, and so the sensitivity cases from the interference test were considered as well together with additional cases to try to achieve a match to both types of data. The additional variants prompted were:

- to consider spatial variations in the types of soil mainly focussed on layers Z1 and Z5, i.e. finer-grained soils around the shores of the lakes and sea,
- to consider vertical versus horizontal anisotropy within the HSD layers, i.e. depth variations in the sedimentation within the defined HSD layers.

It was found that matching both interference test and natural point-water heads would require one or both of these options.

5.3.3 Resulting calibration

An example of the matching of the point-water heads is shown here for HFM boreholes in Figure 5-29 and SFM boreholes in Figure 5-30 for the *stage 2.2 base model simulation*. This is not the best match obtained, but is shown as a reference for the sensitivity cases. Lines indicating the elevation of the topographic surface and the elevation of the soil/bedrock contact are shown for reference.

The simulations predict a distribution of heads in reasonable agreement with the distribution in the data, i.e. heads are generally flat, and where they are more elevated or near to ground surface, this is reproduced. The head in the Quaternary deposits is higher than in the bedrock for almost all boreholes and is generally closer to topography, which suggests groundwater recharge is the prevalent situation for most of the candidate area. However, this case derived mainly from the interference test tends to over-predict the mean heads by nearly 1.6 m for the HFM boreholes, which compares with average seasonal variations of 1.3 m, and so some improvements should be sought.

It may be seen that the head exceeds the topographic height at some locations. This highlights the issue of grid resolution. The simulation grid and the digital elevation map (DEM), provided to define the model top surface, both use a 20 m grid. Depending on undulations in ground surface on scales less than 20 m, then there are inevitably going to be discrepancies in the modelled heads in proportion to the magnitude of these local scale undulations.

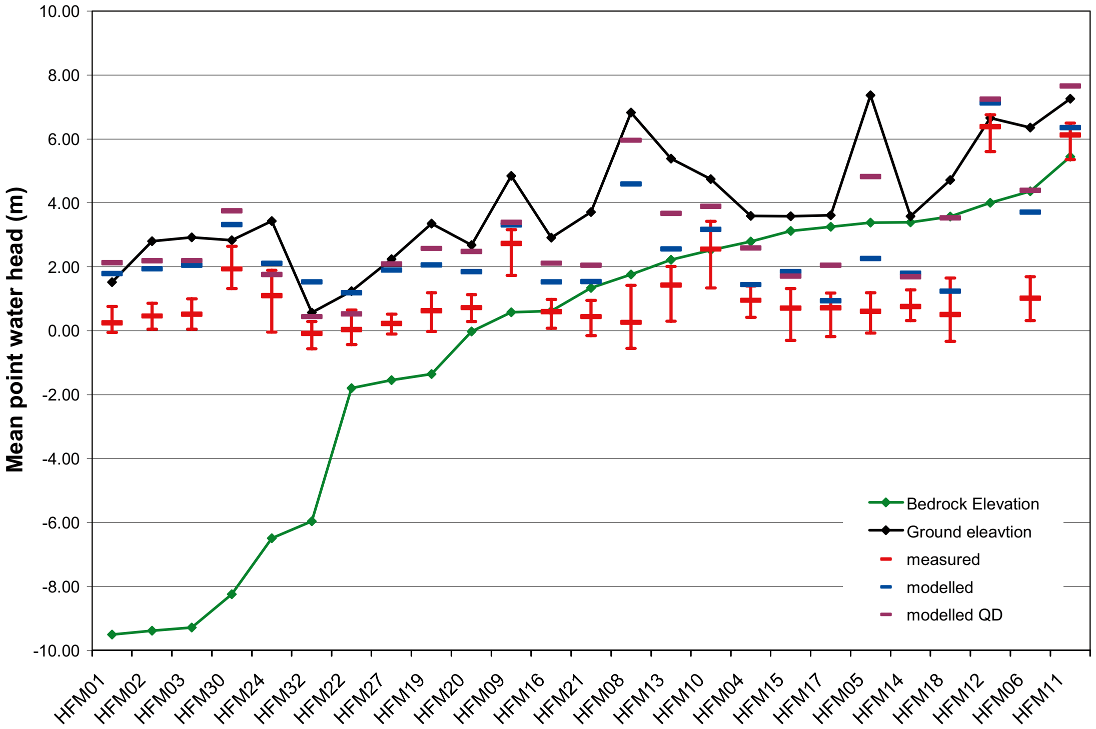

***Figure 5-29.** Comparison of measured heads in percussion drilled boreholes (HFM) with the stage 2.2 base model simulation. For the model, values are given for the QD and as an average over the borehole section in the bedrock. The field data is plotted as mean point-water heads in the bedrock with error bars to show the range of values at different times.*

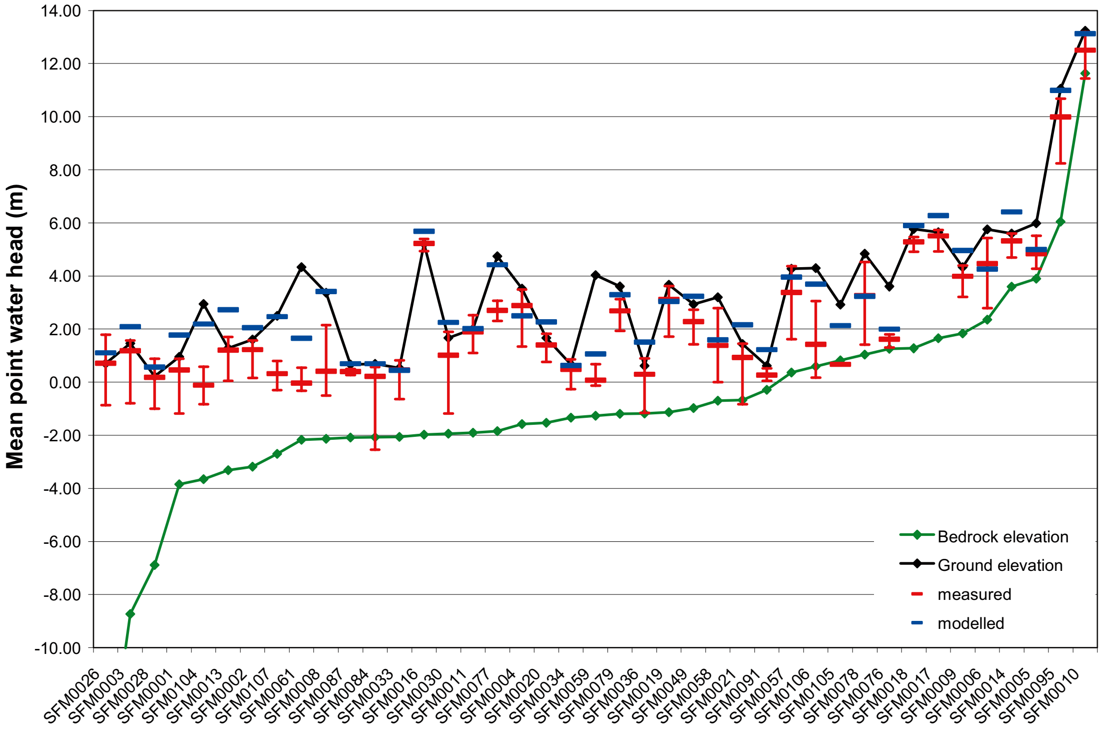

***Figure 5-30.** Comparison of measured heads in soil pipes (SFM) with the stage 2.2 base model simulation. For the model, values are given for the QD only. The field data is plotted as mean point-water heads in the bedrock with error bars to show the range of values at different times. Boreholes are ordered by bedrock elevation.*

5.3.4 Illustration of sensitivities considered during calibration

The same set of sensitivity cases considered for the hydraulic interference test are used here to quantify the importance of uncertainties in HCD, HSD and HRD to the point-water head simulations. A list of the cases and the resulting measures of mean discrepancy between modelled and measured heads is given in Table 5-1. The discrepancies should be viewed relative to the size of the seasonal variations in the measurements, 1.26 m for HFM and 1.62 m for SFM holes. The results show that increases in hydraulic conductivity improve the match, with the best being to use coarse-grained till properties for Z1 and Z5, see Table 3-12, which results in differences well within the data uncertainties. The case with horizontal versus vertical hydraulic anisotropy – using coarse-grained till for K_h and clay and fine-grained till for K_v – gives very similar results for these point-water head simulations as well as good results for the interference test, and so this is probably the most satisfactory model for the HSD properties. The case with high K_h values for the deposits only for areas with topography above 2 m elevation also gives good results. Hence, the HSD properties have the strongest control on the results. Next, increasing the transmissivity of some deformation zones improves the match, probably locally to surrounding HFM holes. The "cage features" have limited effect, probably because they have little effect on the general infiltration to the bedrock. The properties of the HRD also have limited effect, although using the version 1.2 fracture orientations and/or increasing the vertical conductivity of the HRD has a small detrimental effect on the calibration.

The simulated distribution of heads for the case with hydraulic anisotropy in the HSD layers Z1 and Z5 are shown in Figure 5-31 and Figure 5-32. The case uses coarse-grained till properties for K_h and clay and fine-grained till properties for K_v. The results demonstrate the improvement relative to the *stage 2.2 base model simulation*, but still show that recharge conditions dominate, with only HFM22 (close to the shore of the Baltic) and HFM32 (on the island in the centre of Bolundsfjärden) suggesting discharge conditions. Some additional simulations indicated that increasing the horizontal hydraulic conductivity of the layer Z5 by about half an order of magnitude would resolve the remaining over-prediction of the mean head.

Table 5-1. Measures of the average differences between modelled head and mean measured head for HFM and SFM boreholes. The average variation in head between different times for the measurements is 1.26 m for HFM boreholes, and 1.62 m for SFM boreholes. T = transmissivity, K = hydraulic conductivity.

Case	Average head difference in HFM (m)	Average head difference in SFM (m)
stage 2.2 base model simulation	*1.60*	*1.36*
Higher *T* in ENE0060	1.55	1.35
Higher *T* in ENE0401	1.59	1.36
Higher *T* in A8	1.63	1.36
No "cage features"	1.62	1.36
Higher *K* in layers Z1 and Z5	1.03	0.66
Higher K_h in layers Z1 and Z5 (i.e. anisotropy)	1.09	0.73
Higher *K* in layers Z1 and Z5 where topography > 2 m	1.26	0.86
Higher *K* for lake sediments	1.51	1.33
Version 1.2 fracture orientation distributions	1.75	1.37
No reduction in HRD K_v in top 400 m	1.76	1.37
Order of magnitude lower HRD *K* in top 400 m	1.69	1.35
Two orders of magnitude lower HRD *K* in top 400 m	1.67	1.35

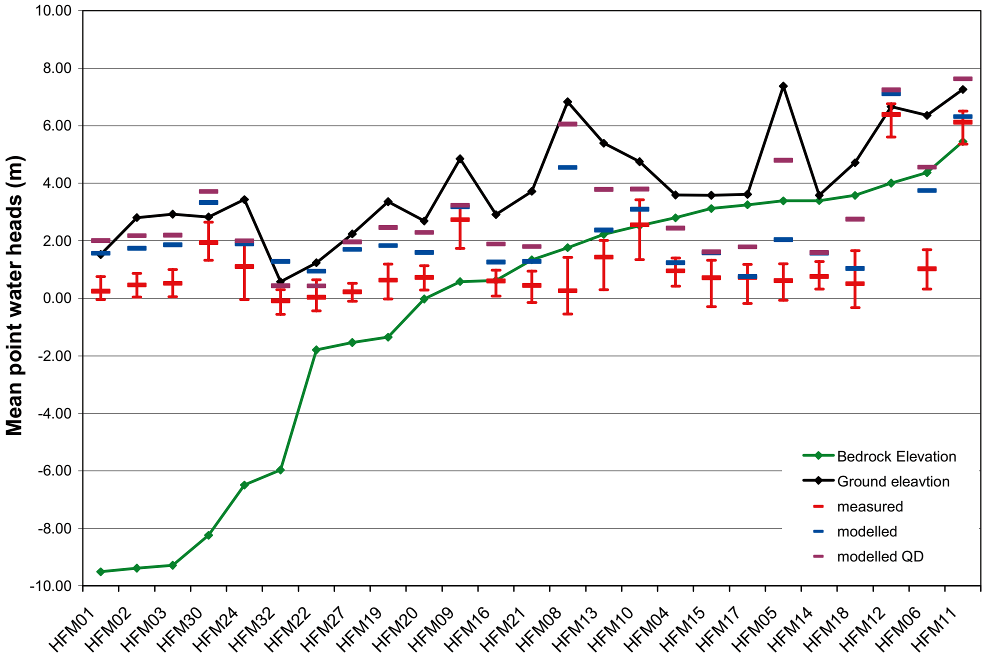

***Figure 5-31.** Comparison of measured heads in HFM boreholes for the sensitivity case with higher K_h in the layers Z1 and Z5, i.e. hydraulic anisotropy. For the model, values are given for the QD and as an average over the borehole section in the bedrock. The field data is plotted as mean point-water heads in the bedrock with error bars to show the range of values at different times. Boreholes are ordered by bedrock elevation.*

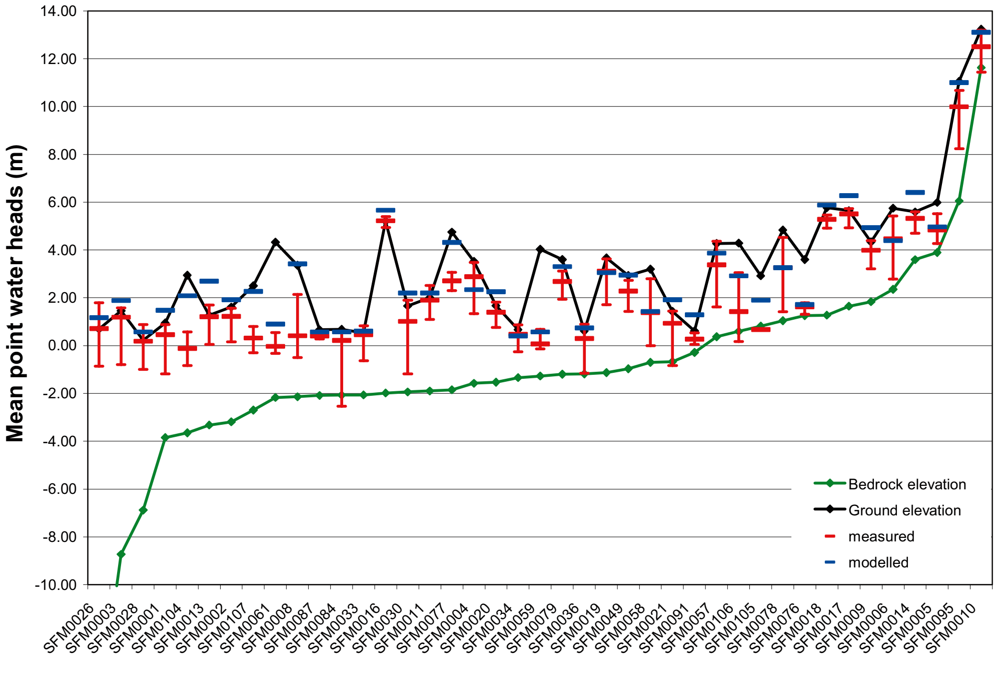

***Figure 5-32.** Comparison of measured heads in SFM boreholes for the sensitivity case with higher K_h in the layers Z1 and Z5, i.e. hydraulic anisotropy. For the model, values are given for the QD only. The field data is plotted as mean point-water heads in the bedrock with error bars to show the range of values at different times. Boreholes are ordered by bedrock elevation.*

For the sake of forthcoming consistency checks with results from the near-surface hydrogeology modelling performed by the surface systems modelling group, average vertical fluxes were calculated over a 4 km by 5 km area covering the candidate area as shown in Figure 5-33. The average of the upward fluxes (discharge) and downward flux (recharge) over the blue area shown in Figure 5-33 are given at various depths in Table 5-2 and Figure 5-34.

Table 5-2. Average vertical fluxes at different depths within the blue sample area shown in Figure 5-33 for the *stage 2.2 base model simulation*. Below sea-level flows area averaged over the whole blue area. Above sea level flows are averaged over that part of the blue area with topographic surface higher than sample height.

Elevation of sample [m RHB 70]	Average upward flux (discharge) [mm/y]	Average downward flux (recharge) [mm/y]
3	6.16	52.85
0	14.60	28.75
–10	7.50	7.68
–50	3.83	3.45
–100	2.57	1.86
–150	0.95	1.03
–200	0.34	0.27
–250	0.26	0.17
–300	0.21	0.09
–400	0.03	0.01
–500	0.02	0.01
–600	0.01	0.00

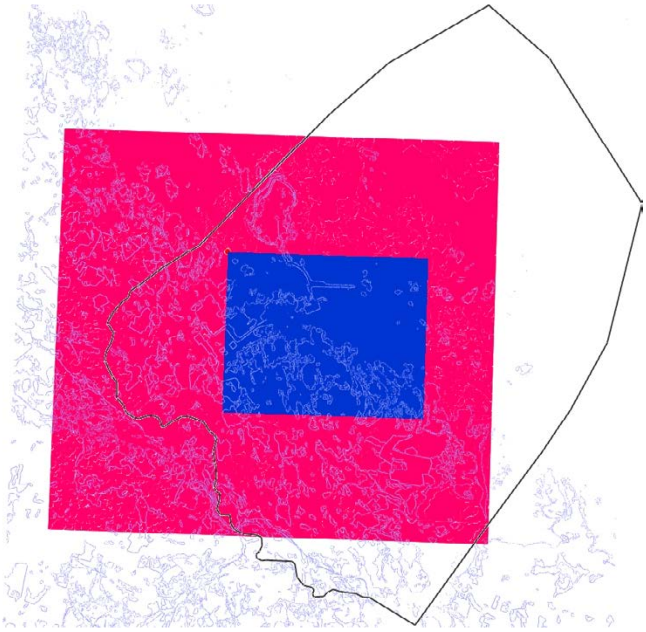

Figure 5-33. *The blue area, 4 km by 5 km, was used to calculate average vertical fluxes through the stage 2.2 base model simulation at different depths. The red area is roughly the extent of the area used for the data specified in the near-surface hydrogeology modelling performed by the surface systems modelling group. The green boundary is the regional model domain used in the work reported here.*

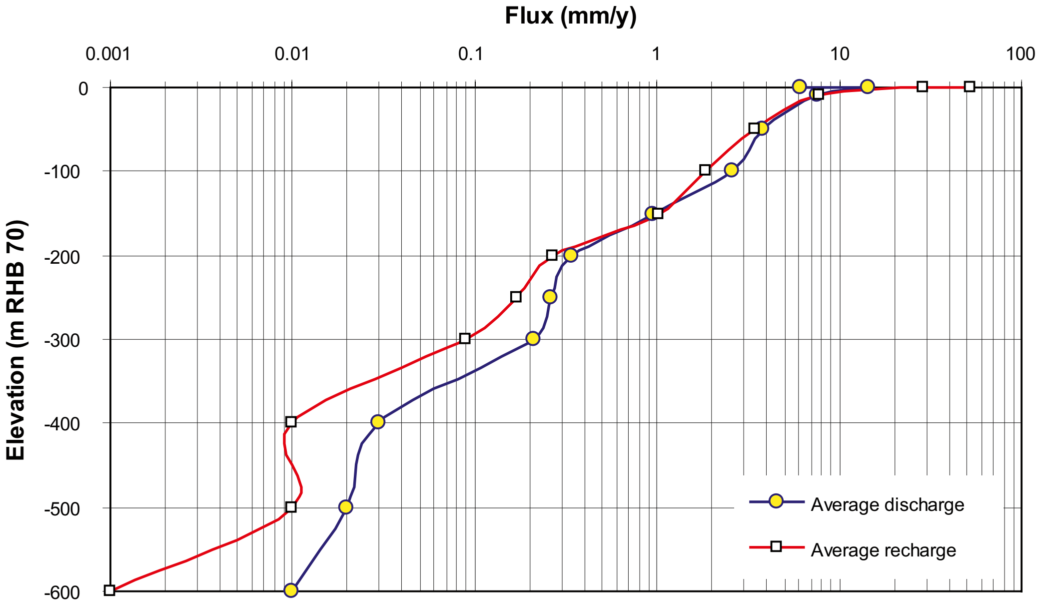

Figure 5-34. *Average vertical fluxes at different depths within the blue sample area shown in Figure 5-33 for the stage 2.2 base model simulation. Below sea-level flows are averaged over the whole blue area. Above sea level flows are averaged over that part of the blue area with topographic surface higher than sample height.*

5.4 Conclusions

Based on the conceptual model and its numerical implementation described in Section 3, it was possible to perform groundwater flow calculations that reproduced many of the characteristics observed in the field according to the hydraulic calibration data described in Section 4. The parameterisation of the numerical model followed the data interpretation of HCD and HRD model elements defined in /Follin et al. 2007b/. The prescription of hydrogeological properties suggested by /Follin et al. 2007b/ is refined in this study in order to improve the calibration of the model, as well as identifying preferred alternatives that are presented in /Follin et al. 2007b/. Other model elements such as HSD and solute transport properties are described here that produce a satisfactory calibration to the hydraulic single-hole and interference tests, as well the point-water heads. In general, the changes in model parameterisation from the initial model described in Section 3 can be viewed as refinements of model definition rather than departures from the conceptual model. The changes necessary to match the data help the understanding of the behaviour of the hydrogeological system in terms of both general and specific features, and provide feedback to the hydrogeological site description and other disciplines. More specifically the following conclusions are made:

HCD

- The description of the hydraulic properties and their depth dependency of deformation zones developed in /Follin et al. 2007b/ appears consistent with the hydraulic measurements. Where there were several transmissivity measurements available in a zone it is generally recommended to use the mean calculated “m-value” from Equation (3-3) rather than the maximum. It is also important to perform local conditioning of transmissivity around the single-hole test intervals.
- As a consequence of /Follin et al. 2007b/, the deformation zones are not necessarily all hydrogeologically significant, but those that do dominate the hydrogeology form a very discrete system.

- The interference test verifies the hydraulic importance of the gently-dipping zone A2. The simulations confirm /Follin et al. 2007b/ that this zone must have high transmissivity and suggest that areas of connected high transmissivity channels persist to at least –400 m RHB 70.
- The steeply-dipping zone ENE0060 also appears to be a significant zone of high connectivity and transmissivity, at least in its upper parts.
- The gently-dipping zone A8 is likely to also be connected to this system to the north, possibly as a splay of A2.
- The hydraulic thickness of zones appears to be thinner than the geological thickness , possibly corresponding to a small number of fractures in any one borehole section giving a very discrete propagation of hydraulic disturbances, rather than a zone of densely connected fractures (see comment in /Follin et al. 2007b, page 117/). This is also implied by the very low storativity of the system.

HRD

- The low hydraulic conductivity derived from the Hydro-DFN model of the fracture domains between the deformation zones derived by /Follin et al. 2007b/ generally gives the right magnitude of hydraulic responses between the HCD, but needs to be made more anisotropic to reduce the vertical leakage and infiltration.
- Using the alternative Hydro-DFN fracture orientation distributions (with higher Fisher concentration in the sub-horizontal set) recommended by /Follin et al. 2007b/ based on data freeze 2.2 data, rather than data freeze 1.2 data, improves the description of the bedrock properties, primarily by defining fractures in the sub-horizontal set to be more sub-parallel reducing the vertical connectivity. Further mechanisms for anisotropy such as a lower transmissivity in sub-vertical sets may also help the simulations.
- The necessary changes suggest a very anisotropic system of water conducting fractures oriented mainly sub-horizontally giving poor or localised vertical communication.
- The horizontal fractures/sheet joints discussed in Section 3 communicate hydraulic disturbances in the north-western parts of the upper bedrock within the candidate area, but these are difficult to map and hence model due to their heterogeneity. The model used in this study possibly under-predicts the hydraulic extent and transmissivity of the “hydraulic cage phenomenon”, though. For the sake of credence, we show in Figure 5-35 a comparison between measurements and the results obtained from the calibrated *stage 2.2 base model simulation* shown in Figure 5-5. Figure 5-35 should be compared with Figure 3-30. The plot suggests that the uppermost bedrock within the target area on a kilometre scale acts like a fairly homogeneous and transmissive “shallow bedrock aquifer”. On smaller scales local compartments may occur, see the spread around five metres of drawdown for an example.

HSD

- The hydraulic properties of the Quaternary deposits required considerable calibration to find consistency with the hydraulic interference test and point-water head measurements.
- The hydraulic contact between the lake and the bedrock appeared to be poor implying tight lake sediments (L1–L3) of the order of 10^{-9}–10^{-8} m/s.
- Similar properties for layers Z1 and Z5 in low lying areas around the shores of lakes, near the coast and beneath the sea were suggested by the modelling, implying areas of clay or fine-grained till.
- Higher conductivity Quaternary deposits may be more prevalent over the candidate area with possible horizontal versus vertical anisotropy.

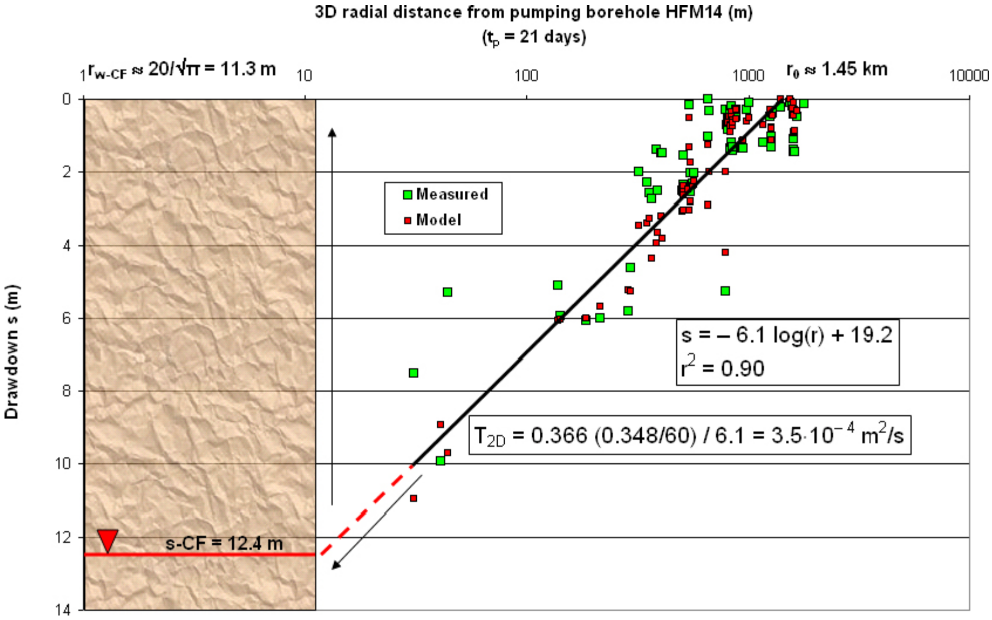

Figure 5-35. *Plot of measured drawdowns (green) and simulated (red) vs. log(3D radial distance) at the end of the 21-day log interference test in HFM14. The measured drawdown in HFM14 was 11.7 m and the simulated 12.4 m using the stage 2.2. base model simulation. The black line shows a least-squares fit to the simulated drawdowns. The value of the correlation coefficient ($r^2 = 0.90$) indicates a less heterogeneous medium than does the regression of the measured data in the real system, cf. Figure 3-30. A 2D steady-state, radial flow approximation using the slope of the least-squares fit for an estimate of Δs (difference in drawdown per log cycle of distance) renders a large-scale effective transmissivity of $3.5 \cdot 10^{-4}$ m²/s. This value is essentially a composite of the transmissivities assigned to A2, the "cage features", and a bit of ENE0060. An extrapolation of the regression model to the edge of the pumped 20 m element matches the simulated drawdown in this cell, ($r_{w\text{-}CF} = 20/\sqrt{\pi} \approx 11.3$ m).*

The conclusions implying poor hydraulic connection between the surface and upper bedrock raise questions for safety assessment about the locations of possible discharge areas. Topography is likely to be less important than geological structures, and hence hydraulic gradients in major deformation zones need to be considered and their contact to the sea. The planned hydraulic interference test in HFM33 on the SFR peninsula with monitoring in boreholes that intercept deformation zones beneath the candidate area is expected to shed some light on these issues.

6 Calibration on hydrochemistry profiles

Following the calibration on hydraulic and hydrogeological data, the hydrochemistry data are used as a series of natural tracer tests to check consistency of the hydraulic parameters and examine the description of transport parameters and concepts for the palaeohydrological development.

6.1 Task D – Matching hydrochemistry profiles in boreholes

6.1.1 Methodology

As described in Section 3, the calibration on hydrochemistry measurements involves the simulation of palaeohydrological development in terms of the evolution of coupled groundwater flow and solute transport from 8000 BC to the present-day. The transport of solutes is modelled in terms of the infiltration and mixing of several different reference waters that are assumed to be transported conservatively, i.e. without reaction, but subject to advection, dispersion, and diffusion in both the fracture and the pore waters (i.e. rock matrix diffusion). Groundwater flow is subject to buoyancy forces that arise due to variations in fluid density according to salinity, temperature (a fixed geothermal gradient is assumed), and total pressure. Variations in fluid viscosity with temperature, salinity and total pressure are also considered. The boundary conditions evolve in time according to both shore-level displacement and variations in marine salinity. The chemical compositions of each reference water are fixed. Therefore, given the simulated mixture of references waters (defined by the mass fraction) at any point in space and time, the concentration of the major ions or environmental isotopes can be calculated by multiplying the reference water fraction by the concentration of the component in that reference water and then summing over the reference waters. The predicted concentrations, or isotope ratios, can then be compared with the data. The chemical composition is calculated both for the mobile water in the fractures and the immobile pore water in the matrix. For simplicity, the simulated values for the pore water used for comparison purposes are essentially an average within the matrix blocks, although CONNECTFLOW stores internally the spatial variation of reference water fractions within the matrix blocks, which could be analysed should such detail be required. The spatial variations of concentration in the pore water between connected fractures are likely to be large at Forsmark since the spacing between water conducting fractures is large, at least at depth. Hence, it should be borne in mind that there may be trends within the pore water data according to where a sample was taken relative to water-bearing fractures that are as important as trends with respect to the absolute elevation of the sample, for example.

6.1.2 Calibration steps

Again, the calibration was initially performed independently of the hydraulic calibration, but directions followed in calibrating to the hydraulic test data followed many common themes as the palaeohydrological calibration. Hence, several cases based on the hydraulic calibration of Section 5 are also considered in the calibration on the hydrochemical data such as the importance of the deformation zones, the fracture orientations in the HRD and a reduction in the vertical hydraulic conductivity of HRD. However, other factors effecting solute transport had to be considered, mainly the kinematic porosity, the flow wetted fracture surface area per unit volume of rock and the initial distribution of groundwater chemistry. A brief summary of the key calibration steps to achieve a match is:

- to use the Alternative Case initial condition including different conditions for the fracture water and pore water,
- to use the HCD parameterisation based on the calibration steps made for the hydraulic data described in Section 5,

- to reduce the vertical hydraulic conductivity of the HRD either by using the alternative fracture orientation distributions recommended by /Follin et al. 2007b/, as also found in the hydraulic calibration steps described in Section 5.2.2, or by reducing the vertical hydraulic conductivity by one or two orders of magnitude,
- to increase the kinematic porosity by a factor of about 5–10, and
- to use low values of the flow wetted fracture surface area per unit volume of rock, so as to maintain a non-equilibrium between the hydrochemistry in the fractures and matrix over thousands of years. Modelling suggests values of $a_r < 0.2–0.3\ m^2/m^3$ are required in line with those derived from PFL-f data (see Table 3-9).

6.1.3 Resulting calibration

First, the quality of the calibration is indicated by the results for a reference calibration case. This has the same parameter setting as the central calibration case used in the hydraulic interference test modelling, see Section 5. Figure 6-1 shows the match between simulated and measured salinity in the fracture system for four groups of boreholes: one group in the hanging wall of A2, and three groups in the footwall. The agreement is generally good with significant salinity encountered from about –100 m RHB 70 associated with *Baltic*/*Littorina Sea Water* concentration and then gradually rising below about –500 m RHB 70. Some data from KFM07A and KFM09A suggest salinity rises rapidly below –500 m RHB 70 in the bordering bedrock, which may be due to localised heterogeneity or upconing by the intrusion of the borehole.

Figure 6-2 through Figure 6-6 then go on to show the comparison of the simulations with data for selected major ions and environmental isotopes for the group of borehole intervals in the hanging wall of zone A2, for the intervals around the border of the tectonic lens and in three groups of boreholes in the footwall of zone A2. The chemical indicators used in these plots are:

- Cl – since it is conservative and indicates the locations of *Littorina Sea* and *Deep Saline Waters*,
- Br/Cl ratio – since both constituents are conservative this ratio can be used to determine the depth at which the origin of saline water changes from a *Littorina Sea Water* (marine) to an older *Deep Saline Water* origin when the ratio increase from around 0.004 to 0.007,
- $\delta^{18}O$ – since this is conservative over the timescales considered in the simulations, where low values indicate remnants of *Holocene Glacial Melt Water* or cold climate water, and
- HCO_3 – since although this is not conservative, it does give a qualitative cross-check on the penetration of recent *Present-day Meteoric Water*.

For the hanging wall of zone A2, shown by Figure 6-2, Cl and Br/Cl give good agreement. However, the high ratios of Br/Cl > 0.007 in the data cannot be reproduced with the chemical composition of the reference waters shown in Table 4-14. The reasons for the high Br/Cl ratios are discussed in /Laaksoharju et al. 2008/. Still, the position of saline water and its change in origin from *Littorina Sea Water* to *Deep Saline Water* appears consistent in KFM02A. The fairly flat distribution of $\delta^{18}O$ is reproduced, suggesting a limited presence of *Holocene Glacial Melt Water*. HCO_3 is simulated with a consistent profile that reproduces the infiltration of recent *Present-day Meteoric Water*. The model predicts a persistence of *Holocene Glacial Melt Water* in KFM03A which is not seen in the data, suggesting the sub-horizontal zones intercepted by KFM03A need higher transmissivity.

The prediction for the boreholes drilled in the bedrock bordering the tectonic lens also appears to reproduce the right behaviour in Figure 6-3. The high salinity seen in KFM09A at –600 m to –500 m RHB 70 may be due to either upconing by the sampling or just reflect effects of spatial heterogeneity in the bedrock outside the tectonic lens which is treated homogeneously in the model due to lack of data.

The simulations for the three groups of footwall boreholes in Figure 6-4 through Figure 6-6 mimic many of the characteristics seen in the data. The onset of Cl at *Baltic-Littorina Sea Water* levels occurs at around –100 m RHB 70 and the transition from *Littorina Sea Water* to *Deep Saline Water* shown by the Br/Cl ratio occurs at about –300 to –400 m RHB 70 in most boreholes.

Figure 6-5 shows a chloride concentration similar to that of the Baltic Sea is measured in KFM05A above –100 m RHB 70, which does not occur until about –150 m RHB 70 in the simulations. The suggested explanation is that KFM05A is inclined beneath Lake Bolundsfjärden for which there is evidence of clayey sediments including gyttja at the bottom. Pockets with *Littorina Sea Water* remnants may still be present in the till layer and in the bedrock beneath the lake cf. /Johansson 2008/. It is noted that the complex stratigraphy under the lakes are modelled in a simplistic fashion in CONNECTFLOW, see Figure 3-52.

The prediction of $\delta^{18}O$ generally agrees with the magnitudes and trends seen in the data for the fracture system with slightly higher values around –300 m RHB 70 and slightly lower values –400 m to –700 m RHB 70. However, the modelled distribution of $\delta^{18}O$ in the pore water is similar to that of *Present-day Meteoric Water* with the Alternative Case initial condition, while the data suggests much warmer climate water with values similar to those of *Littorina Sea Water*, i.e. warm climate water with significantly higher $\delta^{18}O$ than the fracture water in some boreholes such as KFM01D. This suggests that a diffusive equilibrium between the fracture and matrix systems has not been reached at elevations below about –300 m RHB 70. From a conceptual interpretation, this would imply that *Holocene Glacial Melt Water* did not enter a sufficient portion of the fracture system or did not have sufficient time for diffusion to equilibrate with the matrix blocks, cf. /Waber and Smellie 2007/.

Figure 6-7 shows a comparison of the Cl in both the fracture and matrix systems in boreholes KFM01D and KFM06A where both fracture water and pore water samples were available. The data in the fracture system are limited, but do suggest higher Cl in the fracture system than in the matrix, at least in the interval –200 to –500 m RHB 70. Again, this is evidence for the hypothesis that non-equilibrium conditions between hydrochemistry in the fracture and matrix systems persist over many thousands of years as a result of the large spacing between water conducting fractures. However, it is recognised that this interpretation is not necessarily unique. As mentioned, there is certainly a risk for an upconing of *Deep Saline Water* while sampling in transmissive fractures by means of pumping. The *stage 2.2 base model simulation* predicts higher Cl in the fracture system than in the matrix in the interval –200 to –500 m RHB 70 but equilibrium or higher Cl in the matrix in the top 200 m of bedrock, where more recent meteoric water has entered the fracture system. The main property affecting this pattern is the flow wetted fracture surface area per unit volume of rock. The parameters used in the model are taken from Table 3-10 and Table 3-9, and it is the higher flow wetted surface used in FFM02 that is the cause of higher Cl predicted in the top 200 m matrix. Since the pore water data suggest lower Cl, it suggests that the flow wetted fracture surface area per unit volume of rock in FFM02 is also smaller, perhaps around 0.2–0.3 m^2/m^3 as for the upper part of FFM01.

The profiles of other major ions Na, Ca, Mg and SO_4 are shown for the first group of footwall boreholes in Figure 6-8. These ions are non-conservative, subject to reactions, but provide a qualitative comparison with data. Na levels are generally over-predicted by about 1,000 mg/L and Ca is under-predicted by about 500–1,000 mg/L. Mg, associated with *Littorina Sea Water* infiltration is also over-predicted by about a factor 2, but the position of the pulse between about –100 m and –300 m is consistent. SO_4 shows a similar pattern.

Finally, for illustration purposes, the simulated profiles of the *Deep Saline*, *Old Meteoric-Glacial, Holocene Glacial Melt*, *Littorina Sea*, *Present-day Meteoric Waters* are plotted down boreholes KFM01A, KFM02A, KFM03A and KFM07A in Figure 6-9. Profiles of the mixing fractions for both the fracture component are shown together with corresponding M3 interpretations of groundwater samples from these boreholes using the four reference waters defined in Table 3-14: *Deep Saline, Holocene Glacial Melt*, *Littorina Sea*, *Present-day Meteoric*. This is only intended for qualitative comparison and to illustrate how the mix of reference waters varies with depth. KFM01A and KFM07A are both in the footwall of zone A2. Below –400 m RHB 70, the fracture and matrix waters are virtually unchanged from the initial condition. Above this, the *Littorina Sea Water* pulse dominates the fracture water between –100 m to –400 m RHB 70 with *Present-day Meteoric* above. In the matrix, the *Littorina Sea Water* pulse is retarded and only dominates the top 200 m.

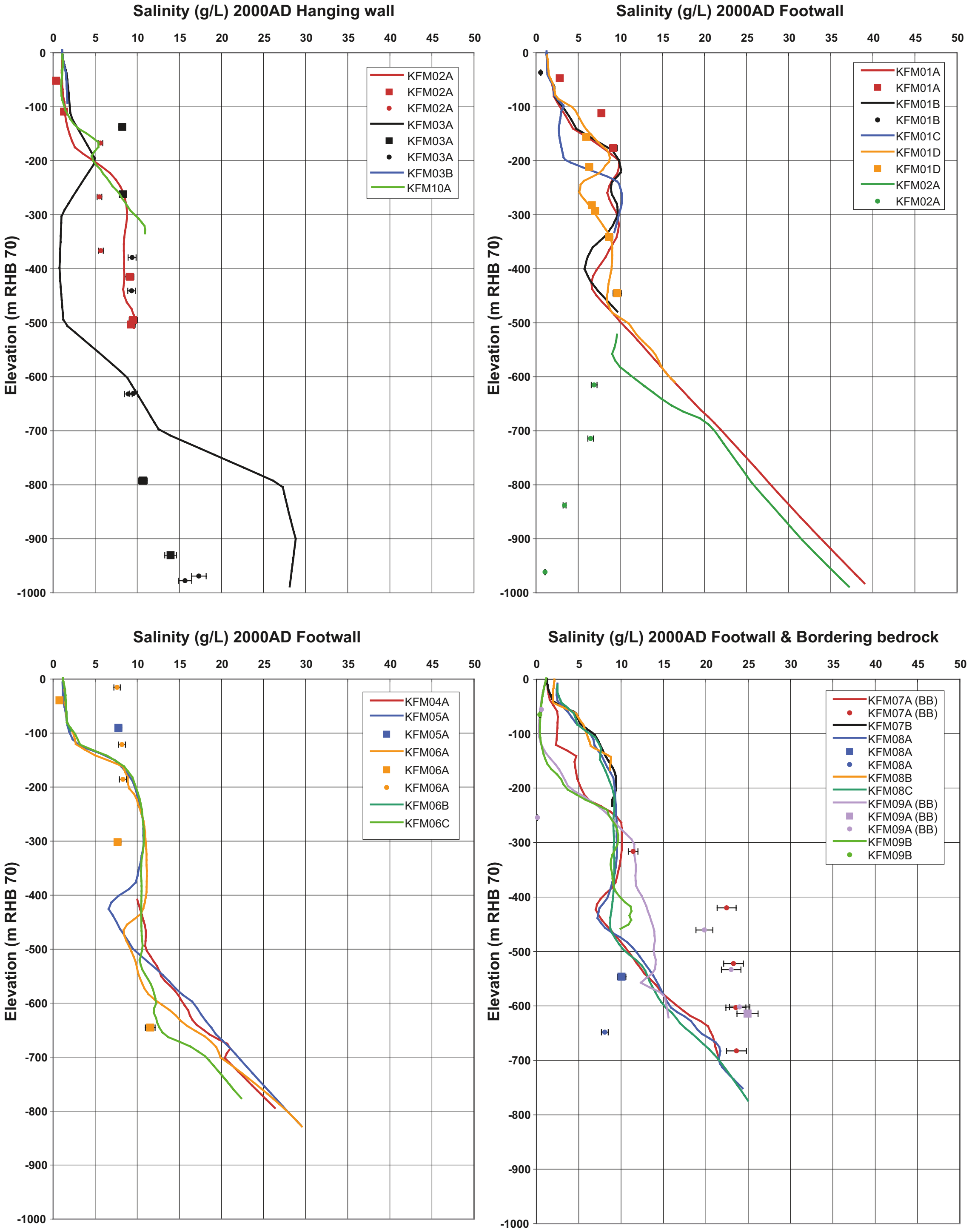

Figure 6-1. *Comparison of modelled and measured distribution of salinity (TDS) in the fracture system for different groups of calibration boreholes. Square symbols are used for the representative and less representative data, and small filled circles for the supplementary data. The error bars on the data only indicate the laboratory analytical error. The solid lines show the simulated distributions in the fracture system. Note that the data in KFM04A above –400 m RHB 70, in KFM07A below –650 RHB 70 and in KFM0 9A below –250 m RHB 70 represent conditions in the bedrock bordering the tectonic lens. It is noted that the supplementary data (small filled circles) are uncertain and should be used with great caution.*

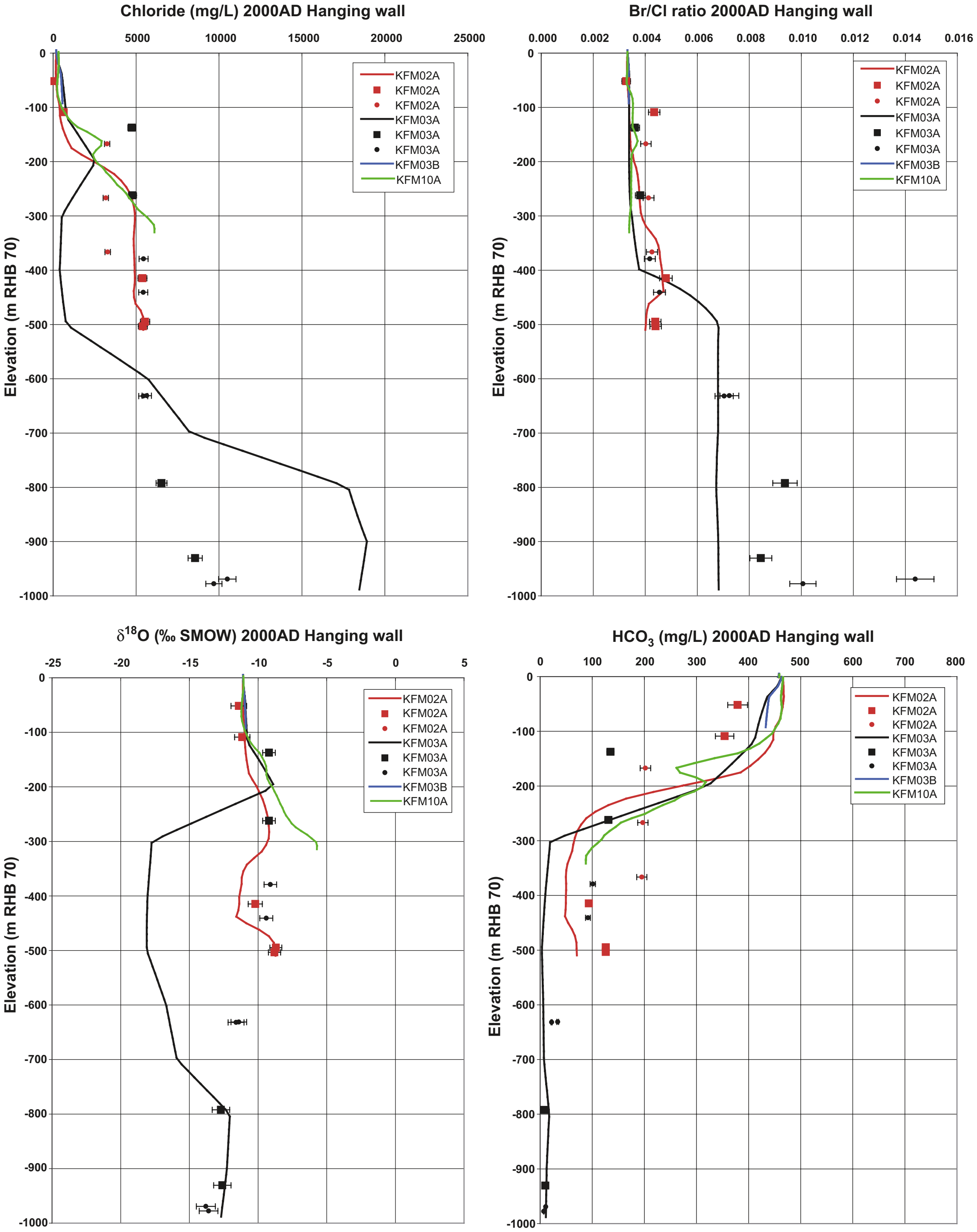

Figure 6-2. *Comparison of modelled and measured Cl, Br/Cl, $\delta^{18}O$ and HCO_3 in the fracture system for boreholes in the hanging wall of A2. Square symbols are used for the representative and less representative data, and small filled circles for the supplementary data. The error bars on the data only indicate the laboratory analytical error. The solid lines show the simulated distributions in the fracture system. It is noted that the supplementary data (small filled circles) are uncertain and should be used with great caution. Moreover, it is noted that ratios of Br/Cl > 0.007 cannot be reproduced with the current chemical composition of the reference waters shown in Table 4-14.*

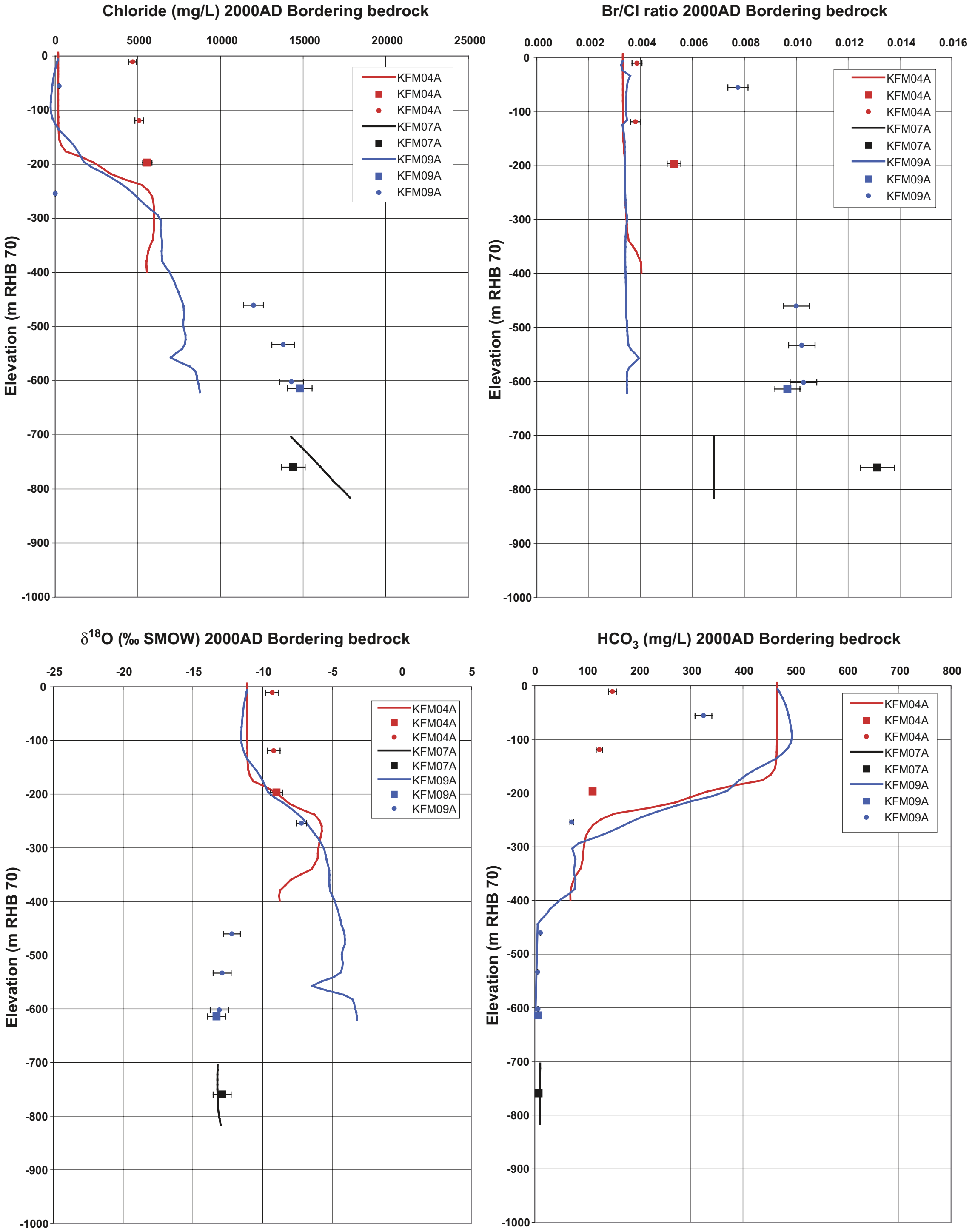

Figure 6-3. *Comparison of modelled and measured Cl, Br/Cl, $\delta^{18}O$ and HCO_3 in the fracture system for the boreholes drilled in the bedrock bordering the tectonic lens. Square symbols are used for the representative and less representative data, and small filled circles for the supplementary data. The error bars on the data only indicate the laboratory analytical error. The solid lines show the simulated distributions in the fracture system. It is noted that the supplementary data (small filled circles) are uncertain and should be used with great caution. Moreover, it is noted that ratios of Br/Cl > 0.007 cannot be reproduced with the current chemical composition of the reference waters shown in Table 4-14.*

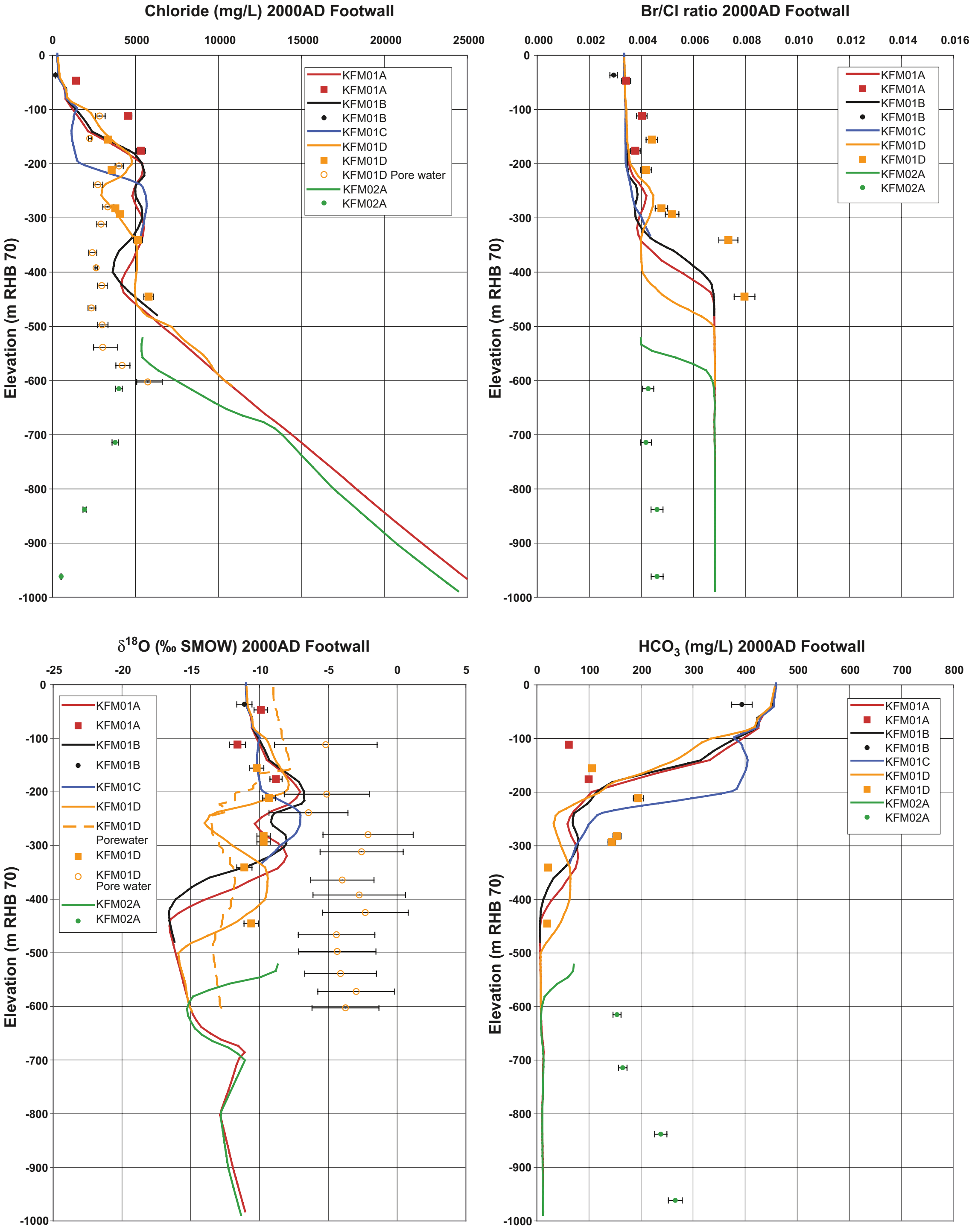

Figure 6-4. *Comparison of modelled and measured Cl, Br/Cl, $\delta^{18}O$ and HCO_3 in the fracture system for the first set of boreholes in the footwall of zone A2. Square symbols are used for the representative and less representative data, and small filled circles for the supplementary data. The pore water data is plotted as open circles. The error bars on the fracture data only indicate the laboratory analytical error, while in the pore water they reflect the uncertainty in the porosity of the rock sample. The solid lines show the simulated distributions in the fracture system, and the dashed lines show the average in the matrix blocks. It is noted that the supplementary data (small filled circles) are uncertain and should be used with great caution. Moreover, it is noted that ratios of Br/Cl > 0.007 cannot be reproduced with the current chemical composition of the reference waters shown in Table 4-14.*

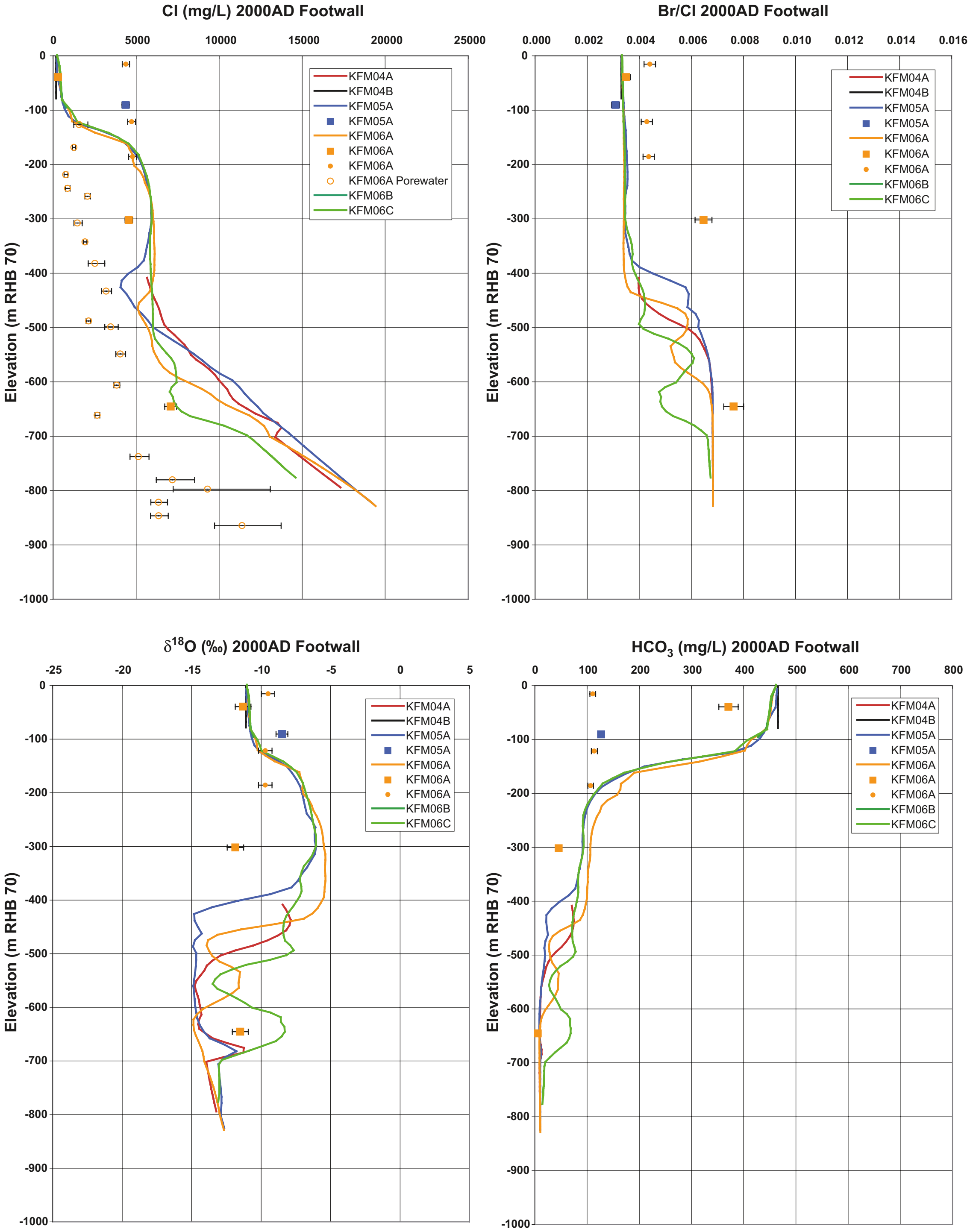

Figure 6-5. *Comparison of modelled and measured Cl, Br/Cl, $\delta^{18}O$ and HCO_3 in the fracture system for the second set of boreholes in the footwall of zone A2. Square symbols are used for the representative and less representative data, and small filled circles for the supplementary data. The pore water data is plotted as open circles. The error bars on the fracture data only indicate the laboratory analytical error, while in the pore water they reflect the uncertainty in the porosity of the rock sample. The solid lines show the simulated distributions in the fracture system. A plausible reason for the "high" chloride concentration in KFM05A around –100 m RHB 70 is discussed in the text. It is noted that the supplementary data (small filled circles) are uncertain and should be used with great caution. Moreover, it is noted that ratios of Br/Cl > 0.007 cannot be reproduced with the current chemical composition of the reference waters shown in Table 4-14.*

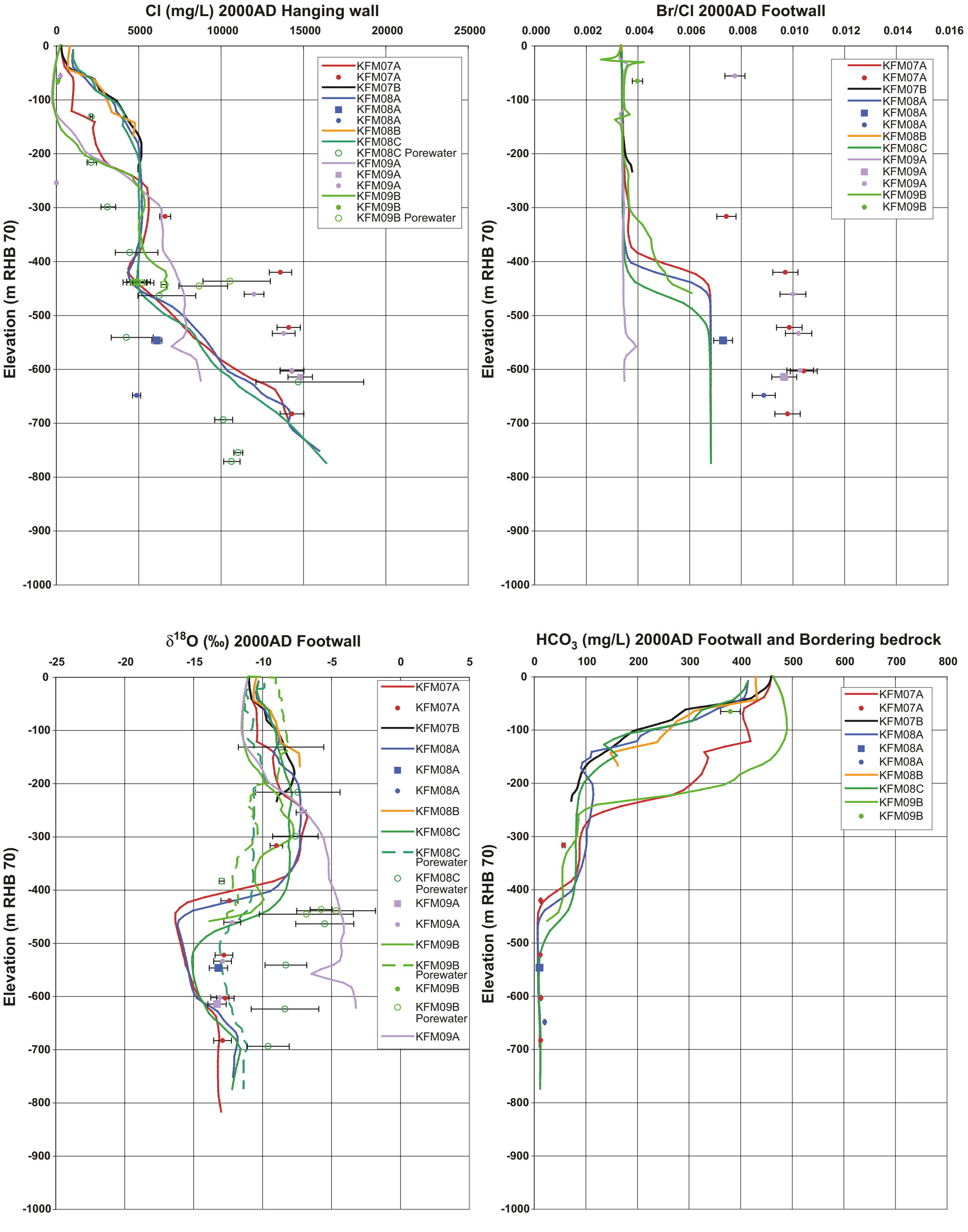

Figure 6-6. *Comparison of modelled and measured Cl, Br/Cl, $\delta^{18}O$ and HCO_3 in the fracture system for the third set of boreholes in the footwall of zone A2. Boreholes KFM07A and -09A the bordering bedrock at depth. Square symbols are used for the representative and less representative data, and small filled circles for the supplementary data. The pore water data is plotted as open circles. The error bars on the fracture data only indicate the laboratory analytical error, while in the pore water they reflect the uncertainty in the porosity of the rock sample. The solid lines show the simulated distributions in the fracture system, and the dashed lines show the average in the matrix blocks. It is noted that the supplementary data (small filled circles) are uncertain and should be used with great caution. Moreover, it is noted that ratios of Br/Cl > 0.007 cannot be reproduced with the current chemical composition of the reference waters shown in Table 4-14.*

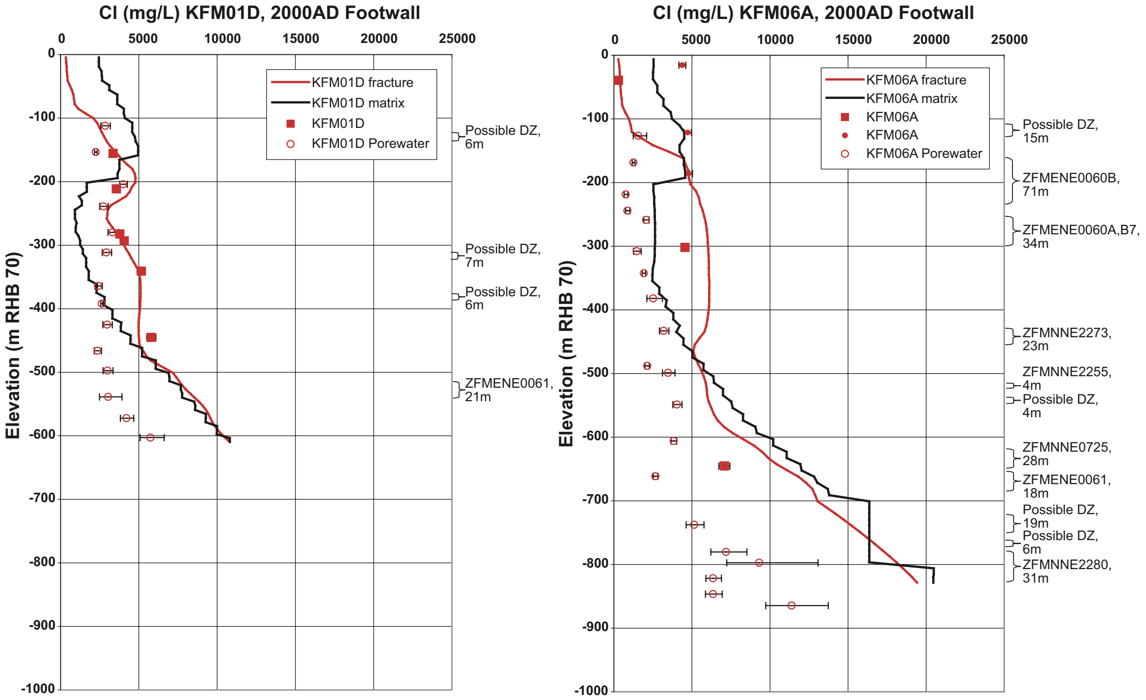

Figure 6-7. *Comparison of modelled and measured Cl in the fracture water and pore water for boreholes KFM01D and KFM06A both in the footwall of zone A2. Square red symbols are used for the representative and less representative fracture data, and small filled circles for the supplementary fracture data. The pore water data is plotted as open circles. The error bars on the fracture data only indicate the laboratory analytical error, while in the pore water they reflect the uncertainty in the porosity of the rock sample. The red lines show the distributions along the boreholes simulated in the fracture system, and the black lines show the average in the matrix blocks. It is noted that the supplementary data (small filled circles) are uncertain and should be used with great caution.*

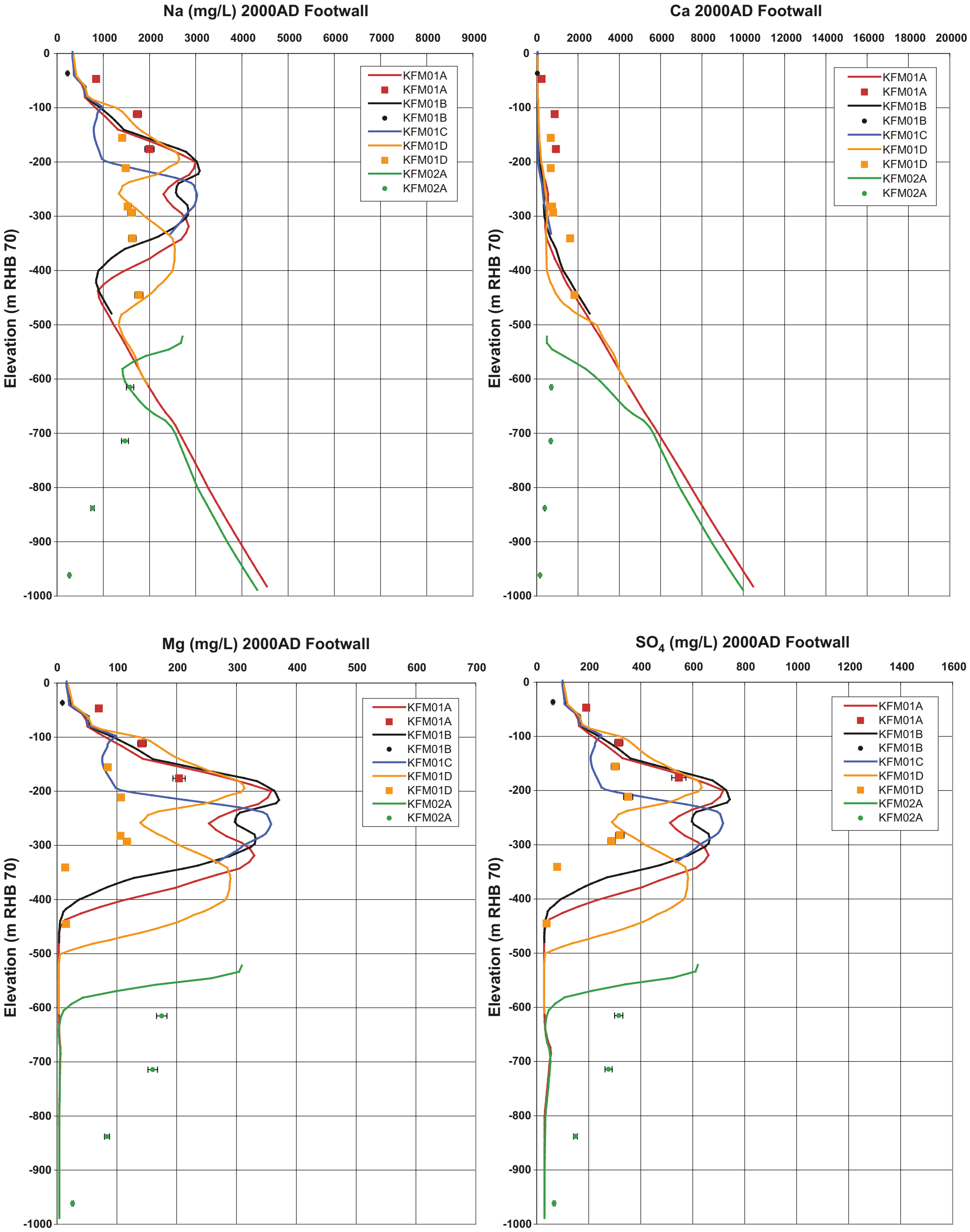

Figure 6-8. *Comparison of modelled and measured Na, Ca, Mg and SO_4 in the fracture system for the first set of boreholes in the footwall of zone A2. Square symbols are used for the representative and less representative data, and small filled circles for the supplementary data. The error bars on the data only indicate the laboratory analytical error. The solid lines show the simulated distributions in the fracture system. It is noted that the supplementary data (small filled circles) are uncertain and should be used with great caution.*

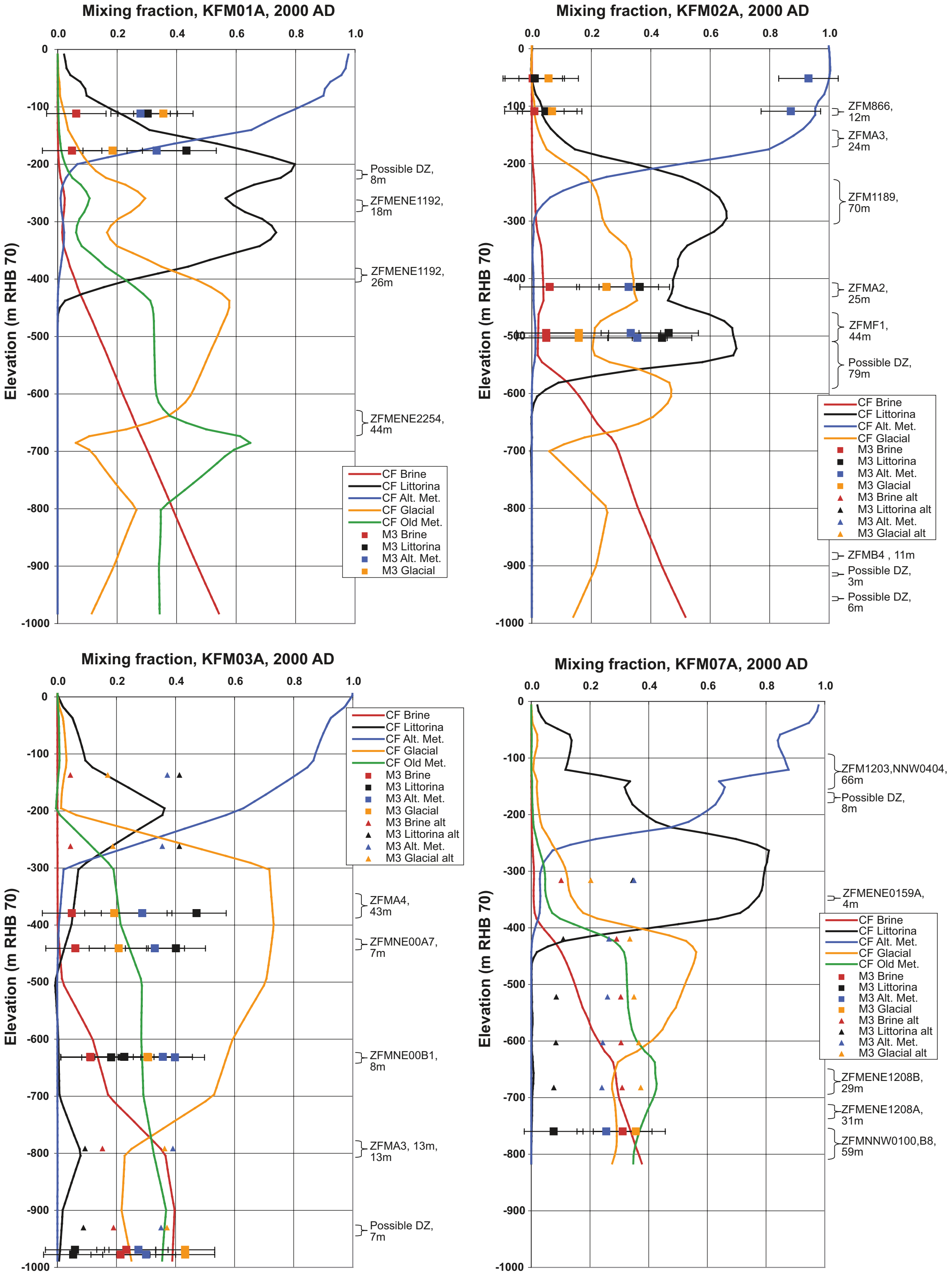

Figure 6-9. *Illustration of simulated mixtures of reference water mass fractions in boreholes KFM01A, KFM02A, KFM03A and KFM07A. Solid lines show simulated reference water fractions in the fracture system. The points show the mixture of the reference waters used in the Base Case model. The values shown are interpreted from the groundwater samples available for modelling in stage 2.2 using the M3 method.*

6.1.4 Illustration of sensitivities considered in the calibration

The reasons for making the calibration steps described in Section 6.1.2 are illustrated by constructing sensitivity cases centred on the *stage 2.2 base model simulation*, i.e. all parameters for the *stage 2.2 base model simulation* are used with individual changes to quantify the sensitivity to a particular quantity or feature. This makes it easier to see the effects of individual parameters whereas the calibration steps tended to change several parameters in sequence.

Sensitivity to HCD

As an example, a sensitivity case to quantify the impact of the deformation zone properties is shown here where the properties used are those prior to any calibration on hydraulic data, i.e. before any of the changes described in Section 5. Figure 6-10 shows the comparison with data for the first group of footwall boreholes for Cl, Br/Cl, Mg and HCO_3. The differences with the *stage 2.2 base model simulation* are moderate. Salinity is deeper in most boreholes by about –100 m RHB 70, e.g. KFM01A, which looking at the Mg and HCO_3 is due to deeper flushing of *Littorina Sea Water* by recent *Present-day Meteoric Water*. This is slightly less consistent with the data, although the scarcity of the data and uncertainties in using non-conservative tracers such as Mg and HCO_3 make it hard to make definitive conclusions. Hence, the changes to HCD properties considered in the calibration exercises on hydraulic data only seem to have a moderate effect on the palaeohydrological modelling.

Sensitivity to HRD

Sensitivities to properties of the HRD parameters are illustrated by a case which uses the fracture set definitions derived in version 1.2, which are less anisotropic. This has a stronger control on the chemistry profiles shown in Figure 6-11 again for Cl, Br/Cl, Mg and HCO_3. For all boreholes except KFM02A, the onset of the *Baltic/Littorina Sea Water* level Cl occurs 100 m deeper (below –200 m RHB 70) than in the *stage 2.2 base model simulation*. The transition from *Littorina Sea Water* to *Deep Saline Water* shown by Br/Cl is also about 100 m lower, below–400 m RHB 70 for all boreholes. The Mg prediction for this variant predicts a *Littorina Sea Water* pulse slightly deeper and penetrating to greater depth in all boreholes apart from KFM02A than the *stage 2.2 base model simulation* and the measured groundwater samples. These simulation results clearly appear to be less well matched to the data, lending more weight to the need to have strong horizontal versus vertical anisotropy in the HRD. Again, it supports careful consideration of the orientations of water bearing fractures.

Another related sensitivity case was performed using the version 1.2 fracture set definitions, but with an order of magnitude reduction in vertical hydraulic conductivity. This was intended to explore further the role of anisotropy in the HRD from a more direct approach than changing orientation distributions in the Hydro-DFN. Comparing the results for this case in Figure 6-12 with Figure 6-11 shows that reducing the vertical hydraulic conductivity by an order of magnitude almost brings the *Littorina Sea Water* pulse back up to the distribution for the central calibrated case. This confirms the importance of anisotropy and that fracture orientation of the sub-horizontal fracturing is part of the explanation.

Sensitivity to transport parameters

The sensitivities above have also been considered in the hydraulic calibration exercises and provide a cross-check in the hydraulic parameterisation for long-timescale natural flows. Other parameters important to safety assessment not measured by the hydraulic tests are the kinematic porosity and flow wetted fracture surface area per unit volume of bedrock, which are best obtained by interpretation of tracer tests. The palaeohydrological evolution is used as a series of natural tracer tests that have occurred over thousands of years.

The initial kinematic porosity was based on summing the connected fracture transport apertures within each grid finite-element as part of the upscaling procedure with the transport aperture based on an empirical relationship between hydraulic aperture and transmissivity given in Section 3.12. This relationship is uncertain, as is the truncation on smallest fracture size necessary in constructing the regional Hydro-DFN.

For the *stage 2.2 base model simulation*, the kinematic porosity was increased by a factor 10 compared to that suggested in Section 3.12. A sensitivity case was considered where the kinematic porosity suggested in Section 3.12 was applied. The results are shown in Figure 6-13. Reducing the kinematic porosity clearly has a large effect on the *Littorina Sea Water* pulse in a similar way to increasing the vertical hydraulic conductivity. The onset of the *Littorina Sea Water* pulse is pushed down to below –200 m RHB 70 giving results for Cl, Br/Cl and Mg less in accordance with the measured profiles. Increasing the kinematic porosity further than in the *stage 2.2 base model simulation* had little effect.

A sensitivity case for the flow wetted fracture surface area per unit volume of rock was based on a uniform value of 0.17 m^2/m^3 which corresponds to a decrease of a factor 4 in FFM02 and the upper part of FFM01. As shown in Figure 6-14, this change has little effect on Cl in the fracture system, but has a significant impact on the matrix profile in the upper 200 m. The results for this sensitivity case seem to agree better with the measured pore water data, suggesting that small values of the flow wetted fracture surface area per unit volume of rock $< 0.3\ m^2/m^3$, are appropriate for all depths. This is less than that suggested for FFM02 in Table 3-9. There may be several reasons contributing to this difference. It may just be local heterogeneity with the properties around KFM01D and KFM06A being different from the overall rock fracture statistics based on all boreholes. Another cause may be the anisotropy fracturing giving matrix blocks that are slab shaped rather than the cubes assumed in the CONNECTFLOW model.

Sensitivity to initial conditions

The calibration step to add additional warm climate reference water, i.e. *Old Meteoric-Glacial Waters*, was prompted by a poor match to $\delta^{18}O$ with just 4 reference waters due to too much cold climate glacial water persisting at depths below –200 m RHB 70. Results for $\delta^{18}O$ for a sensitivity case with just 4 reference waters with the initial freshwater component in the fractures and the pore water all *Holocene Glacial Melt Water* (see Figure 3-63) are shown in Figure 6-15 for two groups of footwall data that also have pore water samples. Comparing with the lower left plots in Figure 6-4 and Figure 6-6 for the *stage 2.2 base model simulation* demonstrates how specifying the initial fracture water according to the Alternative Case model improves the match to $\delta^{18}O$ in the fracture system below –300 m RHB 70. The match between the simulated $\delta^{18}O$ in the matrix and the pore water samples is also significantly improved by specifying the initial fracture water according to the Alternative Case model, but it is recognised that the *stage 2.2 base model simulation* still fails to predict higher $\delta^{18}O$ in the pore water than the fracture water in some of the boreholes. There are several reasonable explanations to this result, where the assumed composition of the *Old Meteoric-Glacial Waters* as reference water probably is the greatest uncertainty.

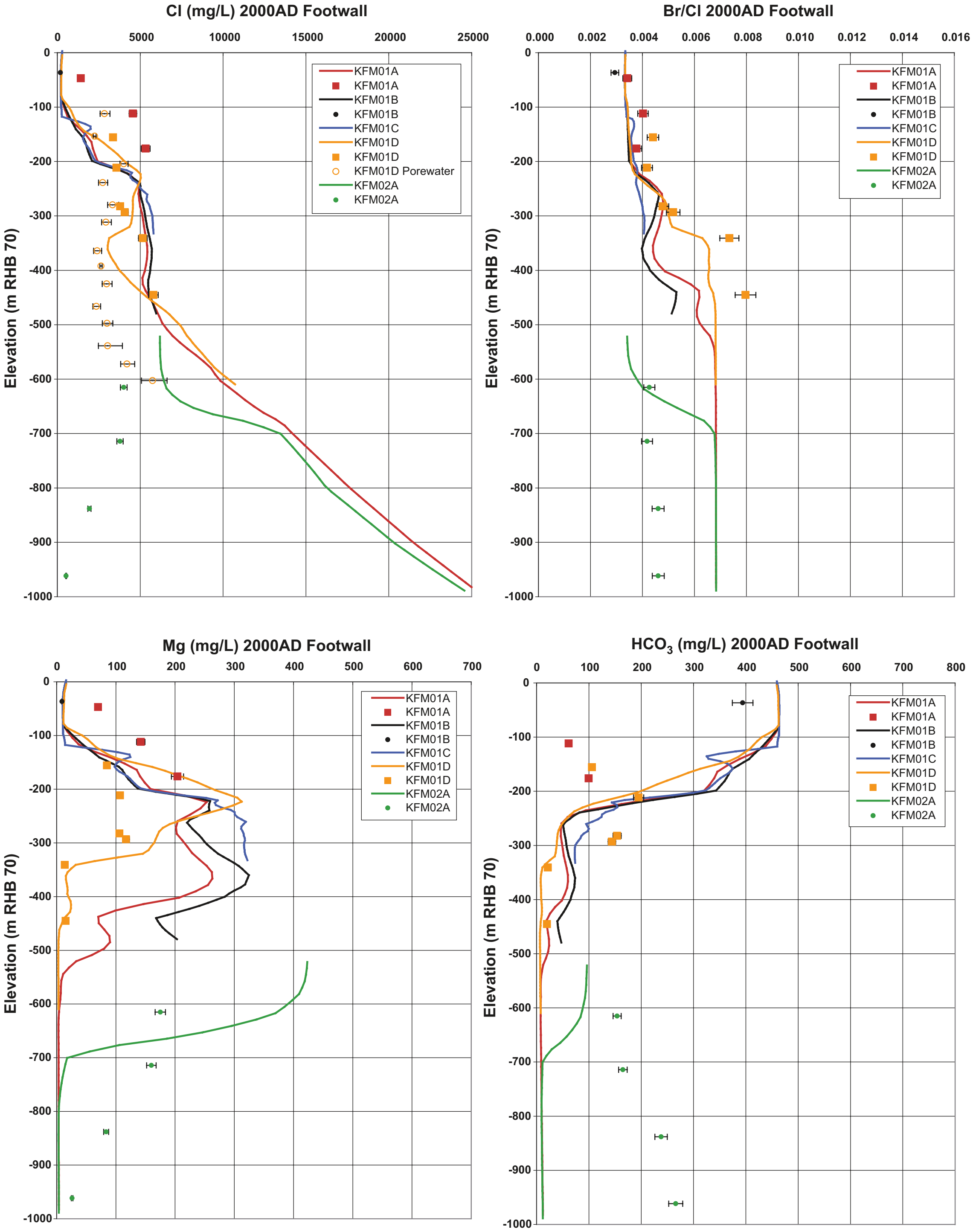

Figure 6-10. *Comparison of result for the sensitivity case before hydraulic conditioning of the HCD and measured Cl, Br/Cl, Mg and HCO$_3$ in the fracture system for the first set of boreholes in the footwall of zone A2. Square symbols are used for the representative and less representative data, and small filled circles for the supplementary data. The pore water data is plotted as open circles. The error bars on the fracture data only indicate the laboratory analytical error, while in the pore water they reflect the uncertainty in the porosity of the rock sample. The solid lines show the simulated distributions in the fracture system. It is noted that the supplementary data (small filled circles) are uncertain and should be used with great caution. Moreover, it is noted that ratios of Br/Cl > 0.007 cannot be reproduced with the current chemical composition of the reference waters shown in Table 4-14.*

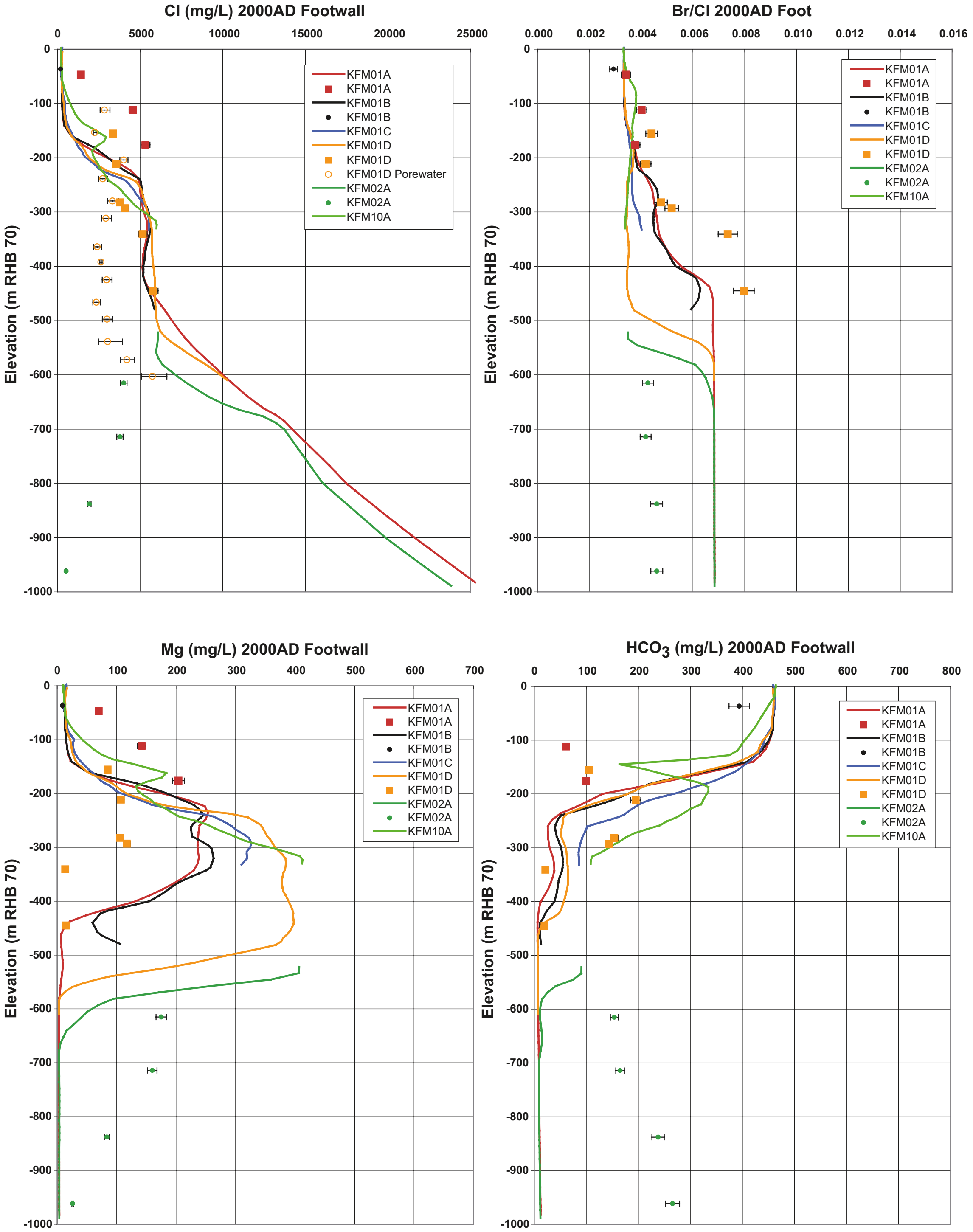

Figure 6-11. *Comparison of result for the sensitivity case with version 1.2 fracture orientations and measured Cl, Br/Cl, Mg and HCO_3 in the fracture system for the first set of boreholes in the footwall of zone A2. Square symbols are used for the representative and less representative data, and small filled circles for the supplementary data. The pore water data is plotted as open circles. The error bars on the fracture data only indicate the laboratory analytical error, while in the pore water they reflect the uncertainty in the porosity of the rock sample. The solid lines show the simulated distributions in the fracture system. It is noted that the supplementary data (small filled circles) are uncertain and should be used with great caution. Moreover, it is noted that ratios of Br/Cl > 0.007 cannot be reproduced with the current chemical composition of the reference waters shown in Table 4-14.*

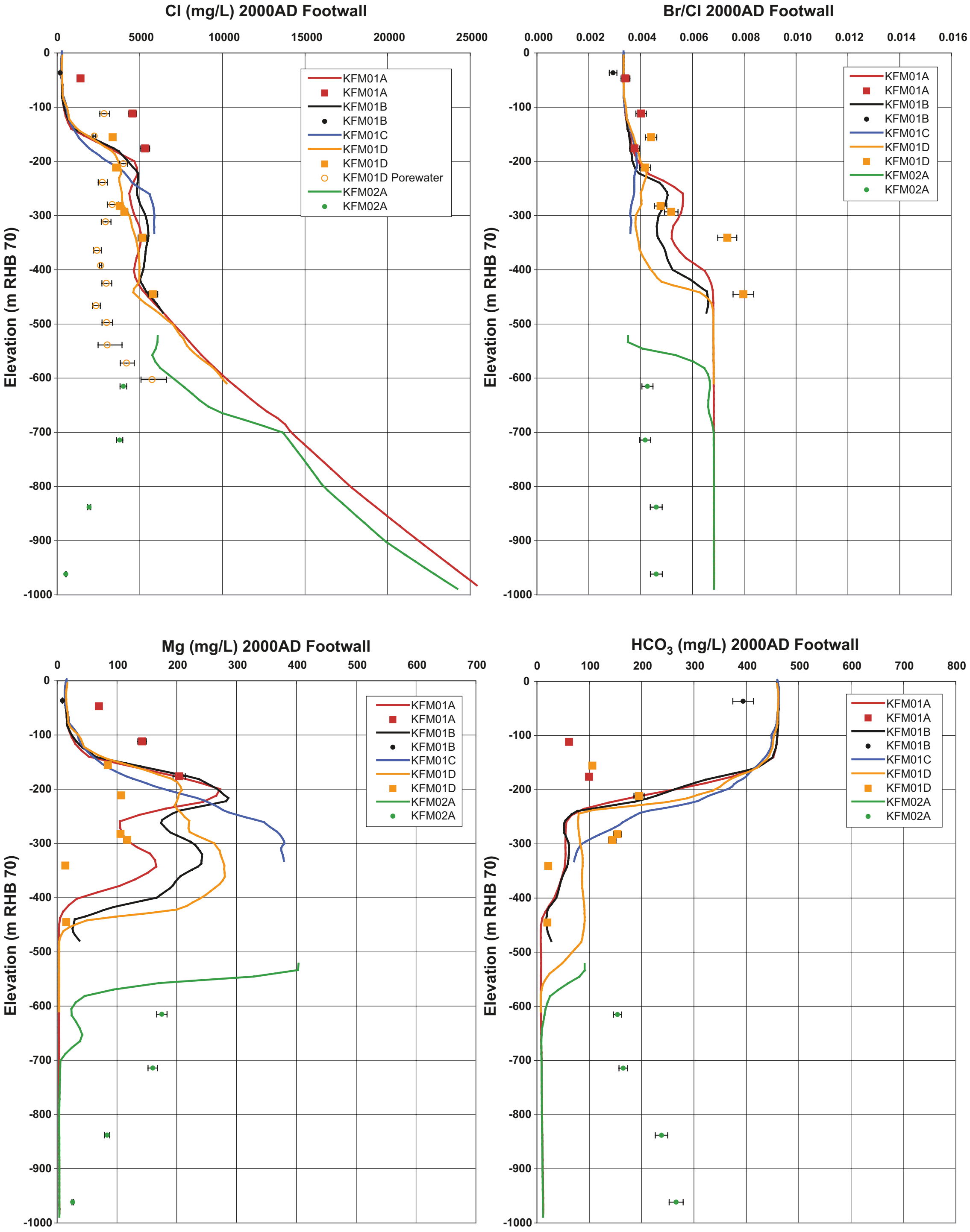

Figure 6-12. *Comparison of result for the sensitivity case with version 1.2 fracture orientations and reduced hydraulic conductivity in the top 400 m of HRD and measured Cl, Br/Cl, Mg and HCO_3 in the fracture system for the first set of boreholes in the footwall of zone A2. Square symbols are used for the representative and less representative data, and small filled circles for the supplementary data. The pore water data is plotted as open circles. The error bars on the fracture data only indicate the laboratory analytical error, while in the pore water they reflect the uncertainty in the porosity of the rock sample. The solid lines show the simulated distributions in the fracture system. It is noted that the supplementary data (small filled circles) are uncertain and should be used with great caution. Moreover, it is noted that ratios of Br/Cl > 0.007 cannot be reproduced with the current chemical composition of the reference waters shown in Table 4-14.*

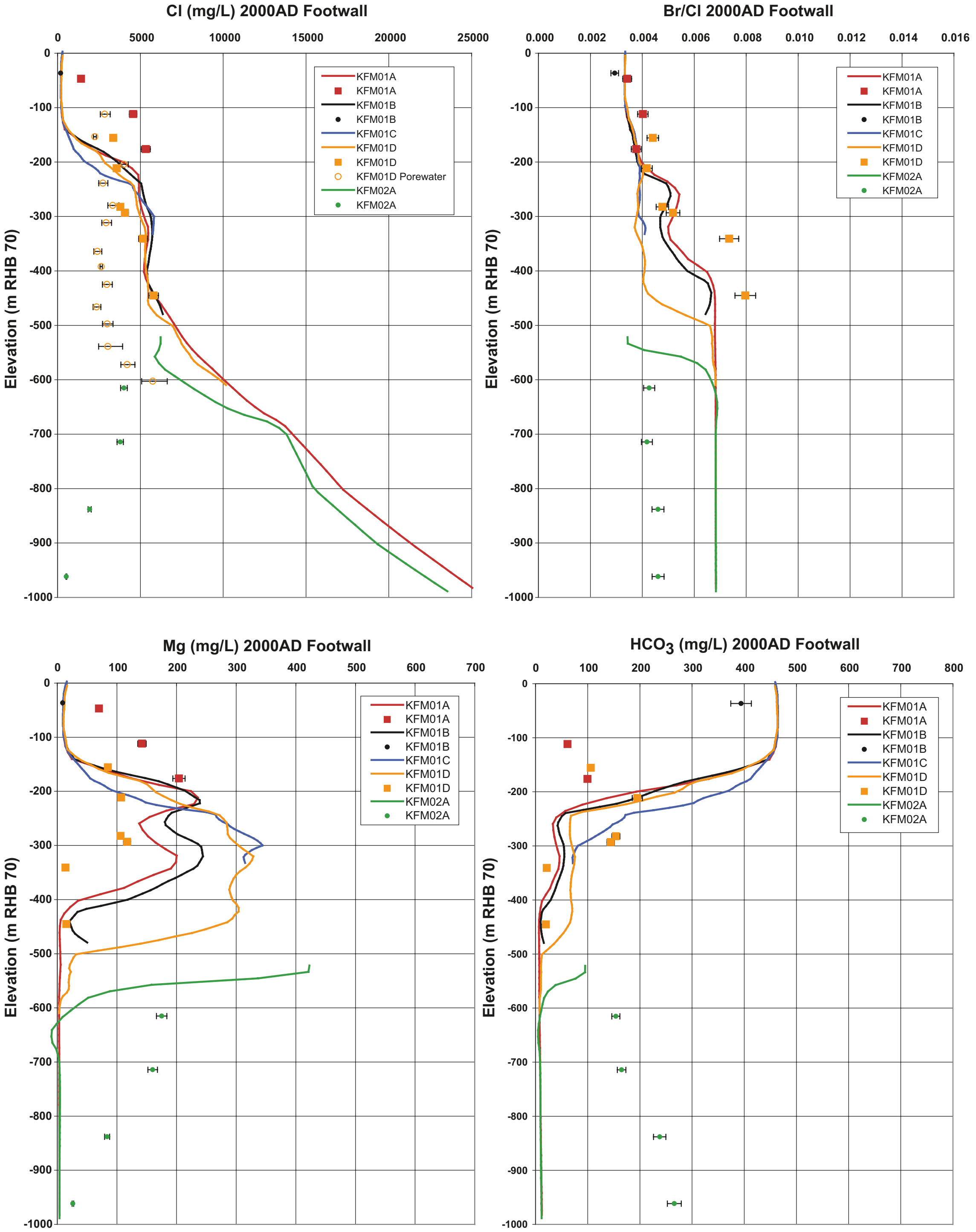

Figure 6-13. *Comparison of result for the sensitivity case with ten times lower kinematic porosity in HRD and HCD and measured Cl, Br/Cl, Mg and* HCO_3 *in the fracture system for the first set of boreholes in the footwall of zone A2. Square symbols are used for the representative and less representative data, and small filled circles for the supplementary data. The pore water data is plotted as open circles. The error bars on the fracture data only indicate the laboratory analytical error, while in the pore water they reflect the uncertainty in the porosity of the rock sample. The solid lines show the simulated distributions in the fracture system. It is noted that the supplementary data (small filled circles) are uncertain and should be used with great caution. Moreover, it is noted that ratios of Br/Cl > 0.007 cannot be reproduced with the current chemical composition of the reference waters shown in Table 4-14.*

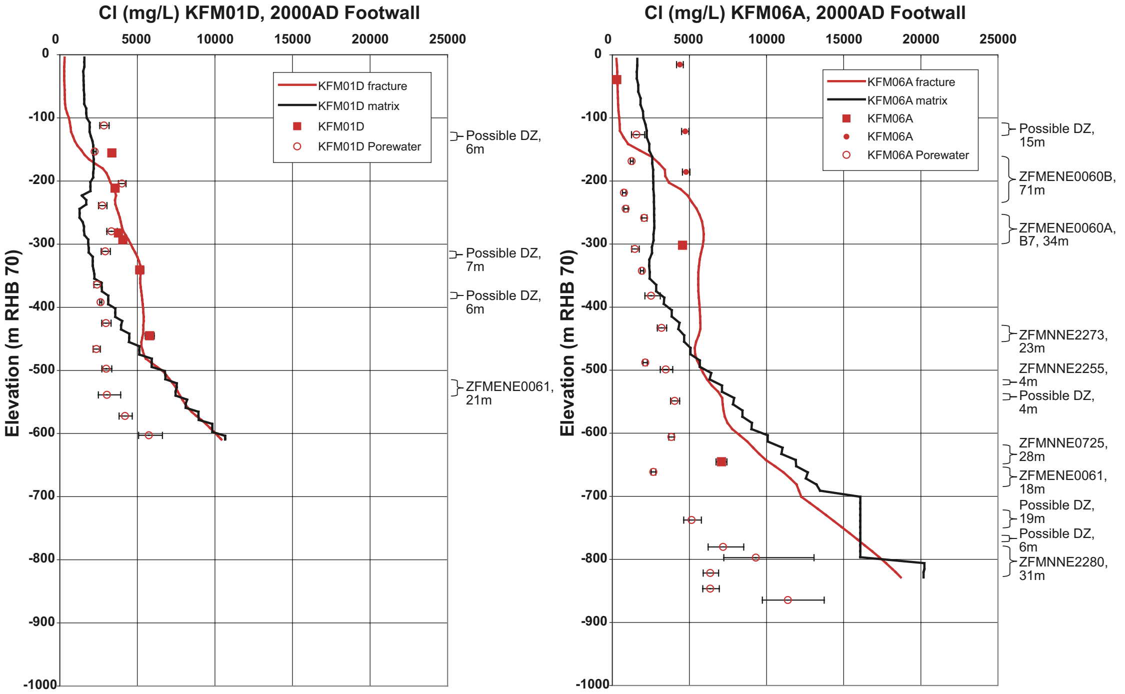

Figure 6-14. *Comparison of result for the sensitivity case with lower flow wetted fracture surface area per unit volume of rock and measured Cl in the fracture water and pore water for boreholes KFM01D and KFM06A both in the footwall of zone A2. Square symbols are used for the representative and less representative fracture data, and small filled circles for the supplementary fracture data. The pore water data is plotted as open circles. The error bars on the fracture data only indicate the laboratory analytical error, while in the pore water they reflect the uncertainty in the porosity of the rock sample. The red lines show the simulated distributions in the fracture system, and the black lines show the average in the matrix blocks. It is noted that the supplementary data (small filled circles) are uncertain and should be used with great caution.*

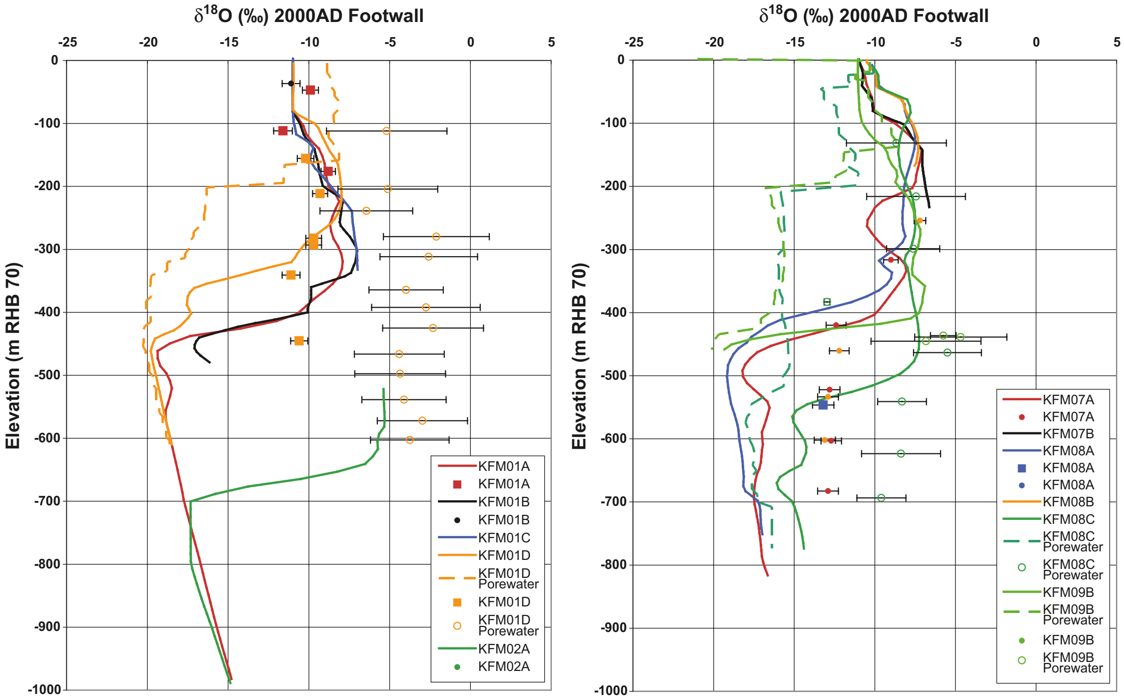

Figure 6-15. *Comparison of results for the sensitivity case without Old Meteoric reference water in the initial condition and measured δ^{18}O in the fracture system for the first and third set of boreholes in the footwall of zone A2. Square symbols are used for the representative and less representative data, and small filled circles for the supplementary data. The pore water data is plotted as open circles. The error bars on the fracture data only indicate the laboratory analytical error, while in the pore water they reflect the uncertainty in the porosity of the rock sample. The solid lines show the simulated distributions in the fracture system, and the dashed lines show the show the average in the matrix blocks. It is noted that the supplementary data (small filled circles) are uncertain and should be used with great caution.*

6.2 Conclusions

Numerical simulations of the palaeohydrological evolution and the predictions of present-day hydrochemistry have been used here as an additional confidence building step and as a calibration tool of model concepts and parameters. A range of sensitivities have been explored to understand the role of alternative model concepts and parameters. Given the constraints on hydrogeological parameters established by the hydraulic test data and modelling, the key remaining sensitivity for the palaeohydrological modelling was found to be the hydrochemical initial conditions. The two possible conceptual models described in Section 3.17.2 were considered with the Alternative Case giving results more consistent with δ^{18}O data for both fracture and pore water samples. Other important parameters were the vertical hydraulic conductivity of the bedrock and the water conducting fracture frequency which controls diffusion into the rock matrix. These sensitivity studies contributed to the description of the *stage 2.2 base model simulation*. This “model” gave a significant improvement in the predictions of present-day hydrochemical data than was achieved in version 1.2.

In terms of individual steps made in the palaeohydrological calibration process, the following conclusions are made:

Usage of hydrochemical data

- The predicted hydrochemistry at depth in the footwall are not always in compliance with all of the measurements, see the upper right plot in Figure 6-1 for an example. It is noted that the observed discrepancies often refer to the usage of hydrochemical data of uncertain representativity, see Section 4.5.1 and Table 4-2. If one would limit the selection of data used to only those that fulfil criteria such as a low level of drilling water residue and full coverage of major ions and isotopes, it would leave a large number of unused samples and little data to calibrate against. Some of the uncertain samples are found at elevations where more representative data are missing. The decision to use some of the uncertain samples as supplementary data in this study was based on the idea to provide more data for the comparison. Uncertain samples must of course be used with a great deal of caution and may serve only as indicative data.
- Moreover, it is noted that the measured ratios of Br/Cl > 0.007 cannot be reproduced with the chemical composition of the reference waters shown in Table 4-14. The reasons for the high Br/Cl ratios are discussed in /Laaksoharju et al. 2008/.

Hydrochemical conceptual model

- Some pore water samples suggest higher $\delta^{18}O$ consistent with an influence of warm climate water. The Alternative Case hydrochemical initial condition suggested here (see Section 3.17.2) gave better predictions for $\delta^{18}O$ data for both fracture and pore water samples than the Base Case hydrochemical initial condition used in version 1.2. The Alternative Case model assumes a limited influx of *Holocene Glacial Melt Water* into the fracture water such that a mixture of *Deep Saline Water* and *Old Meteoric-Glacial Waters* (interglacial) persists even at relatively shallow elevations. Consequently, it is assumed there was little in-diffusion of *Holocene Glacial Melt Water* into the rock matrix during the Holocene, and so the initial pore water is assumed to be only a mixture of *Deep Saline Water* and *Old Meteoric-Glacial Waters*. At this stage, however, such an interpretation is a conjecture supported mainly by numerical simulation. A more robust definition of the chemical composition of *Old Meteoric-Glacial Waters* as reference water appropriate to an interglacial water, for example by analogy to other deep groundwater samples from the Fennoscandian Shield, would help the interpretation of the pore water samples.
- The persistence of an interglacial groundwater composition over the Holocene requires further consideration since it has implications for the description of the long term stability of hydrochemical conditions over glacial cycles.

HCD

- The changes to the hydraulic parameters of the HCD based on the hydraulic data described in /Follin et al. 2007b/ and refined in Section 5 led to a model also consistent with the palaeohydrological calibration and therefore provided a verification of the calibration steps described above.

HRD

- Reducing the vertical hydraulic conductivity of the bedrock improved the calibration. In line with Section 5, this implies greater anisotropy in the Hydro-DFN, which can partly be fulfilled by using the alternative Hydro-DFN fracture orientation distributions recommended by /Follin et al. 2007b/, and
- increasing the kinematic porosity by a factor 10 over that implied by the empirical relationship between fracture aperture and transmissivity improved the results. It should be noted that part of this factor, 2–3, can be accounted for by the truncation of fracture sizes distribution made in the regional Hydro-DFN modelling.

7 Exploration simulations

7.1 Discharge of saline groundwater

The *stage 2.2 base model simulation* was used to predict the present-day spatial distribution of chloride at the surface and at –50 m RHB 70. The simulation results are shown in Figure 7-1 and Figure 7-2, respectively. The interpretation is facilitated by looking at Figure 7-3 and Figure 7-4, which show the exit locations of c. 22,000 particles. The particles were released in a regular mesh of 40 m by 40 m at two different elevations. In Figure 7-3 the particles start at –150 m RHB 70 and in Figure 7-4 the particles start at –500 m RHB 70. The shape of the release area (red points represent start positions) is the same in Figure 7-3 and Figure 7-4 and equates to the border of the model domain used for near-surface hydrogeological modelling /Bosson et al. 2008/. The black line indicates the horizontal extent of the “cage features”.

Table 7-1 shows the predicted chloride concentrations in the till layer below the bottom sediments in Lake Bolundsfjärden, Lake Fiskarfjärden, Lake Eckarfjärden, Lake Gällsboträsket and the Baltic Sea as well as at –50 m RHB 70. The recorded minimum-maximum chloride concentrations measured in the till layer are also shown.

From the information provided by Figure 7-1 through Figure 7-4 we conclude that the particles that were released at –150 m RHB 70 outside the “cage features” are often caught by local flow cells, hence discharge locally. However, below the “cage features” the flow field is different. The particles that were released at –150 m RHB 70 below the “cage features” do not discharge locally but are transported horizontally until they reach the Baltic Sea.

In comparison, we conclude that almost all of the particles that were released at –500 m RHB 70 discharge in the Baltic Sea regardless if they have the “cage features” overlying or not, see Figure 7-4. In addition, many of them discharge along the series of WNW deformation zone traces nearby the Singö deformation zone (WNW0001). The main terrestrial discharge areas, which potentially contain a component of saline groundwater from depth, (i.e. *Deep Saline Water*), are Lake Fiskarfjärden and Lake Gällsboträsket, cf. Section 3.17.5 and Table 7-1. The high salinity groundwater at –50 m RHB below Lake Bolundsfjärden is most likely not *Deep Saline Water*, but a remnant of *Littorina Sea Water* /Tröjbom et al. 2007/. The particles that start at –500 m RHB 70 and discharge below Lake Eckarfjärden are not associated with saline groundwater according to Figure 7-2. This finding is also consistent with data, see Table 7-1.

Table 7-1. Predicted and measured chloride concentrations (mg/L) in the till layer below the bottom sediments in Lake Bolundsfjärden, Lake Fiskarfjärden, Lake Eckarfjärden, Lake Gällsboträsket and the Baltic Sea. Predicted concentrations at –50 m RHB 70 below these water bodies are also shown. The results represent the *stage 2.2 base model simulation*.

Object	Predicted range of Cl in the till	Min–Max range of Cl in the till	Predicted Cl at –50 m RHB 70	Monitoring well
Lake Bolundsfjärden	1,500–2,250	3,520–4,340	250–4,000+	SFM0023
Lake Fiskarfjärden	750–2,250	947–1,300	750–2750	SFM0022
Lake Eckarfjärden	0–250	277–375	0–250	SFM0015
Lake Gällsboträsket	0–1,000	2,160–2,340	750–1,750	SFM0012
Baltic Sea	1,000–3,000	690–3,940	1,500–4,000+	SFM0024, -25, -65, -81

7.2 Flow paths from a tentative repository layout

Figure 7-5 and Figure 7-6 show particle traces for a release area at –500 m RHB 70 coinciding with the tentative D1 layout shown in Figure 3-2. The release area is approximately 1.7 km by 1.7 km and one particle is released every 100 m on a regular mesh. The influence of the "cage features" is evident in these figures and the particle traces are consistent with the conceptual flow field envisaged in Figure 3-21.

A lot of the particles discharge in the Singö deformation zone where this zone intersects the SFR peninsula. Some particles discharge towards ESE along the series of deformation zone traces nearby the Singö deformation zone. The simulation results raise a question about the hydraulic properties of the structural segments in this area. The Singö deformation zone is modelled in the same fashion as all other deformation zones modelled in this report. That is, it is heterogeneous in the vertical direction in steps of 100 m, but homogeneous within each 100 m step, cf. Table L-1 in Appendix L.

7.3 Conclusions

We find the explorative simulation useful for the confidence building process. The results obtained regarding the occurrence of saline groundwater near surface are consistent with the measurements reported by the surface systems modelling group and hence support the hypotheses raised in the conceptual modelling presented in Section 3.

The particle tracking reveals a profound influence of the envisaged "cage features". Whether the interpreted spatial extent of the "cage features" is correct or not will be tested by means of an interference test in borehole HFM33 located on the SFR peninsula, see Figure B-7 in Appendix B. The interference test will also study the hydraulic properties transverse the Singö deformation zone by means of measurements in the boreholes located on the other side of this zone including the boreholes on the SFR peninsula. The hydraulic properties of the Singö deformation zone will also be investigated in stage 2.3 by means of a core-drilled borehole KFM11A, see Figure B-6 in Appendix B. Finally, borehole KFM12A will investigate the properties of the Forsmark deformation zone.

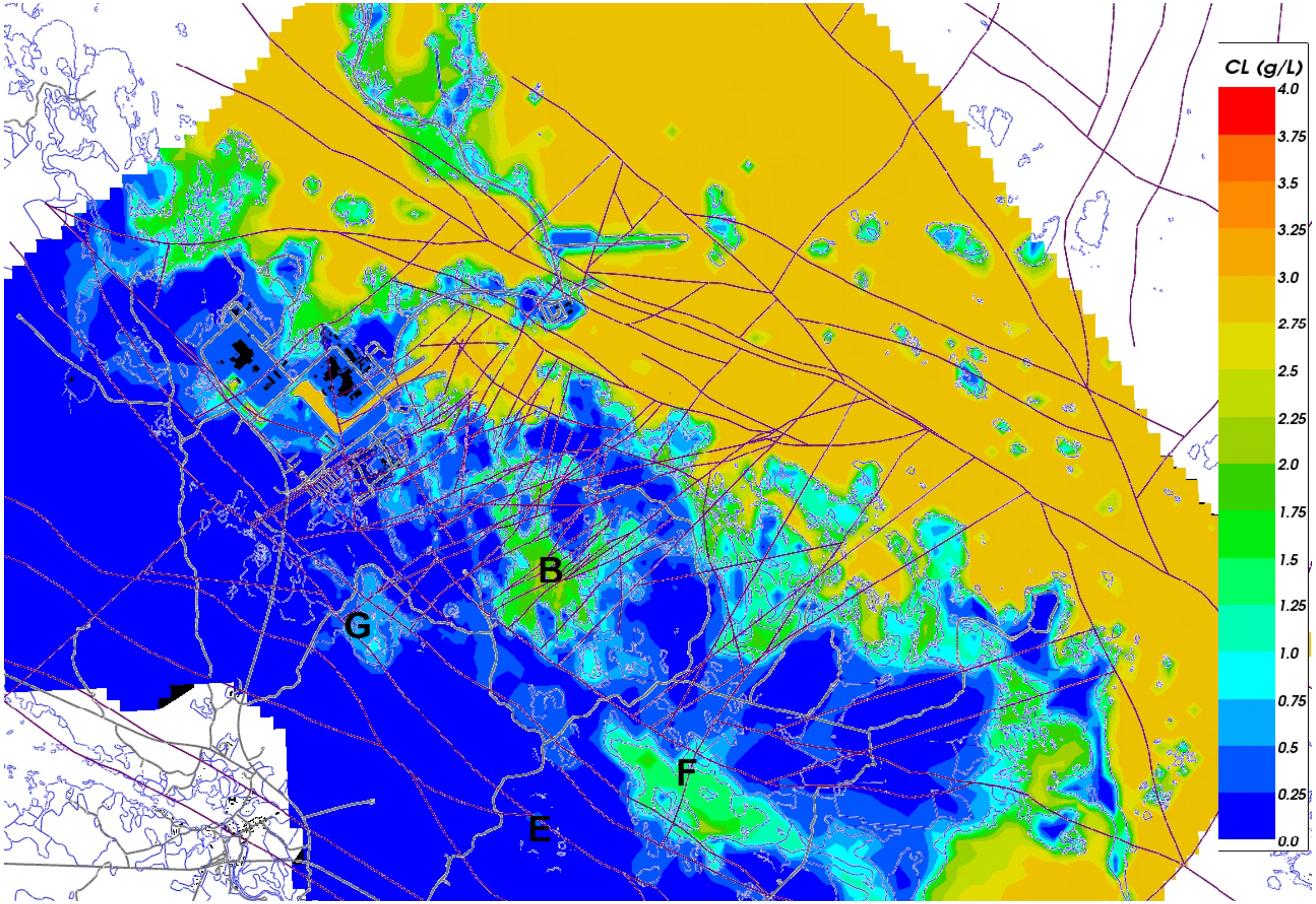

Figure 7-1. *Predicted spatial distribution of chloride at the surface using the stage 2.2 base model simulation. B = Lake Bolundsfjärden, F = Lake Fiskarfjärden, E = Lake Eckarfjärden, G = Lake Gällsboträsket. Saline groundwater discharges in F and G but probably not in E and B.*

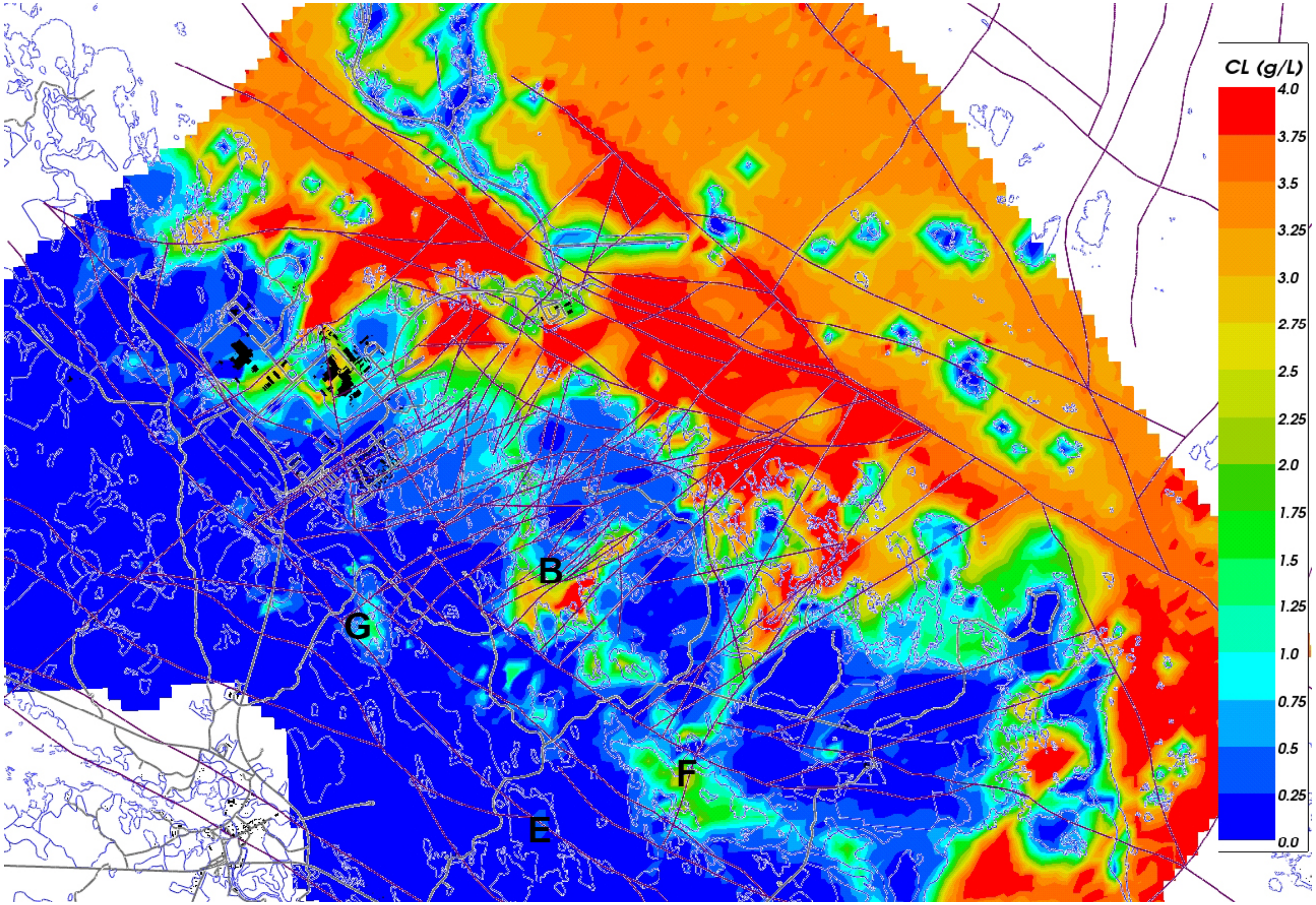

Figure 7-2. Predicted spatial distribution of chloride at –50 m RHB 70 using the stage 2.2 base model simulation. B = Lake Bolundsfjärden, F = Lake Fiskarfjärden, E = Lake Eckarfjärden, G = Lake Gällsboträsket. Saline groundwater discharges in F and G but probably not in E and B.

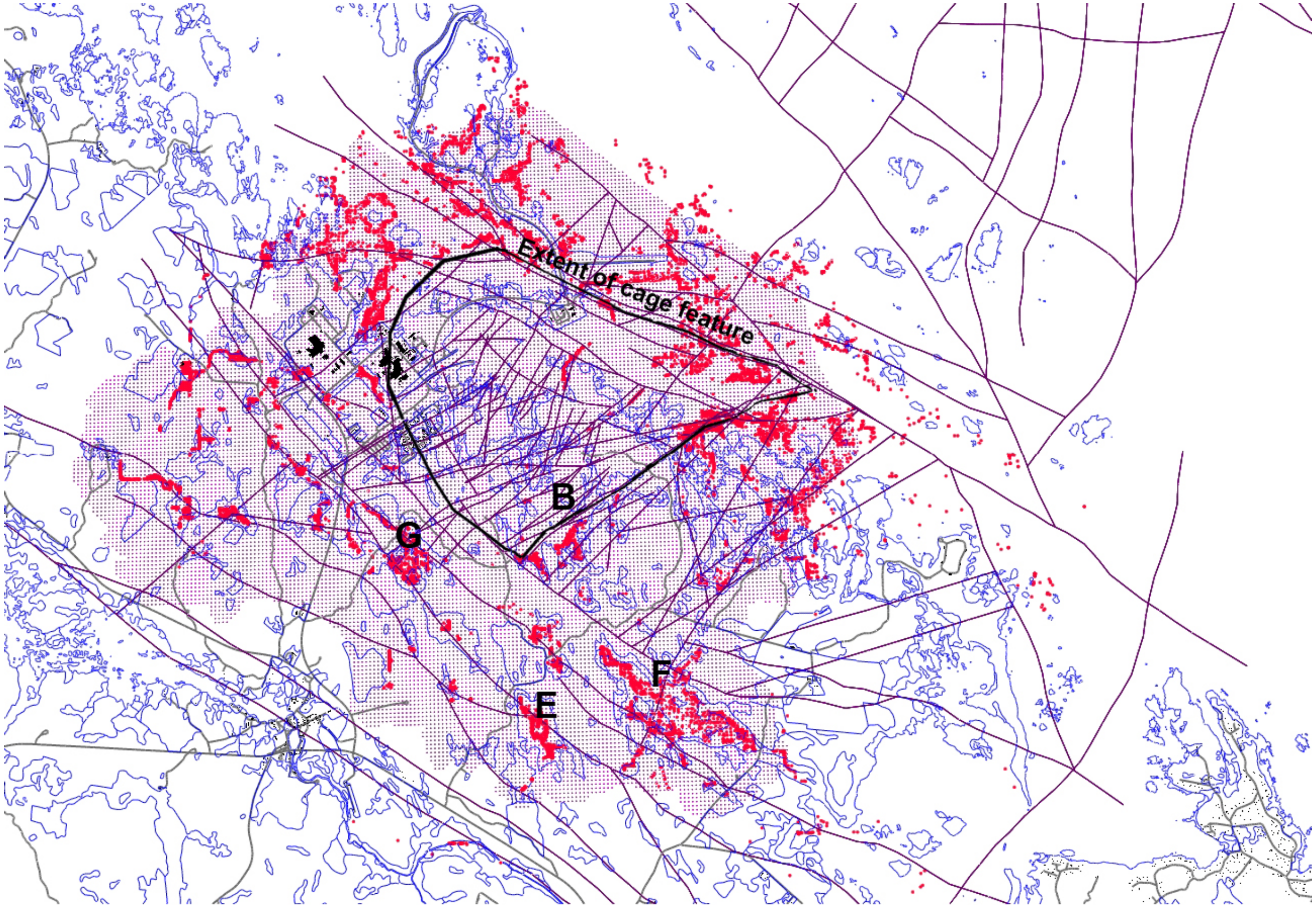

Figure 7-3. *Predicted exit locations at the surface (red dots) of c. 22,000 particles using the stage 2.2 base model simulation. The particles were released in a 40 m by 40 m mesh at –150 m RHB 70. B = Lake Bolundsfjärden, F = Lake Fiskarfjärden, E = Lake Eckarfjärden, G = Lake Gällsboträsket.*

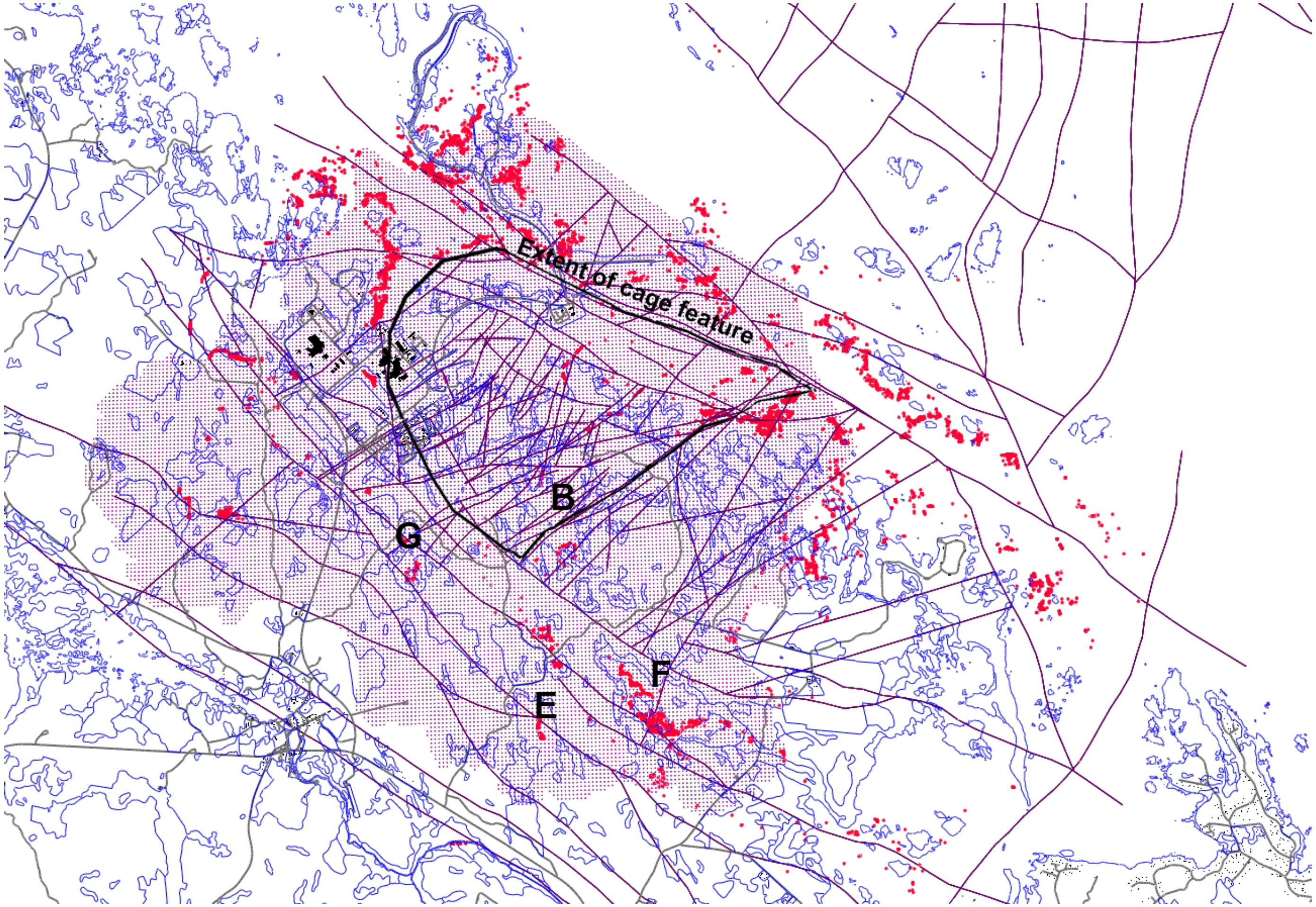

Figure 7-4. *Predicted exit locations) at the surface (red dots) of c. 22,000 particles using the stage 2.2 base model simulation. The particles were released in a 40 m by 40 m mesh at –500 m RHB 70. B = Lake Bolundsfjärden, F = Lake Fiskarfjärden, E = Lake Eckarfjärden, G = Lake Gällsboträsket.*

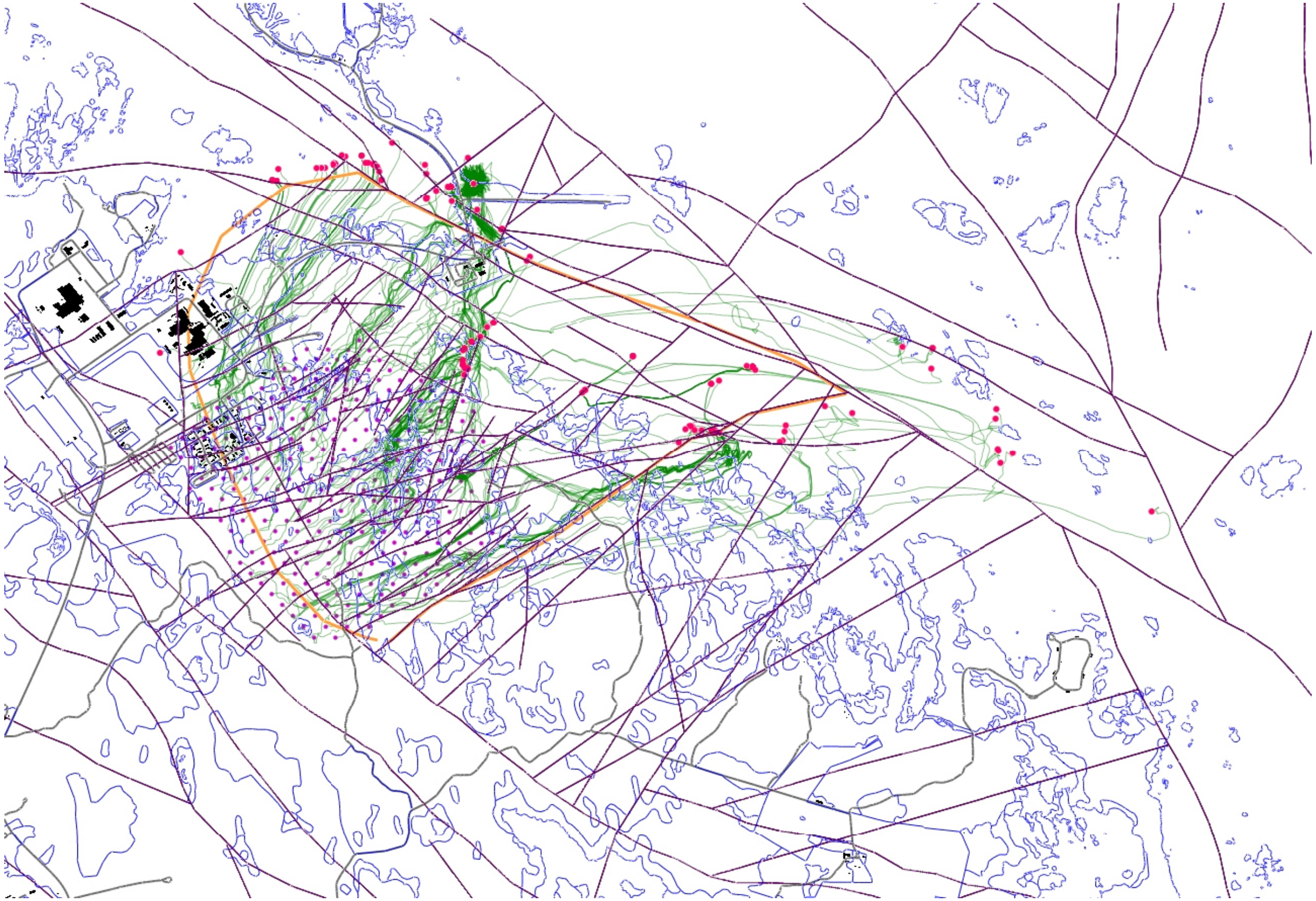

Figure 7-5. *Plane view of the target area with predicted flow paths and exit locations at the surface (red dots) of c. 300 particles using the stage 2.2 base model simulation. The particles were released in a 100 m by 100 m mesh at –500 m RHB 70 using an approximation of the D1 repository layout, see Figure 3-2.*

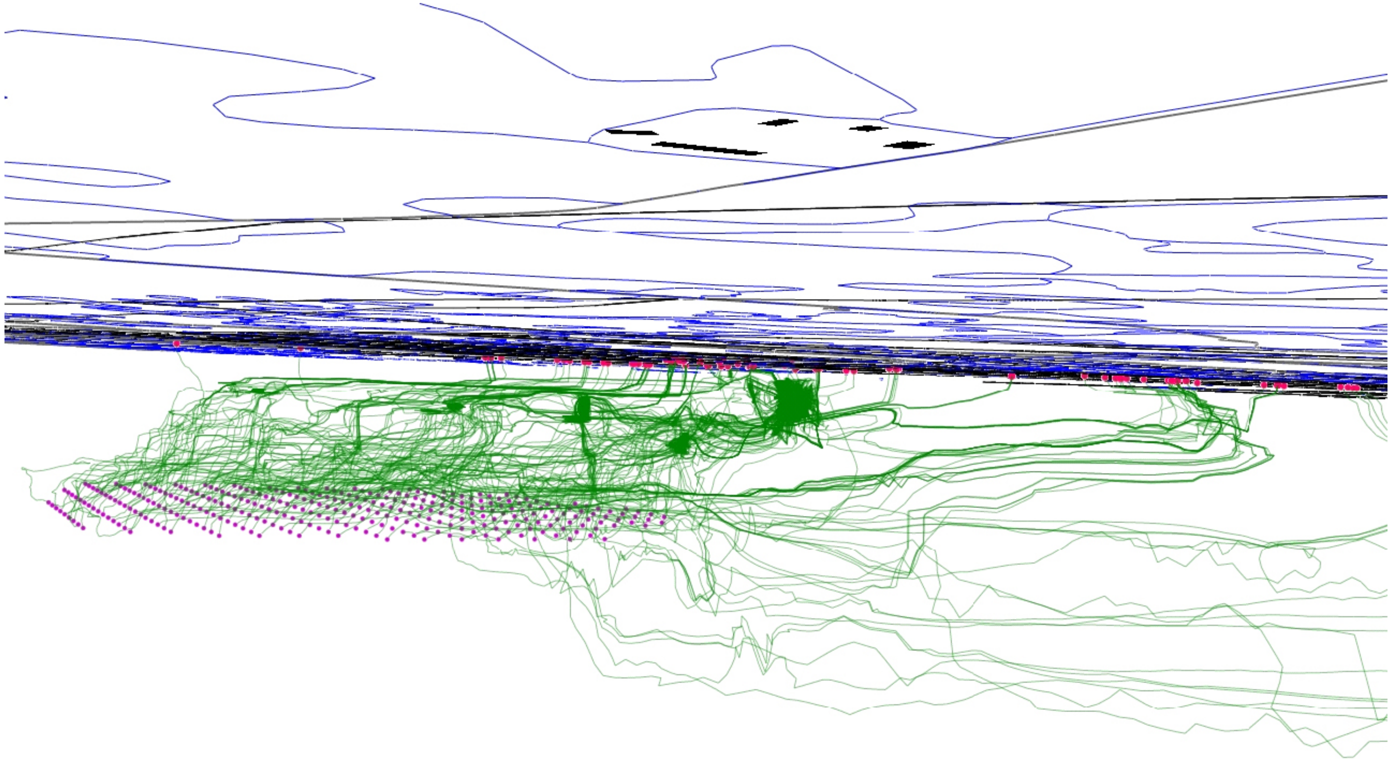

Figure 7-6. *A perspective view towards northwest showing flow paths of c. 300 particles using the stage 2.2 base model simulation. The particles were released in a 100 m by 100 m mesh at –500 m RHB 70 using an approximation of the D1 repository layout, see Figure 3-2. Particles that exit at the surface are indicated by a red dot.*

8 Discussion and conclusions

8.1 Scope and objectives

The work reported here describes the hydrogeological model in stage 2.2 of the SDM-Site project for Forsmark. The primary objectives are:

- to assess and illustrate the hydrogeological conceptual understanding of the Forsmark area, in particular the target volume and its boundaries, and
- to build a numerical groundwater flow and solute transport model and test its functionality against four types of data as a means of approaching the issue of confirmatory testing (cf. Step 4 in Figure 1-1). The four data types treated are single-hole hydraulic tests, hydraulic interference (cross-hole) tests, natural groundwater levels, and hydrochemical data.

8.2 Major findings from the calibration exercises

In the process of calibrating the numerical model to single-hole hydraulic tests, cross-hole tests, natural point-water head measurements and hydrochemistry samples, a number of lessons were learnt in terms of the key features, processes and parameters required to mimic the observed behaviour of the hydrogeological system. Sensitivities to various features and parameters had to be considered to find one or more ways to honour the field data. This prompted relatively few changes to the initial implementation of the hydrogeological conceptual model within the reasonable ranges of uncertainty on parameters. Among the lessons learnt we note in particular:

- **HCD model:** The description of the hydraulic properties and the depth dependency of deformation zones developed in the conceptual model appear consistent with the hydraulic and hydrochemistry measurements, although it is important to condition individual zones where data is available to the single-hole test data.

  Figure 3-35 shows a 3D visualisation of the resulting property model for stage 2.2. Here, the zones are coloured by the hydraulic conductivity within the zones and drawn as volumes to show their assigned hydraulic width. The depth dependency is clearly apparent. A final step would be to add lateral heterogeneity within each zone, but this is not performed until stage 2.3. Because the heterogeneity away from the measurement boreholes is undetermined, this necessarily requires a stochastic modelling approach using at least several realisations.

  The large, horizontal fractures/sheet joints are difficult to map in detail, and hence model, due to uncertainties in their spatial extent and hydraulic heterogeneity. The chosen approach to model them in terms of three deterministic, hydraulically heterogeneous “cage features”, along with interpreted deformation zones, communicates hydraulic disturbances across large distances in the numerical model, which by and large are consistent with the field observations observed in the upper parts of the bedrock. Here, we hypothesised that the “cage features” go all the way to the Singö deformation zone, see Figure 3-31. This hypothesis will be tested in stage 2.3 by an interference test conducted by pumping in borehole HFM33 located on the SFR peninsula, see Figure B-7 in Appendix B.

- **HRD model:** Using the alternative Hydro-DFN fracture set orientation model developed for stage 2.2 (Table 3-8) rather than the model used in version 1.2 (Table 3-7) improved the calibration of the flow and solute transport model, primarily by defining fractures in the sub-horizontal set to be more sub-parallel, which reduced the vertical connectivity and hence increased the hydraulic anisotropy. Further mechanisms for anisotropy such as a lower transmissivity in the sub-vertical sets may also make the simulations correspond better to the observations, although this hypothesis was not tested here.

It is noted that the HRD modelling in stage 2.2 is based on the hypothesis that the Hydro-DFN properties of the poorly investigated fracture domain FFM06 are the same as for FFM01 /Follin et al. 2007b/. Structural-hydraulic data for FFM06 will be available for a comparison in the stage 2.3, which encompasses data from the core-drilled borehole KFM08D, see Figure 8-1.

- **HSD model:** The hydraulic properties of the simplistic HSD model used to represent the complex geometry and stratification of the regolith model suggested for stage 2.2 required considerable calibrations of the hydraulic properties to find consistency with the hydraulic interference test and point-water head measurements. The introduction of anisotropy (lower vertical hydraulic conductivity) being the key step.
- **Solute transport model:** Extra changes to the initial ECPM bedrock transport parameters were necessary for the solute transport modelling of salt including:

  (*i*) increasing the kinematic porosity about one order of magnitude from the initial empirical relationship used to relate fracture transport aperture to transmissivity suggested by /Dershowitz et al. 2003/, and

  (*ii*) increasing the flow wetted fracture surface area per unit volume of rock between up to about two orders of magnitude from the frequency of water bearing fractures measured by the PFL-f technique.

  About 30% of the increase in the kinematic porosity is just a numerical truncation correction factor that we had to apply to make up for the pore space lost by using a truncated size distribution in the regional flow simulations. (The truncated size distribution range between 5.64 m < r < 5.64 m, whereas the location parameter of the power-law size distribution suggested by /Follin et al. 2007b/ is r_0 = 0.038 m.)

  The final values used for the flow wetted fracture surface area per unit volume of rock (a_r) in stage 2.2 vary between 0.15–0.6 m^2/m^3 according to fracture domain and depth. However, below –400 m RHB 70 in FFM01, a_r would actually be < 0.01 m^2/m^3 according to Table 3-4. However, for such a low value the 1D RMD model approximation in CONNECTFLOW of the solute profile in the matrix requires a prohibitively large number of terms in the numerical solution, and hence for pragmatic reasons a minimum value of 0.15 m^2/m^3 is used.

  It can be shown that below about 0.3 m^2/m^3, there is a time lag of a few thousands of years between the solute concentration in the matrix and fracture systems, and for 0.15 m^2/m^3, the lag is about 10,000 years. Hence, using a minimum value of 0.15 m^2/m^3 reproduces the expected behaviour of large matrix blocks with non-equilibrium in solute concentrations between the matrix and fracture systems over the simulation time of 10,000 years. It is noted that in safety assessment calculations, such as SR-Can, cf. /Hartley et al. 2006/, and the upcoming SR-Site, flow wetted fracture surface area per unit volume of rock is calculated explicitly along migration pathways obtained from DFN flow simulations implemented in CONNECTFLOW.

8.3 Confidence and uncertainties in the hydraulic model

The implementation of the hydrogeological conceptual model in a numerical model has been used to demonstrate its consistency with a wide range of field observations such as 1) single-hole hydraulic tests, 2) large-scale cross-hole test responses, 3) natural point-water heads in the bedrock and the Quaternary deposits, and 4) hydrochemistry profiles along the many cored boreholes drilled in close proximity to the so-called target volume. It is noted that a primary idea in stage 2.2 is that the same groundwater flow and solute transport model is used for each type of simulation to make it transparent that a single implementation of the conceptual model could be calibrated against all four types of field observations, although it may have been possible to improve the modelling of a particular data type by refining the model around a relevant observation borehole, for example.

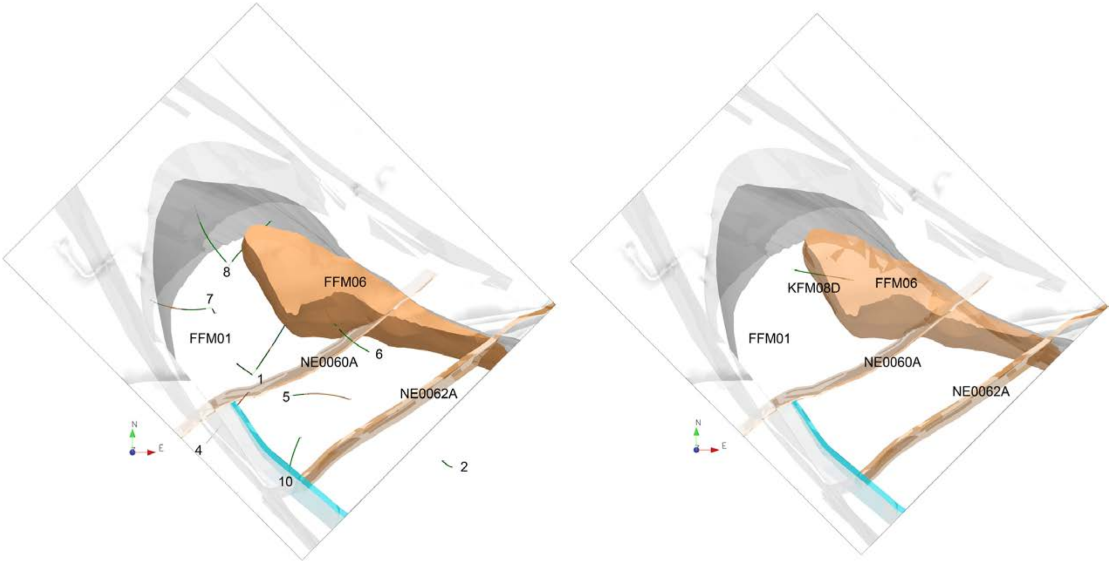

Figure 8-1. *Left: The core-drilled boreholes available for Hydro-DFN modelling of the target volume in stage 2.2 provided little information about FFM06. Right: A prediction of the structural-hydraulic properties along the KFM08D borehole, which penetrated FFM06, was made prior to its drilling and hydraulic testing (Appendix D). Structural-hydraulic data for FFM06 will be available for a comparison in the stage 2.3 report.*

The calibration process has helped narrow uncertainties on some parameters and helped our understanding of the character of the hydrogeological system in the Forsmark area. However, it is emphasised that the results obtained from stage 2.2 represent single realisations. Uncertainties relating to spatial variability in the geometrical and/or hydraulic properties will be quantified in stage 2.3, e.g. sensitivity studies to spatial heterogeneity with deformation zones, and multiple Hydro-DFN realisations.

The 2006 hydraulic interference test in the percussion-drilled borehole HFM14 provided the greatest challenge to the calibration process requiring adjustment to the properties of specific deformation zones, anisotropy in the upper bedrock and several changes to the hydraulic properties of the simplistic HSD model used to represent the complex geometry and stratification of the regolith model suggested for stage 2.2. Reconciling these modifications for the point-water heads narrowed the plausible description of hydraulic properties for the regolith further. The palaeohydrological simulations confirmed the changes made to the hydraulic properties for the bedrock and provided a route for calibrating the transport parameters, mainly the kinematic porosity and flow wetted fracture surface area per unit volume of rock. Figure 8-2 shows a comparison of measured (blue) and modelled (red) drawdown at the end of the 2006 interference test in HFM14 (21 days of pumping) for all monitored borehole intervals. The calibrated model shown in Figure 8-2 is in the work reported here referred to as the *stage 2.2 base model simulation*.

The Alternative Case hydrochemical initial condition suggested in the work reported here assumes a persistence of an interglacial groundwater composition over the Holocene. This hypothesis gave better predictions for both fracture and pore water samples than the Base Case hydrochemical initial condition used in version 1.2. Such a model requires further consideration since it has implications for the description of the long term stability of hydrochemical conditions over glacial cycles.

The simulations imply poor hydraulic contacts between the surface and upper bedrock raise questions for safety assessment about the locations of possible discharge areas. The role of topography for the discharge pattern within the target area is likely to be reduced due to the anisotropy in the Quaternary deposits and the uppermost part of the bedrock. Hence, the hydraulic gradients in the major deformation zones surrounding a repository need to be properly understood as well as the zones' contact with the Baltic Sea.

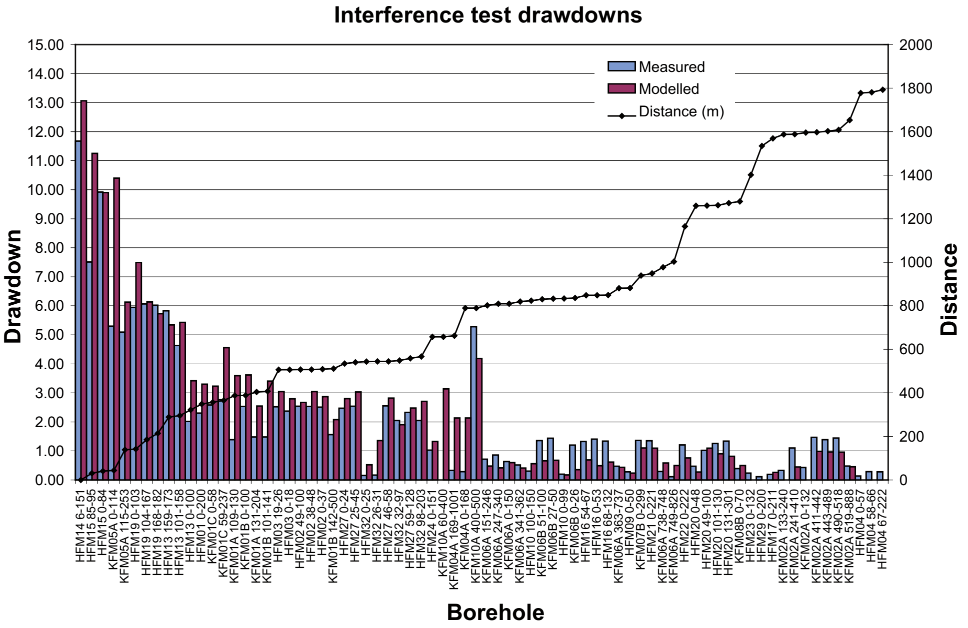

Figure 8-2. *Comparison of measured (blue) and modelled (red) drawdown at the end of pumping (21 days) for all monitored borehole intervals. The borehole intervals are ordered according to the three-dimensional distance (the right axis) of the monitoring intervals to the abstraction borehole HFM14.*

The extent of the "radius of influence" shown in Figure 8-2 demostrates that the uppermost c. 150 m of bedrock communicates hydraulic disturbances across large distances. We present in Appendix J monitoring data from the target area that cannot be explained. From the beginning of June 2006 to the end of October 2006 the sea level is greater than the calculated environmental-water heads in the bedrock in borehole sections HFM32:1–4 and KFM02A:5. Furthermore, the environmental-water heads in borehole section HFM32:2 are in general the lowest. Why the environmental-water heads in boreholes HFM32:1–4 and in KFM02A:5 are lower than the sea level during the dry summer of 2006 is not explained in the present work. However, two hypotheses are: suggested in Appendix J:

1. The pumping underground in the SFR repository on the other side of Singö deformation zone. The total rate of leakage water abstracted from the SFR repository at –140 m RHB is c. 5–6 L/s. (This discharge is close to the pumping rate during the 2006 interference test in HFM14.) There is an outcropping gently-dipping deformation zone below the SFR repository referred to as 871 that connect to the Singö deformation zone, see Figure 3-11. The observed drawdown in 871 at the SFR repository is c. 23–25 m.

   To test this hypothesis four new boreholes, HFM33–HFM35 and KFM11A, are planned to be drilled on the SFR peninsula during stage 2.3, see Figure B-6 and Figure B-7. The aforementioned interference test planned at HFM33 will test if there are extensive horizontal fractures/sheet joints that connect the superficial bedrock in the target area to the Singö deformation zone. During this interference test the monitoring system installed in the SFR repository will be used to check the hydraulic connection across the Singö deformation zone.

2. The pumping in the superficial bedrock below the nuclear power reactor buildings. The total number of pumping wells and their cumulative abstraction rate are a bit uncertain at this point, but there are at least a few wells down to c. –20 m RHB 70 discharging all together at least 1–2 L/s.

The notion behind the two hypotheses is that the pumping rates used are large enough to cause noticeable head changes (drawdowns) at HFM32 and KFM02A during dry periods when the influences of near-surface process are low. There are several examples of groundwater head disturbances in the Forsmark area caused by near-surface processes such as evapotranspiration and precipitation, see Appendix J.:

The hypothesis that the SFR facility disturbs the head field in the target area will be tested using the numerical flow models developed with MIKE SHE and CONNECTFLOW in stage 2.3 by /Bosson et al. 2008/ and /Follin et al. 2008/, respectively.

For the sake of discussion, an analytical model is tested in the present work, see Figure J-8 in Appendix J. The steady-state radial, radial flow model used is a very simple model of the system. For the chosen parameter values, which are based on field data, the model renders a drawdown at HFM32 of 0.5 m for a discharge at SFR of 5.5 L/s. This solution requires that the SFR repository is a sink with a fairly large effective radius (> 150 m) and that the equivalent transmissivity of the bedrock between the SFR and borehole HFM32 is of order $T \approx 1 \cdot 10^{-4}$ m^2/s.

References

Ahlbom K, Svensson U, 1991. The groundwater circulation in the Finnsjön area – the impact of density gradients. SKB TR 91-57, Svensk Kärnbränslehantering AB.

Andersson J-E, Nordqvist R, Nyberg G, Smellie J, Tirén S, 1991. Hydrogeological conditions in the Finnsjön area. Compilation of data and conceptual model. SKB TR-91-24, Svensk Kärnbränslehantering AB.

Andersson J, Ström A, Almén K-E, Ericsson LO, 2000. Vilka krav ställer djupförvaret på berget? Geovetenskapliga lämplighetsindikationer och kriterier för lokalisering och platsutvärdering. SKB R-00-15, Svensk Kärnbränslehantering AB.

Andersson J, 2003. Site descriptive modelling – strategy for integrated evaluation. SKB R-03-05, Svensk Kärnbränslehantering AB.

Auqué L F, Gimeno M J, Gómez J B, Puigdomenech I, Smellie J, Tullborg E-L, 2006. Groundwater chemistry around a repository for spent nuclear fuel over a glacial cycle – Evaluation for SR-Can. SKB TR-06-31, Svensk Kärnbränslehantering AB.

Bath A, Lalieux P, 1999. Technical summary of the SEDE Workshop on the use of hydrogeochemical information in testing groundwater flow models. In: Use of hydrogeochemical information in testing groundwater flow models, Technical summary and proceedings of an NEA Workshop, Borgholm, Sweden, 1–3 September 1997 (organised by the NEA Co-ordinating Group on Site Evaluation and Design of Experiments for Radioactive Waste Disposal (SEDE)). OECD/NEA, Radioactive Waste Management, pp. 13–30.

Berggren M, 1998. Hydraulic conductivity in Swedish bedrock estimated by means of geostatistics, Thesis Report Series 1998:9, Royal Institute of Technology, Stockholm.

Björck S, 1995. A review of the history of the Baltic Sea 13-8 ka. Quaternary International 27, 19–40.

Bosson E, Berglund S, 2006. Near-surface hydrogeological model of Forsmark. Open repository and solute transport applications – Forsmark 1.2. SKB R-06-52, Svensk Kärnbränslehantering AB.

Bosson E, Gustafsson L-Å, Sassner M, 2008. Numerical modelling of surface hydrology and near-surface hydrogeology at Forsmark. Site descriptive modelling, SDM-Site Forsmark. SKB R-08-09, Svensk Kärnbränslehantering AB. (in prep).

Brown G H, 2002. Glacier melt water hydrochemistry. Appl. Geochem., 17, 855–883.

Brunberg A-K, Blomqvist P, 1998. Vatten i Uppsala län 1997. Beskrivning, utvärdering, åtgärdsförslag. Upplandsstiftelsen, Rapport nr 8/1998.

Carlsson A, Christiansson R, 2007. Construction experiences from underground works at Forsmark. Compilation Report. SKB R-07-10, Svensk Kärnbränslehantering AB.

Carrera J, Sanchez-Vila X, Benet I, Medina A, Galarza G, Guimera J, 1998. On Matrix Diffusion: Formulations, Solution Methods, Quantitative Effects, Hydrogeology Journal 6, No. 1, 178–190.

Dershowitz W, Winberg A, Hermanson J, Byegård J, Tullborg E-L, Andersson P, Mazurek M, 2003. Äspö Task Force on modelling of groundwater flow and transport of solutes. Task 6c. A semi synthetic model of block scale conductive structures at the Äspö HRL. Äspö Hard Rock Laboratory, International Progress Report IPR-03-13, Svensk Kärnbränslehantering AB.

DHI, 2004. MIKE SHE. An integrated hydrological modelling system. Users guide. DHI Water & Environment, Hørsholm, Denmark.

Edelman J H, 1947. Over de berekening van grondwaterstromingen, Thesis, Technische Hogeschool Delft.

Fairbanks R, 1989. A 17,000-year glacio-eustatic sea level record: influence of glacial melting rates on the Younger Dryas event and deep-ocean circulation. Nature 342, 637–642.

Follin S, Stigsson M, Svensson U, 2005. Regional hydrogeological simulations for Forsmark – numerical modelling using DarcyTools. Preliminary site description Forsmark area – version 1.2. SKB R-05-60, Svensk Kärnbränslehantering AB.

Follin S, Johansson P-O, Levén J, Hartley L, Holton D, McCarthy R, Roberts D, 2007a. Updated strategy and test of new concepts for groundwater flow modelling in Forsmark in preparation of site descriptive modelling stage 2.2. SKB R-07-20, Svensk Kärnbränslehantering AB.

Follin S, Levén J, Hartley L, Jackson P, Joyce S, Roberts D, Swift B, 2007b. Hydrogeological characterisation and modelling of deformation zones and fracture domains, Forsmark modelling stage 2.2. SKB R-07-48, Svensk Kärnbränslehantering AB.

Follin S, Stigsson M, Svensson U, 2007c. Hydrogeological pre-modelling for Forsmark version 2.2: Sensitivity of the connected open fracture surface area per unit volume to the orientation, size and intensity of Poissonian discrete fracture network (DFN) models, SKB R-07-28, Svensk Kärnbränslehantering AB.

Follin S, Hartley L, Jackson P, Roberts D, Marsic N, 2008. Hydrogeology Forsmark. Site descriptive modelling, SDM-Site Forsmark. SKB R-08-23, Svensk Kärnbränslehantering AB. (in prep).

Forssman I, Zetterlund M, Forsmark T, Rhén I, 2006. Forsmark site investigation, Correlation of Posiva Flow Log anomalies to core mapped features in KFM06A and KFM07A. SKB P-06-56, Svensk Kärnbränslehantering AB.

Fox A, La Pointe P, Hermanson J, Öhman J, 2007. Statistical geological discrete fracture network model for the Forsmark site, stage 2.2. Forsmark modelling stage 2.2. SKB R-07-46, Svensk Kärnbränslehantering AB.

Fredén C (ed.), 2002. Berg och jord. Sveriges nationalatlas. Tredje upplagan.

Gentzschein B, Levén J, Follin S, 2006. A comparison between well yield data from the site investigation in Forsmark and domestic wells in northern Uppland. SKB P-06-56, Svensk Kärnbränslehantering AB.

Gokall-Norman K, Svensson T, Ludvigson L-E, Jönsson S, 2004. Hydraulic interference test. Boreholes HFM18 and KFM03A. Forsmark site investigation. SKB P-04-307, Svensk Kärnbränslehantering AB.

Gokall-Norman K, Ludvigson J-E, Jönsson S, 2005. Hydraulic interference test in borehole HFM01. Forsmark site investigation, SKB P-05-236, Svensk Kärnbränslehantering AB.

Gokall-Norman K, Ludvigson J-E, 2006. Hydraulic interference test in borehole HFM14. Forsmark site investigation, SKB P-06-196, Svensk Kärnbränslehantering AB.

Gokall-Norman K, Ludvigson J-E, Jönsson S, 2006. Hydraulic interference test Boreholes KFM02A and KFM03A. Forsmark site investigation. SKB P-06-09, Svensk Kärnbränslehantering AB.

Hartley L J, Holton D, 2004. CONNECTFLOW (Release 8.0). Technical summary document, Serco Assurance Report SA/ERRA C/TSD02V1.

Hartley L J, Hoch A R, Cliffe K A, Jackson C P, Holton D, 2004a. NAMMU (Release 8.0). Technical summary document, Serco Assurance Report SA/ENV/0626.

Hartley L J, Holton D, Hoch A R, 2004b. NAPSAC (Release 8.0). Technical summary document, Serco Assurance Report SA/ERRA-N/TSD02V1.

Hartley L J, Cox I, Hunter F, Jackson C P, Joyce S, Swift B, Gylling B, Marsic N, 2005. Regional hydrogeological simulations for Forsmark – numerical modelling using CONNECTFLOW, Preliminary site description Forsmark area – stage 1.2. SKB R-05-32, Svensk Kärnbränslehantering AB.

Hartley L J, Hoch A, Jackson C P, Joyce S, McCarthy R, Rodwell W, Marsic N, 2006. Groundwater flow and transport modelling during the temperate period for the SR-Can assessment – Forsmark sub-area – version 1.2. SKB R-06-98, Svensk Kärnbränslehantering AB.

Hedenström A, Sohlenius G, Strömgren M, Brydsten L, Nyman H, 2008. Depth and stratigraphy of regolith at Forsmark. Site descriptive modelling, SDM-Site Forsmark. SKB R-08-07, Svensk Kärnbränslehantering AB. (in prep).

Hjerne C, Jönsson J, Ludvigson J-E, 2004. Single-hole injection tests in borehole KFM03B. Forsmark site investigation. SKB P-04-278, Svensk Kärnbränslehantering AB.

Hoch A R, Jackson C P, 2004. Rock-matrix Diffusion in Transport of Salinity. Implementation in CONNECTFLOW. SKB R-04-78, Svensk Kärnbränslehantering AB.

Johansson P-O, Werner K, Bosson E, Berglund S, Juston J, 2005. Description of climate, surface hydrology, and near-surface hydrogeology. Forsmark 1.2. SKB R-05-06. Svensk Kärnbränslehantering AB.

Johansson P-O, Juston J, 2007. Monitoring of brook levels, water electrical conductivities, temperatures and discharges from April 2004 until March 2007. Forsmark site investigation. SKB P-07-135, Svensk Kärnbränslehantering AB.

Johansson P-O, 2008. Description of surface hydrology and near-surface hydrogeology at Forsmark. Site descriptive modelling, SDM-Site Forsmark. SKB R-08-08, Svensk Kärnbränslehantering AB.

Johansson P-O, Öhman J, 2008. Presentation of meteorological, hydrological and hydrogeological monitoring data from Forsmark. Site descriptive modelling, SDM-Site Forsmark. SKB R-08-10, Svensk Kärnbränslehantering AB.

Juhlin C, Stephens M B, 2006. Gently dipping fracture zones in Palaeoproterozoic metagranite, Sweden: Evidence from reflection seismic and cored borehole data and implications for the disposal of nuclear waste. Journal of Geophysical Research 111, B09302, 19 pp.

Juston J, Johansson P-O, 2005. Analysis of meteorological data, surface water level data, and groundwater level data. Forsmark site investigation. SKB P-05-152, Svensk Kärnbränslehantering AB.

Juston J, Johansson P-O, Levén J, Tröjbom M, Follin S, 2007. Analysis of meteorological, hydrological and hydrogeological monitoring data. SKB R-06-49, Svensk Kärnbränslehantering AB.

Kestin J, Khalifa H E, Correia R J, 1981. Tables of dynamic and kinematic viscosity of aqueous NaCl solutions in the temperature range 20–150°C and the pressure range 0.1–35 MPa, J. Phys. Chem. Ref. Data 10(1).

Konikow L, Bredehoeft J D, 1992. Ground-water models cannot be validated, Advances in Water Resources, 15(1), 1992, 75–83.

Källgården J, Ludvigson J-E, Hjerne C, 2004. Forsmark site investigation. Single-hole injection tests in borehole KFM03A. SKB P-04-194, Svensk Kärnbränslehantering AB.

Laaksoharju M, Wallin B (eds.), 1997. Evolution of the groundwater chemistry at the Äspö Hard Rock Laboratory. Proceedings of the second Äspö International Geochemistry Workshop, June 6–7, 1995. SKB International Co-operation Report ISRN SKB-ICR-91/04-SE. ISSN 1104-3210 Stockholm, Sweden.

Laaksoharju M, Skårman C, Skårman E, 1999. Multivariate Mixing and Mass-balance (M3) calculations, a new tool for decoding hydrogeochemical information. Applied Geochemistry Vol. 14, #7, 1999, Elsevier Science Ltd., pp. 861–871.

Laaksoharju M, Smellie J, Tullborg E-L, Gimeno M, 2008. Bedrock hydrogeochemistry Forsmark. Site descriptive modelling, SDM-Site Forsmark. SKB R-08-47, Svensk Kärnbränslehantering AB.

La Pointe P, Olofsson I, Hermanson J, 2005. Statistical model of fractures and deformation zones for Forsmark. Preliminary site description Forsmark area – version 1.2. SKB R-05-26, Svensk Kärnbränslehantering AB.

Levén J, Carlberg T, Follin S, 2006. Compilation and visualisation of cross discipline borehole data using WellCad. Boreholes KFM01A–KFM07A. Forsmark site investigation. SKB P-06-55, Svensk Kärnbränslehantering AB.

Ludvigson J-E, Jönsson S, 2003. Hydraulic interference tests. Boreholes HFM01, HFM02 and HFM03. Forsmark site investigation. SKB P-03-35, Svensk Kärnbränslehantering AB.

Lusczynski N J, 1961. Head and flow of ground water of variable density. Journal of Geophysical Research, 66(12), pp. 4247–4256.

Martin C D, 2007. Quantifying in situ stress magnitudes and orientations for Forsmark. Forsmark stage 2.2. SKB R-07-26, Svensk Kärnbränslehantering AB.

Morén L, Påsse T, 2001. Climate and shoreline in Sweden during Weichsel and the next 150,000 years. SKB TR-01-19, Svensk Kärnbränslehantering AB.

Munier R, 2004. Statistical analysis of fracture data, adapted for modelling Discrete Fracture Networks – Version 2. SKB R-04-66, Svensk Kärnbränslehantering AB.

NEA-OECD, 1993. Palaeohydrogeological methods and their application, Proceedings of a NEA workshop, Paris, 9–10 November 1992, Co-ordinating Group on Site Evaluation and Design of Experiments for Radioactive Waste Disposal – SEDE.

Nilsson A-C, Borgiel M, 2007. Sampling and analyses of surface waters Results from sampling in the Forsmark area, July 2005–June 2006. Forsmark site investigation. SKB P-07-95, Svensk Kärnbränslehantering AB.

Olofsson I, Simeonov A, Stephens M, Follin S, Nilsson A-C, Röshoff K, Lindberg U, Lanaro F, Fredriksson A, Persson L, 2007. Site descriptive modelling Forsmark, stage 2.2: Presentation of a fracture domain concept as a basis for the statistical modelling of fractures and minor deformation zones, and interdisciplinary coordination. SKB R-07-15, Svensk Kärnbränslehantering AB.

Påsse T, 1996. A mathematical model of the shore level displacement in Fennoscandia. SKB TR 96-24, Svensk Kärnbränslehantering AB.

Påsse T, 1997. A mathematical model of past, present and future shore level displacement in Fennoscandia. SKB TR-97-28, Svensk Kärnbränslehantering AB.

Påsse T, 2001. An empirical model of glacio-isostatic movements and shore-level displacement in Fennoscandia. SKB R-01-41, Svensk Kärnbränslehantering AB.

Rhén I, Gustafson G, Stanfors R, Wikberg P, 1997. Äspö HRL – Geoscientific evaluation 1997/5. Models based on site characterization 1986–1995. SKB TR 97-06, Svensk Kärnbränslehantering AB.

Rhén I, Smellie J, 2003. Task force modelling of groundwater flow and transport of solutes. Task 5 summary report. (ISSN 1404-0344) SKB TR-03-01, Svensk Kärnbränslehantering AB.

Rhén I, Follin S, Hermanson J, 2003. Hydrological Site Descriptive Model – a strategy for its development during Site Investigations. SKB R-03-08, Svensk Kärnbränslehantering AB.

Rouhiainen P, Sokolnicki M, 2005. Difference flow logging in borehole KFM06A. SKB P-05-15, Svensk Kärnbränslehantering AB.

SKB, 2002. Forsmark – site descriptive model version 0. SKB R-02-32, Svensk Kärnbränslehantering AB.

SKB, 2004. Preliminary site description Forsmark area – version 1.1. SKB R-04-15, Svensk Kärnbränslehantering AB.

SKB, 2005a. Preliminary site description Forsmark area – version 1.2. SKB R-05-18, Svensk Kärnbränslehantering AB.

SKB, 2005b. Programme for further investigations of geosphere and biosphere. Forsmark site investigation. SKB R-05-14, Svensk Kärnbränslehantering AB.

SKB, 2005c. Hydrogeochemical evaluation. Preliminary site description Forsmark area – version 1.2. SKB R-05-17, Svensk Kärnbränslehantering AB.

SKB, 2006a. Site descriptive modelling Forsmark stage 2.1 – Feedback for completion of the site investigation including from safety assessment and repository engineering. SKB R-06-38, Svensk Kärnbränslehantering AB.

SKB, 2006b. Hydrogeochemical evaluation of the Forsmark site, modelling stage 2.1 – issue report. SKB R-06-69, Svensk Kärnbränslehantering AB.

SKB, 2006c. Hydrogeochemical evaluation. Preliminary site description Laxemar subarea – version 2.1. SKB R-06-70, Svensk Kärnbränslehantering AB.

SKB, 2006d. Beslut om placering av kärnborrhål KFM08D. Documentum 1062642, Svensk Kärnbränslehantering AB.

SKB, 2007. Prediction of hydraulic properties in KFM08D. Documentum 1071524, Svensk Kärnbränslehantering AB.

Stephens M B, Fox A, La Pointe P R, Isaksson H, Simeonov A, Hermanson J, Öhman J, 2007. Geology – Site descriptive modelling Forsmark stage 2.2. SKB R-07-45, Svensk Kärnbränslehantering AB.

Streltsova T D, 1988. Well testing in heterogeneous formations. John Wiley & Sons.

Terzaghi R, 1965. Sources of error in joint surveys. Geotechnique 15(3): 287–304.

Thiem G, 1906. Hydrologische Methoden, J M Gebhardt, Leipsig.

Thunehed H, Pitkänen T, 2007. Transient electromagnetic soundings at Forsmark and the regional surroundings. Estimations of depth to saline groundwater. Forsmark site investigation. SKB P-07-165, Svensk Kärnbränslehantering AB.

Tröjbom M, Söderbäck B, Johansson P-O, 2007. Hydrochemistry in surface water and shallow groundwater Site descriptive modelling SDM-Site Forsmark. SKB R-07-55, Svensk Kärnbränslehantering AB.

Waber H N, Smellie J A T, 2007. Boreholes KFM01D, KFM08C, KFM09B. Characterisation of pore water. Part 1 Diffusion experiments and pore-water data. Forsmark site investigation. SKB P-07-119, Svensk Kärnbränslehantering AB.

Waber H N, Smellie J A T, 2008. Characterisation of Pore Water in Crystalline Rocks, Paper accepted for publication in Appl. Geochem.

Werner K, Johansson P-O, 2003. Slug tests in groundwater monitoring wells in soil. Forsmark site investigation. SKB P-03-65, Svensk Kärnbränslehantering AB.

Werner K, Bosson E, Berglund S, 2006. Analysis of Water Flow Paths: Methodology and Example Calculations for a Potential Repository in Sweden, Ambio, 35(8), 425–434, Royal Swedish Academy of Science.

Werner K, Johansson P-O, Brydsten L, Bosson E, Berglund S, Tröjbom M, Nyman H, 2007. Recharge and discharge of near-surface groundwater in Forsmark. Comparison of classification methods. SKB R-07-08, Svensk Kärnbränslehantering AB.

Westman P, Wastegård S, Schoning K, Gustafsson B, Omstedt A, 1999. Salinity change in the Baltic Sea during the last 8,500 years: evidence, causes and models. SKB TR-99-38, Svensk Kärnbränslehantering AB.

Wikberg P, 1998. Äspö Task Force on modelling of groundwater flow and transport of solutes. SKB progress report HRL-98-07, Svensk Kärnbränslehantering AB.

Appendix A

Coupled groundwater flow and solute transport

Coupled groundwater flow and solute transport that gives rise to variations in salinity and hence fluid density can be modelled in several ways in CONNECTFLOW. Generally, salinity is modelled in terms of a number of groundwater constituents. This can be modelled either in terms of transport of mass fractions of each of the basic hydrochemical constituents, which are taken to be conservative, or in terms of transport of mass fractions of selected so-called reference waters. Either way, the transport equations are coupled with the overall mass conservation equation for groundwater.

The first approach involves solving transport equations for each of the major ions and stable isotope values with the transient groundwater flow, including a coupling back to the flow via spatial variations in groundwater density due to its varying composition. Since the raw hydrochemistry is analysed in terms of concentrations of major ions, then this option is attractive as it models what is measured. However, the number of transport equations that need to be solved is as large as the number of ions and isotope ratios that are required for the calibration, around ten. Also, it requires that boundary and initial conditions are specified in terms of ion concentrations. This is not entirely straightforward as the hydrochemical conceptual understanding has been developed in terms of the mixing of fractions of reference waters, so in order to specify a boundary condition at any time, one has to first work out the appropriate mixing fractions for that time, and then multiply these by the chemical compositions to get the concentrations of the individual components. Further, although simulating the evolution of ion concentration makes it easy to compare with borehole measurements, it can be difficult to interpret the overall 3D spatial distribution of ions and relate this to the hydrogeology.

In consequence, for this calibration stage it was felt more straightforward and informative to simulate the transport of mass fractions of so-called reference waters. It has to be accepted though that this option makes the approximation that the hydrochemical composition of a mixture of reference waters can be related linearly to the compositions of the individual reference waters (i.e. no reactions), and that transport properties of the major ions (e.g. diffusivities) are similar. (If necessary, these assumptions could be relaxed in stage 2.3.) By working in terms of the transport of reference waters it straightforward to implement the hydrochemical conceptual model and to illustrate how the mixing of the reference waters evolves in time on appropriate slices through the model, for example. At the borehole locations, the calculated reference water fractions can either be converted to concentrations and isotope ratios using the compositions in Table 3-14 and compared with the measured concentrations, or the reference water fractions can be compared with the mixing fractions calculated using hydrochemical Mixing and Mass-balance Modelling (M3) /Laaksoharju et al. 1999/.

The transport of the reference waters, or constituents, is described by equations representing advection, hydrodynamic dispersion and diffusion. The model of diffusion includes both diffusion within the water flowing within the fractures as well as the diffusive transfer between groundwater flowing in fractures and immobile water in the rock matrix between the fractures (Rock-Matrix Diffusion or RMD). The numerical approach used for RMD /Hoch and Jackson 2004/ is based on a method developed by /Carrera et al. 1998/, enhanced to enable potentially larger time steps to be taken. The approach combines an approximation that is accurate for small times with one that is accurate for long times, to give a representation of the diffusion into the rock matrix that is accurate for all times. At early times, the diffusion is represented in terms of the inverse of the square root of time, and at long times it is represented as a series of decaying exponentials. The approach is very efficient computationally, although it is necessary to make the assumption that the groundwater density does not vary in the rock matrix at each location.

In the modelling, the groundwater density and viscosity vary spatially in three dimensions based on equations of state that are a function of total groundwater salinity, total pressure, and temperature. The salinity for a given water composition is just the sum over reference waters of the product of the reference water fraction and the salinity of that reference water. The salinities for the reference waters were calculated from the Total Dissolved Solids (TDS, g L^{-1}) using:

Salinity = TDS / density (A-1)

where density is a function of salinity (and temperature, and total pressure). It was assumed that the data given in Table 3-14 were obtained under laboratory conditions. Therefore, it was assumed that the data correspond to a temperature of 20°C and pressure of one atmosphere. The density and viscosity were obtained using empirical correlations for NaCl type "*Deep Saline Water*" /see SKB 2005c, Kestin et al. 1981/. This corresponds to representing transport of equivalent NaCl for each water type. The approximation made is reasonable, but it will lead to the density and salinity being slightly underestimated for a calcium-rich solution such as the reference water referred to as *Deep Saline Water*.

Assuming a pressure profile down-core (surface ~1atm to ~25 MPa at depth), a salinity profile (surface 0‰ to 72.3‰ (Deep Saline) at depth), and a temperature range (surface 6°C; geothermal gradient 0.01°C m^{-1}; i.e. ~30°C at bottom of model), the groundwater density (ρ) can be calculated from the equation of state. At the surface, the density is around 1,000 kg m^{-3}; and at depth the density is around 1,056 kg m^{-3} (the deepest elevation modelled is 2,300 m RHB 70). The groundwater viscosity (μ) can be similarly calculated. At the surface, the viscosity is around $1.3\cdot10^{-3}$ Pa s^{-1} and at depth, the viscosity at depth is around $0.9\cdot10^{-3}$ Pa s^{-1}.

The equations used to represent the transport of fractions of reference waters, with rock-matrix diffusion, are:

Mass conservation for groundwater:

$$\frac{\partial(n_e\rho)}{\partial t}+\nabla\cdot(\rho\,\mathbf{q})=0 \qquad \text{(A-2)}$$

Transport of reference waters:

$$\frac{\partial(n_e\rho\sigma_i)}{\partial t}+\nabla\cdot(\rho\,\sigma_i\,\mathbf{q})=\nabla\cdot(n_e\,\rho\,\mathbf{D}\nabla\sigma_i)+\zeta\,\rho\,D_{\text{int}}\left.\frac{\partial\sigma_i'}{\partial w}\right|_{w=0} \qquad \text{(A-3)}$$

Rock-matrix diffusion:

$$\alpha_i\frac{\partial\sigma_i}{\partial t}=D_{\text{int}}\frac{\partial^2\sigma_i'}{\partial w^2} \qquad \text{(A-4)}$$

where σ_i is the mass fraction of reference water *i* in the water in the fracture system (mobile water); σ_i' is the mass fraction of reference water *i* in the water in the matrix (immobile water); ***q*** is the Darcy velocity:

$$\mathbf{q}=-\frac{k}{\mu}(\nabla p+\rho\,\mathbf{g}) \qquad \text{(A-5)}$$

D is the dispersion tensor; n_e is the kinematic porosity, ρ is the groundwater density, ζ is the specific surface area of the fractures D_{int} is the intrinsic (or effective) diffusion coefficient, α_i is the capacity factor for the rock matrix (which allows for sorption), *w* is a coordinate into the rock matrix, *k* is the permeability, μ is the fluid viscosity, *p* is residual pressure, *t* is time, and ***g*** is gravitational acceleration. All parameters use SI units.

In fact, the transport equations for the fractions of reference waters are not all independent. Since the sum of the reference water fractions must be equal to one, then it is not necessary to solve explicitly the transport equation for the final reference water. It can simply be evaluated as the remaining water fraction once the other reference water fractions have been computed at each time step.

Appendix B

Drill sites, boreholes and investigations

General

The geological description together with the hydrological, hydraulic and hydrochemical data gathered near the surface and at depth constitute cornerstones in the development of the Forsmark hydrogeological conceptual model. In this appendix we present a summary of the different investigations carried out, or planned to be carried out, in the Forsmark area.

The candidate area and its drill sites

Figure B-1 illustrates the candidate area with its twelve drill sites (DS). The candidate area is approximately 6 km long and 2 km wide, and the north-western part of the candidate area has been selected as the target area for the Complete Site Investigation phase /SKB 2005b/. Figure B-2 presents detailed maps of the drill sites. The work reported here addresses the data gathered in SKB's site characterisation database (Sicada) including data freeze 2.2. It is noted that some of the figures and tables in this section contain information about boreholes that belong, strictly speaking, to data freeze/stage 2.3. The boreholes in mind are the deep, core-drilled boreholes referred to as KFM02B, KFM08D, KFM11A and -12A, located at drill sites 2, 8, 11 and 12, respectively, and the shallow, percussion-drilled boreholes denoted by HFM33–38. The information from these four plus six boreholes was for most parts not available at the time of the work reported here.

Quaternary deposits and surface water hydrological investigations

Table B-1 lists the different kinds of near-surface single-hole investigations carried out, or planned to be carried out, in the Forsmark area with regard to the five data freezes 1.1–2.3. All together, about 70 boreholes (SFM-holes) will be drilled in the Quaternary deposits. About 60 of these will be terrestrial and ten will be marine/lacustrine; that is, drilled through the sea/lake sediments into the underlying till. So-called BAT filter tips are used to collect hydrogeological data in low-permeable sediments such as silt, gyttja and clay. Table B-2 lists the number of BAT tests, slugtests and pumping tests conducted. The hydraulic measurements carried out in the boreholes in the Quaternary deposits are summarised in /Johansson et al. 2005/ and /Johansson 2008/. The properties deduced for hydrogeological modelling of the Quaternary deposits in stages 1.2 and 2.2 are reported in /Bosson and Berglund 2006/ and /Bosson et al. 2008/, respectively. The surface runoff in the brooks, the surface water levels in the lakes and in the sea, and the groundwater levels in the boreholes drilled in the Quaternary deposits as well as in the bedrock are continuously monitored using SKB's hydrological monitoring system (HMS). Figure B-3 shows the network of boreholes used for monitoring the groundwater levels in the Quaternary deposits. Figure B-4 shows the location of stand pipes used for surface water level measurements in the lakes and in the sea. Figure B-5 shows the location of the discharge gauging stations used to monitor the runoff in the brooks.

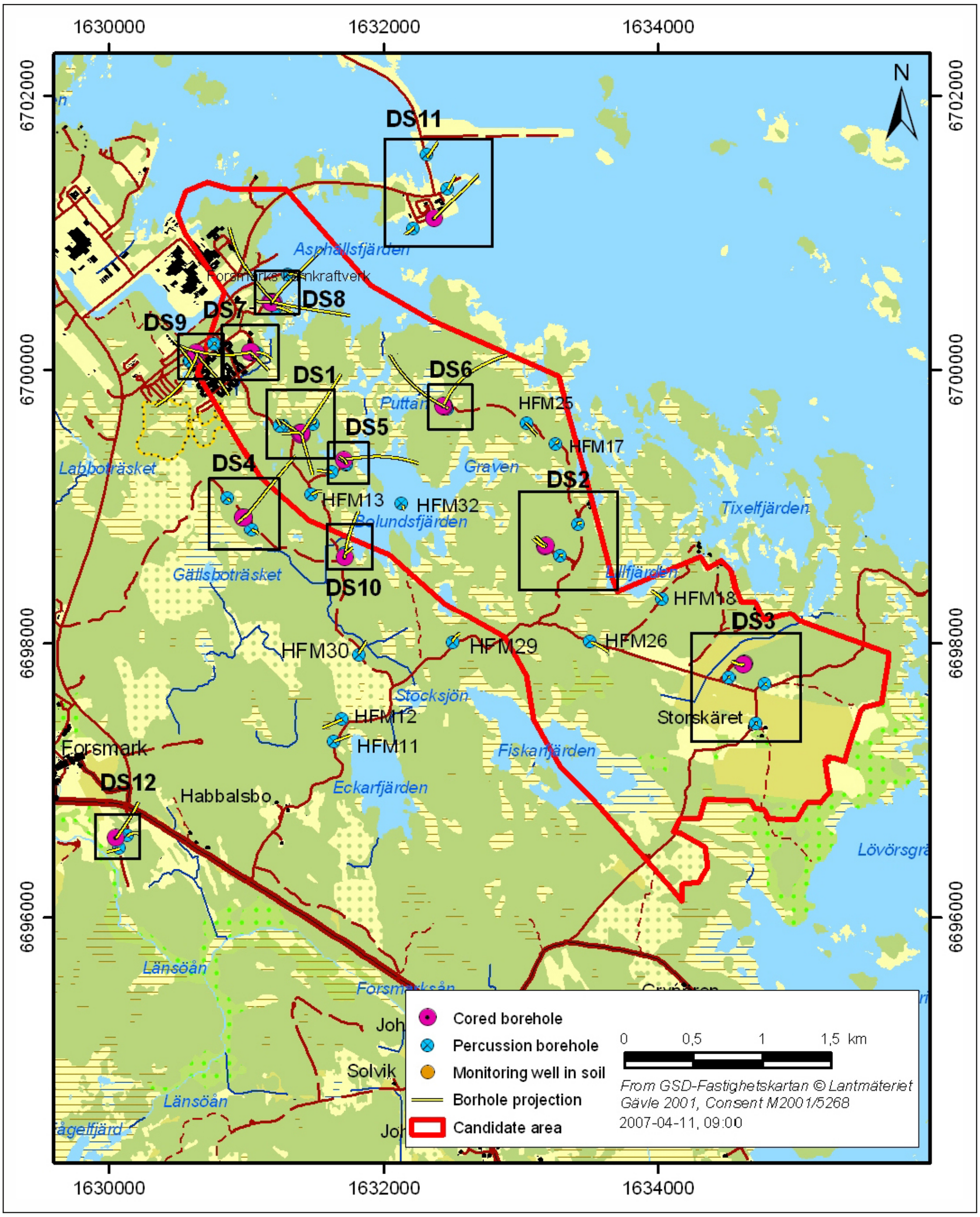

Figure B-1. Drill sites within and close to the candidate area in Forsmark. It is noted that some of the boreholes belong, strictly speaking, to data freeze/stage 2.3. The boreholes in mind are the deep, core-drilled boreholes referred to as KFM02B, KFM08D, KFM11A and -12A, located at drill sites 2, 8, 11 and 12, respectively, and the shallow, percussion-drilled boreholes denoted by HFM33–38. The information from these four plus six boreholes was for most parts not available at the time of the work reported here.

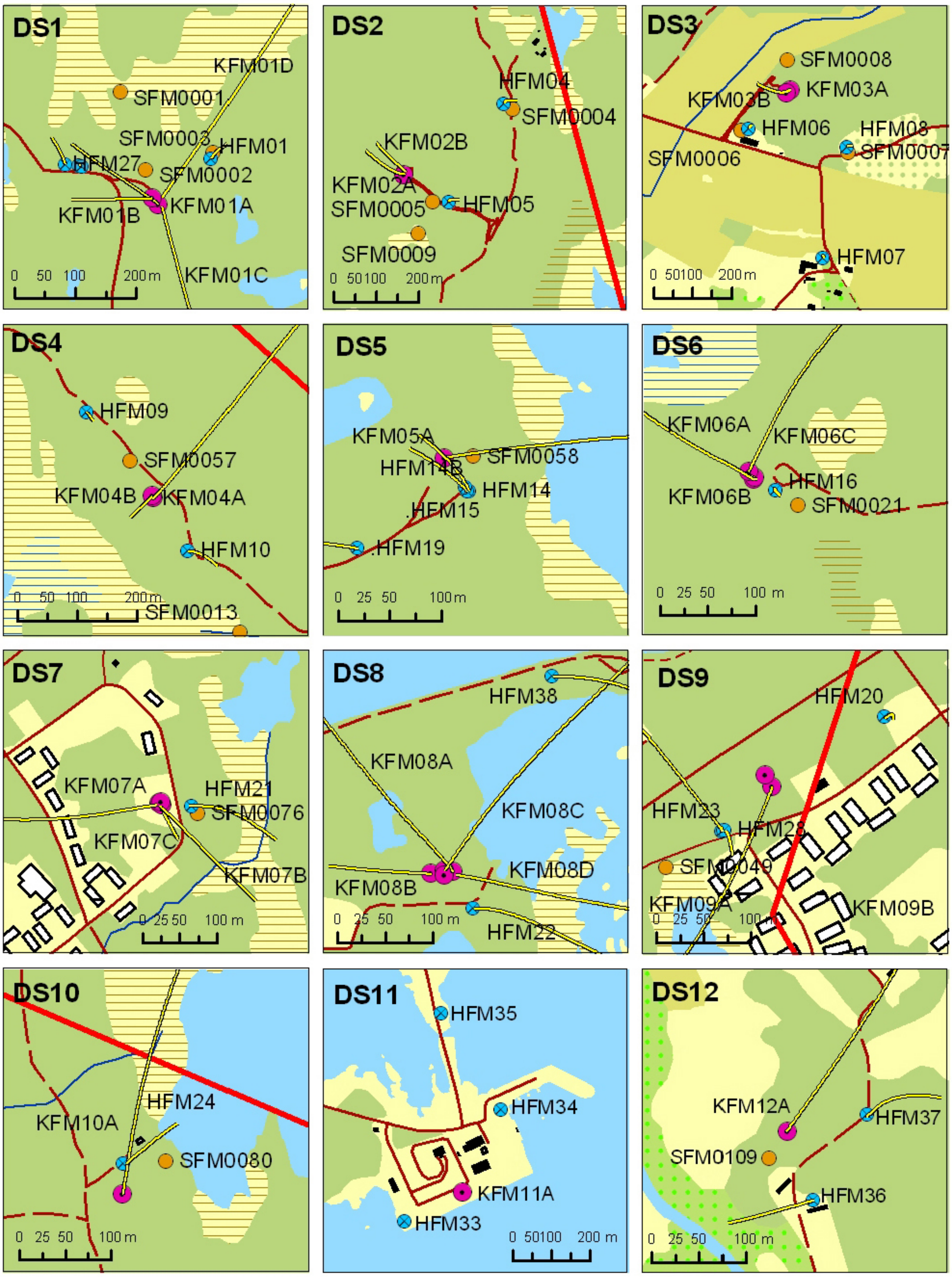

Figure B-2. *Detailed map of the drill sites in Forsmark. The legend is shown in Figure B-1. It is noted that some of the boreholes belong, strictly speaking, to data freeze/stage 2.3. The boreholes in mind are the deep, core-drilled boreholes referred to as KFM02B, KFM08D, KFM11A and -12A, located at drill sites 2, 8, 11 and 12, respectively, and the shallow, percussion-drilled boreholes denoted by HFM33–38. The information from these four plus six boreholes was for most parts not available at the time of the work reported here.*

Table B-1. List of completed and planned boreholes, BAT filter tips and stand pipes for groundwater (GW) levels and hydraulic conductivity (K) with regard to the different data freezes (DF) in Forsmark.

Type of installation	DF 1.1	DF 1.2	DF 2.1	DF 2.2	DF 2.3	Total
Monitoring wells for GW levels and K on land	32	13	3	10	2	60
Monitoring wells for GW levels and K below surface water	6	3	–	1	–	10
BAT filter tips for pore pressure and K	3	–	–	7	–	10
BAT filter tips for water sampling	3	–	–	7	–	10
Stand pipes for lake water levels	3	3	–	–	–	6
Stand pipes for sea water levels	2	–	–	–	–	2

Table B-2. List of completed and planned single-hole slug tests and pumping tests in Quaternary deposits with regard to the different data freezes (DF) in Forsmark.

Type of installation	DF 1.1	DF 1.2	DF 2.1	DF 2.2	DF 2.3	Total
BAT tests	3	–	–	7	–	10
Slug tests	36	12	–	11	–	59
Pumping tests	–	2	–	3	–	5

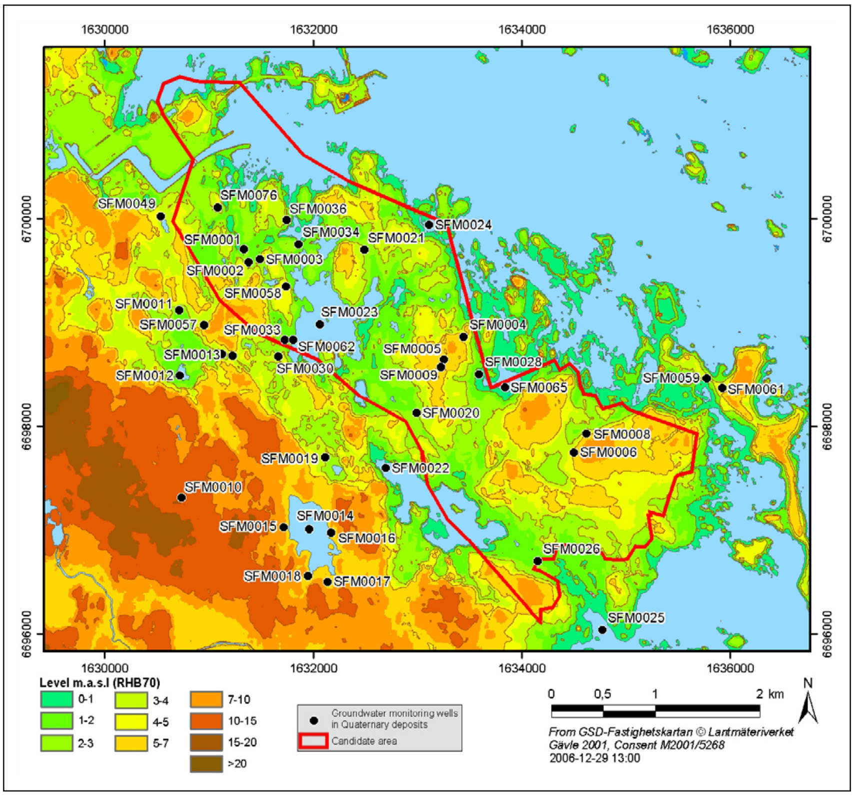

Figure B-3. Locations of groundwater level monitoring wells in Quaternary deposits. Reproduced from /Juston et al. 2007/.

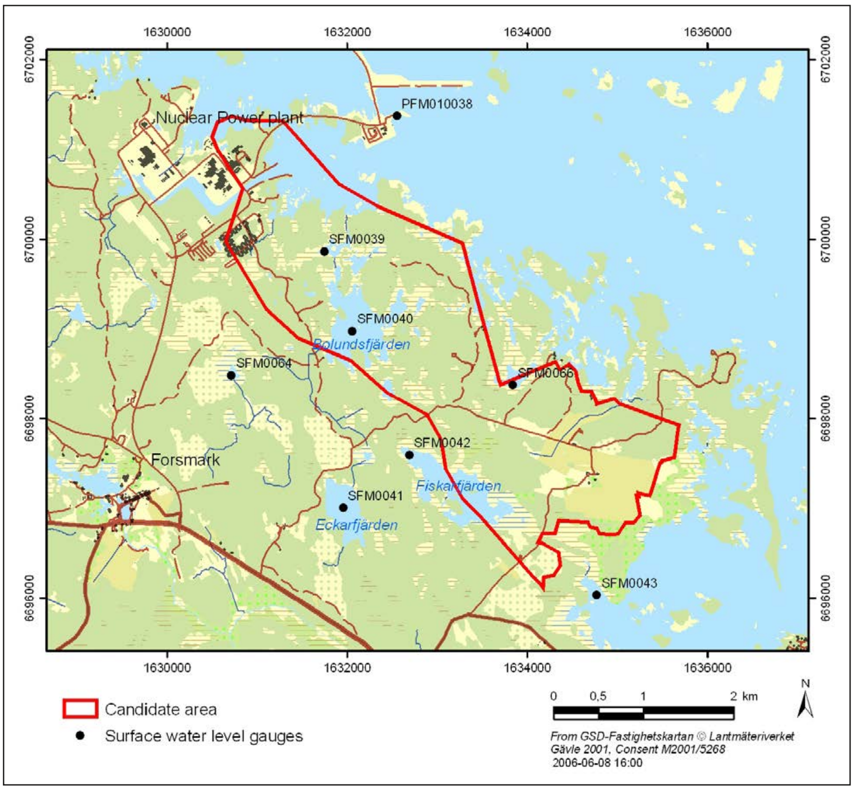

Figure B-4. *Locations of the surface water level gauges. Reproduced from /Juston et al. 2007/.*

Figure B-5. *Locations of discharge gauging stations. Reproduced from /Johansson and Juston 2007/.*

The hydrological time series data gathered are analysed and reported in /Juston and Johansson 2005, Johansson et al. 2005, Juston et al. 2007, Johansson and Juston 2007, Johansson 2008/. The diurnal variations in the monitoring data are modelled in version 1.2 by /Bosson and Berglund 2006/ and in stage 2.2 by /Bosson et al. 2008/. The findings are summarised in /Johansson 2008/. The surface/near-surface modelling is made in 3D using the MIKE SHE code /DHI 2004/.

Mean values of the groundwater level measurements carried out in the Quaternary deposits and the percussion-drilled boreholes are used for the confirmatory testing task referred to as Task C in Figure 1-2.

Single-hole hydraulic bedrock investigations

Figure B-6 shows a map of completed, ongoing and upcoming core-drilled boreholes (KFM-holes) at the time of data freeze 2.2. The map in Figure B-7 shows the corresponding information for the percussion-drilled boreholes (HFM-holes). It is noted that the geological map in these two figures represents the geological interpretation from version 1.2 /SKB 2005a/.

Table B-3 lists the boreholes with regard to the geological information acquired at the time of the different data freezes (stages). Currently, there are 25 core-drilled and 38 percussion-drilled boreholes planned for the site investigations in Forsmark. Table B-4 lists which of the cored boreholes are or will be investigated with the Posiva Flow Log (PLF) unit and the Pipe String System (PSS) unit, respectively. All percussion-drilled boreholes are investigated with the HTHB unit (combined pumping and impeller flow logging) except those with a very poor yield. A detailed description and analysis of the data gathered advantages and disadvantages of using the different test methods is provided in /Follin et al. 2007b/. The data from 20 m section PSS tests are used for the confirmatory testing task referred to as Task A in Figure 1-2.

Table B-3. List of cored and percussion-drilled boreholes with regard to the different data freezes in Forsmark.

Data freeze	No. of core drilled boreholes	KFM-hole	No. of percussion drilled boreholes	HFM-hole
1.1 *2003-04-30*	1	KFM01A	8	HFM01–08
1.2 *2004-07-31*	5	KFM02A–05A KFM01B	11	HFM09–19
2.1 *2005-07-29*	4	KFM06A–07A KFM03B, -06B	3	HFM020–22
2.2 *2006-09-30*	11	KFM08A–10A KFM06B–09B KFM01C, KFM07C–08C KFM01D	10	HFM23–32
2.3 *2007-03-31*	4	KFM11A–12A KFM02B KFM08D	6	HFM33–38
All	25	KFM01A–12A KFM01B–03B KFM06B–09B KFM01C, KFM07C–08C KFM01D, -08D	38	HFM01–38

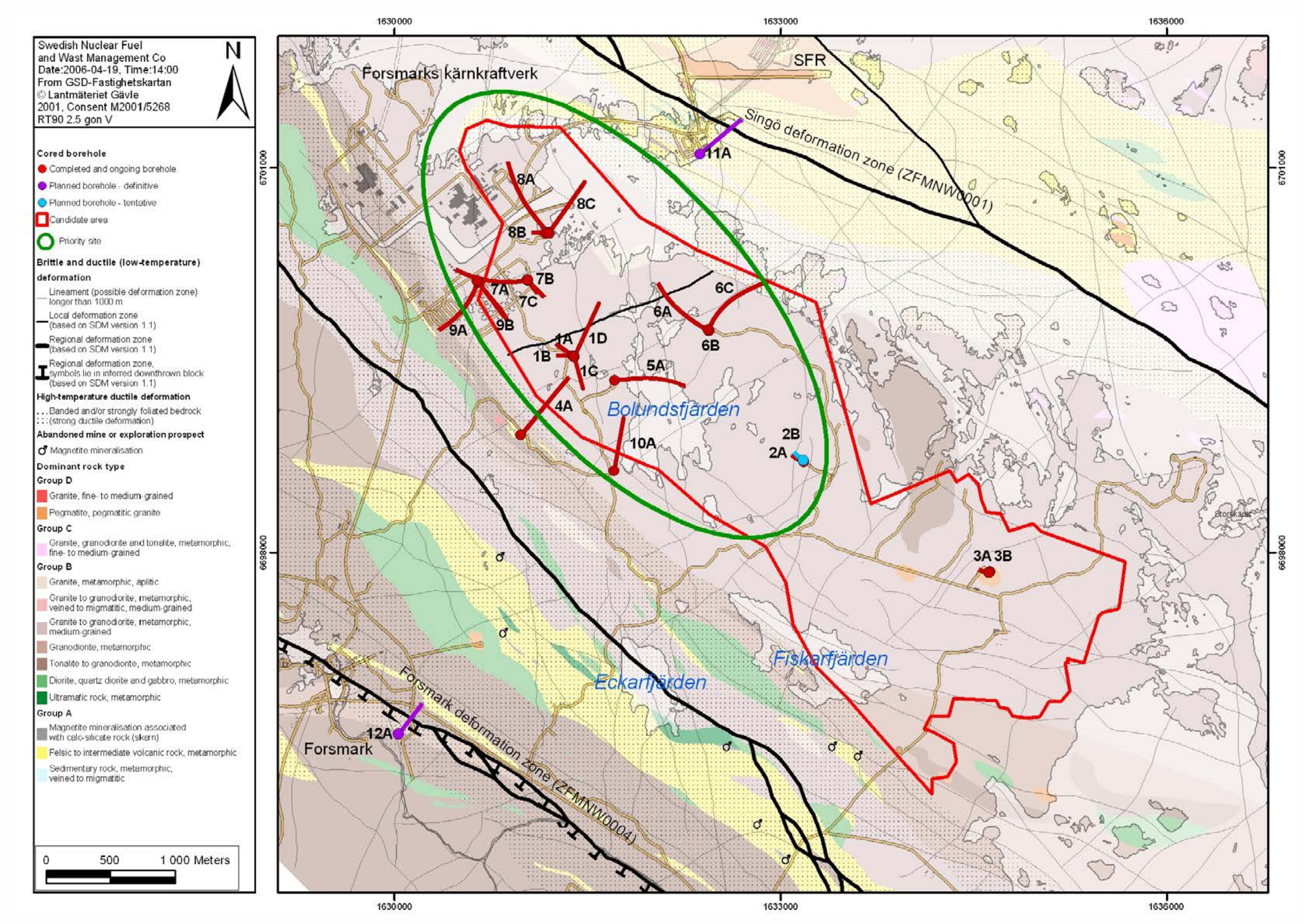

Figure B-6. Completed, ongoing and planned core-drilled boreholes in Forsmark (2006-05-31). The underlying geological map is from version 1.2 /SKB 2005a/. The green ellipse shows the location of the target area.

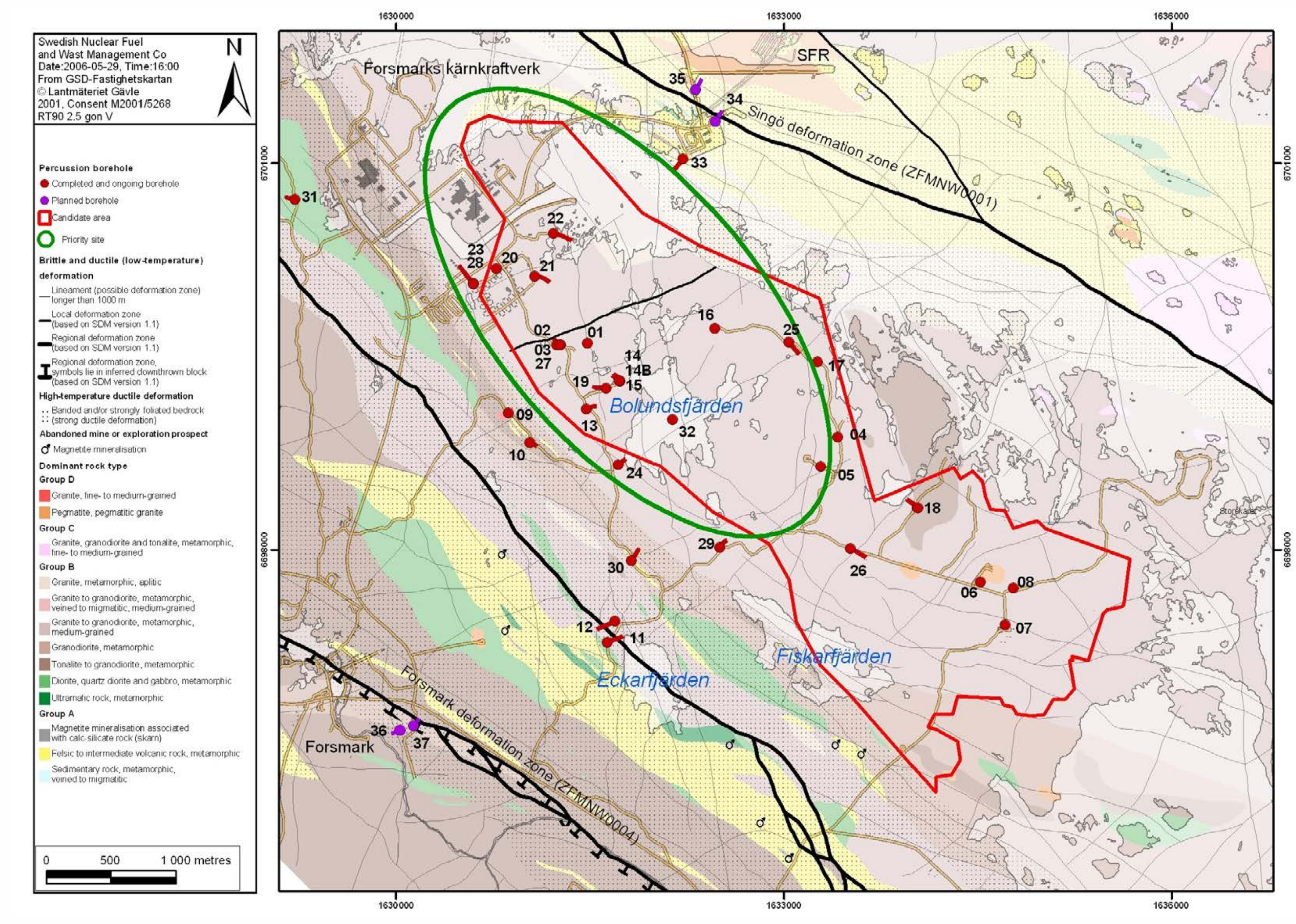

Figure B-7. Completed and upcoming percussion-drilled boreholes in Forsmark (2006-05-31). The underlying geological map is from version 1.2 /SKB 2005a/. The green ellipse shows the location of the target area.

Table B-4. List of PFL and PSS tests, cf. Table B-3.

Data freeze	No. of PFL tested boreholes	Tested boreholes KFM-hole	No. of PSS tested boreholes	Tested boreholes KFM-hole
1.1 *2003-04-30*	1	KFM01A	0	–
1.2 *2004-07-31*	4	KFM02A–05A	3	KFM01A–03A
2.1 *2005-07-29*	2	KFM06A–07A	6	KFM04A–07A KFM03B, -06B
2.2 *2006-09-30*	5	KFM08A, -10A KFM07C–08C KFM01D	8	KFM08A–09A KFM07B–09B KFM01C, -06C KFM01D
2.3 *2007-03-31*	3	KFM11A KFM07C KFM08D	7	KFM10A–12A KFM02B KFM07C–08C KFM08D
All	15	KFM01–08A KFM10A–11A KFM02B KFM07C–8C KFM01D, -08D	24	KFM01A–12A KFM02B–03B, KFM06B–09B KFM01C, KFM06C–08C KFM01D, -08D

Cross-hole hydraulic bedrock investigation

Table B-5 shows completed, ongoing and upcoming pumping tests with the potential to reveal hydraulic properties in the bedrock between adjacent boreholes; that is, cross-hole investigations (interference tests). The most important interference test for the numerical modelling carried out in the work reported here is the interference test conducted year 2006 in HFM14 /Gokall-Norman and Ludvigson 2006/. The data from this interference test are used for the confirmatory testing task referred to as Task B in Figure 1-2.

Table B-5. List of pumping tests in the bedrock intended to function as interference tests.

Data freeze	Pumped borehole	Duration	Target of investigation
1.1 *2003-04-30*	HFM01 HFM02	7 hr 6 hrs	Connectivity between horizontal sheet joints and A2
1.2 *2004-07-31*	HFM11	4 hrs	Eckarfjärden deformation zone
2.1 *2005-07-29*	HFM16 HFM16 HFM18 KFM04A KFM02A	4 hrs 1 day 2 days 5 days 8 days	– A2 – A2 – A4 in hanging wall of A2 – Extent of A2 to southwest – A3 in hanging wall of A2
2.2 *2006-09-30*	HFM01 HFM14	3 weeks 3 weeks	Connectivity between horizontal sheet joints and A2
2.3 *2007-03-31*	–	–	–
Posterior 2.3 *2007-12-31*	KFM02B	8 weeks	– Tracer transport properties in A2 at repository depth
	HFM14	12 weeks	– Tracer transport properties in A2 near surface
	HFM33	not decided yet	– Connectivity of horizontal sheet joints across Singö deformation zone and Asphällsfjärden
	HFM14	not decided yet	– Connectivity with KFM08D

Hydrochemical investigations

The hydrochemical programme encompasses the following constituents:

- major cations and anions (Na, K, Ca, Mg, Si, Cl, HCO_3^-,SO_4^{2-}, S^{2-}),
- trace elements (Br, F, Fe, Mn, Li, Sr, DOC, N, $PO4^{3-}$, U, Th, Sc, Rb, In, Cs, Ba, Tl, Y and REEs),
- stable isotopes (^{18}O, ^{2}H, ^{13}C, ^{37}Cl, ^{10}B, ^{34}S),
- radioactive-radiogenic isotopes (^{3}H, ^{226}Ra, ^{228}Ra, ^{222}Rn, ^{238}U, ^{235}U, ^{234}U, ^{232}Th, ^{230}Th and ^{228}Th),
- microbes, gases and colloids.

The hydrochemical programme in the bedrock and in the Quaternary deposits has been carried out in the same boreholes as the hydrogeological investigations. Figure B-8 shows a map of the sampling locations for the surface water hydrochemistry.

The hydrochemistry available for the confirmatory testing task referred to as Task D in Figure 1-2 (palaeohydrology) was delivered in Excel format in January 2007. Besides fracture water chemistry the database includes pore water hydrochemistry of fresh rock samples.

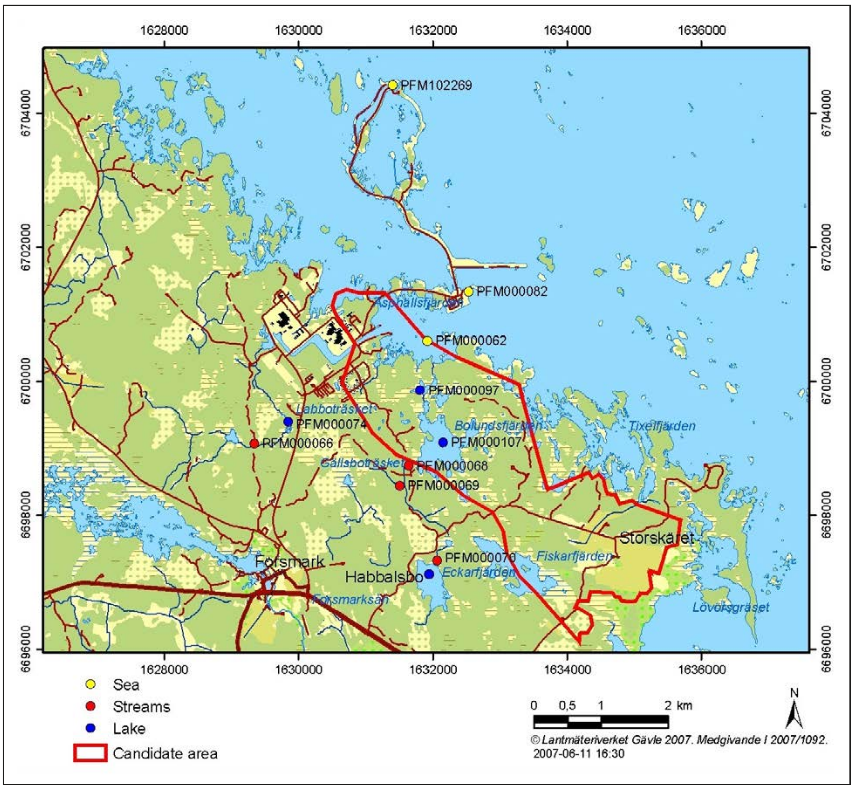

Figure B-8. *Sampling locations for surface water hydrochemistry. Reproduced from /Nilsson and Borgiel 2007/.*

Appendix C

Comparison of DFN model parameters

General

The Geo-DFN and Hydro-DFN modelling tasks were run in parallel in stage 2.2. We present below a simplified comparison between the Geo-DFN and the Hydro-DFN results for fracture domain FFM01, the key fracture domain for a repository in the Forsmark area. The comparison is focussed on the so-called tectonic continuum model.

Background

The geological DFN (Geo-DFN) modelling conducted in stage 2.2 /Fox et al. 2007/ entails different sorts of geological and geophysical data on different spatial scales (lineament data, outcrop data and borehole data). The data were analysed with regard to *a number of different orientation, size, intensity and spatial models* and geological DFN (Geo-DFN) properties were derived for fracture domains FFM01–03 and -06. The Geo-DFN was made without consideration to fracture aperture; that is, the identification of fracture sets and their specific properties (sizes and intensities) were deduced for all fractures (no distinction between sealed and open fractures was made). Moreover, the Geo-DFN modelling did not consider fracture connectivity or hydraulic data such as transmissivity data measured with the PFL-f method.

In comparison, the hydrogeological DFN (Hydro-DFN) modelling conducted in stage 2.2 /Follin et al. 2007b/ was based on data gathered on a single spatial scale, i.e. fracture data and hydraulic data from boreholes. In order to circumvent the lack of geometrical information that follows from this constraint, several geometrical assumptions were invoked. We note in particular the assumptions: (*i*) the global orientation model derived in version 1.2 is appropriate for use also in stage 2.2, (*ii*) the number of features of different sizes follows a power-law relationship, i.e. a tectonic continuum is envisaged (Figure 2-4), and (*iii*) the connectivity of flowing fractures can be appreciated from a connectivity analysis of open fractures that is calibrated against the frequency of flowing fractures observed with the PFL-f method. We present below a simplified comparison between the parameter values derived in the Geo-DFN and Hydro-DFN modelling for the first two assumptions.

Comparison of fracture orientations (fracture sets)

Figure C-1 shows three strereonets of fracture sets. The upper left image shows fracture sets reported from the Geo-DFN modelling conducted in stage 2.2. The upper right image shows the fracture sets reported from the Geo-DFN modelling conducted in version 1.2 /La Pointe et al. 2005/. Pending the results from the Geo-DFN modelling in stage 2.2, /Follin et al. 2007b/ assumed that the version 1.2 fracture sets were appropriate for Hydro-DFN modelling in stage 2.2. Apart from one fracture set (ENE) we conclude that the differences in mean trend and plunges are small. The differences in Fisher concentration are also small except for the sub-horizontal (HZ) set.

As mentioned in Section 3.10.2 suggestions for alternative Fisher orientation distributions were made by /Follin et al. 2007b/. These are shown in the lower image in Figure C-1. Significant properties of the alternative Hydro-DFN for stage 2.2 are the higher Fisher concentration in the sub-horizontal (HZ) set and the convergence of the NS and NE sets. According to the findings reported by /Follin et al. 2007c/ this may lead to stronger horizontal versus vertical anisotropy of fracture flow and also toward NNE within the horizontal direction.

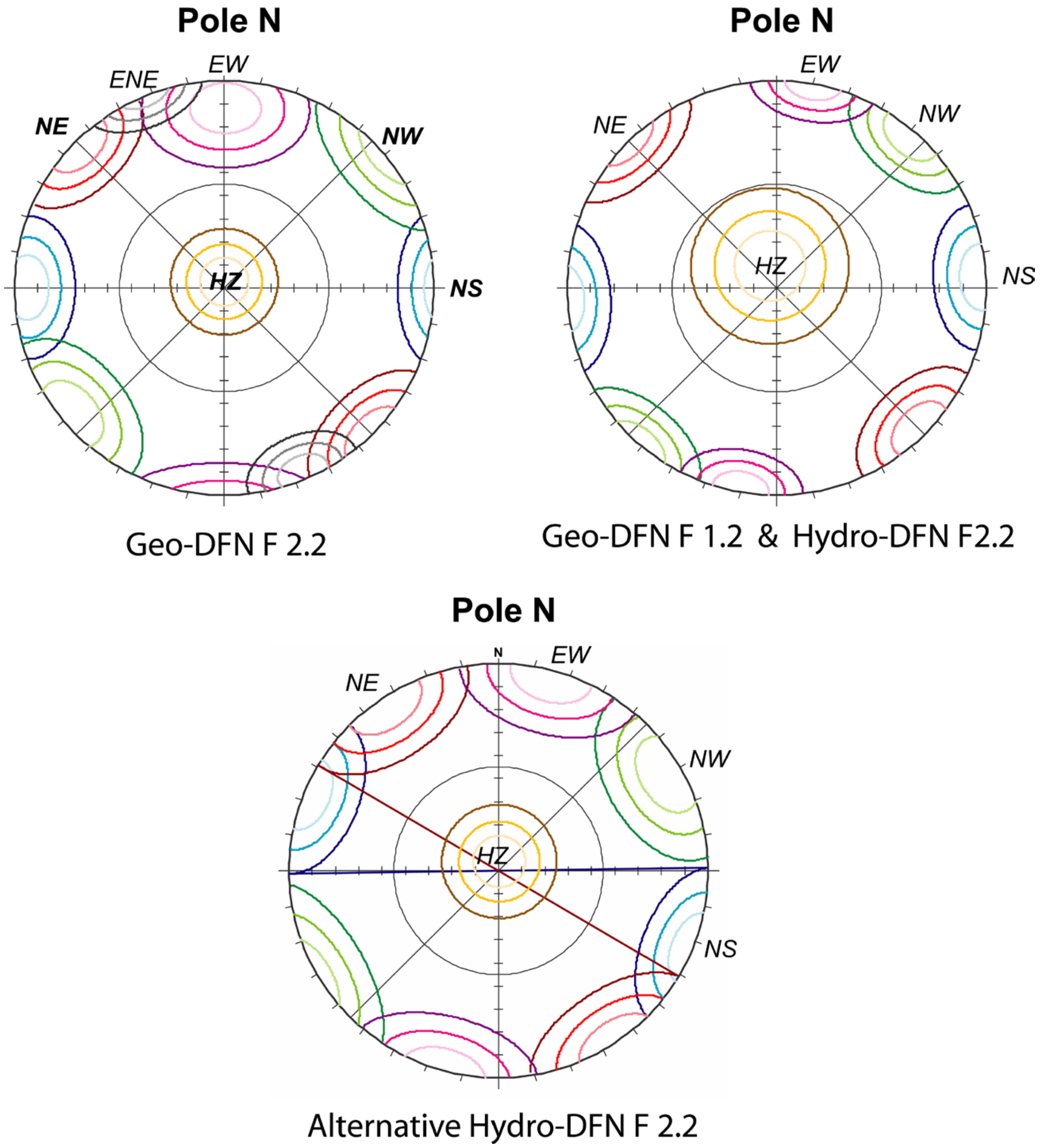

Figure C-1. *Three lower hemisphere strereonets of fracture sets. Upper left: Fracture sets reported from the Geo-DFN modelling conducted in stage 2.2. Upper right: fracture sets reported from the Geo-DFN modelling conducted in version 1.2. Bottom: Alternative fracture sets suggested by /Follin et al. 2007b/. Each fracture set is represented in terms of three coloured lines. These illustrate probability contours – 25%, 50% and 75%. That is, the innermost contour captures 25% of the dispersion around the mean trend and plunge for that fracture set and the outermost contour captures 75% of the dispersion.*

Comparison of fracture size and intensity

The Geo-DFN modelling in stage 2.2 analysed different types of fracture size-intensity relationships/models. We restrict the comparison with the Hydro-DFN modelling to the so-called "tectonic continuum" (TC) model, which prescribes a continuous power-law size-intensity relationship (cf. Figure 2-4). The power-law function for the cumulative fracture surface area per unit volume of rock (intensity P_{32}) can be written as:

$$P_{32}(r \ge r_1) = P_{32}(r \ge r_0)\left(\frac{r_0}{r_1}\right)^{(k_r-2)} \qquad \text{(C-1)}$$

where

r = fracture radius , $r_0 < r_1$
k_r = shape factor , $k_r > 2$
r_0 = location factor

The Hydro-DFN modelling in stage 2.2 assumed that the location factor is equivalent to the borehole radius of the drill cores, i.e. $r_0 = 0.038$ m. Figure C-2 through Figure C-4 shows five plots, one for each fracture set (NS, NE, NW, EW and HZ). In these plots r_1 is set to 564 m, which implies a fracture area of 10^6 m^2. Discrete features above this size are modelled deterministically in SKB' systems approach (cf. Section 2).

The fracture surface intensity of all (sealed + open) fractures is by definition greater than the intensity of open fractures. For large fracture radii, e.g. features greater than 100 m of radius, it is envisaged that most fractures become more or less open, i.e. the sealed fractures become partly open. Hence, the intensity of "all" fractures should approach the intensity of "open" fractures for large values of the fracture radius.

Among the five plots shown in Figure C-2 through Figure C-4 the behaviour envisaged above is observed for the NS fracture set and, perhaps, the HZ and the NE fracture sets. Given the many uncertainties involved in the discrete fracture network (DFN) concept /Munier 2004/ we conclude that the analysis of the differences seen in the five plots cannot be sufficiently dealt with based on the information handled in this appendix alone.

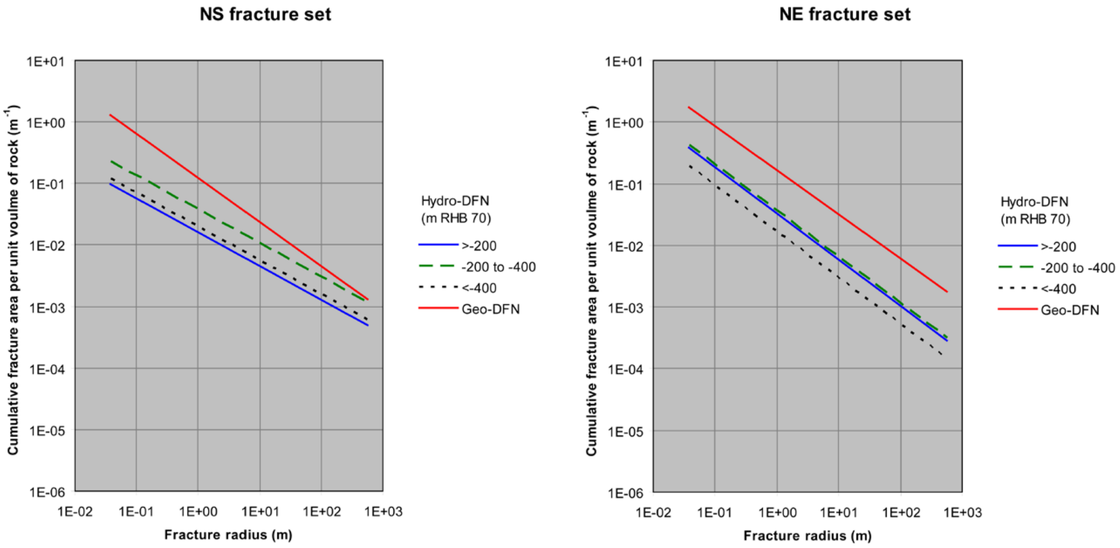

Figure C-2. *Plots of fracture surface area per unit volume of rock (intensity P_{32}) vs. fracture size for the NS fracture set (left) and the NE fracture set (right). The plots are based on the results of stage 2.2 reported by /Fox et al. 2007/ (Geo-DFN) and /Follin et al. 2007b/ (Hydro-DFN).*

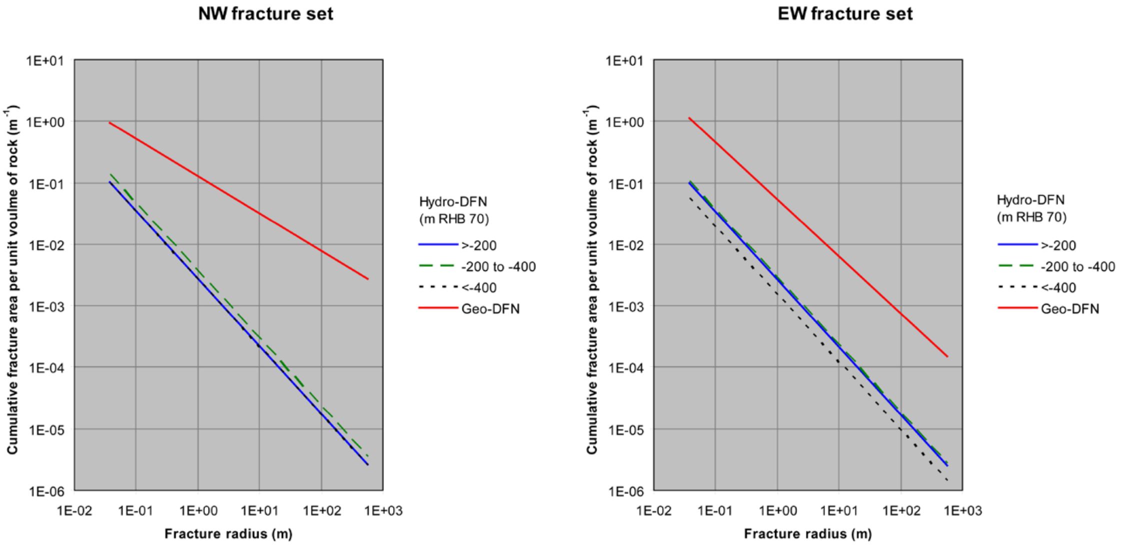

***Figure C-3.** Plots of fracture surface area per unit volume of rock (intensity P_{32}) vs. fracture size for the NW fracture set (left) and the EW fracture set (right). The plots are based on the results for stage 2.2 reported by /Fox et al. 2007/ (Geo-DFN) and /Follin et al. 2007b/ (Hydro-DFN).*

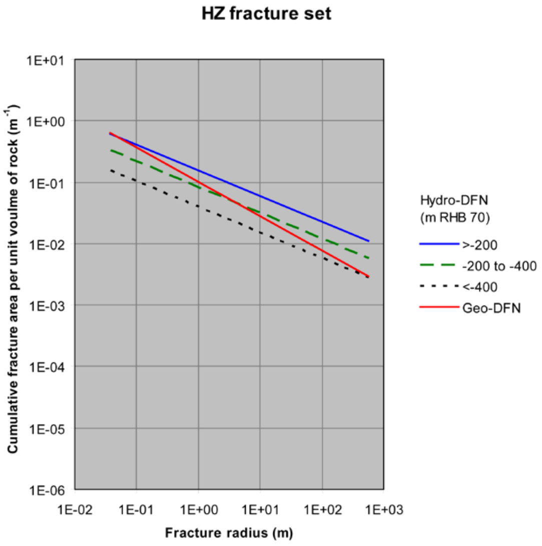

***Figure C-4.** Plot of fracture surface area per unit volume of rock (intensity P_{32}) vs. fracture size for the HZ fracture set. The plot is based on the results for stage 2.2 reported by /Fox et al. 2007/ (Geo-DFN) and /Follin et al. 2007b/ (Hydro-DFN).*

A prediction of hydraulic properties along KFM08D

Background

The deformation zone model in stage 2.2 is based on various kinds of geological and geophysical data. An interesting piece of geophysical information revealed during the later part of the site investigations conducted prior to data freeze 2.2 (2007-09-29) is the structural interpretation of high resolution ground magnetic measurements, see Appendix H. The interpretation suggests a large number of lineaments with a NNE direction in the central and northern parts of the target area. Among the existing cored boreholes it was concluded, at the time, that KFM06A was more or less the only borehole that could provide hydrogeological information at depth of possible deformation zones striking NNE. However, KFM06A did not investigate the hydraulic properties in FFM06 at repository depth. Therefore, it was decided to drill a new borehole, KFM08D /SKB 2006d/. The trajectory of KFM08D is displayed in Figure 3-18 and Figure B-2 in Appendix B. Figure D-1 shows the location of KFM08D with regard to existing cored boreholes, deformation zones traces (version 2.1) at 400 m depth and a tentative repository layout (D1).

A prediction of the hydraulic information along KFM08D was made /SKB 2007/ based the deformation zone model deduced in stage 2.2 /Stephens et al. 2007/. A summary of this prediction is given below.

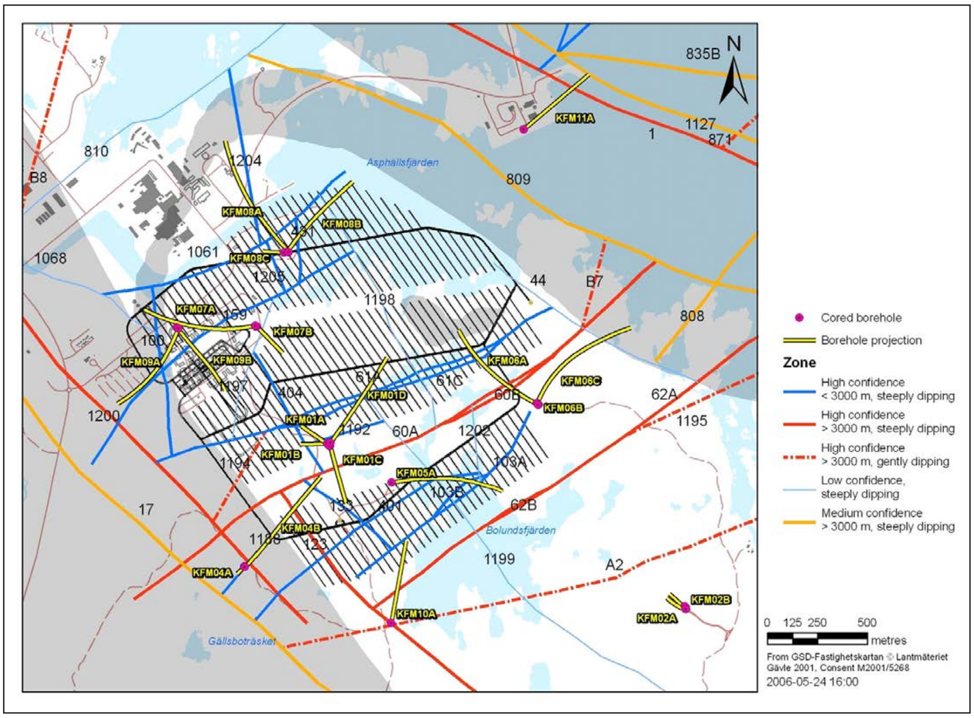

Figure D-1. An illustration showing the location of KFM08D with regard to existing cored boreholes, deformation zones traces (version 2.1) at 400 m depth and a tentative repository layout (version D1). Modified after /SKB 2006a/.

Summary

Figure D-2 shows a horizontal slice through the deformation zone model in stage 2.2. Within the local area the traces of the deformation zones are coloured red, outside they are coloured orange. The location and trajectory of KFM08D is indicated with a yellow line.

Table D-1 shows the predicted intercepts of eight deterministically modelled deformation zones with the trajectory of KFM08D. The prediction is made in SKB's rock visualisation system, RVS. All of the eight deformation zones are steeply dipping and they represent three different orientation sets ENE (-2120, -0159A, -0159B, -2320), NNE (-2309, -2308, -2293) and WNW (-2225). A prediction of the contact between rock domains RFM029 and RFM045, which in this case is equivalent to the contact between fracture domains FFM01 and FFM06, is also shown in Table D-1.

Table D-2 collates the structural geology data presented in Table E-1 in a format that allows for an integration of the hydraulic results (transmissivities) from the PFL-f tests planned to be carried out in KFM08D. The average hydraulic properties in KFM08D, i.e. the number of PFL-f flow anomalies and their cumulative transmissivity value, Σ T PFL-f , were estimated from a comparison with the joint structural-hydraulic data acquired in the eight neighbouring boreholes, KFM01A, -01D, -05A, -06A, -07A, -07C, -08A and -08C, see Figure D-3. /SKB 2007/ provides a detailed presentation of the data and the analyses carried out.

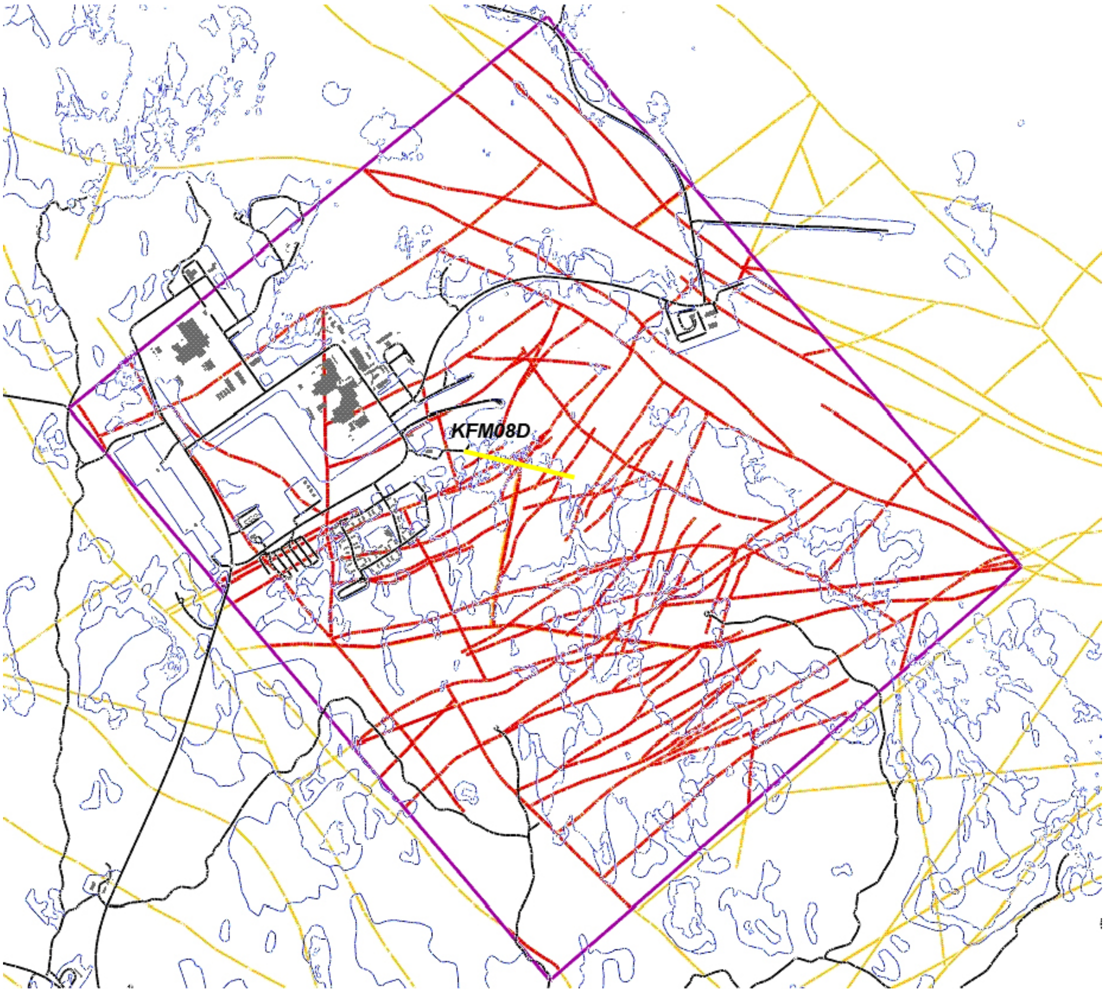

Figure D-2. Horizontal slice through the deformation zones that have been modelled deterministically in stage 2.2. The purple lines indicate the local model area in Forsmark (about 3.7 km by 3.1 km). Traces at –10 m RHB 70 are shown. Within the local area the traces of the deformation zones are coloured red, outside they are coloured orange. The location and the projected trajectory of KFM08D are indicated.

Table D-1. Prediction of intercepts with deterministically modelled deformation zones along the trajectory of KFM08D, and with boundary between fracture domains FFM01 and FFM06. The total length of KFM08D is expected to be 942 m.

Feature #	Deformation zone or fracture domain	Upper/lower intercept, (m borehole length)	Upper/lower intercept, (m RHB 70)
1	ENE2120 – upper	208	–168
1	ENE2120 – lower	234	–189
2	ENE0159A – upper	319	259
2	ENE0159A – lower	359	–292
3	ENE0159B – upper	386	–314
3	ENE0159B – lower	404	–328
4	NNE2309 – upper	441	–358
4	NNE2309 – lower	456	–371
5	NNE2308 – upper	617	–503
5	NNE2308 – lower	639	–521
6	EnE2320 – upper	685	–559
7	NNE22293 – upper	738	–602
6	EnE2320 – lower	760	–620
7	NNE2293 – lower	761	–621
8	WNW2225 – upper	919	750
8	WNW2225 – lower	?	?
9	FFM06 – upper	404	–329

Table D-2. Compilation of structural geology and average hydraulic data predicted for KFM08D. The columns show rock domain (RFM), deformation zone (ZFM), fracture domain (FFM), borehole length [m] (Secup/Seclow) and elevation [m RHB 70] (Depthup/Depthlow).

RFM	ZFM	FFM	Secup	Seclow	Depthup	Depthlow	No. PFL-f	Σ T PFL-f
29		FFM01	–	208	–	–168	14	1E–5
29	ENE2120		208	234	–168	–189	>1	1E–5
29		FFM01	234	319	–189	–259	6	2E–8
29	ENE0159A		319	359	–259	–292	>1	3E–8
29		FFM01	359	386	–292	–314	2	2E–8
29	ENE0159B		386	404	–314	–328	>1	3E–8
45		FFM06	404	441	–327	–358	1	1.4E–9
45	NNE2309		441	456	–358	–371	>1	3E–8
45		FFM06	456	617	–371	–503	0	Nil
45	NNE2308		617	639	–503	–521	>1	1E–8
45		FFM06	639	685	–521	–559	0	Nil
45	NNE2320		685	760	–559	–620	>1	3E–9
45	NNE2293		738	761	–602	–621	>1	3E–8
45		FFM06	761	919	–621	–750	0	Nil
45	WNW2225		919	942+	–750	–782+	>1	1E–9

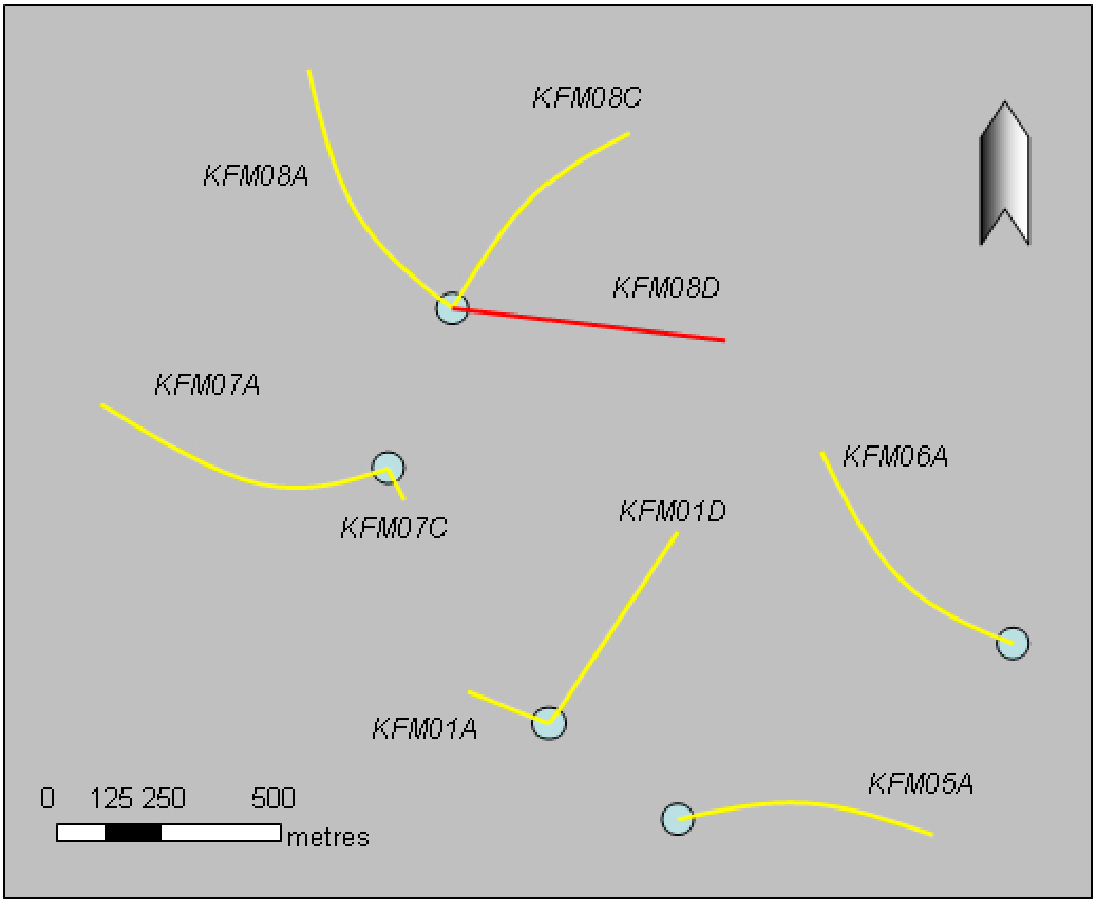

Figure D-3. *A plan view of neighbouring boreholes with regard to KFM08D. All boreholes, except KFM07C, are c. one kilometre long and investigated with the PFL-f method.*

Appendix E

Cumulative density function plots of the dip angle of PFL-f data

Background

The PFL-f data used to calibrate the Hydro-DFN parameters are performed in steeply dipping boreholes (60–90°), so they are largely measuring radial horizontal flow. Hence, our understanding of vertical flows through the fracture network is more uncertain. The Terzaghi correction method /Terzaghi 1965/ was used to estimate the change in the distribution of the dip angle of the PFL-f data. The value of Terzaghi weight was set to 7, which means that the largest angle between the borehole axis and a flowing fracture not affected by the correction was about eight degrees.

We first divided the PFL-f data into three structural segments with regard to the shape of lens and the dominant and gently-dipping deformation zone referred as A2:

- PFL-f data in the bedrock bordering the tectonic lens.
- PFL-f data in the hanging wall bedrock of A2.
- PFL-f data in the footwall bedrock of A2.

Secondly, we divided the PFL-f data in the footwall bedrock into four data sets with regard to fracture domains FFM01 and FFM02:

- PFL-f data in fracture domain FFM02 (excl. ZFM): –100 to –200 m RHB 70.
- PFL-f data in fracture domain FFM01(excl. ZFM): –100 to –200 m RHB 70.
- PFL-f data in fracture domain FFM01(excl. ZFM): –200 to –400 m RHB 70.
- PFL-f data in fracture domain FFM01(excl. ZFM): –400 to –1,000 m RHB 70.

Results

The seven plot suggest that there are clear differences between the hanging wall and the footwall segments and that about 60% of the Terzaghi corrected PFL-f data in the footwall segment has a dip angle of less 25° regardless of fracture domain and elevation.

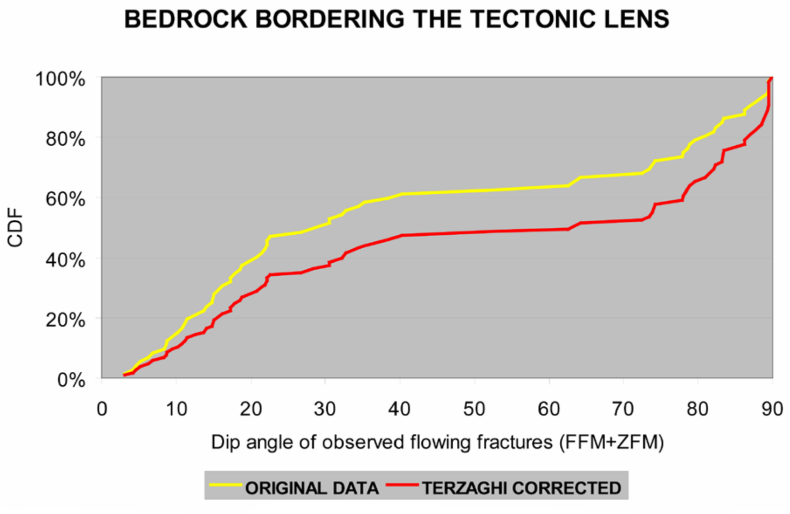
BEDROCK BORDERING THE TECTONIC LENS
100%
80%
60%
40%
20%
0%
CDF
0
10
20
30
40
50
60
70
80
90
Dip angle of observed flowing fractures (FFM+ZFM)
ORIGINAL DATA
TERZAGHI CORRECTED

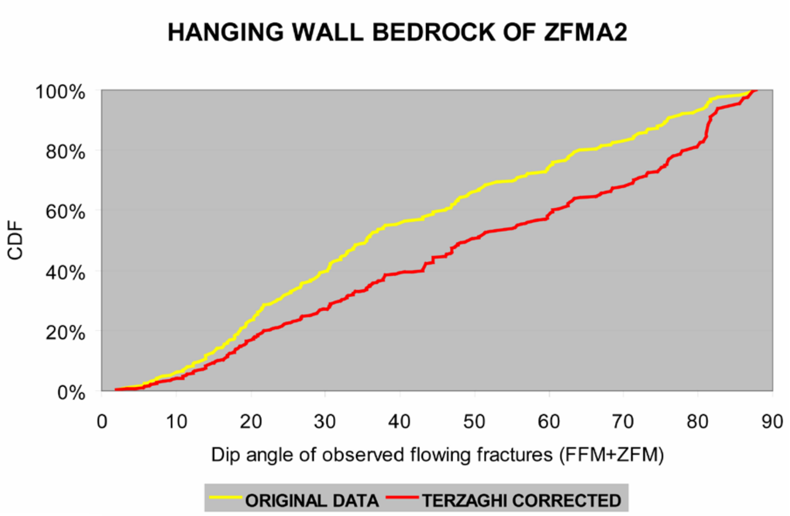
HANGING WALL BEDROCK OF ZFMA2
100%
80%
60%
40%
20%
0%
CDF
0
10
20
30
40
50
60
70
80
90
Dip angle of observed flowing fractures (FFM+ZFM)
ORIGINAL DATA
TERZAGHI CORRECTED

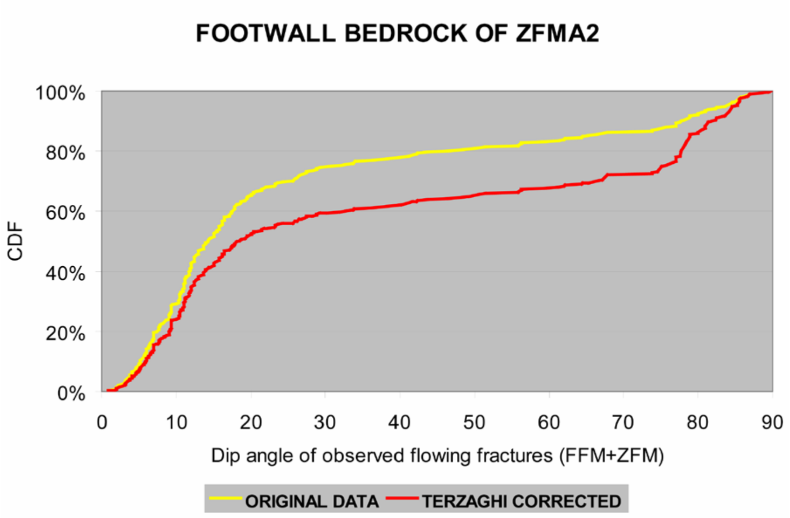
FOOTWALL BEDROCK OF ZFMA2
100%
80%
60%
40%
20%
0%
CDF
0
10
20
30
40
50
60
70
80
90
Dip angle of observed flowing fractures (FFM+ZFM)
ORIGINAL DATA
TERZAGHI CORRECTED

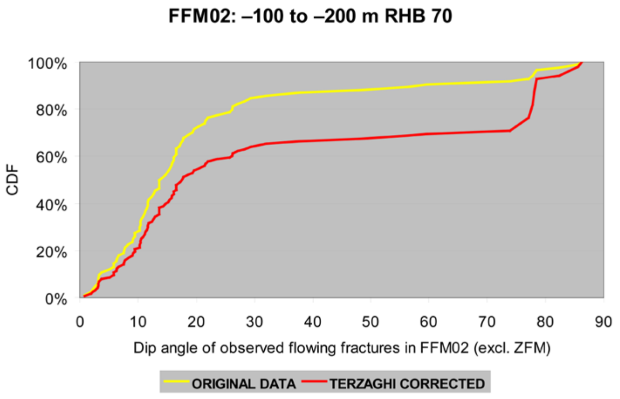
FFM02: –100 to –200 m RHB 70
CDF
100%
80%
60%
40%
20%
0%
0
10
20
30
40
50
60
70
80
90
Dip angle of observed flowing fractures in FFM02 (excl. ZFM)
ORIGINAL DATA
TERZAGHI CORRECTED

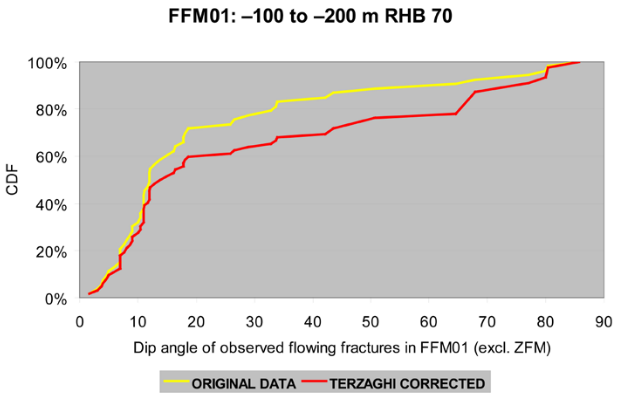
FFM01: –100 to –200 m RHB 70
CDF
100%
80%
60%
40%
20%
0%
0
10
20
30
40
50
60
70
80
90
Dip angle of observed flowing fractures in FFM01 (excl. ZFM)
ORIGINAL DATA
TERZAGHI CORRECTED

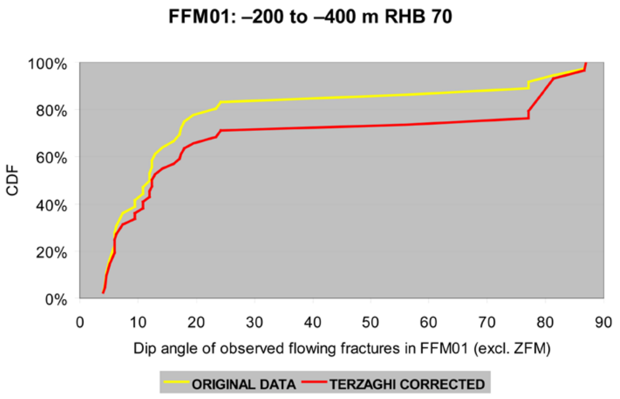
FFM01: –200 to –400 m RHB 70
CDF
100%
80%
60%
40%
20%
0%
0
10
20
30
40
50
60
70
80
90
Dip angle of observed flowing fractures in FFM01 (excl. ZFM)
ORIGINAL DATA
TERZAGHI CORRECTED

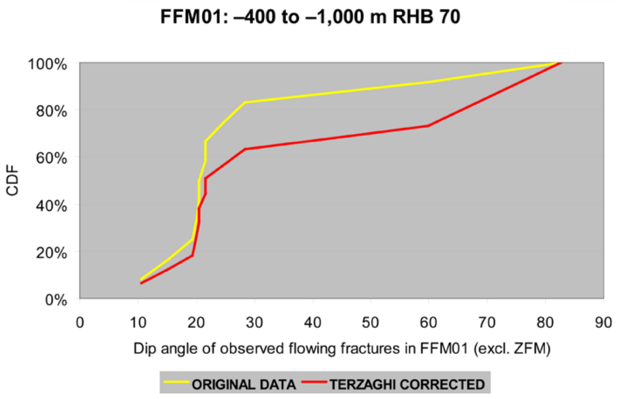
FFM01: –400 to –1,000 m RHB 70
CDF
100%
80%
60%
40%
20%
0%
0
10
20
30
40
50
60
70
80
90
Dip angle of observed flowing fractures in FFM01 (excl. ZFM)
ORIGINAL DATA
TERZAGHI CORRECTED

Appendix F

Hydro-DFN parameter values for FFM01–06

FFM01 and FFM06

The parameterisation of the Hydro-DFN for FFM01 and FFM06 are tabulated in Table F-1. The intensities shown represent the Terzaghi corrected frequency of open fractures. It should be noted that there are no hydraulic information concerning fracture domain FFM06 gathered in data freeze 2.2. The hypothesis made in /Follin et al. 2007b/ is that the properties of FFM06 mimic those of FFM01.

Table F-1. Description of Hydro-DFN parameters for FFM01 and FFM06 with depth dependency above –200 m, –200 m to –400 m and below –400 m RHB 70 /Follin et al. 2007b/.

Fracture domain (m RHB 70)	Fracture set name	Orientation set pole: (trend, plunge), conc.	Size model, power-law (r_0, k_r) (m, –)	Intensity ($P_{32,open}$) valid size interval: (r_0, 564 m) (m^2/m^3)	Transmissivity model Eq. (11-3) Eq. (11-2) Eq. (11-4) in /Follin et al. 2007b/
FFM01 > –200	NS	(292, 1) 17.8	(0.038, 2.50)	0.073	Semi-correlated: (a,b,σ) = ($6.3 \cdot 10^{-9}$, 1.3, 1.0); Correlated: (a,b) = ($6.7 \cdot 10^{-9}$, 1.4); Uncorrelated: (μ, σ) = (–6.7, 1.2)
	NE	(326, 2) 14.3	(0.038, 2.70)	0.319	
	NW	(60, 6) 12.9	(0.038, 3.10)	0.107	
	EW	(15, 2) 14.0	(0.038, 3.10)	0.088	
	HZ	(5, 86) 15.2	(0.038, 2.38)	0.543	
FFM01 –200 to –400	NS	As above	As above	0.142	Semi-correlated: (a,b,σ) = ($1.3 \cdot 10^{-9}$, 0.5, 1.0); Correlated: (a,b) = ($1.6 \cdot 10^{-9}$, 0.8); Uncorrelated: (μ, σ) = (–7.5, 0.8)
	NE	As above	As above	0.345	
	NW	As above	As above	0.133	
	EW	As above	As above	0.081	
	HZ	As above	As above	0.316	
FFM01 < –400	NS	As above	As above	0.094	Semi-correlated: (a,b,σ) = ($5.3 \cdot 10^{-11}$, 0.5, 1.0); Correlated: (a,b) = ($1.8 \cdot 10^{-10}$, 1.0); Uncorrelated: (μ, σ) = (–8.8, 1.0)
	NE	As above	As above	0.163	
	NW	As above	As above	0.098	
	EW	As above	As above	0.039	
	HZ	As above	As above	0.141	

FFM02

The statistical parameterisation of the Hydro-DFN for FFM02 is tabulated in Table F-2. The intensities shown represent the Terzaghi corrected frequency of open fractures.

FFM03, FFM04 and FFM05

The statistical parameterisations of the Hydro-DFN for FFM03, FFM04 and FFM05 are tabulated in Table F-3. The intensities shown represent the Terzaghi corrected frequency of open fractures.

Table F-2. Description of Hydro-DFN parameters for FFM02 /Follin et al. 2007b/.

Fracture domain (m RHB 70)	**Fracture set name**	**Orientation set pole: (trend, plunge), conc.**	**Size model, power-law (r_0, k_r) (m, –)**	**Intensity ($P_{32.open}$) valid size interval: (r_0, 564 m) (m^2/m^3)**	**Transmissivity model Eq. (11-3) Eq. (11-2) Eq. (11-4) in /Follin et al. 2007b/**
FFM02 > –200	NS	(83, 10) 16.9	(0.038, 2.75)	0.342	Semi-correlated: (a,b,σ) = ($9.0 \cdot 10^{-9}$, 0.7, 1.0); Correlated: (a,b) = ($5.0 \cdot 10^{-9}$, 1.2); Uncorrelated: (μ, σ) = (–7.1, 1.1)
	NE	(143, 9) 11.7	(0.038, 2.62)	0.752	
	NW	(51, 15) 12.1	(0.038, 3.20)	0.335	
	EW	(12, 0) 13.3	(0.038, 3.40)	0.156	
	HZ	(71, 87) 20.4	(0.038, 2.58)	1.582	

Table F-3. Description of Hydro-DFN parameters for FFM03, FFM04 and FFM05 with depth dependency above and below –400 m RHB 70. Transmissivity is increased by a factor 2 for FFM04 /Follin et al. 2007b/.

Fracture domain (m RHB 70)	**Fracture set name**	**Orientation set pole: (trend, plunge), conc.**	**Size model, power-law (r_0, k_r) (m, –)**	**Intensity ($P_{32,open}$) valid size interval: (r_0, 564 m) (m^2/m^3)**	**Transmissivity model Eq. (11-3) Eq. (11-2) Eq. (11-4) in /Follin et al. 2007b/**
FFM03 > –400	NS	(292, 1) 17.8	(0.038, 2.60)	0.091	Semi-correlated: (a,b,σ) = ($1.3 \cdot 10^{-8}$, 0.4, 0.8); Correlated: (a,b) = ($1.4 \cdot 10^{-8}$, 0.6); Uncorrelated: (μ, σ) = (–7.2, 0.8)
	NE	(326, 2) 14.3	(0.038, 2.50)	0.253	
	NW	(60, 6) 12.9	(0.038, 2.55)	0.258	
	EW	(15, 2) 14.0	(0.038, 2.40)	0.097	
	HZ	(5, 86) 15.2	(0.038, 2.55)	0.397	
FFM03 < –400 m	NS	As above	As above	0.102	Semi-correlated: (a,b,σ) = ($1.8 \cdot 10^{-8}$, 0.3, 0.5); Correlated: (a,b) = ($7.1 \cdot 10^{-9}$, 0.6); Uncorrelated: (μ, σ) = (–7.2, 0.8)
	NE	As above	As above	0.247	
	NW	As above	As above	0.103	
	EW	As above	As above	0.068	
	HZ	As above	As above	0.250	

Appendix G

A note on the 2005 hydraulic interference test at HFM01

Background

The pumping well, HFM01, and the nearby observation well, HFM02, are both located at drill site 1. The radial distance from drill site 1 to drill site 2, where the core-drilled borehole KFM02A is interpreted to intersect deformation zone A2 at c. 400 m borehole length, is 1.9 km. HFM01 and HFM02 intersect a horizontal fracture/sheet joint in close connection to where A2 outcrops. The elevations of the structure are –42.8 and –43.5 m RHB 70, respectively, see Figure G-1. The distance between HFM01 and HFM02 is c. 220 m and the cross-hole transmissivity at drill site 1 is c. (1.5–4)·10^{-4} m^2/s /Ludvigson and Jönsson 2003, Gokall-Norman et al. 2005/. Figure 3-24 shows the high yield acquired in HFM02 when the horizontal fracture/sheet joint was intersected during the drilling.

The pumping flow rate in HFM01 was c.89 L/min and the drawdown was 26 m implying a specific capacity of HFM01 of about 6·10^{-5} m^2/s. The pumping period lasted close to three weeks and during this period the total amount of precipitation was 15 mm see Figure G-2. The interference test responses are evaluated and reported by /Gokall-Norman et al. 2005/.

In what follows we discuss the hydraulic response in zone A2 due to the precipitation during the interference test. We evaluate the precipitation response in two different ways using methods reported by /Streltsova 1988/ and /Edelman 1947/, respectively, and compare the results with the findings reported /Gokall-Norman et al. 2005/, cf. Figure 3-27.

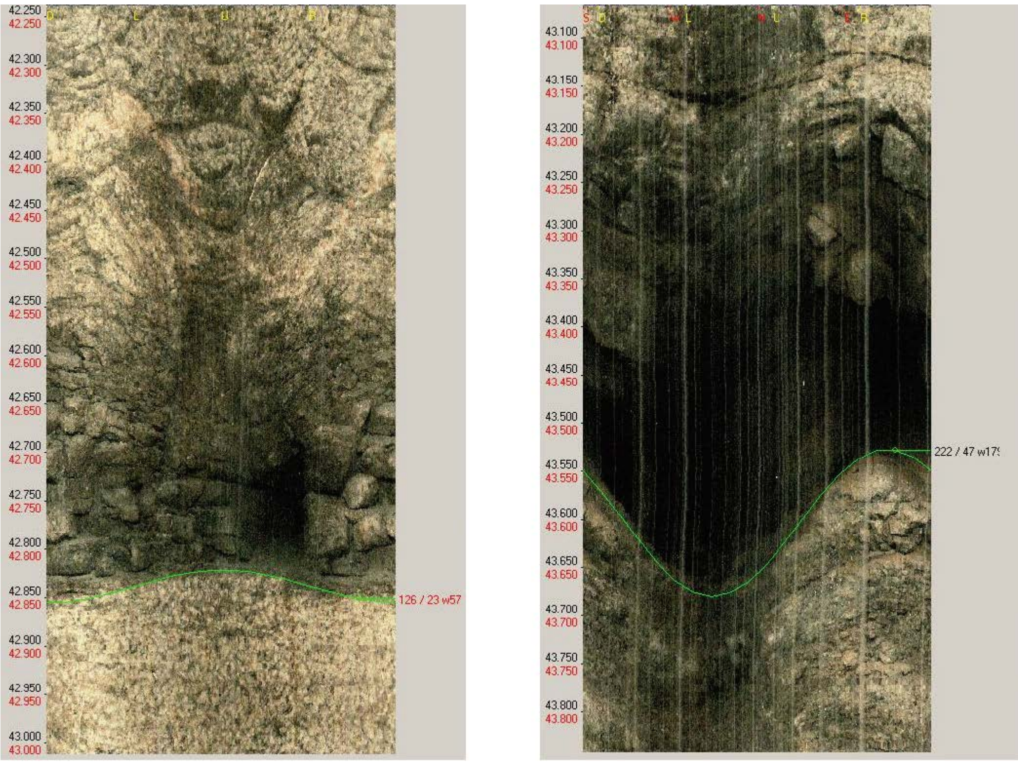

Figure G-1. Two BIPS pictures showing the intersections with the horizontal fracture/sheet joint in close connection to A2 at drill site 1. Left: HFM01; z = –42.8 m RHB 70, strike/dip = 126/23, T = 4.5·10^{-5} m^2/s. Right: HFM02; z = –43.5 m RHB 70, strike/dip = 222/45, T = 5.9·10^{-4} m^2/s. The apertures in the pictures are 1–3 dm wide and show evidence of being channelised due to fill.

Discussion

The precipitation caused a total head response of c. 0.2 m in the monitoring interval HFM02:2 (38–48 m borehole length) at drill site 1 between the 22nd and 26th of July. In the monitoring interval KFM02A:5 (411–442 m borehole length) the maximum head response to the precipitation was c. 0.10–0.15 m, see Figure G-2.

The head responses in zone A2 to the precipitation event are interesting. A tentative guess of the "pressure break-through time" is c. 12–24 hours, cf. Figure G-2 and Figure G-3. The hydraulic diffusivity of A2 was estimated by computing r^2 / dt /Streltsova 1988/. Inserting r = 1,900 m and dt = 18 hours renders a hydraulic diffusivity of 56 m^2/s. The hydraulic diffusivity of A2 evaluated from interference test is in the same range, see Figure 3-27.

Figure G-4 shows a cartoon of the observed precipitation phenomenon. In Figure G-4 we also display a 1D analytical model. A solution to the diffusivity equation for a linearly increasing head at x = 0 is provided by /Edelman 1947/.

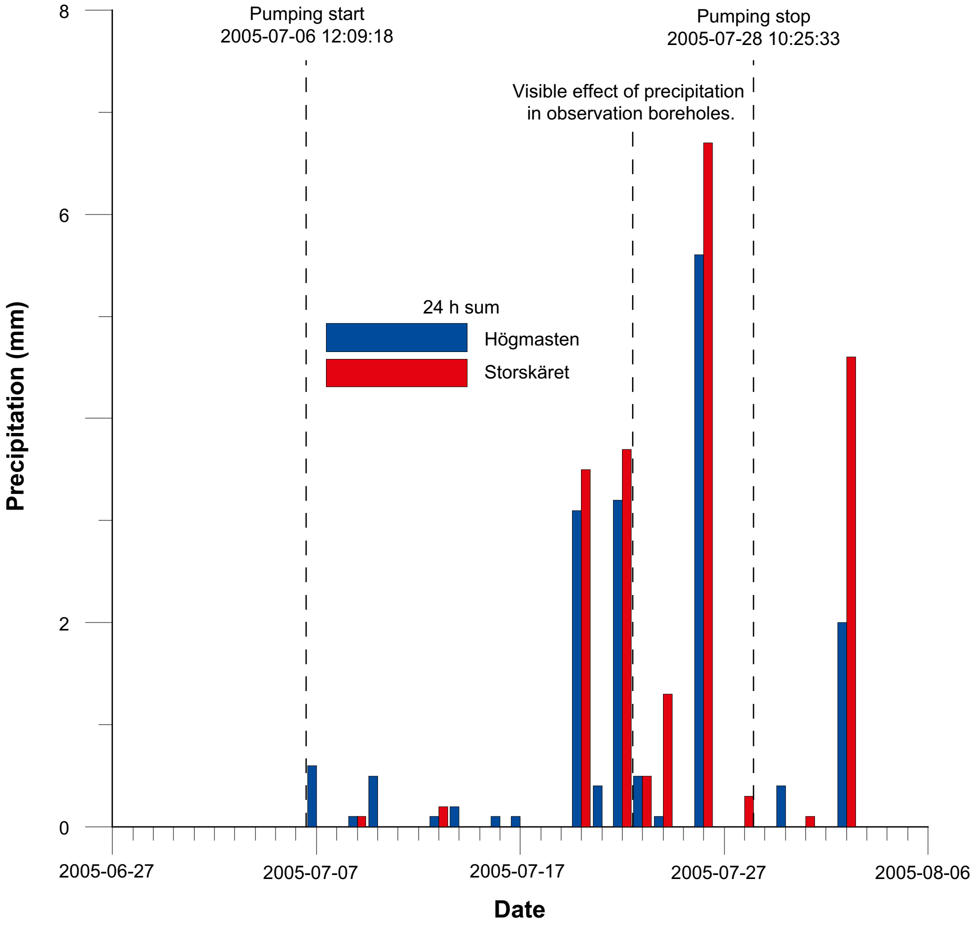

***Figure G-2.** Precipitation observations during the 2005 interference test in HFM01 summed up to 24 hours rates. The station Storskäret is close to KFM03A in the south-eastern part of the candidate area whereas station Högmasten is located in the vicinity of the power plant northwest of the candidate area. Modified after /Gokall-Norman et al. 2005/.*

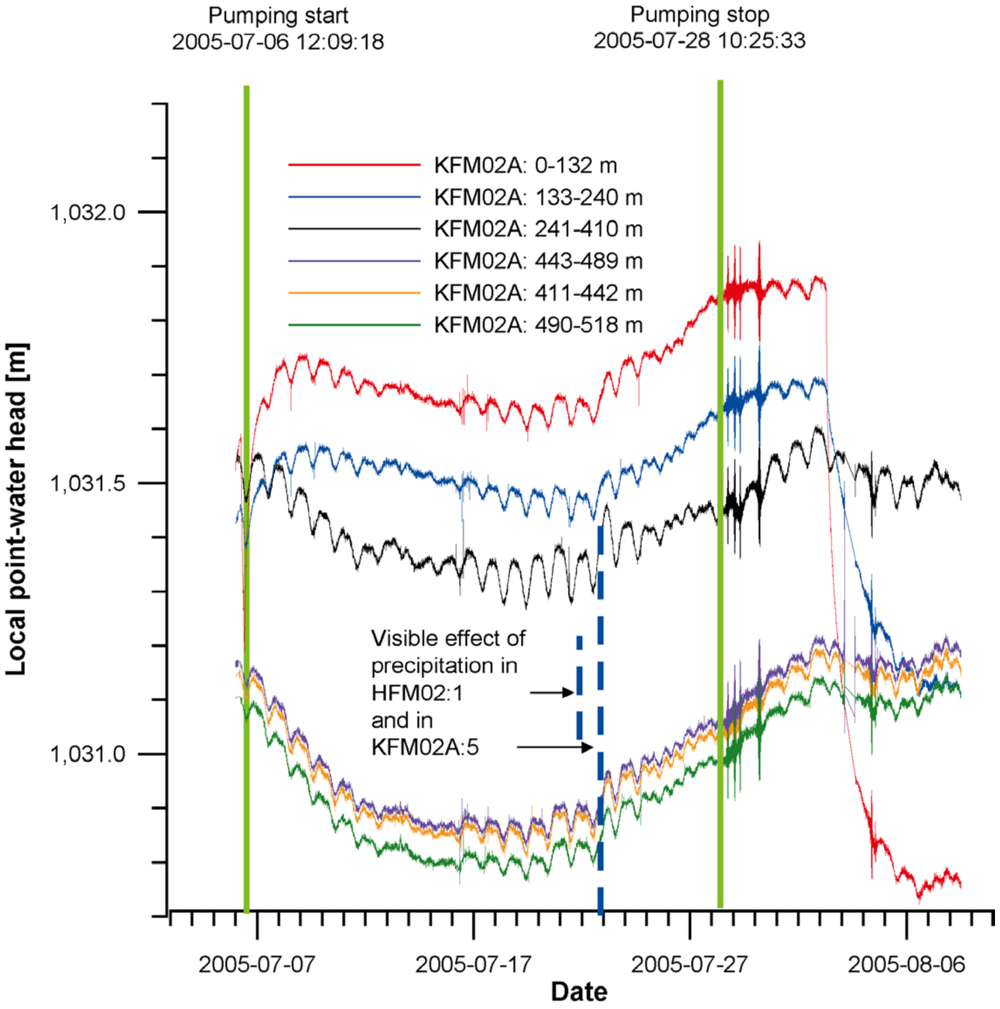

Figure G-3. *Local point-water head responses in KFM02A. Zone A2 intercepts the borehole between 411–442 m borehole length and lays on top of another gently-dipping deformation zone F1. The monitoring interval KFM02A:5 is discussed here. Modified after /Gokall-Norman et al. 2005/.*

Figure G-5 shows the match between the 1D analytical model and field data for three values of the hydraulic diffusivity. The source term is the linear increasing head change at drill site 1, i.e. in monitoring interval HFM02:2. The transient responses at drill site 2, i.e. in monitoring interval KFM02A:5, is matched with a hydraulic diffusivity of 60 m^2/s. The solutions for T/S = 30 m^2/s and T/S = 90 m^2/s are inserted to demonstrate the sensitivity of the model to the value of the hydraulic diffusivity as well as to the uncertainty in the interpreted head response in monitoring interval KFM02:5.

The key conclusion drawn here is that the heads in the gently-dipping deformation zones follow closely the variations in the surface heads that are caused by precipitation events, sea level changes, barometric changes and tidal effects. Indeed, this has previously been demonstrated for the gently-dipping deformation zone A4 in /SKB 2005a/. Zone A4 is intersected by KFM03A at drill site 3 at c. 390 m depth and outcrops in the Baltic Sea some 800–1,000 m away from drill site 3. Sea level changes are observed in KFM03A with a delay of 4 hours, which suggests a hydraulic diffusivity of 40–70 m^2/s.

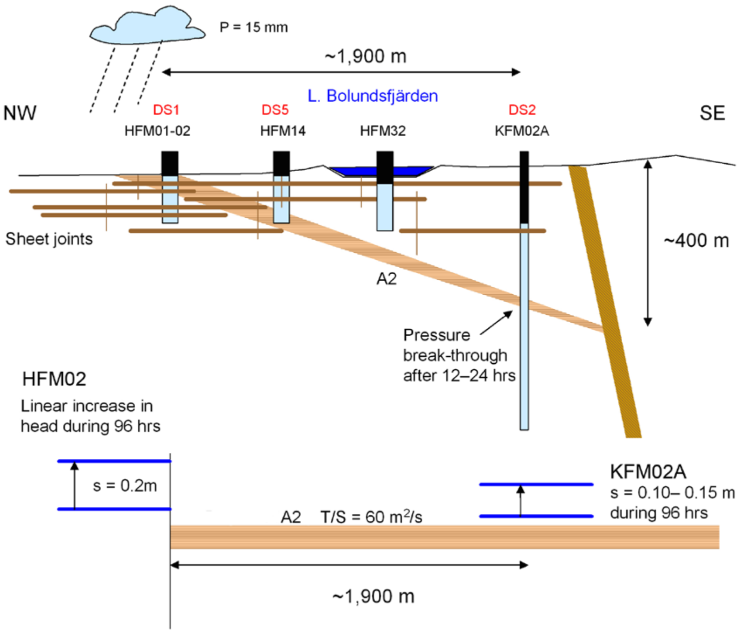

***Figure G-4.** Cartoon of the borehole configuration between drill sites 1 and 2 and the observed precipitation phenomenon. The solution to the one-dimensional model shown in the bottom part of the cartoon is displayed in Figure G-5.*

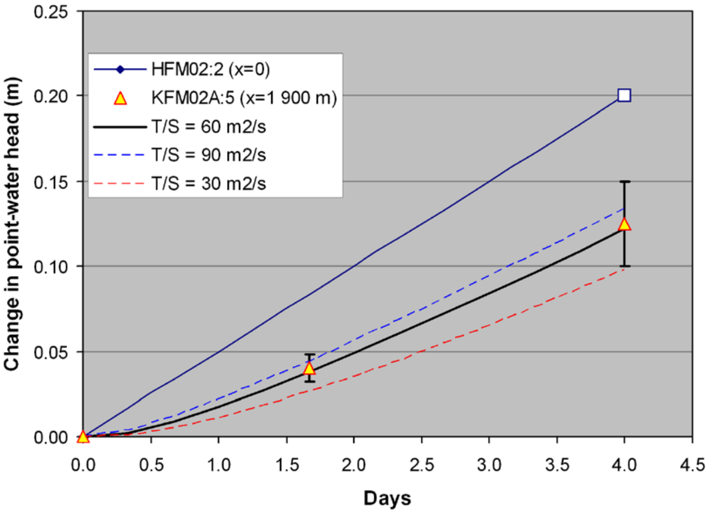

***Figure G-5.** Modelled head responses in monitoring interval KFM02A:5 for a linearly increasing head at drill site 1 using data from monitoring interval HFM02:2 and the mathematical model envisaged in Figure G-4. The three graphs represent different hydraulic diffusivities.*

Appendix H

A note on the 2006 hydraulic interference test in HFM14

Background

The hydraulic responses obtained during the 2005 interference test in HFM01 were confirmed by the interference test conducted the summer of 2006 using percussion-drilled borehole HFM14 as a sink (pumping well) instead of HFM01 (the two boreholes are c. 350 m apart). HFM14 is located at drill site 5 and penetrates the A2 deformation zone in its upper part, see Figure B-2 in Appendix B and Figure G-4 in Appendix G.

The pumping flow rate in HFM14 was c. 348 L/min and the drawdown was c. 12 m implying a specific capacity of HFM01 of about $5 \cdot 10^{-4}$ m^2/s. The pumping period lasted close to three weeks and during this period of time the total amount of precipitation was 4 mm. The interference test responses are evaluated and reported in /Gokall-Norman and Ludvigson 2006/. The pressure break-through time and head responses in the monitoring network from the 2006 interference test in HFM14 are shown in Figure 3-28 and Figure 3-29, respectively. Figure 3-29 also shows the inferred hydraulic diffusivities.

The head responses are used as a calibration target for the numerical modelling work (cf. Task B in Figure 1-2). We discuss below the head responses observed at depth in the monitoring interval installed in the inclined, core-drilled borehole KFM06A at drill site 6, see Figure B-2 in Appendix B. Borehole KFM06A is c. 800 m away from drill site 5 and borehole HFM14.

Discussion

Borehole KFM06A has eight monitoring intervals: 0–150, 151–246, 247–340, 341–362, 363–737, 738–748, 749–826 and 827–1,001 m borehole length. Several of the more shallow intervals show significant head responses due to the pumping at HFM14. Figure H-1 shows a plot of the head responses in three of the deeper intervals: 363–737, 738–748 and 749–826. The drawdowns inferred for these intervals at the test shut-in are: 0.6 m, 0.1 m and 0.1 m, respectively.

Figure H-2 shows a BIPS image of the drill core associated with a PFL-f transmissivity observed in the interval 738–748 m borehole length (c. –620 m RHB 70). The deduced fracture transmissivity is $3 \cdot 10^{-7}$ m^2/s /Rouhiainen and Sokolnicki 2005/. The associated open fracture with this observation has an aperture of c. 4 mm and an orientation of 27/75, i.e. it has a NNE strike and is steeply-dipping towards E /Forssman et al. 2006/. This observation fits well with the deformation zone model in stage 2.2. Figure H-3 shows a map of interpreted ground magnetic lineaments (solid black lines) together with projected trajectories of the cored boreholes belonging to data freeze 2.2. The body of the ground magnetic lineaments strikes NNE and many of then are modelled deterministically in stage 2.2, see Figure 3-9.

Conclusions

In summary, we conclude that the 2006 interference test conducted at HFM14 reveals a visible head response at depth in a deterministically modelled deformation zone NNE0725 intersecting borehole KFM06A at c. –620 m RHB 70 /Follin et al. 2007b/. There are several NNE striking features modelled within the target volume according to Figure 3-9.

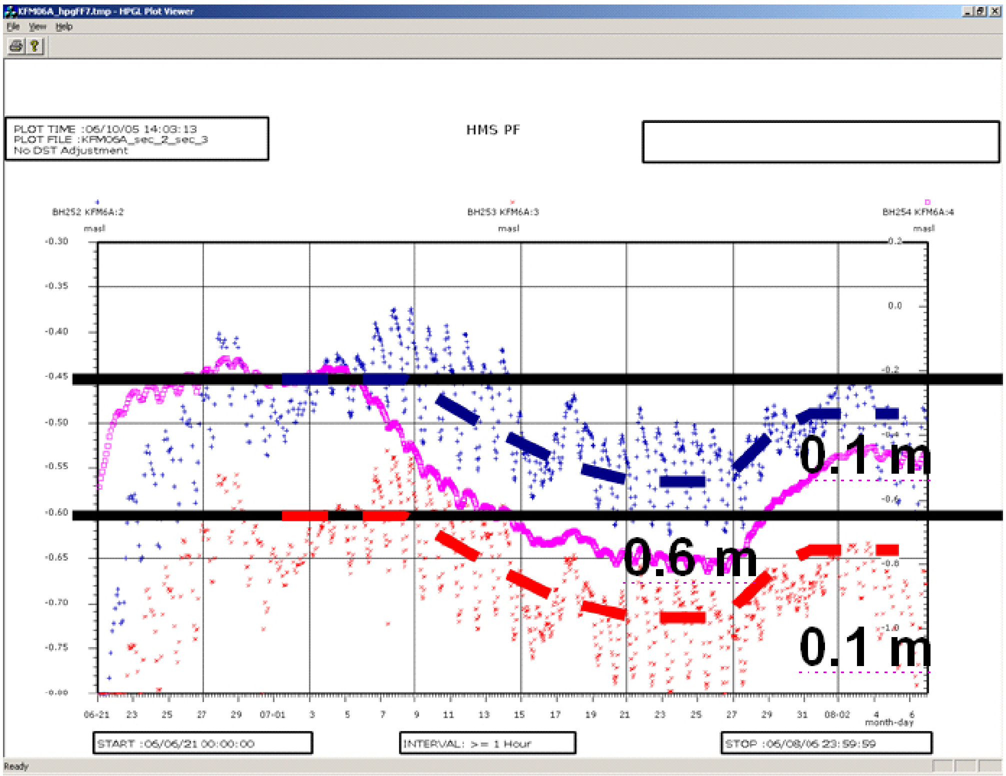

PLOT TIME :06/10/05 14:03:13
PLOT FILE :KFM06A_sec_2_sec_3
No DST Adjustment

START :06/06/21 00:00:00
INTERVAL: >= 1 Hour
STOP :06/08/06 23:59:59

Figure H-1. Interference test responses at different borehole lengths in KFM06A; Red: 738–748 m (c. –620 m RHB 70); Blue: 749–826 m; Pink: 363–737 m.

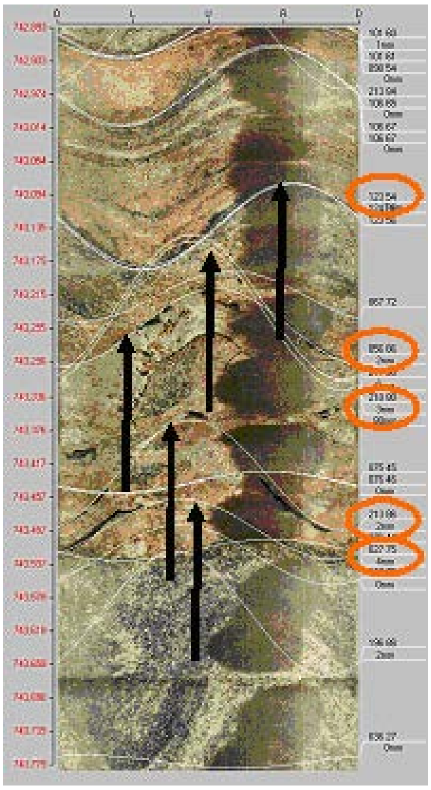

Figure H-2. Open fractures at c. –620 m RHB 70 in KFM06A. The aperture of the bottommost flowing fracture is c. 4 mm and the orientation is 27/75, i.e. NNE and steeply-dipping towards E. Reproduced from /Forssman et al. 2006/.

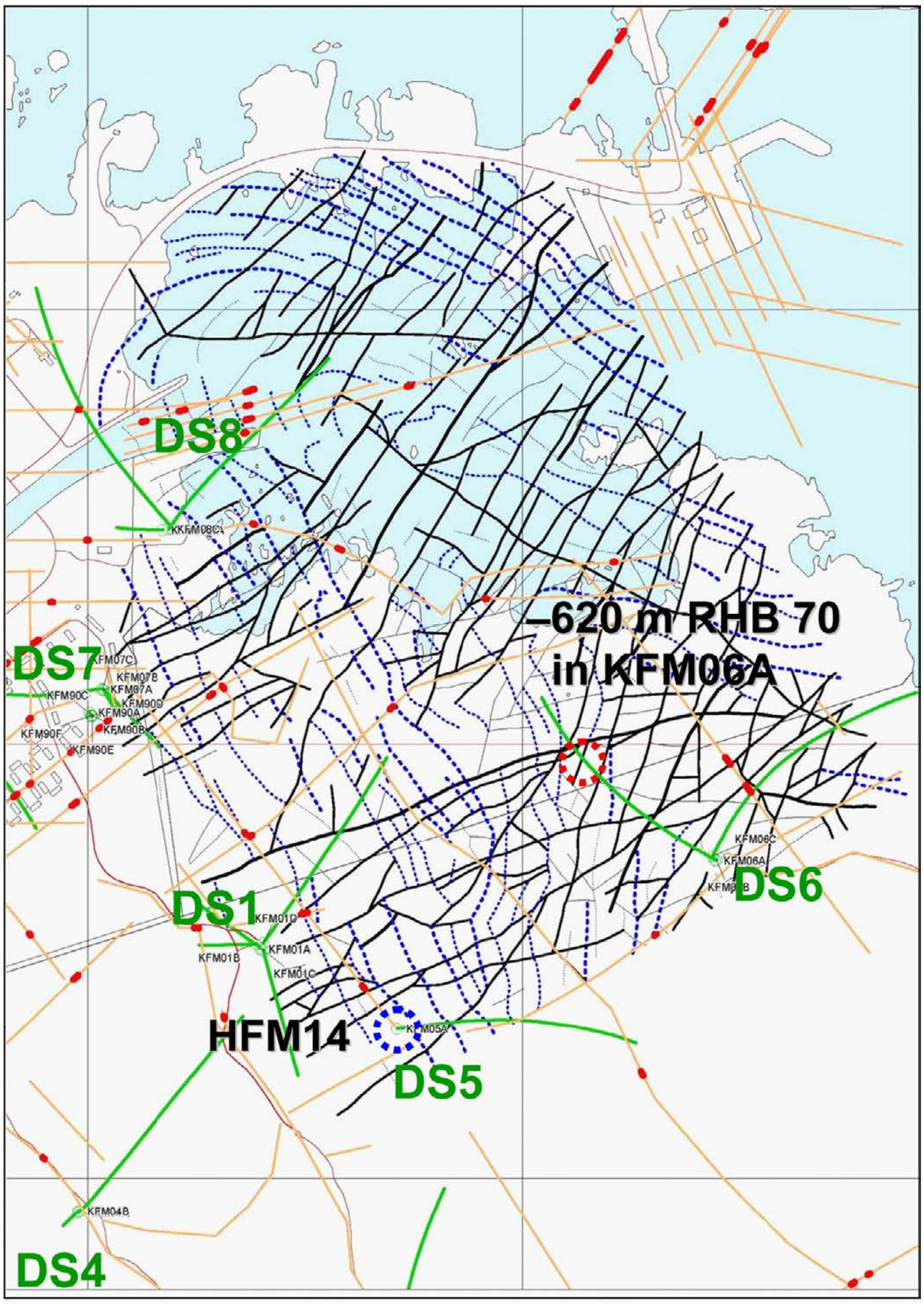

Figure H-3. *Map of interpreted ground magnetic lineaments (solid black lines) (pers. comm. M Stephens 2006-08-22) together with projected trajectories of the cored boreholes belonging to data freeze 2.2 (solid green lines). The body of the ground magnetic lineaments strikes NNE and many are modelled deterministically in stage 2.2. A transmissive fracture at c. –620 m RHB 70 in KFM06A, identified with the PFL-f method /Rouhiainen and Sokolnicki 2005/, is possible to cross-correlate with steeply-dipping fractures in this direction /Forssman et al. 2006/.*

Appendix I

Hydraulic modelling of the near-surface bedrock

Background

Structural, hydrogeological and hydrochemical data gathered up to data freeze 2.2 suggest that the “hydraulic cage phenomenon” is centred geographically in the north-western part of the candidate area, i.e. to the northwest of the area where the gently-dipping deformation zone A2 is outcropping. A horizontal extent for the “hydraulic cage phenomenon” was hypothesised based on the occurrence of high transmissivities to correspond approximately to the domain for FFM02 but stretching north to the Singö deformation zone (WNW001) as shown in Figure 3-31. The chosen bounds are deformation zone WNW001 in the north, and ENE0062A deformation zone in the southeast. The rest of the feature follows the boundary of the FFM02 rock domain with a modification so that the boundary passes between boreholes HFM20 and HFM28. Figure I-1 shows the interpreted horizontal extent of the features causing the “hydraulic cage phenomenon”. The crosses mark the positions of percussion-drilled and core-drilled boreholes for which transmissivity measurements were available.

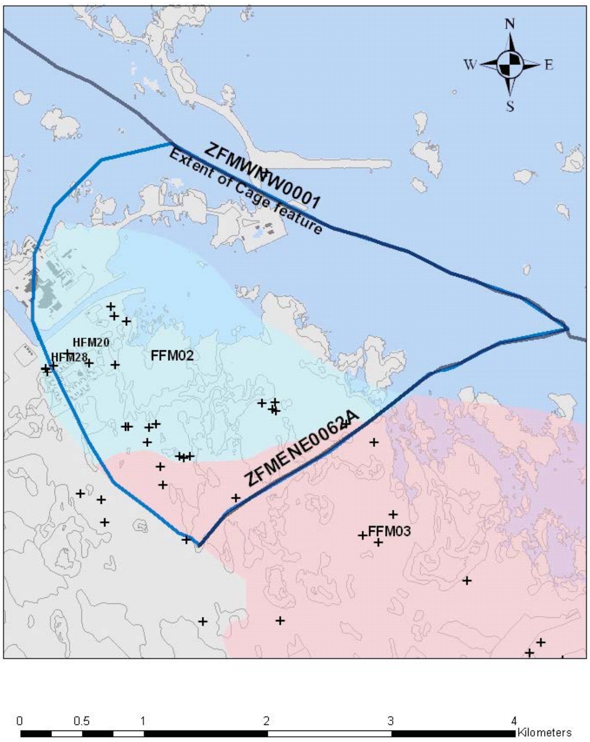

Figure I-1. The interpreted horizontal extent of the discrete features used in this study to model the “hydraulic cage phenomenon”. The crosses mark the positions of percussion- and core-drilled boreholes for which transmissivity measurements were available.

Geostatistical analyses and hydraulic modelling in CONNECTFLOW

The "hydraulic cage phenomenon" is probably formed by a network of structures, where the extent of horizontal sheet joints of varying connectivity and heterogeneous in terms of aperture and fill play a key role. In the previous study /Follin et al. 2007a/, the impact of a single, thin and homogeneous "cage feature" of about $5 \cdot 10^{-4}$ m^2/s was studied. Here, more effort was made to honour the available hydraulic data for the upper bedrock. Still, the computational grid geometry was idealised into three parallel layers within the intervals 0 to –50, –50 to –100 and –100 to –150 m RHB 70 to represent the horizontal sheet joints. In the model implementation, three 1 m thick layers are included at approximately the mid-elevations of these three intervals running parallel to the topographic surface to avoid outcropping on the top surface, cf. Figure 3-21. The three layers were given the form of triangles bounded to the northeast by the Singö deformation zone, (WNW0001), to the southeast by the NE0062A deformation zone, and to the west by the expression of the sheath fold structure in rock domains 32 and 44, as shown in Figure 3-31. The next decision is how to apply hydraulic properties to the three layers. Hydraulic data for the near-surface is available from a combination of PFL-f, PSS and HTHB data, all of which have been interpreted to identify intervals with anomalously high flows.

- The total transmissivity in each borehole in the three intervals 0 to –50, –50 to –100 and –100 to –150 m RHB 70 was summed.
- Some flow anomalies are in the same region as mapped gently-dipping deformation zones; they are still assumed to contribute to the "hydraulic cage phenomenon". That is, we do not exclude a simultaneous occurrence of gently-dipping deformation zones and a horizontal fractures/sheet joints.
- Some boreholes do not have any flow in a particular depth interval, or at least the flow was below the detection threshold of the pumping test technique used. They were assigned a default transmissivity of 10^{-7} m^2 s^{-1} (relatively low for this depth).
- If a core-drilled borehole did not record any PFL-f data it was excluded from the analysis. The reason for the different treatment is that the core-drilled boreholes are in general cased down to approximately –100 m RHB 70, thus excluding any chance for data acquisition (including PSS data).

The resulting distribution of transmissivity data for the three layers is summarised in Table I-1. The values suggest a high degree of heterogeneity in all three layers. Using these values, the distribution of transmissivity was interpolated for each of the three layers forming the "hydraulic cage model".

There are various approaches one might take to producing the interpolated values such as Kriging, nearest neighbour or using an inverse distance weighting. Variograms calculated from the data did not suggest a coherent correlation structure, see Figure I-2, and hence a Kriging approach was not supported. For simplicity, a nearest neighbour approach was used for the final model as this best preserved the varying scale of heterogeneity observed in the measurements and honoured the data at the measurement points. In the following, the three layers forming the hydraulic cage model are referred to as the "cage features".

Table I-1. Transmissivities from impeller logging in near-surface grouped into 50 m intervals for use interpolating transmissivity for the “cage features”.

Borehole name	Log (T) (m^2s^{-1}) 0 to –50 m RHB 70	Log (T) (m^2s^{-1}) –50 to –100 m RHB 70	Log (T) (m^2s^{-1}) –100 to –150 m RHB 70
HFM01	–4.30	–4.87	–7.00
HFM02	–3.23	–7.00	–7.00
HFM03	–3.37	–7.00	–7.00
HFM04	–7.00	–4.10	–7.00
HFM05	–7.00	–7.00	–3.40
HFM06	–3.99	–3.64	–7.00
HFM07	–7.00	–7.00	–7.00
HFM08	–7.00	–4.24	–2.92
HFM09	–3.43	–7.00	–7.00
HFM10	–7.00	–7.00	–3.51
HFM11	–4.65	–4.55	–7.00
HFM12	–7.00	–5.10	–7.00
HFM13	–7.00	–4.68	–3.54
HFM14	–3.46	–3.69	–7.00
HFM15	–3.66	–3.99	–7.00
HFM16	–3.93	–3.39	–7.00
HFM17	–4.41	–7.00	–7.00
HFM18	–3.79	–7.00	–7.00
HFM19	–7.00	–4.40	–3.53
HFM20	–4.24	–5.75	–4.99
HFM21	–3.87	–3.47	–3.68
HFM22	–4.70	–3.84	–7.00
HFM23	–7.00	–7.00	–7.00
HFM24	–3.96	–7.00	–7.00
HFM25	–7.00	–7.00	–7.00
HFM26	–7.00	–7.00	–7.00
HFM27	–4.44	–4.06	–7.00
HFM28	–7.00	–7.00	–7.00
HFM29	–7.00	–7.00	–7.00
HFM30	–7.00	–4.32	–4.06
HFM31	–7.00	–7.00	–7.00
HFM32	–3.02	–7.00	–7.00
KFM01C	–3.01	–3.61	–7.00
KFM01D	–7.00	–4.44	–4.90
KFM02A	–7.00	–3.08	–3.04
KFM03B	–4.65	–4.68	–7.00
KFM04A	–7.00	–4.43	–3.87
KFM05A	–7.00	–5.51	–5.75
KFM06A	–7.00	–4.10	–3.63
KFM06B	–3.22	–4.67	–7.00
KFM06C	–7.00	–4.66	–3.73
KFM07A	–7.00	–2.99	–4.26
KFM08A	–7.00	–5.20	–4.46
KFM08B	–4.41	–7.00	–7.00
KFM09A	–7.00	–7.00	–5.95
KFM09B	–4.37	–5.09	–7.00

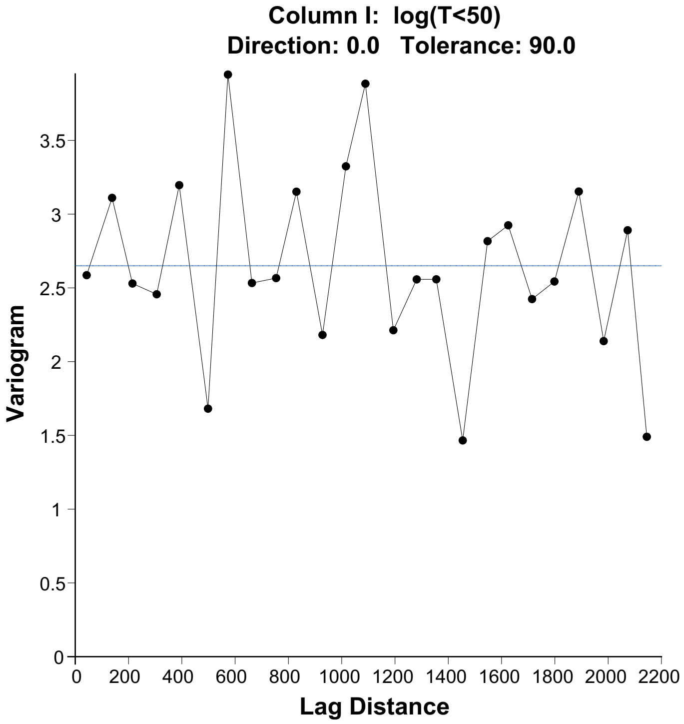

Figure I-2. *Variogram of Log (Transmissivity) from data collected form 0 m–50 m. The variogram appears to show pure nugget behaviour, indicating a lack of spatial correlation in transmissivity, and hence a Kriging approach is not justified.*

A comparison of results obtained using Kriging and nearest neighbour methods for interpolating Log(T) for the top layer, 0 to –50 m RHB 70, is seen in Figure I-3 and Figure I-4. Kriging gives smoother variations in properties at the cost of failing to honour the data where there are large variations in the data over short distances as evident in the nearest neighbour interpolation of Figure I-4. Transmissivity was interpolated over a larger area, but only the part covering the interpreted extent of the hydraulic cage model area was used. The corresponding nearest neighbour interpolations of transmissivity for the other two layers, –50 to –100 and –100 to –150 m RHB 70, are shown in Figure I-5 and Figure I-6. There is limited correlation between the layers. It is clear that for a large part of the "cage features", essentially that part near and under the sea, there is no data to condition the hydraulic cage model.

The three layers were inserted at depth of 35 m, 75 m and 115 m below the topographic surface as 1 m thin layers within the grid layering of 20 m spacing within the candidate area. This meant that were alternating layers of elements that were unaffected by the three layers. Hence, the three layers forming the hydraulic cage model were not connected directly, only where they are intersected by sub-vertical deformation zones. It is considered this is a realistic treatment of the effect of heterogeneous sheet joints in an ECPM model since it creates discrete horizontal stripes of high hydraulic conductivity in the near-surface to represent the extensive sheet joints. Illustrations of how this affected the property assignment on the finite-element grid is shown in Figure I-7 and Figure I-8.

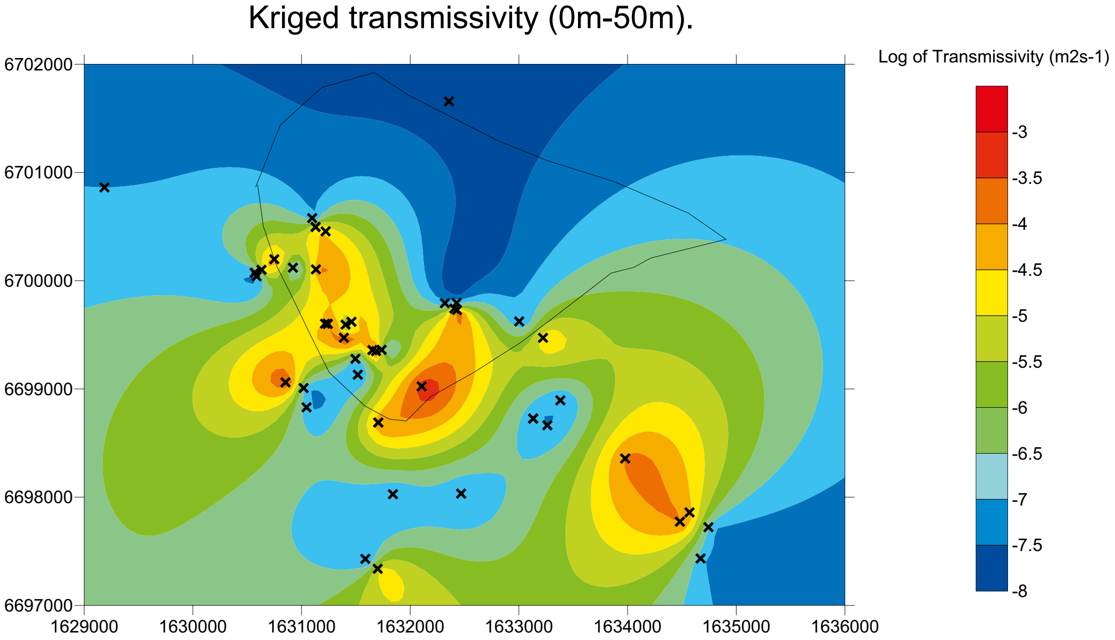

Figure I-3. *Kriged values of Log(Transmissivity) for 0 to –50 m RHB 70. The values given are similar to those from the nearest neighbour approach, but the heterogeneity of the data is less noticeable. The crosses indicate borehole locations and the black line indicate the interpreted extent of the hydraulic cage model.*

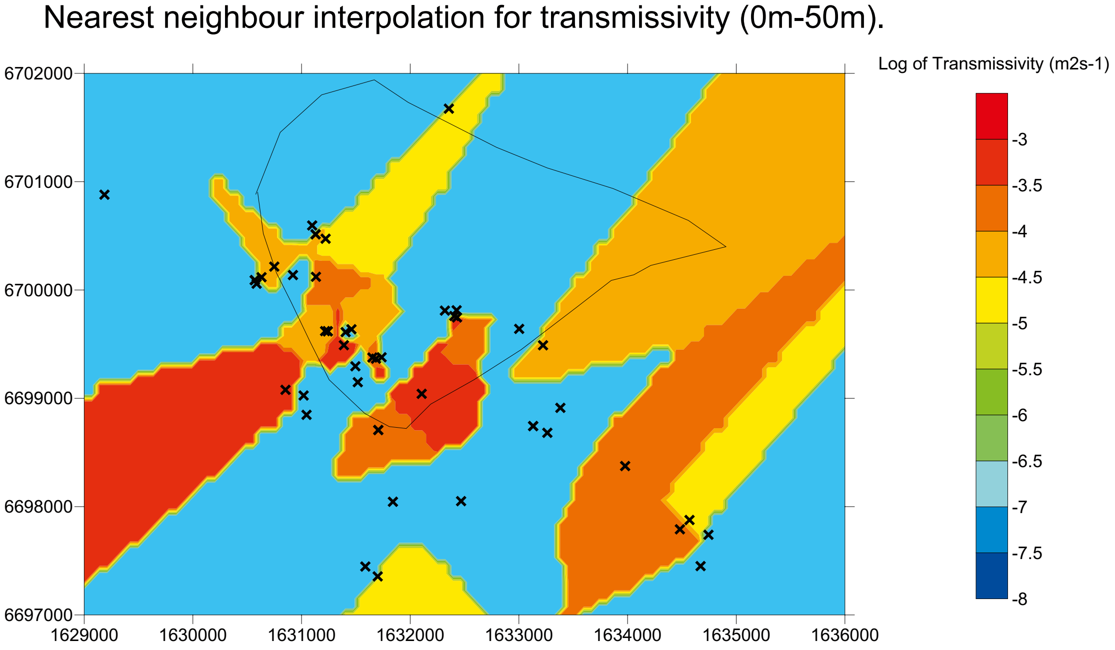

Figure I-4. *Interpolated values of Log(Transmissivity) based on a nearest neighbour approach for 0 to –50 m RHB 70. The crosses indicate borehole locations and the black lines indicate the interpreted extent of the hydraulic cage model.*

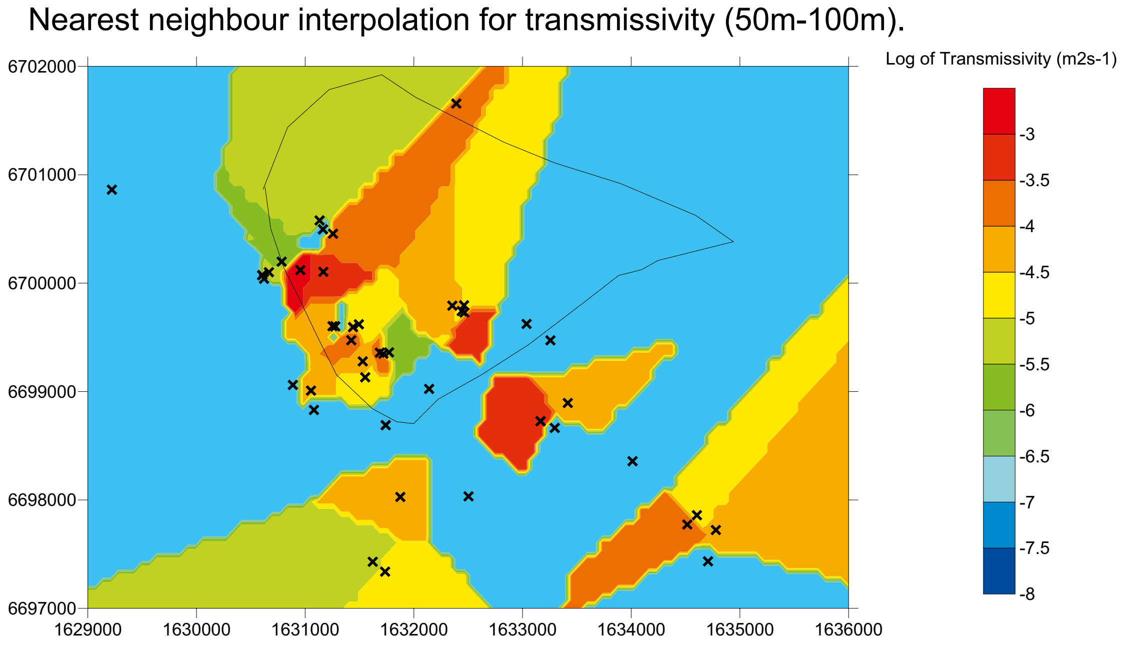

Figure I-5. *Interpolated values of Log(Transmissivity) based on a nearest neighbour approach for –50 to –100 m RHB 70. The crosses indicate borehole locations and the black line indicates the interpreted extent of the hydraulic cage model.*

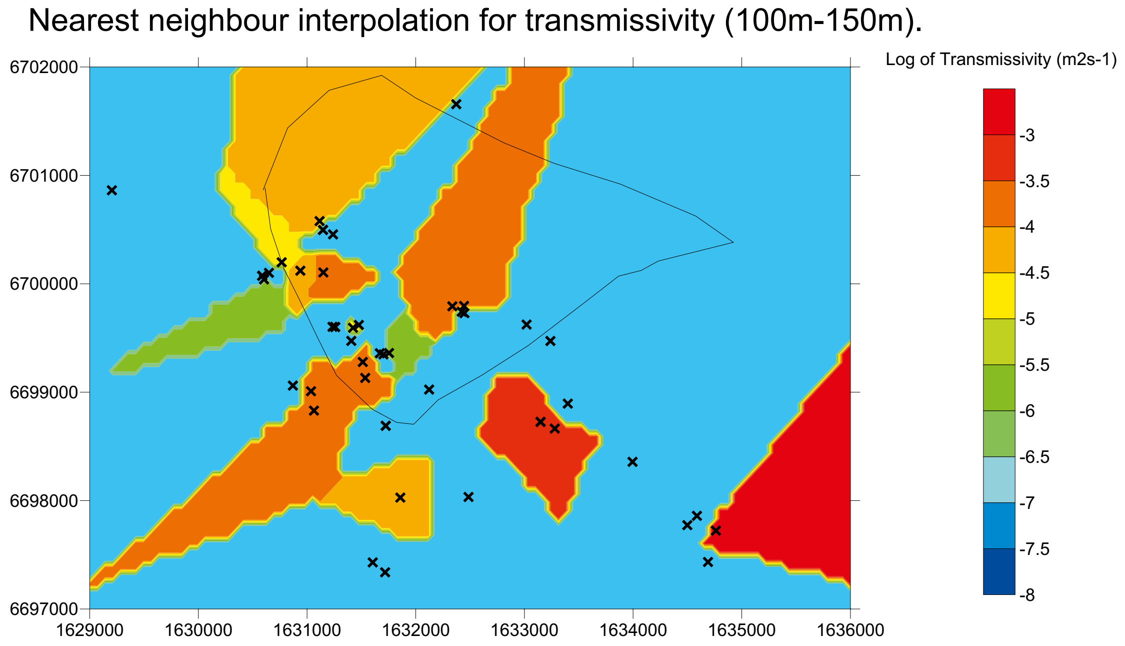

Figure I-6. *Interpolated values of Log(Transmissivity) based on a nearest neighbour approach for –100 to –150 m RHB 70. The crosses indicate borehole locations and the black line indicates the interpreted extent of the hydraulic cage model.*

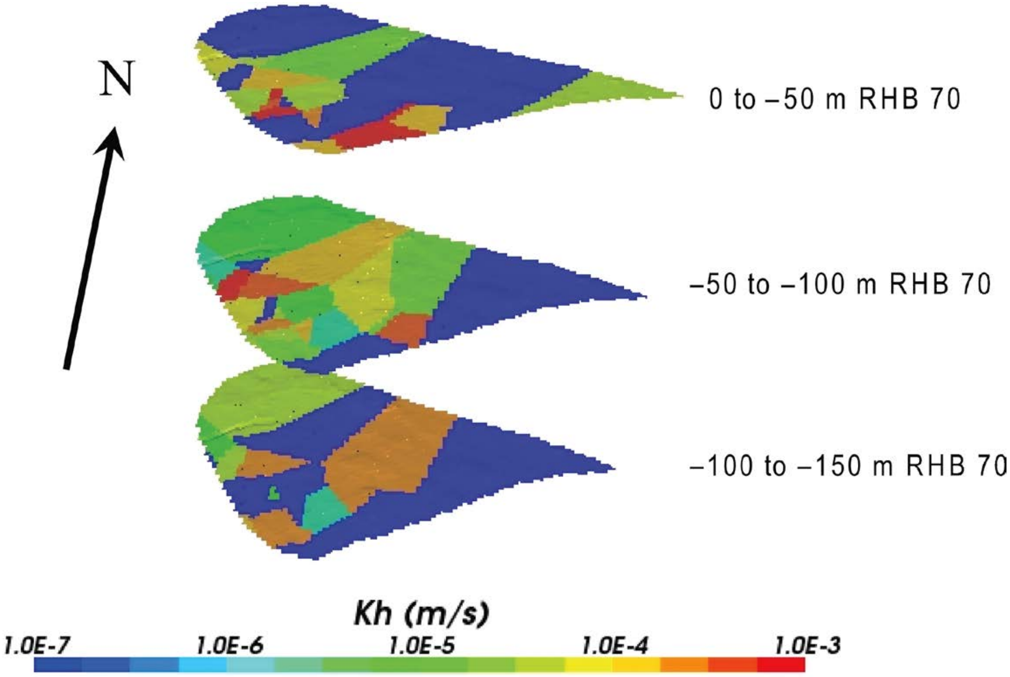

Figure I-7. Visualisation of the three layers forming the hydraulic cage model. The vertical scale has been exaggerated. The colour scale refers to the horizontal conductivity (m/s). The three layers are here referred to as the "cage features".

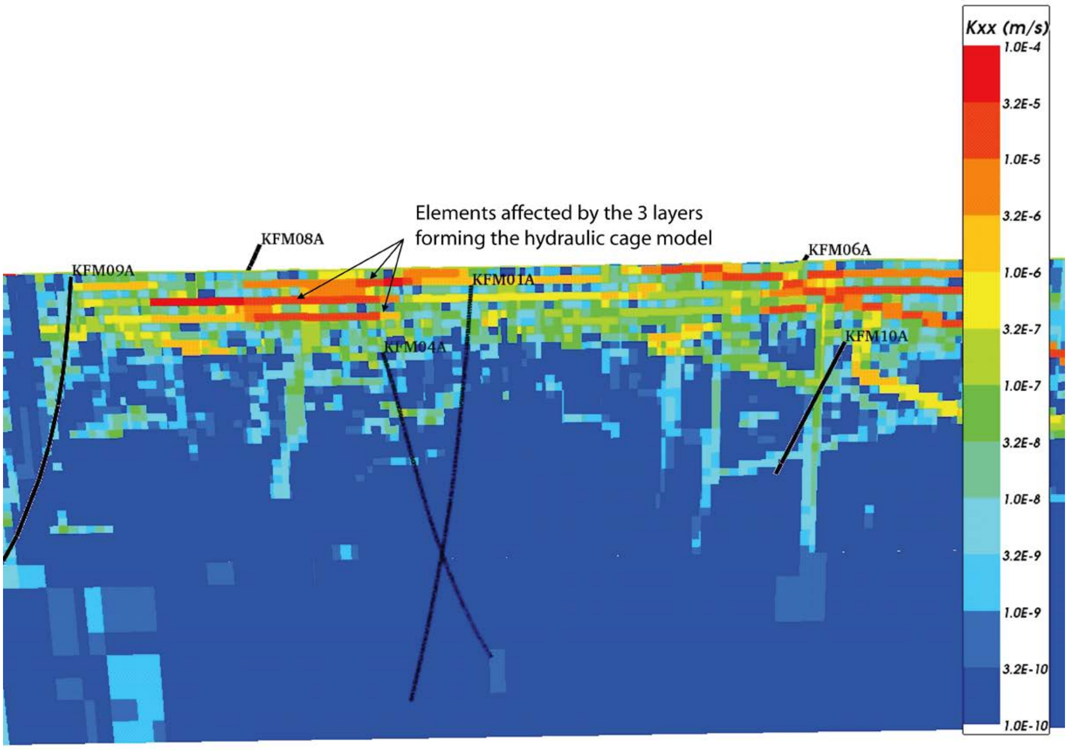

Figure I-8. An illustration of the horizontal hydraulic conductivity in CONNECTFLOW on a N115E vertical slice through the target volume. Note the effect of the three layers forming the hydraulic cage model.

Appendix J

Hydrogeological conditions in HFM32 below Lake Bolundsfjärden

Background

The general situation with lower groundwater levels in superficial bedrock than in the Quaternary deposits shown in Figure 3-47 and Figure 3-49 has been observed even below the middle of Lake Bolundsfjärden. Lake Bolundsfjärden is located in the major topographic depression in the centre of the target area in Forsmark, see Figure B-6. Since the water level in the lake generally is higher than the groundwater level in the Quaternary deposits beneath the lake the two observations combined suggest that the lake may be a source for groundwater recharge rather than a discharge area. The hydraulic conductivity of the gyttja/clay sediments on top of till underlying the lake has not been studied specifically. However, the hydraulic conductivity of the clayey sediments is probably significantly lower than in till beneath, which has a hydraulic conductivity of $3.5 \cdot 10^{-7}$ m/s /Werner and Johansson 2003/. In contrast, the mean equivalent horizontal transmissivity of the uppermost c. 100 m of bedrock is exceptionally high, c. $5 \cdot 10^{-4}$ m^2/s, see Figure 3-30. In the following we take a closer look at the point-water heads below Lake Bolundsfjärden. Figure J-1 shows time series of point-water head data that demonstrate the situation between 2006-02-01 and 2006-09-29 (data freeze 2.2) and Figure J-2 shows a map of the area around Lake Bolundfjärden and the locations of different boreholes and monitoring wells of interest. A useful explanation of the legend in Figure J-1 is:

PFM010038. Surface water level in the Baltic Sea.

SFM0040. Surface water level in Lake Bolundsfjärden.

SFM0023. Groundwater level in the Quaternary deposits (till) beneath the lake sediments (gyttja/clay). The transmissivity of the till layer is estimated to $3.5 \cdot 10^{-7}$ m^2/s.

HFM32. Groundwater level in the superficial bedrock beneath the Quaternary deposits monitored by SFM0023. The groundwater level is monitored by four sections: HFM32:4 [–3 to –25 m RHB 70]; HFM32:3 [–25 to –31 m RHB 70]; HFM32:2 [–31 to –96 m RHB 70] and HFM32:1 [–96 to –198 m RHB 70]. The transmissivity of the intervals [–5 to –28 m RHB 70], [–28 to –120 m RHB 70] and [–120 to –198 m RHB 70] are estimated to c. $8.2 \cdot 10^{-4}$, $1.3 \cdot 10^{-4}$ and $< 1 \cdot 10^{-6}$ m^2/s, respectively.

KFM02A. Groundwater level in the deeper bedrock. KFM02A is located at drill site 2, c. 1,100 m SE of HFM32. The groundwater level in KFM02A is monitored by eight sections. The section KFM02A:5 ranges between –411 to –442 m RHB 70 and monitors the gently-dipping deformation zone A2. The transmissivity of A2 varies with depth. In HFM14, c. 600 m NW of HFM32 the transmissivity is estimated to c. $4.0 \cdot 10^{-4}$ m^2/s and in KFM02:5 the transmissivity is estimated to $2.9 \cdot 10^{-6}$ m^2/s.

The mean water level in Lake Bolundsfjärden is only a few decimetres above the datum plane (RHB 70). The sea level, on the other hand, varies a lot, see Figure J-3. Variations in the sea level between +0.8 and –0.8 m RHB70 are not uncommon, which means that transgressions occur now and then, see Figure J-1 and Figure J-3.

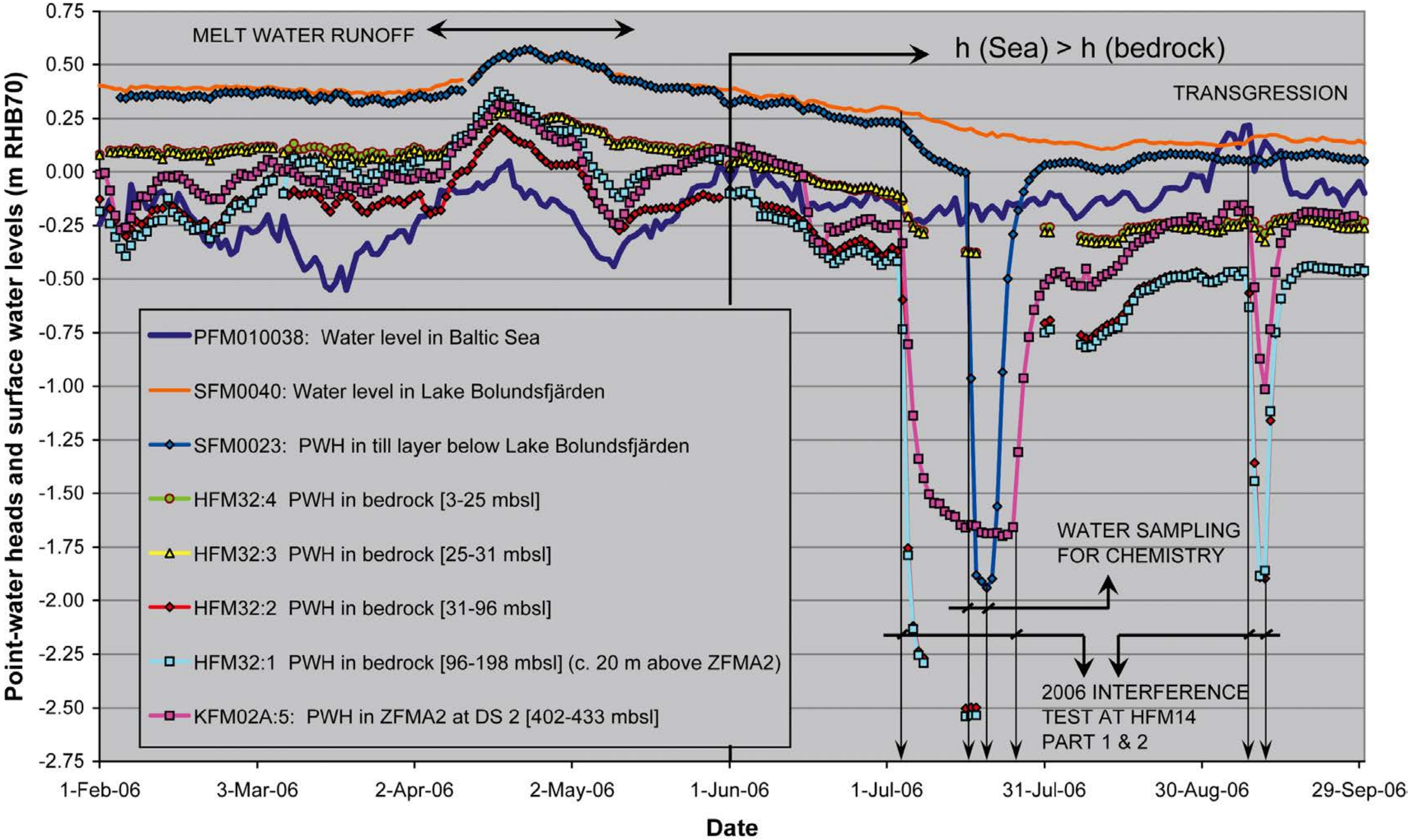

Figure J-1. *Surface water levels and groundwater levels (point-water heads) in the till and in the bedrock below Lake Bolundsfjärden and in KFM02A:5 at drill site 2. The head gradient between the lake and the upper parts of the bedrock below the lake appears to be predominantly downwards suggesting a situation where the lake act as source of recharge to the groundwater rather than as a discharge area. Particular events and disturbances of anomalous character are: Melt water runoff, transgression (backflow from the Baltic Sea into Lake Bolundsfjärden), drawdown from the 2006 interference test in HFM14 and disturbances from water sampling. Note the effects of the interference tests. The hydraulic contact with the till suggests little leakage through the gyttja/clay lake sediments. Furthermore, from the beginning of June the sea level is greater than the recorded point-water heads in the bedrock (HFM32:1–4 and KFM02A:5).*

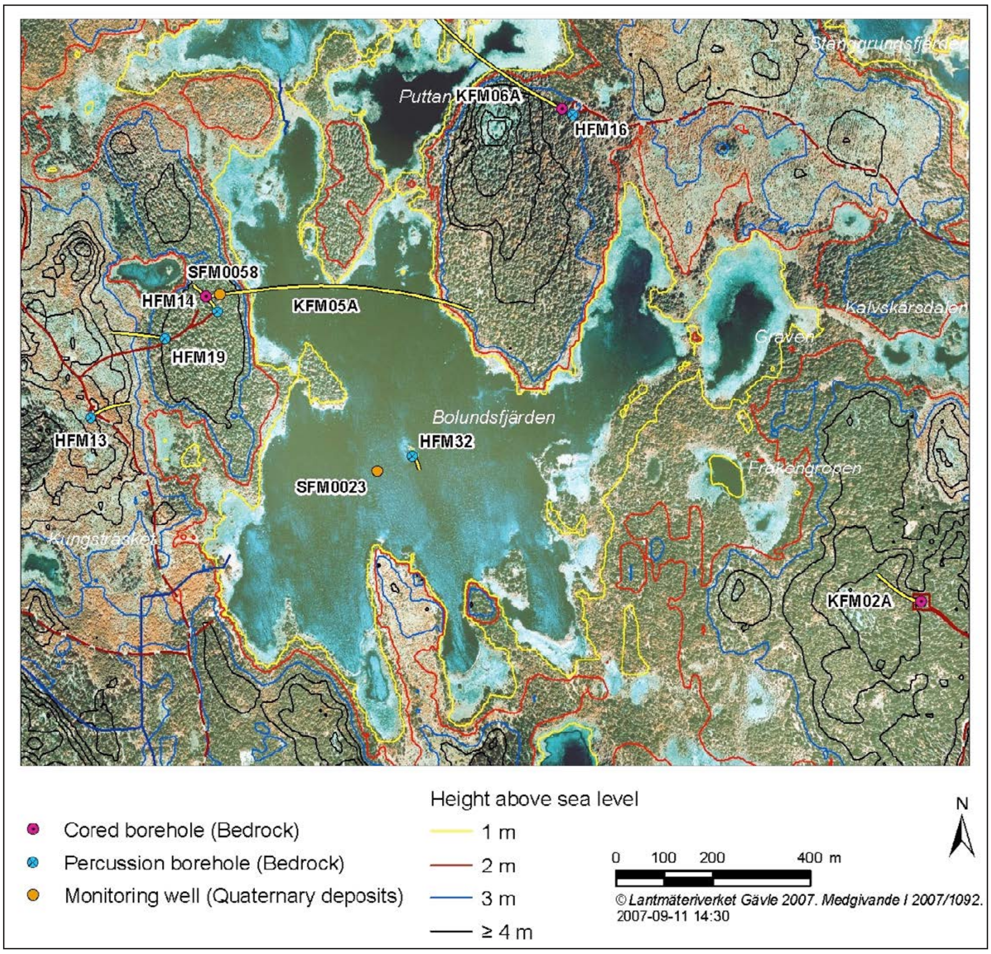

© Lantmäteriverket Gävle 2007. Medgivande I 2007/1092.
2007-09-11 14:30

Figure J-2. *Map showing Lake Bolundfjärden and nearby boreholes and monitoring wells of interest.*

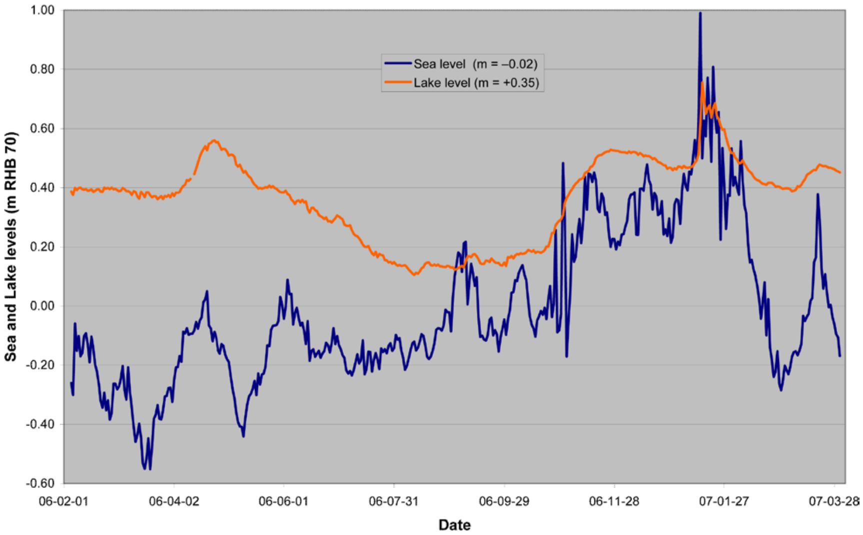

Figure J-3. *Water levels in the Baltic Sea and in Lake Bolundsfjärden between 2006-02-01 and 2007-03-31.*

Observations

The groundwater levels in Figure J-1 are point-water heads, which raises an uncertainty about the direction of the vertical gradients since the groundwater in the Forsmark area is predominantly brackish with a spatially varying fluid density. In Figure J-4 we have transformed the point-water heads to environmental-water heads using the algorithm described in Appendix K. Note that the time series in Figure J-4 are six months longer than the time series shown in Figure J-1; that is, they begin 2006-02-01 and end 2006-03-31 (data freeze 2.3).

The geometrical model used to calculate the environmental-water heads in Figure J-4 is shown in Figure J-5. The estimated depth to the top of the gently-dipping deformation A2 from the bottom of HFM32 is c. 20 m. The estimation is based on Figure J-6, which shows the modelled depth to A2 from the surface. Further, the calculation of environmental-water heads is based on the assumption that the bedrock acts like a continuous porous medium (CPM).

Furthermore, it is assumed in Figure J-4 that the environmental-water heads gathered in KFM02A:5 at drill site 2 are possible to compare with the environmental-water heads gathered in HFM32:1–4 despite the horizontal distance between the two boreholes (c. 1,100 m). Figure J-4 suggests and upward flow gradient from KFM02A:5 to HFM32:1 along A2. Figure J-7 shows the flow directions in KFM02A with depth (green for inflow and red for outflow) as observed with the Posiva Flow Log after the borehole drilling was completed. Figure J-7 suggests an upward flow direction in KFM02A and that the location of the main discharge zone in this borehole is below the casing shoe. This observation suggests an upward flow along zone A2.

Discussion

From the beginning of June 2006 to the end of October 2006 the sea level is greater than the calculated environmental-water heads in the bedrock (HFM32:1–4 and KFM02A:5). Furthermore, the environmental-water heads in borehole section HFM32:2 are in general the lowest. Why the environmental-water heads in HFM32:1–4 and in KFM02A:5 are lower than the sea level during the dry summer of 2006 is currently investigated. Two interesting hypotheses are:

1. The pumping underground in the SFR repository on the other side of Singö deformation zone. The total rate of leakage water abstracted from the SFR repository at –140 m RHB is c. 5–6 L/s. (This discharge is close to the pumping rate during the 2006 interference test in HFM14.) There is an outcropping gently-dipping deformation zone below the SFR repository referred to as 871 that connect to the Singö deformation zone. The observed drawdown in 871 at the SFR repository is c. 23–25 m.

   To test this hypothesis four new boreholes, HFM33–HFM35 and KFM11A, are planned to be drilled on the SFR peninsula during stage 2.3, see Figure B-6 and Figure B-7. An interference test is planned at HFM33 to check if there are extensive horizontal fractures/sheet joints that connect the superficial bedrock in the target area to the Singö deformation zone. During this interference test the monitoring system installed in the SFR repository will be used to check the hydraulic connection across the Singö deformation zone.

2. The pumping in the superficial bedrock below the nuclear power reactor buildings. The total number of pumping wells and their cumulative abstraction rate are a bit uncertain at this point, but there are at least a few wells down to c. –20 m RHB 70 discharging all together at least 1–2 L/s.

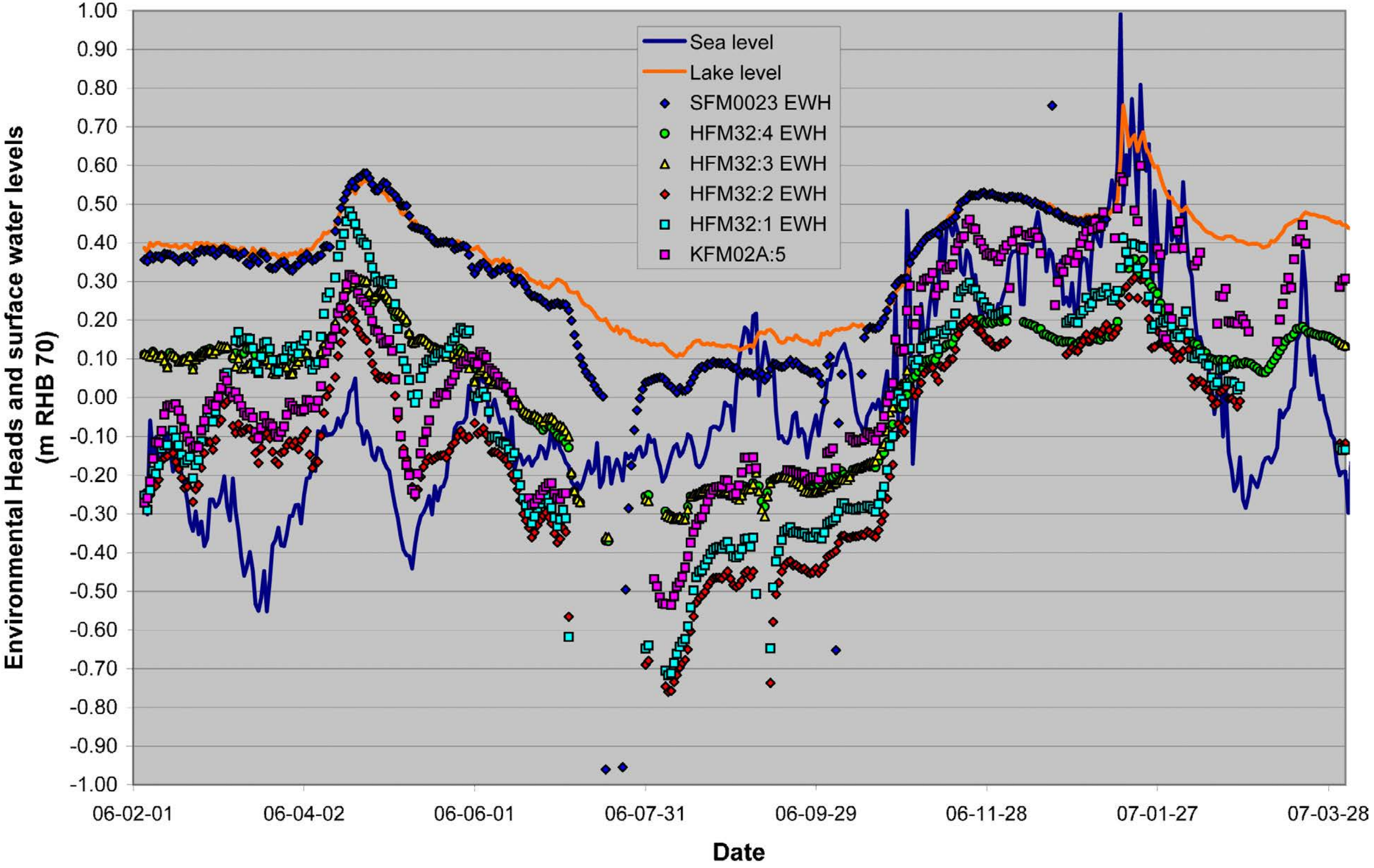

Figure J-4. *Surface water levels and environmental-water heads in the till and in the bedrock below Lake Bolundsfjärden as well as drill site 2. During the dry summer of year 2006 the density corrected heads are lower in the bedrock than in the Baltic Sea. Regardless of season the heads in section HFM32:2 are the lowest.*

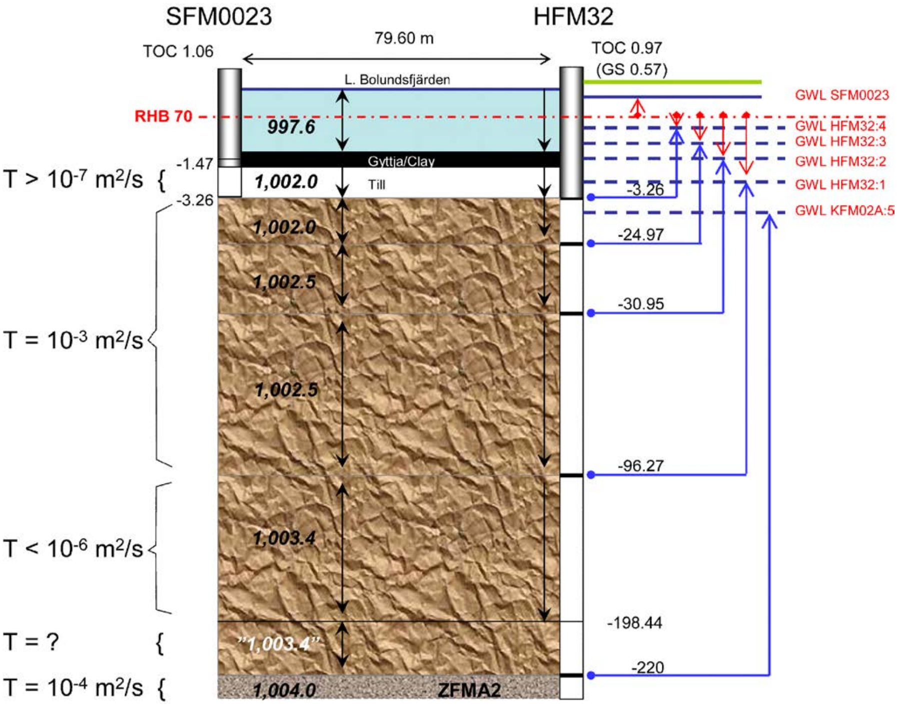

Figure J-5. Illustration of the geometrical configuration and water densities used for the computation of environmental-water heads in a vertical profile under Lake Bolundsfjärden. The salinity in the lake ranges between 997.5–1,000 kg/m^3. The Baltic Sea has a fairly constant water density of c. 1,001.5 kg/m^3. The high density in the till suggests that the lake sediments have a low vertical hydraulic conductivity.

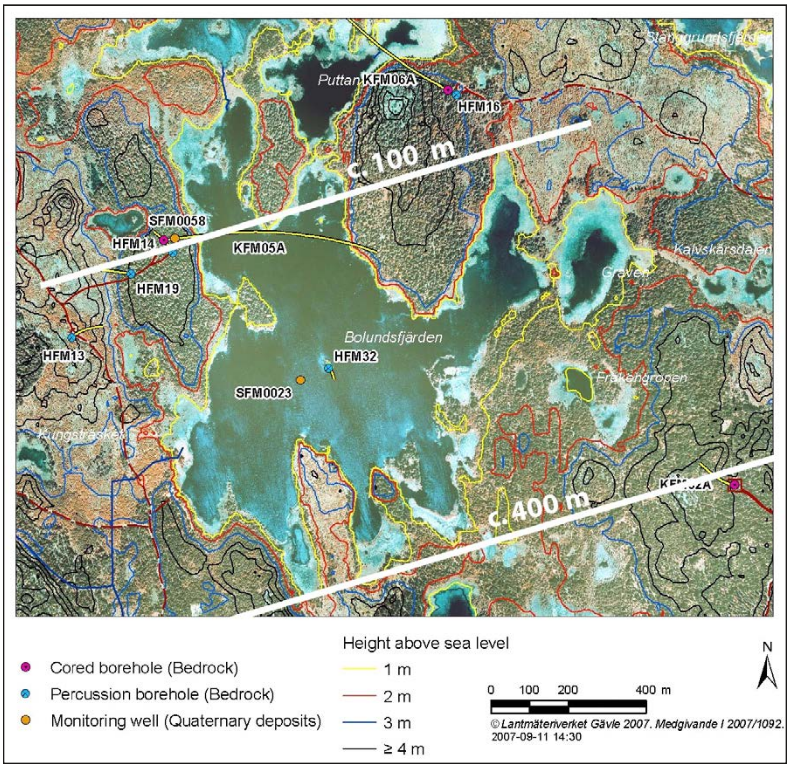

Figure J-6. Map showing the depth to the top of the gently dipping deformation zone A2 from the surface. The vertical distance from the bottom of HFM32 to the top of zone A2 is estimated to c. 20 m.

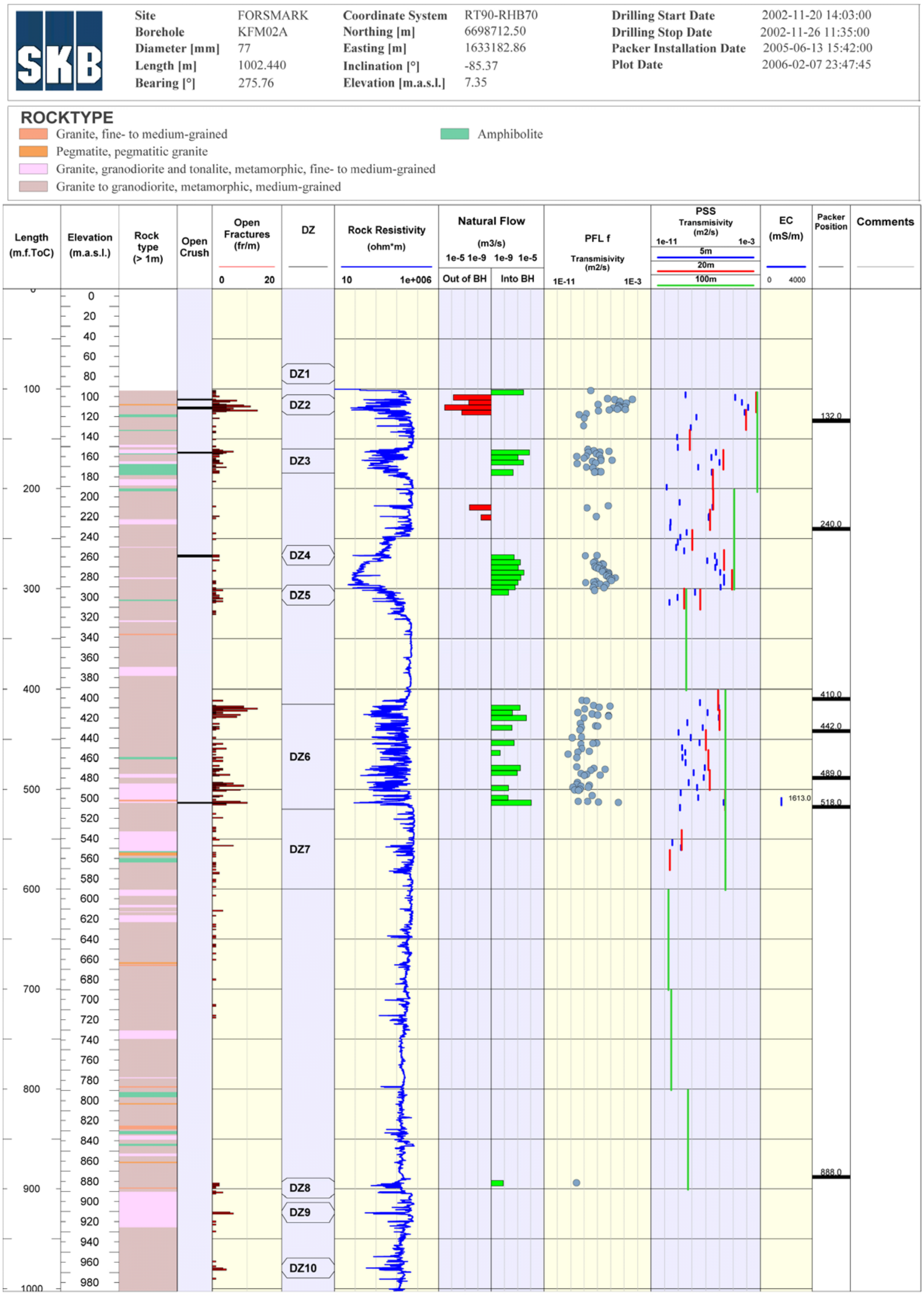

***Figure J-7.** Flow directions in KFM02A with depth (green for inflow and red for outflow) observed with the Posiva Flow Log after the drilling was completed. Reproduced from /Levén et al. 2006/.*

The notion behind the two hypotheses is that the pumping rates used are large enough to cause noticeable head changes (drawdowns) at HFM32 and KFM02A during dry periods when the influences of near-surface process are low. There are several examples of groundwater head disturbances in the Forsmark area caused by near-surface processes such as evapotranspiration and precipitation:

- Figure 3-51 shows an example from drill site 6 where the groundwater level in Quaternary deposits (SFM0021) drops below the groundwater level in the superficial bedrock (HFM16) during the dry summer of year 2006 /Werner et al. 2007/.
- During the dry summer of year 2003 it was noted that the evapotranspiration in the forests around Lake Bolundsfjärden caused a “drawdown” in the till layer underlying the lake sediments (SFM0030) /Johansson et al. 2005/.
- The head response in section KFM02A:5 at c. –400 m RHB 70 at drill site 2 caused by the precipitation event occurring during the 2005 interference test at HFM01. The phenomenon is described and analysed in Appendix G.

Data from the monitoring programme are currently subject for systematic analyses and a soil water budget will be reported in stage 2.3 /Johansson 2008/.

The hypothesis that the SFR facility disturbs the head field in the target area will be tested using flow models. Figure J-8 shows a cartoon of steady-state radial flow model where the discharge at the pumping well (SFR) is set to 5.5 L/s and the distance to the observation well (HFM32) is set to 2,700 m. The drawdowns are set to 23 m and 0.5 m respectively, i.e. in accordance with the observations mentioned above. The unknowns are the effective radius (r_2) of the well and the transmissivity (T) of the “hydraulic feature” connecting the observation point to the well.

The solution to the model can be written as /Thiem 1906/:

$$h_1 - h_2 = \frac{Q}{2\pi T} \ln\left(\frac{r_1}{r_2}\right) \qquad \text{(J-1)}$$

If we base an estimation of the large-scale transmissivity on the analysis provided in Figure 3-30, e.g. $T = 5 \cdot 10^{-4}$ m²/s, the effective radius of the well becomes about 15 m. If we assume the radius of SFR sink to be about 150 m, the large-scale transmissivity becomes about $T = 2 \cdot 10^{-4}$ m²/s.

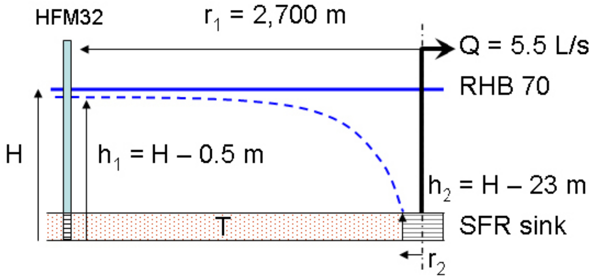

***Figure J-8.** Cartoon showing a steady-state radial flow model of a well (SFR) and an observation well (HFM32). The two points are hydraulically connected.*

Appendix K

Point-water head and environmental-water head

Groundwater level and point-water head

The groundwater density in the Forsmark area increases with depth. It also varies laterally. The groundwater levels (GWL) throughout the area are continuously monitored by means of programmed pressure transducers, which are installed in the many boreholes drilled in the Quaternary deposits (SFM) and in the bedrock (HFM and KFM). The pressure transducers are calibrated once a month using a manually operated water level measurement device (tape). The pressure transducer recordings are stored in SKB's hydrologic monitoring system (HMS). After quality control the data are transferred to SKB's database Sicada and used in modelling.

The groundwater levels recorded in the field are so called point-water heads. The illustration in Figure K-1 shows how they are measured. The borehole in Figure K-1 is intersected by a flowing fracture at point *i* and is completely filled with groundwater of density ρ_i. The fluid pressure p_i reflects the weight of the fluid $g\,\rho_i$ in the borehole above the point *i*. Figure K-2 shows the principle of point-water head measurements with a multipacker system. The different straddle intervals can have different fluid densities.

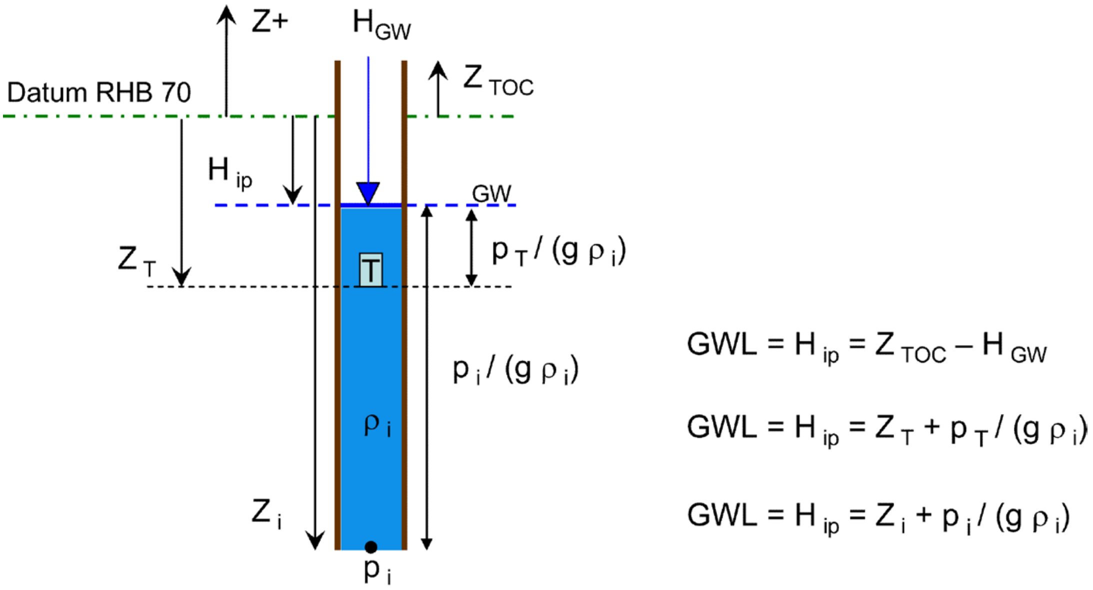

Figure K-1. *The definition of the groundwater level (GWL) in a borehole filled with a fluid of density* ρ_i*. The HMS uses programmed pressure transducers which are calibrated against the levels recorded with a manually operated water level device (tape). TOC = top of casing, GW = groundwater.*

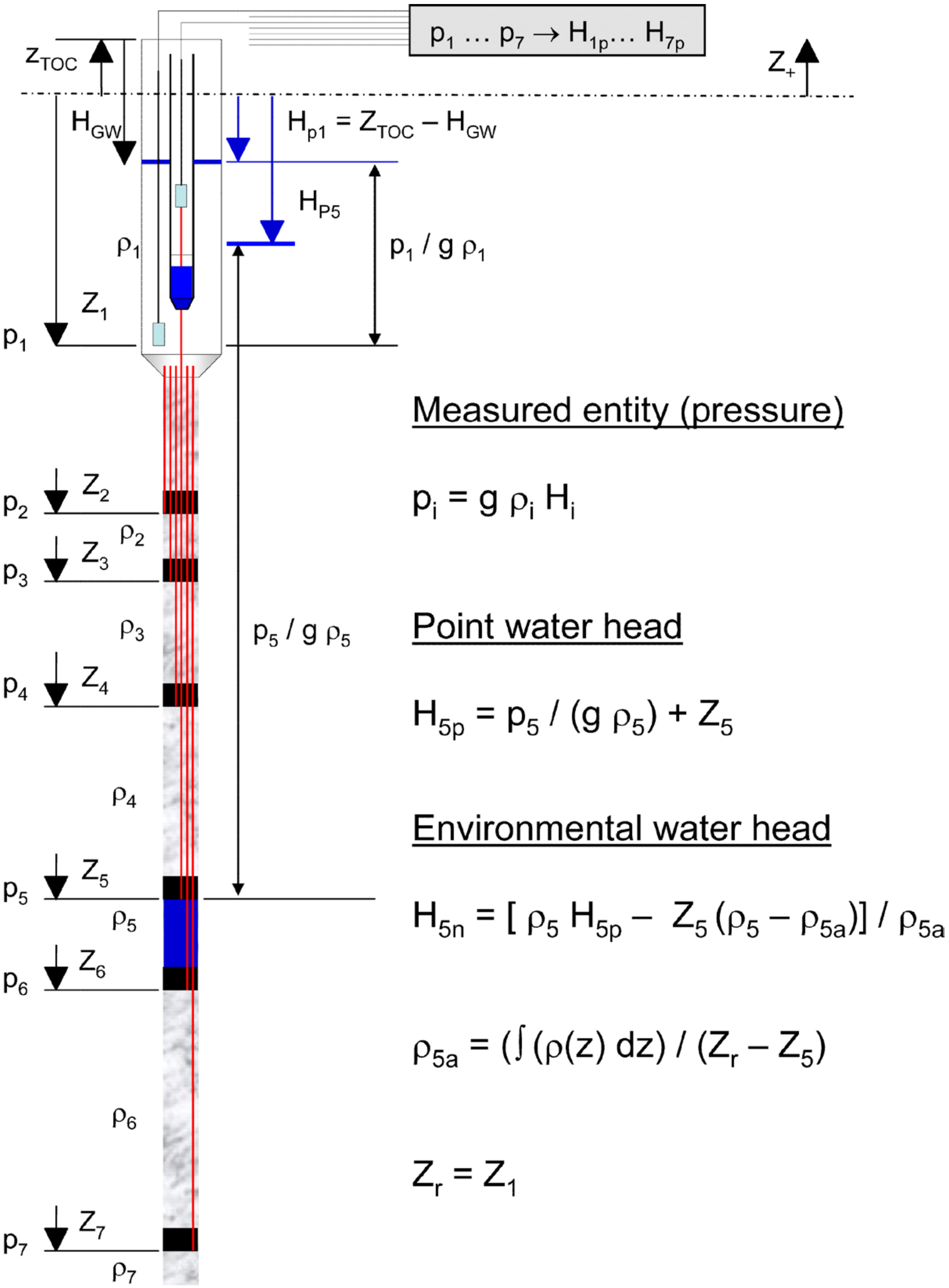

Figure K-2. *Principle for point-water head measurements in a borehole equipped with a multipacker system. /Lusczynski 1961/ is the key reference used in this report for transferring point-water heads* H_{ip} *to environmental water heads* H_{in}*.*

Point-water head and environmental water head

The interpretation of flow gradients from point-water head data in fractured crystalline rock can be quite misleading unless care is taken with regard to uncertainties in the fluid density measurements, geometrical positions of the packers and the structural geology. If a *porous medium* with a continuous density profile in the vertical direction $\rho(z)$ is assumed, the average fluid density ρ_a between the two elevations Z_i and Z_r can be written as /Lusczynski 1961/:

$$\rho_a = \frac{1}{Z_r - Z_i} \int_{Z_i}^{Z_r} \rho(z)\, dz \qquad \text{(K-1)}$$

where

Z_i = elevation of point *i*; elevation measured positively upwards.

Z_r = elevation of a reference point from which the average density of water to point *i* is determined and above which water is constant (e.g. fresh water).

From Figure K-1 we conclude that the pressure p_i is given by $g\,\rho_i\,(H_{ip} - Z_i)$ when the borehole is filled with groundwater of density p_i. By the same token, it is given by $g\,\rho_a\,(H_{in} - Z_i)$ when it is filled with groundwater of average density ρ_a. From this equality, the environmental water head H_{in} may be expressed in terms of the point-water head as:

$$H_{in} = p_i\, H_{ip} - Z_i\,(\rho_i - \rho_a)\,/\,\rho_a \qquad \text{(K-2)}$$

Example

Figure K-3 shows the elevations and point-water densities associated with the multiple packer system in the percussion-drilled borehole HFM19 together with the elevation and fluid density in the fairly nearby monitoring well in the Quaternary deposits (glacial till), SFM0058. The locations of the two boreholes are shown in Figure K-4.

SFM0058 has a hydraulic conductivity of c. $2 \cdot 10^{-5}$ m/s. HFM19 has three monitoring intervals, HFM19:1–3, where HFM19:1 is the deepest. Interval HFM19:1 has a transmissivity of c. $3 \cdot 10^{-4}$ m^2/s, interval HFM19:2 has a transmissivity of c. $2 \cdot 10^{-5}$ m^2/s and interval HFM19:3 has a transmissivity of c. $4 \cdot 10^{-5}$ m^2/s.

Figure K-5 illustrates measured groundwater levels, i.e. point-water heads, gathered in HFM19 and SFM0058 between 2006-01-31 and 2006-06-29. The different graphs react differently to the seasonal hydrological changes, with the largest changes in the glacial till. Interferences with the two pumping tests conducted in HFM14 are seen in the HFM19:1–3 graphs. The location of HFM14 is shown in Figure K-4.

The inset in the upper right shows a schematic illustration of the vertical gradient components if one uses measured point-water heads as a reference. Point-water heads suggest that HFM19 and SFM0058 are primarily located in a recharge area for most parts of the period except during the dry summer months when evapotranspiration make the groundwater level in the Quaternary deposits drop below the point-water head in HFM19:3.

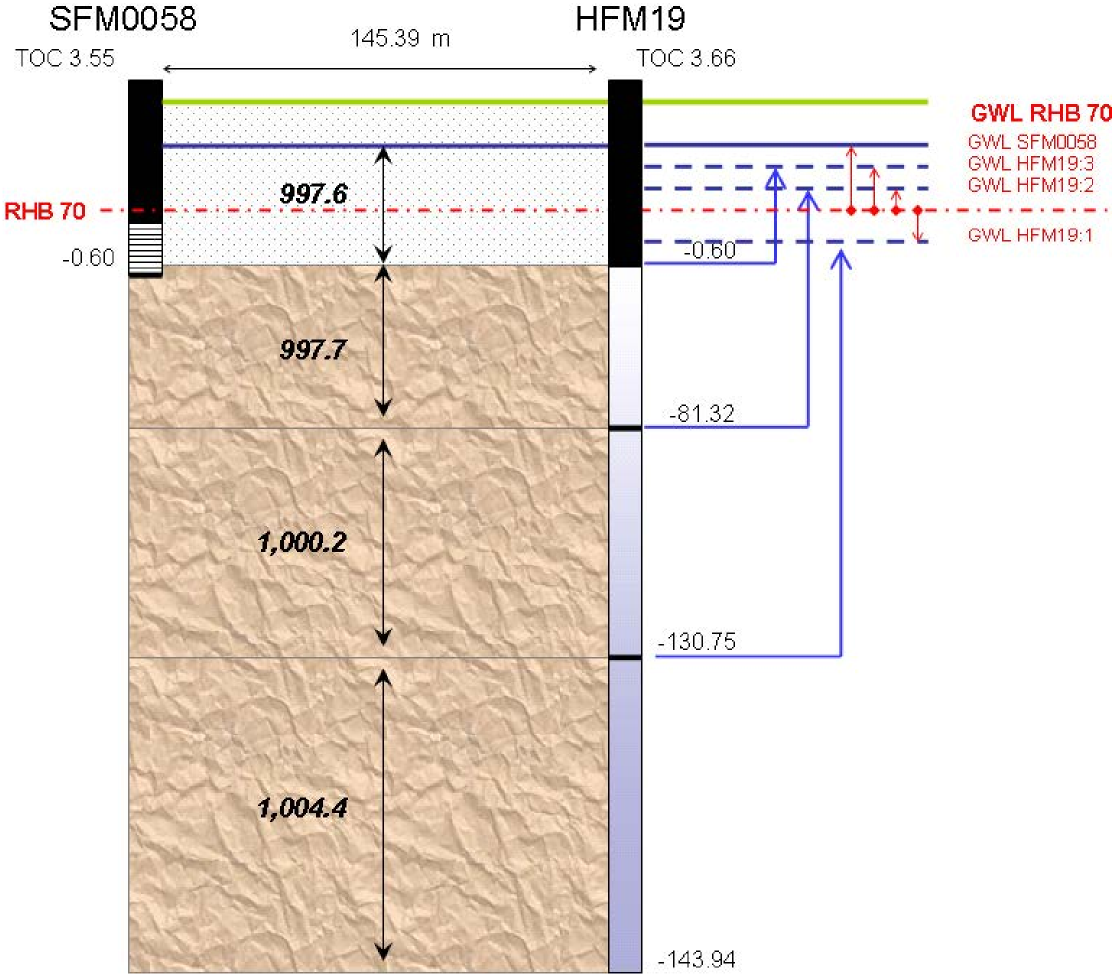

Figure K-3. *Elevations and point-water densities associated with the multiple packer system in the percussion-drilled borehole HFM19 together with the elevation and fluid density in the nearby monitoring well in the Quaternary deposits, SFM0058. Datum is RHB70. TOC = top of casing. Fluid densities between packers are treated as uniform (constant) between packers.*

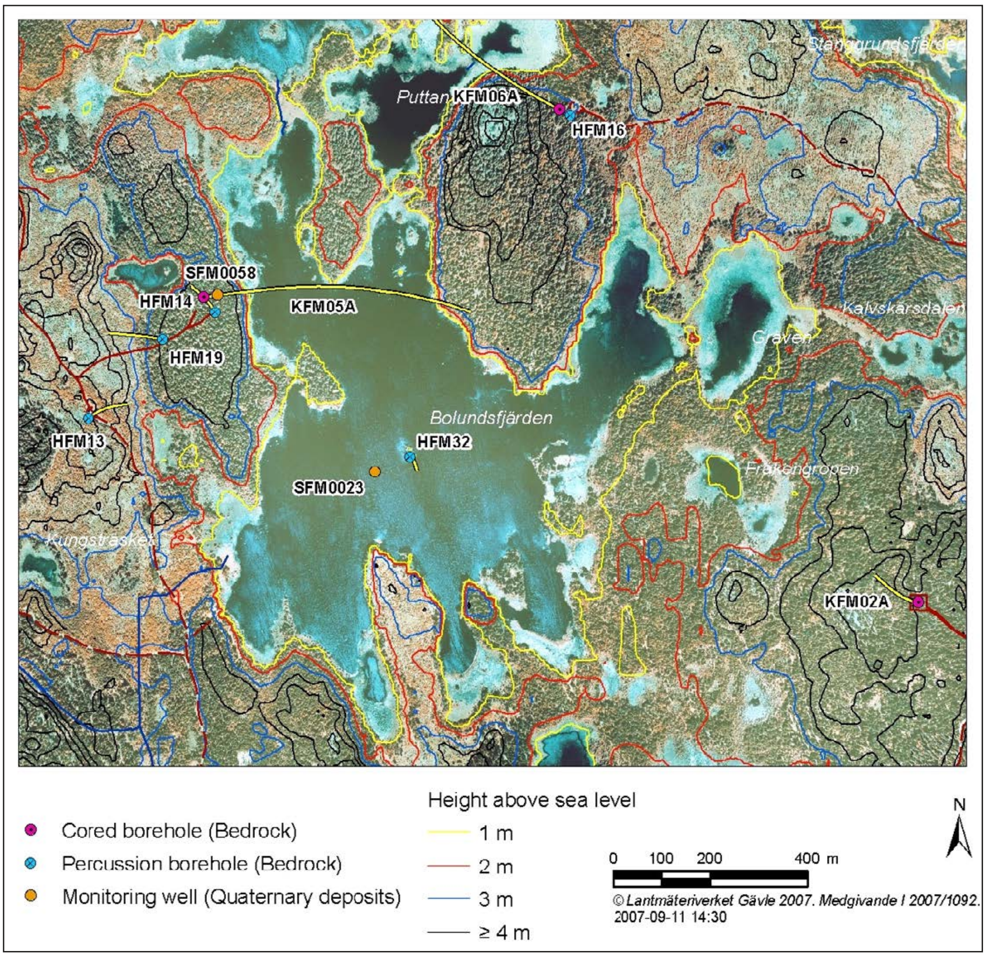

***Figure K-4.** Map showing Lake Bolundfjärden and nearby boreholes and monitoring wells of interest. HFM19 and SFM0058 are located on the western side of the lake.*

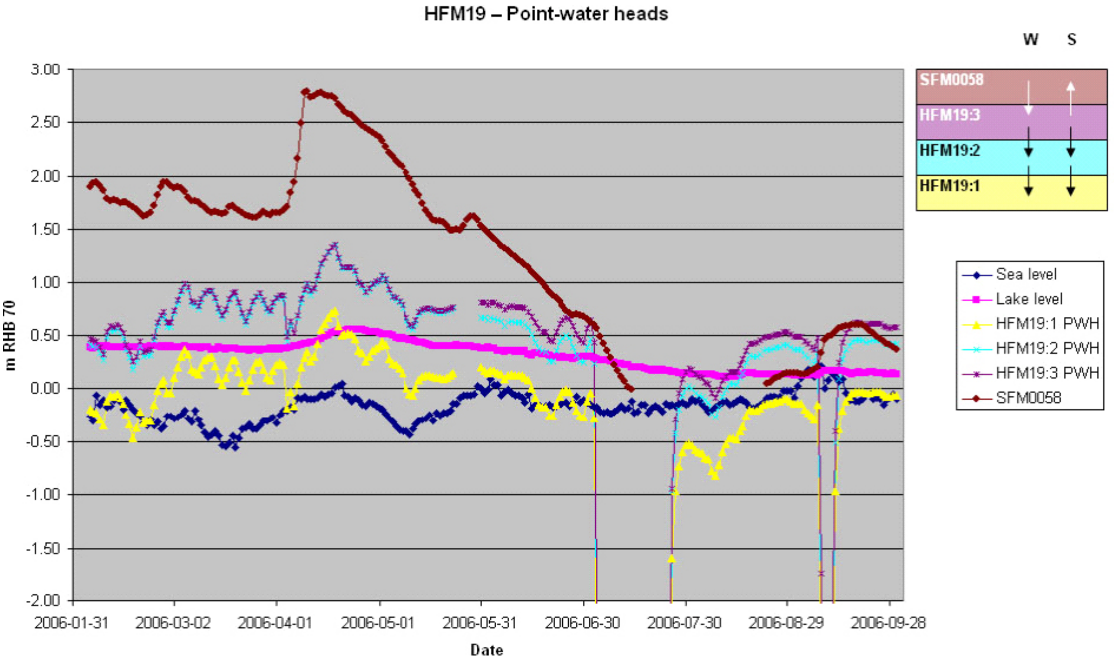

Figure K-5. *Plot of measured groundwater levels, i.e. point-water heads, gathered in HFM19 and SFM0058 from 2006-01-31 to 2006-06-29. The inset in the upper right shows a schematic illustration of the vertical gradient components if one uses point-water heads as a reference; W = winter and S = summer. Two pumping tests were conducted in July and September in HFM14. The location of HFM14 is shown in Figure K-4.*

Figure K-6 illustrates the same information as in Figure K-5 except that the measured groundwater levels have been transformed to environmental water heads. Figure K-6 is based on the assumption of a constant fluid density between packers, cf. Figure K-3. The inset in the upper right shows a schematic illustration of the vertical gradient components if one uses constant-density environmental water heads as a reference.

Constant-density environmental-water heads suggest a complex gradient pattern between the different "intervals" in the bedrock. During the winter period the environmental-water heads in the middle interval, HFM19:2, are apparently greater than the heads in the bedrock intervals both above and below. The heads in the Quaternary deposits, however, are still the greatest, which suggests that the main "discharge interval" is HFM19:3. During the dry summer period evapotranspiration makes the groundwater level in the Quaternary deposits drop below the point-water head in all bedrock intervals.

Discussion and conclusions

Figure K-5 and Figure K-6 demonstrate that the interpretation of the vertical gradients derived from point-water heads or point-water heads must be treated with great caution. This observation was discussed by /Juston et al. 2007/ who also discussed the role of different density profile between the packers than the constant value assumed in this analysis, see Figure K-3. Furthermore, /Juston et al. 2007/ also showed graphs for SFM0058 and HFM19 where the point-water heads in Figure K-5 were transferred to freshwater heads.

The results open up for a discussion about different types of uncertainties. A vital uncertainty is of course the assumption of the density profile in the bedrock outside the borehole HFM19. It is noted that the tentative results shown in Figure K-6 are based on the assumption that fractured crystalline rock is a continuous porous medium, which we know it is not. For instance, interval HFM19:1 is intersected by the extensive and gently dipping deformation zone A2.

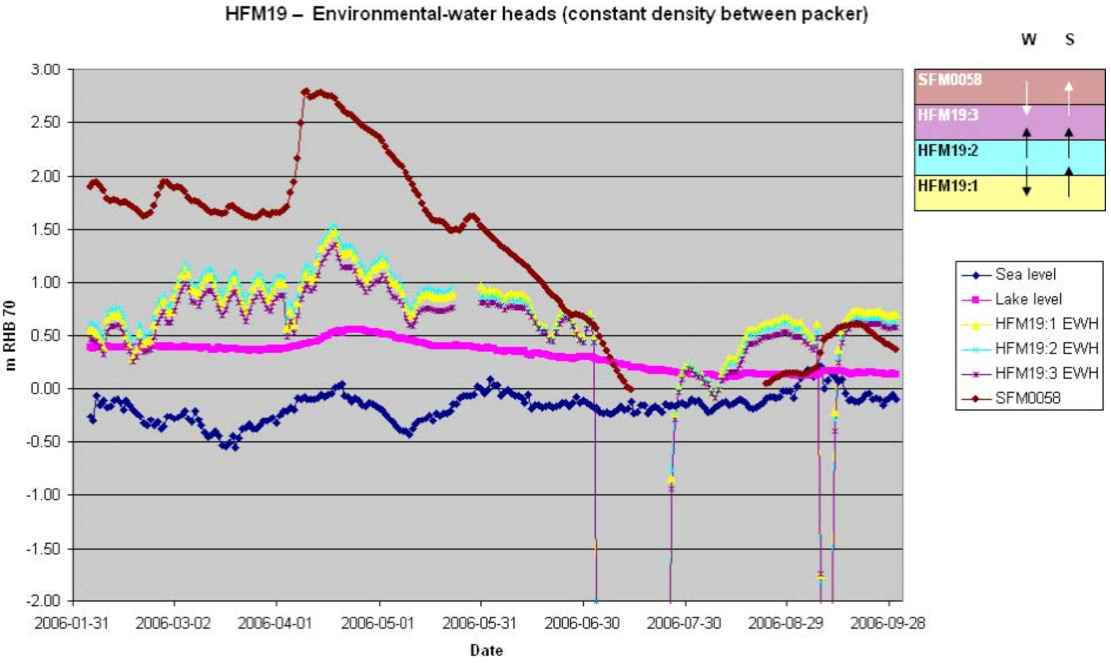

Figure K-6. *Plot of same information as in Figure K-5 after that the measured groundwater levels have been transformed to environmental-water heads. Figure K-6 is based on the assumption of a constant fluid density between packers, cf. Figure A1-2. The inset in the upper right shows a schematic illustration of the vertical gradient components if one uses environmental-water heads as a reference; W = winter and S = summer. Two pumping tests were conducted in July and September in HFM14. The location of HFM14 is shown in Figure K-4.*

Appendix L

Calibration properties for deformation zones

The definition of hydraulic properties used in the central calibration case for the each deformation zone is specified in Table L-1. The depth variation was implemented in CONNECTFLOW as a step-wise change every 100 m of elevation.

Table L-1. Depth variation of hydraulic conductivity K (m/s) and hydraulic thickness, b_h (m), in HCD for 100 m-thick depth zones used for groundwater flow and solute transport in the central calibration case. All elevations are in m RHB 70.

Deformation zone (ZFM)	b_h (m)	Hydraulic conductivity K (m/s) for depth interval (m RHB 70)									
		0 to –100	–100 to –200	–200 to –300	–300 to –400	–400 to –500	–500 to –600	–600 to –700	–700 to –800	–800 to –900	–900 to –1,000
1189	7	$1.26\ 10^{-6}$	$4.69\ 10^{-7}$	$4.00\ 10^{-6}$	$6.47\ 10^{-8}$	$2.40\ 10^{-8}$	$8.92\ 10^{-9}$	$3.31\ 10^{-9}$	$1.23\ 10^{-9}$	$1.00\ 10^{-9}$	$1.00\ 10^{-9}$
1203	10	$1.78\ 10^{-5}$	$6.61\ 10^{-6}$	$2.46\ 10^{-6}$	$9.12\ 10^{-7}$	$3.39\ 10^{-7}$	$1.26\ 10^{-7}$	$4.67\ 10^{-8}$	$1.74\ 10^{-8}$	$6.45\ 10^{-9}$	$2.40\ 10^{-9}$
866	11	$2.31\ 10^{-5}$	$8.59\ 10^{-5}$	$3.19\ 10^{-6}$	$1.19\ 10^{-6}$	$4.40\ 10^{-7}$	$1.64\ 10^{-7}$	$6.07\ 10^{-8}$	$2.26\ 10^{-8}$	$8.38\ 10^{-9}$	$3.11\ 10^{-9}$
871	10	$2.54\ 10^{-5}$	$9.45\ 10^{-6}$	$3.51\ 10^{-6}$	$1.30\ 10^{-6}$	$4.84\ 10^{-7}$	$1.80\ 10^{-7}$	$6.68\ 10^{-8}$	$2.48\ 10^{-8}$	$9.22\ 10^{-9}$	$3.42\ 10^{-9}$
A1	40	$3.98\ 10^{-7}$	$1.48\ 10^{-7}$	$5.50\ 10^{-8}$	$2.04\ 10^{-8}$	$7.59\ 10^{-9}$	$2.82\ 10^{-9}$	$1.05\ 10^{-9}$	$1.00\ 10^{-9}$	$1.00\ 10^{-9}$	$1.00\ 10^{-9}$
A2	5	$5.66\ 10^{-5}$	$5.66\ 10^{-5}$	$5.66\ 10^{-5}$	$5.66\ 10^{-5}$	$1.08\ 10^{-6}$	$4.00\ 10^{-7}$	$1.49\ 10^{-7}$	$5.52\ 10^{-8}$	$2.05\ 10^{-8}$	$7.62\ 10^{-9}$
A3	17	$3.32\ 10^{-8}$	$5.00\ 10^{-6}$	$4.59\ 10^{-9}$	$1.70\ 10^{-9}$	$1.00\ 10^{-9}$	$1.00\ 10^{-9}$	$1.00\ 10^{-9}$	$3.24\ 10^{-10}$	$1.00\ 10^{-9}$	$1.00\ 10^{-9}$
A4	25	$8.97\ 10^{-9}$	$3.33\ 10^{-9}$	$1.24\ 10^{-9}$	$5.00\ 10^{-5}$	$1.00\ 10^{-9}$	$1.00\ 10^{-9}$	$1.00\ 10^{-9}$	$1.00\ 10^{-9}$	$1.00\ 10^{-9}$	$1.00\ 10^{-9}$
A5	10	$2.29\ 10^{-5}$	$8.49\ 10^{-6}$	$3.15\ 10^{-6}$	$1.17\ 10^{-6}$	$4.35\ 10^{-7}$	$1.62\ 10^{-7}$	$6.01\ 10^{-8}$	$2.23\ 10^{-8}$	$8.29\ 10^{-9}$	$3.08\ 10^{-9}$
A6-e	10	$1.04\ 10^{-11}$	$1.00\ 10^{-11}$	$1.00\ 10^{-11}$	$1.00\ 10^{-11}$	$1.00\ 10^{-11}$	$1.00\ 10^{-11}$	$1.00\ 10^{-11}$	$1.00\ 10^{-11}$	$1.00\ 10^{-11}$	$1.00\ 10^{-11}$
A6-w	10	$1.04\ 10^{-11}$	$1.00\ 10^{-11}$	$1.00\ 10^{-11}$	$1.00\ 10^{-11}$	$1.00\ 10^{-11}$	$1.00\ 10^{-11}$	$1.00\ 10^{-11}$	$1.00\ 10^{-11}$	$1.00\ 10^{-11}$	$1.00\ 10^{-11}$
A7	7	$3.39\ 10^{-8}$	$1.26\ 10^{-8}$	$4.68\ 10^{-9}$	$1.74\ 10^{-9}$	$5.00\ 10^{-5}$	$1.00\ 10^{-9}$	$1.00\ 10^{-9}$	$1.00\ 10^{-9}$	$1.00\ 10^{-9}$	$1.00\ 10^{-9}$
A8	5	$7.41\ 10^{-5}$	$2.75\ 10^{-5}$	$1.02\ 10^{-5}$	$3.80\ 10^{-6}$	$1.41\ 10^{-6}$	$5.24\ 10^{-7}$	$1.95\ 10^{-7}$	$7.23\ 10^{-8}$	$2.69\ 10^{-8}$	$9.98\ 10^{-9}$
B1	7	$1.13\ 10^{-4}$	$4.18\ 10^{-5}$	$1.55\ 10^{-5}$	$5.77\ 10^{-6}$	$2.14\ 10^{-6}$	$7.97\ 10^{-7}$	$2.96\ 10^{-6}$	$1.10\ 10^{-7}$	$4.08\ 10^{-8}$	$1.52\ 10^{-8}$
B23	15	$6.22\ 10^{-6}$	$2.31\ 10^{-6}$	$8.59\ 10^{-7}$	$3.19\ 10^{-7}$	$1.18\ 10^{-7}$	$4.40\ 10^{-8}$	$1.63\ 10^{-8}$	$6.07\ 10^{-9}$	$2.25\ 10^{-9}$	$1.00\ 10^{-9}$
B4	15	$6.92\ 10^{-7}$	$2.57\ 10^{-7}$	$9.55\ 10^{-8}$	$3.55\ 10^{-8}$	$1.32\ 10^{-8}$	$4.89\ 10^{-9}$	$1.82\ 10^{-9}$	$1.00\ 10^{-9}$	$1.00\ 10^{-9}$	$1.00\ 10^{-9}$
B5	15	$6.22\ 10^{-6}$	$2.31\ 10^{-6}$	$8.59\ 10^{-7}$	$3.19\ 10^{-7}$	$1.18\ 10^{-7}$	$4.40\ 10^{-8}$	$1.63\ 10^{-8}$	$6.07\ 10^{-9}$	$2.25\ 10^{-9}$	$1.00\ 10^{-9}$
B6	15	$6.22\ 10^{-6}$	$2.31\ 10^{-6}$	$8.59\ 10^{-7}$	$3.19\ 10^{-7}$	$1.18\ 10^{-7}$	$4.40\ 10^{-8}$	$1.63\ 10^{-8}$	$6.07\ 10^{-9}$	$2.25\ 10^{-9}$	$1.00\ 10^{-9}$
B7	28	$9.91\ 10^{-7}$	$3.68\ 10^{-7}$	$1.37\ 10^{-7}$	$5.08\ 10^{-8}$	$1.89\ 10^{-8}$	$7.01\ 10^{-9}$	$2.60\ 10^{-9}$	$1.00\ 10^{-9}$	$1.00\ 10^{-9}$	$1.00\ 10^{-9}$
B8	6	$4.86\ 10^{-5}$	$1.80\ 10^{-5}$	$6.70\ 10^{-6}$	$2.49\ 10^{-6}$	$9.24\ 10^{-7}$	$3.43\ 10^{-7}$	$1.28\ 10^{-7}$	$4.74\ 10^{-8}$	$1.76\ 10^{-8}$	$6.54\ 10^{-9}$
E1	15	$6.22\ 10^{-6}$	$2.31\ 10^{-6}$	$8.59\ 10^{-7}$	$3.19\ 10^{-7}$	$1.18\ 10^{-7}$	$4.40\ 10^{-8}$	$1.63\ 10^{-8}$	$6.07\ 10^{-9}$	$2.25\ 10^{-9}$	$8.38\ 10^{-10}$
F1	44	$8.19\ 10^{-6}$	$3.04\ 10^{-6}$	$1.13\ 10^{-6}$	$4.20\ 10^{-7}$	$1.56\ 10^{-7}$	$5.79\ 10^{-8}$	$2.15\ 10^{-8}$	$7.99\ 10^{-9}$	$2.97\ 10^{-9}$	$1.10\ 10^{-9}$
J1	15	$6.22\ 10^{-6}$	$2.31\ 10^{-6}$	$8.59\ 10^{-7}$	$3.19\ 10^{-7}$	$1.18\ 10^{-7}$	$4.40\ 10^{-8}$	$1.63\ 10^{-8}$	$6.07\ 10^{-9}$	$2.25\ 10^{-9}$	$8.38\ 10^{-10}$
J2	15	$6.22\ 10^{-6}$	$2.31\ 10^{-6}$	$8.59\ 10^{-7}$	$3.19\ 10^{-7}$	$1.18\ 10^{-7}$	$4.40\ 10^{-8}$	$1.63\ 10^{-8}$	$6.07\ 10^{-9}$	$2.25\ 10^{-9}$	$8.38\ 10^{-10}$
K1	15	$6.22\ 10^{-6}$	$2.31\ 10^{-6}$	$8.59\ 10^{-7}$	$3.19\ 10^{-7}$	$1.18\ 10^{-7}$	$4.40\ 10^{-8}$	$1.63\ 10^{-8}$	$6.07\ 10^{-9}$	$2.25\ 10^{-9}$	$8.38\ 10^{-10}$

Deformation zone (ZFM)	**b_h (m)**	**Hydraulic conductivity K (m/s) for depth interval (m RHB 70)**									
		0 to –100	**–100 to –200**	**–200 to –300**	**–300 to –400**	**–400 to –500**	**–500 to –600**	**–600 to –700**	**–700 to –800**	**–800 to –900**	**–900 to –1,000**
ENE0060A	5	$3.45\ 10^{-7}$	$1.28\ 10^{-9}$	$4.76\ 10^{-9}$	$1.77\ 10^{-8}$	$6.56\ 10^{-9}$	$2.44\ 10^{-9}$	$1.00\ 10^{-9}$	$1.00\ 10^{-9}$	$1.00\ 10^{-9}$	$1.00\ 10^{-9}$
ENE0060B	5	$3.99\ 10^{-5}$	$1.48\ 10^{-3}$	$5.51\ 10^{-5}$	$2.05\ 10^{-6}$	$7.60\ 10^{-7}$	$2.82\ 10^{-7}$	$1.05\ 10^{-7}$	$3.89\ 10^{-8}$	$1.45\ 10^{-8}$	$5.37\ 10^{-9}$
ENE0060C	20	$1.06\ 10^{-9}$	$1.00\ 10^{-9}$	$5.00\ 10^{-12}$	$1.00\ 10^{-9}$	$1.00\ 10^{-9}$	$1.00\ 10^{-9}$	$1.00\ 10^{-9}$	$1.00\ 10^{-9}$	$1.00\ 10^{-9}$	$1.00\ 10^{-9}$
ENE0061	11	$2.06\ 10^{-9}$	$7.66\ 10^{-10}$	$2.85\ 10^{-10}$	$1.06\ 10^{-10}$	$3.93\ 10^{-11}$	$1.46\ 10^{-9}$	$9.09\ 10^{-12}$	$9.09\ 10^{-12}$	$9.09\ 10^{-12}$	$9.09\ 10^{-12}$
ENE0062A	44	$1.00\ 10^{-9}$	$1.00\ 10^{-9}$	$1.00\ 10^{-9}$	$1.00\ 10^{-9}$	$1.00\ 10^{-9}$	$1.00\ 10^{-9}$	$1.00\ 10^{-9}$	$1.00\ 10^{-9}$	$1.00\ 10^{-9}$	$1.00\ 10^{-9}$
ENE0062B	10	$6.32\ 10^{-9}$	$2.35\ 10^{-9}$	$1.00\ 10^{-9}$	$1.00\ 10^{-9}$	$1.00\ 10^{-9}$	$1.00\ 10^{-9}$	$1.00\ 10^{-9}$	$1.00\ 10^{-9}$	$1.00\ 10^{-9}$	$1.00\ 10^{-9}$
ENE0062C	5	$1.26\ 10^{-8}$	$4.69\ 10^{-9}$	$1.74\ 10^{-9}$	$1.00\ 10^{-9}$	$1.00\ 10^{-9}$	$1.00\ 10^{-9}$	$1.00\ 10^{-9}$	$1.00\ 10^{-9}$	$1.00\ 10^{-9}$	$1.00\ 10^{-9}$
ENE0103	13	$7.69\ 10^{-9}$	$2.86\ 10^{-9}$	$1.06\ 10^{-9}$	$3.94\ 10^{-10}$	$1.46\ 10^{-10}$	$5.44\ 10^{-11}$	$2.02\ 10^{-11}$	$7.69\ 10^{-12}$	$7.69\ 10^{-12}$	$7.69\ 10^{-12}$
ENE0159A	16	$9.13\ 10^{-8}$	$3.39\ 10^{-8}$	$6.30\ 10^{-9}$	$6.25\ 10^{-12}$	$1.74\ 10^{-11}$	$6.45\ 10^{-11}$	$2.40\ 10^{-11}$	$8.90\ 10^{-12}$	$6.25\ 10^{-12}$	$6.25\ 10^{-12}$
ENE0159B	10	$1.46\ 10^{-8}$	$5.42\ 10^{-9}$	$2.01\ 10^{-9}$	$7.48\ 10^{-10}$	$2.78\ 10^{-10}$	$1.03\ 10^{-10}$	$3.84\ 10^{-11}$	$1.42\ 10^{-11}$	$1.00\ 10^{-11}$	$1.00\ 10^{-11}$
ENE0168	10	$1.46\ 10^{-8}$	$5.42\ 10^{-9}$	$2.01\ 10^{-9}$	$7.48\ 10^{-10}$	$2.78\ 10^{-10}$	$1.03\ 10^{-10}$	$3.84\ 10^{-11}$	$1.42\ 10^{-11}$	$1.00\ 10^{-11}$	$1.00\ 10^{-11}$
ENE0169	15	$9.74\ 10^{-9}$	$3.62\ 10^{-9}$	$1.34\ 10^{-9}$	$4.99\ 10^{-10}$	$1.85\ 10^{-10}$	$6.88\ 10^{-11}$	$2.56\ 10^{-11}$	$9.50\ 10^{-12}$	$6.67\ 10^{-12}$	$6.67\ 10^{-12}$
ENE0401A	5	$8.25\ 10^{-6}$	$3.07\ 10^{-6}$	$1.14\ 10^{-6}$	$4.23\ 10^{-7}$	$1.57\ 10^{-7}$	$5.84\ 10^{-10}$	$2.17\ 10^{-8}$	$8.05\ 10^{-9}$	$2.99\ 10^{-9}$	$1.11\ 10^{-9}$
ENE0401B	5	$1.78\ 10^{-9}$	$6.60\ 10^{-10}$	$2.45\ 10^{-10}$	$9.10\ 10^{-11}$	$2.00\ 10^{-11}$	$2.00\ 10^{-11}$	$2.00\ 10^{-11}$	$2.00\ 10^{-11}$	$2.00\ 10^{-11}$	$2.00\ 10^{-11}$
ENE0810	25	$3.92\ 10^{-8}$	$1.46\ 10^{-8}$	$5.42\ 10^{-9}$	$2.01\ 10^{-9}$	$7.47\ 10^{-10}$	$2.78\ 10^{-10}$	$1.03\ 10^{-10}$	$3.83\ 10^{-11}$	$1.42\ 10^{-11}$	$5.28\ 10^{-12}$
ENE1057	10	$9.81\ 10^{-8}$	$3.64\ 10^{-8}$	$1.35\ 10^{-8}$	$5.03\ 10^{-9}$	$1.87\ 10^{-9}$	$6.94\ 10^{-10}$	$2.58\ 10^{-10}$	$9.57\ 10^{-11}$	$3.56\ 10^{-11}$	$1.32\ 10^{-11}$
ENE1061A	45	$2.32\ 10^{-8}$	$8.60\ 10^{-9}$	$3.19\ 10^{-7}$	$1.19\ 10^{-9}$	$4.41\ 10^{-10}$	$1.64\ 10^{-10}$	$2.22\ 10^{-12}$	$2.22\ 10^{-12}$	$8.39\ 10^{-12}$	$3.12\ 10^{-12}$
ENE1061B	2	$2.72\ 10^{-8}$	$1.01\ 10^{-8}$	$3.75\ 10^{-9}$	$1.39\ 10^{-9}$	$5.18\ 10^{-10}$	$1.92\ 10^{-10}$	$7.14\ 10^{-11}$	$5.00\ 10^{-11}$	$5.00\ 10^{-11}$	$5.00\ 10^{-11}$
ENE1192	3	$1.52\ 10^{-6}$	$3.33\ 10^{-11}$	$3.33\ 10^{-11}$	$3.33\ 10^{-11}$	$3.33\ 10^{-11}$	$3.33\ 10^{-11}$	$3.33\ 10^{-11}$	$3.33\ 10^{-11}$	$3.33\ 10^{-11}$	$3.33\ 10^{-11}$
ENE1208A	20	$6.75\ 10^{-7}$	$2.51\ 10^{-10}$	$9.31\ 10^{-11}$	$3.46\ 10^{-11}$	$1.28\ 10^{-11}$	$5.00\ 10^{-12}$	$5.00\ 10^{-12}$	$5.00\ 10^{-11}$	$5.00\ 10^{-12}$	$5.00\ 10^{-12}$
ENE1208B	20	$1.31\ 10^{-5}$	$4.86\ 10^{-9}$	$1.81\ 10^{-9}$	$6.71\ 10^{-10}$	$2.49\ 10^{-10}$	$9.26\ 10^{-11}$	$5.00\ 10^{-12}$	$1.28\ 10^{-11}$	$5.00\ 10^{-12}$	$5.00\ 10^{-12}$
ENE2120	12	$1.27\ 10^{-11}$	$8.33\ 10^{-12}$	$8.33\ 10^{-12}$	$8.33\ 10^{-12}$	$8.33\ 10^{-12}$	$8.33\ 10^{-12}$	$8.33\ 10^{-12}$	$8.33\ 10^{-12}$	$8.33\ 10^{-12}$	$8.33\ 10^{-12}$
ENE2248	38	$8.30\ 10^{-10}$	$3.08\ 10^{-10}$	$1.15\ 10^{-10}$	$4.25\ 10^{-11}$	$1.58\ 10^{-11}$	$5.87\ 10^{-12}$	$2.63\ 10^{-12}$	$2.63\ 10^{-12}$	$2.63\ 10^{-12}$	$2.63\ 10^{-12}$
ENE2254	3	$1.29\ 10^{-8}$	$4.81\ 10^{-9}$	$1.79\ 10^{-9}$	$6.63\ 10^{-10}$	$2.46\ 10^{-10}$	$9.15\ 10^{-11}$	$3.40\ 10^{-11}$	$3.33\ 10^{-11}$	$3.33\ 10^{-11}$	$3.33\ 10^{-11}$
ENE2283	10	$2.99\ 10^{-9}$	$1.11\ 10^{-9}$	$4.12\ 10^{-10}$	$1.53\ 10^{-10}$	$5.69\ 10^{-11}$	$2.11\ 10^{-11}$	$1.00\ 10^{-11}$	$1.00\ 10^{-11}$	$1.00\ 10^{-11}$	$1.00\ 10^{-11}$
ENE2320	40	$6.90\ 10^{-10}$	$2.56\ 10^{-10}$	$1.81\ 10^{-9}$	$3.53\ 10^{-11}$	$1.31\ 10^{-11}$	$4.88\ 10^{-12}$	$2.50\ 10^{-12}$	$2.50\ 10^{-12}$	$2.50\ 10^{-12}$	$2.50\ 10^{-12}$
ENE2325A	30	$1.29\ 10^{-9}$	$4.79\ 10^{-10}$	$1.78\ 10^{-10}$	$4.35\ 10^{-12}$	$4.35\ 10^{-12}$	$9.12\ 10^{-12}$	$3.39\ 10^{-12}$	$3.33\ 10^{-12}$	$3.33\ 10^{-12}$	$3.33\ 10^{-12}$
ENE2325B	10	$1.26\ 10^{-6}$	$4.69\ 10^{-7}$	$1.74\ 10^{-7}$	$6.47\ 10^{-8}$	$2.40\ 10^{-8}$	$8.93\ 10^{-9}$	$3.32\ 10^{-9}$	$1.23\ 10^{-9}$	$4.58\ 10^{-10}$	$1.70\ 10^{-10}$
ENE2332	15	$9.50\ 10^{-8}$	$3.53\ 10^{-8}$	$1.31\ 10^{-8}$	$4.87\ 10^{-9}$	$1.81\ 10^{-9}$	$6.72\ 10^{-10}$	$2.50\ 10^{-10}$	$9.27\ 10^{-11}$	$3.44\ 10^{-11}$	$1.28\ 10^{-11}$
ENE2383	34	$4.73\ 10^{-9}$	$1.76\ 10^{-9}$	$6.53\ 10^{-10}$	$2.42\ 10^{-10}$	$9.01\ 10^{-11}$	$3.35\ 10^{-11}$	$1.24\ 10^{-11}$	$4.62\ 10^{-12}$	$2.94\ 10^{-12}$	$2.94\ 10^{-12}$
ENE2403	4	$1.10\ 10^{-10}$	$4.07\ 10^{-11}$	$2.50\ 10^{-11}$	$2.50\ 10^{-11}$	$2.50\ 10^{-11}$	$2.50\ 10^{-11}$	$2.50\ 10^{-11}$	$2.50\ 10^{-11}$	$2.50\ 10^{-11}$	$2.50\ 10^{-11}$
EW0137	30	$1.25\ 10^{-9}$	$1.00\ 10^{-9}$	$1.00\ 10^{-9}$	$1.00\ 10^{-9}$	$1.00\ 10^{-9}$	$1.00\ 10^{-9}$	$1.00\ 10^{-9}$	$1.00\ 10^{-9}$	$1.00\ 10^{-9}$	$1.00\ 10^{-9}$
EW1156	25	$1.50\ 10^{-9}$	$1.00\ 10^{-9}$	$1.00\ 10^{-9}$	$1.00\ 10^{-9}$	$1.00\ 10^{-9}$	$1.00\ 10^{-9}$	$1.00\ 10^{-9}$	$1.00\ 10^{-9}$	$1.00\ 10^{-9}$	$1.00\ 10^{-9}$
EW2311	10	$3.74\ 10^{-9}$	$1.39\ 10^{-9}$	$5.16\ 10^{-10}$	$1.92\ 10^{-10}$	$7.12\ 10^{-11}$	$2.64\ 10^{-11}$	$1.00\ 10^{-11}$	$1.00\ 10^{-11}$	$1.00\ 10^{-11}$	$1.00\ 10^{-11}$

Deformation zone (ZFM)	b_h (m)	Hydraulic conductivity K (m/s) for depth interval (m RHB 70)									
		0 to –100	–100 to –200	–200 to –300	–300 to –400	–400 to –500	–500 to –600	–600 to –700	–700 to –800	–800 to –900	–900 to –1,000
NE0065	26	1.00 10^{-9}	1.00 10^{-9}	1.00 10^{-9}	1.00 10^{-9}	1.00 10^{-9}	1.00 10^{-9}	1.00 10^{-9}	1.00 10^{-9}	1.00 10^{-9}	1.00 10^{-9}
NE0808A	30	1.25 10^{-9}	1.00 10^{-9}	1.00 10^{-9}	1.00 10^{-9}	1.00 10^{-9}	1.00 10^{-9}	1.00 10^{-9}	1.00 10^{-9}	1.00 10^{-9}	1.00 10^{-9}
NE0808B	10	3.74 10^{-9}	1.39 10^{-9}	1.00 10^{-9}	1.00 10^{-9}	1.00 10^{-9}	1.00 10^{-9}	1.00 10^{-9}	1.00 10^{-9}	1.00 10^{-9}	1.00 10^{-9}
NE0808C	15	2.49 10^{-9}	1.00 10^{-9}	1.00 10^{-9}	1.00 10^{-9}	1.00 10^{-9}	1.00 10^{-9}	1.00 10^{-9}	1.00 10^{-9}	1.00 10^{-9}	1.00 10^{-9}
NE0811	10	3.74 10^{-9}	1.39 10^{-9}	5.16 10^{-10}	1.92 10^{-10}	7.12 10^{-11}	2.64 10^{-11}	1.00 10^{-11}	1.00 10^{-11}	1.00 10^{-11}	1.00 10^{-11}
NE0870	2	1.87 10^{-8}	6.95 10^{-9}	2.58 10^{-9}	9.58 10^{-10}	3.56 10^{-10}	1.32 10^{-10}	5.00 10^{-11}	5.00 10^{-11}	5.00 10^{-11}	5.00 10^{-11}
NE1188	3	7.12 10^{-7}	2.64 10^{-7}	1.96 10^{-8}	7.30 10^{-10}	1.36 10^{-8}	5.03 10^{-9}	1.87 10^{-9}	6.94 10^{-10}	2.58 10^{-10}	9.58 10^{-11}
NE2282	11	1.77 10^{-10}	6.56 10^{-11}	2.44 10^{-11}	9.09 10^{-12}	9.09 10^{-12}	9.09 10^{-12}	9.09 10^{-12}	9.09 10^{-12}	9.09 10^{-12}	9.09 10^{-12}
NE2374	10	3.74 10^{-9}	1.39 10^{-9}	5.16 10^{-10}	1.92 10^{-10}	7.12 10^{-11}	2.64 10^{-11}	1.00 10^{-11}	1.00 10^{-11}	1.00 10^{-11}	1.00 10^{-11}
NE2384	10	3.74 10^{-9}	1.39 10^{-9}	5.16 10^{-10}	1.92 10^{-10}	7.12 10^{-11}	2.64 10^{-11}	1.00 10^{-11}	1.00 10^{-11}	1.00 10^{-11}	1.00 10^{-11}

Deformation zone (ZFM)	b_h (m)	Hydraulic conductivity K (m/s) for depth interval (m RHB 70)									
		0 to –100	–100 to –200	–200 to –300	–300 to –400	–400 to –500	–500 to –600	–600 to –700	–700 to –800	–800 to –900	–900 to –1,000
NNE0130	10	8.27 10^{-8}	3.07 10^{-8}	1.14 10^{-8}	4.24 10^{-9}	1.57 10^{-9}	5.85 10^{-10}	2.17 10^{-10}	8.07 10^{-11}	3.00 10^{-11}	1.11 10^{-11}
NNE0725	6	1.84 10^{-5}	6.84 10^{-6}	2.54 10^{-6}	9.44 10^{-7}	3.51 10^{-7}	1.30 10^{-7}	2.42 10^{-7}	1.80 10^{-8}	6.67 10^{-9}	2.48 10^{-9}
NNE0828	35	2.36 10^{-8}	8.78 10^{-9}	3.26 10^{-9}	1.21 10^{-9}	1.00 10^{-9}	1.00 10^{-9}	1.00 10^{-9}	1.00 10^{-9}	1.00 10^{-9}	1.00 10^{-9}
NNE0842	25	3.31 10^{-8}	1.23 10^{-8}	4.56 10^{-9}	1.70 10^{-9}	1.00 10^{-9}	1.00 10^{-9}	1.00 10^{-9}	1.00 10^{-9}	1.00 10^{-9}	1.00 10^{-9}
NNE0860	35	2.36 10^{-8}	8.78 10^{-9}	3.26 10^{-9}	1.21 10^{-9}	1.00 10^{-9}	1.00 10^{-9}	1.00 10^{-9}	1.00 10^{-9}	1.00 10^{-9}	1.00 10^{-9}
NNE0869	10	8.27 10^{-8}	3.07 10^{-8}	1.14 10^{-8}	4.24 10^{-9}	1.57 10^{-9}	5.85 10^{-10}	2.17 10^{-10}	8.07 10^{-11}	3.00 10^{-11}	1.11 10^{-11}
NNE0929	35	2.36 10^{-8}	8.78 10^{-9}	3.26 10^{-9}	1.21 10^{-9}	1.00 10^{-9}	1.00 10^{-9}	1.00 10^{-9}	1.00 10^{-9}	1.00 10^{-9}	1.00 10^{-9}
NNE1132	35	2.36 10^{-8}	8.78 10^{-9}	3.26 10^{-9}	1.21 10^{-9}	1.00 10^{-9}	1.00 10^{-9}	1.00 10^{-9}	1.00 10^{-9}	1.00 10^{-9}	1.00 10^{-9}
NNE1133	40	2.07 10^{-8}	7.68 10^{-9}	2.85 10^{-9}	1.06 10^{-9}	1.00 10^{-9}	1.00 10^{-9}	1.00 10^{-9}	1.00 10^{-9}	1.00 10^{-9}	1.00 10^{-9}
NNE1134	40	2.07 10^{-8}	7.68 10^{-9}	2.85 10^{-9}	1.06 10^{-9}	1.00 10^{-9}	1.00 10^{-9}	1.00 10^{-9}	1.00 10^{-9}	1.00 10^{-9}	1.00 10^{-9}
NNE1135	30	2.76 10^{-8}	1.02 10^{-8}	3.80 10^{-9}	1.41 10^{-9}	1.00 10^{-9}	1.00 10^{-9}	1.00 10^{-9}	1.00 10^{-9}	1.00 10^{-9}	1.00 10^{-9}
NNE2008	6	3.85 10^{-7}	1.43 10^{-7}	5.31 10^{-7}	1.97 10^{-8}	7.33 10^{-9}	2.72 10^{-9}	1.01 10^{-9}	3.76 10^{-10}	1.40 10^{-10}	5.18 10^{-11}
NNE2255	2	2.28 10^{-8}	8.48 10^{-9}	3.15 10^{-9}	1.17 10^{-9}	4.35 10^{-10}	1.61 10^{-10}	6.00 10^{-11}	5.00 10^{-11}	5.00 10^{-11}	5.00 10^{-11}
NNE2263	30	1.44 10^{-7}	5.34 10^{-8}	1.98 10^{-8}	3.33 10^{-12}	2.74 10^{-9}	1.02 10^{-9}	3.78 10^{-10}	1.40 10^{-10}	5.21 10^{-11}	1.93 10^{-11}
NNE2273	9	5.69 10^{-10}	2.12 10^{-10}	7.86 10^{-11}	2.92 10^{-11}	1.11 10^{-11}	1.11 10^{-11}	1.11 10^{-11}	1.11 10^{-11}	1.11 10^{-11}	1.11 10^{-11}
NNE2280	14	1.26 10^{-8}	4.67 10^{-9}	1.73 10^{-9}	6.44 10^{-10}	2.39 10^{-10}	8.88 10^{-11}	3.30 10^{-11}	1.23 10^{-11}	7.14 10^{-12}	7.14 10^{-12}
NNE2293	15	5.51 10^{-8}	2.05 10^{-8}	7.61 10^{-9}	2.83 10^{-9}	1.05 10^{-9}	3.90 10^{-10}	1.45 10^{-10}	5.38 10^{-11}	2.00 10^{-11}	7.42 10^{-12}
NNE2298	10	8.27 10^{-8}	3.07 10^{-8}	1.14 10^{-8}	4.24 10^{-9}	1.57 10^{-9}	5.85 10^{-10}	2.17 10^{-10}	8.07 10^{-11}	3.00 10^{-11}	1.11 10^{-11}
NNE2299	10	8.27 10^{-8}	3.07 10^{-8}	1.14 10^{-8}	4.24 10^{-9}	1.57 10^{-9}	5.85 10^{-10}	2.17 10^{-10}	8.07 10^{-11}	3.00 10^{-11}	1.11 10^{-11}
NNE2300	10	8.27 10^{-8}	3.07 10^{-8}	1.14 10^{-8}	4.24 10^{-9}	1.57 10^{-9}	5.85 10^{-10}	2.17 10^{-10}	8.07 10^{-11}	3.00 10^{-11}	1.11 10^{-11}
NNE2308	15	5.51 10^{-8}	2.05 10^{-8}	7.61 10^{-9}	2.83 10^{-9}	1.05 10^{-9}	3.90 10^{-10}	1.45 10^{-10}	5.38 10^{-11}	2.00 10^{-11}	7.42 10^{-12}
NNE2309	10	8.27 10^{-8}	3.07 10^{-8}	1.14 10^{-8}	4.24 10^{-9}	1.57 10^{-9}	5.85 10^{-10}	2.17 10^{-10}	8.07 10^{-11}	3.00 10^{-11}	1.11 10^{-11}
NNE2312	43	1.36 10^{-7}	5.04 10^{-8}	1.87 10^{-8}	6.95 10^{-9}	2.58 10^{-9}	9.59 10^{-10}	3.56 10^{-10}	1.32 10^{-10}	4.92 10^{-11}	1.83 10^{-11}

Deformation zone (ZFM)	**b_h (m)**	**Hydraulic conductivity K (m/s) for depth interval (m RHB 70)**									
		0 to –100	**–100 to –200**	**–200 to –300**	**–300 to –400**	**–400 to –500**	**–500 to –600**	**–600 to –700**	**–700 to –800**	**–800 to –900**	**–900 to –1,000**
NNW0100	41	$2.66\ 10^{-12}$	$2.44\ 10^{-12}$	$2.44\ 10^{-12}$	$2.44\ 10^{-12}$	$2.44\ 10^{-12}$	$2.44\ 10^{-12}$	$2.44\ 10^{-12}$	$2.44\ 10^{-12}$	$2.44\ 10^{-12}$	$2.44\ 10^{-12}$
NNW0101	20	$8.40\ 10^{-10}$	$3.12\ 10^{-10}$	$1.16\ 10^{-10}$	$4.31\ 10^{-11}$	$1.60\ 10^{-11}$	$5.94\ 10^{-12}$	$5.00\ 10^{-12}$	$5.00\ 10^{-12}$	$5.00\ 10^{-12}$	$5.00\ 10^{-12}$
NNW0404	10	$1.68\ 10^{-9}$	$6.24\ 10^{-10}$	$2.32\ 10^{-10}$	$8.61\ 10^{-11}$	$3.20\ 10^{-11}$	$1.19\ 10^{-11}$	$1.00\ 10^{-11}$	$1.00\ 10^{-11}$	$1.00\ 10^{-11}$	$1.00\ 10^{-11}$
NNW0823	25	$1.00\ 10^{-9}$	$1.00\ 10^{-9}$	$1.00\ 10^{-9}$	$1.00\ 10^{-9}$	$1.00\ 10^{-9}$	$1.00\ 10^{-9}$	$1.00\ 10^{-9}$	$1.00\ 10^{-9}$	$1.00\ 10^{-9}$	$1.00\ 10^{-9}$
NNW1204	4	$5.47\ 10^{-7}$	$2.03\ 10^{-7}$	$7.54\ 10^{-8}$	$2.80\ 10^{-7}$	$1.04\ 10^{-8}$	$3.86\ 10^{-9}$	$1.44\ 10^{-9}$	$5.33\ 10^{-10}$	$1.98\ 10^{-10}$	$7.36\ 10^{-11}$
NNW1205	15	$1.22\ 10^{-9}$	$6.67\ 10^{-12}$	$1.68\ 10^{-10}$	$6.25\ 10^{-11}$	$2.32\ 10^{-11}$	$8.63\ 10^{-12}$	$6.67\ 10^{-12}$	$6.67\ 10^{-12}$	$6.67\ 10^{-12}$	$6.67\ 10^{-12}$
NNW1209	2	$8.40\ 10^{-9}$	$3.12\ 10^{-9}$	$1.16\ 10^{-9}$	$4.31\ 10^{-10}$	$1.60\ 10^{-10}$	$5.94\ 10^{-11}$	$5.00\ 10^{-11}$	$5.00\ 10^{-11}$	$5.00\ 10^{-11}$	$5.00\ 10^{-11}$
NW0002	75	$3.27\ 10^{-7}$	$1.22\ 10^{-7}$	$4.52\ 10^{-8}$	$1.68\ 10^{-8}$	$6.23\ 10^{-9}$	$2.31\ 10^{-9}$	$1.00\ 10^{-9}$	$1.00\ 10^{-9}$	$1.00\ 10^{-9}$	$1.00\ 10^{-9}$
NW0003	53	$3.92\ 10^{-7}$	$1.46\ 10^{-7}$	$5.40\ 10^{-8}$	$2.01\ 10^{-8}$	$7.46\ 10^{-9}$	$2.77\ 10^{-9}$	$1.03\ 10^{-9}$	$1.00\ 10^{-9}$	$1.00\ 10^{-9}$	$1.00\ 10^{-9}$
NW0017	64	$3.86\ 10^{-6}$	$1.44\ 10^{-6}$	$5.33\ 10^{-7}$	$1.98\ 10^{-7}$	$7.36\ 10^{-8}$	$2.73\ 10^{-8}$	$1.02\ 10^{-8}$	$3.77\ 10^{-9}$	$1.40\ 10^{-9}$	$1.00\ 10^{-9}$
NW0805	10	$2.46\ 10^{-6}$	$9.12\ 10^{-7}$	$3.39\ 10^{-7}$	$1.26\ 10^{-7}$	$4.67\ 10^{-8}$	$1.74\ 10^{-8}$	$6.45\ 10^{-9}$	$2.40\ 10^{-9}$	$1.00\ 10^{-9}$	$1.00\ 10^{-9}$
NW0806	80	$3.07\ 10^{-7}$	$1.14\ 10^{-7}$	$4.23\ 10^{-8}$	$1.57\ 10^{-8}$	$5.84\ 10^{-9}$	$2.17\ 10^{-9}$	$1.00\ 10^{-9}$	$1.00\ 10^{-9}$	$1.00\ 10^{-9}$	$1.00\ 10^{-9}$
NW0854	95	$2.58\ 10^{-7}$	$9.60\ 10^{-8}$	$3.57\ 10^{-8}$	$1.32\ 10^{-8}$	$4.92\ 10^{-9}$	$1.83\ 10^{-9}$	$1.00\ 10^{-9}$	$1.00\ 10^{-9}$	$1.00\ 10^{-9}$	$1.00\ 10^{-9}$
NW1173	60	$4.09\ 10^{-7}$	$1.52\ 10^{-7}$	$5.65\ 10^{-8}$	$2.10\ 10^{-8}$	$7.79\ 10^{-9}$	$2.89\ 10^{-9}$	$1.07\ 10^{-9}$	$1.00\ 10^{-9}$	$1.00\ 10^{-9}$	$1.00\ 10^{-9}$
NW1200	47	$2.71\ 10^{-7}$	$1.00\ 10^{-7}$	$3.73\ 10^{-8}$	$1.39\ 10^{-8}$	$5.15\ 10^{-9}$	$6.00\ 10^{-11}$	$1.00\ 10^{-9}$	$1.00\ 10^{-9}$	$1.00\ 10^{-9}$	$1.00\ 10^{-9}$

Deformation zone (ZFM)	**b_h (m)**	**Hydraulic conductivity K (m/s) for depth interval (m RHB 70)**									
		0 to –100	**–100 to –200**	**–200 to –300**	**–300 to –400**	**–400 to –500**	**–500 to –600**	**–600 to –700**	**–700 to –800**	**–800 to –900**	**–900 to –1,000**
WNW0001	165	$1.49\ 10^{-7}$	$5.53\ 10^{-9}$	$1.03\ 10^{-7}$	$7.63\ 10^{-9}$	$2.83\ 10^{-9}$	$1.05\ 10^{-9}$	$1.00\ 10^{-9}$	$1.00\ 10^{-9}$	$1.00\ 10^{-9}$	$1.00\ 10^{-9}$
WNW0004	160	$1.53\ 10^{-7}$	$5.70\ 10^{-8}$	$2.12\ 10^{-8}$	$7.86\ 10^{-9}$	$2.92\ 10^{-9}$	$1.09\ 10^{-9}$	$1.00\ 10^{-9}$	$1.00\ 10^{-9}$	$1.00\ 10^{-9}$	$1.00\ 10^{-9}$
WNW0016	45	$1.76\ 10^{-9}$	$1.00\ 10^{-9}$	$1.00\ 10^{-9}$	$1.00\ 10^{-9}$	$1.00\ 10^{-9}$	$1.00\ 10^{-9}$	$1.00\ 10^{-9}$	$1.00\ 10^{-9}$	$1.00\ 10^{-9}$	$1.00\ 10^{-9}$
WNW0019	45	$1.76\ 10^{-9}$	$1.00\ 10^{-9}$	$1.00\ 10^{-9}$	$1.00\ 10^{-9}$	$1.00\ 10^{-9}$	$1.00\ 10^{-9}$	$1.00\ 10^{-9}$	$1.00\ 10^{-9}$	$1.00\ 10^{-9}$	$1.00\ 10^{-9}$
WNW0023	45	$1.76\ 10^{-9}$	$1.00\ 10^{-9}$	$1.00\ 10^{-9}$	$1.00\ 10^{-9}$	$1.00\ 10^{-9}$	$1.00\ 10^{-9}$	$1.00\ 10^{-9}$	$1.00\ 10^{-9}$	$1.00\ 10^{-9}$	$1.00\ 10^{-9}$
WNW0024	45	$1.76\ 10^{-9}$	$1.00\ 10^{-9}$	$1.00\ 10^{-9}$	$1.00\ 10^{-9}$	$1.00\ 10^{-9}$	$1.00\ 10^{-9}$	$1.00\ 10^{-9}$	$1.00\ 10^{-9}$	$1.00\ 10^{-9}$	$1.00\ 10^{-9}$
NW0029	30	$2.64\ 10^{-9}$	$1.00\ 10^{-9}$	$1.00\ 10^{-9}$	$1.00\ 10^{-9}$	$1.00\ 10^{-9}$	$1.00\ 10^{-9}$	$1.00\ 10^{-9}$	$1.00\ 10^{-9}$	$1.00\ 10^{-9}$	$1.00\ 10^{-9}$
WNW0035	35	$2.26\ 10^{-9}$	$1.00\ 10^{-9}$	$1.00\ 10^{-9}$	$1.00\ 10^{-9}$	$1.00\ 10^{-9}$	$1.00\ 10^{-9}$	$1.00\ 10^{-9}$	$1.00\ 10^{-9}$	$1.00\ 10^{-9}$	$1.00\ 10^{-9}$
WNW0036	55	$1.44\ 10^{-9}$	$1.00\ 10^{-9}$	$1.00\ 10^{-9}$	$1.00\ 10^{-9}$	$1.00\ 10^{-9}$	$1.00\ 10^{-9}$	$1.00\ 10^{-9}$	$1.00\ 10^{-9}$	$1.00\ 10^{-9}$	$1.00\ 10^{-9}$
WNW0044	39	$1.32\ 10^{-6}$	$4.88\ 10^{-7}$	$1.81\ 10^{-7}$	$6.74\ 10^{-8}$	$1.25\ 10^{-7}$	$9.30\ 10^{-9}$	$3.45\ 10^{-9}$	$1.28\ 10^{-9}$	$4.77\ 10^{-10}$	$1.77\ 10^{-10}$
WNW0123	52	$1.00\ 10^{-9}$	$1.00\ 10^{-9}$	$1.00\ 10^{-9}$	$1.00\ 10^{-9}$	$1.00\ 10^{-9}$	$3.84\ 10^{-11}$	$1.00\ 10^{-9}$	$1.00\ 10^{-9}$	$1.00\ 10^{-9}$	$1.00\ 10^{-9}$
WNW0809A	25	$3.17\ 10^{-9}$	$1.18\ 10^{-9}$	$1.00\ 10^{-9}$	$1.00\ 10^{-9}$	$1.00\ 10^{-9}$	$1.00\ 10^{-9}$	$1.00\ 10^{-9}$	$1.00\ 10^{-9}$	$1.00\ 10^{-9}$	$1.00\ 10^{-9}$
WNW0809B	15	$5.28\ 10^{-9}$	$1.96\ 10^{-9}$	$1.00\ 10^{-9}$	$1.00\ 10^{-9}$	$1.00\ 10^{-9}$	$1.00\ 10^{-9}$	$1.00\ 10^{-9}$	$1.00\ 10^{-9}$	$1.00\ 10^{-9}$	$1.00\ 10^{-9}$
WNW0813	15	$5.28\ 10^{-9}$	$1.96\ 10^{-9}$	$7.29\ 10^{-10}$	$2.71\ 10^{-10}$	$1.01\ 10^{-10}$	$3.73\ 10^{-11}$	$1.39\ 10^{-11}$	$6.67\ 10^{-12}$	$6.67\ 10^{-12}$	$6.67\ 10^{-12}$
WNW0835A	25	$3.17\ 10^{-9}$	$1.18\ 10^{-9}$	$1.00\ 10^{-9}$	$1.00\ 10^{-9}$	$1.00\ 10^{-9}$	$1.00\ 10^{-9}$	$1.00\ 10^{-9}$	$1.00\ 10^{-9}$	$1.00\ 10^{-9}$	$1.00\ 10^{-9}$
WNW0835B	15	$5.28\ 10^{-9}$	$1.96\ 10^{-9}$	$1.00\ 10^{-9}$	$1.00\ 10^{-9}$	$1.00\ 10^{-9}$	$1.00\ 10^{-9}$	$1.00\ 10^{-9}$	$1.00\ 10^{-9}$	$1.00\ 10^{-9}$	$1.00\ 10^{-9}$
WNW0836	30	$2.64\ 10^{-9}$	$1.00\ 10^{-9}$	$1.00\ 10^{-9}$	$1.00\ 10^{-9}$	$1.00\ 10^{-9}$	$1.00\ 10^{-9}$	$1.00\ 10^{-9}$	$1.00\ 10^{-9}$	$1.00\ 10^{-9}$	$1.00\ 10^{-9}$
WNW0851	25	$3.17\ 10^{-9}$	$1.18\ 10^{-9}$	$1.00\ 10^{-9}$	$1.00\ 10^{-9}$	$1.00\ 10^{-9}$	$1.00\ 10^{-9}$	$1.00\ 10^{-9}$	$1.00\ 10^{-9}$	$1.00\ 10^{-9}$	$1.00\ 10^{-9}$
WNW0853	60	$1.32\ 10^{-9}$	$1.00\ 10^{-9}$	$1.00\ 10^{-9}$	$1.00\ 10^{-9}$	$1.00\ 10^{-9}$	$1.00\ 10^{-9}$	$1.00\ 10^{-9}$	$1.00\ 10^{-9}$	$1.00\ 10^{-9}$	$1.00\ 10^{-9}$
WNW0974	30	$2.64\ 10^{-9}$	$1.00\ 10^{-9}$	$1.00\ 10^{-9}$	$1.00\ 10^{-9}$	$1.00\ 10^{-9}$	$1.00\ 10^{-9}$	$1.00\ 10^{-9}$	$1.00\ 10^{-9}$	$1.00\ 10^{-9}$	$1.00\ 10^{-9}$
WNW1053	25	$3.17\ 10^{-9}$	$1.18\ 10^{-9}$	$4.37\ 10^{-10}$	$1.62\ 10^{-10}$	$6.03\ 10^{-11}$	$2.24\ 10^{-11}$	$8.32\ 10^{-12}$	$4.00\ 10^{-12}$	$4.00\ 10^{-12}$	$4.00\ 10^{-12}$
WNW1056	15	$5.28\ 10^{-9}$	$1.96\ 10^{-9}$	$7.29\ 10^{-10}$	$2.71\ 10^{-10}$	$1.01\ 10^{-10}$	$3.73\ 10^{-11}$	$1.39\ 10^{-11}$	$6.67\ 10^{-12}$	$6.67\ 10^{-12}$	$6.67\ 10^{-12}$
WNW1068	15	$5.28\ 10^{-9}$	$1.96\ 10^{-9}$	$7.29\ 10^{-10}$	$2.71\ 10^{-10}$	$1.01\ 10^{-10}$	$3.73\ 10^{-11}$	$1.39\ 10^{-11}$	$6.67\ 10^{-12}$	$6.67\ 10^{-12}$	$6.67\ 10^{-12}$
WNW1127	35	$2.26\ 10^{-9}$	$1.00\ 10^{-9}$	$1.00\ 10^{-9}$	$1.00\ 10^{-9}$	$1.00\ 10^{-9}$	$1.00\ 10^{-9}$	$1.00\ 10^{-9}$	$1.00\ 10^{-9}$	$1.00\ 10^{-9}$	$1.00\ 10^{-9}$
WNW2225	25	$1.86\ 10^{-8}$	$6.92\ 10^{-9}$	$2.57\ 10^{-9}$	$9.55\ 10^{-10}$	$3.55\ 10^{-10}$	$1.32\ 10^{-10}$	$4.89\ 10^{-11}$	$1.82\ 10^{-11}$	$6.75\ 10^{-12}$	$4.00\ 10^{-12}$

CM Gruppen AB, Bromma, 2008